Raman Spectroscopy for Chemical Analysis

CHEMICAL ANALYSIS

A SERIES OF MONOGRAPHS OF ANALYTICAL CHEMISTRY AND ITS APPLICATIONS

Editor
J. D. WINEFORDNER

VOLUME 157

A JOHN WILEY & SONS, INC., PUBLICATION

New York / Chichester / Weinheim / Brisbane / Singapore / Toronto

Raman Spectroscopy for Chemical Analysis

RICHARD L. McCREERY

The Ohio State University
Columbus, Ohio

A JOHN WILEY & SONS, INC., PUBLICATION

New York / Chichester / Weinheim / Brisbane / Singapore / Toronto

This book is printed on acid-free paper. ♾

Published simultaneously in Canada.

For ordering and customer service, call 1-800-CALL-WILEY.

Library of Congress Cataloging-in-Publication Data:

McCreery, Richard L.
Raman spectroscopy for chemical analysis / by Richard L. McCreery.
p. cm. — (Chemical analysis ; v. 157)
"A Wiley-interscience publication
Includes index
ISBN 0-471-25287-5 (alk. paper)
1. Raman spectroscopy. 2. Chemistry, Analytic. I. Title. II. Series.
QC454.R36.M33 2000
543'.08584 — dc21 99-086491

Printed in the United States of America.

10 9 8 7 6 5 4 3 2

CONTENTS

PREFACE

This book was inspired by the transition of Raman spectroscopy from a technically demanding research technique to a useful and practical method of chemical analysis. There are many fine texts and thousands of scientific articles on research in Raman spectroscopy, primarily oriented toward understanding the Raman effect itself and using Raman scattering to probe molecular structure and dynamics. These research efforts have reached a high level of sophistication and have yielded valuable chemical and physical insights, but they rarely resulted in practical techniques for chemical analysis until approximately 1986. The impediments to broad applications of Raman spectroscopy to chemical analysis were mainly technological rather than fundamental. The instrumentation required to observe the weak Raman effect was too cumbersome and expensive for routine analysis, and interference from fluorescence precluded application to a broad range of industrial samples. As a result, the advantages of Raman spectroscopy over more common infrared absorption techniques were not exploited in analytical problems.

Major technological and scientific innovation in the past 10 to 15 years has significantly broadened the applicability of Raman spectroscopy, particularly in chemical analysis. Fourier transform (FT)–Raman, charge-coupled device (CCD) detectors, compact spectrographs, effective laser rejection filters, near-infrared lasers, and small computers have contributed to a revolution in Raman instrumentation and made routine analytical applications possible. An increase in instrumental sensitivity by factors as large as 10^5, plus decreases in both interferences and noise resulted from this "revolution." The number of vendors of Raman spectrometers increased from 3 to 12 over a 10-year period, and integrated commercial spectrometers led to turnkey operation and robust reliability.

This book is intended to introduce a student or practitioner of analytical chemistry to the technical elements and practical benefits of the "Raman revolution." It is *not* intended to describe "high-end" Raman techniques such as nonlinear or time-resolved Raman spectroscopy, nor does it attempt to describe the many theoretical treatments of Raman scattering. The book emphasizes the concepts and technology important to applications of Raman spectroscopy in chemical analysis, with attention to calibration, performance, and sampling modes. While many recent innovations in analytical Raman spectroscopy are

technically sophisticated, their objectives are reliability, accuracy, reduction of interferences, and ease of operation rather than ultimate spectral resolution or sensitivity. The emphasis of both the theory and instrumentation discussions in this book is the practical analysis that has resulted from recent technological developments. Techniques such as nonlinear Raman (CARS, hyperRaman, stimulated Raman, etc.), picosecond transient Raman, single-crystal Raman, gas-phase Raman,and so forth are excluded not because they are unimportant, but because they currently have limited use in routine chemical analysis.

The audience for this book should include graduate students, practicing chemists, and Raman spectroscopists who seek information on recent instrumentation developments. It is not a comprehensive review but more of a textbook intended as an introduction to modern Raman spectroscopy. In most cases, the techniques discussed are available in commercially available spectrometers, and the book should be useful to chemists who are implementing Raman spectroscopy in industrial or academic laboratories. Although a large number of useful Raman applications involve custom-built instrumentation, the book emphasizes configurations and components used by current vendors of integrated Raman spectrometers.

Since commercial spectrometers can be constructed in a variety of configurations, instruments from different manufacturers often differ significantly in applicability and performance. Specific manufacturers are mentioned in the text to identify a particular approach or optical configuration. Available commercial units differ widely in performance and are often optimized for particular sample types. Mention of a manufacturer in the text does not imply an endorsement but may be useful to the reader in order to appreciate differences in design objectives. There is no "best" manufacturer or configuration, but certain designs are more applicable to certain situations, depending on the sample and analytical objective. It will become obvious that the sample dictates the choice of spectrometer type, and no single Raman system covers all possible applications.

The book is divided into roughly three general areas on theory and instrumentation. Chapters 1 to 4 cover the origin and magnitude of Raman scattering and the major factors determining the signal/noise ratio. Chapters 5 to 10 discuss instrumental components and configurations and methods of calibration. Chapters 11 to 13 address the widely studied specialty areas of Raman microscopy, fiber-optic sampling, and Raman spectroscopy of surfaces. In most chapters , many examples of applications to Raman spectroscopy to analytical problems are provided.

Notes on Conventions

The definitions of several symbols and certain conventions are not used uniformly in the Raman spectroscopy literature, and some choices were

required to retain internal consistency in this book. Raman shifts are plotted from left (low shift) to right (high shift), in opposition to the usual practice for Fourier transform infrared (FTIR) frequencies. Furthermore, the Raman shift axis shows only Stokes-shifted bands unless noted otherwise. The differential Raman cross section is assigned the symbol β instead of $d\sigma/d\Omega$ often used in the literature. As explained in Chapter 2, β has specific significance and is a more convenient symbol for equations. Modern CCD Raman spectrometers count photons rather than measure power, and it is more convenient to define power and intensity as photons per second and power density as photons per square centimeter per second (Chapter 2). The sampled volume discussed in several texts is explicitly defined herein as the detected area, A_D, times the sampling depth, dz. There are several additional and more minor differences in definitions between this book and certain treatments from the literature, and a complete list of symbols is provided to reduce possible confusion.

ACKNOWLEDGMENTS

First and foremost, I thank my wife and children for their support and understanding during the long process of writing this book. Much of the technical information was provided by graduate students in my research group, both past and present. I appreciate their willingness to acquire data not directly related to their research projects. Many technical discussions with practicing spectroscopists were very valuable to the effort, particularly those with Bruce Chase, Chris Frank, Rick Van Duyne, Jack Spencer, Fritz Allen and Jun Zhao. Valuable collaborations with the technical staff at Chromex provided many of the illustrative examples in the book, as well as some innovations in instrument design. Finally, I appreciate the efforts of Margaret Dodd and Anna McCreery with preparation of the manuscript and figures.

LIST OF SYMBOLS

α	polarizability
A_D	sample area monitored by spectrometer, cm^2
α_F	scattering coefficient of fibers, dB/m
α_L	scattering and absorption coefficient at laser wavelength, cm^{-1}
α_R	scattering and absorption coefficient at laser wavelength, cm^{-1}
α_o	polarizability in the absence of vibrations
β	differential Raman cross section ($d\sigma/d\Omega$), cm^2 molecule^{-1} sr^{-1}
B	observed intensity due to background, e^-
$\dot{B}$	rate of background accumulation, e^- sec^{-1}
β°	frequency independent differential Raman cross section, cm^6 sr^{-1} molecule^{-1}
b	sample thickness, cm
β_S	differential Raman cross section for a surface species, cm^2 molecule^{-1} sr^{-1}
c	speed of light, cm sec^{-1}
C	collection function for Raman spectrometer, usually cm^2 sr e^- photon^{-1} cm^{-1}
D	number density, molecules cm^{-3}
d	distance between mirrors, cm
D_S	surface number density, molecule cm^{-2}
$d\Omega$	increment of observation angle
dz	path length increment, cm
δ	CCD gain, e^-/ADU (analog-to-digital converter unit)
δa	spectrometer depth of field, cm
$\delta\bar{\nu}$	spectral resolution, cm^{-1}
ϵ	molar absorptivity, M^{-1}, cm^{-1}
ϵ	blur diameter, cm
E	electric field, V cm^{-1}
E_G	grating efficiency into first order
$f/\#$	aperture ratio (f number)
f_1	focal length

F_S	figure of merit for Raman signal
F_{SNR}	figure of merit based on signal-to-noise ratio, using power density, cm^3 sr e^- $(\text{photon})^{-1}$
F'_{SNR}	cm^3 sr e^- $(\text{photon})^{-1}$
γ	CCD gain, e^-/ADU (analog-to-digital converter unit)
Γ	mirror velocity in an interferometer, cm sec^{-1}
h	Planck's constant
I_0	incident laser intensity, W
I_R	Raman intensity, W
k	Boltzman constant
K	geometric factor depending on observation geometry, units vary with the situation
λ	wavelength, cm
L	specific intensity, photons sec^{-1} cm^{-2} sr^{-1}
L_a	specific intensity of analyte, photons sec^{-1} cm^{-2} sr^{-1}
λ_0	laser wavelength, nm or cm
M	molar concentration, mol/liter
m	diffraction order
ν	frequency of light, Hz
N_C	number of channels along spectral axis of a multichannel detector
n	refractive index
ν_0	laser frequency
N_R	number of resolution elements in a given spectrum
$\overline{\nu}$	frequency expressed in wavenumbers
$\overline{\nu}_j$	vibrational frequency of mode j, expressed in wavenumbers; also Raman shift, in cm^{-1}
ν_p	frequency of an electronic transition, cm^{-1}
P	polarization, V cm^{-1}
P_D	incident laser power density, photons sec^{-1} cm^{-2}
P_0	incident laser intensity, in photons sec^{-1}
P_R	scattered Raman intensity, photons sec^{-1}
Φ_d	rate of dark signal accumulation, e^- sec^{-1}
Φ_S	average flux of e^- generated by photons reaching the detector, photons sec^{-1}
Q	quantum efficiency of detector, e^- photon^{-1}
Q_j	jth normal vibrational mode
Q_j°	amplitude of Q_j
R_F	reflectivity of focusing mirror

σ_j	integrated Raman cross section, cm^2 $molecule^{-1}$
S	Raman signal, in electrons, e^-
σ'_j	integrated Raman cross section, with intensity stated as photons sec^{-1}
S_a	Raman signal, due to analyte band of interest, e^-
$\bar{S}$	mean value of Raman signal, e^-
$\dot{S}$	signal rate, dS/dt, e^- sec^{-1}
$\dot{S}_a$	rate of analyte signal accumulation, e^- sec^{-1}
$S(i)$	signal in ith channel (e^-)
$S'(i)$	signal in ith channel, in analog-to-digital units (or counts)
$S_{\text{bias}}(i)$	bias electrons in ith channel
$S_{\text{dark}}(i)$	dark electrons in ith channel
σ_B	standard deviation of the background (or blank)
σ_{bk}	standard deviation of a blank "sample"
σ_d	standard deviation of dark signal, sometimes called *dark noise*
σ_F	flicker noise
σ_r	readout noise
σ_S	standard deviation of analyte Raman signal
σ_y	standard deviation of peak height
σ_j°	frequency-independent cross section of mode j, cm^6 $molecule^{-1}$
SNR	signal noise ratio
sr	steradian
R_C	reflectivity of collimating mirror
T	transmission of optics or spectrograph, unitless
T	absolute temperature, K
t_g	global image acquisition time
t_M	total spectrum acquisition time, sec.
T_S	spectrometer transmission
t_s	single-channel measurement time, or time of observation for a single Raman shift
T_l	line focus image acquisition time
T_P	transmission of polarization scrambler
T_p	point-to-point image acquisition time
v	vibrational quantum number
W_D	total width of detector
w_0	radius of beam waist, cm
W_P	width of pixel or exit slit
z	depth into sample
Ω	solid angle of collection
Ω_D	solid angle observed by the spectrometer at the sample

CHEMICAL ANALYSIS

A SERIES OF MONOGRAPHS ON ANALYTICAL CHEMISTRY AND ITS APPLICATIONS

J. D. Winefordner, *Series Editor*

Vol. 1. **The Analytical Chemistry of Industrial Poisons, Hazards, and Solvents.** *Second Edition.* By the late Morris B. Jacobs

Vol. 2. **Chromatographic Adsorption Analysis.** By Harold H. Strain (*out of print*)

Vol. 3. **Photometric Determination of Traces of Metals.** *Fourth Edition*
Part I: General Aspects. By E. B. Sandell and Hiroshi Onishi
Part IIA: Individuals Metals, Aluminum to Lithum. By Hiroshi Onishi
Part IIB: Individuals Metals, Magnesium to Zirconium. By Hiroshi Onishi

Vol. 4. **Organic Reagents Used in Gravimetric and Volumetric Analysis.** By John F. Flagg (*out of print*)

Vol. 5. **Aquametry: A Treatise on Methods for the Determination of Water.** *Second Edition (in three parts).* By John Mitchell, Jr. and Donald Milton Smith

Vol. 6. **Analysis of Insectidies and Acaricides.** By Francis A. Gunther and Roger C. Blinn (*out of print*)

Vol. 7. **Chemical Analysis of Industrial Solvents.** By the late Morris B. Jacobs and Leopard Scheltan

Vol. 8. **Colorimetric Determination of Nonmetals.** *Second Edition.* Edited by the late David F. Boltz and James A. Howell

Vol. 9. **Analytical Chemistry of Titanium Metals and Compounds.** By Maurice Codell

Vol. 10. **The Chemical Analysis of Air Pollutants.** By the late Morris B. Jacobs

Vol. 11. **X-Ray Spectrochemical Analysis.** *Second Edition.* By L. S. Birks

Vol. 12. **Systematic Analysis Surface-Active Agents.** *Second Edition.* By Milton J. Rosen and Henry A. Goldsmith

Vol. 13. **Alternating Current Polarography and Tensammetry.** By B. Breyer and H. H. Bauer

Vol. 14. **Flame Photometry.** By R. Hermann and J. Alkemade

Vol. 15. **The Titration of Organic Compounds** (*in two parts*). By M. R. F. Ashworth

Vol. 16. **Complexation in Analytical Chemistry: A guide for the Critical Selection of Analytical Methods Based on Complexation Reactions.** By the late Anders Ringbom

Vol. 17. **Electron Probe Microanalysis.** *Second Edition.* By L. S. Birks

Vol. 18. **Organic Complexing Reagents: Structure, Behaviour, and Application to Inorganic Analysis**. By D. D. Perrin

Vol. 19. **Thermal Analysis**. *Third Edition*. By Wesley Wm. Wendlandt

Vol. 20. **Amperometric Titrations**. By John T. Stock

Vol. 21. **Reflectance Spectroscopy**. By Wesley Wm. Wendlandt and Harry G. Hecht

Vol 22. **The Analytical Toxicology of Industrial Inorganic Poisons**. By the late Morris B. Jacobs

Vol. 23. **The Formation and Properties of Precipitates**. By Alan G. Walton

Vol. 24. **Kinetics in Analytical Chemistry**. By Harry B. Mark, Jr. And Garry A. Rechintz

Vol. 25. **Atomic Absorption Spectroscopy**. *Second Edition*. By Morris Slavin

Vol. 26. **Characterization of Organometallic Compounds** (*in two parts*). Edited by Minoru Tsutsui

Vol. 27. **Rock and Mineral Analysis**. *Second Edition*. By Wesely M. Johnson and John A. Maxwell

Vol. 28. **The Analytical Chemistry of Nitrogen and Its Compounds** (*in two parts*). Edited by C. A. Streuli and Philip R. Averell

Vol. 29. **The Analytical Chemistry of Sulphur and Its Compounds** (*in three parts*). By J. H. Karchmer

Vol. 30. **Ultramicro Elemental Analysis**. By Günther Tölg

Vol. 31. **Photometric Organic Analysis** (*in two parts*). By Eugene Sawicki

Vol. 32. **Determination of Organic Compounds: Methods and Procedures**. By Frederick T. Weiss

Vol. 33. **Masking and Demasking of Chemical Reactions**. By D. D. Perrin

Vol. 34. **Neutron Activation Analysis**. By D. De Soete, R. Gijbels, and J. Hoste

Vol. 35. **Laser Raman Spectroscopy**. By Marvin C. Tobin

Vol. 36. **Emission Spectrochemical Analysis**. By Morris Slavin

Vol. 37. **Analytical Chemistry of Phosphorous Compounds.** Edited by M. Halmann

Vol. 38. **Luminescence Spectromoetry in Analytical Chemistry**. By J. D. Winefordner, S. G. Schulman and T. C. O'Haver

Vol. 39. **Activation Analysis with Neutron Generators**. By Sam S. Nargolwalla and Edwin P. Przybylowicz

Vol. 40. **Determination of Gaseous Elements in Metals**. Edited by Lynn L. Lewis, Laben M. Melnick, and Ben D. Holt

Vol. 41. **Analysis of Silicones**. Edited by A. Lee Smith

Vol. 42. **Foundations of Ultracentrifugal Analysis**. By H. Fujita

Vol. 43. **Chemical Infrared Fourier Transform Spectroscopy**. By Peter R. Griffiths

Vol. 44. **Microscale Manipulations in Chemistry**. By T. S. Ma and V. Horak

Vol. 45. **Thermometric Titrations**. By J. Barthel

Vol. 46. **Trace Analysis: Spectroscopic Methods for Elements**. Edited by J. D. Winefordner

Vol. 47. **Contamination Control in Trace Element Analysis**. By Morris Zief and James W. Mitchell

Vol. 48. **Analytical Applications of NMR**. By D. E. Leyden and R. H. Cox

Vol. 49. **Measurement of Dissolved Oxygen**. By Michael L. Hitchman

Vol. 50. **Analytical Laser Spectroscopy**. Edited by Nicolo Omenetto

Vol. 51. **Trace Element Analysis of Geological Materials**. By Roger D. Reeves and Robert R. Brooks

Vol. 52. **Chemical Analysis by Microwave Rotational Spectroscopy**. By Ravi Varma and Lawrence W. Hrubesh

Vol. 53. **Information Theory As Applied to Chemical Analysis**. By Karl Eckschlager and Vladimir Stepanek

Vol. 54. **Applied Infrared Spectroscopy: Fundamentals, Techniques, and Analytical Problem-solving**. By A. Lee Smith

Vol. 55. **Archaeological Chemistry**. By Zvi Goffer

Vol. 56. **Immobilized Enzymes in Analytical and Clinical Chemistry**. By P. W. Carr and L. D. Bowers

Vol. 57. **Photoacoustics and Photoacoustic Spectroscopy**. By Allan Rosenewaig

Vol. 58. **Analysis of Pesticide Residues**. Edited by H. Anson Moye

Vol. 59. **Affinity Chromatography**. By William H. Scouten

Vol. 60. **Quality Control in Analytical Chemistry**. *Second Edition*. By G. Kateman and L. Buydens

Vol. 61. **Direct Characterization of Fineparticles**. By Brain H. Kaye

Vol. 62. **Flow Injection Analysis**. By J. Ruzicka and E. H. Hansen

Vol. 63. **Applied Electron Spectroscopy for Chemical Analysis**. Edited by Hassan Windawi and Floyd Ho

Vol. 64. **Analytical Aspects of Enviromental Chemistry**. Edited by David F. S. Natusch and Philip K. Hopke

Vol. 65. **The Interpretation of Analytical Chemical Data by the Use of Cluster Analysis**. By D. Luc Massart and Leonard Kaufman

Vol. 66. **Solid Phase Biochemistry: Analytical and Synthetic Aspects**. Edited by William H. Scouten

Vol. 67. **An Introduction to Photoelectron Spectroscopy**. By Pradip k. Ghosh

Vol. 68. **Room Temperature Phosphorimetry for Chemical Analysis**. By Tuan Vo-Dinh

Vol. 69. **Potentiometry and Potentiometric Titrations**. By E. P. Serjeant

Vol. 70. **Design and Application of Process Analyzer Systems**. By Paul E. Mix

Vol. 71. **Analysis of Organic and Biological Surfaces**. Edited by Patrick Echlin

Vol. 72. **Small Bore Liquid Chromatography Columns: Their Properties and Uses**. Edited by Raymond P. W. Scott

Vol. 73. **Modern Methods of Particle Size Analysis**. Edited by Howard G. Barth

Vol. 74. **Auger Electron Spectroscopy**. By Michael Thompson, M. D. Baker, Alec Christie, and J. F. Tyson

Vol. 75. **Spot Test Analysis: Clinical, Enviromental, Forensic and Geochemical Applications**. By Ervin Jungreis

Vol. 76. **Receptor Modeling in Enviromental Chemistry**. By Philip K. Hopke

Vol. 77. **Molecular Luminescence Spectroscopy: Methods and Applications** (*in three parts*). Edited by Stephen G. Schulman

Vol. 78. **Inorganic Chromatographic Analysis**. Edited by John C. MacDonald

Vol. 79. **Analytical Solution Calorimetry**. Edited by J. K. Grime

Vol. 80. **Selected Methods of Trace Metal Analysis: Biological and Enviromental Samples**. By Jon C. VanLoon

Vol. 81. **The Analysis of Extraterrestrial Materials**. BY Isidore Adler

Vol. 82. **Chemometrics**. By Muhammad A. Sharaf, Deborah L. Illman, and Bruce R. Kowalski

Vol. 83. **Fourier Transform Infrared Spectrometry**. By Peter R. Griffiths and James A. de Haseth

Vol. 84. **Trace Analysis: Spectroscopic Methods for Molecules**. Edited by Gary Christian and James B. Callis

Vol. 85. **Ultratrace Analysis of Pharmaceuticals and Other Compounds of Interest**. Edited by S. Ahuja

Vol. 86. **Secondary Ion Mass Spectrometry: Basic Concepts, Instrumental Aspects, Applications and Trends**. By A. Benninghoven, F. G. Rüdenauer, and H. W. Werner

Vol. 87. **Analytical applications of Lasers**. Edited by Edward H. Piepmeier

Vol. 88. **Applied Geochemical Analysis**. By C. O. Ingamells and F. F. Pitard

Vol. 89. **Detectors for Liquid Chromatography**. Edited by Edward S. Yeung

Vol. 90. **Inductively Coupled Plasma Emission Spectroscopy: Part 1: Methodology, Instrumentation, and Performance; Part II: Applications and Fundamentals**. Edited by J. M. Boumans

Vol. 91. **Applications of New Mass Spectrometry Techniques in Pesticide Chemistry**. Edited by Joseph Rosen

Vol. 92. **X-Ray Absorption: Principles, Applications, Techinques, of EXAFS, SEXAFS, and XANES**. Edited by D. C. Konnigsberger

Vol. 93. **Quantitative Structure-Chromatographic Retention Relationships**. By Roman Kaliszan

Vol. 94. **Laser Remote Chemical Analysis**. Edited by Raymond M. Measures

Vol. 95. **Inorganic Mass Spectrometry**. Edited by F. Adams, R. Gijbels, and R. Van Grieken

Vol. 96. **Kinetic Aspects of Analytical Chemistry**. By Horacio A. Mottola

Vol. 97. **Two-Dimensional NMR Spectroscopy**. By Jan Schraml and Jon M. Bellama

Vol. 98. **High Performance Liquid Chromatography**. Edited by Phyllis R. Brown and Richard A. Hartwick

Vol. 99. **X-Ray Fluorescence Spectrometry**. By Ron Jenkins

Vol. 100. **Analytical Aspects of Drug Testing**. Edited by Dale G. Deustch

Vol. 101. **Chemical Analysis of Polycyclic Aromatic Compounds**. Edited by Tuan Vo-Dinh

Vol. 102. **Quadrupole Storage Mass Spectrometry**. By Raymond E. March and Richard J. Hughes

Vol. 103. **Determination of Molecular Weight**. Edited by Anthony R. Cooper

Vol. 104. **Selectivity and Detectability Optimization in HPLC**. By Satinder Ahuja

Vol. 105. **Laser Microanalysis**. By Lieselotte Moenke-Blankenburg

Vol. 106. **Clinical Chemistry**. Edited by E. Howard Taylor

Vol. 107. **Multielement Detection Systems for Spectrochemical Analysis**. By Kenneth W. Busch and Marianna A. Busch

Vol. 108. **Planar chromatography in the Life Sciences.** Edited by Joseph C. Touchstone

Vol. 109. **Fluorometric Analysis in Biomedical Chemistry: Trends and Techinques Including HPLC Applications**. By Norio Ichinose, George Schwedt, Frank Michael Schnepel, and Kyoko Adochi

Vol. 110. **An Introduction to Laboratory Automation**. By Victor Cerdá and Guillermo Ramis

Vol. 111. **Gas Chromatography: Biochemical, Biomedical, and Clinical Applications**. Edited by Ray E. Clement

Vol. 112. **The Analysis Chemistry of Silicones**. Edited by A. Lee Smith

Vol. 113. **Modern Methods of Polymer Characterization**. Edited by Howard G. Barth and Jimmy W. Mays

Vol. 114. **Analytical Raman Spectroscopy**. Edited by Jeanette Graselli and Bernard J. Bulkin

Vol. 115. **Trace and Ultratrace Analysis by HPLC**. By Satinder Ahuja

Vol. 116. **Radiochemistry and Nuclear Methods of Analysis**. By William D. Ehmann and Diane E. Vance

Vol. 117. **Applications of Fluorescence in Immunoassays**. By Ilkka Hemmila

Vol. 118. **Principles and Practice of Spectroscopic Calibration**. By Howard Mark

Vol. 119. **Activation Spectrometry in Chemical Analysis**. By S. J. Parry

Vol. 120. **Remote Sensing by Fourier Transform Spectrometry**. By Reinhard Beer

Vol. 121. **Detectors for Capillary Chromatography**. Edited by Herbert H. Hill and Dennis McMinn

Vol. 122. **Photochemical Vapor Deposition**. By J. G. Eden

Vol. 123. **Statistical Methods in Analytical Chemistry**. By Peter C. Meier and Richard Zünd

Vol. 124. **Laser Ionization Mass Analysis**. Edited by Akos Vertes, Renaat Gijbels, and Fred Adams

Vol. 125. **Physics and Chemistry of Solid State Sensor Devices**. By Andreas Mandelis and Constantinos Christofides

Vol. 126. **Electroanalytical Stripping Methods**. By Khjena Z. Brainina and E. Neyman

Vol. 127. **Air Monitoring by Spectroscopic Techniques**. Edited by Markus W. Sigrist

Vol. 128. **Information Theory in Analytical Chemistry**. By Karel Eckschlager and Klaus Danzer

Vol. 129. **Flame Chemiluminescence Analysis by Molecular Emission Cavity Detection**. Edited by David Stiles, Anthony Calokerinos, and Alan Townshend

Vol. 130. **Hydride Generation Atomic Absorption Spectrometry**. By Jiri Dedina and Dimiter L. Tsalev

Vol. 131. **Selective Detectors: Enviromental, Industrial, and Biomedical Applications**. Edited by Robert E. Sievers

Vol. 132. **High Speed Countercurrent Chromatography**. Edited by Yoichiro Ito and Walter D. Conway

Vol. 133. **Particle-Induced X-Ray Emission Spectrometry**. By Sven A. E. Johansson, John L. Campbell, and Klas G. Malmqvist

Vol. 134. **Photothermal Spectroscopy Methods for Chemical Analysis**. By Stephen E. Bialkowski

Vol. 135. **Element Speciation in Bioinorganic Chemistry**. Edited by Sergio Caroli

Vol. 136. **Laser-Enhanced Ionization Spectrometry**. Edited by John C. Travis and Gregory C. Turk

Vol. 137. **Fluorescence Imaging Spectroscopy and Microscopy**. Edited by Xue Feng Wang and Brain Herman

Vol. 138. **Introduction to X-Ray Powder Diffractometry**. By Ron Jenkins and Robert L. Snyder

Vol. 139. **Modern Techinques in Electroanalysis**. Edited by Petr Vanýsek

Vol. 140. **Total Reflection X-Ray Fluorescence Analysis**. By Reinhold Klockenkamper

Vol. 141. **Spot Test Analysis: Clinical, Enviromental, Forensic, and Geochemical Applications, Second Edition**. By Ervin Jungreis

Vol. 142. **The Impact of Stereochemistry on Drug Development and Use**. Edited by Hassan Y. Aboul-Enein and Irving W. Wainer

Vol. 143. **Macrocyclic compounds in Analytical Chemistry**. Edited by Yury A. Zolotov

Vol. 144. **Surface-Launched Acoustic Wave Sensors: Chemical Sensing and Thin-Film Characterization**. By Michael Thompson and David Stone

Vol. 145. **Modern Isotope Ratio Mass Spectrometry**. Edited by T. J. Platzner

Vol. 146. **High Performance Capillary Electrophoresis: Theory, Techinques, and Applications**. Edited by Morteza G. Khaledi

Vol. 147. **Solid Phase Extraction: Principles and Practice**. By E. M. Thurman

Vol. 148. **Commercial Biosensors: Applications to Clinical, Bioprocess and Enviromental Samples**. Edited by Graham Ramsay

Vol. 149. **A Practical Guide to Graphite Furnace Atomic Absorption Spectrometry**. By David J. Butcher and Joesph Sneddon

Vol. 150. **Principles of chemical and Biological Sensors**. Edited by Dermot Diamond

Vol. 151. **Pesticide Residue in Foods: Methods, Technologies, and Regulations**. By W. George Fong, H. Anson Moye, James N. Seiber, and John P. Toth

Vol. 152. **X-Ray Fluorescence Spectrometry**. *Second Edition*. By Ron Jenkins

Vol. 153. **Statistical Methods in Analytical Chemistry**. *Second Edition*. By Peter C. Meier and Richard E. Zünd

Vol. 154. **Modern Analytical Methodologies in Fat and Water Soluble Vitamins**. Edited by Won O. Song, Gary R. Beecher and Ronald R. Eitenmiller

Vol. 155. **Modern Analytical Methods in Arts and Archaeology**. Edited by Enrico Ciliberto and Guiseppe Spoto

Vol. 156. **Shpol'skii Spectroscopy and Others Site Selection Methods: Applications in Enviromental Analysis, Bioanalytical Chemistry and Chemical Physics**. Edited by C. Goojier, F. Ariese and J. W. Hofstraat

Vol. 157. **Raman Spectroscopy for Chemical Analysis**. By Richard L. McCreery

Raman Spectroscopy for Chemical Analysis

Raman Spectroscopy for Chemical Analysis. Richard L. McCreery

ISBN: 0-471-25287-5

CHAPTER

1

INTRODUCTION AND SCOPE

1.1. HISTORY PRECEDING 1986

The discovery of Raman scattering by Krishna and Raman in 1928 is well documented (1), and the phenomenon has been the subject of thousands of research papers and at least a dozen monographs. Examples of general discussions of Raman spectroscopy include those emphasizing theory (2–4), instrumentation (5–8), applications (9–13), and compilations of spectra and frequencies (14–18). Until approximately 1986, the Raman literature was dominated by physical and structural investigations, with relatively few reports of Raman spectroscopy applied to chemical analysis. The application of Raman spectroscopy for "real-world" chemical analysis was impeded by both fundamental and technical issues, including weak intensity, fluorescence interference, and inefficient light collection and detection. The prospects for routine chemical analysis took a major turn for the better starting in 1986, with the introduction of Fourier transform (FT)–Raman (19), charge-coupled devices (5,8), small computers, and near-infrared lasers. These developments overcame the major impediments and resulted in a Raman renaissance in the context of chemical analysis.

Several fundamental issues underlying Raman utility are illustrated in Figures 1.1 and 1.2. When monochromatic light of energy $h\nu_0$ encounters matter (gas, solid, or liquid), there is a small probability that it will be scattered at the same frequency. If the object in question (e.g., a molecule) is much smaller than the wavelength of the light, the scattering is Rayleigh scattering, as shown in Figure 1.1. The "virtual state" is not necessarily a true quantum state of the molecule but can be considered a very short lived distortion of the electron cloud caused by the oscillating electric field of the light. Blue light is more efficiently scattered than red (by a factor of ν^4, with ν the frequency of the light), and Rayleigh scattering is responsible for the blue sky. The electron cloud of the molecule is also perturbed by molecular vibrations, and it is possible for the optical and vibrational oscillations to interact, leading to Raman scattering. Raman scattering is shown in Figure 1.1 in which the scattered photon is lower in energy by an amount equal to a vibrational transition, $h\nu_1$.

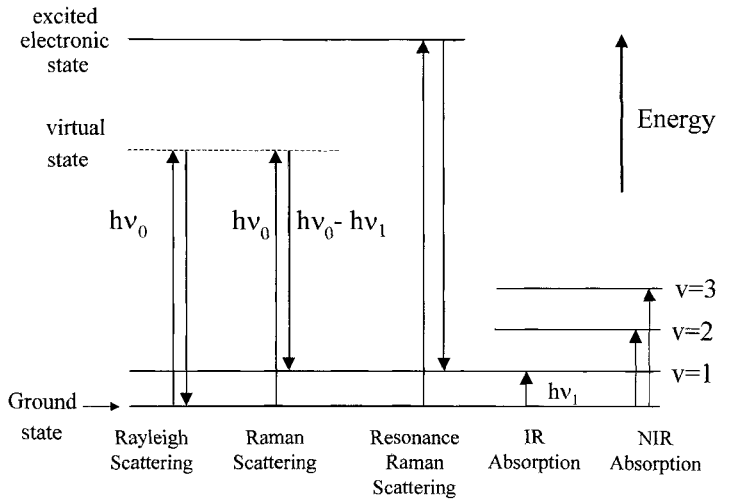

Figure 1.1. Spectroscopic transitions underlying several types of vibrational spectroscopy. ν_0 indicates laser frequency, while v is the vibrational quantum number. The virtual state is a short-lived distortion of the electron distribution by the electric field of the incident light.

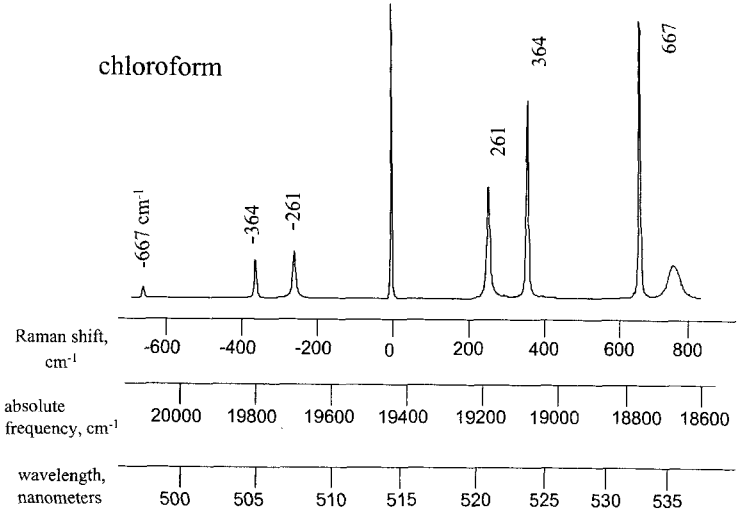

Figure 1.2. Raman spectrum of room-temperature chloroform obtained with 514.5 nm light. Rayleigh scattering at zero Raman shift is heavily attenuated by a band reject filter and is actually several orders of magnitude more intense than the Raman scattering. The x axis is shown in three different scales but is normally plotted as Raman shift in reciprocal centimeters relative to the laser frequency (19,435 cm^{-1} in this case). Although the Stokes Raman to the right is actually a negative frequency shift, convention assigns Stokes Raman shifts as positive numbers.

A Raman spectrum consists of scattered intensity plotted vs. energy, as shown in Figure 1.2. Each peak corresponds to a given Raman shift from the incident light energy $h\nu_0$. If the molecule happens to be in an excited vibrational state when an incident photon is scattered, the photon may gain energy when scattered, leading to anti-Stokes Raman scattering. The Stokes and anti-Stokes Raman peaks are symmetrically positioned about the Rayleigh peak, but their intensities are very different except for low vibrational energies.

Infrared absorption, often called Fourier transform infrared (FTIR) or mid-IR absorption, also depends on molecular vibrations, as shown in Figure 1.1. Although Raman spectroscopy probes vibrational transitions indirectly by light scattering, the Raman shift has the same energy range as FTIR absorption, and in many cases, the same energies are observed. The selection rules for Raman scattering and FTIR are different (as noted in Chapter 2), but the chemical information is similar. A fundamental difference between absorption and Raman scattering is probability, with absorption usually being a far more likely event. For example, a typical sample for an absorption experiment (10^{-3}M, $\epsilon = 1000$, $M^{-1}cm^{-1}$) absorbs 90 per cent of the incident light over a 1 cm path length, but only about 1 in 10^{10} incident photons will undergo Raman scattering. The first major impediment to using Raman spectroscopy is the weakness of the effect, with Raman scattering being roughly 10^{-10} as likely as the corresponding mid-IR absorption in typical experimental situations.

A second problem with Raman spectroscopy is another competitive effect, fluorescence. The visible light typically used for Raman spectroscopy before 1986 often excites fluorescence of the analyte of interest or of impurities. Fluorescence is not a scattering process, and fluorescence emission from most liquids and solids does not have the vibrational fine structure observed in Figure 1.2. Figure 1.3 illustrates the energy levels and appearance of fluorescence emission compared to Raman scattering. Even weak fluorescence can be much stronger than Raman scattering, easily overwhelming the weak Raman signal. With pre-1986 technology and excitation with 400 to 650 nm light, fluorescence of either the analyte or impurities in the sample prevented the observation of Raman scattering in a large fraction of samples of practical importance. Accordingly, avoidance of fluorescence was critical to the utility of Raman spectroscopy for practical applications.

Near-infrared (NIR) absorption spectroscopy is another technique of importance to the context of the development of analytical Raman spectroscopy. The method is generally referred to as NIR, despite the unfortunate confusion with NIR-Raman. NIR absorption is based on overtone and combination bands of mid-IR transitions, as shown in Figure 1.1. Such transitions are quantum mechanically forbidden and significantly weaker than mid-IR fundamentals. However, the higher energy photons involved in NIR absorption are transmitted by fiber optics and common optical materials, and the method has

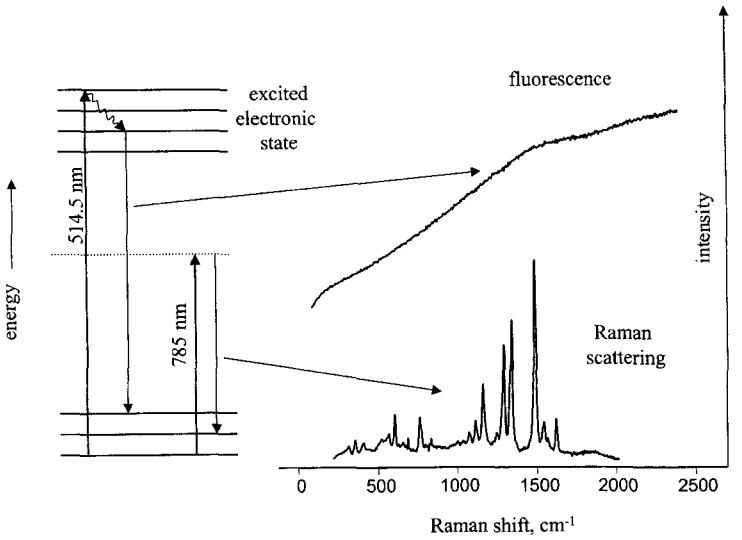

Figure 1.3. Energy levels associated with 514.5 and 785 nm light incident on a fluorescent sample. Energy and intensity scales are not to scale, and fluorescence intensity is several orders of magnitude greater than Raman scattering. Raman shift axis is relative to the incident laser frequency.

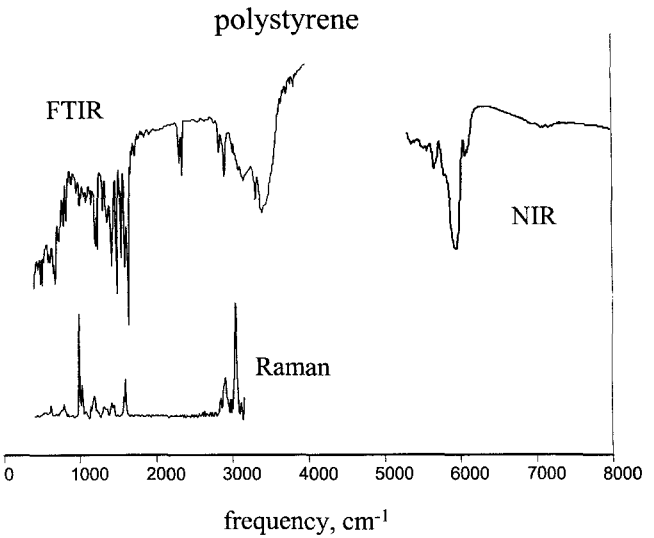

Figure 1.4. Raman scattering, IR transmission, and NIR transmission spectra of polystyrene, plotted on a single energy scale. Intensity scales are very different, with NIR absorption being much weaker than IR absorption. In this case, the sample concentrations for NIR and Raman (solid polystyrene) were much greater than that for FTIR (dilute powder in KBr).

substantial advantages in sampling and instrumentation. Figure 1.4 compares Raman, FTIR, and NIR spectra of polystyrene, plotted on the same energy scale but very different intensity scales. As we will discuss later, NIR absorption techniques have provided some of the motivation for Raman spectrometer development.

1.2. TECHNOLOGICAL ADVANCES

The post-1986 developments that caused the Raman renaissance are mainly technological, but they largely overcome the fundamental problems of a weak Raman signal and interference from fluorescence. To be sure, there were major technical developments preceding 1986, such as photon counting detection and the introduction of the laser, but the more recent technical innovations have been responsible for the transition of Raman spectroscopy from the research lab to the real world. These advances are listed here and discussed in detail in subsequent chapters.

1.2.1. Fourier Transform Raman Spectroscopy

Before 1986, it was generally accepted that the combination of a Michelson interferometer and Fourier transform techniques, as employed in FTIR, would not be useful for Raman spectroscopy because of the "multiplex disadvantage." The increase in shot noise when the signal is multiplexed onto a single detector negates the advantage of multiplex spectroscopy when the instrument is operating in the shot noise limit, as is usually the case for visible lasers (Chapter 4). However, when FT techniques are combined with laser excitation in the NIR, for example, at 1064 nm, significant advantages result. Although the Raman scattering is weaker at 1064 nm compared to visible excitation (e.g., 514.5 nm), the fluorescence background is often orders of magnitude weaker. NIR excitation is sufficiently lower in energy that most of the electronic transitions responsible for fluorescence are not excited (6,19,20,21). Referring to Figure 1.3, the virtual state becomes too far in energy from the electronic excited states to cause fluorescence. An example is shown in Figure 1.5, for rhodamine 6G, a fluorescent laser dye. With 514.5 nm excitation the spectrum is completely dominated by fluorescence, while at 1064 nm, the Raman scattering is easily observed with an FT-Raman spectrometer. Regardless of the detection method (FT or dispersive), longer wavelength excitation yields a higher ratio of Raman scattering to fluorescence for the vast majority of samples. Even though the Raman scattering is weaker and detection is more difficult than in the visible region, the reduction in fluorescence permits a much wider range of samples to be examined with Raman spectroscopy.

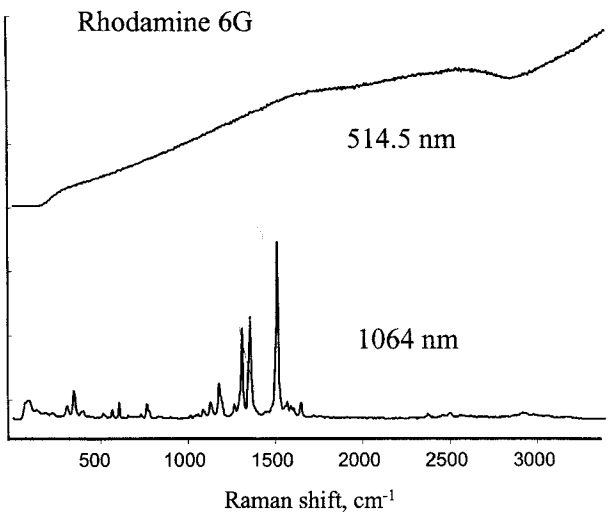

Figure 1.5. Spectra of rhodamine 6G obtained with a 514.5 nm laser and dispersive spectrometer (upper) or an FT-Raman spectrometer and 1064 nm laser (lower). Intensity scales differ greatly, with the upper spectrum being much more intense.

In addition to reduced fluorescence, FT-Raman also provides excellent frequency precision and many other benefits common to FTIR instrumentation (6). In many cases, FT-Raman instruments are modified FTIRs, and several FTIR vendors added Raman accessories to their product line. FT-Raman was responsible for a surge of interest in analytical Raman spectroscopy during the period 1986 to 1990, and steady growth since.

1.2.2. Multichannel Detectors and Charge-Coupled Devices

A parallel but unrelated development was the introduction of multichannel detectors capable of monitoring many Raman shifts simultaneously. Intensified photodiode arrays (IPDA) were used as early as 1982, and charge-coupled devices (CCDs) were first applied to Raman spectroscopy in 1985 (5,8). These detectors differ greatly in their electronic design and specifications, but both permit multiwavelength detection. The benefits of multichannel detection are addressed in Chapters 3 and 4, but for now suffice it to say that they greatly increase the signal and signal/noise ratio (SNR) for a given measurement time, or they permit much faster acquisition times. CCDs have better noise characteristics and are simpler than IPDAs, and have replaced IPDAs in all but a few specialized applications. As shown in Figure 1.6, a CCD spectrometer permits both faster acquisition and higher SNR than a state-of-the-art dispersive spectrometer of 1985 vintage.

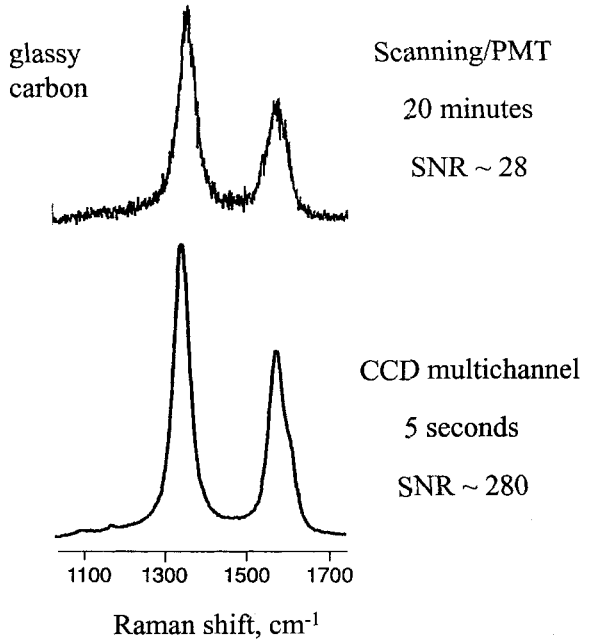

Figure 1.6. Spectra of solid glassy carbon obtained with a state-of-the-art spectrometer in 1985 (Spex 1403 double monochromator with photon counting PMT) and a multichannel/CCD spectrometer of 1996 (Chromex 250 spectrograph, back thinned silicon CCD); 514.5 nm laser at 50 mW in both cases; measurement times and signal/noise ratios (SNR) as shown.

Some people would argue that multiplex detection from FT-Raman and multichannel detection with CCDs are the major instrumental advances responsible for the Raman Renaissance. However, there are several other innovations that were important to broadening the applications of Raman spectroscopy:

1.2.3. Fiber-Optic Sampling

Since Raman spectroscopy measures a frequency shift, the laser wavelength can be chosen to be compatible with fiber optics or other optical components. Mid-IR light necessary for FTIR absorption is difficult to transmit through any existing optical fiber for more than a few meters, but Raman scattering can be conducted hundreds of meters in readily available fibers. For example, fiber optics may be used to carry the laser light to a reactor vessel in a chemical production plant, then collection fibers can bring the scattered light back to the spectrometer (Chapter 12). Fiber optics permit both simplified alignment

and remote sampling, and increase the attractiveness of Raman spectroscopy for process monitoring and control.

1.2.4. Laser Rejection Filters

Any Raman spectrometer must observe weak Raman scattering in the presence of much stronger Rayleigh scattering or diffuse reflection occurring at the laser frequency. So Raman spectrometers must have outstanding stray light rejection, often achieved with bulky and inefficient double monochromators and triple spectrographs. Fortunately, new filter designs based on holograph optics, improved dielectric filters, or semiconducting absorbers can effectively reject the intense Rayleigh light. The rejection (or *notch*) filter shown schematically in Figure 1.7 is small and simple and permits the use of a small, single-stage spectrograph. A notch filter and a single spectrograph can be much smaller and more efficient than a traditional double or triple spectrometer, reducing both the size and cost of the spectrometer.

1.2.5. Compact Imaging Spectrographs

An imaging spectrograph differs from a conventional (e.g., Czerny-Turner) design in that it maintains the one-to-one correspondence of the entrance slit and its image at the detector. So a circular fiber positioned at the entrance

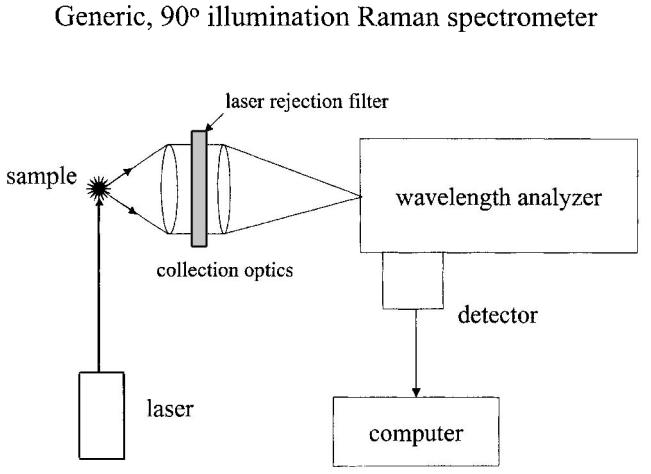

Figure 1.7. Generic Raman spectrometer showing main components: laser, collection optics, wavelength analyzer, detector, computer. Many variations of geometry and components are in common use. Laser rejection filter is often called a notch filter.

slit produces a circular image at the focal plane. Imaging spectrographs are particularly important when constructing an image of a heterogeneous sample which is also wavelength (or Raman shift) specific. More generally, imaging spectrographs require aberration corrections that also permit shorter focal lengths. The end result is a spectrograph with lower aperture ratio ($f/\#$) and higher light-gathering ability. In addition, imaging spectrographs perform well with CCD having possibly large areas, say 1×2.5 cm. Maintaining good focus and resolution over a large detector area often requires the aberration corrections inherent in an imaging spectrograph.

1.2.6. Diode Lasers

Pre-1986 Raman spectrometers generally employed physically large lasers such as argon or krypton ion, which require 208 or 480 V electrical power and significant cooling water. Maintenance costs were fairly high, and such lasers are generally impractical for routine analytical applications. Diode lasers and diode-pumped Nd:YAG (yttrium–aluminum–garnet) lasers are much smaller, air cooled, powered by 110 V, and much lower maintenance. Common examples are Nd:YAG (1064 nm), doubled Nd:YAG (532 nm), and Al:GaAs diode lasers (750 to 900 nm). Not only are these lasers amenable to routine applications in analytical instruments, they can operate in the NIR wavelengths where fluorescence is less prominent.

1.2.7. Personal Computers

Both CCD and FT techniques require significant computing power, which added substantially to system cost before the advent of personal computers. Now, the required computing power is available at a cost that is insignificant compared to the rest of the instrument. Furthermore, sophisticated data analysis software is available for calibration, quantitative multivariate analysis, and information storage and management. Although small computers are now integrated into a variety of analytical instrumentation, they are both enabling and essential to modern Raman spectroscopy.

1.2.8. Integrated Raman Spectrometers

These somewhat disparate technical developments progressed more or less in parallel but converged during the evolution of Raman instrumentation starting approximately in 1986. A major result was the emergence of integrated Raman spectrometers that incorporated laser, spectrometer, sampling accessories, and software into a complete system. These newer instruments were not only much more capable than previous systems, but they were also more reliable

and simpler to use. The major impediments to widespread Raman application were addressed by a huge improvement in sensitivity and a large reduction of fluorescent interferences. For example, an integrated CCD/dispersive spectrometer available in 1997 provides approximately 50,000 times more signal (and >100 times the SNR) compared to a single-channel system of 1985, for comparable total measurement times. Operation with NIR lasers reduced the number of fluorescent samples greatly, so that many previously intractable samples are now amenable to Raman spectroscopy. Most importantly, the convergence of technological advances permitted the analytical chemist to exploit the benefits of Raman spectroscopy, such as noninvasive sampling, compatibility with water, and high spectral information content, while avoiding the old impediments of low sensitivity and fluorescence interference. Furthermore, the availability of integrated, "turnkey" Raman spectrometers greatly decreased experimental complexity and increased reliability.

1.3. COMPARISON TO FTIR AND NIR ABSORPTION

Returning to Figure 1.4, it is useful to compare Raman spectroscopy with FTIR and NIR absorption in the context of chemical analysis. Since all three techniques probe molecular vibrations, they are often used for similar analytical problems. FTIR is the oldest and most developed, and accounts for several hundred million dollars per year of the chemical instrumentation market in the United States. Some advantages of FTIR are summarized in Figure 1.8, and most derive from the fact that FTIR involves absorption by fundamental (i.e., $\Delta v = 1$) vibrations. FTIR spectra have narrow linewidths and rich spectral detail, such that different molecules have distinguishable "fingerprints." A good fingerprint permits reliable qualitative analysis by comparison to spectral libraries, and both printed and electronic FTIR libraries are available. FTIR instrumentation is highly refined due to its widespread use, and interferometers possess excellent wavelength precision and stability.

While FTIR is currently the most widely used vibrational spectroscopy in both research and application labs, it does have some drawbacks. Mid-IR light does not penetrate many common optical materials, thus restricting sampling flexibility. For example, it is not possible to use FTIR to sample a solid inside a glass vial without removing the solid. Water absorbs mid-IR light strongly, so aqueous samples may be probed only as thin films, and water is a common interferent. In many cases, FTIR requires nontrivial sample preparation, such as a KBr pellet, Nujol null, and the like. These procedures are time consuming, destructive, or both. Although FTIR absorption is both popular and powerful, it does have some limitations that are fundamental to the wavelength range involved.

FTIR Absorption	NIR Absorption
Narrow linewidths	Noninvasive, simple sampling
Good fingerprint; libraries available	Fiber optics, remote sampling
Fundamental vibrations	Water compatible
(Sampling often difficult)	*(wide linewidths)*
(water absorbs strongly)	*(calibration complex)*
	(poor fingerprint)

Raman Scattering	
Narrow linewidths	water compatible
Fibers, remote sampling OK	easy sampling, often noninvasive
No moving parts (sometimes)	Resonance and surface enhancement possible
Low frequency modes observable	
(low sensitivity)	*(interferences)*

Figure 1.8. Some features and shortcomings of FTIR, NIR, and Raman spectroscopy. Italics indicate disadvantages.

NIR absorption uses shorter wavelength light than FTIR, in the range of 1 to 2.5 μm instead of 2.5 to 25 μm. The resulting compatibility with fiber optics, common glass, and water was a major incentive for NIR development for chemical analysis. NIR spectra may be obtained noninvasively from samples inside glass containers or remotely down a fiber-optic cable. Although water still absorbs in the 1 to 2.5 μm range, the absorption is much weaker than in the FTIR region and is often used to quantify water content. However, NIR is based on overtones of FTIR fundamentals, and NIR absorptions are both weaker and broader than FTIR bands. The result is a loss of spectral information (apparent in Fig. 1.4). Furthermore, the overtones observed with NIR absorption are generally from C—H, O—H, and N—H stretches, and

often lack the structural specificity common to the fingerprint region of FTIR. Due to the relatively broad and often overlapped features in NIR, multivariate calibration is generally required for quantitative analysis. Such procedures require a fairly large training set (10 to 20 standard samples) and are often sensitive to instrumental drift or small variations in sample properties, such as water content.

Although NIR spectra are not as information-rich or specific as FTIR spectra, the technique has experienced rapid growth. The increasing popularity of NIR absorption is driven mainly by sampling advantages, particularly the ability to obtain spectra noninvasively or with fiber optics. Since sample preparation is often not required, NIR analysis can be fast, inexpensive, and nondestructive.

The attraction of Raman spectroscopy for chemical analysis is derived from the combination of many of the advantages of FTIR with those of NIR absorption, plus a few benefits unique to Raman (10,13,21,22). Like NIR, Raman spectra can be acquired noninvasively, and sampling can be simple and fast. Like FTIR, Raman scattering probes fundamental vibrations with high spectral resolution. Although the selection rules differ for FTIR and Raman, the information is similar and both are amenable to spectral libraries and fingerprinting. As summarized in Figure 1.8, Raman combines the high spectral information content of FTIR with the sampling ease and convenience of NIR absorption. In addition, Raman has some added features based on resonance and/or surface enhancement, polarization measurements, and compatibility with aqueous samples. Figure 1.8 also notes the historical impediments to the widespread use of Raman spectroscopy for chemical analysis: low sensitivity and interference from fluorescence. Progress in addressing these weaknesses has enabled the application of Raman spectroscopy to a variety of analytical problems.

In summary, the Raman renaissance began when the attractiveness of Raman scattering for chemical analysis could be exploited as a result of technological improvements. The large gain in sensitivity and the reduction in fluorescent background resulting from new hardware and techniques permitted Raman spectroscopy applications to a wide range of samples of practical analytical importance. Much of the stimulus for the renewed development of analytical Raman spectroscopy is the ease and versatility of sampling modes and the high spectral information content.

1.4. OVERVIEW OF THE BOOK

The central topic of this book is analytical Raman spectroscopy in terms of both techniques and applications. While there are many elegant treatments

of Raman fundamentals available, Raman theory is not emphasized here. Similarly, the current text will not address the interpretation of Raman spectra to determine molecular structure, nor will it provide a large compilation of Raman vibrational frequencies. Such compendia of spectra and frequencies have already been cited (14–18) and should be consulted as required. Those aspects of Raman theory and spectrum interpretation that bear directly on chemical analysis will be discussed, particularly with regard to the constraints they impose on instrument design and applicability. This approach necessarily excludes many aspects of Raman spectroscopy from the current treatment, such as nonlinear Raman, group theory, time-resolved Raman, and so forth. Although these and many other topics of interest to Raman spectroscopists may become relevant to chemical analysis, they are not presently of central analytical interest.

Chapters 2, 3, and 4 discuss Raman scattering magnitude, signal collection, and signal/noise ratio and form the theoretical basis of analytical measurements. Chapter 5 summarizes instrumentation issues, particularly those relevant to selecting a spectrometer design for a given application. Chapters 6 and 7 describe Raman sampling configurations and common lasers currently used in spectrometers intended for analytical applications. Dispersive (Chapter 8) and Fourier transform spectrometers (Chapter 9) are addressed next, with attention to relative merits and applicability. Chapter 10 is a general discussion of calibration and validation issues, for both frequency and intensity. The book closes with three chapters on analytical Raman techniques of currently active interest, Raman microscopy (Chapter 11), fiber-optic sampling (Chapter 12), and Raman spectroscopy of surfaces, including surface-enhanced Raman spectroscopy (Chapter 13).

REFERENCES

1. R. S. Krishnan and R. K. Shankar, *J. Raman Spectosc.*, **10**, 1 (1981).
2. D. A. Long, *Raman Spectroscopy*, McGraw Hill, New York, 1977.
3. J. R. Ferraro and K. Nakamoto, *Introductory Raman Spectroscopy*, Academic Press, Boston, 1994.
4. M. Diem, *Introduction to Modern Vibrational Spectroscopy*, Wiley, New York, 1993.
5. J. J. Laserna, ed., *Modern Techniques in Raman Spectroscopy*, Wiley, New York, 1996.
6. P. Hendra, C. Jones, and G. Warner, *Fourier Transform Raman Spectroscopy; Instrumentation and Applications*, Ellis Harwood, New York, 1991.
7. D. S. Trommen and J. Nakamoto, *Laboratory Raman Spectroscopy*, Wiley, New York, 1984.

8. R. L. McCreery, in J. Sweedler, K. Ratzlaff, and M. B. Denton, eds., *Charge Transfer Devices in Spectroscopy*, VCH, New York, 1994.
9. P. J. Hendra and J. K. Agbenvega, *The Raman Spectroscopy of Polymers*, Wiley, New York, 1993.
10. J. Grasseli and B. Bulkin, *Analytical Raman Spectroscopy*, Wiley, New York, 1991.
11. J. Grasselli, M. Snavely, and B. Bulkin, *Chemical Applications of Raman Spectroscopy*, Wiley, New York, 1981.
12. J. M. Chalmers and G. Dent, *Industrial Analysis with Vibrational Spectroscopy*, Royal Society of Chemistry, Cambridge, 1997.
13. J. M. Chalmers, *Spectroscopy in Process Analysis*, CRC Analytical Chemistry Series, Vol. 4, CRC Press, Boca Raton, FL, 1999.
14. B. Schrader, *Raman and Infrared Atlas of Organic Compounds*, VCH, New York, 1989.
15. F. R. Dollish, W. G. Fateley, and F. F. Bentley, *Characteristic Raman Frequencies of Organic Compounds*, Wiley, New York, 1974.
16. D. Lien-Vien, N. Colthup, W. G. Fateley, and J. Grasselli, *Handbook of Infrared and Raman Characteristic Frequencies of Organic Molecules*, Academic Press, Boston, 1991.
17. K. Nakamoto, *Infrared and Raman Spectra of Inorganic and Coordination Compounds*, Wiley, New York, 1986, 2nd ed., 1995.
18. R. A. Nyquist, C. L. Putzig, and M. A. Leugers, *The Handbook of Infrared and Raman Spectra of Inorganic Compounds and Organic Salts*, Academic Press, San Diego, 1997.
19. D. B. Chase, *J. Am. Chem. Soc.*, **108**, 7485 (1986).
20. D. B. Chase, *Anal. Chem.*, **59**, 881A (1997).
21. D. B. Chase, J-F. Rabolt, *Fourier Transform Raman Spectroscopy: From Concept to Experiment*, Academic Press, New York, 1994.
22. M. J. Pelletier (ed.), *Analytical Applications of Raman Spectroscopy*, Blackwell Science Ltd., London, 1999.

Raman Spectroscopy for Chemical Analysis. Richard L. McCreery

ISBN: 0-471-25287-5

CHAPTER

2

MAGNITUDE OF RAMAN SCATTERING

2.1. THEORETICAL OVERVIEW

The classical description of Raman scattering depicted in Figure 2.1 is that of a polarization induced in the molecule by the oscillating electric field of the incoming light. This induced dipole then radiates scattered light, with or without exchanging energy with vibrations in the molecule. The strength of the induced polarization, P, scales with the polarizability, α, and the incident electric field, E:

$$P = \alpha E \tag{2.1}$$

Both classical and quantum mechanical treatments of Raman scattering are based on Eq. (2.1), and such treatments are very valuable in understanding the effect and interpreting spectra (1–5). One of the more analytically important results of Raman theory is the Raman scattering cross section, σ_j, which will be discussed at some length below. Before considering the factors that affect σ_j, it is useful to review several aspects of Raman theory.

A classical treatment of Raman scattering (3,4) is based on the effects of molecular vibrations on the polarizability, α, in Eq. (2.1). Consider the incident optical electric field to be governed by Eq. (2.2):

$$E = E_0 \cos 2\pi\nu_0 t \tag{2.2}$$

where ν_0 is the frequency of the laser light. The molecular vibrations are usually considered to be composed of normal modes, Q_j, of which there are $3N$-6 (or $3N$-5 for a linear molecule) in a molecule with N atoms.

$$Q_j = Q_j^\circ \cos 2\pi\nu_j t \tag{2.3}$$

where ν_j is the characteristic harmonic frequency of the jth normal mode. The polarizability of electrons in the molecule will be modulated by the molecular vibration so that

$$\alpha = \alpha_0 + \left(\frac{\delta\alpha}{\delta Q_j}\right) Q_j + \cdots \tag{2.4}$$

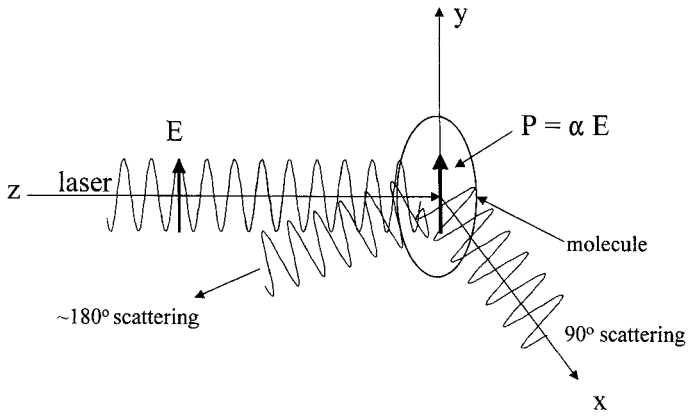

Figure 2.1. Polarization (P) induced in a molecule's electron cloud by an incident optical electric field E. Scattering may be in various directions, but 90° and ~180° are shown.

From Eq. (2.1), the polarization is the product of Eq. (2.2) and (2.4), which yields (2.5) after noting that $\cos a \cos b = [\cos(a+b) + \cos(a-b)]/2$, and ignoring higher order terms in Eq. (2.4):

$$P = \alpha_0 E_0 \cos 2\pi\nu_0 t + E_0 Q_j^\circ \left(\frac{\delta\alpha}{\delta Q_j}\right) \frac{\cos 2\pi(\nu_0 + \nu_j)t + \cos 2\pi(\nu_0 - \nu_j)}{2} \tag{2.5}$$

After assuming (classically) that the polarized electrons will radiate light at the frequency of their oscillations, Eq. (2.5) demonstrates that light will be scattered at three frequencies. The first term is Rayleigh scattering, which is at the same frequency as the laser, and has a magnitude proportional to α_0, the inherent polarizability of the molecule. The second term is anti-Stokes Raman scattering, which occurs at $\nu_0 + \nu_j$, and the third term is Stokes Raman scattering at $\nu_o - \nu_j$. The transitions associated with Rayleigh and Stokes Raman scattering were shown in Figure 1.1. Note that ν_j is the same frequency that would be observed with infrared (IR) absorption for a given vibrational mode, if allowed by symmetry.

Although Eq. (2.5) was derived classically and is incomplete, it does provide some useful insights. First, polarization and scattering (both Rayleigh and Raman) intensities are linear with the laser intensity. Nonlinear Raman scattering can occur at high values of E_0 but is generally not an issue in analytical applications. Second, only vibrations that change the polarizability (and consequently $\delta\alpha/\delta Q \neq 0$) yield Raman scattering. This statement is the basis of the primary selection rule for Raman scattering and its effect is quite evident in the spectra of Figure 2.2. The polarizability of the C=C bond

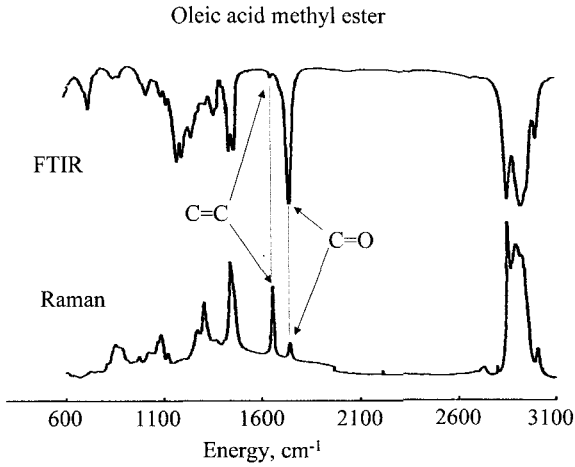

Figure 2.2. FTIR (upper) transmission and Raman scattering (lower) of oleic acid methyl ester.

changes significantly with a vibration associated with the stretch of the C=C bond. So the Raman scattering from a C=C bond is strong, while that of a C=O bond is relatively weak. In contrast, infrared absorption requires a dipole moment change for a given vibration to be IR active, so the C=C vibration is very weak toward IR absorption and the C=O stretch is strong. A third consequence of Eq. (2.5) is that Raman shifts may be both positive and negative. Since anti-Stokes Raman intensity depends on the population of the first vibrationally excited state, its intensity is related to temperature by the Boltzmann distribution, given by Eq. (2.6) for the case of a nondegenerate vibration (2):

$$\frac{I_R(\nu_0 + \nu_j)}{I_R(\nu_0 - \nu_j)} = \frac{(\nu_0 + \nu_J)^4}{(\nu_0 - \nu_j)^4} \exp\left(\frac{-h\nu_j}{kT}\right) \tag{2.6}$$

Fourth, $\delta\alpha/\delta Q_j$ may vary significantly for different molecules and for different modes in a given molecule, leading to wide variations in Raman scattering intensity. Fifth, although it is not apparent from Eq. (2.5), $\delta\alpha/\delta Q_j$ is generally much smaller than α_0, and Raman scattering is much weaker than Rayleigh scattering.

The observed intensity of Raman scattering is proportional to the cross section, σ_j, with units of square centimeters per molecule. The magnitude of σ_j is related to $\delta\alpha/\delta Q_j$, and significant theoretical treatment of this issue is available (1,4). One consequence of this theory is the variation of Raman

intensity, I_R, with frequency:

$$I_R = \mu(\nu_0 \pm \nu_j)^4 \alpha_j^2 Q_j^2 \tag{2.7}$$

where μ is a constant. Equation (2.7) indicates that Raman intensity varies with the fourth power of the observed frequency for normal Raman scattering, which, in turn, depends on laser frequency. The ν^4 factor is derived from the classical treatment of scattering from an oscillating induced dipole, with the intensity expressed in watts. As noted later, modern Raman spectrometers, which usually measure photons/seconds rather than watts, are governed by a slightly different frequency dependence.

It is conventional to express frequency in terms of wavenumbers (in reciprocal centimeters) rather than hertz, using the symbol $\bar{\nu}$ ($\bar{\nu} = \nu/c = \lambda^{-1}$, with c the speed of light and λ the wavelength). Accordingly, Eq. (2.7) becomes (2.8), with the factor of c^4 contained in the constant μ':

$$I_R = \mu'(\bar{\nu}_0 \pm \bar{\nu}_j)^4 \alpha_j^2 Q_j^2 \tag{2.8}$$

The Raman shift $\bar{\nu}_j$ (in reciprocal centimeters) is sometimes labeled $\Delta\bar{\nu}_j$ in the literature, while the scattered light occurs at an absolute frequency $\bar{\nu}_0 \pm \bar{\nu}_j$.

Figure 2.2 and Eq. (2.8) lead to two distinctions between Raman scattering and IR absorption spectroscopy that have significant practical consequence. First, IR requires a dipole moment change for an allowed absorption, while Raman requires a finite polarizability change. IR and Raman spectra may differ greatly in the relative intensities of the observed molecular vibrations because of the different selection rules. The Fourier transfor IR (FTIR) and Raman spectra of a fatty acid ester in Figure 2.2 reveal very different relative intensities for the C=O stretch (strong in IR, weak in Raman) and C=C stretch (strong in Raman, weak in IR). For molecules with a center of inversion, IR and Raman modes are mutually exclusive. Second, IR is an absorption technique while Raman involves scattering. Absorption measurements generally involve transmission or reflection geometry, while Raman experiments can involve light collection at a variety of angles relative to the source. Obviously, a choice between Raman and FTIR for an analytical problem may depend on the selection rules applied to the analyte of interest, as well as the experimental geometry.

Extensive compilations of IR and Raman frequencies are available, in some cases with FTIR and Raman spectra plotted together for comparison (6–9). A few frequencies for organic compounds are listed in Table 2.1, in part to illustrate differences in IR and Raman intensities. Symmetric vibrations such as the acetylenic C—C stretch, the —S—S— stretch, and ring breathing modes are generally strong in the Raman but forbidden in the infrared, while

Table 2.1. Examples of Raman and IR Frequencies[a]

	Frequency (cm^{-1})	IR[a]	Raman[b]
Alkanes			
CH_3 sym stretch	2862–2882	vs	vs
C—C stretch	1040–1100	—	s
Cyclopentane ring breathing	889	—	s
Alcohol O—H stretch	3635–3644	m	w
Acetylene C—H bend	825–640	s	w
Acetylene C≡C	2230–2237	—	s
C≡N stretch in R—CN	2230–2250	s	vs
Cyanate C≡N	2245–2256	s	vs
C—H in R—CHO	2800–2850	m	—
C=O in R—CHO	1730–1740	vs	w
R—NO_2 asym stretch	1530–1600	vs	m–w
R—NO_2 sym stretch	1310–1397	s	vs
C—S stretch	580–704	—	vs
S—H stretch	2560–2590	w	s
R_2 S_2 S—S stretch	507–512	m–w	s
Benzene ring breathing	992	—	vs
Primary R—Cl	650–660	s	s
Primary R—Br	565–560	s	vs
Primary R—I	500–510	s	vs

[a]Taken from Reference 8.
[b]vs = very strong, m = medium, w = weak, dash = absent.

many asymmetric vibrations such as C—H and C=O in aldehydes are strong in the IR but weak in Raman. Of course, Raman and IR frequencies are identical for the same vibration, for fundamental reasons. However, apparent frequency shifts between the two methods can occur if IR and Raman select different modes from a group of closely spaced vibrations.

A second important difference between Raman and IR is the typical wavelength region employed for the analysis. Both techniques yield vibrational frequencies from the IR region, but Raman uses ultra violet–visible–near-infrared (UV–Vis–NIR) light rather than IR light. Mid-IR radiation of greatest interest to vibrational spectroscopy (220 to 4000 cm^{-1}) does not penetrate many common cell and optical materials and has a very short penetration depth in water and many other solvents. The wavelengths used for Raman spectroscopy (400 to 1064 nm, and sometimes 200 to 400 nm) are compatible with water and common optical materials, thus simplifying optical design and broadening applicability. Several examples that exploit these practical issues are discussed in later chapters.

2.2. DEFINITION OF RAMAN CROSS SECTION

Although one should be aware of the effects of polarizability, laser wavelength, and the like, on Raman intensity, it is often the case in analytical applications that the important parameter is the empirically determined cross section, σ_j. In many cases, the investigator may be dealing with weak scattering or with distinguishing scattering from several components, and the magnitude of the cross section is critical. In addition, the observation geometry, polarization, and laser wavelength are often invariant and are determined by the instrument for analytical applications, so an empirical cross section for a given Raman band in that geometry is adequate for estimating signal strength. The use of a single cross section for a given laser wavelength and observation geometry is clearly a major simplification of reality, but this pragmatic approach is often both adequate and desirable for analytical situations. Parameter σ_j is proportional to the probability of an incident photon being scattered as a Raman-shifted photon with a particular Raman shift. Although cross sections are not in common use as such in other types of analytical spectroscopy, they are the dominant convention for Raman, due mainly to historical reasons. A more familiar quantity to analytical chemists is the molar absorptivity from Beer's law, with units of reciprocal molar per centimeter. The molar absorptivity is a cross section for absorption and can be converted from the usual units of reciprocal molar per centimeter to centimeters squared per molecule by dividing by Avogadro's number (molecules/mole) and multiplying by 1000 cm^3/liter. It is certainly possible to convert the conventional Raman cross section to a molar equivalent based on moles and liters,* but that convention is currently not in use and would be unfamiliar to Raman spectroscopists. At least for the time being, the cross section with units of centimeters squared per molecule will be employed, rather than any related quantity based on molar concentration.

For a classical treatment, Eq. (2.9) relates the Raman scattering (in watts) to the cross section, with laser intensity (I_0) in watts.

$$I_R = I_0 \sigma_j D \, dz \tag{2.9}$$

where D is the number density of scatters (molecules per cubic centimeter) and dz is the path length of the laser in the sample (or the spectrometer depth of field, as explained in Chapter 6). In this case, σ_j would track $\bar{\nu}_j^4$, as stated in Eq. (2.8). The frequency dependence depicted in Eq. (2.8) is sometimes used to determine a cross section that is independent of frequency (10). For a scatterer that is not resonant or preresonant, and follows the classical $\bar{\nu}^4$

* $\sigma_j(\text{molar}^{-1}\ \text{cm}^{-1}) = \sigma_j\ (\text{cm}^2\ \text{molecule}^{-1}) \times 10^{-3} N_A$, where N_A = Avogadro's number.

dependence, a frequency independent cross section σ_j° may be defined by Eq. (2.10):

$$\sigma_j^\circ = \frac{\sigma_j}{(\bar{\nu}_0 - \bar{\nu}_j)^4} \tag{2.10}$$

where σ_j° has units of centimeters to the sixth power per molecule when $\bar{\nu}_0$ and $\bar{\nu}_j$ are expressed in wavenumbers (in reciprocal centimeters). Note that $\bar{\nu}_j$ is the vibrational frequency (in reciprocal centimeters) of the Raman mode, and $\bar{\nu}_0 - \bar{\nu}_j$ is the absolute frequency (in reciprocal centimeters) of the scattered light.

A complication to the frequency dependency of σ_j arose when photon counting detectors were introduced into Raman instrumentation. Virtually all modern spectrometers count photons rather than measure watts, and the two differ by a factor of $h\nu$. Since the incident and scattered photons differ in energy, the ratio of scattered to incident power differs from the ratio of scattered to incident photon flux. The consequences of this difference are quantitatively fairly minor, but conceptually important. Derivations based on photons/second and photon counting are more consistent with a quantum mechanical treatment where a cross section is effectively a statement of probability, whereas the classical treatment is based on induced dipoles. If Eq. (2.9) is rewritten for photon counting systems, Eq. (2.11) results:

$$P_R = P_0 \sigma_j' D\, dz \tag{2.11}$$

Now, P_0 and P_R haves units of photons per second, and σ_j' has a different frequency dependence than that of Eq. (2.10). Substituting σ_j from Eq. (2.10) into Eq. (2.9) yields (2.11):

$$I_R = I_0 \sigma_R^\circ (\bar{\nu}_0 - \bar{\nu}_j)^4 D\, dz \tag{2.12}$$

Since $I_R = P_R hc(\bar{\nu}_0 - \bar{\nu}_j)$ and $I_0 = P_0 hc\bar{\nu}_0$, Eq. (2.12) becomes

$$P_R = P_0 \sigma_j^\circ \bar{\nu}_0 (\bar{\nu}_0 - \bar{\nu}_j)^3 D\, dz \tag{2.13}$$

and

$$\sigma_j' = \sigma_j^\circ \bar{\nu}_0 (\bar{\nu}_0 - \bar{\nu}_j)^3 \tag{2.14}$$

Therefore, when P_R is measured as photons per second, as is always the case with modern spectrometers, the Raman intensity scales with $\bar{\nu}_0(\bar{\nu}_0 - \bar{\nu}_j)^3$ rather than $(\bar{\nu}_0 - \bar{\nu}_j)^4$. *For all further discussions, the Raman scattering and incident power will be expressed in units of photons per second, as in Eq. (2.13), unless stated otherwise.*

Returning to Eq. (2.11) σ_j is the integrated cross section for Raman scattering and includes scattering in all directions. The integrated cross section σ_j is "integrated" in two respects: over all directions from the sample, and over the wavelength range of an entire Raman band. Measurement of P_R in Eq. (2.11) would require light collection over all 4π steradians around the sample and integration over the entire Raman band. In practice, only a relatively small range of solid angle is observed, in one of several scattering directions from the sample. Thus, it is more useful to define the differential Raman cross section, $d\sigma_j/d\Omega$, where Ω represents the solid angle of collection. We will use the symbol β for this differential cross section, as in Eq. (2.15):

$$\beta(\text{cm}^2 \text{ molecule}^{-1} \text{ sr}^{-1}) = \frac{d\sigma_j}{d\Omega} \tag{2.15}$$

The symbol β is used here rather than the more common $d\sigma_j/d\Omega$ to explicitly distinguish β from the integrated σ_j and from the cross section differentiated both with respect to observation angle and with respect to wavelength (β', defined below). β° is analogous to σ_j° and denotes the differential cross section with units of centimeters to the sixth power per molecule per steradian.

Theoretical curves for β calculated from Eq. (2.10), (2.14) and (2.15) are shown in Figure 2.3, with both based on $\beta^\circ = 5.05 \times 10^{-48}$ cm^6 sr^{-1} molecule^{-1} for N_2 (10). Experimentally observed cross sections are included in Figure 2.3 for the case where both laser and Raman intensities are measured in watts. The difference between the cross sections determined from Eq. (2.9) and (2.14) is 9 per cent at 350 nm and 27 per cent at 900 nm. This difference can be significant when comparing results with different laser wavelengths or when measuring the magnitude of resonance effects (11). If the laser wavelength is far from any absorption bands of the sample and resonance effects are negligible, Eq. (2.14) and (2.15) may be used to adjust the cross section for one laser wavelength to another. A curve of the ratio of the two cross sections is also shown in Figure 2.3, illustrating that the difference is larger at longer wavelengths. However, many analytical applications are based on a cross section observed empirically for a given laser wavelength, and the underlying frequency dependence is not important.

β is often a strong function of the angle of observation and polarization, and those parameters should be specified for a particular reported value of β. Using the classical description of Raman scattering, the induced dipole will radiate more strongly in a direction perpendicular to its axis, leading to a higher β for observation from the dipole "side" rather than "end." Referring to Figure 2.1, classical theory predicts that minimal scattering will occur in the direction of the y axis if the incident light is polarized parallel to the y axis as shown. So β measured with the spectrometer along the y axis is

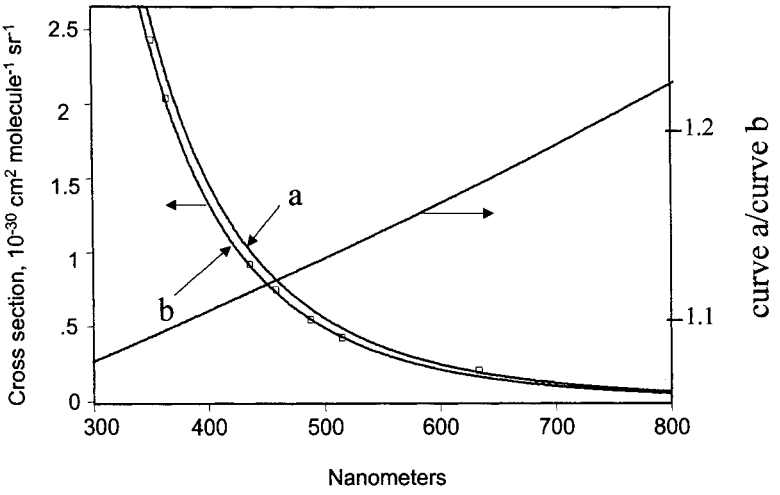

Figure 2.3. Differential Raman cross section, β, for N_2 gas calculated from Eqs. (2.10) and (2.15) (curve b) and (2.14) and (2.15) (curve a), with $\beta^\circ = 5.05 \times 10^{-48}$ cm^6 sr^{-1} molecule^{-1}. Squares indicated experimental results for conditions appropriate to curve b. An overlay of the ratio of curve a to curve b is plotted as well, illustrating the greater difference between the two at longer laser wavelength.

near zero. For any observation point in the xz plane, however, β is finite and independent of the observation angle relative to the incident beam. This is exactly the behavior observed for "polarized" vibrations, where the scattering intensity (and β) along the axis of the laser electric field vector is near zero. The practical consequence of this anisotropic scattering is the necessity to define and reproduce scattering geometry for a given experimental procedure, and to be aware of scattering geometry when comparing results from different laboratories. The use of the integrated cross section σ (in centimeters squared per molecule) avoids the variation of β (in square centimeters per molecule per steradian) with direction but is experimentally cumbersome. For nearly all practical applications, β is the more useful form of the cross section, but it must be remembered that β depends on observation geometry.

Note that σ_j is also integrated over the Raman bandwidth, as is β. However, the usual representation of a spectrum is scattering signal vs. Raman shift, $\bar{\nu}_j$, and the signal depends on β at a particular Raman shift. We will define β' to account for this fact, with:

$$\beta'(\text{cm}^2 \text{ molecule}^{-1} \text{ sr}^{-1} \text{ wavenumber}^{-1}) = \frac{\delta^2 \sigma_j}{\delta\Omega \, \delta(\Delta\bar{\nu})} \tag{2.16}$$

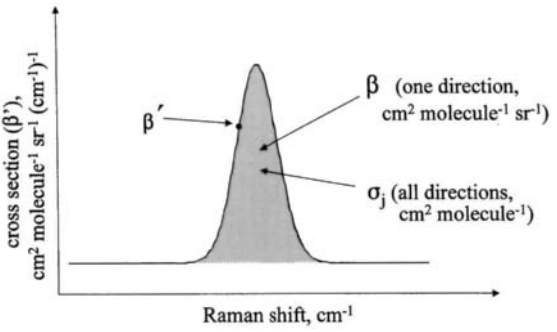

Figure 2.4. Definitions of β, β', and σ_R for to a generic Raman band. β' is the cross section at a particular Raman shift and direction; β is integrated over the bandwidth, and σ_j is integrated over both bandwidth and direction.

Note that β' depends both on observation direction and on Raman shift. Figure 2.4 shows the relationships between β, β', and σ_j for a hypothetical Raman band. In a real measurement, the scattering over a range of angles (those within the acceptance cone of the spectrometer) and a range of $\overline{\nu}$ (those within the spectrometer's instrumental linewidth, ILW). As we will see, these facts can lead to some confusion when comparing spectra from different instruments and/or geometries. A particularly thorny consequence is the dependence of the spectrum on ILW, which can change the value of β' and the peak height of a Raman feature. For the common case of a dispersive spectrometer with an array detector, β' can depend on the relative magnitude of the Raman bandwidth, the entrance slit width, and the detector pixel width. Fortunately, these complications can be accommodated fairly simply with proper calibration techniques (Chapter 10). As noted earlier, the most commonly reported form of the cross section is β, accompanied by a statement of the observation and excitation geometry.

2.3. MAGNITUDE OF RAMAN CROSS SECTIONS

Raman cross sections are commonly determined by quantitatively comparing the Raman signal for an unknown to that for a standard with known cross section. The standard cross sections were determined by comparison to some radiometric standard, with painstaking attention to collection variables and geometry. Table 2.2 lists several cross sections determined for some common materials. When available, the frequency–independent cross section (σ_j°) defined by Eq. (2.9) is listed. The cross sections in Table 2.1 show good agreement among several labs and are considered very reliable, provided the conditions are fixed.

Table 2.2. Absolute Raman Cross Section[a]

Sample	Laser λ (nm)	β^b(cm^2 sr^{-1} molecule^{-1}, $\times 10^{30}$)	β^c(cm^6 sr^{-1} molecule, $\times 10^{48}$)	Reference[c]
Benzene liquid, 992 cm^{-1}	647	10.6		14
	514.5	30.6		12
	514.5	28.6		13
	514.5	27.0	235	10
	488	36.5		12
	441.6	44.6		12
	407	64		23
	351	160		23
	337	392	580	10
	325	440		12
	351–694		259 ± 66[d]	14
Benzene liquid, 3060 cm^{-1}	514.5	45.3		12
	488.0	57.1		12
	441.6	68.3		12
	325.0	477		12
Benzene gas, 992 cm^{-1}	514.5	7.0	61	10
Cyclohexane liquid, 802 cm^{-1}	647	2.1		23
	514.5	5.2		23
	488	9.06		25
	407	17.6		23
Cyclohexane liquid, 1028 cm^{-1}	448	5.37		25
Cyclohexane liquid, 1267 cm^{-1}	488	4.61		25
Cyclohexane liquid, 1444 cm^{-1}	488	6.17		25
Cyclohexane liquid, all C-H	647	12.7		23
	514.5	43		23
	488	75.2		25
	407	127		23
Cacodylate, 608 and 628 cm^{-1}	647	3.2		23
	514.5	14.3		23
	407	39		23
N_2 gas 2331 cm^{-1}	514.5	0.43	5.01	10
	488.0	0.54	5.06	10
	457.9	0.74	5.1	10
	351.1	2.43	5.2	10
O_2 gas 1555 cm^{-1}	514.5	0.58	5.0	10
CH_3Cl gas, 725 cm^{-1}	514.5	1.73	14.1[a]	10

(*continued next page*)

Table 2.2. (*continued*)

Sample	Laser λ (nm)	β^b(cm^2 sr^{-1} molecule^{-1}, $\times 10^{30}$)	β°(cm^6 sr^{-1} molecule, $\times 10^{48}$)	Reference[c]
CH_2Cl_2 gas, 2997 cm^{-1}	546.1	1.71	23.4[a]	10
CH_2Cl_2 gas, 713 cm^{-1}	546.1	2.29	18.6[a]	10
$CHCl_3$ gas				
3032 cm^{-1}	514.5	0.59	8.2[e]	10
1221 cm^{-1}	514.5	0.19	1.7[e]	10
758 cm^{-1}	514.5	1.1	8.7[e]	10
667 cm^{-1}	514.5	1.7	13.8[e]	10
364 cm^{-1}	514.5	1.7	12.6[e]	10
261 cm^{-1}	514.5	1.8	13.3[e]	10
CCl_4 gas				
459 cm^{-1}	514.5	4.7	36.4	10
221 cm^{-1}	514.5	2.4	17.9	10
$CHCl_3$ liquid[b]				
3032 cm^{-1}	514.5	4.4		f
758 cm^{-1}	514.5	3.2		f
667 cm^{-1}	514.5	6.6		f
364 cm^{-1}	514.5	6.3		f
261 cm^{-1}	514.5	7.0		f

[a]Both parallel and perpendicular polarizations observed.
[b]Based on classical $\bar{\nu}^4$ dependence. May be converted to dependence of Eq. (2.14) by multiplying by $\nu_0/(\nu_0 - \nu_j)$.
[c]Reference 10 contains many more gas-phase cross sections. β° values listed here are averaged when Reference 10 lists several values. Spatially integrated cross sections from reference 23 were divided by 4π.
[d]Mean and standard deviation of 19 values from Reference 14.
[e]β° based on 546.1 nm excitation, β calculated for 514.5 using ν^4 dependence.
[f]Determined from average of gas–phase β° values from p. 151 of Reference 10, multiplied by average of liquid/gas ratios on p. 162.

Many more cross sections in the literature were determined by comparison of Raman intensity of an "unknown" to that from one of the standards in Table 2.2. Provided the measurement conditions are the same and the spectrometer response function is known, the ratio of the peak areas of two bands adjusted for relative number density will equal the ratio of cross sections. One such procedure is described in Chapter 10, but cross sections for a variety of samples are listed in Table 2.3. These values were not critically evaluated for accuracy and should not be considered as accurate as those in Table 2.3. Nevertheless, they are useful for observing comparative magnitudes and trends.

Cross sections from different labs often show significant (30 to 50 per cent) variations, even when experimental conditions are very similar.

Since the Raman scattering intensity and the observed Raman signal depend directly on β, Table 2.3 provides a useful indication of the expected range of Raman signals compared to absorption and fluorescence. Raman cross sections are nearly always very small compared to these competing processes. Normal Raman scattering* cross sections are often 6 to 8 orders of magnitude smaller than fluorescence cross sections, leading to the common problem of fluorescence interference. Many aspects of experimental design are dictated by the need to reduce fluorescence. Notice that the "normal" Raman scatterers in Table 2.3 have a fairly narrow range of β values, about 2 orders of magnitude.

Tables 2.2 and 2.3 provide some illustrations of factors controlling the magnitude of β. For example:

1. β is larger for molecules with extended π systems since the electrons are more easily polarized. The increase in β for the series benzene–naphthalent–anthracene is a factor of about 20 for the strongest Raman modes of each molecule (Table 2.3).
2. Molecules with only single C—H, C—O, and C—C bonds (e.g., glucose) generally have small cross sections.
3. Molecules containing large or electron-rich aroms, such as sulfur or iodine, often have high β. The S—S bond stretch in peptides and the CCl_4 symmetric stretch are examples.
4. Small molecules without electron-rich atoms, such as H_2, CO, and N_2 have small cross sections.
5. Multiple bond stretches generally have high β values, which are higher still if they are conjugated with another π system.
6. Very large increases in β can occur if resonant (e.g., β-carotene) or preresonant [e.g., bis(2-methyl styryl) benzene] effects are present. In addition, cross sections in solutions often differ from the neat liquid.
7. Cross sections in liquids are generally higher by factors of 2 to 4 than those for the same vibration in gases, due to the local field effects (10,11). In addition, cross sections in solution often differ from those of pure liquids.

It was established long ago that resonance effects can greatly increase the cross section when the incident light approaches an electronic absorption of the sample molecule. β-carotene is one of the strongest resonance-enhanced molecules, with a 10^5 enhancement in cross section when the laser wavelength

* "Normal Raman" will be used to describe scattering without resonance or surface enhancement. The older literature often uses the term "spontaneous Raman."

Table 2.3. Relative Raman Cross Sections

Sample[a]	Laser λ (nm)	Raman Shift (cm^{-1})	$\beta \times 10^{30}$[b,c] (cm^2 molecule^{-1} sr^{-1})	Reference
SO_4^{-2} in H_2O (as Na_2SO_4)	514.5	981	9.9	17
CH_3CN	514.5	918	1.01	16,17
CH_3CN	514.5	2249	8.2	16,17
H_2O, liquid	514.5	1595	0.11	19
ClO_4^- in H_2O	514.5	932	12.7	17
Cyclohexane, neat	514.5	802	8.3	10
Cyclohexane in benzene	514.5	801	11.9	18
Glucose in H_20	514.5	1126 cm^{-1}	5.6	19
1.4 Bis-(2-methylstyryl) benzene in benzene	514.5	1593	6200	18
1.4 Bis-(2-methylstyryl) benzene in benzene	514.5	1177	1900	18
β-Carotene in benzene	514.5	1520	1.1×10^7	18
β-Carotene in benzene	514.5	1005	2.2×10^6	18
Benzene, neat	514.5	992	28.6	18
Naphthalene in benzene	514.5	1382	82	13
Anthracene in benzene	514.5	1402	540	18
$C_6H_5NO_2$	488	1345	10	18
H_2 (gas)	488	4161	7.9	10
CO (gas)	488	2145	3.3	20
$C_6H_5CH_3$	514.5	1002	13.8	20
$C_6H_5NO_2$	514.5	1345	89	10
CCl_4	514.5	459	16.9	10
1% C_6H_6 in CH_3 CN	514.5	992	19.2	11
	220	992	15,200	11
$CHCl_3$ liquid	785.0	3032	0.58	d
	785.0	758	0.57	d
	785.0	667	1.19	d
	785.0	364	1.14	d
	785.0	261	1.29	d
Diamond	514.5	1332	3.4[e]	15
Absorption $\epsilon = 1000$ M^{-1} cm^{-1}			2×10^{-18} cm^2 molecule^{-1}	
Fluorescence $\epsilon = 1000$, quantum yield = 0.01			2×10^{-19} cm^2 molecule^{-1} sr^{-1}	

[a]Sample and solvent (where applicable). Samples are pure liquids or solutions unless stated otherwise.

[b]Determined by comparison to benzene 992 cm^{-1} band, acquired under the same conditions.

[c]$\beta = \beta_j^e[\bar{\nu}_0(\bar{\nu}_0 - \bar{\nu}_j)^3]$. The results reported used photon counting, so the $\bar{\nu}_0(\bar{\nu}_0 - \bar{\nu}_j)^3$ factor applies.

[d]Calculated from values listed in Table 2.2.

[e]Calculated from Reference 15, as cm^2 sr^{-1} $atom^{-1}$.

is near the absorption maximum of 482 nm (21). Preresonant scattering occurs when the laser wavelength approaches an absorption maximum but is not yet within the absorption band. A pragmatic definition of preresonant scattering is when the cross section begins to deviate from the ν^4 dependence expected for normal scattering (10,11). However, the boundaries between normal, preresonant, and resonance Raman are often not well defined. The importance of resonance effects in analytical applications is the large β they generate, and the ability to select a laser wavelength which causes (or avoids) resonance scattering. In some cases, resonance effects can be used to selectively observe a particular scatterer in a complex matrix.

There have been extensive theoretical treatments of resonant and preresonant Raman scattering, which reveal the important factors affecting the magnitude of β. However, it is difficult to theoretically predict β from molecular structure, and the theory is normally used to predict laser frequency dependence and deduce the relationship between resonance Raman spectra and molecular structure. Albrecht and Hutley (22) derived an expression for the laser frequency dependence of the cross section:

$$\beta = k\bar{\nu}_0(\bar{\nu}_0 - \bar{\nu}_j)^3 \left[\frac{\bar{\nu}_P^2 + \bar{\nu}_0^2}{(\bar{\nu}_P^2 - \bar{\nu}_0^2)^2}\right]^2 \tag{2.17}$$

where ν_P is the frequency of an electronic transition in the sample molecule, and k is a constant. When ν_0 is distinct from ν_P, the term in brackets changes slowly with ν_0, and the usual ν^4 dependence of β is observed. However, as ν_0 approaches ν_P, β increases more quickly than expected from ν^4, and the system is considered to be preresonant. Several experimental reports support the validity of Eq. (2.17), based on the dependence of the cross section on laser wavelength (11,12,23,24). For example, a fit of observed cross sections for the cyclohexane 802 cm^{-1} band for excitation wavelengths from 239 to 647 nm to Eq. (2.7) yielded $k = 7.2 \times 10^{-27}$ cm^2 $molecule^{-1}$ sr^{-1} and $\bar{\nu}_P = 115,000$ cm^{-1} (23).

The electronic transition associated with ν_P need not be identical to an absorption observed in a visible absorption spectrum; ν_P could lie beyond the usual UV–Vis wavelength range (e.g., at 180 nm) or be a shoulder on a larger absorption band. An important aspect of resonance Raman spectroscopy is the association between enhanced Raman modes and the chromophore associated with ν_P. The enhanced vibrations are those involving the atoms and bands in the chromophore, and vibrations originating in distant parts of the molecule are not enhanced. This feature can be very useful analytically since resonance enhancement can amplify scattering from the vibrations of interest above a possibly complex background. For example, the resonance Raman scattering from the heme group in a protein can be observed with minimal interference

from the remainder of the molecule, if the laser wavelength is close to the absorption of the heme group at ~410 nm.

2.4. RAMAN SCATTERING INTENSITY

Returning now to expressions of Raman intensity, Eq. (2.11) may be restated in terms of β:

$$P_R = P_0 \beta D \, dz \tag{2.18}$$

where P_R is now the Raman scattering in a steradian of collection solid angle, rather than total scattering in all directions. It is often convenient to express the incident laser light in terms of power density (P_D, photons per square centimeter per second) rather than power (photons per second), in which case P_R is generated by a beam with a 1 cm^2 cross section and a path length of dz:

$$P_R \text{ (photons cm}^{-2} \text{ sr}^{-1} \text{ sec}^{-1}) = P_D \beta D \, dz \tag{2.19}$$

Note that for a 1 cm^2 beam, $D\,dz$ equals the total number of illuminated molecules. There are many experiments where the total beam area cannot be observed, in which case P_R is more usually stated as specific intensity, L:

$$L \text{ (photons sr}^{-1} \text{ cm}^{-2} \text{ sec}^{-1}) = P_D \beta D K \tag{2.20}$$

Specific intensity is sometimes referred to as *radiance*, although neither term is used consistently in the literature. If one considers a sample area that is evenly illuminated by some power density P_D, then L is the number of Raman photons scattered from 1 cm^2 of the sample, into 1 steradian of solid angle in 1 second; K is used to denote a geometric factor that depends on observation geometry. Its significance is illustrated in Figure 2.5, and it will be discussed in detail in Chapter 6. For the case of 180° backscattering geometry with a thin sample, K is the sample depth observed by the spectrometer, in centimeters. Figure 2.5 illustrates the specific intensity for a large beam incident on a sample and Raman observation at ~180°; A_D and Ω_D are the sampled area and collection angle, defined in Chapter 3.

The specific intensity is an important quantity because it depends mainly on sample (β, D) and laser (P_D) variables and not on spectrometer parameters such as collection angle, quantum efficiently, and the like; L indicates "what the spectrometer has to work with" while collecting and detecting scattered light. If we consider the example of a clear sample and 180° backscattered geometry with $K = 0.1$ cm (as in Fig. 2.5), then L can be calculated for a variety of samples. Table 2.4 lists several specific intensities for samples of

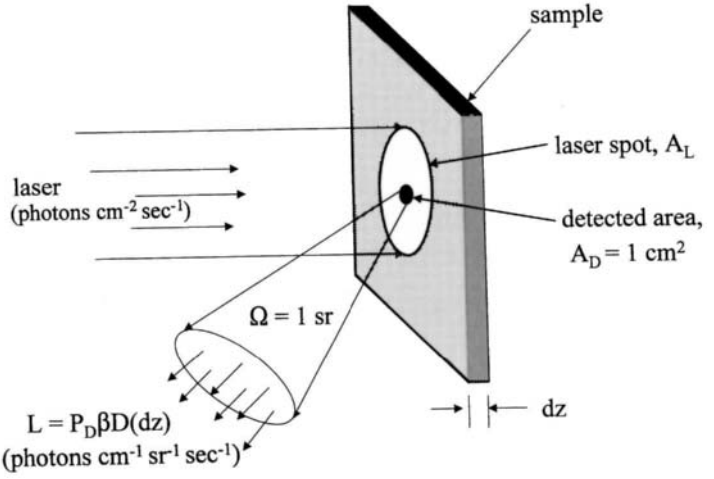

Figure 2.5. Schematic representation of the specific intensity, L, where L is the photons/sec scattered by a 1 cm^2 area (A_D) into a 1 steradian solid angle (Ω), assuming constant power density over the illuminated area.

Table 2.4. Some Specific Intensities for 180° Geometry,[a] 514.5 nm laser

Sample	L^b photons cm^{-2} s^{-1} sr^{-1}
Neat benzene (992 cm^{-1})	1.0×10^{13}
0.10 M SO_4^{-2}(981 cm^{-1})	7.5×10^{10}
10^{-3} M glucose in water (1126 cm^{-1})	1.7×10^{8}
H_2O neat (1600 cm^{-1})	1.9×10^{11}
10^{-6} M β-carotene (1520 cm^{-1})	3.3×10^{11}
Benzene monolayer (1.0×10^{-10} mol/cm^2)	8.9×10^{5}

[a]100 mW of 514.5 nm light in a 0.05 × 1 mm area ($P_D = 5.2 \times 10^{20}$ photons cm^{-2} s^{-1}), K = 0.1 cm.
[b]Integrated over spectral bandwidth, calculated from Eqn. (2.20).

various types. As will be shown in Chapter 3, the Raman signal of analytical value ultimately depends on how well the spectrometer collects and detects light from the specific intensity at the sample.

Obviously, β and D are characteristics of the sample and cannot readily be varied by the analyst. The laser power density can be increased, however, to a limit determined by the available laser or by sample radiation damage. A longer path length through the sample can increase scattering provided the longer path length can be observed by the spectrometer. Chapter 6 will present

some cases where path length is a major factor, but the main point here is the limitations imposed on the Raman signal by the product $P_D\beta_D$. Ultimately, the upper limit on Raman signal, even for a 100 per cent efficient spectrometer, is governed by variables of the sample (β and D) and the maximum value of P_D allowed by sample damage.

A further comment is useful at this point, on the modifications to Eq. (2.19) and (2.20) for "surface" vs. "volume" samples. If the sample is very thin relative to the depth sampled by the spectrometer, D may be expressed as D_s (moles per square centimeter), and K set to 1. Equation (2.18) becomes

$$P_R = P_O\beta D_S \tag{2.21}$$

and (2.20) becomes

$$L = P_D\beta D_S \tag{2.22}$$

When dealing with volume scatterers (e.g., clear liquids), Eqs. (2.18) and (2.20) apply to thin slices of the sample but must be integrated over the path length to yield total scattering. These cases will be discussed in Chapters 3 and 6. Many texts use the term *scattering volume* to indicate the sample volume actually monitored by the spectrometer.

As a final note of practical importance, the L values in Table 2.4 cover a wide range for a single laser power (100 mW) and could cover an even wider range for commonly used laser powers (1 to 5000 mW). However, even very weak scattering, such as that from a single molecular layer of benzene, generates about 10^6 photons cm^{-2} sr^{-1} sec^{-1}. Modern instrumentation permits single photon counting, and signals much smaller than 10^6 photons are observable, even if only a fraction (say, 0.1 per cent) of the available specific intensity is collected and detected. We will see that modern Raman measurements are rarely limited by the size of the signal but rather are more dependent on noise and background. In the absence of background and noise, observation of very low light levels is straightforward with modern equipment. Success in acquiring Raman spectra is often more dependent on reducing noise (from the detector, laser, etc.) and background (from fluorescence, stray light, solvent, etc.) than it is on generating sufficient signal.

REFERENCES

1. H. A. Szymanski, ed., *Raman Spectroscopy, Theory and Practice*, Vol. 1 and 2, Plenum, New York, 1967.
2. D. A. Long, *Raman Spectroscopy*, McGraw-Hill, New York, 1977.
3. J. G. Graselli and B. Bulkin, *Analytical Raman Spectroscopy*, Wiley, New York, 1991, Chapter 1.

4. J. Tang and A. C. Albrecht, in H. A. Szymanski, ed., *Raman Spectroscopy, Theory and Practice*, Vol. 2, Plenum, New York, 1967, Chapter 2.
5. A. Weber, ed. *Raman Spectroscopy of Gases and Liquids, Topics in Current Physics*, Vol. 11, Springer, New York, 1979.
6. B. Schrader, *Raman/Infrared Atlas of Organic Compounds,* 2nd ed., VCH, New York, 1989.
7. F. R. Dollish, W. G. Fateley, and F. F. Bentley, *Characteristic Raman Frequencies of Organic Compounds,* Wiley, New York, 1974.
8. D. Lin-Vien, N. Colthup, W. G. Fateley, and J. Grasselli, *Handbook of Infrared and Raman Characteristic Frequencies of Organic Molecules*, Academic Press, New York, 1991.
9. K. Nakamoto, *Infrared and Raman Spectra of Inorganic and Coordination Compounds*, 2nd ed., Wiley, New York, 1996.
10. H. W. Schrötter and H. W. Klöckner, A. Weber, ed., *Raman Spectroscopy of Gases and Liquids, Topics in Current Physics*, Vol. 11, Springer, New York, 1979, Chapter 4.
11. S. A. Asher and C. R. Johnson, *J. Phys. Chem.*, **89**, 1375, (1985).
12. K. T. Schomacker, J. K. Delaney, and P. M. Champion, *J. Chem. Phys.*, **85**, 4240 (1986).
13. N. Abe, M. Wakayama, and M. Ito, *J. Raman, Spectra.*, **6**, 38 (1977).
14. C. J. Petty, P. J. Hendra, and T. Jawhari, *Spectrochim. Acta*, **47A**, 1189 (1991).
15. N. Wada and S. A. Solin, *Physica*, **105B**, 353 (1981).
16. J. M. Dudik, C. R. Johnson, and S. A. Asher, *Chem. Phys.*, **82**, 1732 (1985).
17. M. A. Fryling, PhD. Dissertation, The Ohio State University, 1994.
18. M. R. Kagan, PhD. Dissertation, The Ohio State University, 1996.
19. Kenneth Ray, The Ohio State University, unpublished data.
20. R. P. Van Duyne, in C. B. Moore, ed., *Chemical and Biological Applications of Lasers*, Vol. IV, Academic Press, New York, 1979.
21. S. Saito, M. Tasami, and C. H. Eugster, *J. Raman Spec.*, **14**, 299, (1983).
22. A. C. Albrecht and M. C. Hutley, *J. Chem. Phys.*, **55**, 4438 (71).
23. M. O. Trulson and R. A. Mathies, *J. Chem. Phys.*, **84**, 2068 (1986). Spatially integrated cross sections were divided by 4π to yield β values in Table 2.3.
24. B. Li and A. B. Myers, *J. Phys. Chem.*, **94**, 4051 (1990).
25. J. R. Nestor and E. R. Lippincott, *J. Raman Spec.*, **1**, 305 (1973).

Raman Spectroscopy for Chemical Analysis. Richard L. McCreery

ISBN: 0-471-25287-5

CHAPTER

3

COLLECTION AND DETECTION OF RAMAN SCATTERING

3.1. SIGNAL MAGNITUDE AND COLLECTION FUNCTION

Equations (2.19) and (2.20) permit prediction of the overall Raman scattering, P_R, and the specific intensity, L. These quantities are functions of the sample and laser power and may be varied within the limits discussed in Chapter 2. In order to produce an analytical signal, some fraction of the Raman scattered light must be collected and detected. Except for increasing laser power to a limit imposed by sample damage, there is not much an analyst can do to increase either P_R or L for a given sample. However, there has been an enormous improvement in our ability to collect and detect Raman light in recent years, driven mainly by detector technology, Fourier transform (FT)–Raman, and novel optics. In fact, technological developments in the form of FT-Raman, low-noise multichannel detectors, and compact, efficient spectrometers have been essential to the rapid growth of Raman spectroscopy applications since approximately 1985. Because Raman instrumentation development has been so dramatic, many discussions of Raman spectrometer design are obsolete, and one should rely on relatively recent treatments of the subject (1–4). Since collection and detection technology is critical to the rebirth of Raman spectroscopy as a technique for chemical analysis, considerable attention will be paid to understanding the factors that determine the ability to transform the scattering magnitude given by Eq. (2.19) into a usable Raman signal. In order to relate instrument response to scattering magnitude, our objective is to determine the fraction of Raman scattered light producing signal, stated in terms of spectrometer design parameters such as transmission, $f/\#$, and the like.* Restricting the discussion to the measurement of a single Raman shift increment (so-called single-channel operation), we may define a collection function C, with units of cm^2 sr e^- $photon^{-1}$ (electrons steradians, square centimeters per photon) such that

$$S_a(e^-) = L_a C t_s \tag{3.1}$$

* The *aperture ratio* or *f number* will be designated by $f/\#$, with a specific case stated as $f/4.5$, $f/2$, etc.

where S_a is the signal due to the analyte of interest, expressed in electrons, and L_a is the specific intensity for a Raman band of a particular analyte. Most modern Raman spectrometers operate in "single-photon" mode, meaning that photons incident on the detector are converted to electrons that are counted by one of several methods; t_s is the measurement time for the particular Raman shift value being observed.† A schematic representation of the collection process is shown in Figure 3.1 for ~180° backscattered geometry. We will also define $\dot{S}_a$ as the rate of electron accumulation:

$$\dot{S}_a(\mathrm{e^- sec^{-1}}) = L_a C \tag{3.2}$$

It is instructive to maintain a clear conceptual distinction between experimental factors that determine L and those that determine C; L is a function of the sample and laser power (and, to some extent, the collection geometry), while C depends on collection and detection characteristics. For a given specific intensity, a larger value of C yields a larger signal.

Unfortunately, any discussion of Raman signal dependence on spectrometer variables is complicated by the many different ways experiments can be performed. Laser spot size, spectrometer slit area, depth of field, and several other variables affect the magnitude of C, and, in some cases, the way it

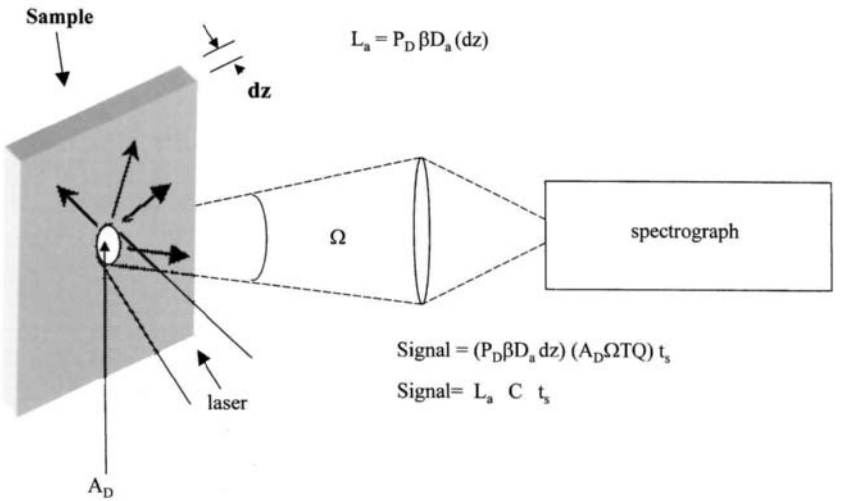

Figure 3.1. Schematic of the collection variables for ~180° backscattering. L_a indicates specific intensity, C is collection function.

† t_s refers to single-channel measurement time, as opposed to t_M, the total acquisition time, which will be defined later.

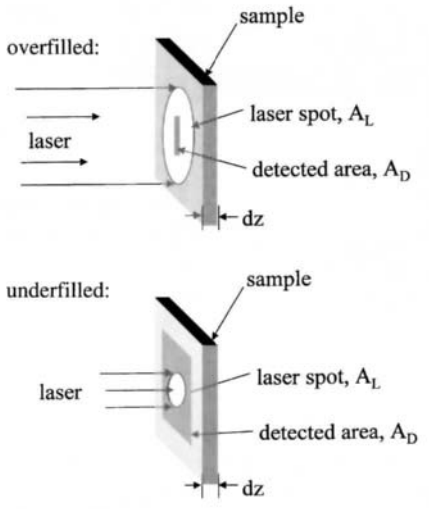

Figure 3.2. Relationship of area illuminated by laser (A_L) to area detected by spectrometer (A_D).

is defined (5,6). For example, the spectrometer can be "underfilled," which means that the entire cross section of the region illuminated by the laser can enter the spectrometer entrance aperture (Fig. 3.2, lower drawing). In this case, many authors use Eq. (2.18) to describe the Raman scattering, and laser power is more convenient to use than power density. Alternatively, the spectrometer may be "overfilled," meaning that the scattering is emanating from a region too large to be collected by the spectrometer (Fig. 3.2, upper drawing). In this case, Eq. (2.19) is more convenient, with the laser input in terms of power density. To the extent possible, we will unify these two common approaches to arrive at a single expression for the total signal. We will see in Chapter 10 that these complexities can be accommodated during calibration with proper experimental design.

3.2. INSTRUMENTAL VARIABLES COMPRISING THE COLLECTION FUNCTION

In order to relate S_a to specific spectrometer variables such as $f/\#$, transmission, and the like, we must define C in terms of these variables. Equation (3.3) is such a definition, with the four variables explained in succeeding paragraphs:

$$C(\text{cm}^2 \text{ sr e photon}^{-1}) = A_D \Omega_D T Q \tag{3.3}$$

Here A_D is the sample area monitored by the spectrometer and collection optics. For a fixed L, the signal will obviously increase if more scattering area is monitored. Also A_D is usually determined by a limiting aperture in the spectrometer, such as the entrance slit or detector area. Since some magnification often occurs between the sample and the spectrometer, it is important to define A_D as the area observed at the sample. As will be shown later, A_D can vary greatly for different spectrometers, with a corresponding effect on signal size. In the end, the Raman signal is proportional to the sample area, which is both illuminated by the laser and observed by the collection optics.

In Eq. (3.3) Ω_D is the solid angle in steradians (sr) collected by the spectrometer and transmitted into the wavelength analyzer. It is useful to note that Ω_D varies with the square of the $f/\#$ of the optics at the sample position. Furthermore, Ω_D is defined specifically as the collection solid angle at the sample. As shown in Figure 3.3, Ω varies through the optical system, as do the cross-sectional area and the local $f/\#$. Ω_D is related to $f/\#$ by Eq. (3.4), with $(f/\#)_D$ being that measured at the sample:

$$\Omega_D = \frac{\pi}{4(f/\#)_D^2} \tag{3.4}$$

In Eq. (3.3) T is transmission, equal to the fraction of light within the A_D and Ω_D monitored by the spectrometer that reaches the detector. It consists of at least two factors, the transmission of the collection and focusing optics and the transmission within the spectrometer itself. The transmission of the collection optics incorporates any losses from reflection of lenses, mirrors, or a sample cell, while the transmission of the spectrometer incorporates grating efficiency, mirror reflectivity, beamsplitter losses, and the like. In addition, T includes losses from optical filters that may be used between the collection optics and the spectrometer; Q [Eq. (3.3)] is the quantum efficiency (e^- photon^{-1}), the fraction of photons reaching the detector producing an electron, which is subsequently counted.

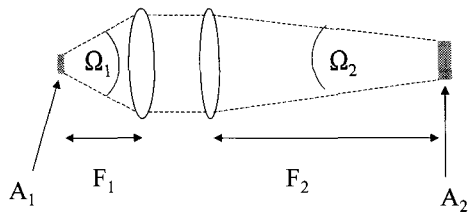

Figure 3.3. Example of constancy of $A\Omega$ product during magnification. A_2 is larger than A_1 by the factor $(F_2/F_1)^2$, but Ω_2 is smaller than Ω_1 by the same factor.

All four variables comprising C in Eq. (3.3) may vary over significant ranges, yielding widely varying signals for a given specific intensity. In addition, L itself can vary significantly for a given sample, due mainly to variations in focal spot size and depth of field. Considering a given L for the moment, the magnitude of C indicates signal size for a given spectrometer configuration; A_D may range from $\sim 1\ \mu m^2$ for a microprobe to $\sim 1\ mm^2$ for an FT-Raman system, a factor of 10^6 in area; Ω_D typically ranges from 0.05 sr ($f/4$ collection) to 0.8 sr ($f/1$ collection), while T may be as small as 0.05 to as much as 0.5; and Q could be <0.10 for a photomultiplier to as much as 0.90 for a changed-coupled device (CCD) or germanium detector operating at its optimum wavelength.

Table 3.1 illustrates the effects of these variations on C for several common configurations. The "spectrometers" should be considered generic and hypothetical but are chosen to approximate real systems. Recall that the value of C indicates the relative signal magnitude for a given sample and power density. Table 3.1 does not incorporate the multichannel advantage so important to many modern spectrometers, but it does illustrate several points. First, lower $f/\#$ strongly affects Ω_D and therefore C. Second, single-stage spectrometers with low $f/\#$ provide a large gain in C relative to multistage spectrometers. Third, spectrometer 4 in Table 3.1 is approximately the current state-of-the-art for dispersive systems and can collect at $f/1.4$ with 50 per cent transmission. Fourth, the FT-Raman systems are quite efficient due to large A_D and Q.

It is instructive to use Eq. (3.2) to estimate what fraction of the total Raman photons are detected in a typical experiment. Consider neat benzene in a 0.10 cm-deep cell, with an L of 1.0×10^{13} photons cm^{-2} see^{-1} sr^{-1} (Table 2.4).

Table 3.1. Typical Values of A_D, Ω_D, T, and Q

	Spectrometer[a]	A_D^b, (cm^2)	Ω_D, (sr)	T	Q	$C \times 10^5$ cm^2 sr e photon^{-1}
1.	Double, PMT[c]	0.004 (0.02 × 0.2)	0.4 ($f/2$)	0.1	0.15	2.4
2.	Single, PMT	0.002 (0.01 × 0.2)	0.05 ($f/4$)	0.3	0.15	0.45
3.	Single, CCD	0.002	0.05 ($f/4$)	0.3	0.5	1.5
4.	Single, CCD	0.002	0.40 ($f/1.4$)	0.5	0.8	32
5.	Triple, CCD	0.002	0.4 ($f/2$)	0.05	0.5	2.0
6.	FT-Raman	0.01 (1 mm spot)	0.78 ($f/1$)	0.1	0.7	55
7.	MCFT[d]	0.04 (2 mm spot)	~0.4	0.1	0.5	80

[a]"Single," "double," "triple" refer to dispersive spectrometer type, PMT (photomultiplier tube), and CCD (charge-coupled device) refer to the detector.

[b]Parentheses indicate A_D geometry.

[c]Photomultiplier tube.

[d]Multichannel Fourier transform spectrometer, described in Chapter 9.

For a 0.1 × 2 mm area, and scattering into 4π sr, this yields 2.5×10^{11} photons sec^{-1} into the entire sphere around the sample. For the case of spectrometer 4 in Table 3.1, Eq. (3.2) predicts that 3.2×10^9 photon/sec, or 1.3 per cent of the total scattering, will be collected. Even with a state-of-the-art spectrometer, a relatively small fraction of the available Raman photons are detected. This observation is due to the fact that even with $f/1$ optics, only the scattered photons in about 1 out of 4π steradians are monitored, and, of those, many are lost in the spectrometer and detector. This issue will be considered in more detail in Chapter 8.

Returning to the general expression for Raman signal, Eq. (3.1), we can observe that C represents the fraction of the specific intensity that results in detected signal. Now we can substitute C from Eq. (3.3) and L from Eq. (2.20) into (3.1) to yield (3.5) and (3.6):

$$S(e^-) = LA_D\Omega_D TQt_s \tag{3.5}$$

$$S(e^-) = (P_D\beta DK)(A_D\Omega_D TQ)t_s) \tag{3.6}$$

Equation (3.6) is quite useful for estimating the effects of spectrometer or geometric variables on signal, and we will often modify it for particular common configurations. If we define A_L as the cross sectional area of the laser beam at the sample, then $P_D = P_0/A_L$, where P_0 is laser power in photons per second. Substituting for P_D in Eq. (3.6) yields

$$S = P_0\beta DK\frac{A_D}{A_L}\Omega_D TQt_s \tag{3.7}$$

Equations (3.6) and (3.7) may be applied to the underfilled and overfilled cases, provided care is used in defining A_D and A_L. For the underfilled case, $A_D = A_L$ and

$$S = (P_0\beta DK)\Omega TQt_s \tag{3.8}$$

Note that A_D is determined by the laser spot size rather than the spectrometer aperture and no longer affects the signal magnitude for the underfilled case. For this case, changes in power density from variations in laser beam diameter are exactly compensated by variations in the number of molecules in the beam. A practical consequence of this observation is the relatively strong signal observed with a Raman microprobe (Chapter 11) in which a very small quantity of sample is illuminated with quite high power density. For the overfilled case, $A_D < A_L$, and either Eq. (3.6) or (3.7) applies directly, with $P_0 = P_D A_L$.

We have defined A_D and Ω_D as the detected area and collection angle *at the sample*, since they can be used to determine the signal magnitude. A more general definition of these variables leads to the *étendue* or the $A\Omega$ product for the optical system. Here A is the area of the limiting aperture that occurs at some point in the spectrometer, and Ω is the solid angle at the same point. As noted previously for Figure 3.3, A and Ω vary through the system as the collected light is magnified, focused, and so forth. However, the $A\Omega$ product or *étendue remains constant through the entire optical system.*

For the example of Figure 3.3, suppose that the magnification between the sample and the entrance slit is 2, meaning that the area monitored at the sample has one-half the linear dimensions as the entrance slit. In this case, the area of the slit is 4 times the area at the sample, but Ω at the slit is one-fourth Ω at the sample. Stated differently, the $f/\#$ at the slit is twice that at the sample, and Ω varies with $1/(f/\#)^2$.

An important qualifier is required for the statement that *étendue* remains constant through the system. The usable *étendue* is determined by the *minimum* $A\Omega$ product for the system. This minimum could be determined by the laser spot size, the entrance slit, or the detector area and is often related to the "limiting aperture" applied to the definition of $f/\#$. For many Raman applications, the *étendue* is determined by the spectrometer/detector combination (e.g., the $f/\#$ of a spectrograph and the area of a CCD pixel). Increasing the $A\Omega$ product has provided much of the motivation for building Raman spectrometers with lower $f/\#$ and maximum *étendue.*

3.3. SPECTROMETER RESPONSE FUNCTION

In Eq. (3.6) T and Q are determined by spectrometer and detector design and will be discussed in some detail in Chapter 8. Also Q and, to a lesser degree, T can vary significantly with wavelength, and the choice of optical components and detectors is a strong function of the laser wavelength for a given measurement. With current technology, the maximum values for T and Q are 0.5 and 0.9, respectively, but these values can be much smaller for many situations. The magnitude and wavelength dependence of T and Q can have significant consequences for both qualitative and quantitative analysis, unless they are compensated by appropriate calibration. Considering the entire $A_D\Omega TQ$ product, most of its variation with wavelength stems from variations in T (due, e.g., to grating and filter efficiency) and Q (which varies with detector type and materials). Thus, the observed signal in Eq. (3.6) depends on instrumental variables in addition to the more fundamentally interesting variations in β. This fact leads to the unhappy situation of observing quite different relative Raman intensities for different spectrometers observing the

same sample, because they may have different TQ products. This problem is illustrated in Figure 3.4 for the case of methylene chloride. Spectrum 3.4c shows accurate relative Raman intensities, obtained by correction of experimental spectra. This spectrum is what Mother Nature intended, with relative peak areas reflecting relative cross sections for various Raman features. Spectrum 3.4a is an uncorrected spectrum obtained with a 514.5 nm laser, and 3.4b is from a 785.0 nm laser. The Q for the CCD detector employed varied significantly within and between the wavelength regions where the Raman features occurred (515 to 620 nm for the 514.5 nm laser, 785 to 1050 nm for the 785 nm laser), yielding very different relative intensities.* This variation is an instrumental artifact and will occur when comparing spectra from instruments of different designs or even from different units of the same design. A plot of the collection function vs. wavelength or Raman shift is often referred to as the instrument response function. It is the output of the spectrometer for a "white" source with a specific intensity that is constant with Raman shift. For example, the product of the true spectrum in Figure 3.4c and the instrument response function yields the observed spectrum 3.4b.

The distortion of relative intensities illustrated in Figure 3.4 is an example of a general problem with Raman spectroscopy, compared to more common

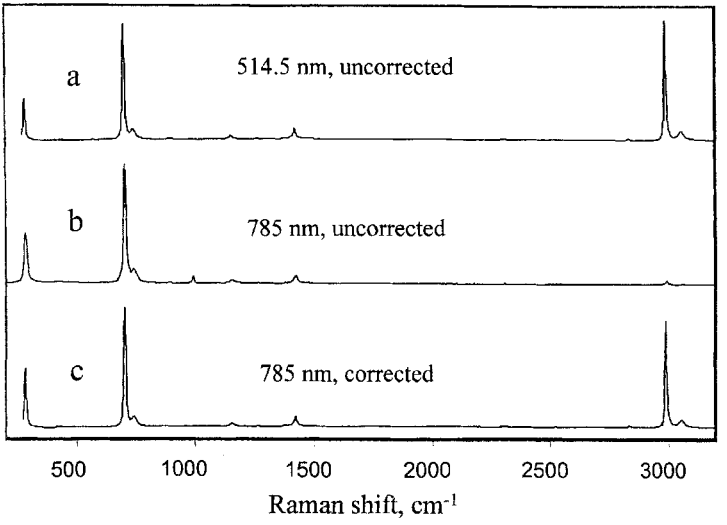

Figure 3.4. Effect of instrument response function on relative intensities for CH_2Cl_2. Spectrum c is corrected for response variation with wavelength and shows correct relative intensities.

* The relative intensities for CH_2Cl_2 vary slightly between these two wavelengths due to cross-section variation, but this factor is quite small, less than 10 per cent.

techniques based on absorption, such as FTIR spectroscopy. An absorption measurement is based on the ratio of incident and transmitted light and always involves a correction for detector or spectrometer sensitivity. This correction is accomplished by using a double-beam spectrometer or by recording a single-beam response with and without the sample present. In this way, a given measurement of transmitted light is compared to the incident light of the same wavelength, and spectrometer T and Q (as well as source variation) are ratioed out. Almost all Raman spectra in the literature are uncorrected and in that sense are "single-beam" spectra. As is obvious from Figure 3.4, correction of Raman spectra is essential if spectra from different labs are to be compared quantitatively. Methods for accomplishing this correction will be discussed in Chapter 10.

The concept of an instrument response function can be applied more generally, in light of the many variables involved in the Raman signal expressions of Eq. (3.5) through (3.8). It is quite unusual to determine all of the instrumental variables in these expressions independently, so it is rare to actually predict a Raman signal expected for a given sample. However, if the instrument is stable and sampling is reproducible, it is possible to compare a sample to a standard. As discussed in Chapter 10, reproducibility is sufficient for certain spectrometer designs so that quantitative analysis is possible without specific evaluation of all the variables in the Raman signal expressions.

3.4. MULTIPLEX AND MULTICHANNEL SPECTROMETERS

The development that is most responsible for the major increase in Raman applications to analytical problems is the introduction of multiplex and multichannel spectrometers in the 1980s. Although the two techniques have similarities in the way they reduce acquisition time and increase signal, they differ fundamentally in both instrumental design and in their effects on the signal/noise ratio. A *multichannel* spectrometer monitors many (typically 512 to 1024) wavelengths simultaneously, using many detectors operating in parallel. A common example is a grating-based dispersive spectrograph with a CCD at its focal plane. Since a multichannel system monitors many wavelengths simultaneously, it acquires a spectrum faster than a scanning, single-channel system that must monitor each wavelength in turn. A *multiplex* spectrometer does not separate the different wavelengths scattered by the sample but rather modulates them at frequencies dependent on their wavelengths. The result is a single beam, detected by a single detector, which contains all wavelengths of interest. Since each wavelength is modulated at a different frequency, a Fourier transform of the multiplex detector output yields a Raman spectrum. An example is FT-Raman in which a modified

FTIR interferometer is used to monitor Raman scattered light. The two approaches are shown schematically in Figure 3.5 and will be discussed in detail in Chapters 5, 8, and 9. It is important to appreciate that a multichannel spectrometer disperses the light for detection by many parallel detectors, while a multiplex spectrometer directs all of the scattered light onto a single detector. This difference between multichannel and multiplex approaches has major effects on the characteristics of the Raman spectrum, in terms of resolution, spectral coverage, signal magnitude, and signal/noise ratio (SNR).

Returning to the general signal expression (3.6), the measurement time must be reconsidered in light of multiplex and multichannel spectrometers. The time, t_s, is defined in Eq. (3.1) as the time for which photons are collected in a given resolution element. For a single-channel system, t_s is the time spent at a given Raman shift interval before moving on to the next. For a multiplex system such as FT-Raman, the measurement time for each resolution element is much longer than t_s since all wavelengths are monitored simultaneously. We will define t_M as the time required for the entire spectral acquisition. For the case of an FT-Raman instrument, t_M is the total interferometer scan time during which photons are collected. To acquire a complete spectrum, a single-channel spectrometer would spend a time equal to t_s on each resolution element, then move to the next. The entire spectrum would require a time equal to $N_R t_s$ for acquisition, where N_R is the number of resolution elements. For multiplex and multichannel instruments, all of the resolution elements are monitored at once, so that the time for each resolution element can be much longer than it was for a single-channel instrument for complete spectrum acquisition. This

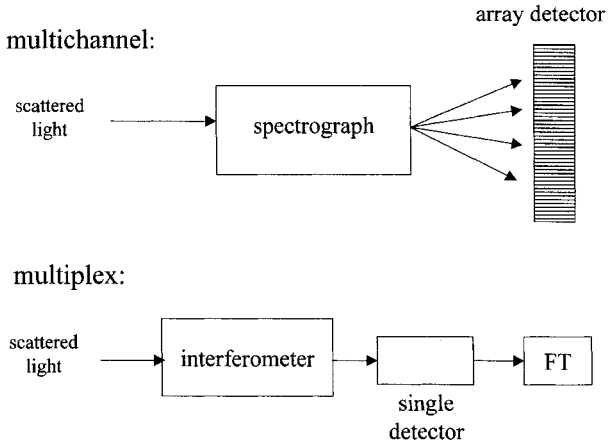

Figure 3.5. Block diagrams for multichannel and multiplex Raman spectrometers. FT indicates computer for performing a Fourier transform.

difference leads to two familiar statements about multichannel (or multiplex) spectrometers compared to single-channel systems. First, for the same total spectral acquisition time, a multichannel or multiplex system can yield N_R times longer collection time in each resolution element:

$$t_M = N_R t_s \tag{3.9}$$

For either multiplex (e.g., FT-Raman) or multichannel (e.g., CCD) spectrometers, t_M is the appropriate time to insert in Eq. (3.6) or (3.7). Second, a multichannel system can obtain a complete spectrum $1/N_R$ times faster than a single-channel system, while maintaining the same measurement time and signal strength per resolution element. Of course, both of these statements assume that other variables are equal for both spectrometer types. In Chapter 4, we will see that t_M strongly affects SNR, but that the effects are fundamentally different for multichannel as opposed to multiplex spectrometers.

With all of its variables identified, Eq. (3.6) provides a means to evaluate the effect of sample and instrument parameters on observed signal. An additional application of Eq. (3.6) is the comparison of different spectrometers for instrumental sensitivity. Stated differently, "how much signal results from a particular sample for a given laser power and measurement time?" Rearrangement of Eq. (3.6) and (3.9) yields (3.10), which applies to the multichannel case (6):

$$F_S = \frac{S(\mathrm{e}^-)}{P_D \beta D t_M} = A_D \Omega T Q K \tag{3.10}$$

where F_S is a "figure of merit" for the Raman signal, and indicates the signal magnitude for a given sample (βD), laser power density (P_D), and measurement time (t_M). Also F_s may be defined in terms of power rather than power density, as in Eq. (3.11):

$$F'_S = \frac{S(\mathrm{e}^-)}{P_0 \beta D t_M} = \frac{A_D \Omega T Q K}{A_L} \tag{3.11}$$

For a single-channel spectrometer, t_M/N_R is substituted for t_s in Eq. (3.6), yielding:

$$F_S(\text{single channel}) = \frac{S}{P_D \beta D t_M} = \frac{A_D \Omega T Q K}{N_R} \tag{3.12}$$

$$F'_S(\text{single channel}) = \frac{S}{P_0 \beta D t_M} = \frac{A_D \Omega T Q K}{A_L N_R} \tag{3.13}$$

In both (3.12) and (3.13), t_M is the total spectrum acquisition time to permit comparison to multichannel spectrometers. For the single-channel case, the figure of merit is reduced because each resolution element can collect less signal for a given t_M. Table 3.2 lists figures of merit calculated from Eq. (3.10) and (3.12) and the spectrometers described in Table 3.1. The signal for a sample of liquid benzene and a constant total measurement time is also listed, using the specific intensity from Table 2.4. The benzene signal is proportional to F_S for a given sample and laser power density, but S will vary with sample and laser power while F_S depends only on collection variables. Notice that a modern CCD spectrometer (spectrometer 4 in Table 3.2) has an F_S and signal about 10,000 times that of a "classical" system from 1985 (spectrometer 1). This large increase in signal provides much of the driving force for the increased utility of Raman spectroscopy in analytical applications.

In practical laboratory applications, it is tedious to determine A_D, Ω, T, Q, and A_L, but it is relatively simple to determine P_0 and t_M for a given sample. So F'_S may be measured for different spectrometers and a given sample with known βD product; F'_S and F_S provide a direct comparison of spectrometer sensitivity, normalized for laser power and t_M.

As defined here, F_s and F'_s were derived in terms appropriate to a dispersive spectrometer, either single or multichannel. Multiplex systems such as FT-Raman spectrometers have much the same dependence on experimental variables as that described by Eq. (3.10) and (3.11), but the signal S is not the same. Although an FT-Raman system still monitors photons, its output is the magnitude of the interferogram and is not directly comparable to $S(e^-)$ as defined in Eq. (3.10) and (3.11). Thus the F_S or F'_S for FT-Raman cannot be meaningfully compared to that for single or multichannel spectrometers. We will define a figure of merit for SNR in Chapter 4 that *is* directly comparable

Table 3.2. Figures of Merit for Generic Spectrometers

Spectrometer (from Table 3.1)	F_S^a	F_S^b (single channel)	$S^c(e^-)$ for Neat Benzene, 992 cm^{-1}	Relative F_S
1		2.3×10^{-9}	1.4×10^7	1
2		4.4×10^{-10}	2.6×10^6	0.18
3	1.5×10^{-6}		9.0×10^9	640
4	3.2×10^{-5}		1.9×10^{11}	13,600
5	2.0×10^{-6}		1.2×10^{10}	860
6	Not applicable			

[a]From Eq. (3.10) for $K = 0.1$ cm, units are (e^- cm^3 sr $photon^{-1}$).
[b]From Eq. (3.12), $N_R = 1024$, $K = 0.1$ cm.
[c]100 mW, 514.5 nm, 0.5 × 1 mm area, $K = 0.1$, $t_M = 60$ sec. $L = 1.0 \times 10^{13}$ photons cm^{-2} s^{-1} sr^{-1}.

among the three spectrometer types. Furthermore, the signal for all types may be normalized to an intensity standard to permit quantitative comparison of spectra.

REFERENCES

1. J. J. Laserna, ed., *Modern Techniques in Raman Spectroscopy*, Wiley, New York, 1996.
2. J. R. Ferraro and K. Nakamoto, *Introductory Raman Spectroscopy*, Academic Press, San Diego, 1994.
3. G. Turrell and J. Corset, *Raman Microscopy*, Academic Press, New York, 1996.
4. P. J. Hendra, *Fourier Transform Raman Spectroscopy: Instrumentation and Chemical Applications*, Ellis Harwood, New York, 1991.
5. R. T. Packard and R. L. McCreery, *Anal. Chem.*, **59**, 2631 (1987).
6. M. Fryling, C. J. Frank, and R. L. McCreery, *App. Spectrosc.*, **47**, 1965 (1993).

Raman Spectroscopy for Chemical Analysis. Richard L. McCreery

ISBN: 0-471-25287-5

CHAPTER

4

SIGNAL-TO-NOISE IN RAMAN SPECTROSCOPY

The ability to extract analytical information from any spectroscopic technique is usually limited by the signal-to-noise ratio (SNR) for the conditions employed. For example, the limit of detection in quantitative analysis is often defined as the concentration of analyte yielding an SNR of 3.* Stated differently, an instrument with higher SNR for a given concentration yields a lower limit of detection. Since Raman scattering is quite weak compared to fluorescence or absorption, Raman measurements have historically pushed the limits of existing technology to reduce noise and increase SNR. Particularly in the past 10 years, Raman signals have increased and noise sources have decreased for technological reasons, yielding much larger SNR for a given sample. In fact, the recent (post-1985) renaissance of Raman spectroscopy is due in large part of increases in signal from multichannel and multiplex techniques and reduction in noise from longer wavelength excitation (to reduce background) and low noise detectors [such as charge-coupled devices (CCDs)]. Since noise and SNR are so critical to applications of Raman spectroscopy, they must be understood in detail in order to develop and apply Raman techniques in analysis.

4.1. DEFINITION AND MEASUREMENT OF SNR

The SNR for particular measurement is rigorously defined as the inverse of the relative standard deviation of the measured value. For example, the SNR for the peak intensity of a Raman band is the average peak height, $\overline{S}$ (usually above the baseline), divided by the standard deviation of the peak height (σ_y). As with any determination of standard deviation, the accuracy of the SNR improves with the number of measurements averaged:

$$\text{SNR} = \frac{\overline{S}}{\sigma_y} \tag{4.1}$$

* The limit of detection can also be defined relative to the standard deviation of the blank rather than the signal. In many Raman measurements, the two definitions yield equal limits of detection.

It is often possible to predict the SNR from fundamental principles of counting statistics combined with instrumental characteristics, as will be demonstrated later.

Although the definition of SNR is straightforward, it is not consistently applied to experimental spectra in the literature. Consider Figure 4.1, which shows a spectrum of glassy carbon (A) and the difference of two successive spectra (B). $\bar{S}$ is defined as the mean peak height above background, σ_y is the standard deviation of the peak height, and σ_B is the standard deviation of the background. The SNR is most accurately determined by acquiring several repetitions of spectrum 4.1A, then determining $\bar{S}$ and σ_y at a single peak frequency. If the density of points on the frequency axis is high enough, σ_y may be determined from one spectrum, by using the several points at the top of the Raman band. A more accurate method is to substract two successive spectra to remove the contributions of the Raman band and background, and leave only the noise (spectrum 4.1B). Then σ_y is equal to the standard deviation of Figure 4.1B in the peak region divided by $\sqrt{2}$. It is instructive to note that the noise is significantly larger when the intensity is higher on the peaks. Since the case shown in Figure 4.1 is shot noise limited, the magnitude of the noise (and its standard deviation) vary with the square root of the signal magnitude. As discussed in Section 4.2.1, the SNR for this case equals $S/\sqrt{S}$ or $\sqrt{S}$.

Once an acceptable value of σ_y is in hand, the SNR may be calculated directly from Eq. (4.1). Unfortunately, the SNR is often calculated in the literaure as $\bar{S}/\sigma_B$, which is a fundamentally different quantity from the SNR defined in Eq. (4.1). Generally σ_B is *not* related to σ_y, and equating σ_B with σ_y can yield unreasonable conclusions. For example, consider the spectrum of Figure 4.2A, where the $\bar{S}$ is 100 photons. If the background is zero, then $\bar{S}/\sigma_B$ is infinite, implying an infinite SNR. However, the highest possible SNR defined by Eq. (4.1) is $100^{1/2}$, for the case of the analyte shot noise limit discussed below. Figure 4.2B shows a real spectrum acquired under shot-noise-limited conditions in which the SNR for the large band is ~100, as expected from the peak height, while the S/σ_B is an erroneously high "SNR" of 1000. Although the quantity $\bar{S}/\sigma_B$ can indicate useful information about the experiment, it can lead to erroneously high SNR if it is used in lieu of Eq. (4.1). Figure 4.3 shows a sequence of spectra acquired near the detection limit, illustrating the criterion of SNR = 3 to reliably detect an analyte. In this case, an SNR of 2.8 yielded correct identification of the unknown by a search of a 300-member spectral library.

We will discuss SNR measurements for particular spectrometer configurations in Chapters 8 and 9, but throughout the general discussion in this chapter, we will abide by Eq. (4.1). There are a few situations where the ratio $\bar{S}/\sigma_B$ yields a correct approximation of true SNR, and these will be noted as they occur.

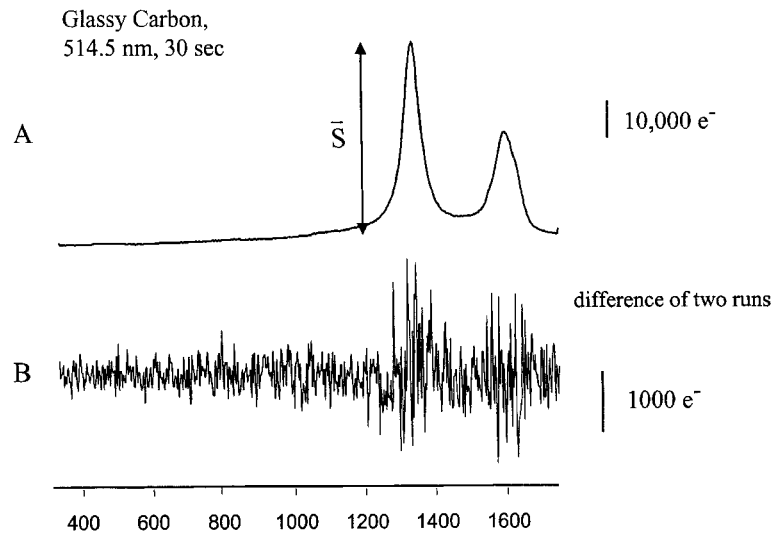

Figure 4.1. Definition of $\bar{S}$ as the mean signal above baseline for the case of a Raman signal on a non-negligible background (curve A). Curve B is the difference of two successive spectra similar to curve A. The correct SNR is $\bar{S}/\sigma_y$, determined at the peak intensity. σ_y is the standard deviation of spectrum B at the peak of interest, divided by $\sqrt{2}$.

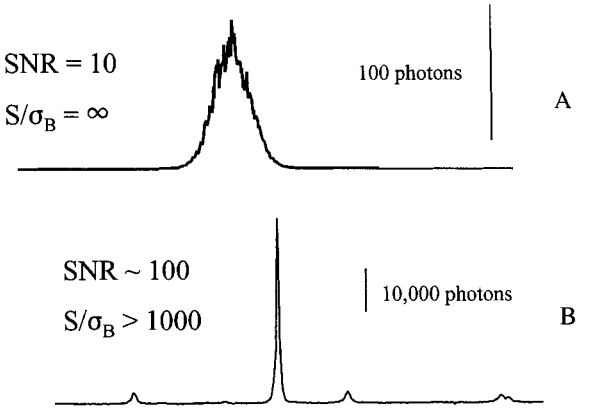

Figure 4.2. Signal-to-noise ratios for a peak with $\bar{S} = 100$ photons on a zero background (curve A) and for a spectrum of neat benzene (curve B). The ratio of signal-to-background noise can seriously overstate the true SNR.

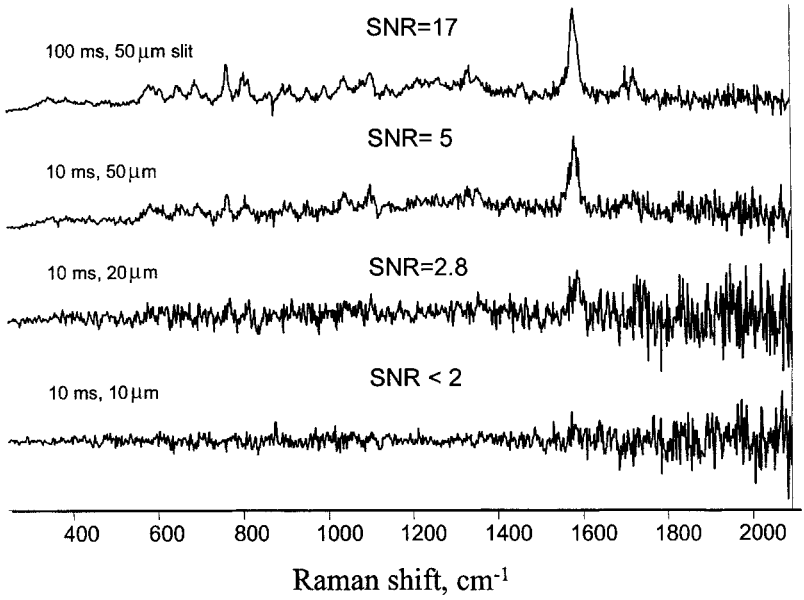

Figure 4.3. Raman spectra of calcium ascorbate with progressively shorter integration times and narrower entrance slit. The observed SNR for the 1548cm^{-1} peak is indicated and illustrates the visual appearance of the spectrum for various SNR.

4.2. NOISE SOURCES

The magnitude of $\bar{S}$ in Eq. (4.1) is described by the appropriate equation from Chapter 3, so we need an estimate of σ_y in order to evaluate SNR. In Raman measurements σ_y has contributions from a number of sources, as indicated by Eq. (4.2):

$$\sigma_y = (\sigma_S^2 + \sigma_B^2 + \sigma_d^2 + \sigma_F^2 + \sigma_r^2)^{1/2} \tag{4.2}$$

where σ_S = standard deviation of signal, from the analyte or band of interest
σ_B = standard deviation of the background
σ_d = standard deviation of dark signal, usually $(\phi_d t)^{1/2}$, where ϕ_d is the dark rate (electrons per second, or $e^- sec^{-1}$)
σ_F = flicker noise
σ_r = readout noise

Equation (4.2) is more conveniently stated as:

$$\sigma_y = (S + B + \phi_d t + \sigma_F^2 + \sigma_r^2)^{1/2} \tag{4.3}$$

Equations (4.2) and (4.3) neglect noise contributions from stray light not originating in the laser or sample, such as room light reaching the detector. These sources can be difficult to predict but certainly must be negligible in Eq. (4.3) is to be correct.

4.2.1. Signal Shot Noise

We defined S as the signal, in electrons, resulting from the Raman scattering of the analyte of interest, as described in Chapter 3. In the absence of other noise sources, the standard deviation of S is determined by the shot noise limit:

$$\sigma_S = S^{1/2} \tag{4.4}$$

The shot noise limit is fundamental to spectroscopy and occurs when counting anything governed by Poisson statistics (1). Stated differently, the standard deviation when counting any random event equals the square root of the number of events counted. As an analogy, consider a person counting cars passing on a highway, when the cars occur randomly but at a constant average rate. If only a few cars are counted, the relative standard deviation (σ_S/S) is high. As the number of cars counted increases (by increasing the observation time), the standard deviation, σ_S increases, but the relative standard deviation (σ_S/S) *decreases* and the SNR (S/σ_S) *increases*. Clearly, the relative precision of the determination of the average number of cars/minute improves as the measurement time increases and more cars are observed.

Counting scattered photons follows the same logic, with random photon arrival leading to Eq. (4.4). If signal shot noise is the only noise source, Eq. (4.5) and (4.6) also apply, where $S = \dot{S}t$:

$$\text{SNR} = S/\sigma_S = S^{1/2} \tag{4.5}$$

$$\text{SNR} = \dot{S}t^{1/2} \tag{4.6}$$

In the shot noise limit, we observe the familiar increase in SNR with $t^{1/2}$. It is worth noting that the SNR cannot exceed that given by Eq. (4.6), even for a perfect spectrometer. The best possible Raman measurement, with 4π collection, 100 per cent spectrometer transmission, 100 per cent quantum efficiency, and zero background is still limited in SNR by Eq. (4.6). As long as the photons arrive randomly (and any other case is hard to envision), the maximum SNR will be given by Eq. (4.5) and (4.6). Figure 4.4 is an example of a Raman spectrum with an SNR determined mainly by sample shot noise.

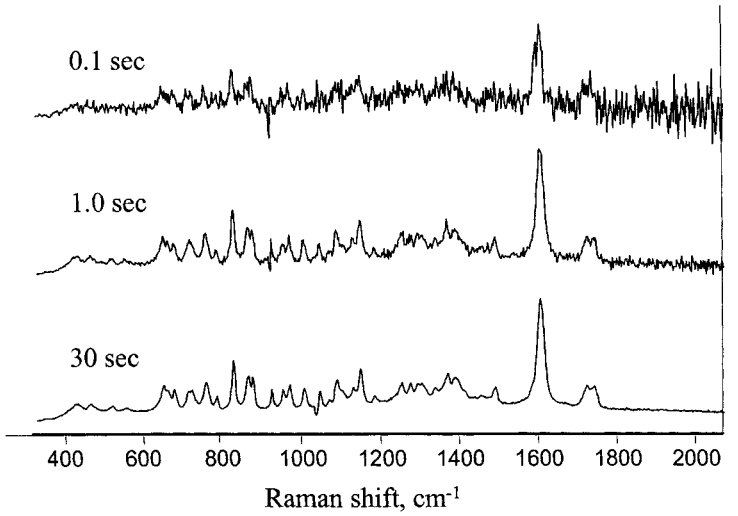

Figure 4.4. Three spectra of calcium ascorbate at various measurement times. Improvement in SNR with longer integration time is due mainly to decreased shot noise, as stated in Eq. (4.6).

4.2.2. Background Shot Noise

"Background" is a fairly general term, but we will use it here to mean any detected photons arising from the laser and sample other than Raman photons from the analyte at the frequency of interest. In particular, background includes lumminescene of cell, sample, or optics (e.g., fluorescene, thermal emission), and stray laser light, including Rayleigh scattering, reflection from optics or dust, and the like. Stray light includes any elastically scattered laser light that is not removed by filters or by the spectrometer itself. It is important to distinguish background from detector or readout noise because background noise depends on laser intensity and the presence of luminescene from sample components or the analyte itself, while detector and readout noise do not.

Background magnitude can be expressed by an equation similar to (3.6), if βD is redefined slightly:

$$B = P_D \beta_B D_B K A_D \Omega T Q t \tag{4.7}$$

where $\beta_B D_B$ is the cross section–number density product for sample components generating the background; $\beta_B D_B$ would apply directly to a fluorescent impurity but would be more loosely defined if the background source were stray light, lens liminescene, and the like. In the latter cases, β_B and D_B are not meaningful, but their product does indicate the fraction of detected photons

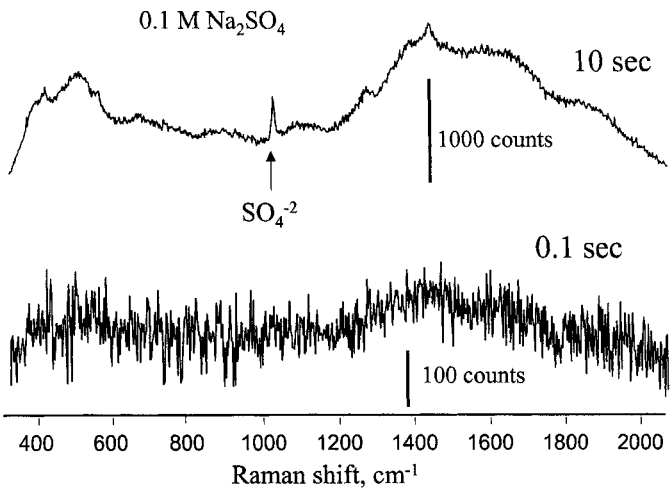

Figure 4.5. Spectra of 0.1 M Na_2SO_4 dominated by background noise from the water and cell. At short measurement time, SNR is too low to permit observation of the SO_4^{-2} Raman band [see Eq. (4.21)].

arising from these sources, and their contribution to background is proportional to laser intensity.

Background is also governed by shot noise, so Eq. (4.8) applies, with B expressed as electrons:

$$\sigma_B = B^{1/2} = \dot{B}^{1/2} t^{1/2} \tag{4.8}$$

Figure 4.5 shows a spectrum with an SNR dominated by background shot noise. The noise on the sulfate peak is due mostly to background from the water and cell, which overwhelms the signal for short integration time. The situation is fairly common in Raman spectroscopy, and reduction of background shot noise was a major motivation for using longer wavelength lasers to minimize fluorescence.

4.2.3. Detector Dark Noise

In Eq. (4.3) ϕ_d is the rate of spontaneous generation of electrons in the detector, the so-called dark signal. All detectors currently in use in Raman spectroscopy have a finite dark signal, caused mainly by thermal generation of electrons from a photomultiplier cathode or within a solid-state detector. Thus ϕ_d is usually strongly temperature dependent, thus providing the motive for detector cooling; ϕ_d covers a wide range of values, from nearly negligible values ($\prec 0.001$ $e^- sec^{-1}$) for liquid-nitrogen-cooled CCD detectors to

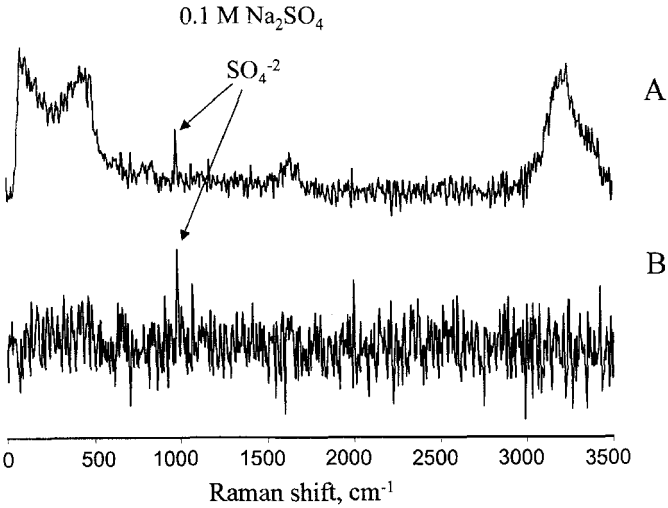

Figure 4.6. Spectra of 0.1 M Na_2SO_4 dominated by detector noise. Spectrum A is 0.1 M Na_2SO_4 in water, spectrum B is after subtraction of a spectrum of the cell containing only water. Spectra are from an FT-Raman spectrometer with a germanium detector.

$\succ$ 100 $e^- sec^{-1}$ for near-infrared (NIR) detectors used in Fourier transform (FT)–Raman. For a given experiment, the contribution of dark signal to the total signal is $\phi_d t$.

Since "dark" electrons are counted in the same way as signal or background, they contribute to the shot noise, as stated in Eq. (4.9):

$$\sigma_d = (\Phi_d t)^{1/2} \tag{4.9}$$

Although the dark signal contributes to the observed signal, it is distinguished from the background defined in Section 4.2.2 by the fact that it does not depend on laser intensity or sample variables. In fact, one test for detector noise is to run a spectrum with the laser completely off. The observed noise in this situation is due to detector and readout noise. Figure 4.6 shows a spectrum dominated by detector noise. The detector noise remains after the contributions of the cell and water are subtracted.

4.2.4. Flicker Noise

Flicker noise is commonly defined classically for absorption and emission spectroscopy (see Ref. 1, pp. 144–145) but also applies to Raman spectroscopy. Variation in laser intensity at both low and high frequencies will

cause proportional variation in Raman scattering and in the measured Raman signal. An example of a servere effect of flicker noise is a single-channel spectrometer scanning at a rate of 1 $cm^{-1}sec^{-1}$ and a laser output varying on a 1 to 10 sec cycle. The laser flicker would appear as variations in Raman intensity as a given Raman band is observed, thus degrading the SNR.

Spectrometer designs vary in their sensitivity to flicker noise as will be discussed in Chapters 8 and 9. For example, a multichannel spectrometer is fairly immune to flicker noise because all wavelengths are monitored in parallel, while a scanning system is very sensitive to flicker noise depending on the flicker frequency. Interferometers used in FT-Raman are sensitive to flicker noise when the sampling frequency is comparable to the flicker frequncy.

4.2.5. Readout Noise

Readout refers to the process of converting electrons from the detector to a useful form, usually a digital value stored in a computer. Here σ_r is the standard deviation of a large number of readouts from a constant detector signal. For example, if a CCD pixel contains exactly 1000 e^-, and those electrons are digitized to a numerical value in a computer, σ_r is the standard deviation of the numerical value for many repetitions. Note that σ_r does not depend on signal magnitude according to this definition and does not depend on measurement time. For the common case of a CCD detector, σ_r is the standard deviation associated with the analog-to-digital conversion of the current from the electrons stored in CCD. It has contributions from the amplifiers between the CCD and the analog-to-digital converter, and from Johnson (thermal) noise in electronic components. σ_r varies greatly with detector type but can vary from a few electrons for a scientific CCD to several thousand electrons for a photodiode array.

4.2.6. General SNR Expressions

Equation (4.2) provides the total standard deviation of the observed signal when all five noise sources are included. For the remainder of the chapter, we will ignore flicker noise and state the total noise as:

$$\text{Noise} = \sigma_y = (\sigma_s^2 + \sigma_B^2 + \sigma_d^2 + \sigma_r^2)^{1/2} \tag{4.10}$$

Flicker noise could indeed contribute, but it is difficult to address theoretically and may vary significantly for different spectrometer configurations and lasers. For a well-designed experiment, flicker noise can usually be reduced to a negligible level.

If we define the signal as that from the Raman band of interest, and therefore governed by Eq. (3.6), the SNR is defined by:

$$\text{SNR} = \frac{S}{(\sigma_S^2 + \sigma_B^2 + \sigma_d^2 + \sigma_r^2)^{1/2}} \tag{4.11}$$

where S is rigorously defined as the average value of the signal due to the Raman band above the signal due to a blank. In practice, S is often defined as the signal due to the Raman feature above a baseline interpolated between spectral regions on either side of the Raman band. S may be defined either as peak height or peak area (both above baseline), with a corresponding definition of σ_S.

There is a common misconception about background subtraction that should be dispelled at this point. It is common to subtract the background obtained from a blank Raman spectrum before quantitative analysis in order to remove background and dark signal from the signal of interest. Such subtraction is quite useful for observing small Raman features on top of much stronger features, such as those from the solvent or background fluorescence. However, this subtraction does not remove the *noise* from the background. By definition, noise is random and cannot be reproduced for the sample and the blank. The background has shot noise (at least), and this shot noise is added to the signal of interest when background is present. Subtracting B from raw signal to yield S will not reduce total noise.*

These issues are illustrated in Figure 4.6, for the case of a relatively small Raman feature on a large background. Clearly, subtraction of the blank spectrum will not remove the shot noise originating in the blank. This point may be confirmed by considering Eq. (4.11) with σ_d and σ_r equal to zero for simplicity. Table 4.1 lists several situations with varying magnitudes of S and B. Lines 1 and 2 indicate the increase in SNR with the size of the signal, as expected. Lines 2 to 5 show the degradation in SNR even though the signal size above background is constant. This simple but important observation demonstrates that background noise cannot be subtracted out and that large backgrounds will eventually make the signal unobservable. The only recourse to improve SNR when faced with high background is to increase the signal + background, for example, by longer measurement time (line 6 in Table 4.1). Even with a large background contribution, the SNR still increases with the square root of the measurement time.

A familiar analogy for the influence of background on SNR in Raman experiments is the attempt to observe stars in the daytime. The stars are easily observed at night, in the absence of background, but are not observable in the

* Subtraction actually increases noise by $\sqrt{2}$, since the variances in signal and blank are additive.

Table 4.1. Effect of Background Shot Noise on SNR

	$S(e^-)$	$B(e^-)$	σ_y^a (noise)	SNR[a]
1.	100	0	10	10
2.	1000	0	31	31
3.	1000	1000	45	22
4.	1000	10^4	105	9.5
5.	1000	10^6	1000	1.0
6.	10^5	10^8	10^4	10

[a]Calculated from Eq. (4.11), assuming negligible dark and readout noise.

daytime, in the presence of scattered and reflected sunlight. Even with an excellent detector (much better than our eyes), the shot noise from scattered sunlight would overwhelm the starlight, and the SNR ratio would approach zero.

4.2.7. Limiting SNR Situations

Attempting to observe stars in the daytime is one example of a limiting case for SNR in which the noise stems principally from one source. Although shot noise and flicker noise from the star are present, they are negligible compared to the large solar background. There are several limiting cases for SNR based on Eq. (4.11) that are relevant to Raman spectroscopy. The limiting cases often dictate the way the spectrometer is designed and the experiment is carried out and will be discussed here in general terms before specific designs are discussed in Chapters 8 and 9.

The *sample shot noise limit* occurs when σ_B, σ_d, and σ_r are small compared to σ_S in Eq. (4.11). This limiting case was discussed in Section 4.2.1 and leads to Eq. (4.6). The SNR increases with $t^{1/2}$ for a constant $\dot{S}(e^- sec^{-1})$. As stated earlier, the shot noise limit yields the highest SNR possible for a given value of $\dot{S}$

The *background shot noise limit* is often encountered in samples containing fluorescent materials. A relatively small Raman peak is superimposed on a high background, but the noise originates almost totally in the background. In this case, $\sigma_B = (\dot{B}t)^{1/2}$ and

$$\text{SNR}_B = \frac{\dot{S}t}{(\dot{B}t)^{1/2}} = \frac{\dot{S}}{\dot{B}^{1/2}} t^{1/2} \tag{4.12}$$

As was the case with sunlight and stars, $\dot{B}$ can be so much larger than S that SNR approaches zero. It is also interesting to note that the SNR in the

background shot noise limit is linear in $\dot{S}$ while SNR scales with $\dot{S}^{1/2}$ in the sample shot noise limit.

The *detector noise limit* occurs commonly in FTIR spectroscopy and in most FT-Raman measurements. If σ_d is much larger than σ_S, σ_B, or σ_r, Eq. (4.13) applies:

$$\mathrm{SNR}_D = \frac{\dot{S}}{\Phi_d^{1/2}} t^{1/2} \tag{4.13}$$

SNR_D is always smaller than that for the sample shot noise limit, all else (other than detector noise) being equal. As ϕ_d is decreased by improvements in the detector, SNR_D approaches the value determined by sample and background shot noise.

The readout noise limit is not encountered frequently with modern spectrometers, but can be important for samples with very weak scattering. If σ_r in Eq. (4.11) is dominant, the SNR is linear in S:

$$\mathrm{SNR}_R = \frac{\dot{S}t}{\sigma_r} \tag{4.14}$$

Since σ_r is not time dependent, the SNR increases linearly with time, and it would be possible to collect signal until σ_r is negligible. An exception would be an experiment with a very small $\dot{S}$, such as Raman scattering from low-pressure gas or a submonolayer film, for which the signal is so weak that an impractically long integration time would be required for the signal to exceed the readout noise. In such cases, the experimenter must ensure that the detector has low readout noise. An example of the effects of readout noise on SNR for weak signals is shown in Figure 4.7. A spectrum of dextrose powder was obtained with low laser power, and the SNR in spectrum 4.7A is dominated by readout noise. Increasing the integration time 50-fold greatly improves the SNR, as predicted by Eq. (4.14). However, a signal average of 50 spectra similar to 4.7A does *not* yield an SNR improvement, even though the total acquisition times for 4.7B and 4.7C are equal. During signal averaging, both the numerator and denominator of Eq. (4.14) increase with the square root of the number of averages, leading to no gain in SNR. So signal averaging will not improve SNR when readout noise is significant, as each readout adds to the noise.

In many practical applications, Eq. (4.11) has a significant impact on experimental design. Generally speaking, the experimenter should choose an instrument for which σ_r and σ_d are negligible, so the SNR is determined by the sample and not the spectrometer. After that, σ_B is reduced as much as possible by judicious choice of laser wavelength or sample pretreatment. It is easier said than done, but ultimately, experimental conditions are selected that

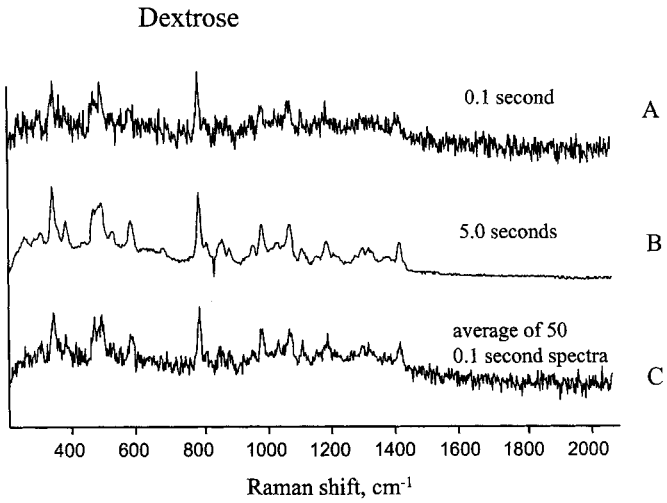

Figure 4.7. Spectra of solid dextrose, obtained with 785 nm excitation and a dispersive/CCD spectrometer. Spectrum C is an average of fifty 0.1 sec CCD integrations and shows no improvement in SNR over a single 0.1 sec integration (spectrum A), due to the dominance of readout noise.

minimize the denominator of Eq. (4.11) while maximizing the signal. Tactics for maximizing SNR in this manner will be discussed later.

4.3. SIGNAL-TO-NOISE RATIO EXPRESSIONS

The expression for Raman signal from Chapter 3 may be combined with Eq. (4.11) to arrive at the dependence of experimental SNR on various sample and measurement variables. SNR is a generally more important indicator of the utility of the measurement than raw signal, since SNR determines the detection limit and overall information content. In addition, SNR may be compared for spectra with quite different intensity units, such as dispersive/CCD and FT-Raman instruments. In the remainder of this chapter, we will derive SNR expressions for several situations, and define a figure of merit for SNR.

4.3.1. SNR for Analyte Shot Noise Limit

For the case where the observed signal is due solely to Raman scattering from the analyte of interest, Eq. (3.6) may be substituted into Eq. (4.6) to yield

(4.15) or (4.16):

$$\mathrm{SNR}_A = (P_D \beta_A D_A K A_D \Omega_D T Q t_s)^{1/2} \tag{4.15}$$

$$\mathrm{SNR}_A = L_A^{1/2} C^{1/2} t_s^{1/2} \tag{4.16}$$

SNR_A is used to denote the analyte shot noise limit, and β_A, D_A, L_A refer only to analyte variables. Recall that t_s is the measurement time for each resolution element and does not necessarily equal the total measurement time t_M. As expected, SNR_A varies with $t_s^{1/2}$.

An obvious but useful observation based on Eq. (4.15) is the dependence of SNR_A on $P_D^{1/2}$ and $(A_D \Omega_D T Q)^{1/2}$. Improvements in the instrument that increase $A_D \Omega_D T Q$ or increases in power density yield only a square root improvement in SNR in the shot noise limit. For example, increasing Q by a factor of 2 might be quite expensive or may restrict the experiment in terms of laser wavelength or other parameters. The resulting SNR_A improvement of 1.4 may not justify the cost or effort.

The analyte shot noise limit illustrates the fundamental importance of multichannel detection for improving SNR. Equations (4.15) and (4.16) are valid for each resolution element in the system in a single or multichannel spectrometer (but not for a multiplex spectrometer). As noted in Section 3.4 and Eq. (3.9), a spectrometer that can monitor N_R resolution elements simultaneously increases the measurement time for each resolution element by a factor of N_R over the time required for a single-channel system. Since $t_M = N_R t_S$,

$$\mathrm{SNR}_A = (L_A C t_M)^{1/2} = (L_A C N_R t_S)^{1/2} \tag{4.17}$$

In effect, each resolution element of a multichannel spectrometer collects signal for a time t_M, while the single-channel systems collect signal for $t_S (= t_M / N_R)$. *If L_A and C are equal for both the single and multichannel spectrometers,* Eq. (4.18) yields the relative SNRs:

$$\frac{\mathrm{SNR}_A(\text{multichannel})}{\mathrm{SNR}_A(\text{single channel})} = \left(\frac{t_M}{t_S}\right)^{1/2} = N_R^{1/2} \tag{4.18}$$

The large improvement in SNR available with multichannel spectrometers is illustrated in Figure 4.8. Note that the higher SNR was achieved for a shorter measurement time and lower laser power. Although (4.18) states the often quoted $N_R^{1/2}$ "multichannel advantage," it should be emphasized that all other experimental parameters were assumed equal. This is rarely the case (and was not in Fig. 4.8), but there is nevertheless a major gain in SNR for multichannel spectrometers. As additional warning deals with *multiplex* as

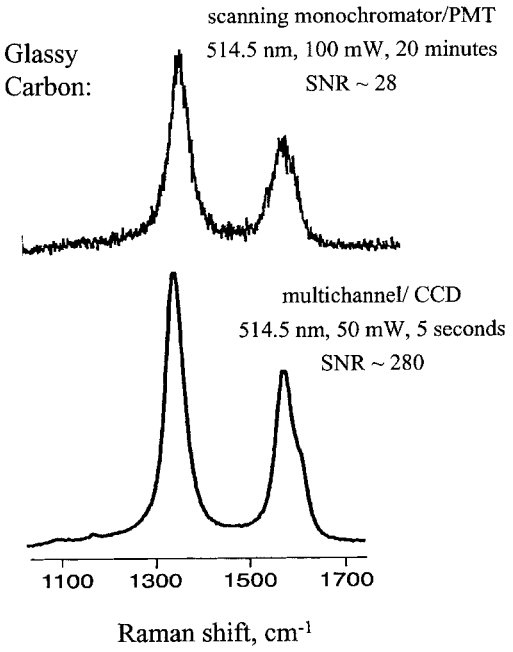

Figure 4.8. Spectra of glassy carbon (a hard form of sp^2 carbon) with single-channel and multichannel spectrometers. The multichannel system ($N_R = 512$) achieved higher SNR with shorter measurement time and lower laser power.

distinguished from *multichannel* spectrometers. Multiplex systems, such as those used in FT-Raman, *do* lead to an increase in measurement time, but *do not* have the noise characteristics noted in Eqs. (4.17) and (4.18). Multiplex detection will be treated in a Section 4.6.

4.3.2. SNR for the Sample Shot Noise Limit

We define the sample shot noise limit, SNR_S, as that occuring when σ_d, σ_F, and σ_r are negligible, and the noise is due solely to analyte and background shot noise. This is a common cause in dispersive/CCD Raman spectrometers and deserves treatment in some detail.

Combining Eqs. (3.6) and (4.7) yields the total signal derived from analyte and background scattering:

$$S + B = (\beta_A D_A + \beta_B D_B) P_D K C t \tag{4.19}$$

Recall that S is the analyte signal above the background, so the signal of interest is given by Eq. (3.6). Thus SNR_S is given by:

$$\mathrm{SNR}_S = \frac{S}{(S+B)^{1/2}} = \frac{\beta_A D_A}{(\beta_A D_A + \beta_B D_B)^{1/2}} (P_D K C t_S)^{1/2} \tag{4.20}$$

As with analyte shot noise limit, SNR_S scales with $t^{1/2}$, but SNR_S is always less than SNR_A due to the contribution from background shot noise. Equation (4.20) itself has two limiting cases, depending on the relative magnitudes of $\beta_A D_A$ and $\beta_B D_B$. For small $\beta_B D_B$, Eq. (4.20) reduces to (4.16), the analyte shot noise limit. If $\beta_B D_B$ is much larger than $\beta_A D_A$, the background shot noise limit, SNR_B, is reached:

$$\mathrm{SNR}_B = \frac{\beta_A D_A}{(\beta_B D_B)^{1/2}} (P_D K C t_S)^{1/2} \tag{4.21}$$

Equation (4.21) applies for a small analyte signal on top of a large background in which case the analyte shot noise contributes little to the total noise. Since SNR_S and SNR_B are proportional to $t^{1/2}$, they both are subject to an $N_R{}^{1/2}$ multichannel advantage, analogous to that in Eq. (4.18). For equal measurement conditions, SNR_S cannot exceed SNR_A, and background scattering can only degrade SNR_S compared to SNR_A.

4.3.3. SNR for Dark Noise Limit

If σ_d is dominant in Eq. (4.11), the combination of (3.6) and (4.9) yields an expression for SNR_d:

$$\mathrm{SNR}_d = \frac{P_D \beta_A D_A K C t^{1/2}}{\phi_d{}^{1/2}} \tag{4.22}$$

SNR_d scales with $t^{1/2}$ but is always less than SNR_A. As $(P_D \beta_A D_A K C)$ increases to the point where it significantly exceeds ϕ_d, analyte shot noise will exceed dark noise ($\sigma_S \gg \sigma_d$), and Eq. (4.22) will revert to Eq. (4.16). As always, the best one can do is the analyte shot noise limit, when other noise sources become insignificant.

4.3.4. Readout Noise Limit

If σ_r dominates the denominator of Eq. (4.11), the readout noise limit occurs:

$$\mathrm{SNR}_r = \frac{P_D \beta_A K C t}{\sigma_r} \tag{4.23}$$

As noted earlier, this is a rare case, resulting from a very weak signal or a high σ_r (such as a photodiode array). Unlike the analyte, sample, or dark noise limits, SNR_r is linear with t rather than $t^{1/2}$.

4.4. SNR FIGURE OF MERIT

Rearrangement of Eq. (4.15) permits definition of an SNR figure of merit (F_{SNR}), which is useful for comparing spectrometer performance (2). It is generally more useful than the figure of merit for signal defined in Eqs. (3.10) and (3.11). Equation (4.24) defines F_{SNR} based on Eq. (4.15).

$$F_{SNR} = \frac{SNR_A}{(P_D \beta_A D_A t_M)^{1/2}} = (A_D \Omega Q T K)^{1/2} \tag{4.24}$$

Equation (4.24) is based on total measurement time, t_M, in part to remain consistent with F_S defined in Eq. (3.10). The analyte shot noise limit is used in (4.24), although a similar expression could be defined for SNR_B or SNR_S. If P_0/A_L is substituted for P_D, an alternative expression results:

$$F'_{SNR} = \frac{SNR_A}{(P_0 \beta_A D_A t_M)^{1/2}} = \left(\frac{A_D}{A_L} \Omega Q T K\right)^{1/2} \tag{4.25}$$

In practice, F_{SNR} or F'_{SNR} may be determined for a given spectrometer experimentally by measuring the SNR for a sample with known βD. For example, F'_{SNR} could be determined for a given spectrometer by measuring the SNR for neat benzene ($\beta D = 1.93 \times 10^{-7} sr^{-1} cm^{-1}$) and noting the laser power at the sample (P_0) and measurement time t_M. In principle, one could also determine F'_{SNR} from determinations of A_D, A_L, Ω, Q, T, and K; but these variables are much more difficult to measure accurately. The units of F'_{SNR} ($sr^{1/2} cm^{1/2} photons^{-1/2}$ or $W^{-1/2} sr^{1/2} cm^{1/2} sec^{-1/2}$) are not very informative but should be consistent for any comparisons of F'_{SNR}.

The utility of F'_{SNR} stems from the adjustment of SNR for sample, power, and t_M. Since Raman spectroscopists use a wide variety of conditions, it is generally difficult to meaningfully compare the SNRs from different labs. F'_{SNR} will adjust for only some of these experimental differences. If one knows the F_{SNR} or F'_{SNR} for a given spectrometer, the SNR can be predicted for a particular laser power and t_M, if the βD product is known. In addition, F'_{SNR} is based on a function of six parameters on the right side of Eq. (4.25) and permits a fast evaluation of the magnitude of the aggregate of these variables. Finally, F'_{SNR} is not dependent on absolute signal magnitude but rather on a ratio of observable signal and noise, so that quite different spectrometers

(e.g., FT-Raman and dispersive) may be compared in terms of their SNR for a given $P_0\beta D t_M$ product.

Although F_{SNR} and F'_{SNR} differ only in the use of P_D vs. P_0, this difference can lead to important consequences. F'_{SNR} is easier to measure since A_L need not be known. Most spectroscopists record P_0 and t_M, so F'_{SNR} is easily determined. For an underfilled spectrometer ($A_D = A_L$), F'_{SNR} will be independent of laser spot size and therefore independent of focusing parameters. However, if the spectrometer is overfilled ($A_L > A_D$), then a tighter laser focus will lead to a higher F'_{SNR}. In this case, F_{SNR} yields a more reliable estimate of the figure of merit. Overall, F_{SNR} is more reliable (meaning more constant for different sample and focus parameters) than F'_{SNR}, but it is less convenient.

F_{SNR} and F'_{SNR} as defined in Eq. (4.24) and (4.25) assumed the case of the analyte shot noise limit, with negligible contribution from background scattering or detector noise. If the background noise is considered, as in Eq. (4.20) and (4.21), the F_{SNR} and F'_{SNR} expressions are more complex and probably less useful. However, F_{SNR} and F'_{SNR} still vary with $(P_D t_S)^{-1/2}$ or $(P_0 t_S)^{-1/2}$, respectively, for a given sample.

A consequence of this issue arises for tightly focused laser beams, such as occur in a Raman microprobe. For a spectrometer with a given F_{SNR} (and, therefore, $A_D\Omega QTK$), the observed SNR can be increased by tighter focusing, since for a constant P_0, P_D increases as the laser spot becomes smaller. This is fine, provided the sample is not subject to radiation damage. If sample damage is an issue (e.g., for a biological sample), Eq. (4.24) is more useful, with insertion of the maximum permissible P_D. Stated differently, the F'_{SNR} may be varied at will by changing the laser focus, even if unacceptable power densities are reached. F_{SNR} is not subject to this variation for the overfilled case and can be defined with a maximum P_D in mind.

To illustrate the potential utility of F_{SNR}, consider a scientist deciding on a purchase of one of two spectrometers, X and Y. A sample of neat benzene ($\beta D = 1.93 \times 10^{-7}\text{sr}^{-1}\text{cm}^{-1}$) in spectrometer X, was illuminated by 515 nm laser light with a P_D of 3×10^{17} photons $\text{sec}^{-1}\text{cm}^{-2}$ with t_M of 10 sec. The SNR, properly measured as S/σ_S for the 992-cm^{-1} band, is 26. The F'_{SNR} calculated from these parameters and Eq. (4.24) is $3.4 \times 10^{-5}\text{sr}^{1/2}\text{cm}^{3/2}$ $\text{photon}^{-1/2}$. Suppose a similar measurement on spectrometer Y yielded an F_{SNR} of 17×10^{-5}. The fivefold higher F_{SNR} for spectrometer Y indicates that the SNR will be 5 times higher than for X, for the same sample, power density, and t_M. If readout noise is negligible, this statement is true for a wide range of t_M and P_D, as well as for other samples with very different βD. Furthermore, the SNR for Y will be five times that of X if there is background present and Eq. (4.20) or (4.21) apply.

Despite the theoretical appeal of F_{SNR}, it is likely that F'_{SNR} will be more widely used, with units of $\text{W}^{-1/2}\text{sr}^{1/2}\text{cm}^{3/2}\text{sec}^{-1/2}$. From a practical

standpoint, it is easy to measure power in watts and measurement time for a sample with known βD. However, this less rigorous definition of F'_{SNR} brings with it the warning about variations in power density and possible sample damage.

As was the case for F_S, minor modification of F_{SNR} is necessary for the case of a single channel instrument. The time that determines SNR is t_S, which would occur instead of t_M in Eq. (4.24) for a single-channel instrument. Keeping F_{SNR} as a parameter based on total measurement time requires the substitution $t_S = t_M/N_R$, and

$$F_{\mathrm{SNR}}(\text{single channel}) = \frac{\mathrm{SNR}_A}{(P_D\beta_A D_A t_M)^{1/2}} = \frac{(A_D\Omega QTK)^{1/2}}{N_R^{1/2}} \tag{4.26}$$

So F_{SNR} is decreased for the single-channel instrument when compared to a multichannel system with N_R resolution elements.

As a final note on F_{SNR}, it should be emphasized that a figure of merit for SNR is not in common use for comparison of Raman spectrometers. In fact, there is no standard in general use for assessing performance, except for comparison of spectra of particular samples of interest to the user. Some of these are described in Chapter 5. Here F_{SNR} and F'_{SNR} are defined in the hope that they will lead to a common standard for spectrometer comparison, at least for a few common sample types such as clear liquids or thin films. At the very least, F'_{SNR} provides a means to adjust observed SNR for variations in laser power and integration time. For example, the CCD spectrometer used for Figure 4.8 has an F'_{SNR} that is 219 times as large as that for the scanning system, based on the observed SNRs, laser power, and measurement times. Stated differently, the CCD system should have an SNR 219 times larger than that for the scanning system, for the same laser power and total measurement time.

4.5. SNR AND DETECTION LIMITS

We noted earlier that the detection limit is directly related to SNR and is often defined as an analyte concentration yielding a signal that is some factor, k, larger than the standard deviation of the blank, σ_{bk}. It is useful to define the detection limit for Raman spectroscopy as the minimum detectable value of the cross section–number density product, or $(\beta D)_{\mathrm{MIN}}$. Of course, the concentration detection limit in terms of D or molarity will depend on the magnitude of β, but $(\beta D)_{\mathrm{MIN}}$ is a more general definition that directly indicates spectrometer performance. In the vast majority of analytical Raman measurements at low values of βD, the SNR is background noise limited, so $\sigma_{\mathrm{bk}} \approx \sigma_B$. In

this case, Eq. (4.11) leads to

$$(\mathrm{SNR})_{\mathrm{MIN}} = \frac{S_{\mathrm{MIN}}}{\sigma_B} = \frac{S_{\mathrm{MIN}}}{\sigma_{\mathrm{bk}}} = \frac{k\sigma_{\mathrm{bk}}}{\sigma_{\mathrm{bk}}} = k \tag{4.27}$$

where S_{MIN} and $(\mathrm{SNR})_{\mathrm{MIN}}$ are the signal magnitude and SNR at the detection limit. For example, if the requirement is that the signal be three times the standard deviation of the blank at the detection limit ($k = 3$), then $(\mathrm{SNR})_{\mathrm{MIN}}$ is 3. An equivalent definition of S_{MIN} is based on the slope, m, of a plot of signal vs. (βD) (see Ref. 1, p. 173):

$$(\beta D)_{\mathrm{MIN}} = \frac{k\sigma_{\mathrm{bk}}}{m} \tag{4.28}$$

In both approaches, one is determining the $(\beta D)_{\mathrm{MIN}}$ value, which yields a detectable signal, S_{MIN}, meeting the requirement that the signal exceeds the standard deviation of the background by a factor of k. In practice, one would determine $(\beta D)_{\mathrm{MIN}}$ from Eq. (4.28).

The detection limit is related to F_{SNR} through rearrangement of Eq. (4.24) to yield

$$(\beta D)_{\mathrm{MIN}} = \frac{(\mathrm{SNR})^2_{\mathrm{MIN}}}{(P_D t_M) F^2_{\mathrm{SNR}}} \tag{4.29}$$

If power instead of power density is preferred, Eq. (4.30) applies:

$$(\beta D)_{\mathrm{MIN}} = \frac{(\mathrm{SNR})^2_{\mathrm{MIN}}}{P_0 t_M (F'_{\mathrm{SNR}})^2} \tag{4.30}$$

and $(\mathrm{SNR})_{\mathrm{MIN}}$ is generally set equal to 3. Note that $(\beta D)_{\mathrm{MIN}}$ depends on power and measurement time and is a strong function of the SNR figure of merit. Equations (4.29) and (4.30) permit estimation of the detection limit in terms of $(\beta D)_{\mathrm{MIN}}$ directly from the SNR figure of merit.

4.6. SNR FOR MULTIPLEX SPECTROMETERS

As noted in Section 3.4, multiplex and multichannel spectrometers can monitor many wavelengths simultaneously, although they do it in different ways. For the same measurement time, these spectrometers can monitor each wavelength N_R times longer than a single-channel instrument. Most of the discussion in this chapter has dealt with multichannel systems, which have a large number of identical detectors monitoring N_R different wavelengths in parallel. Each

detector is assumed to have properties approximating those of a single-channel detector, so the main effect on signal is a lengthening of the collection time for each detector by a factor of N_R [Eq. (3.9)].

Multiplex spectrometers operate in a fundamentally different mode, with major consequences to the SNR. As noted earlier, the term *multiplex* means that photons of different wavelengths are detected by a *single* detector, then some postacquisition processing is used to sort out the contributions from different wavelengths. For example, FT-Raman uses a Michelson interferometer to modulate all wavelengths before detection by a single detector, then the wavelengths are sorted according to modulation frequency by a Fourier transform.

SNR analysis for multiplex and FT spectrometers is fairly complex and largely beyond the scope of this book (3–5). However, a nonrigorous discussion is useful for comparing FT-Raman and other multiplex techniques to dispersive systems. The signal for a multiplex system follows Eq. (3.6), with each wavelength (or, actually, the range of wavelengths contained in a given resolution element) being monitored for a time, t_M; and t_M might be the interferometer scan time or the total time for several scans that are co-added. Restricting the discussion to FT-Raman for the remainder of this section, Eq. (3.6) may be recast as:

$$S_{\mathrm{FT}} = (P_D \beta D K)(A_D \Omega T Q)_{\mathrm{FT}} t_M \tag{4.31}$$

Equation (4.31) applies to a particular wavelength or Raman shift, but the observed interferogram is actually the sum of all monitored wavelengths, after each is modulated at a different frequency by the interferometer. After Fourier transformation, the response for a given Raman shift will be proportional to S_{FT}. An additional observation of experimental significance is that $(A_D \Omega T Q)_{\mathrm{FT}}$ may differ greatly from the same quantity for a dispersive system.

If we assume a stable laser and negligible readout noise, Eq. (4.11) reduces to contributions from shot noise and detector noise:

$$\sigma_{\mathrm{FT}} = (\sigma_A^2 + \sigma_B^2 + \sigma_d^2)^{1/2} \tag{4.32}$$

Substituting for the σ values in (4.32) yields

$$\sigma_{\mathrm{FT}} = [(\dot{S} + \dot{B} + \phi_d) t_M]^{1/2} \tag{4.33}$$

Now, the big difference between multichannel and multiplex techniques arises because a single detector in FT-Raman is collecting all the modulated wavelengths at once. Consider a single data acquisition in an FT experiment, with the interferometer at a fixed position. The detector collects light from

all Raman shift values and does not "know" whether the photons are from one analyte band or another or from background. *So the shot noise in the data point thus acquired has contributions from all wavelengths in the spectral region observed.* The shot noise in a given data acquisition is the sum of all contributions, as stated in:

$$\sigma_{\mathrm{FT}} = \left[\sum_{N_R}(\dot{S}_i + \dot{B}_i) + \phi_d\right]^{1/2} t_M^{1/2} \tag{4.34}$$

The essential point here is that the signal magnitude for a given Raman shift value, as plotted in the spectrum after Fourier transformation, is proportional to the photons observed for that Raman shift only, while the noise has contributions from all Raman shift values. If we define ϕ_S as the rate of electron electron generation from photons reaching the detector, averaged over all N_R resolution elements:

$$\phi_S = \frac{\sum_{N_R}(\dot{S}_i + \dot{B}_i)}{N_R} \tag{4.35}$$

then:

$$\sigma_{\mathrm{FT}} = (\phi_S N_R + \phi_d)^{1/2} t^{1/2} \tag{4.36}$$

Note that since ϕ_S is an average, it is not wavelength dependent, so the noise in an FT-Raman spectrum is equal across the entire wavelength range monitored.

In the detector noise limit that is often observed for FT experiments,

$$(\mathrm{SNR})_{\mathrm{FT}} = \frac{\dot{S}_i t_M^{1/2}}{\phi_d} = \frac{L_i(A_D \Omega T Q)_{\mathrm{FT}} t_M^{1/2}}{\phi_d^{1/2}} \tag{4.37}$$

In this limit, the SNR increases with $t_M^{1/2}$, and the familiar $N_R^{1/2}$ "multiplex advantage" over a single-channel system results. Although this $N_R^{1/2}$ advantage is the same as that observed for multichannel systems [Eq. (4.18)], it has a very different origin and applies to a different limit (detector noise limited as opposed to shot noise limited). $\mathrm{SNR}_{\mathrm{FT}}$ in the detector noise limit is always lower than that observed for the shot noise limit, since by definition, ϕ_d was assumed to be much greater than ϕ_S.

If detector noise decreases to values much smaller than ϕ_S, the $(\mathrm{SNR})_{\mathrm{FT}}$ is governed by:

$$(\mathrm{SNR})_{\mathrm{FT}} = \frac{\dot{S}_i t_M^{1/2}}{(\phi_S N_R)^{1/2}} \tag{4.38}$$

The magnitude of $(SNR)_{FT}$ compared to the SNR for a single or multichannel system depends on the magnitude of ϕ_S, the average signal across the spectrum. If there is only one sharp peak in the spectrum, then $\phi_S = S_i/N_R$, and $(SNR)_{FT}$ equals SNR_A from the multichannel system [Eq. (4.17)]. As the spectrum becomes more complex, ϕ_S increases, and $(SNR)_{FT}$ degrades. The additional spectral features contribute to the shot noise for S_i and all other Raman bands. In the extreme of a nearly flat spectrum (such as might be observed for high background), $\phi_S = S_i$ and (4.38) becomes

$$(SNR)_{FT} = \frac{\dot{S}_i t_M^{1/2}}{\dot{S}_i^{1/2} N_R^{1/2}} = \frac{\dot{S}_i^{1/2} t_M^{1/2}}{N_R^{1/2}} = \dot{S}_i t_S^{1/2} \tag{4.39}$$

The multiplex advantage has been lost completely, and the FT spectrometer has the same SNR as a single-channel scanning system, in the case of a flat spectrum. For spectra more complex than a single peak, but not to the limit of a flat (i.e., "white") spectrum, SNR_{FT} will lie between the limits described by Eqs. (4.38) and (4.39).

As a rule of thumb, an FT spectrometer will exhibit a significant multiplex advantage when detector noise is present, compared to a single-channel spectrometer. As the detector noise becomes negligible, the $N_R^{1/2}$ multiplex advantage is lost unless the spectrum consists of only a few lines on a low background. For the common case of a broad background with superimposed Raman features, SNR_{FT} is comparable to a single-channel system. In contrast, multichannel spectrometers retain the $N_R^{1/2}$ advantage even with complex spectra, high background, or significant detector noise. As we will see in Chapters 8 and 9, multiplex spectrometers can have significantly larger $A_D\Omega$ products than multichannel systems, and this factor can partly equalize the SNR for a given measurement performed with both spectrometer types.

REFERENCES

1. J. D. Ingle and S. R. Crouch, *Spectrochemical Analysis*, Prentice Hall, Englewood Cliffs, NJ, 1988, pp. 141–142.
2. M. Fryling, C. J. Frank, and R. L. McCreery, *Appl. Spectrosc.*, **47,** 1965 (1993).
3. N. Everall and J. Howard, *Appl. Spectrosc.*, **43**, 778 (1989).
4. C. Brennan and I. Hunter, *Appl. Spectrosc.*, **49**, 1086 (1995).
5. A. G. Marshall and F. R. Verdum, in *Fourier Transforms in NMR, Optical, and Mass Spectroscopy*, Elsevier, New York, 1990, p. 49.

Raman Spectroscopy for Chemical Analysis. Richard L. McCreery

ISBN: 0-471-25287-5

CHAPTER

5

INSTRUMENTATION OVERVIEW AND SPECTROMETER PERFORMANCE

As noted in Chapter 1, the relatively recent explosion in Raman instrumentation started with Fourier transform (FT)–Raman in 1986 and accelerated with the introduction of charge-coupled devices (CCDs), diode lasers, holographic optics, and the like starting about 1987. These advances resulted in a rather daunting array of possible configurations for Raman spectrometers, often intended for different applications. A new user considering a Raman application must decide which of many available configurations is best for either the specific problem or more generally for the anticipated mix of samples and applications. Before discussing major components in detail in Chapters 6 to 9, we will consider some general instrumental issues and their importance to selecting or building a Raman spectrometer. In several cases, choices about particular instrument components have major effects on the entire spectrometer design. For example, the laser wavelength might dictate the spectrometer type (dispersive or nondispersive), the detector (single or multichannel), and the maximum achievable signal-to-noise ratio (SNR). As always, the choice from many instrumental configurations is dictated by the application and sample requirements.

5.1. MAJOR SPECTROMETER COMPONENTS

The generic spectrometer shown in Figure 1.7 will be one of two fundamentally different designs, dispersive (Fig. 5.1) (1,2) or nondispersive (Fig. 5.2) (3). In both cases, the objective is a plot of Raman intensity (photons per second) vs. Raman shift (in reciprocal centimeters), but this result is accomplished by very different procedures. The laser and sampling module may be similar for the two designs (although the laser wavelength is probably not), and both systems are amenable to fiber optics, microscopes, and other sampling accessories. The dispersive system separates wavelengths spatially, to be scanned across a single detector or monitored by many parallel detectors. Nondispersive spectrometers do not spatially separate different wavelengths but usually modulate them so that each wavelength has a characteristic modulation frequency. The composite modulated signal is then monitored by a

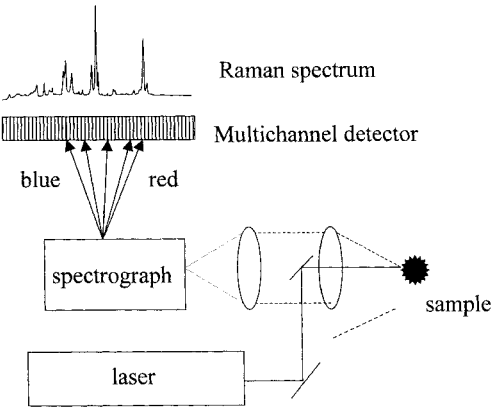

Figure 5.1. Schematic of the operation of a dispersive multichannel Raman spectrometer. Each detector element detects photons of a different Raman shift, and the spectrum is read out directly in terms of intensity (number of photons) vs. detector position (Raman shift).

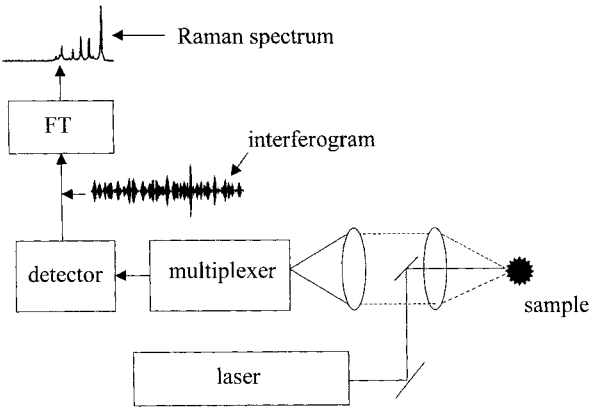

Figure 5.2. Schematic of a nondispersive, FT-Raman spectrometer. A single detector monitors photons with all Raman shifts, after each has been modulated by a multiplexer such as an interferometer. Raman spectrum is obtained by Fourier transformation of the detector output (interferogram).

single detector and demodulated by a Fourier transform. The advantages and shortcomings of each method are discussed below and in subsequent chapters, but the choice between the two is clearly an important criterion when selecting a spectrometer.

The choice of laser wavelength is critical to the success of Raman for a given application and has major effects both on the observed spectrum and

Table 5.1. Criteria for Raman Spectrometer Selection

1.	Laser wavelength and power
	a. Is fluorescence background a major problem?
	b. Are low detection limits required?
	c. Are electrical and cooling requirements important?
2.	Dispersive vs. nondispersive wavelength analyzer
	a. How important are spectral coverage and resolution?
	b. Does the application require high sensitivity?
	c. Does the application require tolerance to vibrations or temperature variation?
3.	Sampling mode
	a. Are samples open powders? Liquids in vials? Inside containers?
	b. Is sample microheterogeneity important?
	c. Is the sample in a harsh or dangerous environment or remote from the spectrometer (or both)?
	d. Is automated sample handling required?
4.	Data analysis
	a. Is data analysis primarily qualitative, such as compound identification?
	b. Is it primarily quantitative analysis of one component?
	c. Is it quantitative analysis of multiple components?
5.	Capital and operating costs
	a. Purchase price of spectrometer and laser
	b. Installation, including cooling water (possibly) and power
	c. Utilities and maintenance
	d. Samples/hour of operator time

the instrument design. Sampling mode could be "conventional" 90° or 180° backscattering from a sample compartment, microscopic through an optical microscope or imaging system, or remote, with fiber optics. Detector choice depends in turn on laser wavelength and spectrometer type and will be dictated by speed, spectral coverage, and sensitivity. Finally, the data acquisition and analysis system may vary from a simple, "one-button" operation to complex multivariate techniques and Fourier transformations.

The many options are discussed briefly below and in more detail in Chapters 6 to 9, but for now, it is useful to list the selection criteria for a Raman spectrometer. The list is in order of decreasing priority, and in several cases decisions made early in the sequence restrict later options. These criteria are outlined in Table 5.1, along with several questions affecting a user's decision.

5.2. LASER WAVELENGTH

Before beginning a detailed discussion of spectrometer design, the first two criteria in Table 5.1 deserve special note. The choice of laser wavelength

usually involves trade-offs among three factors: Raman cross section, detector sensitivity, and background scattering from the sample. As noted in Chapter 2, most Raman cross sections decrease with increasing laser wavelength, but some scatterers exhibit resonance effects that can be very large. If resonance enhancement of a particular analyte is essential for a given application, then that requirement dictates the laser wavelength. In the absence of resonance effects, a shorter laser wavelength will yield larger cross sections and sensitivity, with a $1/\lambda^4$ dependence. In addition, shorter wavelengths can usually be detected with higher quantum efficiency and less noise, thus improving sensitivity. However, shorter wavelengths also are more likely to excite fluorescence since more electronic transitions occur in the ultraviolet (UV) and visible than in the infrared regions. So, if a significant number of potentially fluorescent samples is anticipated, the laser wavelength should be as long as permitted by sensitivity requirements. As noted in Chapter 4, one is trading off the higher sensitivity at shorter laser wavelengths vs. the lower background at longer wavelengths, with the ultimate objective being maximum SNR. Some practical effects of laser wavelength are summarized in Table 5.2.

The effect of laser wavelength is illustrated in Figure 5.3 for a human breast biopsy sample. Six Raman spectra were acquired with lasers ranging from 406 to 830 nm. At 406 nm, fluorescence is sufficiently intense that the Raman signal is unrecoverable from background. This is the background shot noise limit [Eq. (4.21)] in which the SNR for the Raman signal approaches zero because of high background. With a 514.5 nm laser, carotenoids (related to β-carotene) are resonance enhanced and easily observable above a still high background. Carotene is a minor component (<1 per cent) but a very strong scatterer. If the objective were to monitor carotenoids in biological samples, resonance effects should obviously be exploited. For laser wavelengths of 691 nm and longer, the carotene resonance enhancement is absent (or at least much smaller) and the spectrum of fatty acids is apparent. These features are smaller than they were for a 514.5 nm laser, but the background is much lower and the SNR is higher. Referring to Eq. (4.20), the SNR improved when the laser wavelength increased because the background ($\beta_B D_B$) decreased much

Table 5.2. Generalizations on Laser Wavelength

Shorter Wavelength	Longer Wavelength
Larger cross section	Smaller cross section
Lower detector noise	
Dispersive spectrometer	Nondispersive spectrometer
Higher background	Lower background
Often background shot noise limited	Generally detector noise limited
Generally much higher SNR	Lower SNR requires higher laser power

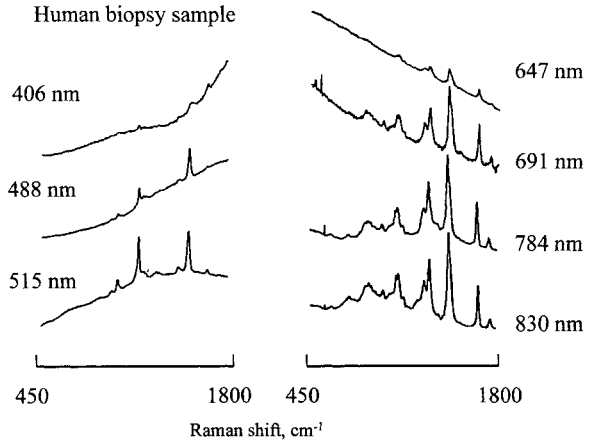

Figure 5.3. Raman spectra (uncorrected) of a normal human breast biopsy specimen obtained with lasers of various wavelength between 406 and 830 nm. (Adapted from Reference 4, with permission.)

more than the signal ($\beta_A D_A$). As longer wavelengths are employed, the background continues to decrease. Eventually, the SNR will degrade again as the lower detector Q or higher dark noise become factors.

The effect of detector noise is shown in Figure 5.4, for the common throat medicine Chloraseptic. At 514.5 nm, the red dye fluoresces and obscures the Raman scattering. At 785 nm, the greatly reduced fluorescence permits observation of Raman scattering from phenol, glycerin, and saccharin. At 1064 nm, the background is still lower, but detector noise has become a significant factor. In this case, the 1064 nm laser dictates the choice of a noisier detector, since the CCD used at 785 nm is insensitive above about 1050 nm. This example illustrates an important rule of thumb: The laser wavelength should be as long as required to avoid fluorescence, but not so long that signal strength and detector noise become problems (2,4). Stated in terms of Eq. (4.11), the objective is to maximize SNR by choosing a laser wavelength that yields the largest S while minimizing $(\sigma_B^2 + \sigma_d^2)$.

A quite different approach to improving signal and reducing background involves excitation with ultraviolet lasers in the range of 220 to 260 nm. UV-Raman at these wavelengths often exhibits resonance enhancement from aromatic rings, for example, and is sometimes called UV resonance Raman (UVRR) spectroscopy (5–7). Although UV-Raman is instrumentally more demanding than visible or FT-Raman, its advantages for analytical applications have been pointed out by Asher and co-workers (8–12). First, cross sections in the UV are larger due to the ν^4 factor and can be enhanced further by

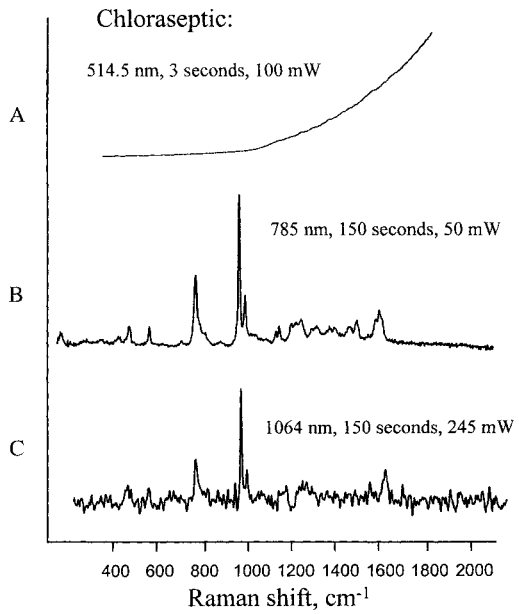

Figure 5.4. Spectra of Chloraseptic throat medicine obtained with different spectrometers. (A) 514.5 nm laser, 100 mW, 5 sec integration; (B) 785 nm, 50 mW, 150 sec integration, 4 cm^{-1} resolution, CCD detector; (C) FT-Raman, 150 sec acquisition time, 100 mW, 4 cm^{-1} resolution.

resonance. Second, many fluorophors are inactive when excited by deep UV (<260 nm), thus reducing background. An impressive case is the observation of Raman scattering from aromatic hydrocarbons in coal liquids (12). Third, UV Raman is much less sensitive to black-body background, and spectra may be obtained for hot samples. At present, lasers are expensive and CCDs are not as sensitive in the UV region, but doubled argon lasers show significant promise (10). In this author's opinion, there are some technical and safety issues to overcome before UV-Raman can compete with visible and near-infrared (NIR) Raman in an analytical setting. However, the special advantages of UV-Raman may justify the cost in certain applications.

5.3. DISPERSIVE VS. NONDISPERSIVE SPECTROMETERS

At the time of this writing, the Raman spectrometer market is approximately split between dispersive (spectrograph/CCD) and nondispersive (FT-Raman) instruments. Both types have their pros and cons, which enter into a selection for a given application. Several generalizations are listed in Table 5.3. These

Table 5.3. Comparison of Spectrometer Types

Dispersive/CCD	FT-Raman
ADVANTAGES	
Sensitive	Excellent frequency precision
Higher SNR	Higher AΩ
Laser $\lambda = 200-800$ nm (limited by response CCD)	Always ≥ 1064 nm
Lower laser power	Better fluorescence avoidance
No moving parts (often)	Good libraries
DISADVANTAGES	
Spectral coverage/resolution trade-off	Lower SNR
More fluorescence	Often high laser power
Resolution varies across spectrum	Full spectral coverage with constant resolution

comparisons are somewhat dependent on current technology, while others are inherent to the wavelength analysis technique. The relationship between wavelength choice and spectrometer type evident in Tables 5.2 and 5.3 is technical rather than fundamental. With today's technology, a spectrometer with a laser wavelength longer than 850 nm will be nondispersive, since suitable multichannel detectors are not available for Raman-shifted wavelengths longer than about 1000 nm. Furthermore, there are good reasons to avoid laser wavelengths below 850 nm with a nondispersive system (in general) due to the multiplex disadvantage discussed in Chapter 4. There is a major technical separation of spectrometer type into those designed to operate with Raman-shifted light below 1000 nm and those for longer wavelengths. This separation is currently dictated by the silicon photoresponse curve (discussed in Chapter 8) and by the currently poor noise characteristics of multichannel detectors for wavelengths above 1000 nm. Since this separation is technical rather than fundamental, it may change with evolving technology. However, it currently has a major effect on the way Raman spectrometers are designed and selected and on their suitability for particular applications.

5.4. PERFORMANCE CRITERIA

Several benchmarks for spectrometer performance are listed below, which vary in relative importance depending on the anticipated applications. Similar

parameters will be discussed later for particular components, but those listed here are characteristics of complete, integrated spectrometers. Whatever the properties of the components, the success of the measurement depends on the performance of the entire instrument.

5.4.1. Frequency Precision and Accuracy

Assignment of Raman features, library searching, and spectral subtraction depend on reproducible Raman shift values. Frequency accuracy becomes increasingly important as spectral databases become available, since spectra from a wide variety of spectrometers will contribute to the database. A consequence of frequency imprecision is shown in Figure 5.5 for a commercial tablet containing the pain reliever ibuprofen. With accurate Raman shifts, the ibuprofen spectrum from a library can be subtracted to yield the spectrum of a coating component, titanium dioxide (spectrum 5.5B). If the frequency is offset by 3 cm^{-1}, however, significant artifacts remain after subtraction (spectrum 5.5C). Unfortunately, peak frequencies in the literature often vary by several reciprocal centimeters for a given Raman feature, but accuracy of substantially better than ± 1 cm^{-1} is routinely achievable. In some spectrometers, <1 cm^{-1} accuracy is both routine and automatic (Chapter 10).

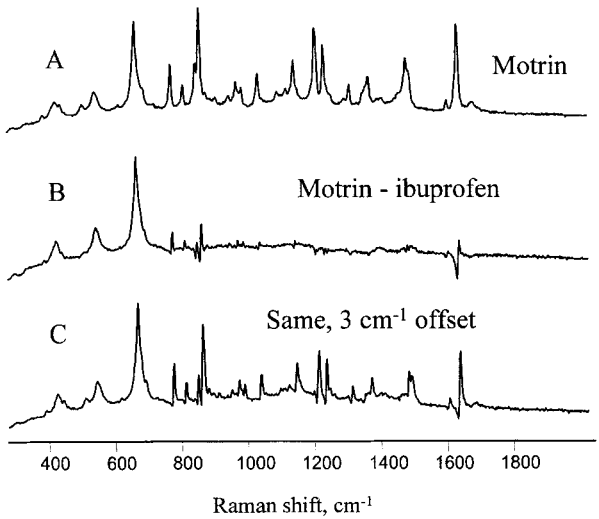

Figure 5.5. Raman spectra of Motrin anti-inflammatory tablet obtained with a 785 nm laser (A). Spectrum B was obtained by subtracting a reference spectrum of ibuprofen from spectrum A, revealing the TiO_2 coating on the Motrin tablet. Spectrum C shows the effect of a 3 cm^{-1} frequency offset preceding spectral subtraction.

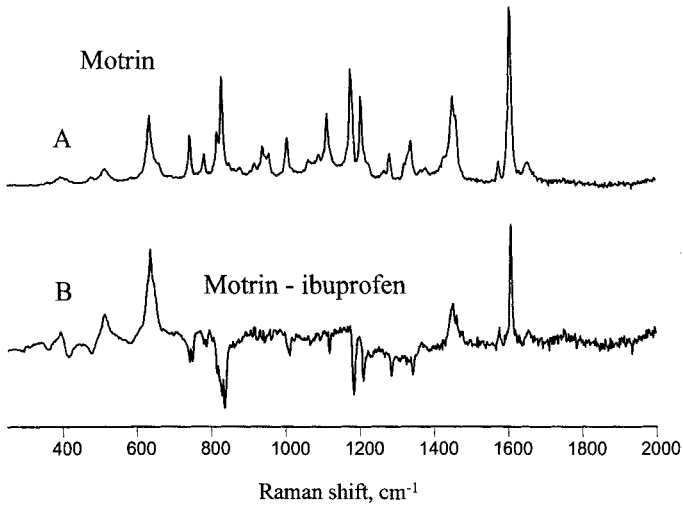

Figure 5.6. Spectrum of Motrin obtained with a 785 nm laser, but not corrected for instrument response function (spectrum A). Spectrum B results from subtraction of a corrected library spectrum for ibuprofen from spectrum A. Residual ibuprofen features result from differences in relative intensity between the corrected and uncorrected spectra.

5.4.2. Reproducibility of Relative and Absolute Peak Intensities

Although less important than peak frequencies, peak intensities obviously play a role in quantitative analysis and, in many cases, qualitative identification. Multivariate calibration techniques and their transferability depend on reproducible relative peak heights. A possibly lengthy method development procedure may fail when a different spectrometer is used, if the observed intensities vary. Reproducibility of absolute signal is difficult to achieve between labs or even between instruments of the same design, but it is important for a particular instrument. Absolute intensities can at least be used to evaluate day-to-day instrument performance and to detect hardware or alignment problems.

Calibration of relative intensities will be discussed in Chapter 10, but an illustration of its importance is provided in Figure 5.6. If the Motrin spectrum exhibits different relative peak intensities from those in a library, spectral subtraction leaves a residue from the subtracted spectrum.

5.4.3. Figures of Merit

The figures of merit, F_S and F_{SNR}, defined in Chapters 3 and 4, permit comparison of spectrometers for a given sample and laser power. Equation 4.29 shows

that F_{SNR} is directly related to the limit of detection, while both F_S and F_{SNR} permit estimation of the measurement time required for a given signal or SNR. Both figures of merit are useful when evaluating spectrometers for applications involving weak or dilute scatterers or where measurement time is an issue.

5.4.4. Available Laser Power

The figures of merit are normalized to a given laser power since they apply to collection rather than excitation of Raman scattering. Referring to Eq. (3.10) and (4.24), increasing laser power will increase the signal and SNR for a given value of the spectrometer figure of merit, F_S or F_{SNR}. While high laser power is desirable in this regard, there are limitations. High power, or more precisely high power density, can cause thermal or photolytic damage to the sample, ultimately limiting the acceptable power density. Sample damage requires an increase in F_S in order to lower the power density and maintain the signal. A second limitation on laser power is more pragmatic, involving cost or utility requirements. With today's technology, lasers with outputs of greater than about 500 mW require cooling water or external heat exchangers and are impractical for many requirements.

5.4.5. Environmental Requirements

Spectrometer designs differ in their sensitivity to vibration, dust, temperature changes, and the like, and in the utilities they require. On-line or at-line applications generally require a rugged instrument with minimal periodic maintenance. For routine use, cooling water or liquid nitrogen are often impractical, and stand-alone operation on only 110 V power is desirable. In addition, ambient light is usually not controlled in on-line or at-line applications, and resistance to stray light should be designed into the system.

In some cases, these environmental requirements are met by locating the spectrometer remotely from the sampling point, in a cleaner, more controlled environment. Fiber-optic probes, described in Chapter 12, have been used successfully when the sampling point is located 100 m or more from the spectrometer. Depending on the application, fiber-optic sampling may be a critical performance requirement.

5.4.6. Capital and Operating Costs

In addition to original purchase cost, spectrometers vary in their lifetime operating expense. At this writing, the largest maintenance cost relates to the laser, as currently popular lasers require expensive tube or diode replacement every 5000 to 10,000 h of operation. In addition, lasers differ greatly in the

cost and convenience of electrical power and cooling water (Chapter 7). The high sample throughput of modern Raman spectrometers is likely to provide competitive per-sample costs compared to Fourier transform infrared (FTIR), liquid chromatography (LC), and the like, thus mitigating the currently high capital cost.

5.5. SAMPLES FOR SPECTROMETER EVALUATION

Given the wide range of capabilities of various instruments, it is ultimately up to the user (or buyer) of a spectrometer to determine which performance criteria to emphasize. Instrumental specifications are important, but a more direct measure of performance is the quality of spectra obtained for samples representative of the type the user intends to examine. It is usually possible to require vendors to run a prospective buyer's samples before purchase. A more general approach is to evaluate spectrometers with samples that are chosen to "exercise" certain aspects of spectrometer performance. If such samples are commonly available and have known spectra, they can provide useful comparisons. The list of samples presented below is by no means comprehensive in that not all aspects of spectrometer performance are evaluated. However, the samples described in Sections 5.5.1 to 5.5.9 provide an initial set of readily obtainable materials that can reveal important strengths and weaknesses of particular spectrometers. The samples are listed under the performance criteria they are intended to evaluate, and sample spectra are provided in Figures 5.7 to 5.17.

5.5.1. Frequency Accuracy

As described in more detail in Chapter 10, the American Society for Testing and Materials (ASTM) has established several compounds as frequency standards (13). The Raman shifts for these materials were determined by at least six independent laboratories, and the standard deviation of each frequency was less than 1 cm^{-1}. Figure 5.7 shows a spectrum of 4-acetamidophenol, the active ingredient of Tylenol and several other analgesics. The indicated frequencies were determined with both 514.5- and 1064 nm lasers and did not show any laser wavelength dependence.

5.5.2. Low Raman Shift Performance

The requirement to suppress the much stronger signal from elastically scattered laser light in order to observe weak Raman features becomes more problematic at low Raman shifts. As noted in Section 8.2.1, this stray light

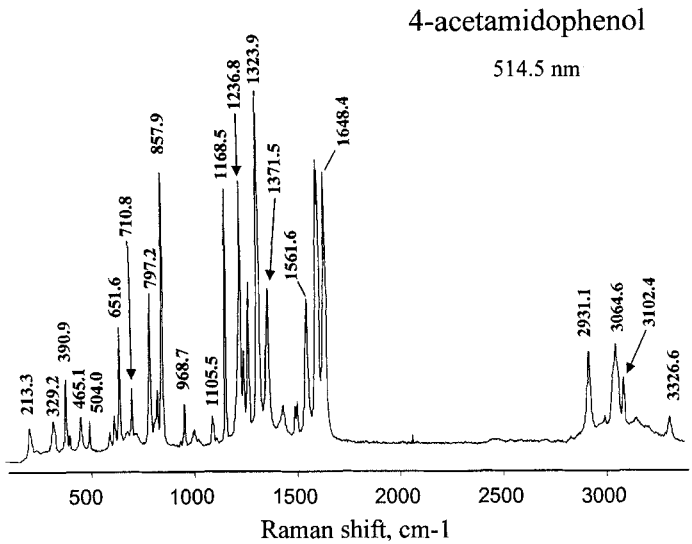

Figure 5.7. Spectrum of 4-acetamidophenol obtained with a Spex 1403 double monochromator, photon counting PMT, and 514.5 nm laser. Frequencies are from ASTM Standard E 1840. Standard deviations of all frequencies except 213.3 and 3326.6 are less than 1 cm^{-1} for determination by six independent laboratories.

interference becomes stronger as the laser frequency is approached. In general, spectrometers differ significantly in their ability to observe Raman shifts below approximately 300 cm^{-1}, due to the methods used to reject stray laser light. Elemental sulfur has several low-frequency Raman bands (Fig. 5.8) that test the ability to observe low Raman shifts. It should be noted that sulfur is a very strong Raman scatterer and will not simultaneously provide a good measure of sensitivity and low Raman shift performance. Another sample that is often recommended is the amino acid cystine, which has a Raman band at 7 cm^{-1}.

5.5.3. Weak, Clear Scatterers

Solutions in clear solvents (including water) are common samples for Raman spectroscopy, and spectrometer design can have a large effect on the size of the signal and the SNR. Na_2SO_4 dissolved in water is a convenient example of a clear solution containing a relatively weak Raman scatterer. For the conditions of Figure 5.9, the intensity of the 981 cm^{-1} band of 0.1 M Na_2SO_4 is approximately as large as that from the cell and spectrometer background. Repeated determination of the area of the 981 cm^{-1} band yielded a relative standard deviation for the conditions employed of 0.5 per cent, corresponding to a SNR of 200. Spectra of more dilute SO_4^{-2} solutions are shown in Figure 5.10. The

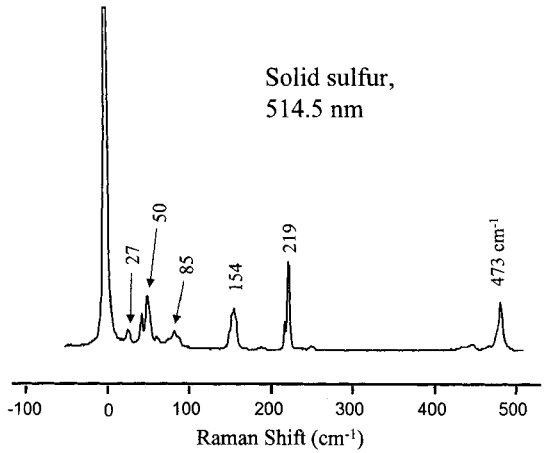

Figure 5.8. Raman spectrum of elemental sulfur obtained at 514.5 nm with a Dilor X-Y triple spectrometer and CCD detector.

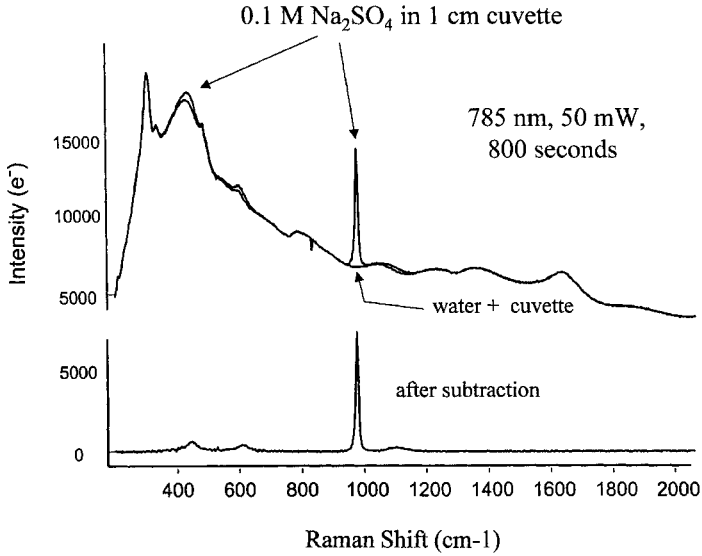

Figure 5.9. Spectra of 0.1 M Na_2SO_4 in a 1 cm quartz cuvette in water obtained with a Chromex Raman 2000 spectrometer and EEV 15-11 deep depletion CCD (−90°C), 50 mm slit, 600 line/mm grating, 50 mW of 785 nm light at sample, 20 integrations of 40 sec each were averaged. Lower spectrum is difference between the two upper spectra.

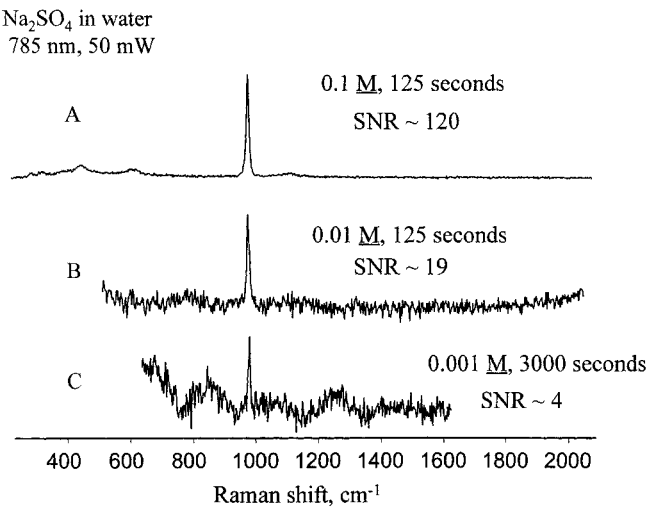

Figure 5.10. Spectra of Na_2SO_4 solutions, all after subtraction of water in cuvette background. Conditions as in Figure 5.9, except: (A) 0.1 M Na_2SO_4, average of five 25 sec integrations; (B) 0.01 M Na_2SO_4, average of five 25 sec integrations; (C) 0.001 M Na_2SO_4, average of sixty 50 sec integrations.

relatively long laser wavelength in this case (785 nm) yields a modest detection limit (for SNR ~3) for this system of just under 0.001 M.

5.5.4. White Solid with Weak Raman Scattering

White powders can present a challenge, since they generate a large elastic scattering signal. Several percent of the incident laser light may be scattered elastically into the spectrometer, representing a signal that is 10^4 to 10^8 times as strong as the Raman scattering. When the white solid is also a weak Raman scatterer, the sample becomes a severe test of both spectrometer sensitivity and laser light rejection. Powdered sucrose, lactose, dextrose, and the like are good examples of strong elastic scatterers with moderate Raman signals, and reasonable spectra should be obtainable with most spectrometers (e.g., see Fig. 5.16). Carbopol is a pharmaceutical excipient that is quite challenging, as it also has moderate fluorescence. Figure 5.11 shows spectra obtained with a 785 nm dispersive system and an FT-Raman system.

5.5.5. Fluorescent Samples

A discussed in Section 5.2, the choice of laser wavelength is often governed by background fluorescence, which generally decreases at longer wavelength. Rhodamine 6G is an example of a strongly fluorescent sample when observed

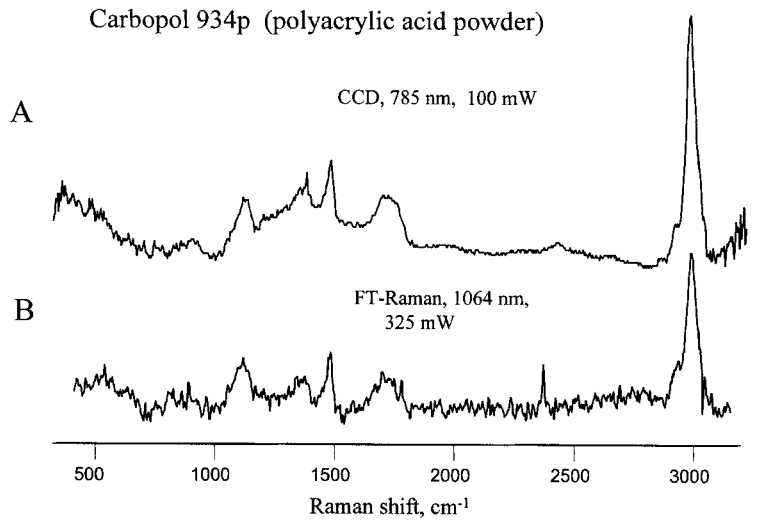

Figure 5.11. Spectra of polyacrylic acid homopolymer (Carbopol 934p, also "carbimer" resin, CAS registry 9003-01-4) unpacked powder. Spectrum A is an open powder obtained with the conditions of Figure 5.9, except 100 mW at sample and averaging of forty 3.5 sec integrations. A multipoint baseline was subtracted to yield spectrum A. Spectrum B obtained with a Bruker IFS 66 FT-Raman, germanium detector, 325 mW at sample, 1024 scans, 30 min total acquisition time, 4 cm^{-1} resolution.

with 514.5 nm light, but quite suitable for Raman spectroscopy for laser wavelengths above approximately 700 nm. Figure 5.12 shows an R6G spectrum demonstrating Raman scattering superimposed on a slowly declining fluorescence "tail." As the laser wavelength is increased, the tail becomes less intense relative to Raman scattering. Chloraseptic throat medicine is illustrated in Figure 5.13, as an example of a fluorescent solution of low concentration (1 per cent phenol in water, plus saccharin, glycerol, coloring). The acquisition time and laser power of the FT-Raman spectrum in Figure 5.13 were significantly larger than those of Figure 5.4, to improve SNR.

5.5.6. Opaque Solids

The penetration depth of the laser into a black solid can be quite short (< 1 μm), thus reducing the effective path length (dz or K from Chapter 2) and the Raman signal. Even samples with large cross sections, such as graphite, can yield quite weak Raman signals because both the laser and scattered light are severely attenuated in the sample (see Section 6.3.2). The spectrum of a silicon wafer used for integrated circuit fabrication is shown in Figure 5.14. It

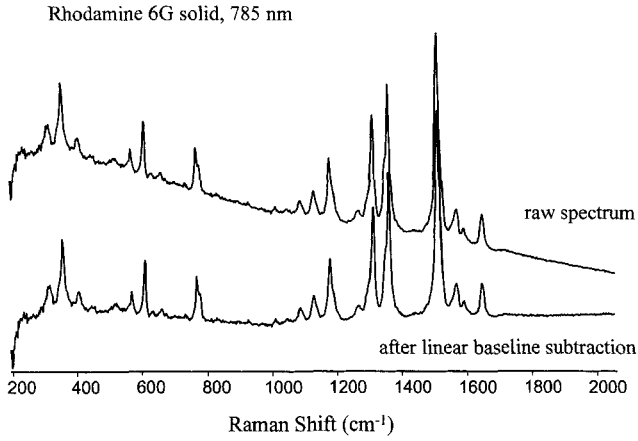

Figure 5.12. Rhodamine 6G laser dye (open powder, Exciton), observed with conditions of Figure 5.9, except average of twenty 0.2 sec integrations. Both spectra are response corrected, but lower spectrum is after a linear baseline was subtracted.

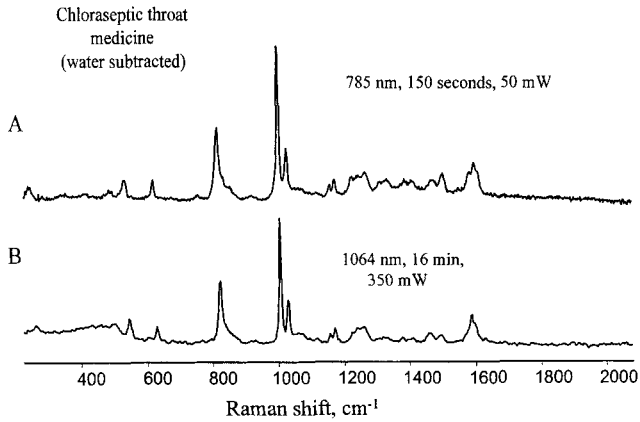

Figure 5.13. Chloraseptic (Procter & Gamble) throat medicine (1 per cent phenol, in water, plus glycerol, saccharin, dye) following subtraction of water and cuvette background. (A) conditions of Figure 5.9, average of five 30 sec integrations. (B) conditions of Figure 5.11B, using 512 scans and 16 min total acquisition time.

will be pointed out later that microprobe Raman systems often provide strong spectra for opaque solids, since their power density is high and depth of field is small (Chapter 11). Graphite from pencil lead is more readily available than silicon, although more variable in properties, but still provides a simple test of a spectrometer for strongly absorbing samples (Fig. 5.15).

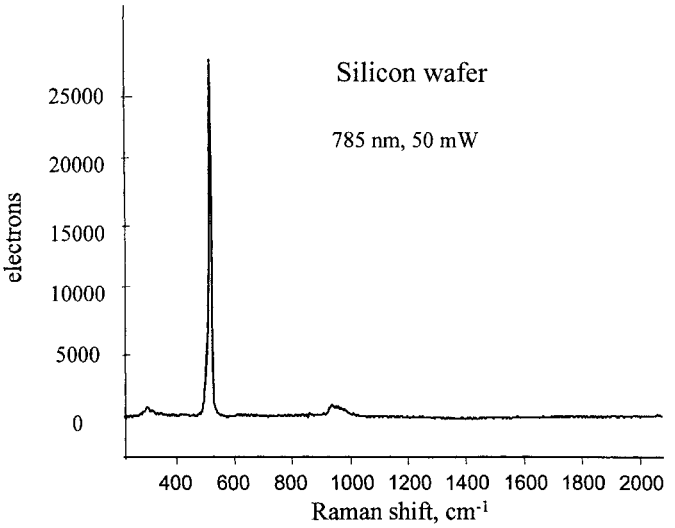

Figure 5.14. Unpolished side of Si (100) wafer, after subtraction of spectrometer background. Conditions same as Figure 5.9, but using a single 10 sec integration.

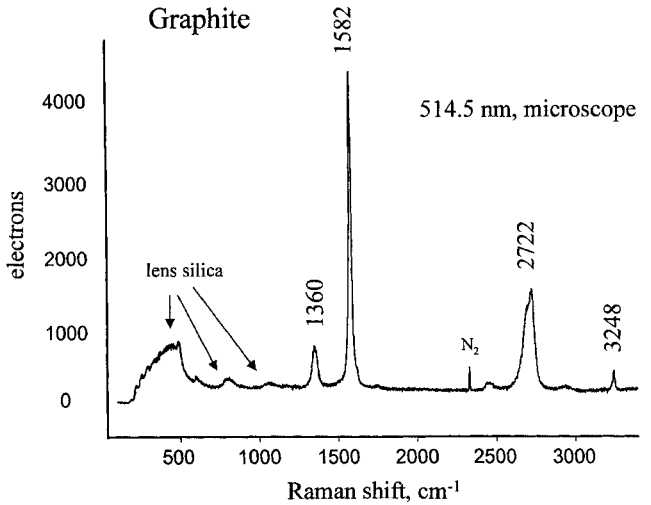

Figure 5.15. Spectrum of graphite in No. 2 pencil lead obtained with Dilor microscope and 50× objective. Five spectral segments with total acquisition time of 20 min; 5 mW at sample, 100 μm slit, resolution of ~4 cm^{-1}.

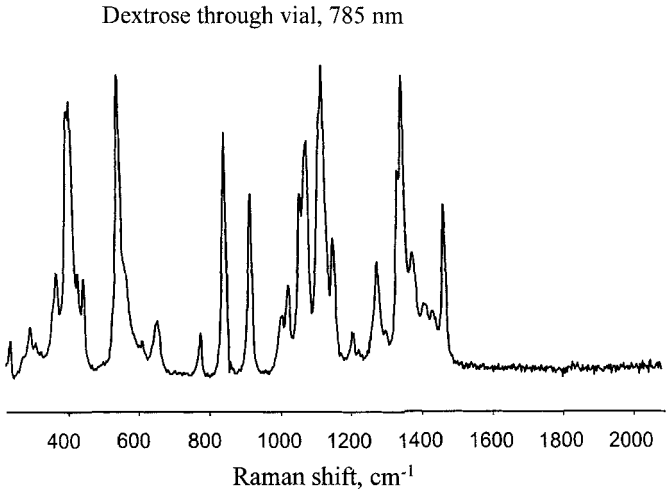

Figure 5.16. ACS reagent grade dextrose (glucose) solid inside USP amber vial. Conditions of Figure 5.9, average of five 10 sec integrations. Beam entered through bottom of USP vial, and vial spectrum was subtracted.

5.5.7. Through-Glass Sampling

The ability to obtain spectra of samples contained in glass or plastic vials without sample preparation is an attractive feature of Raman spectroscopy, since it permits noninvasive and nondestructive sampling. Not all spectrometer configurations can successfully observe samples in vials, due to optical geometry, working distance, or unsuitable laser wavelength. Of course, sample containers vary widely in thickness, shape, and material, but one example is shown in Figure 5.16. A USP (United States Pharmacopeia) amber vial is a standard container (with reproducible properties) used in the pharmaceutical industry, with a thickness of amber glass of about 3 mm (14). Figure 5.16 shows a spectrum obtained with 785 nm light directly through the bottom of the USP vial, with 180° geometry.

5.5.8. Response Uniformity

As noted in Section 5.4.2 and discussed in detail in Chapter 10, the relative peak heights observed in Raman spectra are strong functions of instrumental variables. These variations can be corrected, but it is useful to have a standard with known intensities in order to evaluate the instrument and the correction procedure. Figure 5.17 shows raw and response-corrected spectra of cyclohexane for 785 excitation. The relative peak areas for cyclohexane vary with

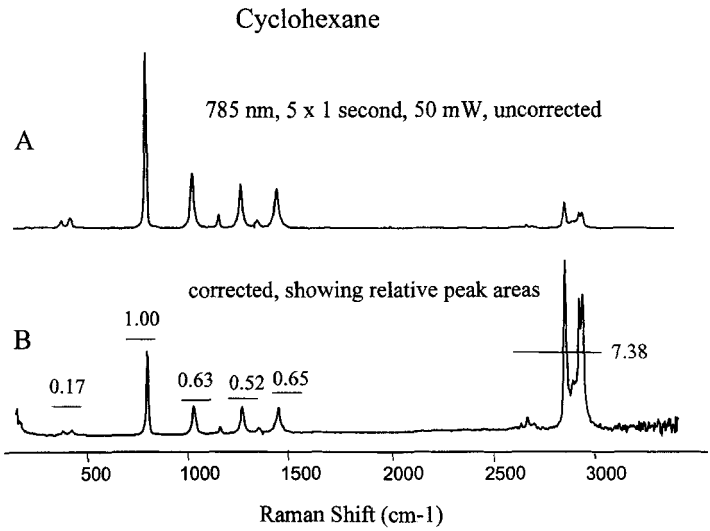

Figure 5.17. Spectrum of cyclohexane in 1 cm cuvette before (A) and after (B) instrument response correction as described in Chapter 10. Numbers above peaks indicate relative peak areas over the integration ranges shown. Spectrum A obtained with conditions of Figure 5.9, except using a 300 line/mm grating (see also footnote *e* of Table 10.7).

laser wavelength, but fairly weakly (see Chapter 10). The large difference in relative intensities between the raw spectrum and the "true" values of the corrected spectrum illustrates that instrumental effects on spectral appearance can be large. A detailed description of response correction is provided in Chapter 10, but Figure 5.17B is a visual representation of the corrected cyclohexane spectrum for 785 nm excitation (15).

5.5.9. Spectral Resolution

The ability to distinguish closely spaced peaks in spectroscopy has received much attention in the classical literature, and many of the same principles apply to Raman spectroscopy. Raman does require fairly high frequency precision and resolution, since one is observing relatively small frequency shifts from a particular laser frequency (see Chapter 10 for more detail). In the context of spectrometer evaluation, it should be noted that most analytical Raman applications involve liquids and solids in which Raman bandwidths are significantly greater than those in the gas phase. The narrowest linewidths encountered in most liquid and solid samples are in the range of 3 to 10 cm^{-1}.

At present, there is no agreed upon standard for resolution of Raman spectrometers. A pragmatic criterion for spectral resolution is the instrumental

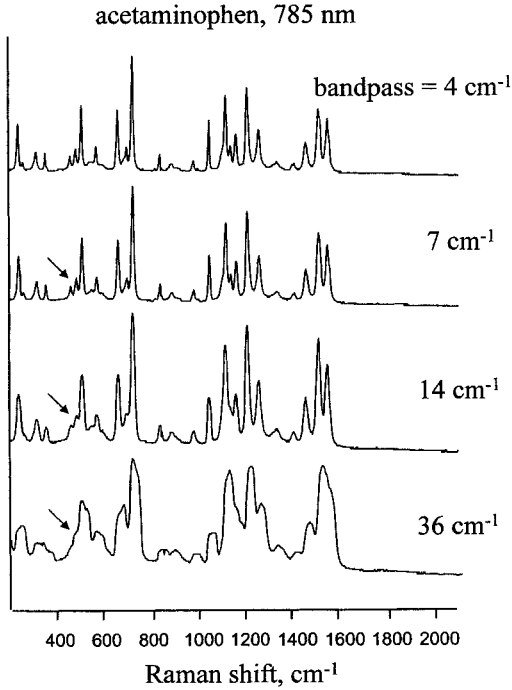

Figure 5.18. Spectra of an acetaminophen pellet obtained at 785 nm with a 250 mm, 600 line/mm spectrograph and varying slit width. The bandpass is an indication of instrumental linewidth and is a linear function of slit width [Eq. (8.7)]. The cases shown used 50-, 100-, 200-, and 500 μm slit widths. Arrows indicate features that are quite resolution dependent.

linewidth, which is fairly easily determined. If a hypothetical Raman band were infinitely narrow, the spectrometer would cause some apparent broadening due to its finite resolution arising from finite dispersion and pixel size in a dispersive system or finite mirror travel in an FT-Raman system. The spectrum of the narrow source would appear as a band on the final spectrum, and the observed bandwidth is often defined as the instrumental linewidth (ILW). Usually, the ILW is equated to the full width at half maximum (FWHM) of the observed "Raman" band of a very narrow source. An additional commonly used term describing resolution is the "spectral bandpass," which is similar but not identical to the ILW. The factors that determine bandpass are described in Chapter 8.

A low-pressure atomic emission lamp such as neon or argon emits atomic lines of sufficiently narrow linewidth to be considered "infinitely narrow" for most Raman spectrometers (an example is shown in Fig. 10.1). The width of atomic emission lines depends on temperature and pressure, but is generally

less than 0.001 nm. Thus 0.001 nm width corresponds to $<0.03\ cm^{-1}$ at 600 nm or $0.01\ cm^{-1}$ at 1000 nm, much narrower than solid or liquid Raman bands. So the observed FWHM of an emission line from a simple neon bulb is a good indication of instrumental linewidth. A more detailed specification for using atomic emission sources to determine ILW is currently under discussion by the ASTM Raman subcommittee.

Two Raman samples that provide indications of spectral resolution are cyclohexane and 4-acetamidophenol. The $801\ cm^{-1}$ band of liquid cyclohexane (Fig. 5.17) has a true linewidth (FWHM) of $4.0\ cm^{-1}$, and an observed linewidth larger than $4\ cm^{-1}$ indicates some degree of instrumental broadening. The Raman band of 4-acetamidophenol at $\sim 1614\ cm^{-1}$ (Fig. 5.7) is split into two bands approximately $8\ cm^{-1}$ apart. The spectral resolution required to resolve these two features as distinct peaks is adequate for the vast majority of analytical applications. The effect of resolution on the appearance of a typical Raman spectrum is shown in Figure 5.18 in which the slit width of a dispersive/CCD system was varied to change the spectral resolution. The bandpass was determined from the slit width and grating, as described in Chapter 8. As the bandpass increases, the spectral resolution worsens, peaks become broader, and closely spaced features merge into broader bands. For the example shown (and for many solid samples), a $7\ cm^{-1}$ bandpass or less is sufficient.

REFERENCES

1. R. L. McCreery, in J. Sweedler, K. Ratzlaff, and M. B. Denton, eds., *Charge Transfer Devices in Spectroscopy*, VCH, New York, 1994.
2. R. L. McCreery, in J. J. Laserna, ed., *Instrumentation for Dispersive Raman Spectroscopy*, Wiley, New York, 1996, pp. 41–72.
3. P. Hendra, in J. J. Laserna, ed., *Modern Techniques in Raman Spectroscopy*, Wiley, London, 1996.
4. C. J. Frank, D. C. B. Redd, T. S. Gansler, and R. L. McCreery, *Anal. Chem.*, **66**, 319 (1994).
5. S. A. Asher, C. R. Johnson, and J. Murtaugh, *Rev. Sci. Instrum.*, **54**, 1657 (1983).
6. C. M. Jones, V. L. Devito, P. A. Harmon, and S. A. Asher, *Appl. Spectrosc.*, **41**, 1268 (1987).
7. M. Ludwig and S. A. Asher, *Appl. Spectrosc.*, **42**, 1458 (1988).
8. S. A. Asher, C. H. Munro, and Z. Chi, *Laser Focus World*, **July**, 99 (1997).
9. S. A. Asher, *Anal. Chem.*, **65**, 59A (1993).
10. S. A. Asher, R. W. Bormett, X. G. Chen, D. H. Lemmon, N. Chao, P. Peterson, M. Arrigoni, L. Spinelli, and J. Cannon, *Appl. Spectrosc.*, **47**, 628 (1993).
11. V. Pascini, C. H. Munro, R. W. Bormett, R. E. Witkowski, and S. A. Asher, *Appl. Spectrosc.*, **51**, 81 (1997).

12. S. A. Asher and C. R. Johnson, *Science*, **July**, 224 (1984).
13. American Society for Testing and Materials, Standard Guide for Raman Shift Standards for Spectrometer Calibration, Standard E-1840-96, 1998.
14. R. L. McCreery, A. J. Horn, J. Spencer, and E. Jefferson, *J. Pharm. Sci.*, **87**, 1 (1998).
15. K. J. Frost and R. L. McCreery, *Appl. Spectrosc.*, **52**, 1614 (1998).

Raman Spectroscopy for Chemical Analysis. Richard L. McCreery

ISBN: 0-471-25287-5

CHAPTER

6

SAMPLING MODES IN RAMAN SPECTROSCOPY

6.1. SAMPLING OVERVIEW

The sampling geometry and collection optics are critical to efficient applications of Raman spectroscopy for several reasons. The design and execution of the alignment between laser, sample, and collection aperture have a huge effect on the magnitude and reproducibility of the signal and the signal-to-noise ratio (SNR). Remote sampling or Raman microscopy permit applications to a wider range of problems, some of which are uniquely suited to Raman spectroscopy. Furthermore, the stability and simplicity of sampling geometry can be the determining factors in whether Raman is practical for a particular analytical application. One must always keep in mind that Raman spectroscopy is a scattering technique with a generally weak signal, and the optical requirements are much more demanding than those of an absorption method such as Fourier transform infrared spectroscopy (FTIR). When sampling techniques for Raman are sufficiently robust and practical, the special advantages of Raman can be realized, such as noninvasive sampling, compatibility with fiber optics, and often trivial sample preparation. Conversely, an ineffective or cumbersome sample interface can prevent acceptance of Raman for a particular application. Given the importance of sampling, it will be discussed before other instrumental issues dealing with analysis and detection of scattered light.

Sampling modes for Raman can be divided into three general categories, of which only the first is discussed in this chapter. *Conventional sampling* is shown in Figure 6.1, which illustrates the 90° and 180° geometries common to traditional and many of today's spectrometers. Conventional sampling is the most similar to common analytical techniques such as ultraviolet-visible (UV–Vis) and FTIR absorption spectroscopy, and the samples are generally liquids in vials or cuvettes or solids such as pellets or powders. A second general type of sampling involves *remote sampling* using fiber optics, as depicted schematically in Figure 6.2. The fiber-optic head can be quite small and the fibers long, so Raman spectra may be obtained remotely many meters or even kilometers away from the spectrometer. For example, the sample may be in a pipe in a chemical plant or in a hazardous environment where batch sampling is impractical. Furthermore, a chemical process may be monitored continuously (so-called *process monitoring*), and the analytical data

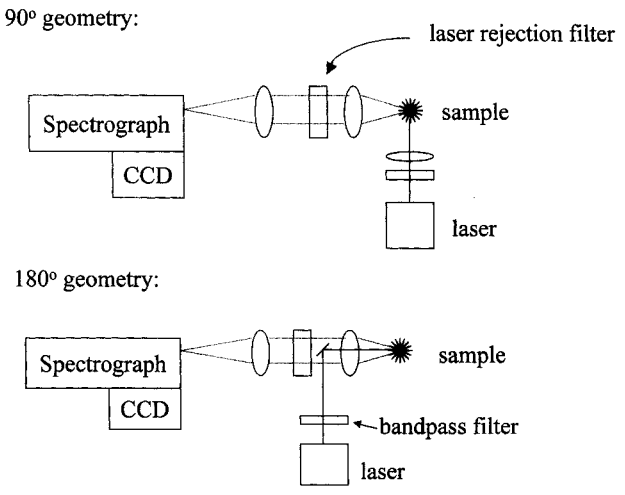

Figure 6.1. Common sampling geometries for Raman spectroscopy. Dispersive spectrometers are shown, but similar sample arrangements are used for FT-Raman.

may be used to control the chemical process (*process control*). Fiber-optic sampling has significantly stimulated analytical Raman applications and will be discussed in Chapter 12.

A third class of sampling geometries involves Raman microscopy and closely related Raman imaging techniques. Combination of a Raman spectrometer with a modified optical microscope permits spectra to be obtained from very small sample regions, down to less than 1 μm laterally and a few microns in depth (Fig. 6.3). *Raman microspectroscopy* is a term generally used to describe this spatially resolved technique in which spectra are obtained

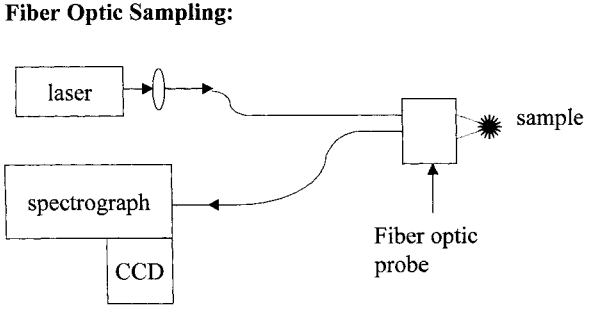

Figure 6.2. Schematic of fiber-optic sampling configuration. Fiber lengths between probe and laser/spectrometer can be quite long, up to several hundred meters.

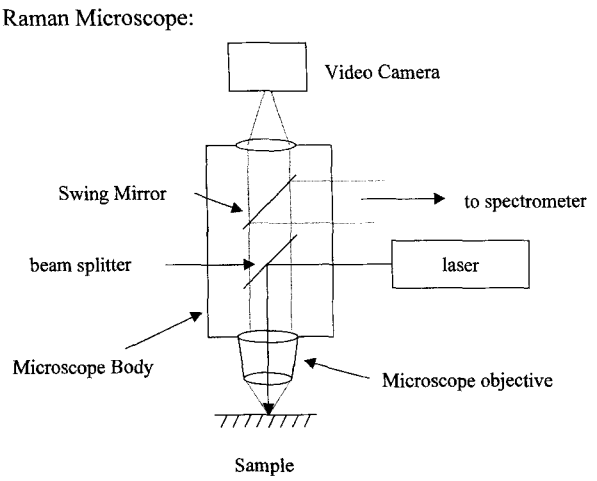

Figure 6.3. Schematic of a Raman microprobe. A modified optical microscope directs an image onto a video camera or Raman light to a spectrometer. Various arrangements are available for sample motion and imaging.

from microscopic domains of a sample, usually a solid or thin film. *Raman imaging* refers to techniques in which a two-dimensional image, sometimes depth resolved, is constructed using Raman scattered light. For example, a Raman image of an integrated circuit using the 521 cm^{-1} Raman mode of elemental silicon would show a pattern of exposed silicon but not silicon oxide or aluminum. There are a variety of techniques for obtaining Raman images, and they will be described in Chapter 11. In the current chapter, the conventional and most common sample geometries will be described.

6.2. PERFORMANCE CRITERIA

As discussed in Chapters 2 and 3, a scattering experiment has several more variables than an absorption method, leading to a more complicated dependence on sampling and optical design parameters. There are many ways to obtain Raman spectra, and often small variations can lead to large effects on signal and SNR. It can be argued that there are "too many choices" in sampling modes, and lack of standardization has been an impediment to widespread application of Raman in chemical analysis. Most of the design issues will be addressed in this chapter, but it is important to be aware of how these issues affect analytical performance. Sampling criteria are a more specific component of the general performance criteria listed in Table 5.1 and include at least the topics discussed in Sections 6.2.1 to 6.2.4.

6.2.1. Effective Sampling Volume

In Chapter 3, we noted that Raman signal is proportional to the total number of illuminated molecules monitored by the spectrometer. From Eq. (3.6), we see that

$$\#\text{ of scattering molecules} = DKA_D$$

where K is a geometric factor depending on sample properties and configuration. K may be determined by sample thickness, dz, as in Figure 3.1, or by spectrometer properties such as depth of field. Several examples of K for different situations are discussed below. Sampling volume is one factor determining signal magnitude but is also of obvious importance to the degree of spatial resolution achieved in microscopy.

6.2.2. *Étendue* at the Sample

The $A\Omega$ product (*étendue*) defined in Section 3.2 also contributes to the signal magnitude and varies greatly for different sample configurations. The $A\Omega$ product is usually limited by some inherent constraint in the spectrometer, such as detector or slit area, and the sampling optics should not impose a further limit on its magnitude.

6.2.3. Power Density at Sample, P_D

Although Raman signal strength increases with power density, sample damage ultimately imposes a limit on the magnitude of P_D. And P_D can vary from <10 W/cm^2 for a "macro" sample to $>10^6$ W/cm^2 in a microscope. Table 6.1 illustrates the wide variation in power density for common sampling configurations. Acceptable P_D depends on the absorption properties of the sample as well as its thermal or photochemical damage threshold.

6.2.4. Reproducibility of Raman Signal

Since alignment and focus of Raman spectrometers strongly affect signal strength, their reproducibility is important to quantitative measurements. Different sampling geometries have varying sensitivity to focus. It will be illustrated later that a short focal length collection system is efficient but quite sensitive to focusing. An extreme case is a microscope, where a few microns of motion along the optical axis can reduce the signal by half or more. The 90° geometry is often more sensitive to sample positioning than the 180° geometry. So a 180° configuration with a relatively long collection focal length generally

Table 6.1. Power Density, P_D, of Laser Light at Sample

Power (mW)	Beam Dimensions at Sample	P_D (W/cm^2)	P_D,[a] (photons/sec cm^2)	P_D, Relative to 1 mm circle
100	25 μm circle[b]	20,400	5.2×10^{22}	158
100	50 μm circle	5,100	1.3×10^{22}	39
100	100 μm circle	1,270	3.3×10^{21}	10
1,000	1 mm circle	127	3.3×10^{20}	1.00
100	50 × 2000 μm rectangle	100	2.6×10^{20}	0.8
5	50 × 2000 μm rectangle	5	1.3×10^{19}	0.04
10	1 μm circle	1.3×10^{6}	3.3×10^{24}	10^4
10	5 μm circle	5.2×10^{4}	1.3×10^{23}	394

[a]For 514.5 mm light.
[b]Circular dimensions refer to beam diameter at sample.

results in better signal reproducibility, while short collection focal length often yields larger signal. This and similar trade-offs often influence spectrometer design and selection.

6.3. 180° BACKSCATTERING GEOMETRY

As noted earlier, the 180° backscattered geometry is experimentally convenient and has become quite common in commercial instruments. Most fiber-optic probes and Raman microscopes also use 180° backscattered geometry, so similar principles apply in all three sampling categories.

6.3.1. 180° Optical Configurations

Figures 6.4 and 6.5 show more detailed examples of the general 180° geometry of Figure 6.1. In all cases, the laser beam is coaxial with the collection "beam," and a beamsplitter or mirror is used to combine the two beams. Modes A, C, and D permit rapid exchange of lens L1, thus permitting variation in working distance and depth of field. Mode B is used in several FT-Raman instruments because the laser focus can be varied (by changing L3) without affecting collection. Modes A, C, and D can exhibit background from lens L1, if the lens material is prone to luminescent or Raman background. Similarly, mode C can exhibit background from the beamsplitter. While these background sources can generally be avoided with proper choice of optical materials, there are some specialized 180° configurations shown

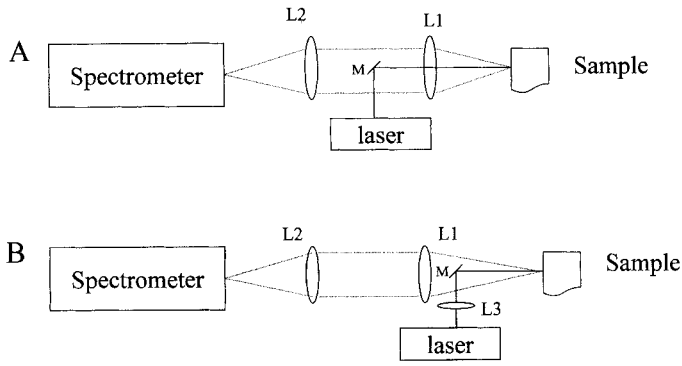

Figure 6.4. Two variations of the 180° sampling geometry. The laser beam is inserted colinearly with the collection axis by a small mirror, *M*.

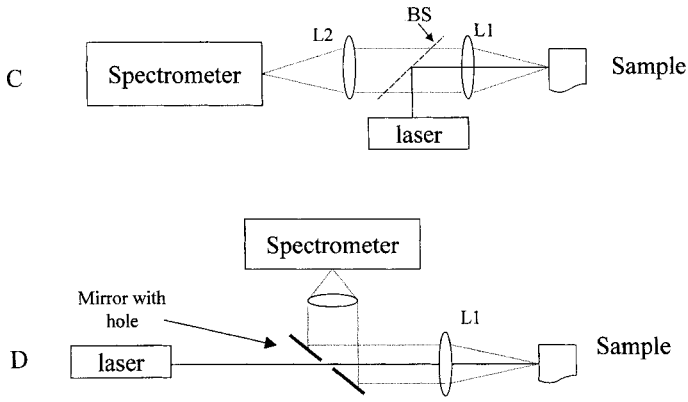

Figure 6.5. Additional 180° configurations. Schematic 6.5C uses a beamsplitter (BS) to combine laser and collection axes. BS is often a dichroic mirror that selectively reflects the laser wavelength. Schematic 6.5D uses a plane mirror with a small hole, large enough to pass the laser beam.

in Figure 6.6 that use reflective optics to avoid them altogether. An off-axis paraboloid (OAP) is a specialized mirror formed from a section of a parabolic reflector.

An important advantage of the 180° geometry is the possibility of noninvasive sampling through a window or sample container, as shown in Figure 6.7. The working distance between the lens and sampled region can be quite long (several centimeters), so a suitable window may be placed between the spectrometer and the sample. For example, Figure 6.7A shows a pipe in a

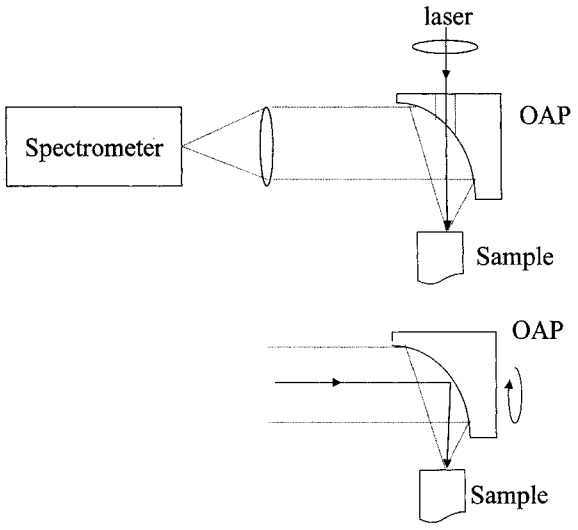

Figure 6.6. 180° configurations using reflective optics based on an off-axis paraboloid (OAP). Upper drawing shows a hole in the OAP, lower drawing assumes laser and collection axes have been combined, as in Figure 6.4A, 6.5C, or 6.5D.

chemical plant with a flat window for on-line monitoring. The window material (often quartz or sapphire) is out of focus and usually contributes negligibly to the background. The laser and the collected light pass through the same surfaces, so curved vials or bottles can be tolerated (Fig. 6.7B). Many plastics are transparent enough to act as windows, so samples may be probed in various common containers. Figure 6.8 shows Raman spectra of acetamidophenol (active ingredient of Tylenol) as both an open powder and in an amber vial. In the latter case, the geometry of Figure 6.5D was used, and the beam penetrated about 3 mm of optically imperfect amber glass on the bottom of the vial. The glass attenuates the signal by about 60 per cent, but there is little distortion of intensities. Spectral effects of the window material are correctable with the procedures of Chapter 10.

The 180° geometry is an example of the sampling convenience that is a major driving force for the development of analytical Raman instrumentation. A similar geometry is often used for near-infrared (NIR) absorption spectroscopy, where noninvasive sampling with little or no sample preparation has become quite valuable. With the 180° geometry and Raman spectroscopy, one retains the ease of sampling while adding high-resolution vibrational information to generally low-resolution NIR spectra. The geometry of Figure 6.7 has obvious applications to a wide variety of problems in chemical processing and quality control.

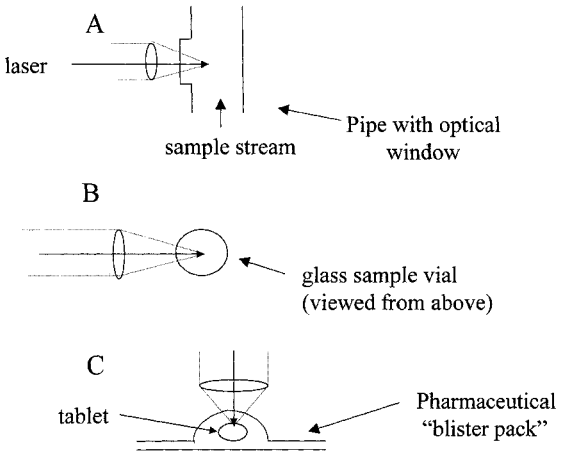

Figure 6.7. Noninvasive 180° sampling into a flowing stream (A), sample vial (B), or pharmaceutical blister pack (C). Optical window in case 6.7A is often made of sapphire to withstand possibly high pressure.

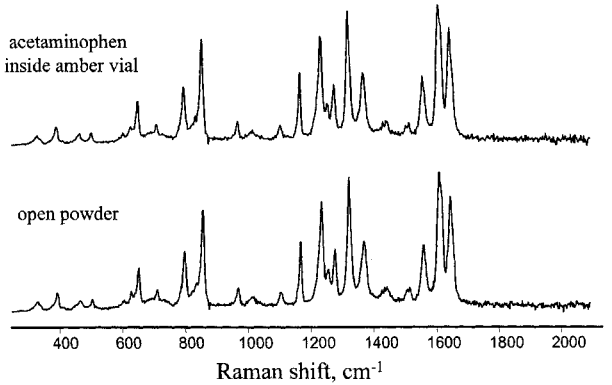

Figure 6.8. Spectra of acetamidophenol (active ingredient of Tylenol) obtained with geometry of Figure 6.7B. Spectra were response corrected as described in Chapter 10. Despite attenuation by amber vial, the corrected spectra differ by less than 5 per cent.

6.3.2. Sampling Volume for 180° Geometry

Chapter 3 and Eqs. (3.6) to (3.8) demonstrated that a Raman signal is proportional to a "geometric" factor K, which is related to sampling volume. For the case of 180° geometry shown in Figures 3.1 and 3.2, K is the incremental path length (dz) in the sample monitored by the spectrometer and illuminated by

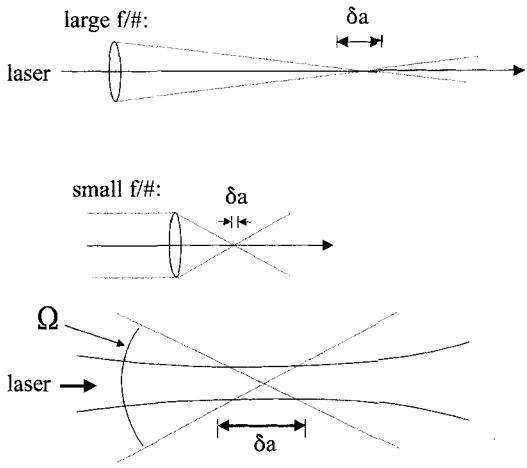

Figure 6.9. Spectrometer depth of field, δa, for large and small $f/\#$. The region sampled by the spectrometer is the overlap between the depth of focus and the sample volume illuminated by the laser.

the power density P_D. For the 180° geometry, K can be considered the effective path length determined from the integration of dz over the sample region illuminated by the laser and collected by the spectrometer. The magnitude of K can be affected by several aspects of the sample and the spectrometer design and will be addressed in some detail. Although the discussion applies to the 180° geometry, similar concepts bear on other sampling geometries as well. The three primary factors that determine K are spectrometer depth of field, sample thickness, and sample optical density.

The spectrometer depth of field, δa, is the same parameter that applies to photography and depends primarily on the $f/\#$ of the collection optics. One expression for δa is given by Eq. (6.1), where ϵ is the "blur diameter" (1):

$$\delta a \simeq \epsilon(f/\#) \tag{6.1}$$

The blur diameter is related to the size of the slit image at the sample and approximately equals the diameter of a point source at the sample after it is imaged at the slit. For a clear, thick sample, K equals δa, and Eq. (6.1) indicates that the effective sampling depth for the collection optics is proportional to the collection $f/\#$. Figure 6.9 illustrates this fact for low and high $f/\#$.

The laser has a depth of focus that depends on the laser divergence and the focal length of the focusing lens, f_1 (e.g., L1 in Fig. 6.4). The minimum spot

diameter for the laser is twice the beam waist, w_0, and is given by:

$$\text{Spot diameter} = 2w_0 = f\theta_d \tag{6.2}$$

where θ_d is the full angle divergence of the laser in radians and f is the focusing lens focal length. The depth of focus of the laser (δa) is given either by Eq. (6.3) in the diffraction limit (2,3):

$$\delta a = \sqrt{3}\pi w_0^2/\lambda_0 \tag{6.3}$$

or by Eq. (6.1) for the ray-optic limit (where the $f/\#$ refers to the laser, not the lens). For the ray-optic limit, the $f/\#$ of the laser is larger than that for the collection optics, so the laser focal depth does not limit the path length (see Fig. 6.9). Strictly speaking, K is the integral of dz over the overlap region for the laser and spectrometer depth of fields. In the situations shown in Figures 6.4 to 6.6, this overlap usually equals the spectrometer depth of field from Eq. (6.1), since the spectrometer $f/\#$ is usually smaller than the laser $f/\#$.

Although the depth of field and therefore K are proportional to the collection $f/\#$, Ω_D is proportional to $(f/\#)^{-2}$ via Eq. (3.4). The product of K and Ω_D yields

$$K\Omega = \frac{\epsilon\pi}{4(f/\#)_D} \tag{6.4}$$

If all else were constant and Eq. (3.6) or (3.8) applies, the signal would vary inversely with $f/\#$ for a case limited by spectrometer depth of field.

The effective path length for the case where K is limited by spectrometer depth of field ranges from less than 100 μm to several millimeters for typical conditions. If the sample is clear, it is generally possible to make the sample depth greater than the spectrometer depth of field. However, for thin samples (or optically dense samples, as discussed below), the opposite limit may apply in which the sample is thin compared to δa, and K is determined solely by the sample thickness. For example, a biological membrane or a sheet of plastic wrap will be thinner than the depth of field of most conventional spectrometers. In this case, the integral of dz is simply the sample thickness (b), and $K = b$, yielding

$$S = P_D\beta DbA_D\Omega TQt \tag{6.5}$$

where K no longer depends on collection $f/\#$, but Ω_D does, so the signal will scale with Ω_D, or $(f/\#)^{-2}$. The functional dependence of $K\Omega_D$ on several collection variables is summarized in Table 6.2. All else being equal, Raman signal scales with $K\Omega_D$.

Table 6.2. Dependence of Effective Path Length and $K\Omega_D$ on Sample and Collection Variables, 180° Geometry

Sample Type	K	$K\Omega_D$
Thick[a], transparent, $b \gg \delta a$	$\epsilon(f/\#)$	$\dfrac{\epsilon\pi}{4(f/\#)}$
Thin[a], transparent, $b \ll \delta a$	b	$\dfrac{b\pi}{4(f/\#)^2}$
Optically dense[b]	$(\alpha_L + \alpha_D)^{-1}$	$\dfrac{\pi}{4(f/\#)^2(\alpha_L + \alpha_D)}$

[a]"Thick" and "thin" refer to the sample depth (b_{max}) being much greater or much less than the collection depth of field.
[b]Case where sample thickness is greater than $(\alpha_L + \alpha_D)^{-1}$ but less than δa.

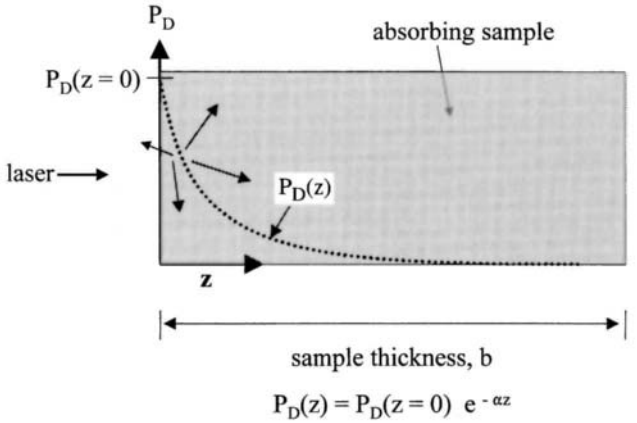

Figure 6.10. Attenuation of incident laser power density by an absorbing sample. $P_D(z)$ is the power density at various sample depths. Raman light is also attenuated by the sample absorption, resulting in Eq. (6.9).

An optically dense sample is a special case of a thin sample in which the sampling depth is determined by the absorption or scattering properties of the sample. *Scattering* in this context refers to mainly elastic scattering such as might occur in a powder. The effects on Raman sampling are illustrated in Figure 6.10. The incident laser light is attenuated by absorption and scattering in the sample but results in Raman-shifted light over some sample depth. This Raman light is attenuated as it leaves the sample, resulting in shorter sampling depth for more optically dense samples. The decrease in laser intensity is approximated by Eq. (6.6), and the signal from the emerging Raman light

by Eq. (6.7):

$$P_D(z) = P_D(z = 0)e^{-\alpha_L z} \tag{6.6}$$

$$S = \int_0^b P_D(z)e^{-\alpha_R z}(\beta D A_D \Omega T Q)\, dz \tag{6.7}$$

The Raman light that escapes the sample will be proportional to the integral of the product of the local power density and the attenuation of escaping Raman light, as in Eq. (6.7) (4). The terms α_L and α_R are the attenuation coefficients for the laser and Raman-shifted light and are generally considered to equal the sum of a scattering constant and an absorption constant, each with units of reciprocal centimeters.

The combination of Eqs. (6.6) and (6.7) leads to an effective path length K given by:

$$K = \int_0^b e^{-(\alpha_L+\alpha_R)z}\, dz = \frac{1 - e^{-(\alpha_L+\alpha_R)b}}{\alpha_L + \alpha_R} \tag{6.8}$$

provided the spectrometer depth of field is large compared to the total sampling depth. Finally, if the sample is fairly optically dense so that $b \gg (\alpha_L + \alpha_R)^{-1}$, the path length reduces to $(\alpha_L + \alpha_R)^{-1}$ and Eq. (6.9) applies. Examples of common samples that meet these conditions include graphite (Fig. 5.15) and elemental silicon (Fig. 5.14), in which K is less than 1000 Å.

$$S = \frac{P_D \beta D A_D \Omega_D T t}{\alpha_L + \alpha_R} \tag{6.9}$$

An extreme case of a thin sample is a monolayer or submonolayer on a surface, a situation of great interest to research in catalysis, electrochemistry, and surface chemistry. The simplest example is a flat surface with complete or partial coverage by a single molecular layer of some adsorbate. Equation (6.5) may be applied directly with K equal to the thickness of the monolayer and D with units of molecules per centimeter cubed. However, it is more convenient and conventional to express D for surface monolayers with units of molecules per centimeter square, in which case $K = 1$ (5). Using D_S to indicate the surface concentration, Eq. (6.5) becomes

$$S = P_D \beta D_S A_D \Omega_D T Q t \tag{6.10}$$

The dependence of the $K\Omega_D$ on $f/\#$ for a surface monolayer is the same as the "thin, transparent" case of Table 6.2. Surface monolayers are discussed in greater detail in Chapter 13.

6.3.3. A_D and *Étendue* Effects on Raman Signal

Table 6.2 summarizes the effects of sample and $f/\#$ on effective path length, but additional variables are important for determining the overall signal for the 180° geometry. In most Raman experiments, the laser power P_0 (photons per second) is controlled, rather than the power density, P_D (photons per second per square centimeter). It is useful to consider a question posed in practical terms: For a given laser power, how does the Raman signal depend on the collection lens (L1 in Figs. 6.4 and 6.5)? This question is relevant not only to the choice of a collection lens, but also to the available working distance between the lens and the sample. We will consider the answer for two limiting cases, the *underfilled* and *overfilled* situations illustrated in Figure 3.2. The geometry of Figure 6.4A will be assumed, but the conclusions apply to others as well, with minor modification.

The *overfilled* case is illustrated in more detail in Figure 6.11A. The image of the laser focus at the spectrometer is larger than the slit (or other entrance aperture). The $A_D\Omega_D$ is determined by the spectrometer and will not vary with f_1, since A_D and Ω_D vary with f_1^2 and f_1^{-2}, respectively. The power density varies with f_1^{-2} if P_0 is constant since the laser spot diameter equals $f_1\theta_d$ [Eq. (6.2)]. For a thick sample, K increases linearly with f_1 (since $f/\#$ is

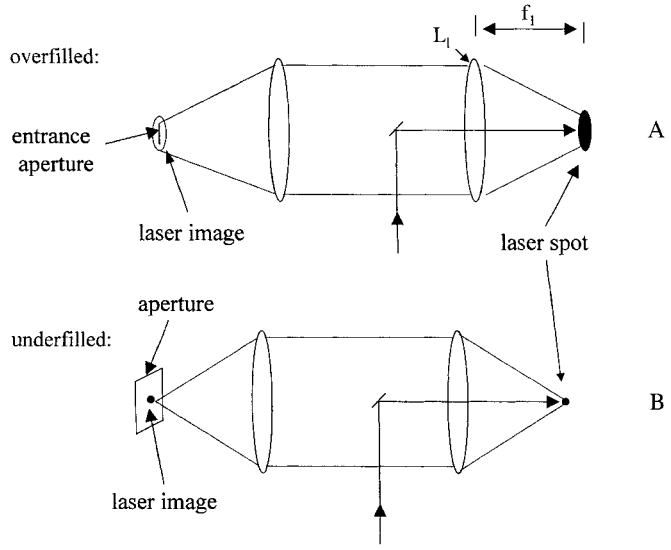

Figure 6.11. Examples of "overfilled" (A) and "underfilled" (B) illumination for the 180° geometry of Figure 6.4A. In overfilled case (A), the image of the laser spot is larger than the entrance aperture.

Table 6.3. Dependence of Raman Signal on Collection Focal Length for Constant Laser Power and 180° Geometry[a]

Sample	Underfilled Case	Overfilled Case
Thick, constant lens diameter d_1	$\frac{\epsilon\pi d_1}{f_1}$	$\frac{4\epsilon(A_D\Omega_D)}{\theta_d^2 f_1 d_1 \pi}$
Thick, variable d_1	$\frac{\epsilon\pi}{(f/\#)}$	$\frac{4\epsilon(f/\#)^2}{\theta_d^2 f_1^2 \pi}$
Thin, constant d_1	$\frac{\pi d_1^2 b}{4f_1^2}$	$\frac{4A_D\Omega_D b}{\theta_d^2 f_1^2 \pi}$
Thin, variable d_1	$\frac{\pi b}{4(f/\#)^2}$	$\frac{4A_D\Omega_D b}{\theta_d^2 f_1^2 \pi}$

[a]Raman signal equals table entry times ($P_0\beta DTQt$).

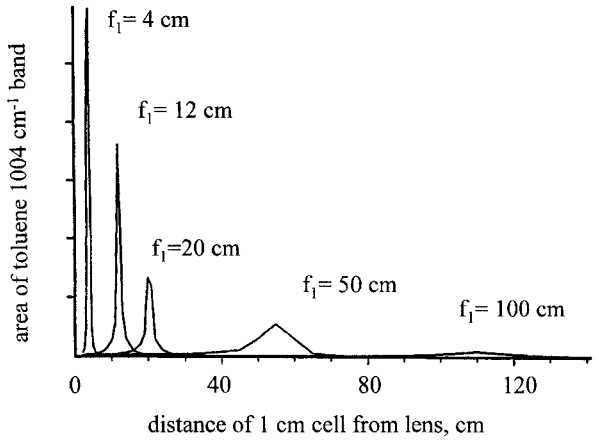

Figure 6.12. Raman signal for the geometry of Figure 6.4A, for the 1004 cm^{-1} band of toluene in a 1 cm cuvette. The focal length of lens L1 was varied as indicated. (Adapted from Reference 6 with permission.)

proportional to f_1) and for a thin sample, K is independent of f_1. The product of all the variables of Eq. (3.7) that are affected by f_1 is $A_D\Omega_D K/A_L$. This product varies with f_1^{-1} for a thick sample and f_1^{-2} for a thin sample for constant laser power and an overfilled spectrometer, as indicated in Table 6.3.

For the *underfilled* case (Fig. 6.11B), the laser image at the spectrometer is smaller than the entrance aperture, and the laser spot determines the *étendue* rather than the spectrometer. Equation (3.7) in Ω_D varies with f_1^{-2} [or $(f/\#)^{-2}$], $A_D = A_L$, and K has the dependence of Table 6.2. Now,

the variables in Eq. (3.7) affected by f_1 are K and Ω_D, whose product determines the signal [as in Eq. (3.8)]. For a thick sample, this product varies with f_1^{-1} or $(f/\#)^{-1}$, while for a thin sample, it varies with f_1^{-2} of $(f/\#)^{-2}$. These observations are summarized in Table 6.3, with the Raman signal equaling the terms in the table times $P_0\beta DTQt$.

The details of Table 6.3 are generally of more value to the spectrometer designer than to the Raman practitioner, but some practical conclusions are available that affect analytical applications. First, the signal almost always decreases with increasing working distance (which approximately equals f_1), mainly because Ω_D decreases. This decrease is more rapid for thin samples (f_1^{-2}) than for thick, transparent samples (f_1^{-1}). Second, the working distance can be increased with less signal loss if the $f/\#$ is maintained by increasing d_1 for longer f_1. Third, for an underfilled spectrometer, the signal depends on $f/\#$ but not f_1, so the laser spot size (equal to $f_1\theta_d$) could be arbitrarily small. This is important to a Raman microscope, since a signal for a given laser power is not decreased as spatial resolution improves. The power density increases for smaller spots, however, so one is still limited by sample damage. Some experimental results on the effects of f_1 on signal magnitude are provided in Chapter 11 and Table 11.2 in the context of Raman microscopy.

The effect of f_1 on the signal for the case of constant lens diameter is illustrated experimentally in Figure 6.12. A 1 cm cuvette containing toluene was moved along the optical axis for the geometry of Figure 6.4A and lenses of varying focal length. The area of the 1004 cm^{-1} peak is plotted vs. distance from lens L_1 in Figure 6.11 (6). The peak signal at optimum focus decreases with increasing f_1, as expected. However, the longer focal length lenses sample a much greater sample path length, partially compensating for the decreased signal. The conditions of this experiment are not such that quantitative comparisons with Table 6.3 are expected to be valid, but the trends are as predicted. Notice also that quite long working distances are possible, up to 1 m in this case. Using a slightly different 180° geometry, Angel and co-workers (7) obtained good-quality Raman spectra from samples located 16.7 or 20 meters from the spectrometer.

6.3.4. Accuracy and Reproducibility of 180° Geometry

As pointed out in Section 3.3, Raman spectroscopy is usually a "single-beam" method, and the observed spectrum is the product of the actual Raman scattering and an instrument response function. Correction of relative intensities across a Raman spectrum is possible, although not common, using the techniques described in Chapter 10. For quantitative analysis, however, one must be concerned about the reproducibility of the observed magnitude

of a given Raman feature as well as the relative intensities of several features. At the least, one must know how reliably an observed intensity depends on concentration, measurement time, and the like. This issue will be considered at two levels: one involving the prediction of absolute Raman intensities for a given experiment and one the reproducibility of observed intensities from sample to sample and day to day.

In principle, one could use expressions for Raman signal in terms of number density, laser power, and so forth, such as Eq. (3.6) or (6.5), to directly calculate the expected Raman signal for a given experiment. This signal should vary predictably with different experimental conditions such as collection $f/\#$, detector quantum efficiency, and the like. In practice, direct prediction of Raman signal is quite difficult and generally impractical. Some of the instrumental variables, such A_D, T, Ω, and Q, are not easily measured and may even vary with focus and sample conditions. Equations similar to (3.6) and (6.5) are very useful for evaluating how experimental variables affect signal magnitude and to determine if performance approximately meets expectations. But it is unlikely that direct calculation of Raman signal would be useful for quantitatively relating signal to concentration.

A far more practical approach is construction of a calibration curve of observed signal as a function of concentration. Provided all of the variables in Eq. (3.6), for example, are constant, signal should precisely track concentration. The success of this approach depends on the reproducibility of the Raman signal for a given sample signal. Reproducibility depends in turn on the nature and rigidity of the optical arrangement and on the reproducibility of the focus of the laser and collection optics on the sample. Once the optical components and sample holder are held rigidly, the 180° geometry yields quite reproducible signals. Since the laser and collection axes are rigid and colinear, the signal is affected only by motion along the optical axis. When changing the sample, it is imperative that repositioning be as precise as possible, particularly along the focal axis. In addition, any adjustments that affect the alignment of the laser focus relative to the slit image should be held firmly and not readily accessible to accidental adjustment.

The reproducibility of signal strength when samples are removed and replaced depends strongly on sample type and collection parameters. The key issue is the relationship between the sample position and the focal volume of the spectrometer. For a clear sample (such as a liquid in a cuvette) with a thickness larger than the depth of field, δa, the signal is fairly insensitive to focus, as long as δa is within the sample. A thin sample, or a shallow depth of field, will be much more sensitive to focus. As indicated by Eq. (6.1), δa depends on collection $f/\#$ and to some degree on the collection focal length. For example, Raman microscopes usually collect at low $f/\#$, $f/1$ or less. For thin or optically dense samples (such as powders) these systems are very

sensitive to focus. Other designs use relatively large $f/\#$ collection, say $f/4$, and correspondingly higher depth of field. For example, Figure 6.13 is a plot of signal vs. sample position along the focal axis for a silicon wafer observed with several spectrometers. A clear sample produces a constant signal over a range of focal positions, since the focal region is merely moving in a clear liquid. A thin sample (silicon) varies much more with focus, and the variation depends strongly on collection parameters. The $f/2$ system is more sensitive to focus than the $f/4$ because δa is smaller for a given slit width. The $f/4$ signal varies only slightly within about 1 mm of optimum focus, making it less prone to focusing errors. The FT instrument collects at low $f/\#$ but has a relatively large δa because its entrance aperture (and therefore blur diameter) is much larger than a typical slit in a dispersive spectrometer.

A more quantitative indication of reproducibility is provided by repetitive acquisition of spectra from a given sample, with removal and replacement of the sample between acquisitions. The standard deviation of the mean of several runs indicates the overall precision of the measurement, including sample placement. Of course, precision will vary for different spectrometers and collection parameters, but the observations of Table 6.4 provide some examples. The 180° geometry was that for Figure 6.5D, in a commercially available spectrometer (Chromex Raman 2050). For a clear liquid (lines 3 and 4 of Table 6.4), the relative standard deviation (rsd) is less than 1 per cent and improves with longer observation time, as expected from Eq. (4.15) and (4.20). Removal and replacement of a liquid sample in a cuvette introduces only slight additional error compared to repetitive runs, provided a rigid mount for the cuvette is provided (lines 4 and 5). Homogenous (line 6) and opaque (lines 1 and 2) samples also exhibit rsd's of less than 1 per cent.

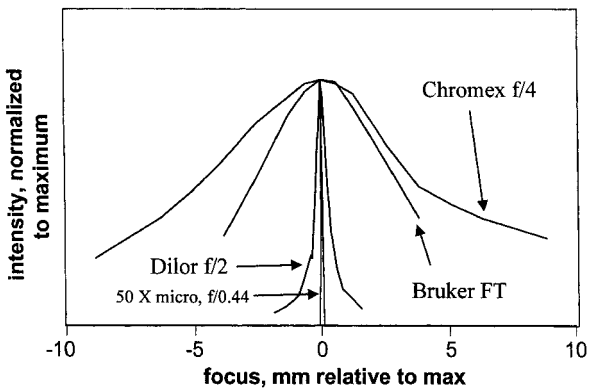

Figure 6.13. Raman intensity for a silicon wafer positioned at various distances from the lens of a 180° geometry sampling system. Each curve is normalized to its maximum value.

Table 6.4. Reproducibility of Raman Signal for 180° Geometry[a]

Sample	Integration Time[b] (sec)	Relative Standard Deviation[c] (%)
1. Silicon wafer, motionless	10	0.42
2. Silicon wafer, remove and replace	10	0.78
3. CH_2Cl_2 in cuvette, motionless	0.5	0.63
4. CH_2Cl_2 in cuvette, motionless	2.5	0.31
5. CH_2Cl_2, remove and replace	2.5	0.82
6. Clear, solid polystyrene	2.5	0.78
7. Calcium ascorbate in amber vial	30	4.9
8. Heterogeneous tablet,[d] motionless	1.5	0.70
9. Tablet,[d] incremental lateral motion	1.5	12.6
10. Tablet,[d] remove and replace	1.5	13
11. Tablet, defocused, remove and replace	1.5	3.1
12. Tablet, line focus, remove and replace	1.5	6.0
13. Tablet, line focus, spinning, remove and replace sample	1.5	1.5

[a]Chromex Raman 2050, configuration of Figure 6.4D, $L_f = 75$ mm, $f/4$.
[b]For each run.
[c]From peak heights of 10 spectra.
[d]Acetaminophen, cellulose, magnesium stearate pressed tablet, heterogeneous on a roughly 50 μm scale.

Table 6.4 also illustrates a possible source of irreproducibility when dealing with solid samples. Mixtures of solids pressed into pellets are heterogeneous on a size scale comparable to the particles or microcrystallites of the solids involved. A common example is a pharmaceutical tablet, consisting of a physical mixture of drug and excipient (and possibly other components). As shown in Figure 6.14, the small laser focus (usually less than 50 μm) may preferentially sample one sample component or another, even if the focus is reproduced perfectly. Depending on the relative population of sample components under the beam, the apparent composition may vary with sample position. This effect is apparent for lines 8 to 12 of Table 6.4, which deal with a tablet of acetamidophenol formulated with magnesium stearate and microcrystalline cellulose. Although the reproducibility for a homogeneous solid was <1 per cent, the Raman signal for the tablet varied by 13 per cent when the tablet was removed and replaced. This variation was also observed for incremental lateral motion of the tablet, which did *not* affect the focus. If the focus was intentionally degraded so a larger region of the tablet was sampled, the run-to-run reproducibility improved from 11.3 to 3.1 per cent. Thus, the irreproducibility in

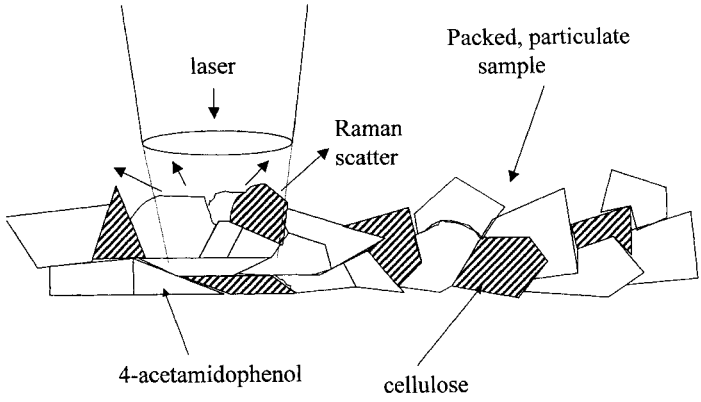

Figure 6.14. Schematic of laser focus on a heterogeneous sample consisting of acetamidophenol and cellulose pressed into a tablet. For repeated positioning of samples at the laser focus, the relative amounts of the two materials will vary.

this case was caused by a sampled volume that was small compared to sample heterogeneity. As described in Section 6.5, a line focus of the laser can cover more sample area without losing signal, thus averaging out much of the sample heterogeneity. The "line" focus of line 12, Table 6.4, samples an approximately 50 × 2000 μm area of the tablet and reduces the rsd for repeated replacement of the sample from 12 to 6 per cent. Further spatial averaging may be achieved by spinning the sample under the line focus, thus covering the much larger sample area shown in Figure 6.15. As noted in Table 6.4, sample spinning combined with a line focus reduces the rsd to about 1.5 per cent for repetitive replacement of a heterogeneous sample.

6.3.5. Summary of 180° Characteristics

The performance criteria noted in Section 6.2 can vary over wide ranges for the 180° geometry, mainly depending on the choice of collection lens focal length. A short collection lens yields higher sensitivity, but also shorter working distance, higher power density at the sample, and shorter depth of field. A longer collection focal length relaxes the requirement for accurate focusing (due to greater depth of field) but at the cost of sensitivity. In both cases, the 180° geometry is quite reproducible because the laser and collection axes are coincident. Overall, the 180° geometry is more versatile than the 90° geometry and generally easier to use. If one includes microscopes and fiber-optic problems as examples of the 180° geometry, it is certainly the most popular collection configuration in commercial spectrometers.

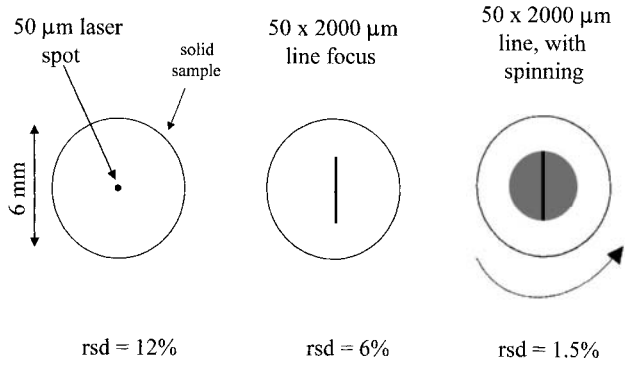

Figure 6.15. Schematic of point and line focus of the laser on a tablet. The right-hand drawing shows spinning combined with a line focus, with the gray region indicating the tablet area sampled by the spectrometer. Relative standard deviations (rsd) are shown for experiments on the tablet described in Figure 6.14.

6.4. 90° SAMPLING GEOMETRY

The 90° geometry of Figure 6.1 is historically quite common, although it has receded into the minority in modern spectrometers. There are some advantages to keeping the laser and collection axes separate, and there are differences between 90° and 180° geometry in the way polarization is analyzed (described in Section 6.7). In many cases, the angle between laser and collection axes is indeed 90°, but it is often less. We will treat any geometry in which the laser and collection axes differ from colinear in the current section.

6.4.1. 90° Optical Configurations

Some variations on the 90° geometry are shown in Figure 6.16. In Figure 6.16A, a transparent sample is free standing or contained in a cuvette or capillary, and the laser is focused by L3. The laser focus is positioned to match the slit image in the sample, so the laser focal cylinder is imaged onto the entrance slit or spectrometer entrance aperture. The diameter of the laser beam in the sample is determined by Eq. (6.2), using the focal length of L3. The configuration of Figure 6.16B may be used for opaque or translucent samples, which are positioned so the specularly reflected laser beam does not enter the collection optics. Configuration 6.16C is similar, except it does not retain the true 90° geometry.

A pragmatic disadvantage of the 90° geometry relates to the alignment of laser, sample, and collection optics. For the 180° geometry, the laser and collection axes are coincident, so the sample position cannot affect their

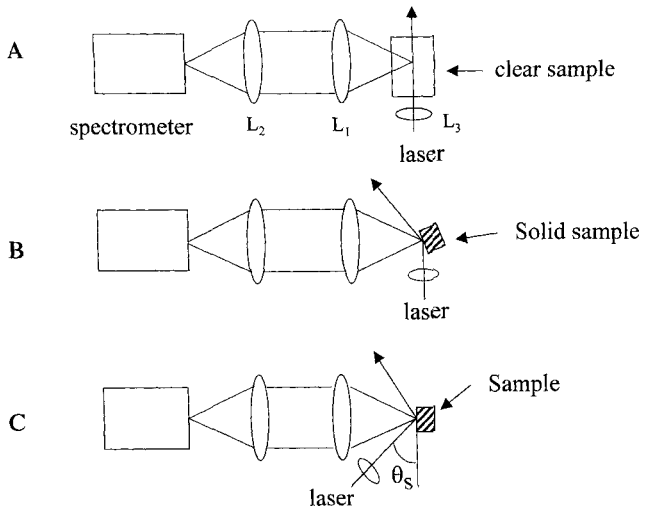

Figure 6.16. Variations on 90° sampling geometry. Case C is not a true 90° configuration but retains many of its properties.

alignment, except for focus. The same is true of Figure 6.16A, but not B and C. Motion of the sample on the z axis moves the laser focus laterally relative to the collection axis, thus making the signal more sensitive to focusing and alignment stability. The practical result is decreased convenience and reduced signal reproducibility.

6.4.2. Sampled Volume for 90° Geometry

The sampling volume is quite different for the 90° geometry compared to the 180° geometry because the focal cylinder is monitored from the side rather than end-on. For the configuration of Figure 6.16A with a transparent sample, it will usually be the case that the focussed laser beam radius, w_0, will be smaller than the spectrometer depth of field. In this case, the specific intensity L will be given by the Raman scattering occurring within the focal cylinder:

$$L = \frac{P_D \beta D \pi w_0^2 d}{2\pi w_0 d} \tag{6.11}$$

where d is the length of the focal cylinder observed by the spectrometer. Equation (6.11) yields a value of $w_0/2$ for K in Eq. (3.6). For the case of a

transparent thick sample ($w_0 \ll \delta a$), Eq. (3.6) becomes

$$S = \frac{P_D \beta D A_D \Omega_D T Q t w_0}{2} \tag{6.12}$$

The signal decreases for a smaller laser beam radius because fewer scatterers are illuminated by a constant power density.

The definitions of *overfilled* and *underfilled* for the 90° case are illustrated in Figure 6.17. If the power is kept constant rather than the power density, Eq. (3.7) becomes (6.13) (with $A_L = \pi w_0^2$) for the overfilled case (5):

$$S = \frac{P_0 \beta D A_D \Omega_D T Q t}{2\pi w_0} \tag{6.13}$$

Now, the signal increases with decreasing radius and constant P_0 because the power density is increasing. For an underfilled case, $A_D = 2w_0 d$ because the cylinder is viewed from the side, and Eq. (3.7) becomes

$$S = \frac{P_0 \beta D d \Omega_D T Q t}{\pi} \tag{6.14}$$

Equation (6.14) assumes that the slit image is smaller than the length of the focal cylinder given by Eq. (6.1) or (6.3). Note that Eq. (6.14) predicts that the signal is independent of the beam diameter because the power density tracks

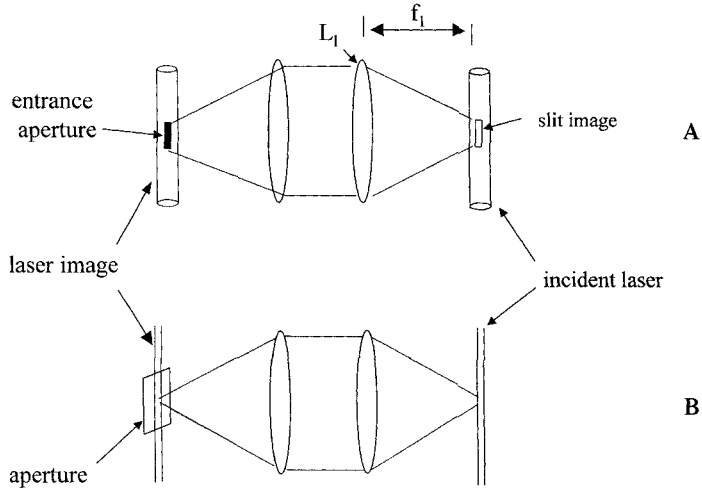

Figure 6.17. Overfilled (A) and underfilled (B) situations for 90° sampling through a transparent sample. In overfilled case, the image of the laser beam is larger than the entrance aperture.

w_0^{-2}, while the number of scatterers tracks w_0^2. Note also that the signal is larger for longer d, since a larger volume of sample is observed. An advantage of configuration 6.16A is a fairly long sampling depth (equal to the length of the slit image at the sample) while maintaining a high power density. The dependence of signal on conditions is summarized in Table 6.5.

6.4.3. Reproducibility of 90° Geometry

For clear samples, the geometry of Figure 6.16A exhibits a fairly reproducible signal once the laser and collection alignment is fixed securely. As was the case for the 180° geometry, sample position is noncritical to the signal provided the clear sample includes the overlap region of the laser focus and the slit image. For the configurations of Figure 6.16B and 6.16C, however, the signal depends more strongly on positioning than for the 180° geometry. The sample position along the focal axis can affect the alignment of the laser and slit image, as shown in Figure 6.18. When the sample is in focus, the laser, slit image, and sample surface are all coincident and the maximum Raman light enters the slit. A small displacement of the sample along the focal axis not only defocuses the collection optics, but it also displaces the laser laterally away from the slit image. The result is high sensitivity to sample positioning, making quantitative signal reproducibility significantly more difficult than for the 180° geometry. Even if the collection optics have a fairly large depth of focus, the slit is generally narrow and "easy to miss."

A more subtle effect of positioning occurs with dispersive spectrometers, when the distribution of light across the slit is altered by sample motion. A change in this distribution causes a shift in position at the detector, yielding a small apparent frequency shift. This frequency jitter can amount to a wavenumber or more and sometimes affects spectral subtraction or background correction.

Table 6.5. Signal Dependence of 90° Geometry

	K	$(KA_D\Omega_D/A_L)^a$
Thick, clear sample overfilled	$w_0/2$	$\dfrac{A_D\Omega_D}{2\pi w_0}$
Thick, clear underfilled	$w_0/2$	$\dfrac{d\Omega_D}{\pi}$
Thin, overfilled	b^c	$\dfrac{A_D\Omega_D}{\pi w_0^2 \sin\theta s}$
Thin, underfilled	b^c	Ω_D^b

[a] Raman signal equals this value times $P_0\beta DTQt$.
[b] θ_s = angle between beam and surface; see Figure 6.16.
[c] Sample thickness, cm.

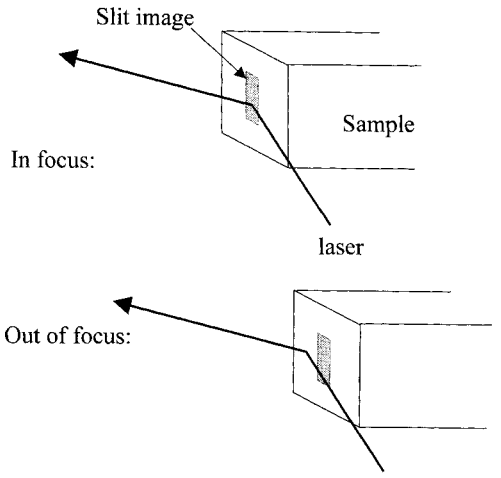

Figure 6.18. Illustration of the sensitivity of the 90° geometry to sample position. Lateral motion of the sample (in the case shown) not only defocused the collection optics and laser focus but also shifts the laser focus off the entrance slit image.

6.4.4. Summary of 90° Geometry Characteristics

The fact that the 90° geometry separates the laser beam and the collection axis, combined with historical reasons, provide most of the motivation for using the 90° geometry. It is common when the laser spot and collection region must be controlled independently. The orientation of the laser focal cylinder along the entrance slit can increase A_D while maintaining high power density, thus providing strong signals for clear samples. However, the alignment difficulty and irreproducibility of the design make it generally less attractive than the 180° configuration.

6.5. REDUCING THE LASER POWER DENSITY AT THE SAMPLE

As noted earlier, the maximum specific intensity of Raman light is limited by available laser power density and ultimately sample damage. Focusing hundreds of milliwatts (possibly) to a small sample area can thermally or photochemically damage a variety of samples. Depending upon the collection optics, it is often possible to maintain signal while reducing the power density by monitoring a larger sample area (A_D). For constant laser power, the product $P_D A_D$ is constant as A_D is increased and P_D decreased, and the signal remains constant as long as the larger A_D is monitored with the same $A_D \Omega_D$ product.

For example, FT-Raman spectrometers have relatively large input apertures and *étendue*, and can often collect light reasonably efficiently from an unfocused laser spot. It is possible to position the smaller laser mirror in Figure 6.4A on the sample side of L1, allowing the laser to be unfocused or at least less tightly focused. If the laser spot is 1 mm instead of 100 μm, the power density decreases by a factor of 100 (Table 6.1). This procedure generally causes loss of signal compared to the focused case, but by a factor much smaller than 100.

For dispersive spectrometers involving an entrance slit, the laser may be focused to a line rather than a point. If this line is imaged onto the entrance slit and monitored by the detector, up to 1 cm or more of the focal line can be monitored. For example, a 50 μm-wide entrance slit may be arranged to observe a 50 μm-wide laser spot, with the configuration of Figure 6.4A. If the same laser power is focused to a 50 μm × 2 mm line and all of this line is within the detected area, the signal will be unchanged but the power density at the sample will decrease by a factor of 40.

A line focus for either the 180° or 90° geometries may be produced with a cylindrical lens, as shown in Figure 6.19. In Figure 6.19A, the length of the focal line depends on the focal length of L4, while in 6.17B, the line will be as long as the unfocused laser beam diameter. Figure 6.20 shows spectra of a silicon wafer obtained under identical conditions, except for the insertion of a cylindrical lens to produce a line focus. As long as the entire length of the line is imaged onto the active region of the CCD, the signal strength is maintained while the power density is decreased by a large factor.

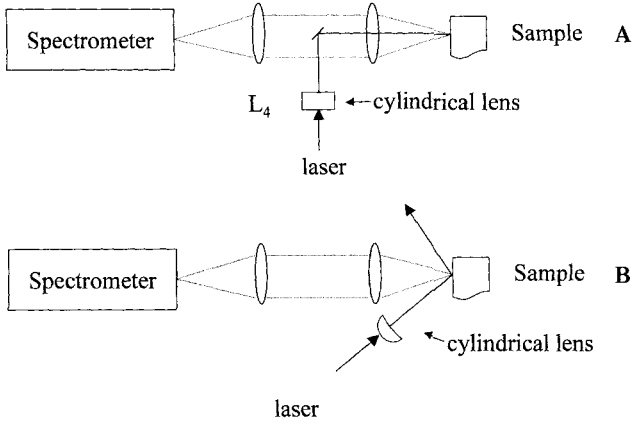

Figure 6.19. Reduction of power density using a cylindrical lens. Figure shows 180° (A) and 90° (B) configurations viewed from above, so the entrance slit is perpendicular to the plane of the figure.

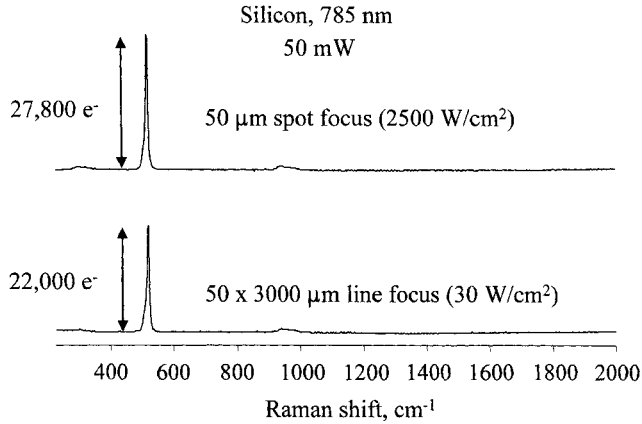

Figure 6.20. Spectra of silicon wafer with a point focus (A) and line focus (B). Same total power at sample, but line has ~1 per cent as high a power density.

6.6. PATH LENGTH ENHANCEMENT

As discussed in Section 6.3.2, the sampling volume and Raman signal magnitude depend upon the optical properties of the sample, laser focus, and collection optics. Several cases were considered in Tables 6.2 and 6.3, but the situation of relevance here is the thick, optically transparent sample such as a clear liquid or solution. For a thick sample such as a large cell or other container, where the depth of field is much less than the sample thickness, the sampling depth is determined by the collection optics. One cannot arbitrarily increase δa , since it is a function of $f/\#$, slit width, and the like and is limited in practice to at most a few millimeters.

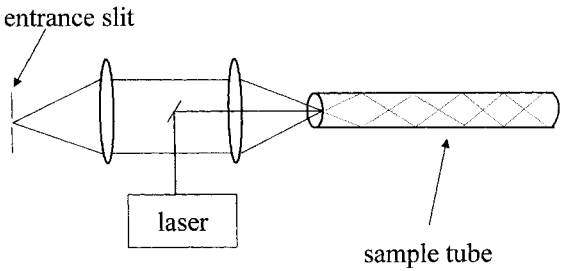

Figure 6.21. Path length enhancement for a transparent sample by reflection of laser and scattered light inside a small-diameter tube.

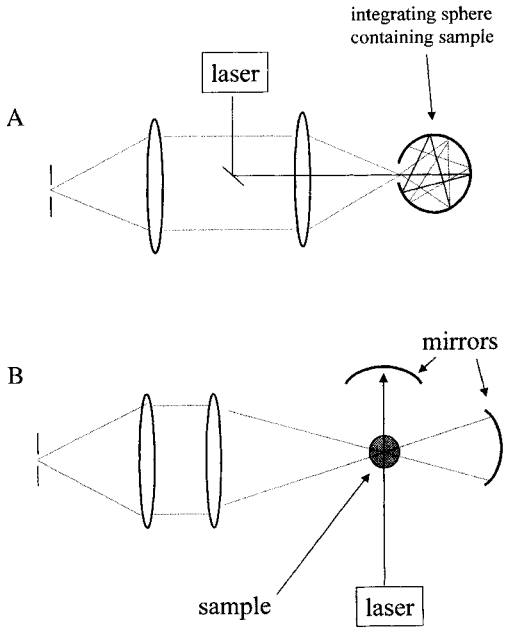

Figure 6.22. (A) Path length enhancement for a clear sample inside an integrating sphere. (B) Additional mirrors to provide a double laser pass through the sample and increased collection efficiency.

Several modifications to conventional sampling geometry have been devised to increase the effective path length without sacrificing collection efficiency, some of which are shown schematically in Figures 6.21 and 6.22. The dual-pass optics of Figure 6.22B reflect the laser back through the sample and also collect light from two sides of the samples. Ignoring losses in the cell, this arrangement increases signal by a factor of 4. Integrating spheres (Fig. 6.22A), extend this approach to provide multiple laser passes and collection from a larger range of solid angles. The increase in signal varies with conditions, but a factor of 10 is readily achievable (8). A sample tube (Fig. 6.21) may be substituted for a cuvette in the conventional 180° geometry to contain both the laser and the collected light. If the sample has a higher refractive index than the tube, internal reflection directs the laser down the tube, and a significant fraction of the scattered light returns to the opening of the tube. For the more common case of samples with refractive index lower than the tube material, the tube may be coated with a reflective film. The effect is to increase the value of b in Eq. (6.5), or more generally to increase K in Eq. (3.6) to (3.8). The magnitude of K is a complex function of the tube dimensions and

optical parameters, but signal enhancements of factors of 30 to 50 have been reported (9).

Any scheme for increasing effective path length will obviously depend on the optical properties of the sample, particularly absorption. The sample must be transparent to both the laser and Raman-shifted wavelengths. This condition is often satisfied for visible light and clear liquids but is sometimes an issue for the same samples in the near infrared. For example, water has weak absorptions in the 700 to 2000 nm region resulting from overtones of the O—H stretch. These absorptions can substantially reduce the enhancement expected from the techniques depicted in Figures 6.21 and 6.22. It is generally necessary, and certainly advisable, to calibrate the path length with standards prepared in the solvent of interest. It is dangerous to assume that the same enhancement will apply to samples with varying refractive index or absorbance. Some related methods for path length enhancement using fiber optics are discussed in Chapter 12.

6.7. POLARIZATION MEASUREMENTS

The polarization of Raman scattering relative to the input laser polarization has been studied extensively and can be of significant analytical value. It was noted in Chapter 2 and Figure 2.1 that the laser induces a polarization in the sample that is parallel to the incident electric field. For a totally symmetric vibration, such as the symmetric stretch of CCl_4, the Raman-scattered light retains the polarization of the incident light. As a consequence, the observed intensity of the CCl_4 symmetric stretch is much weaker when viewed from the y axis of Figure 2.1 than from the z or y axis. The associated Raman band is said to be *polarized.* A *depolarized* band exhibits significant scattering along the x, y, and z axes and results from vibrations that are not totally symmetric. Figure 6.23 shows spectra obtained for benzene along an axis parallel to the incident electric field (y axis in Fig. 2.1, e.g.) and perpendicular to the incident field (y axis in Fig. 2.1). Note that certain bands are much weaker in perpendicular observation (992 and 3060 cm^{-1}), and these bands are said to be *polarized.* The depolarization ratio, ρ, defined as $I_\perp/I_\parallel$, is small for *polarized* bands and is close to 0.75 for *depolarized* bands. Vibrations that preserve molecular symmetry (so-called totally symmetric vibrations) have ρ values in the range of 0.0 to 0.75 but generally close to 0.0. Asymmetric vibrations should have ρ values close to 0.75 for liquids and gases. These simple rules apply to randomly oriented molecules, usually liquids or gases, and polarization effects become considerably more complex for crystals (10). Some examples of depolarization values for the case of liquid benzene are shown in Figure 6.23.

Several aspects of Raman polarization measurements are of value for chemical analysis. First, polarization provides a means to determine the symmetry

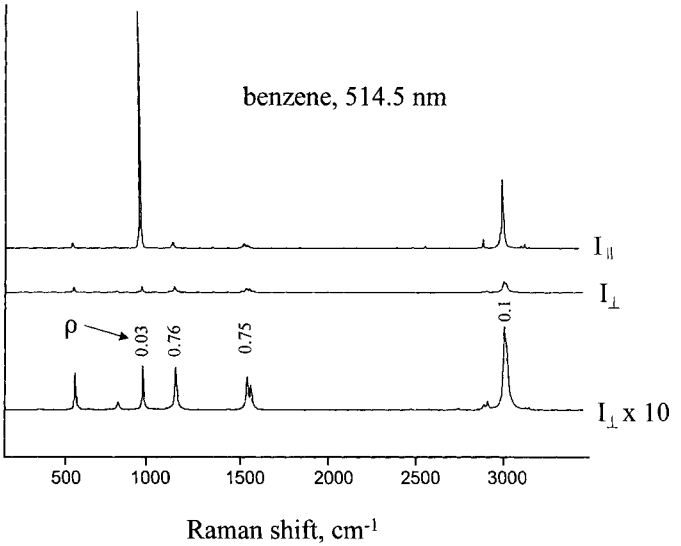

Figure 6.23. Raman spectra of liquid benzene observed with parallel and perpendicular polarization analyzers, 180° geometry (as in Fig. 6.22). Upper spectrum is parallel observation, middle is perpendicular. The lower spectrum is magnified by 10 to illustrate relative peak heights. Numbers indicate depolarization ratios, $\rho = I_{\perp}/I_{\parallel}$.

of the vibrations underlying observed spectral features. There is no analog in FTIR spectroscopy, and polarization measurements can assist assignment of observed Raman features. Second, any nonrandom molecular orientation will affect the observed polarizations, so Raman may provide information about such orientation. For example, partial orientation of polymer chains in synthetic fibers can be deduced from Raman spectra, so that fiber fabrication may be controlled to enhance or avoid preferential orientation. Polarization of scattering from molecules adsorbed on surfaces indicates the molecular orientation of the adsorbate relative to the surface (11). Third, polarization may be used to distinguish preferentially oriented molecules (such as those on a surface) from randomly oriented molecules (such as those in the adjacent solution).

Both the 90° and 180° sampling geometries can provide equivalent information about the polarization of Raman spectral features, but the measurement is performed differently for each case. Figure 6.24 shows the 180° geometry, which requires a polarization analyzer between the sample and spectrometer. Assuming the laser's electric field is polarized parallel to the y axis, the polarization analyzer is rotated to transmit y-polarized light ($I_{\parallel}$) or x-polarized light ($I_{\perp}$). After suitable calibration, the depolarization ratio is simply the ratio, $\rho = I_{\perp}/I_{\parallel}$, determined by obtaining spectra with the polarizer in two orthogonal positions.

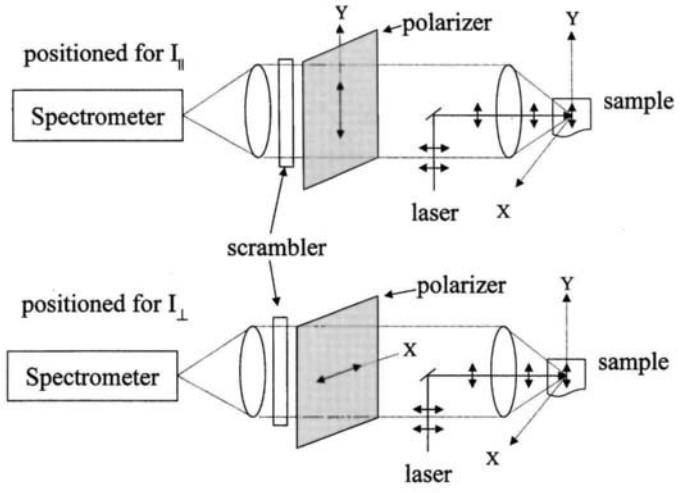

Figure 6.24. Position of polarization analyzer (polarizer) in 180° geometry. Double-headed arrows indicate direction of laser electric field vector and direction of maximum transmission of the polarizers.

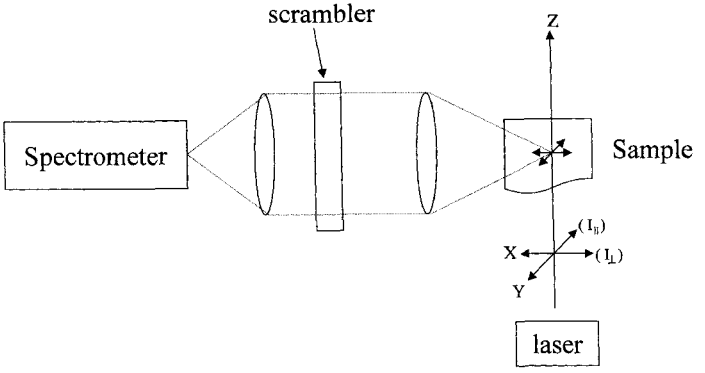

Figure 6.25. Polarization analysis for 90° geometry. Observed polarization is changed by rotating the polarization of the incident laser, as shown.

The 90° geometry of Figure 6.25 does not require a polarizer to determine ρ but does require rotation of the laser polarization. The intensity ($I_{\parallel}$) is determined with the laser electric field oriented on the y axis, with the observation axis along the x axis. Then the laser electric field is rotated 90° (usually with a quarter wave plate) to position it parallel to the x axis. The observed intensity is now $I_{\perp}$, and ρ may be calculated directly from the two spectra.

Both dispersive and nondispersive spectrometers can exhibit preferential transmission of light depending on its polarization. The efficiency of diffraction gratings and the polarization sensitivity of the beamsplitter can cause errors in the observed depolarization ratio, depending on several variables such as experimental geometry and Raman shift region. For this reason, it is often important to place a polarization scrambler between the sample and any polarization-sensitive components of the spectrometer other than the polarization analyzer itself. In addition, it is good practice to measure ρ for a few known systems to verify accuracy of the apparatus.

REFERENCES

1. L. Levi, *Applied Optics*, Vol. 1, Wiley, New York, 1968, p. 469.
2. M. Young, *Optics and Lasers*, Springer, NewYork, 1991, p. 206ff.
3. W. Driscoll and W. Vaughn, eds., *Handbook of Optics*, McGraw-Hill, NewYork, 1978, pp. 14–9ff.
4. Y. W. Alsmeyer and R. L. McCreery, *Anal. Chem.*, **63**, 1289 (1991).
5. M. A. Fryling, C. J. Frank and R. L McCreery, *Appl. Spectrosc.*, **47**, 1965 (1993).
6. M. A. Fryling, Ph.D. Disseration, The Ohio State University, 1994.
7. S. M. Angel, T. J. Kulp and T. M. Vess, *Appl. Spectrosc.*, **46**, 1085 (1992).
8. J. Zhao and R. L. McCreery, *Appl. Spectrosc.*, **51**, 1687 (1997).
9. S. D. Schwab and R. L. McCreery, *Appl. Spectrosc.*, **41**, 126 (1987).
10. D. A. Long, *Raman Spectroscopy,* McGraw-Hill, New York, 1977.
11. J. Zhao and R. L. McCreery, *Langmuir*, **11**, 4036 (1995).

Raman Spectroscopy for Chemical Analysis. Richard L. McCreery

ISBN: 0-471-25287-5

CHAPTER

7

LASERS FOR RAMAN SPECTROSCOPY

7.1. OVERVIEW

As noted in Sections 5.2 and 5.3, Raman spectrometers that operate at laser wavelengths of less than 900 nm are most commonly dispersive systems, while those with lasers of 1064 nm and above are usually nondispersive Fourier transform (FT)–Raman systems. This distinction is mainly technological and is controlled by the signal/noise ratio (SNR) considerations discussed in Section 4.5. With currently available technology, SNR is maximized for dispersive multichannel systems using silicon charge-coupled devices (CCDs), and therefore Raman scattering at wavelengths below the silicon cut-off at 1100 nm. For longer wavelengths, particularly those scattered from 1064 nm lasers, the multiplex spectrometers used in FT-Raman are preferred. Although the sampling issues discussed in Chapter 6 apply to both dispersive and nondispersive spectrometers, the wavelength analysis and detection principles for the two approaches differ substantially (see Chapter 5). When one examines spectrometers designed for chemical analysis, practical and technological considerations result in a relatively limited number of instrument configurations. Virtually all integrated FT-Raman systems use 1064 nm lasers, while integrated dispersive systems commonly use lasers operating at 488.0, 514.5, 632.8, 532, and 785 nm. This chapter emphasizes the laser sources of common use in analytical chemical applications, in both dispersive and nondispersive spectrometers. The wavelength analysis and detection systems for dispersive and non dispersive spectrometers are discussed in Chapters 8 and 9, respectively. General texts on laser fundamentals (1,2) and analytical applications (3–5) should be consulted for more detailed information than provided here.

A very wide range of laser wavelengths and types has been used for Raman spectroscopy, ranging from the hard ultra violet (UV) (<200 nm) to near-infrared (NIR) (≥1064 nm). Relatively few of these are of interest for analytical applications, and several are listed in Table 7.1 and shown graphically in Figure 7.1. Some general characteristics deserve note before discussing particular designs. First, many pulsed lasers have been used for Raman spectroscopy (6–8), but these are generally undesirable for analytical applications. Their high peak powers result in safety concerns as well as an increased likelihood of sample damage or photochemical effects. The lasers listed in

Table 7.1. CW Lasers for Analytical Raman Spectroscopy

Type	λ(nm[a])	Power (typical)	Comments
Doubled Ar^+	244, 257, 229	15–200 mW	*b,c,d*
Ar^+ (air cooled)	488.0, 514.5	5–50 mW	
Ar^+ (water cooled)	351.1	0.1–10 W	*b,c,d*
	479.9		
	476.5		
	488.0		
	496.5		
	514.5		
	528.7		
He–Ne	632.8	5–100 mW	
Kr^+	413.1	0.1–4 W	*b,c,d*
	647.1		
	752.5		
Nd:YAG	1064	0.1–10 W	*e*
Doubled Nd:YAG	532	0.05–5 W	*e*
Diode	670–865 nm	0.01–1 W	*f*

[a]Commonly available output wavelengths. Others available as noted in Table 7.2.
[b]Requires water cooling.
[c]Requires 208 or 480 V power.
[d]Tunable to one of indicated lines.
[e]Some versions require water cooling and/or 208 V power.
[f]Continuously tunable wavelength within limited range.

Table 7.1 are *continuous wave* (CW), not pulsed. Second, frequency stability to <1 cm^{-1} is important to assure Raman shift precision and avoid line broadening. Although the Raman shift axis is usually calibrated periodically, the laser frequency must remain stable between calibrations. Third, lasers vary significantly in output linewidth, from hundreds of reciprocal centimeters to much less than 1 cm^{-1}. For the majority of samples of analytical interest, a laser linewidth below 1 cm^{-1} is sufficient. Laser linewidths are often quoted in terms of frequency rather than wavenumber, in which case 1 cm^{-1} equals 30 GHz. Lasers are available with <1 MHz linewidths ($<10^{-4}$ cm^{-1}), but such lasers would be unnecessarily narrow for most analytical Raman applications. Fourth, lasers differ in their output of light at wavelengths other than the laser line itself. Gas lasers (Ar^+, Kr^+, He–Ne) emit atomic lines (*plasma lines*), and solid-state lasers luminesce, both of which can interfere with Raman scattering. Essentially all lasers require a bandpass filter or monochromator to reduce these extraneous emissions.

Beam divergence is a less common laser consideration of importance to Raman applications. No optical beam is perfectly collimated, and diffraction

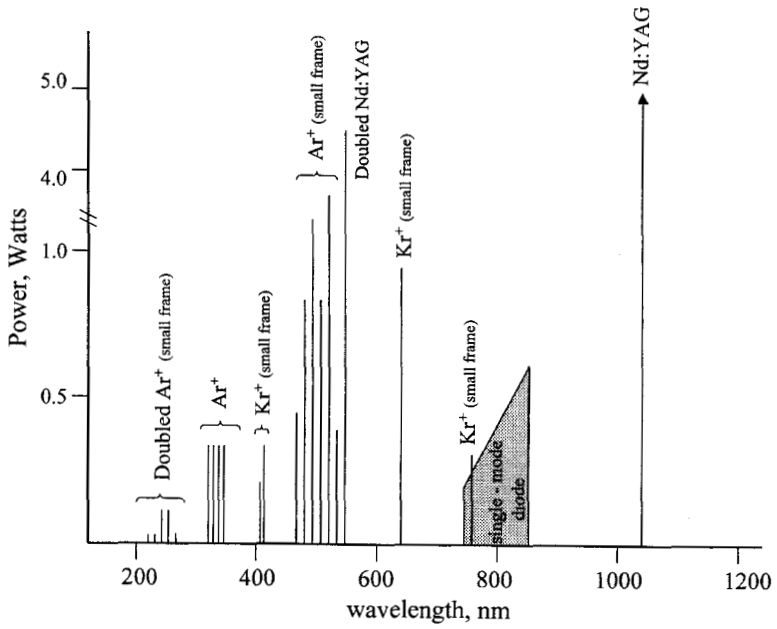

Figure 7.1. Wavelengths and available power ranges of commercial lasers commonly used for Raman spectroscopy. Note discontinuity in power axis above 1 W. Diode lasers are available over a range of wavelengths and are to some extent tunable. Numerical details are in Tables 7.1 to 7.4.

effects make a strictly parallel beam physically impossible. All laser beams diverge at some rate, usually stated as the full-angle divergence in radians, θ_d. This value is the angular spread of the beam as it leaves the laser, and equals zero for a perfectly collimated beam. Divergence is a function of laser design, wavelength, and the like but varies from $<10^{-3}$ rad (0.06°) for an Ar^+ laser to as much as 0.5 rad (30°) for a diode laser. Divergence is of obvious practical importance to how the laser beam propagates through the focusing optics to the sample but also results in a more fundamental constraint on the laser beam diameter and cross-sectional area. For a beam focused by a lens with focal length f_1, the minimum beam radius at the focal point, w_O, is given by:

$$2w_O = f_1\theta_d \tag{7.1}$$

For example, if $\theta_d = 1$ mrad and $f_1 = 5$ cm, the laser spot diameter at the focal point (often called the *beam waist*) is 50 μm. This minimum may define a limit in power density or spatial resolution and can affect the choice of laser.

Divergence is usually stated as one of the manufacturer's specifications for a given laser system.

Some additional practical issues noted in general terms in Table 5.1 also apply to the choice of laser. Water cooling or electrical power requirements other than 110 V can be inconvenient in an analytical lab, particularly for field or portable operation. As indicated in Table 7.1, the more powerful lasers such as Ar^+ often have such requirements. In addition, the capital and operating costs of the lasers in Table 7.1 differ significantly and may be an issue in laser or spectrometer choice. Of the lasers listed, the diode, Nd:YAG (fundamental and doubled) and He–Ne lasers are relatively inexpensive and do not require special cooling or power, while the Ar^+, Kr^+, and doubled Ar^+ lasers are more expensive and require special installation.

7.2. Ar^+ AND Kr^+ ION LASERS

7.2.1. Water-Cooled Ion Lasers

The workhorse lasers for Raman spectroscopy until approximately the early 1990s were the argon and krypton ion lasers. They continue to be used widely, but alternatives have emerged that have lower cost and utility demands, such as the doubled Nd:YAG and diode lasers. The argon and krypton lasers are generally referred to as "ion lasers" because the lasing species is a singly ionized Ar^+ or Kr^+. The wide use of ion lasers has resulted in the development of reliable and sophisticated designs, but the principle is simple and is shown schematically in Figure 7.2. A direct current (DC) electron discharge through low-pressure Ar or Kr forms a plasma, which is magnetically confined inside a resonant cavity consisting of one highly reflecting mirror and one partially transmitting (~95 per cent) mirror. In addition to a variety of nonlasing atomic and ionic emission lines, a few transitions can lase with sufficient gain to support CW laser output.

Table 7.2 is a more detailed listing of wavelengths and power for commercially available ion lasers. *Small-frame* ion lasers use 208 V, three-phase power, with total consumption of 10 to 15 kW. *Large frame* implies 480 V, three-phase power, 50 to 60 kW total. The ion lasers listed in Table 7.2 require water cooling, but lower power air-cooled versions are available (see Section 7.2.2). Ion lasers are quite inefficient in terms of converting electrical to optical energy because much of the power is used to create the ions rather than exciting the laser transition. Roughly 0.01 to 0.05 per cent of the electrical energy is converted to laser light, making ion lasers among the least efficient types in common use. Obviously, this inefficiency leads to the high electrical power and water cooling requirements.

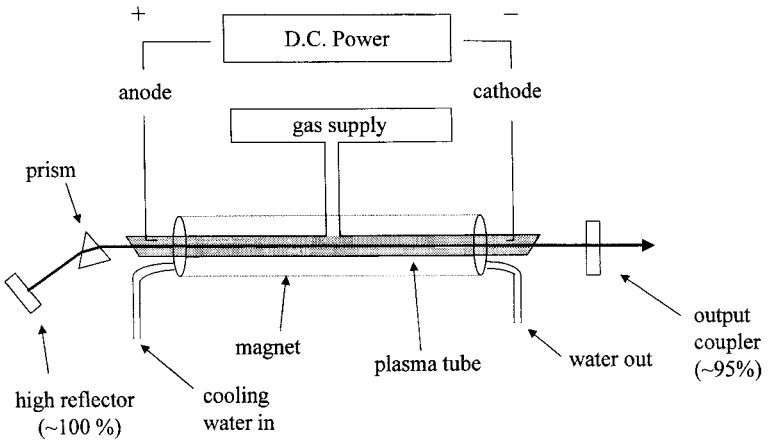

Figure 7.2. Schematic of argon ion laser, including a cylindrical magnet to confine the plasma.

The last line of Table 7.2 indicates the total optical output power for each ion laser, in terms of "multiline visible" power. However, this power is distributed among many wavelengths and is not useful directly for Raman spectroscopy. Multiline output is often used to pump dye lasers or titanium: sapphire lasers, but these cases are fairly rare in analytical applications. Most often, a prism is added to the laser cavity to select one of the wavelengths listed in Table 7.2. As apparent in the table, Ar^+ and Kr^+ have a few strong lines that are popular for Raman (e.g., 488, 514.5, and 647.1 nm) plus several more at lower power. The mixed-gas Ar^+/Kr^+ laser provides less power but covers a wider range of visible wavelengths than Ar^+ or Kr^+ alone.

Ion lasers have been popular for Raman spectroscopy and other uses because of their high power output, variety of output wavelengths, and relatively long lifetime. The output wavelength is very stable and accurately known, since it depends on a particular atomic transition. A modern Ar^+ laser tube lasts 5000 h or more, but the replacement cost is high. Small-frame Ar^+ lasers cost $30,000 to $50,000 at the time of this writing, and a replacement plasma tube costs $12,000 to $15,000. As noted earlier, the utility requirements are high for water-cooled ion lasers, making them less practical for routine use. Mainly for this reason, many analytical Raman systems use the smaller, less demanding doubled Nd:YAG laser operating at 532 nm (Section 7.4.2).

7.2.2. Air-Cooled Ar^+ and Kr^+ Lasers

The air-cooled Ar^+ system avoids the need for water cooling but with a substantial reduction in power. Most air-cooled ion lasers operate on 110 V

Table 7.2. Visible Wavelengths and Powers (W) for Typical Ion Lasers

	Ar^+		Kr^+		
Wavelength (nm)	Small Frame[a]	Large Frame[b]	Small Frame[c]	Large Frame[d]	Mixed Gas[e]
791–799			0.03	0.3	
752.5			0.10	1.2	0.03
676.4			1.15	0.9	
647.1			0.80	3.5	0.25
568.2			0.15	1.1	0.15
530.9			0.20	1.5	0.15
528.7	0.42	1.8			
520.8			0.07	0.70	0.13
514.5	2.40	10.0			0.25
501.7	0.48	1.8			
496.5	0.72	3.0			
488.0	1.80	8.0			0.25
482.5			0.03	0.40	
476.5	0.72	3.0	0.05	0.40	0.10
472.7	0.24	1.3			
468.0					
465.8	0.18	0.80			
457.9	0.42	1.5			0.03
454.5	0.14	0.80			
415.4					
413.1			0.30	1.8	
406.7			0.20	0.9	
Multiline visible	7.0	25	0.6–1.0[f]	3.0–4.6[f]	2.5

[a]For example, Coherent Innova 307.
[b]For example, Coherent Innova Sabre-DBW 25.
[c]For example, Coherent Innova 302.
[d]For example, Coherent Innova Sabre Krypton.
[e]For example, Coherent Innova Spectrum.
[f]Depends on mirror selection and spectral region.

power, or occasionally single phase 208 V. Total output power is $\leq$ 100 mW, with most of that available in the 488 or 514.5 nm lines. Air-cooled Ar^+ lasers are generally less expensive than doubled Nd:YAG lasers, but their low power leads to marginal performance in many Raman applications.

7.2.3. Ultraviolet Ion Lasers

Ultraviolet output is available from both Ar^+ and Kr^+ lasers, sometimes with relatively minor modification. For a conventional large-frame Ar^+ laser, the

Table 7.3. Ultraviolet Wavelengths and Powers (W) of Ion Lasers

Wavelength (nm)	Ar^{+a}	Kr^{+a}	Doubled Ar^{+b}
351.6–385.8	3.0		
333.6–363.8	5.0		
337.5–356.4		2.0	
245.4–305.5	0.60		
264			0.02 (0.10)[a]
257			0.10 (1.0)[a]
248			0.03 (0.30)[a]
244			0.10 (0.50)[a]
238			0.03 (0.10)[a]
229			0.01 (0.04)[a]

[a]Large frame.
[b]Small frame.

mirrors may be changed to optimize UV performance, and the UV outputs listed in Table 7.3 result. These "lines" are often in closely spaced groups, as indicated in the table. An alternative approach uses an intracavity nonlinear crystal (beta barium borate, or BBO) to frequency double the fundamental Ar^+ visible wavelengths into the UV (9). A small-frame Ar^+ laser is modified with a temperature-controlled doubling crystal, and the output mirror is coated to reflect visible light but transmit ultraviolet. Table 7.3 includes output powers for doubled Ar^+ lines in the range of 229 to 264 nm. Several doubling crystals are required to cover all six lines, and variation of output wavelength by the operator is usually infrequent.

7.3. HELIUM–NEON LASERS

The familiar 632.8 nm output of the He–Ne laser is available in several integrated Raman spectrometers of analytical interest. Unlike ion lasers, the lasing transition in the He–Ne is an atom (neon), so power need not be consumed to create excited ions. Helium ions and electrons carry the current in the He–Ne laser tube, but energy is transferred to Ne atoms before lasing, and the process is much more efficient than that of ion lasers. Ordinary 110 V electrical power and air cooling are sufficient, and He–Ne lasers are generally much smaller (and less expensive) than ion lasers. However, the output optical power is much lower for the He–Ne laser compared to Ar^+ lasers, with the common

range being 0.5 to 100 mW at 632.8 nm. He–Ne lasers with outputs above 50 mW are quite large and not practical for routine use.

Since the He–Ne is based on emission of gas-phase atoms, the frequency accuracy is excellent, and the output linewidth is sufficiently narrow for most Raman applications without special accessories such as an intracavity etalon. Like ion lasers, He–Ne lasers exhibit a variety of atomic emission lines from the DC discharge that must be filtered out before reaching the sample.

He–Ne lasers are attractive for Raman applications with modest power requirements and compatibility with 632.8 nm excitation. Their long life, low cost, and frequency precision are significant advantages, when low power is sufficient. In addition, 632.8 nm results in Raman scattering in the 633 to 815 nm wavelength range, which includes the most sensitive region of silicon CCDs. However, the likelihood of fluorescence interferences decreases with longer laser wavelength and 632.8 nm is often not red enough. As illustrated in Figure 5.3 for the example of a complex medical sample, the fluorescence observed at 647 nm is lower than that at 488 or 514.5 nm, but not as low as that at 785 nm.

In summary, the He–Ne laser is a good choice for applications in which low power is acceptable and fluorescence interference is not a major issue. An example is routine identification of pure materials or concentrated liquids. The low capital and operating cost of the He–Ne laser is a significant advantage for less demanding applications.

7.4. NEODYMIUM–YAG (Nd:YAG)

Nd:YAG lasers differ fundamentally from He–Ne and ion lasers in that the lasing medium is a solid rather than a gas. The density of excited states can be much higher, and the gain medium much smaller. YAG is yttrium aluminum garnet ($Y_3Al_5O_{12}$), usually in the shape of a rod a few millimeters in diameter and few centimeters in length. The YAG is a host to Nd^{3+} ions, which are actually the lasing medium. YAG has more attractive optical and heat transfer properties than the glass used in large, pulsed Nd:glass lasers. The Nd:YAG is a "four-level" laser and is much more efficient than its historical predecessor, the three-level ruby laser based on Cr^{3+} in an Al_2O_3 host (1). Nd:YAG lasers are available in a wide variety of configurations, including CW versions with well above 10 W of fundamental output, and pulsed lasers with peak powers exceeding 10^9 W in a several nanosecond pulse. The fundamental (1064 nm) and frequency doubled (532 nm) CW Nd:YAG lasers are widely used in both FT and dispersive Raman and are the most popular of the rare-earth lasers for analytical Raman applications. A schematic of the CW Nd:YAG is shown in Figure 7.3.

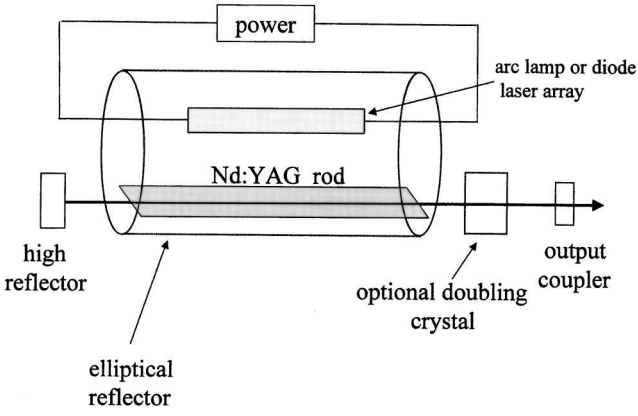

Figure 7.3. Schematic of Nd:YAG laser, pumped by an arc lamp or diode laser array. Doubling crystal converts 1064 nm light to 532 nm.

7.4.1. Fundamental Nd:YAG Laser, 1064 nm

The earliest Nd:YAG lasers were pumped by a flashlamp and emitted pulses with durations of several microseconds. While such lasers and their Q-switched versions have been used extensively for Raman spectroscopy, there is always concern that their high peak powers will damage the sample or generate spectra of photoexcited states or fragments. A simplified energy level diagram for the Nd^{3+} ion in a YAG host is shown in Figure 7.4. Optical pumping by an arc lamp or diode laser can occur over a range of energies in the red and near-infrared regions. Nonradiative decay occurs to populate the upper state ($^4F_{3/2}$) of the lasing transition, so that a population inversion occurs for the $^4F_{3/2}$ to $^4I_{11/2}$ transition. Rapid depopulation of the $^4I_{11/2}$ state by decay to the $^4I_{9/2}$ ground state helps maintain the population inversion. As stated, Nd:YAG is a four-level laser and can be pumped continuously to generate CW output at 1064 nm. Many Nd:YAG lasers use high-pressure xenon arc lamps to pump the Nd:YAG rod, with both lamp and rod cooled by recirculating water. These lasers are capable of output powers exceeding 10 W at 1064 nm and can be mode locked to permit frequency doubling and mixing. Water-cooled Nd:YAG lasers are often the basic lasers acting as pumps for picosecond dye lasers used in time-resolved Raman spectroscopy.

An alternative to the arc-lamp-pumped Nd:YAG, which is attractive to analytical applications, is the diode-pumped Nd:YAG laser, introduced in the early 1990s. An array of diode lasers operating in the range of 800 to 900 nm is directed at the Nd:YAG rod, and pumps the Nd^{3+} to its excited state. Diode lasers are more efficient and compact than arc lamps, and a much larger

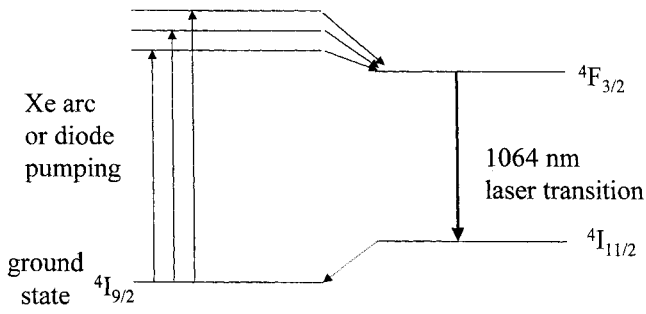

Figure 7.4. Simplified energy levels diagram of Nd^{3+} ion, showing the transition responsible for 1064 nm laser action.

fraction of their output is absorbed by the Nd^{3+} ions. Air-cooled diode-pumped YAG laser heads can be quite small (~2 × 2 × 12 in.) and have high output at 1064 nm (>500 mW). Their high efficiency avoids the requirement for water cooling, and they usually operate on 110 V power. They have become the laser of choice for FT-Raman spectroscopy and are usually an integral component of commercial FT-Raman spectrometers. Output power is usually variable by the operator.

7.4.2. Frequency-Doubled Nd:YAG Lasers (532 nm)

As noted earlier, the reliability and power of the Ar^+ laser has resulted in the common use of 514.5 nm for Raman spectroscopy. However, Ar^+ lasers usually require water cooling and special electrical power. If a single green laser wavelength is sufficient, and the Ar^+ lines other than 514.5 nm are not of interest, the doubled Nd:YAG operating at 532 nm is an attractive alternative. These lasers use an intracavity crystal to double a significant fraction of the 1064 nm light from an otherwise conventional Nd:YAG laser to 532 nm, which is allowed to exit the cavity. The efficiency of diode pumping permits generation of up to several watts of 532 nm output without external cooling water or special electrical power, in a compact laser head.

Commercially available doubled Nd:YAG lasers occur in two general types, which vary in size and power. Integrated systems incorporating power supply and laser head in one unit are available with 50 to 200 mW output powers. Their small size (about 4 × 6 × 12 in.) and turnkey, 110 V, air-cooled operation make them attractive components for integrated Raman spectrometers. More powerful versions in the 2 to 5 W range have separate laser heads and power supplies. The heads are still relatively small (5 × 6 × 18 in.), but the power supplies add significant volume (typically an additional 7 × 18 × 18 in.

module). The high power output of these doubled Nd:YAG lasers, combined with their relatively low utility demands, have led to the replacement of many Ar^+ lasers for Raman spectroscopy. The 532 nm is close enough to 514.5 nm that the rest of the spectrometer requires minimal modification. The most significant scientific cost of changing from Ar^+ to the doubled Nd:YAG is the loss of the other Ar^+ wavelengths, such as 457 and 488 nm.

7.5. DIODE LASERS

Diode lasers based on optical emission from semiconductor junctions were developed initially from light-emitting diodes for applications in communications and displays (2). Their relatively long wavelengths (800 to 1500 nm) were not attractive to Raman spectroscopy until the benefits of NIR excitation and CCDs were appreciated. In addition, there has been a continuous effort to extend diode laser output wavelengths into the visible and blue parts of the spectrum, thus providing a wider range of diode laser wavelengths. For unrelated reasons, diode laser technology has become more useful to Raman applications, while at the same time Raman spectroscopy has evolved to better exploit the red and NIR outputs of diode lasers. The small size, modest power requirements and relatively low cost make diode lasers particularly attractive for integrated Raman spectrometers.

7.5.1. Diode Laser Principles

A schematic of a diode laser is shown in Figure 7.5. Doped semiconductors, often based on gallium arsenide, are joined to form a junction between *p*-type (rich in holes) and *n*-type (rich in electrons) materials. When the junction is forward biased, as shown in Figure 7.5A, electrons are injected into the conduction band of the *p*-type material. These electrons then combine with holes, releasing energy equal to or exceeding the band gap (E_g) of the material. As shown in Figure 7.5B, this recombination annihilates an electron/hole pair, and the energy can be released as light. Without any further modification, the *pn* junction device shown in Figure 7.5 is a light-emitting diode, with ability to convert current to light, at often high efficiency (~30 per cent conversion of electrical to optical power). The output wavelength varies over a range of several tens of nanometers for a given material and may be varied over most of the visible and NIR range by using semiconductors with different band gaps.

If the current density across the *pn* junction is high enough, there are enough electron/hole pairs to cause stimulated emission. For many diode lasers, the faces perpendicular to the junction layer are polished to create

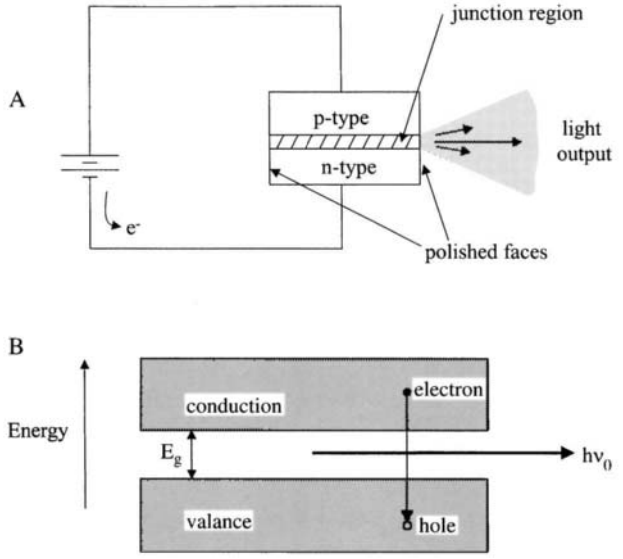

Figure 7.5. (A) Schematic of semiconductor diode laser junction and (B) corresponding energy diagram. Junction region is only a few micrometers thick, and light output is quite divergent. E_g is the semiconductor bandgap.

a resonant cavity. The high refractive index of the semiconductor yields fairly high reflectivity of the semiconductor/air interface, resulting in oscillation of the light between the polished faces. Once a threshold current density is exceeded, the optical gain of the junction region becomes positive and lasing begins. In most diode lasers, additional layers of semiconductors with varying composition are added to the junction to form a "heterojunction" such as AlGaAs. These lasers can support higher current density and efficiency and operate near room temperature.

Diode lasers are quite attractive for spectroscopy in general and Raman in particular for several reasons. First, their high efficiency minimizes power and cooling requirements. Second, they can be very small, since the laser itself is only a few square millimeters in size. When support electronics are included, the laser still may be only a few cubic inches in volume. Third, diode lasers suitable for Raman are available over a range of wavelengths, from approximately 670 to 860 nm, and individual diode lasers are tunable within a more limited range. Fourth, diode lasers can be inexpensive, although significant costs are added to maintain stability (see below). For example, a 691 nm, 20 mW, single-mode diode laser is available for $125 (in 1998) and is adequate for many Raman applications (10). Fifth, diode lasers are available

with sufficient power for the majority of analytical Raman applications, with many in the 0.5 to 1 W range.

However, diode lasers have some negative characteristics that must be overcome for use in Raman spectroscopy. Their broad gain curves permit drift in the output wavelength, and their mode structure is difficult to stabilize. The result is uncertainty in output wavelength and observed Raman shift. Diode lasers of the type shown in Figure 7.5 have high divergence and are less easily filtered and focused than ion or Nd:YAG lasers. Modifications to alleviate these problems are described in the next section.

7.5.2. Diode Laser Adaptation to Raman Spectroscopy

Frequency stabilization is critical before a diode laser is suitable for Raman spectroscopy. Since the laser output frequency is not determined by an atomic line, as in Ar^+ or Nd^{3+}, it can vary in a diode laser for at least two reasons. Temperature affects the gain curve, so that the output wavelength varies at a rate of several reciprocal centimeters per degree Celsius. Temperature control is therefore critical, and most diode lasers systems useful for Raman control the diode temperature to $\pm 0.01°C$. In many cases, a thermistor is built into the laser chip itself, to improve temperature stability by feedback control of a cooling device. In addition, many diode lasers operate on more than one cavity mode, as shown in Figure 7.6. Laser output is maximized when an integral number of wavelengths fits in the cavity between the polished surface, comprising a "longitudinal cavity mode." Since the wavelength is short compared to the cavity length, many modes are possible, and they are closely spaced. Left to itself, the laser depicted in Figure 7.5A has an output similar to that of Figure 7.6D, with each sharp peak resulting from a longitudinal mode. If used for Raman, this multimode laser would generate a Raman spectrum for each mode, yielding a spectrum consisting of several overlapped but slightly shifted Raman spectra. It is not simple to select one of the modes of Figure 7.6A with a filter because they are very closely spaced, and multimode lasers are not readily adapted to Raman unless line broadening and/or multiple peaks are acceptable. The particular AlGaAs diode laser shown in Figure 7.6 yields a single-mode output at higher power (Fig. 7.6A).

Single-mode diode lasers have a modified chip design that preferentially amplifies one cavity mode. The output is a single line (as in Fig. 7.6A) with a linewidth well below 1 cm^{-1}. Single-mode lasers generate good Raman spectra but are still subject to instability. Very small temperature changes cause changes in the gain curve or cavity length, and the laser can suddenly jump from one mode to another. These "mode hops" result in the single-mode output unpredictably changing from one of the modes in Figure 7.6A to another. Modes are typically 5 to 10 cm^{-1} apart, so mode hops can seriously affect frequency accuracy. Mode hops can be eliminated in a few specialized

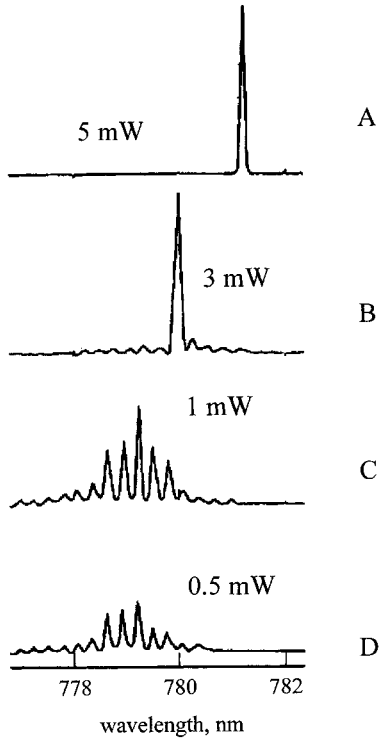

Figure 7.6. Output of an AlGaAs diode laser operating at the indicated optical output powers. For this device, low-power operation (C and D) results in multimode output covering about 2 nm of wavelength. At higher powers (A and B), a single mode operates with a linewidth of ~0.2 nm. (Adapted from Reference 2, p. 338.)

diode lasers based on "distributed Bragg reflection (DBR)." One face of the laser chip is microfabricated to act as a diffraction grating, so the cavity becomes selective for a particular wavelength. The technique successfully yields stable, single-mode operation, but so far has been used in lasers with a limited range of power and wavelength (11). Currently available DBR diode lasers have output powers below 100 mW and wavelengths near 860 nm. A more expensive but more versatile approach to stabilization is based on an external cavity added to a diode laser.

7.5.3. External Cavity Diode Lasers

A semiconductor junction driven with sufficient electrical current exhibits positive optical gain, meaning that it generates more light than it takes in, via

stimulated emission. In the diode lasers discussed so far, the polished faces of the semiconductor act as mirrors to comprise an optical resonator. In an external cavity diode laser, the reflection at the faces is greatly reduced by antireflection coatings, and the mirrors are mounted external to the diode. The diode acts only as a gain medium, analogous to the Ar^+ plasma in an ion laser. A schematic of an external cavity diode laser is shown in Figure 7.7. The diode itself is still quite small, with a junction region only a few micrometers thick. But the cavity is now large, several inches in length. A diffraction grating at one end selects and stabilizes the output wavelength and also permits tunability over an approximately 10 nm range. The diode gain medium is quite sensitive to stray light reflected back into the laser and can be destabilized or even damaged by even small amounts of back-reflected light. To avoid this problem, an isolator is often included that rotates the polarization of exiting light, thus negating the effects of back reflection.

External cavity diode lasers are available as integrated systems that include electronics and power supply in a small (about $4 \times 6 \times 12$ in.) package that runs on 110 V and is air cooled. Alternatively, separate laser heads and power supplies are available, with the laser itself being a few cubic inches in volume. Output powers range from <30 mW to >1 W for single-mode, stabilized output. Linewidths vary over a wide range, from $<10^{-3}$ to 0.3 cm^{-1}, and nearly all external cavity systems are sufficiently narrow for Raman applications. Their frequency stability is excellent, and mode hops are absent. They have an additional advantage over simple diode lasers in beam quality. Their beam is well collimated ($\Theta_d \sim 1$ mrad) and small ($\sim$1.5 mm diameter) and is quite similar in beam characteristics to an ion or Nd:YAG laser. Several diode lasers and typical performance characteristics are listed in Table 7.4. A

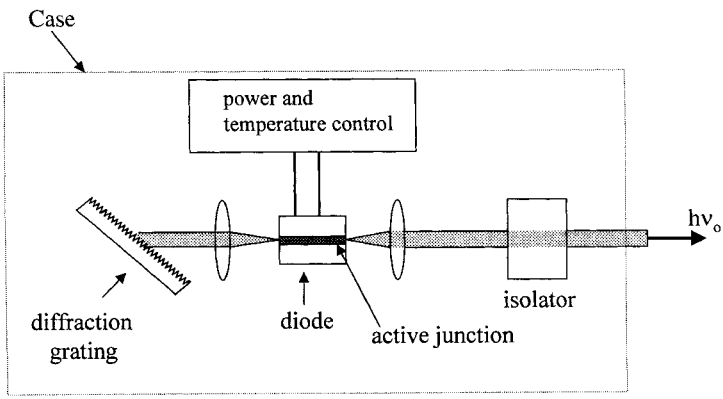

Figure 7.7. External cavity diode laser, such as the Spectra Diode Labs 8530. All components are contained in a $3 \times 4 \times 10$ in. case, and the output power is 300 mW.

Table 7.4. Diode Lasers of Interest to Raman Spectroscopy

Type	Output λ (nm)	Power	Linewidth	Θ_d (rad)	Comments
Multimode	650–900	5 mW–1 W	>5 cm^{-1}	~0.5	[a,b]
Single mode	750–900	1–100 mW	<1 cm^{-1}	~0.5	[b]
Distributed Bragg reflector	852	100 mW	<0.01 cm^{-1}	~0.5	[c]
External cavity, fixed λ	785	300 mW	<0.3 cm^{-1}	0.001	[c,d]
External cavity, variable λ	670, 780, 850[e]	1–30 mW	<0.01 cm^{-1}		[e,f]
External cavity, variable λ	780–1060[e]	500 mW	0.3 cm^{-1}	<0.001	[g]
External cavity, large area	790–804	300 mW	0.01 cm^{-1}		[h]

[a]Multiple simultaneous output wavelengths.
[b]Mode hops likely.
[c]For example, Spectra Diode Labs SDL 5712-H1.
[d]For example, Spectra Diode Labs 8530.
[e]Multiple diodes required.
[f]Tunable over about 10 nm. Similar to New Focus Model 6102.
[g]For example, Spectra Diode Labs SDL 8630.
[h]Described in Reference 12.

recent addition to the collection is a powerful, single-mode diode laser with very narrow linewidth (~0.015 cm^{-1}) and large emitting area (12).

In summary, diode lasers have major advantages for analytical Raman spectroscopy due to their small size, low utility demands, and efficient operation. At present, they are expensive due to the cost associated with frequency stabilization. It is likely that commercial integrated Raman spectrometers will be offered with diode lasers when operation in the 700 to 850 nm range is desired. It appears unlikely that diode lasers will replace Nd:YAG, doubled Nd:YAG, or argon systems for visible and 1064 nm operation.

7.6. LASER WAVELENGTH FILTERING

Although the vast majority of light output from a laser occurs at the lasing wavelength(s), all lasers emit additional wavelengths from various sources. Atomic emission lines from Ar, Ar^+, Kr^+, He, Ne, for example, were mentioned earlier, and solid-state lasers such as Nd:YAG and diode lasers have broad, near continuum output off the laser wavelength. An example is shown in Figure 7.8 for a silicon sample excited with the 514.5 nm line of an Ar^+

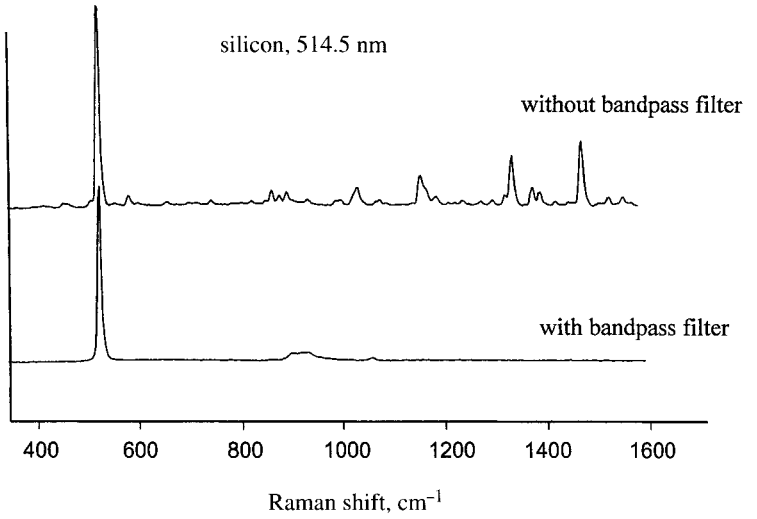

Figure 7.8. Spectra of a silicon wafer obtained without (upper) and with (lower) a bandpass filter between the laser and sample (positioned as shown in Fig. 6.1); 180° geometry, 514.5 nm. Only the lines at 521 and ~960 cm^{-1} are due to silicon, the remainder are emissions from the Ar^+ laser.

laser. Since Raman scattering is weak, even small amounts of nonlasing light from the laser can interfere. Elastic scattering from these interfering lines is collected and analyzed along with the Raman light, leading to the interfering lines apparent in upper spectrum of Figure 7.8. These lines are removed by adding a dielectric bandpass filter between the laser and the sample (as shown in Fig. 6.1). The intensity of nonlasing lines can be as high as a few percent of the laser line itself and therefore much stronger than most Raman features. The bandpass filter used to remove nonlasing lines should have a high optical density off the laser line, at least 3.0 or greater.

All lasers in current use for analytical Raman spectroscopy must be filtered to reduce laser interferences. A perfect filter would exhibit 100 per cent transmission of the laser line, while totally blocking all other light a few reciprocal centimeters away from the laser. In reality, several different types of filters are used for Raman, which approximate ideal performance to varying degrees. Of interest here are interference filters and premonochromators.

7.6.1. Interference Filters

The bandpass filters used in many Raman spectrometers are essentially high-performance interference filters of conventional design. Typically, low-cost

interference filters have optical densities (OD) of about 3 outside the passband, meaning that light at wavelengths other than the filter center is attenuated by a factor of 1000 or more. An OD of 3 is marginally adequate for Raman applications and will usually allow too much laser interference, particularly for samples with large elastic scatter (e.g., white solids). The OD can be increased to values above 6 by using multiple cavities in the filter. The filter manufacturer numerically optimizes the thickness and refractive index of several dielectric layers to adjust both transmission wavelength, bandpass width, and off-line OD. An example of the transmission characteristics of multilayer dielectric filters is shown in Figure 7.9. Note that the ordinate is optical density, hence it is logarithmic in transmitted light intensity. The "six-cavity" filter shown has an OD above 7 about 15 nm from the laser line. Note also that interference can exhibit "harmonics" at which the transmission increases off the intended transmission wavelength (e.g., 400 nm in Fig. 7.9). Such harmonics are usually "blocked" by adding a suitable absorber that prevents transmission at harmonic wavelengths.

The physical size of interference filters is commonly 1 in. diameter by 5 to 10 mm thick, including protective mount. Optical properties important to Raman can usually be specified at the time of purchase, and their relative importance depends on the application. First, the transmission at the laser

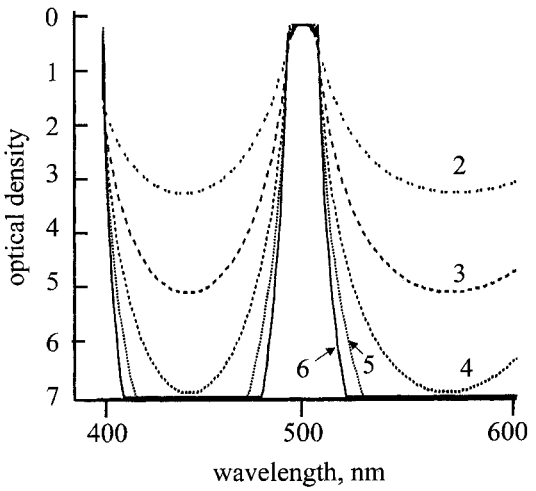

Figure 7.9. Optical density of an interference bandpass filter designed to transmit 500 nm light. Labels on curves refer to the number of cavities in the filter (see text). (Adapted from Omega product literature.)

wavelength determines how much laser light reaches the sample, and is usually in the range of 40 to 60 per cent. Filter bandwidth is usually stated as a full width at half maximum (FWHM) for the filter transmission curve. As the FWHM becomes smaller, the peak transmission usually decreases, so there is a trade-off of maximum laser power versus spectral purity. Third, the OD off the peak wavelength increases with wavelength, at a rate similar to that shown in Figure 7.9. As noted already, it is important to have a high OD at wavelengths where Raman scattering is observed. However, if a sufficient OD is achieved at a high Raman shift (e.g., 1000 cm^{-1}), the OD may not be sufficient at lower Raman shift, close to the laser line. Table 7.5 illustrates the effect, based on a 785 nm laser and filter, FWHM of 10 nm, and six-cavity filter of the type shown in Figure 7.9. For Raman shifts above 250 cm^{-1}, the performance described in Table 7.5 is adequate. For lower Raman shifts, laser interference is possible, with its magnitude depending on the relative strengths of the laser emission and the Raman scattering at each Raman shift value. In effect, the bandpass filter performance influences the ability to observe Raman scattering at low Raman shifts. The band reject filters discussed in Chapters 8 and 9 also affect low-frequency performance.

In addition to their transmission characteristics, interference filters also differ in maximum power tolerance and sensitivity to incidence angle. Damage can occur at high laser powers, but usually at levels above a few watts. Filter damage is therefore unlikely at laser powers used in routine Raman spectroscopy. The transmission curves similar to that in Figure 7.9 vary with angle of incidence, with the center wavelength varying approximately with the cosine of the incidence angle relative to the surface normal of the filter. A few degrees of tilt have minor effects, but larger angles should be avoided. In addition, poorly collimated light results in a range of incidence angles and will allow additional nonlasing light to pass through the filter.

Table 7.5. Transmission of 785 nm Interference Filter[a]

Wavelength (nm)	Raman Shift (cm^{-1}) Relative to 785 nm	Transmission	Optical Density
785	0	0.6	0.2
790	80	0.3	0.5
792	113	0.01	2
793	138	10^{-3}	3
794	145	10^{-4}	4
796	177	10^{-5}	5
800	>250	$<10^{-6}$	>6

[a]Six cavities, FWHM = 10 nm, similar to Omega 785DF10.

7.6.2. Premonochromators as Filters

Figure 7.10 shows a small monochromator designed explicitly for a collimated laser beam. A diffraction grating selected to be most efficient at or near the laser wavelength disperses the laser light into the main beam and extraneous wavelengths. The grating angle is adjusted, usually with a small micrometer, so the diffracted laser beam exits through a circular aperture of diameter approximately equal to the original beam diameter. Undesired laser light leaves the grating at a different angle and is blocked by the aperture or monochromator body. The transmission wavelength of the filter may be tuned over a wide range merely by adjusting the grating angle. Tunability is a major advantage over interference filters, as a multiline (such as Ar^+) or tunable (dye, diode) laser may be used without requiring a filter for each wavelength.

Grating premonochromators are excellent in terms of selectivity for the desired wavelength, with rejection of extraneous light at least as good as the best interference filters. They do require collimated light and a fairly small beam diameter, typical of ion, He–Ne, and Nd:YAG lasers. Their transmission is generally close to 50 per cent, with most of the loss due to the grating efficiency. They are more bulky and more expensive than interference filters and are subject to mechanical misalignment by rough treatment. Overall, a grating premonochromator is attractive for applications where the laser wavelength is changed frequently or when extraneous light near the laser line must be blocked.

A holographic bandpass filter is conceptually similar to a grating premonochromator, but has higher overall transmission. A volume diffraction grating may be generated in a suitable photosensitive emulsion by an interference pattern from a laser beam (13). Such a grating disperses light much like a reflection grating, but for transmitted light (see Fig. 7.11). The grating may be embedded in a cube of optical glass, so that the desired wavelength diffracts

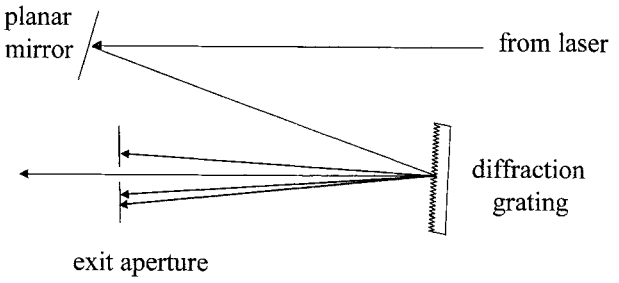

Figure 7.10. Schematic of a grating premonochromator configured to filter out plasma lines from a collimated laser beam.

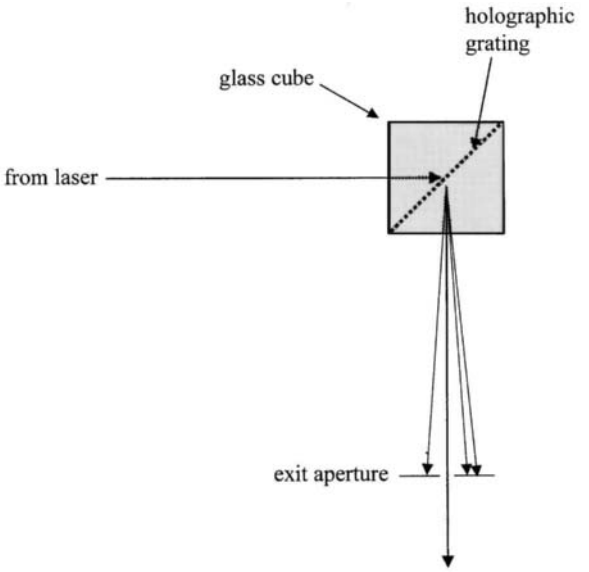

Figure 7.11. Premonochromator based on a holographic diffraction grating mounted in a glass cube.

at 90°. The grating density is chosen to match the laser wavelength, and is fixed at the time of manufacture. Extraneous light is diffracted at angles other than 90° and blocked by a circular aperture. Even better selectivity may be achieved by focusing the diffracted light through a pinhole, then recollimating. The holographic bandpass filter of Figure 7.11 can be quite compact, with the cube itself being less than 1 in. on a side. The main attraction is high transmission, with 80 per cent or more of the laser light exiting the aperture after filtering. The holographic system may be angle tuned by rotating the cube, but over a more limited range than the grating system of Figure 7.10.

REFERENCES

1. P. W. Milonni and J. H. Eberly, *Lasers*, Wiley-Interscience, New York, 1988.
2. J. Hecht, *The Laser Guidebook*, 2nd ed., McGraw-Hill, New York, 1992.
3. E. H. Piepmeier, *Analytical Applications of Lasers*, Wiley-Interscience, New York, 1986.
4. J. Sneddon, T. Thiem, and Y.-I. Lee, eds, *Lasers in Analytical Atomic Spectroscopy*, VCH, New York, 1997.
5. D. Andrews, *Lasers in Chemistry*, Springer, New York, 1997.

6. S. A. Asher, C. R. Johnson, and J. Murtaugh, *Rev. Sci. Instrum.*, **54**, 1657 (1983).
7. C. M. Jones, V. L. Devito, P. A. Harmon, and S. A. Asher, *Appl. Spectrosc.*, **41**, 1268, (1987).
8. S. A. Asher, *Anal. Chem.*, **65**, 59A (1993).
9. S. A. Asher, R. W. Bormett, X. G. Chen, D. H. Lemmon, N. Chao, P. Peterson, M. Arrigoni, L. Spinelli, and J. Cannon, *Appl. Spectrosc.*, **47** , 628 (1993).
10. J. Zhao and R. L. McCreery, *Langmuir*, **11**, 4036 (1995).
11. J. Cooper, P. Flecher, S. Albin, T. Vess, and W. Welch, *Appl. Spectrosc.*, **49**, 1692 (1995).
12. R. Claps, J. Sabbaghzadeh, and M. Fink, *Appl. Spectrosc.*, **53**, 491 (1999).
13. J. Tedesco, H. Owen, D. M. Pallister, and M. Morris, *Anal. Chem.*, **65**, 441A (1993).

Raman Spectroscopy for Chemical Analysis. Richard L. McCreery

ISBN: 0-471-25287-5

CHAPTER

8

DISPERSIVE RAMAN SPECTROMETERS

8.1. OVERVIEW

As discussed in Chapter 5, all Raman spectrometers built before 1986 were dispersive, with the Fourier transform (FT) systems being a popular alternative since then when the laser wavelength is longer than about 1.0 μm. Dispersive Raman designs cover a wide range of types and configurations, and only the most common will be addressed in this chapter. Until ca. 1980, dispersive spectrometers were single-channel, scanning systems based on single, double, or occasionally triple monochromators. Since 1990, multichannel dispersive systems superceded single-channel designs due to the speed and sensitivity gains noted in Chapters 3 and 4. In the current chapter, we will consider single grating dispersive spectrometers initially, in order to illustrate dispersive principles. The majority of the chapter is on multichannel systems and charge-coupled devices CCD, as this combination currently dominates dispersive designs.

Dispersion of light by a diffraction grating, shown schematically in Figure 8.1, is the principle of the most common type of dispersive wavelength analyzer. As noted in Chapter 1, the *wavelength analyzer* is a subunit within a Raman *spectrometer* that allows separation of wavelengths and eventually Raman shifts. A *spectrograph* disperses light along a *focal plane.* A spectrograph with a multichannel detector at the focal plane is a key component in a multichannel spectrometer. If an exit slit is placed at the focal plane, a small range of wavelengths (the *bandpass*) is transmitted, and the device is a *monochromator.* Strictly speaking, a monochromator is used only with a single-channel detector, but in common usage, the spectrograph preceding a multichannel detector is often referred to as a monochromator.

Before considering specific spectrometer designs, a few general points that apply to all dispersive systems deserve note. Nearly all dispersive Raman spectrometers are based on diffraction gratings, shown schematically in Figure 8.1. Gratings disperse the light according to *wavelength*, not *wavenumber*, resulting in a linear spread of wavelengths at the focal plane of the spectrometer. The lower portion of Figure 8.1 shows the coverage of wavelength along the focal

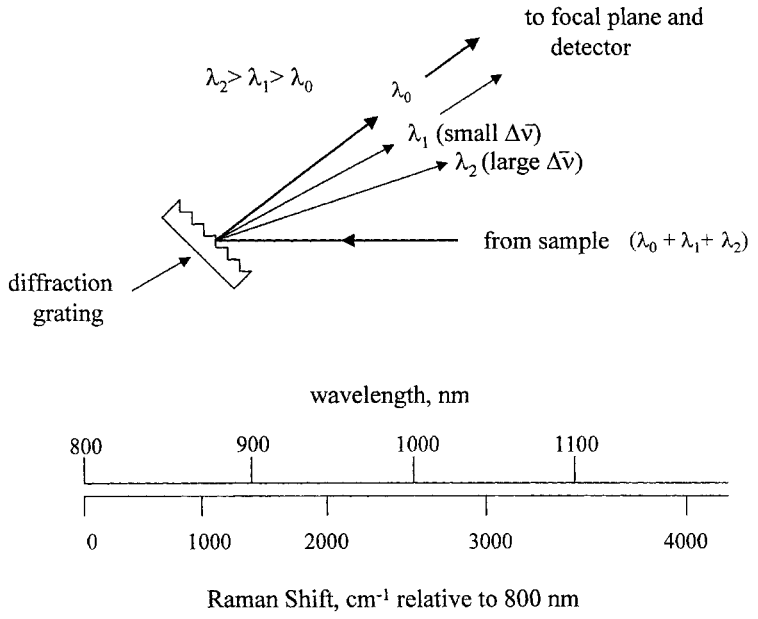

Figure 8.1. Schematic of wavelength dispersion by a diffraction grating. Wavelength and Raman shift scales illustrate the nonlinear dispersion of Raman shift for diffraction of scattering from a 785 nm laser. Scales shown are linear in wavelength but nonlinear in Raman shift.

plane, with linear* dispersion of wavelength (1). This spread of wavelengths is often described by a constant linear dispersion, $dl/d\lambda$, with units of millimeters per nanometer. However, if the same range of wavelengths is plotted as Raman shift, the dispersion is nonlinear. The dispersion in terms of $dl/d(\Delta\bar{\nu})$, with units of millimeters per reciprocal centimeter is not constant with $\Delta\bar{\nu}$. For example, the 10 nm between 800 and 810 nm contains 154 cm^{-1}, while the range 1000 to 1010 nm contains only 99 cm^{-1}.

When either a slit or a detector element is placed at the focal plane, it will collect a constant range of wavelength along the spectrum, but a nonconstant range of Raman shift. A slit width sufficient to collect 0.1 nm at 800 nm will also collect 0.1 nm at 1000 nm. But the same slit will collect 1.6 cm^{-1} at 800 and 1.0 cm^{-1} at 1000 cm^{-1}. This effect is described algebraically by Eq. (8.1), obtained by differentiating the relation $\bar{\nu} = 1/\lambda$:

$$d\bar{\nu} = \frac{1}{\lambda^2} d\lambda \tag{8.1}$$

* There is a small nonlinearity that depends on the cosine of the diffraction angle, as discussed in Section 8.2.1.

The nonlinear dispersion of Raman shifts is fundamental to wavelength dispersive spectrometers because the physics underlying dispersion is based on wavelength rather than energy. The effect is larger at longer laser wavelengths because the typical Raman shift range of interest (0 to 3500 cm^{-1}) covers a wider range of wavelength in the red and near-infrared (NIR) regions of the spectrum. For example, the dispersion $(dl/d(\Delta\bar{\nu}))$ over a 0 to 3500 cm^{-1} Raman shift range varies by 30 per cent for a 457 nm laser but 47 per cent for a 785 nm laser. The main consequences of this nonlinear Raman shift dispersion is nonconstant spectral resolution noted below and effects on response correction discussed in Chapter 10.

A second general property of dispersive spectrometers is a trade-off of resolution, spectral coverage, and acquisition time. High resolution over a wide Raman shift range requires a large number of intensity measurements. For the case of a scanning spectrometer, this means that a large number of wavelength increments must be monitored, leading to a long acquisition time. A multichannel system greatly improves this problem by monitoring many wavelengths at once, but it still has a finite number of channels. Increasing the dispersion improves resolution but decreases spectral coverage since the multichannel detector is of finite size. The problem is illustrated in Figure 8.2 for the case of a 1024-element CCD. *Low* and *high* dispersion refer to a 250 mm focal length spectrograph with 300 or 1200 line/mm gratings, respectively. For the example shown, one has the choice of a 3300 cm^{-1} spectral coverage with 2 to 4 cm^{-1} resolution or 850 cm^{-1} coverage with <1 cm^{-1} resolution. As will be discussed in Section 8.6, this trade-off may be mitigated by multiple CCD exposures or scanning/multichannel hybrids, but at the cost of increased measurement time.

8.1.1. Definitions

Referring back to Figure 1.7, the dispersive wavelength analyzer must receive an image of the Raman sample as illuminated by the laser, then reimage this input after dispersing the light according to wavelength. The dispersed image is formed at the focal plane of the analyzer and a spatially displaced image will appear for each wavelength increment. The important parameters that determine analyzer design are dispersion, $f/\#$, transmission, stray light, and image quality. The parameters are defined with reference to the generic single grating system of Figure 8.3.

1. *Dispersion.* The linear dispersion (in millimeters per nanometer) described above is often converted to reciprocal linear dispersion ($d\lambda/dl$, units of nm/mm) when stated in the manufacturer's literature. It describes how much of the spectrum (in nanometers) is covered in a unit of focal plane. If

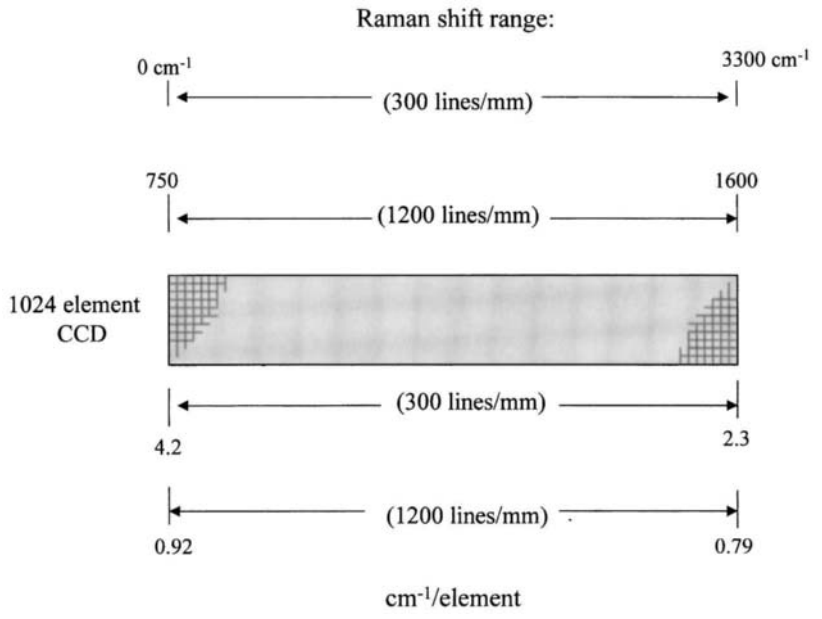

Figure 8.2. Raman shift coverage and resolution for two different gratings (300 and 1200 lines/mm) and a 25 mm wide CCD in a 250 mm spectrograph. For a constant number of CCD elements, resolution improves as spectral coverage decreases.

the image is formed on a CCD detector, the spectral range for each pixel is given by:

$$\frac{\text{nm}}{\text{pixel}} = \left(\frac{d\lambda}{dl}\right) W_p \tag{8.2}$$

where W_P is the physical width of the detector channel along the wavelength axis. For a single-channel spectrometer, an exit slit would be positioned at the focal plane. The bandpass in nanometers would be given by Eq. (8.2), with the slit width substituting for W_P (1).

2. $f/\#$. As was the case with the collection optics, the wavelength analyzer also has an f number. To a first approximation, the $f/\#$ is the ratio of the focal length of the collimating mirror to the limiting aperture diameter, usually determined by the grating. So short focal length and large mirrors and gratings yield a low $f/\#$. As stated in Eq. (3.4), a lower $f/\#$ yields a larger collection angle for the analyzer and more efficient collection of Raman scattering.

3. *Transmission.* The transmission of the wavelength analyzer is the fraction of light of a given wavelength entering the entrance slit that reaches

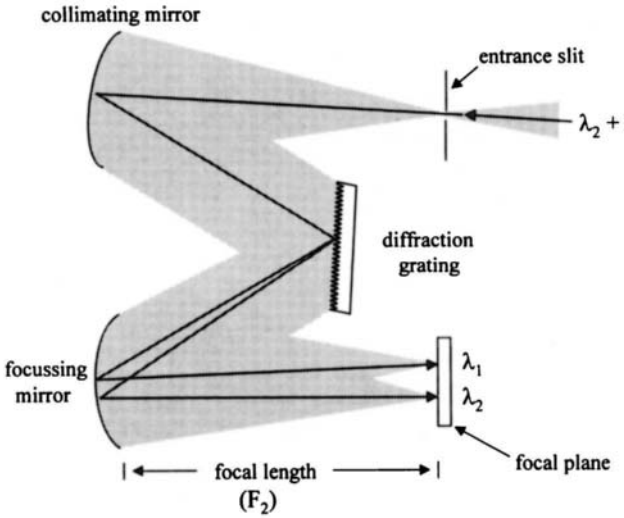

Figure 8.3. Schematic of a single grating Czerny-Turner spectrograph. Shading indicates envelope of light passing through the instrument, which disperses and focuses wavelengths at the focal plane.

the detector. It is unitless and covers a wide range from less than 5 per cent to above 50 per cent. It can vary with incident angle, and should be determined for light that fills the collection aperture of the wavelength analyzer. A measurement using solely on-axis light (such as a laser) will usually overstate the transmission. The largest transmission losses in dispersive systems usually occur at the grating.

4. *Stray Light.* When a wavelength analyzer is adjusted to observe a particular wavelength, a small amount of light of other wavelengths will reach the detector. Low stray light is critical in Raman spectroscopy because one is observing weak Raman scattering in the presence of much stronger laser light. The wavelength analyzer must be able to reject the intense laser light, while efficiently transmitting Raman light. An example of the problem is shown in Figure 8.4. The high background in the upper spectrum is stray laser light striking the detector at unintended positions. Stray light appears on the spectrum at wavelengths other than that of the laser, but, in fact, it is unshifted laser light striking the detector in the wrong place. The problem is greatly reduced by adding a filter that blocks only the laser light. Stray light magnitude is often measured differently by various manufacturers, but one method is to observe the intensity of a laser at some wavelength other than that of the laser itself. For example, a monochromator with a bandpass of 2 nm might be set for 642.8 nm, and a He–Ne laser (632.8 nm) is directed into the entrance slit. If

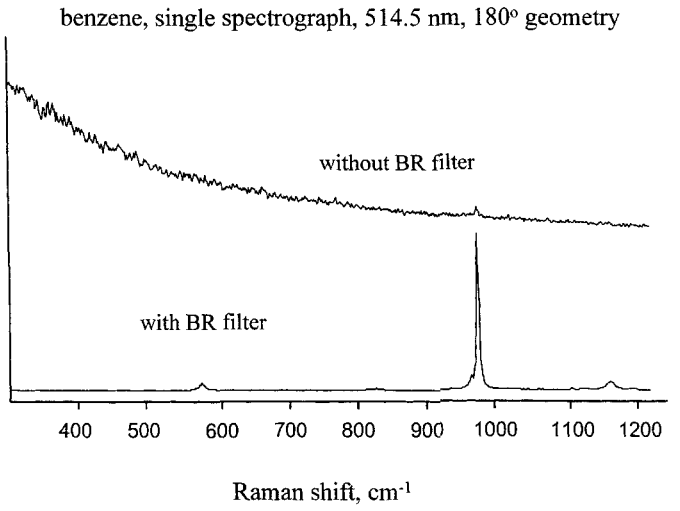

Figure 8.4. Raman spectrum of liquid benzene from a single spectrograph with and without a holographic laser rejection filter between the sample and the entrance slit. Intensity scales differ greatly between the two spectra.

the signal at 642.8 nm is 10^{-5} times that of the laser, the stray light would be "10^{-5} at five bandpasses away from the incident wavelength." In other words, moving the monochromator setpoint by 10 nm reduced transmission a factor of 10^5.

5. *Imaging and Flat Field.* Like any real optical system, a dispersive analyzer design has aberrations that result in nonideal performance. These aberrations arise from the mirrors operating off-axis (as in Fig. 8.3), chromatic aberrations in the optics, and the designer usually chooses to minimize one type of aberration at the expense of another. For example, the classical Czerny-Turner configuration of Figure 8.3 provides good dispersion across a relatively wide focal plane but does distort the slit image along the slit axis. If the user is concerned only about determining Raman shift, such distortion is acceptable. In an "imaging" application, however, distortion along both the wavelength and slit axes is reduced as much as possible. This property is illustrated in Figure 8.5 for the case of a source containing solely three monochromatic wavelengths of 400, 500, and 600 nm. The imaging spectrograph produces three slit images on the focal plane, with the image width ideally equal to the entrance slit width. Furthermore, the registry of the entrance slit and focal plane image is maintained in the imaging system. For a conventional system (e.g., Czerny-Turner), aberration causes broadening and curvature when the image occurs off the optical axis, and registry between slit and image is

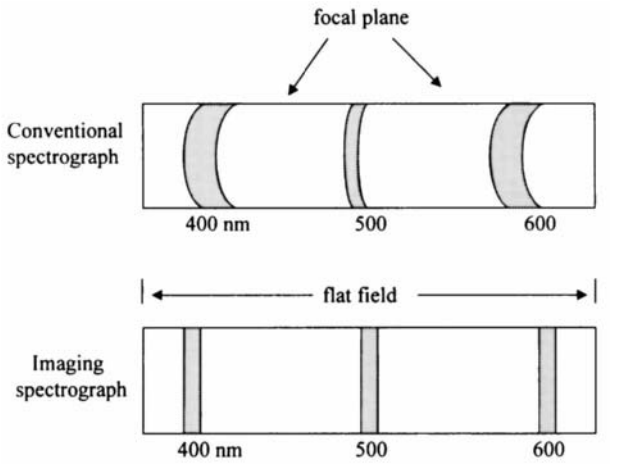

Figure 8.5. Images of the entrance slit for monochromatic light of 400, 500, and 600 nm at the focal plane of a conventional (nonimaging) spectrograph and an ideal imaging spectrograph. Distortion of slit image in conventional system varies significantly for different configurations.

not retained. The area of the focal plane in which the slit image is maintained on imaging systems is known as the *flat field*. The height and width of the flat field dictate the detector size that can be used without serious degradation of spectral or spatial resolution or imaging. It is not easy to quantitatively specify image quality, but a practical test is the observation of a monochromatic point source imaged at various positions on the focal plane. For good imaging quality, the point will not increase in diameter significantly over the entire flat field. The imaging capability of a spectrograph is important when considering Raman microscopy (Chapter 11) or fiber optics (Chapter 12).

8.2. DISPERSIVE SPECTROMETER CONFIGURATIONS

8.2.1. Single Grating Spectrographs

The single grating instrument depicted in Figure 8.3 is very common in optical spectroscopy (1), but its application to Raman is relatively recent because of inadequate stray light rejection. The introduction of effective laser rejection filters (Section 8.2.5) removed this limitation and single spectrographs became attractive. They are simpler and more efficient than double or triple systems and usually much more compact. Variations of the classical Czerny-Turner

design (Fig. 8.3) are now quite common in Raman spectrometers, although they vary in focal length, $f/\#$, and dispersion.

The reciprocal linear dispersion of the single spectrograph in Figure 8.3 is given by:

$$\frac{d\lambda}{dl} = \frac{d\cos\theta}{mF_2} \tag{8.3}$$

where d is the distance between rulings on the diffraction grating, m is the diffraction order (0, 1, 2,...), F_2 is the focal length of the focusing mirror, θ is the angle of diffracted light leaving the grating (relative to the grating surface normal), and $\cos\theta$ is usually considered to be constant over the limited range of wavelengths to be analyzed (2). Note that $d\lambda/dl$ is nearly constant over a limited range of θ, when stated in terms of wavelength rather than wavenumber. For example, $d\lambda/dl$ changes by less than 2 per cent over a 100 nm wavelength range for a 1200 line/mm grating in a 250 mm spectrograph.

The dispersion in terms of $\bar{\nu}$ or Raman shift is not as constant, however, as noted in Section 8.1. Differentiation of the relationship between λ and $\bar{\nu}$ leads to Eq. (8.4), and combination with (8.3) yields (8.5):

$$\frac{d\bar{\nu}}{d\lambda} = \frac{-1}{\lambda^2} = -(\bar{\nu})^2 \tag{8.4}$$

$$\frac{d\bar{\nu}}{dl} = \frac{d\cos\theta}{mF_2\lambda^2} = \frac{d\cos\theta(\bar{\nu})^2}{mF_2} \tag{8.5}$$

Since $d\bar{\nu}/dl$ depends on $(\bar{\nu})^2$, it will vary both with Raman shift magnitude and with laser wavelength, as noted in Eq. (8.6) after substituting $\bar{\nu}_R = \bar{\nu}_O - \bar{\nu}_j$ in Eq. (8.5):

$$\frac{d\bar{\nu}}{dl} = \frac{d\cos\theta(\bar{\nu}_O - \bar{\nu}_j)^2}{mF_2} \tag{8.6}$$

Several values of the dispersion for various laser, grating, and focal length combinations are listed in Table 8.1. Since $d\bar{\nu}/dl$ describes how widely a Raman shift increment is spread over an increment of focal plane, a lower $d\bar{\nu}/dl$ implies higher spectral resolution. Stated differently, a slit or detector element of fixed width will collect a smaller range of Raman shifts for smaller values of $d\bar{\nu}/dl$. As expected, the dispersion is higher (and $d\bar{\nu}/dl$ smaller) for higher density gratings (small d) and longer focal lengths (large F_2). It is also apparent from Table 8.1 that the dispersion varies over the Raman shift range, more so at longer laser wavelengths.

Table 8.1. Reciprocal Linear Dispersion for Several Single Spectrograph Designs

Laser Wavelength (nm)	Grating Density (lines/mm)	Focal Length (mm)	$\frac{d\bar{\nu}}{dl}$ (cm^{-1}/mm) for $\Delta\bar{\nu}$ =		
			100 cm^{-1}	1500 cm^{-1}	3000 cm^{-1}
514.5	600	100	623	536	450
514.5	600	250	249	214	180
514.5	600	500	125	107	90
514.5	600	1000	62	54	45
514.5	1200	100	312	268	225
514.5	1200	250	125	107	90
514.5	1200	500	62	54	45
514.5	1200	1000	31	27	23
514.5	1800	100	208	179	150
514.5	1800	250	83	71	60
514.5	1800	500	42	36	30
514.5	1800	1000	21	18	15
785	300	100	532	421	316
785	300	250	213	168	126
785	300	500	106	84	63
785	300	1000	53	42	32
785	600	100	266	211	158
785	600	250	106	84	63
785	600	500	53	42	32
785	600	1000	27	21	16
785	1200	100	133	105	79
785	1200	250	53	42	32
785	1200	500	27	21	16
785	1200	1000	13.3	10.5	7.9

8.2.1.1 Resolution and Spectral Coverage

The practical consequences of Eq. (8.6) lie in both resolution and spectral coverage. High dispersion (small $d\bar{\nu}/dl$) yields high resolution (small $\Delta\bar{\nu}$ range per pixel or slit width), according to:

$$d\bar{\nu} = \left(\frac{d\bar{\nu}}{dl}\right) W_P \tag{8.7}$$

In this case, $d\bar{\nu}$ is the Raman shift increment observable with a slit or pixel of width W_P. However, an array detector has a finite number of pixels, and the flat field of the spectrograph is of finite width, so there is a limit on the range

of Raman shifts observable with a given spectrograph/detector combination. Temporarily ignoring the variation of $d\bar{\nu}/dl$ with $\Delta\bar{\nu}$, the Raman shift range observable with a given detector width is provided *approximately* by:

$$\text{Spectral range} = \left(\frac{d\bar{\nu}}{dl}\right)_{1500} W_D = \frac{d\bar{\nu}}{dl} W_p N_C \tag{8.8}$$

The subscript 1500 is the reciprocal linear dispersion at a Raman shift of 1500 cm^{-1} (approximately the center of the spectrum), W_D is the total detector width and N_C is the number of channels along the wavelength axis. Combining with Eq. (8.6) (and assuming $m = 1$, $\cos\theta = 1$), yields

$$\text{Spectral range} \_ \frac{d(\bar{\nu}_0 - 1500)^2 W_D}{F_2} \tag{8.9}$$

A more accurate but less convenient expression is given by:

$$\text{Spectral range } (cm^{-1}) = \bar{\nu}_0 - \bar{\nu}_j - \left[(\bar{\nu}_O - \bar{\nu}_j)^{-1} + \frac{dW_D}{mF_2}\right]^{-1} \tag{8.10}$$

where $\bar{\nu}_0$ is the absolute wavenumber of the laser and $\bar{\nu}_j$ is the lowest Raman shift to be observed (in reciprocal centimeters). The spectral range calculated from the approximate Eq. (8.8) is generally within 10 per cent or less of the accurate value calculated from Eq. (8.10). Table 8.2 provides several examples of $d\bar{\nu}$ and spectral range for a 250 mm spectrograph. The relationships of dispersion, coverage, and resolution are shown graphically in Figure 8.6. The numbers accompanying each curve are the grating density (lines/millimeter) in a spectrograph with $F_2 = 250$ mm. The ordinate is labeled with $d\bar{\nu}/dl$ and $d\bar{\nu}$ per pixel (25 μm width) on the left and spectral coverage for a 25 mm detector on the right. The horizontal lines labeled with italics indicate the Raman shift range for various common laser wavelengths. As an example, consider a 250 mm spectrograph, 25 mm detector, and 785 nm laser. The coverage is given approximately by the grating curves of Figure 8.6 at points below the midpoint of the 785 nm Raman shift range. Coverage is about 3700 cm^{-1} for the 300-line/mm grating, 2200 cm^{-1} for the 600-line/mm grating (indicated by the asterisk on the 600-line/mm curve), and 1200 cm^{-1} for the 1200-line grating. Furthermore, the resolution for the 600-line grating (indicated by the black circles) varies from about 2.4 cm^{-1} per pixel at low Raman shift (high absolute wavenumber) to about 1.2 cm^{-1} per pixel at 3500 cm^{-1}.

It should be noted that the actual spectral resolution is a fairly complex function of the slit width, pixel width, and spectrograph dispersion. The image of the entrance slit on the CCD may be wider or narrower than the pixel width

Table 8.2. Bandpass and Spectral Coverage for Several Single Spectrograph Designs

Laser Wavelength (nm)	Grating Density (lines/mm)	Focal Length (mm)	Bandpass[a] for 25 μm Slit or Pixel at 1500 cm^{-1}	Spectral[b] Coverage over 25 mm Detector
514.5	600	100	13.4	8697
514.5	600	250	5.4	4756
514.5	600	500	2.7	2709
514.5	600	1000	1.3	1456
514.5	1200	100	6.7	5602
514.5	1200	250	2.7	2709
514.5	1200	500	1.3	1456
514.5	1200	1000	0.67	756
514.5	1800	100	4.5	4132
514.5	1800	250	1.8	1894
514.5	1800	500	0.89	996
514.5	1800	1000	0.45	511
785	300	100	10.5	6560
785	300	250	4.2	3797
785	300	500	2.1	2231
785	300	1000	1.05	1223
785	600	100	5.26	4417
785	600	250	2.11	2231
785	600	500	1.05	1223
785	600	1000	0.53	642
785	1200	100	2.63	2672
785	1200	250	1.05	1223
785	1200	500	0.53	642
785	1200	1000	0.26	329

[a]Calculated from Eq. (8.6), assuming $m = 1$, $\cos\theta = 1$, and $\bar{\nu}_j = 1500\ cm^{-1}$.
[b]Calculated from Eq. (8.10), with $m = 1$, $\cos\theta = 1$, and $\bar{\nu}_j = 100\ cm^{-1}$.

depending on the physical slit width and the spectrograph magnification (if any). For example, the image of a 100 μm slit on a CCD with 25 μm pixels will project a given wavelength onto four pixels. In this case, the resolution is determined by the slit width rather than the pixel width in Eq. (8.7). Conversely, decreasing the slit image width to a value smaller than the pixel width will not improve resolution but will decrease the signal. As a rule of thumb, the resolution is determined by the *larger* of the pixel width and the slit image width, multiplied by $d\bar{\nu}/dl$.

Figure 8.7 shows an experimental example of the trade-off of spectral coverage and resolution for three gratings in a 330 mm spectrograph and

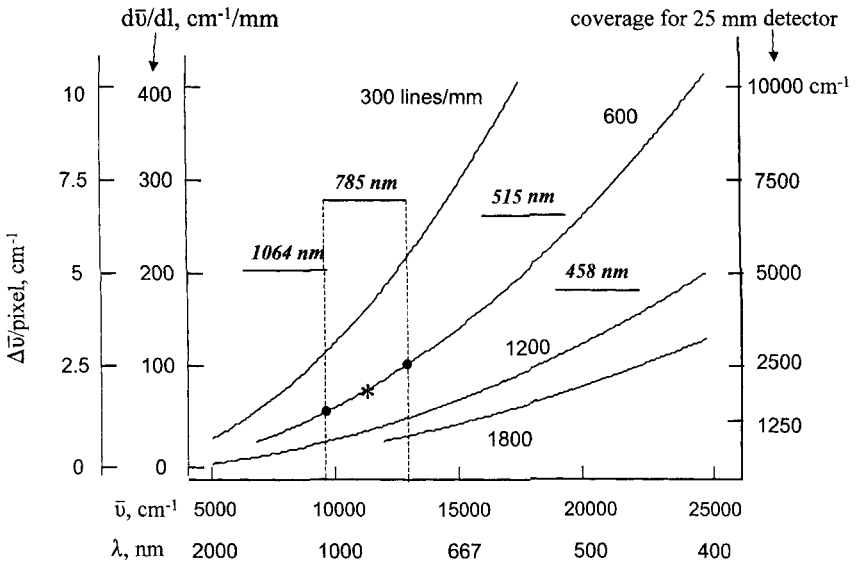

Figure 8.6. Dispersion and coverage for 250 mm focal length single spectrograph, 25 mm detector, and 25 μm pixel width. Curves correspond to gratings with 300, 600, 1200, or 1800 lines/mm, and italics indicate the Raman shift range for several laser wavelengths. Reciprocal linear dispersion ($d\bar{\nu}/dl$) and resolution for a 25 μm pixel ($\Delta\bar{\nu}$) are on the left ordinate and may be determined directly for a given grating and wavelength. Approximate coverage is given for different gratings and wavelengths. The asterisk indicates spectral coverage and black dots indicate resolution and high and low Raman shift limits for the case of a 785 nm laser and 600 line grating.

27 mm-wide detector. Equation (8.9) predicts approximate coverages of 3400, 1720, and 860 cm^{-1} for 300-, 600-, and 1800-line/mm gratings, respectively. Notice that the resolution improves for the higher density gratings, while the spectral coverage decreases.

Several observations of practical importance are available from Tables 8.1 and 8.2 and Figures 8.6 and 8.7. First, dispersion in terms of Raman shift varies over the common Raman shift range, as noted in Section 8.1, with a greater relative effect for longer laser wavelengths. Second, bandpass and spectral coverage are strong functions of grating density, focal length, and laser wavelength. For this reason, many dispersive Raman spectrographs can mechanically select among two or three gratings to permit both high- and low-resolution operation. Third, the fundamental trade-off between resolution and coverage is obvious from Table 8.2 and Figure 8.7. Since the number of pixels is finite, wider spectral coverage requires a larger bandpass and lower resolution. Fourth, the user can choose one of several combinations of focal length and grating density to achieve a particular coverage and resolution.

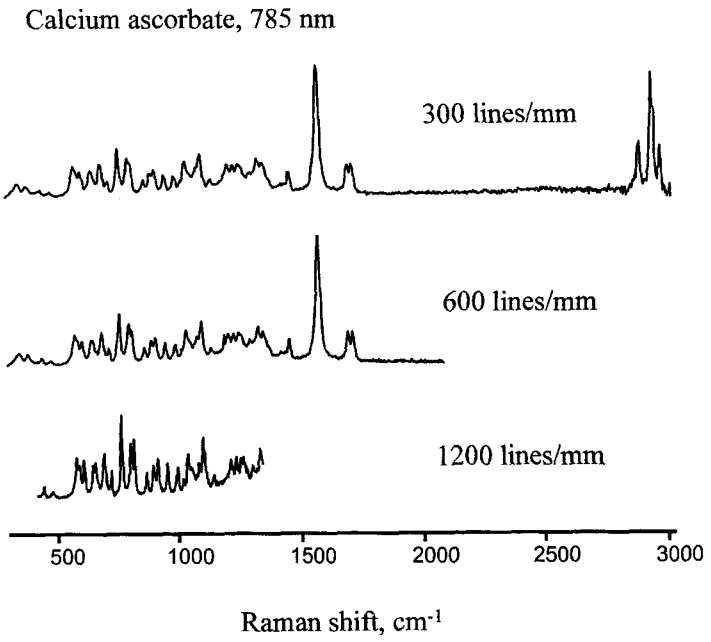

Figure 8.7. Spectra of calcium ascorbate acquired with a Chromex 2000 spectrometer, 25 mm detector, and three different gratings. Each spectrum is a single CCD exposure using the indicated gratings. Intensity scales differ in the three cases.

Either the user or the manufacturer must choose these parameters according to other requirements such as detector size, $f/\#$, physical size, and so forth. It is common practice to splice several spectral segments to cover a wider spectral range, as will be discussed in Section 8.6.

8.2.1.2 Transmission and Collection

The transmission of a single spectrograph is the simple product of the efficiencies of each optical component, including mirrors, lenses, the grating, and any filters. For the spectrograph of Figure 8.3, the overall transmission is the product of the reflectivities of both mirrors and the grating. These values depend on wavelength, coating materials, and grating design, and there is no ideal combination that maintains high transmission over a wide spectral range. Components are generally selected by the spectrograph designer to maximize transmission over a particular wavelength range. For example, aluminum-coated mirrors have high reflectivity through the visible region,

but gold-coated mirrors have higher reflectivity above 600 nm and into the infrared.

Diffraction grating efficiency is strongly dependent on both wavelength and polarization. Examples of grating efficiency curves are shown in Figure 8.8. Grating designers specify an optimum wavelength (often called "blaze" wavelength) at which the grating diffracts the maximum fraction of incident light in first order. Efficiency decreases away from this maximum, usually more slowly on the side of the curve corresponding to longer wavelengths. Figure 8.8 also illustrates the effect of polarization of the incident light relative to the grating surface, due in part to differences in reflectivity. Since Raman bands differ in their degree of polarization, discrimination of the spectrograph against one polarization will lead to errors in relative band intensities. For this reason, a polarization scrambler is often inserted between the sample and the spectrograph to randomize the polarization striking the grating. A scrambler is critical for accurate determination of polarization ratios, since they rely on relative peak intensities.

The overall transmission, T_S (λ), of a single spectrograph of the type depicted in Figure 8.3 is given by:

$$T_S(\lambda) = T_P R_C E_G R_F \tag{8.11}$$

where T_P is the scrambler transmission, R_C and R_F are collimating and focusing mirror reflectivities, and E_G is the grating efficiency for randomly

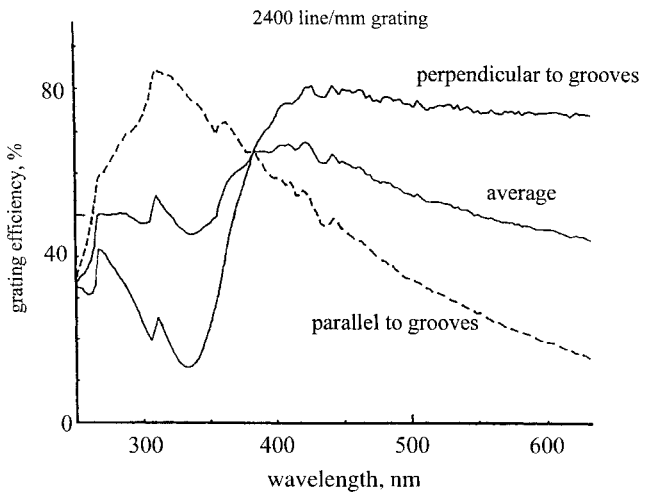

Figure 8.8. Typical grating efficiency (fraction of incident light diffracted into first order) for different incident polarizations. Each grating design has a different set of curves.

polarized input light. All of the factors in (8.11) are wavelength dependent, resulting in a T_S (λ) that varies across the Raman spectrum. This variation contributes to the overall instrument response function, which ultimately determines the collection efficiency, C, in Eq. (3.1). T_S is typically in the range of 0.10 to 0.50 for single grating spectrographs. The dependence of T_S on wavelength and its effects on the system response may be calibrated using the methods described in Chapter 10.

The $f/\#$ of the spectrograph determines its light collection ability and therefore the magnitude of the Raman signal. According to Eq. (3.4), the solid angle of light collected by the spectrograph depends on $(f/\#)^{-2}$, so lowering the $f/\#$ significantly increases collection. The Ω_D discussed in Chapter 3 refers to overall light collection at the sample, to which the spectrograph Ω contributes. Assuming Ω_D is not limited by a component other than the spectrograph, a lower $f/\#$ spectrograph will increase sensitivity. All else being equal, signal strength increases with $(f/\#)^{-2}$, so a decrease from $f/8$ to $f/4$ results in 4 times the signal magnitude. This simple relation assumes that the collection optics are not limiting Ω_D and are therefore $f/4$ or lower.

While it may appear that lower $f/\#$ is always better, there are some substantial constraints (3). Since $f/\#$ is the ratio of focal length to aperture diameter, lower $f/\#$ requires shorter focal length or larger optics. Both of these measures increase aberrations and stray light, and a shorter focal length requires higher grating density to achieve the same dispersion. It is a challenge to the spectrograph designer to maintain dispersion and image quality over the relatively large flat field of a modern CCD, and the problem is escalated when the $f/\#$ is reduced. At least with current dispersive technology, the goal is to reduce the $f/\#$ as much as possible while retaining dispersion and flat field performance.

An additional factor driving the reduction in $f/\#$ is the transition from photomultiplier tubes (PMTs) to CCDs as detectors (4,5). Recall that the Raman signal is ultimately determined by the minimum $A_D\Omega$ product of the entire system (Section 3.2). PMTs have relatively large photoresponsive areas (e.g., 3 × 10 mm), while a CCD pixel is much smaller (25 μm × several millimeters when binned). The reduction in A with a CCD requires a larger Ω (and smaller $f/\#$) to maintain the $A_D\Omega_D$ product. The multichannel advantage and high quantum efficiency of the CCD more than justify this requirement, but it does provide additional incentive to design smaller, lower $f/\#$ spectrographs. Table 8.3 lists several single spectrographs in common use for Raman spectroscopy.

8.2.1.3 Stray Light

As illustrated in Figure 8.4, stray light can interfere with Raman scattering unless it is adequately rejected by the spectrograph. Rayleigh scattering is

Table 8.3. Examples of Single Spectrographs for Raman Spectroscopy

Configuration	Focal Length (mm)	$f/\#$	Ω^a, (sr)	Number of Interchangeable Gratings[b]
Czerny-Turner[c]	640	5.5	0.026	1
Czerny-Turner[d]	500	4.0–6.9	0.049–0.016	2
Modified Czerny-Turner (imaging)[e]	250	4.0	0.049	3
Modified Czerny-Turner (imaging)[f]	190	3.9	0.052	3
Holographic (imaging)[g]	85	1.5–1.8	0.35–0.24	1

[a]From Eq. (3.4), using manufacturer's stated $f/\#$.
[b]Without disassembly or realignment.
[c]Instruments SA HR 640.
[d]ISA 500 M.
[e]Chromex 250 IS (input focal length is 250 mm, output is 330 mm).
[f]ISA Triax 190.
[g]Kaiser Holospec $f/1.8$.

often 10^4 to 10^6 times stronger than Raman scattering, so a stray light specification of 10^{-5} or less is required to avoid overwhelming the Raman signal with elastic scattering. Many single spectrographs have stray light in the region of 10^{-5}, so they can sometimes be used without additional filtering for relatively strong scatterers that are transparent (e.g., neat solvents). For the great majority of samples, however, a single spectrograph by itself has too much stray light. Elastic scattering from solid samples, optics, dust, and the like, can easily exceed Rayleigh scattering by orders of magnitude, totally obscuring the Raman signal. For virtually all Raman instruments based on single spectrographs, a laser rejection filter is included to provide an additional factor of 10^4 to 10^6 in stray light reduction. These filters are described in Section 8.2.5.

In the spectrograph itself, stray light has several sources, including optical imperfections, dust, and reflections from interior components. Stray light is generally more severe for short focal lengths and small $f/\#$, since random scattering and reflections can more efficiently reach the detector. As spectrograph $f/\#$'s are reduced to improve the $A\Omega$ product, stray light becomes an increasing concern. Fortunately, advances in laser rejection filters have enabled the use of relatively high stray light spectrographs since the strong laser light is greatly attenuated before entering the spectrograph.

8.2.1.4 Holographic Grating Spectrographs

The technology associated with holographic optical elements (HOEs) existed for some time before applications to spectroscopy but were applied to Raman

spectroscopy starting in the early 1990s. HOEs consist of layers of photoactive emulsion between glass or quartz plates, which are exposed to interference patterns that generate a holographic image in the emulsion. The image consists of variations in refractive index that can be patterned to form a diffraction grating, a wavelength-selective reflector, or a variety of other optical elements (6). A holographic grating produced by this procedure differs fundamentally from a conventional grating in that it is used in transmission rather than reflection mode. An HOE grating should not be confused with a "holographically ruled grating," which is a reflection grating whose "rulings" are produced holographically. Figure 8.9 shows a spectrograph suitable for Raman spectroscopy produced with HOE components. The light is dispersed by the HOE grating while undergoing a 90° (average) turn. The dispersion is equivalent to that of a 2400-line/mm grating, but operating in transmission rather than reflection mode. Note that the achromatic lenses replace the mirrors of the reflection design.

The HOE design of Figure 8.8 has several advantages over the conventional Czerny-Turner configuration of Figure 8.3. First, the optical axis is normal to the lenses (so-called on-axis design), significantly reducing optical aberrations and maintaining image quality. Second, the transmission design improves grating efficiency, leading to high spectrograph transmission. Third, the axis design and high dispersion permit a very low $f/\#$, in the range of 1.5 to 1.8. Fourth, low aberrations result in a relatively large flat field and good compatibility with CCD detectors.

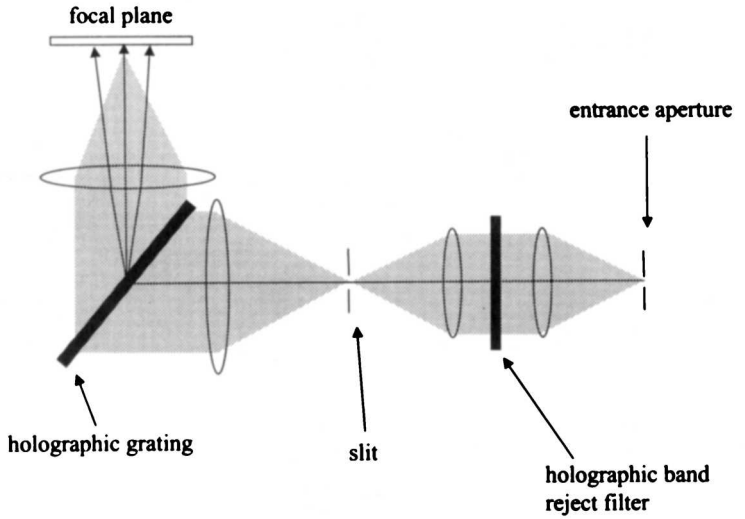

Figure 8.9. Schematic of axial transmission holographic spectrograph, such as the Kaiser 1.8i.

Disadvantages of the HOE spectrometer deal mainly with flexibility. The grating is fixed, so the spectral range can be changed only by exchanging the grating. The spectrograph is generally configured during installation for a particular laser wavelength and spectral range. The peak efficiency of the grating is higher than a reflection grating but falls off faster away from the optimum wavelength. In addition, existing HOE emulsions do not permit operation in the ultraviolet region of the spectrum. The low $f/\#$ and high imaging quality of the holographic spectrometer are very attractive for Raman spectroscopy, particularly for a fixed laser wavelength. Additional discussion of HOE filters appears in Section 8.2.5.2.

8.2.2. Double Monochromators

Many Raman spectrometers used in the pre-multichannel era were double monochromators such as that diagramed in Figure 8.10. By combining two single-grating monochromators in series, with a common "intermediate" slit, the light is dispersed twice and the bandpass can be quite narrow. More importantly, the stray light becomes the product of the stray light levels for the single stages, leading to excellent rejection of elastic scattering. A double monochromator of the configuration shown in Figure 8.10 has stray light in the region

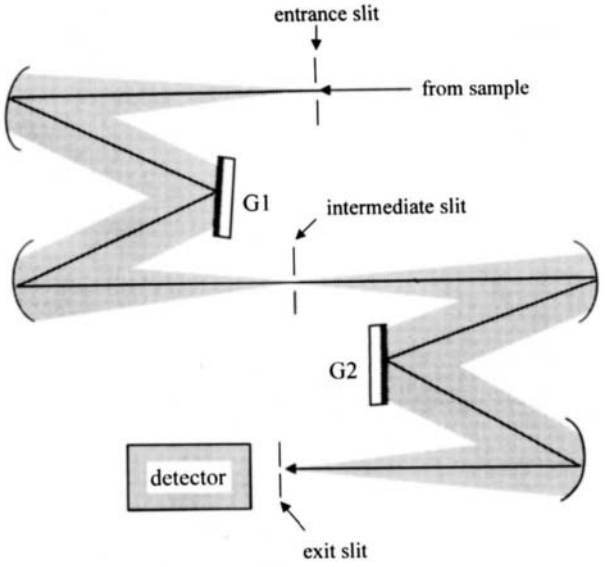

Figure 8.10. Schematic of a double monochromator, such as the Spex 1403.

of 10^{-10} to 10^{-12}, permitting observation of highly scattering samples such as white powders, at low Raman shift values if desired. For a conventional double monochromator used for Raman, the two gratings are positioned for "additive dispersion," and the gratings are mechanically locked together so the two stages transmit the same wavelength. A double monochromator used widely for Raman in the 1970s (Spex model 1403) has an 850 mm focal length, a dispersion of 10 cm^{-1}/mm, and stray light below 10^{-10}.

The high dispersion and low stray light of double monochromators are attractive for single channel systems with a relatively large detector area, such as a PMT. The two gratings are typically scanned synchronously and each Raman shift increment is collected in series. High dispersion provides a sensitivity advantage in this case because a wider slit permits higher A_D and $A_D\Omega$ product. It is common to magnify the sample region when matching collection optics to the double monochromator in order to exploit the relatively large detector area. This approach also permits arbitrarily wide spectral coverage, although the acquisition time increases linearly with spectral range and inversely with bandpass. Acquisition times are typically much longer than those for multichannel systems, often by factors of 100 to 1000. A high-resolution spectrum obtained with a scanning double monochromator is shown in Figure 8.11.

Since multichannel detectors have relatively small pixels (otherwise a 1000-channel detector would be prohibitively large), the high dispersion of an additive double monochromator is unnecessary or even undesirable. A dispersion of 10 cm^{-1}/mm and a 25 mm detector would cover only 250 cm^{-1} at a time, requiring many detector exposures to assemble a 3000 cm^{-1}-wide

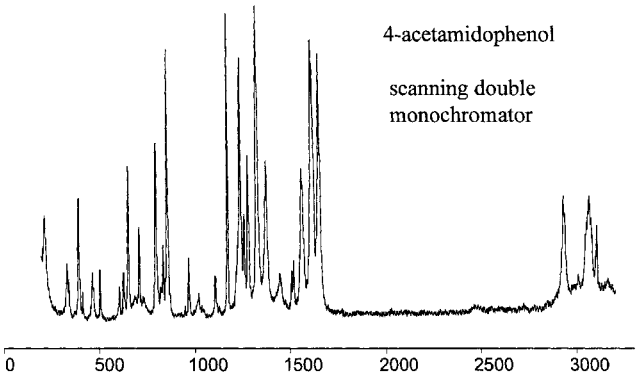

Figure 8.11. Spectrum of acetamidophenol obtained by scanning a double monochromator onto a photon counting PMT: 514.5 nm, total acquisition time about 40 min.

spectrum (see Section 8.6). The low stray light of a double monochromator remains attractive, but there are better alternatives for use with multichannel detectors.

8.2.3. Triple Spectrographs

As discussed in Section 8.2.1, single spectrographs meet most of the requirements of Raman spectroscopy and have particular advantages in high transmission and compact size. However, their insufficient stray light requires the addition of a laser rejection filter (Section 8.2.5), which is constructed to reject a single, narrow range of laser wavelengths. A different excitation wavelength requires a different rejection filter, and a tunable laser source would require an impractically large array of filters. The double monochromator has low stray light without filters and can be used with a wide range of excitation wavelengths but is not generally useful with multichannel detectors. So, how can one achieve multichannel operation with low stray light while also permitting many excitation wavelengths?

The triple spectrographs achieve these objectives, albeit with a cost in transmission and complexity. Triple spectrographs are often specified for applications involving varying excitation wavelengths, but also when the observation of low Raman shifts (<100 cm^{-1}) is important. A triple spectrograph is shown schematically in Figure 8.12. It has three gratings and up to four slits but can be viewed as a single spectrograph (stage C) preceded by a specialized premonochromator (stages A and B). In effect, stages A and B act as a tunable bandpass filter preceding an otherwise conventional single spectrograph. This combination achieves very low stray light ($<10^{-12}$) and may be tuned over a wide range of wavelengths.

Stages A and B comprise a tunable filter that is generally configured as a subtractive dispersion double monochromator. Stage A disperses the light onto an intermediate "slit" that blocks all but a certain wavelength range. Stage B is configured to recombine this range of wavelengths and focus them on the spectrograph entrance slit. The term "subtractive dispersion" stems from the opposing dispersion directions of stages A and B. Although no net dispersion results after stage B, the device discriminates strongly against light that is outside the passband resulting from the intermediate slit. Figure 8.13 illustrates triple spectrograph operation in simplified form. Slit 1 is the entrance slit for stage A, onto which the scattered light is imaged for wavelength analysis. Stage A disperses the light onto an intermediate slit S2, which is usually wide enough to transmit the entire wavelength range of interest. This range does not include the laser wavelength, however, so much of the elastic scatter is blocked at S2. Stage B recombines the light transmitted by S2 (so-called "subtractive dispersion") to focus to a point at S3. Stage C then disperses this filtered

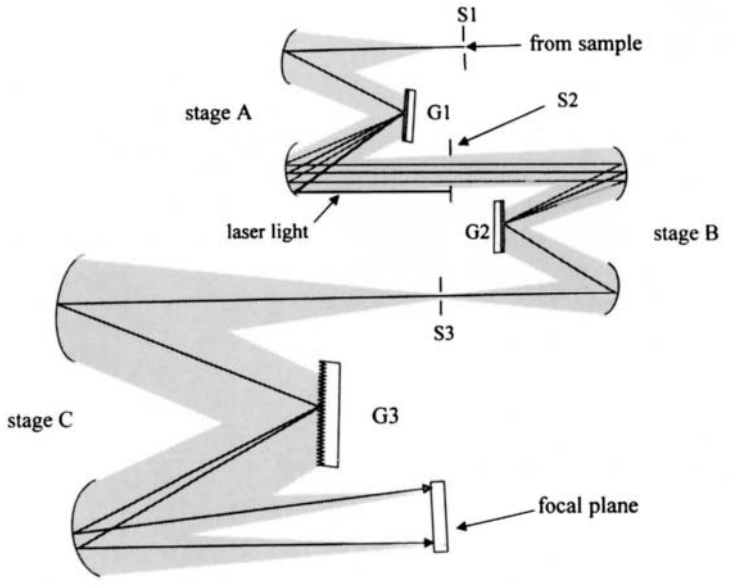

Figure 8.12. Schematic of a triple spectrograph, consisting of a subtractive dispersion double monochromator preceding a single spectrograph. Similar to Spex "Triplemate" or Dilor "X-Y."

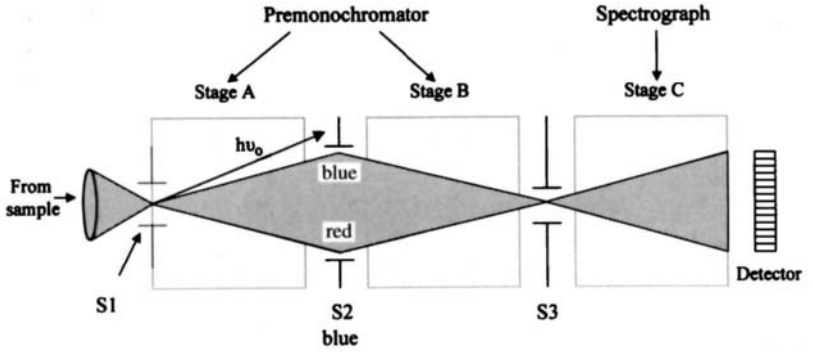

Figure 8.13. Simplified diagram illustrating operation of a triple spectrograph. The light dispersed in stage A is recombined after passing through S2, but the laser light is blocked. The shaded region within each stage represents light dispersed (or recombined) by each grating.

light onto the detector, just like the single spectrograph described earlier. S1 and S3 are usually the same width, and S2 is generally set to transmit a range of wavelengths equal to that dispersed on the detector. Stages A and B are mechanically synchronized, but the center of the passband may be adjusted by rotating the gratings. The passband position may usually be

varied independently of stage C, but obviously the passband and spectrograph coverage must overlap.

As noted earlier, the outstanding stray light rejection and tunability of a triple spectrograph come at the cost of transmission. A triple has three gratings and seven to nine mirrors, each with a reflection loss and efficiency curve. Assuming 50 per cent grating efficiency and 95 per cent mirror reflectivity, the transmission of a triple spectrograph is approximately 5 to 9 per cent. Compared to 30 to 50 percent for single spectrographs, this decrease in transmission is significant. Even with its low transmission, however, a triple may be essential for observing low Raman shifts. The laser rejection filters required to use a single spectrograph rarely work effectively at Raman shifts below 50 to 100 cm^{-1} (Section 8.2.5), while triple spectrographs can maintain excellent stray light rejection down to <10 cm^{-1}. When such low Raman shifts are of interest, or when excitation wavelength tunability is important, a triple spectrograph may be the only acceptable option for use with multichannel detectors.

8.2.4. Performance Comparisons

It should be clear by now that a user or designer must choose from a wide array of possibilities when configuring a dispersive spectrograph. Choices of grating density, focal length, $f/\#$, and the like affect resolution, Ω, and T differently, and often one must compromise performance in one area for that in another. At least with current technology, no one spectrograph has superior simultaneous performance in transmission, stray light, collection, and dispersion, so a spectrograph choice is usually dictated by which features are important to a particular mix of applications.

It is instructive to consider several examples of spectrograph configurations to illustrate the strengths and weaknesses of various common designs. The instruments listed in Table 8.4 are generic but are similar to commercially available systems. Generally speaking, better stray light rejection leads to lower transmission and collection (Ω). Maximum flexibility requires compromises in throughput and Ω. As a broad generalization, single spectrographs with band rejections filters provide excellent sensitivity but limited flexibility in that they are less tunable (due to the filters) and have difficulty at very low Raman shifts. On the other hand, triple spectrographs are tunable and operate well down to Raman shifts of less than 10 cm^{-1}, but are less sensitive and more complex. Figure 8.14 illustrates the excellent performance of a triple spectrograph for low Raman shifts, but the signal at 200 and 400 cm^{-1} is substantially weaker than that from a single spectrograph under similar conditions.

Table 8.4. Performance Comparisons of Generic Dispersive Spectrographs

Configuration	$f/\#$	Focal length (mm)	T	Ω (sr)	Stray Light	Comments
Single, Czerny-Turner	4	250	0.4	0.049	$\sim 10^{-5}$	Efficient, limited tunability, limited performance at Raman shift <200 cm^{-1}.
Single + OD6 BR filter	4	250	0.3	0.049	$\sim 10^{-11}$	
Holographic + OD6 BR filter	1.8	85	0.5	0.24	$\sim 10^{-11}$	
Double	8	850	0.1	0.012	$<10^{-10}$	Limited flat field, tunable over wide range, good for low Raman shifts.
Triple	6	600	<0.1	0.022	$<10^{-12}$	Tunable over wide range, good for low Raman shifts.

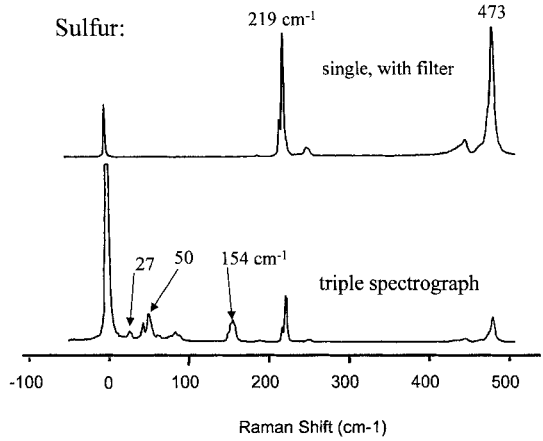

Figure 8.14. Spectrum of solid sulfur obtained with a single spectrograph and holographic laser rejection filter (upper) or a triple spectrograph (lower).

8.2.5. Laser Rejection Filters

As noted in Section 8.2.4, and Table 8.4, single spectrographs are efficient in terms of collection and transmission but rely on a laser rejection filter to decrease stray light from about 10^{-5} to 10^{-10} or less. In the vast majority

of real samples, laser rejection filters permit single grating spectrographs to yield acceptable stray light performance while retaining their high efficiency. One could argue that rejection filters were critical to enabling the major gains in sensitivity that resulted in "modern" Raman spectroscopy. For dispersive spectrometers, the three most common types are dielectric, holographic, and absorption filters.

8.2.5.1 Dielectric Notch and Edge Filters

The multilayer dielectric technology used for laser bandpass filters (Section 7.6.1) can also be used to construct rejection filters for use in Raman spectroscopy (7,8). By varying the thickness, order, and refractive index of dielectric coatings on a flat, transparent substrate, the manufacturer may produce a variety of optical transmission functions. For example, a *notch filter* has a relatively narrow (5 to 10 nm) spectral region with a high optical density, centered on the laser wavelength. This notch rejects (usually by reflection) a high fraction of the elastic laser scatter but transmits wavelengths a few nanometers different from the laser wavelength. The observed transmission of a dielectric notch filter is shown in Figure 8.15, for a filter intended for use with a 514.5 nm laser. The transmission at 514.5 is low by design and is usually expressed as optical density (OD), defined as the negative logarithm of the transmission. Commercial notch filters vary from OD 3 (0.1 per cent transmission) to OD 6, and there is usually a trade-off of OD with maximum off-laser transmission. The sharpness of the rise from high optical density to high transmission is important, since it determines the ability to observe low (<200 cm^{-1}) Raman shift. For example, a Raman feature located 200 cm^{-1} on the Stokes side of 514.5 nm appears at 519.8 nm. In order to observe Raman scattering at 200 cm^{-1}, the notch filter transmission must rise from $<10^{-5}$ to $>10^{-1}$ when the wavelength changes by only 5 nm. This rather stiff requirement generally limits low Raman shift performance for dielectric filters to approximately 100 cm^{-1}.

Figure 8.15 also shows that the transmission at wavelengths above the filter cut-on is not 100 per cent and usually exhibits oscillations from interference effects. Maximum transmission is usually above 50 per cent and the oscillations may be minimized with careful design. It is not uncommon to observe filter oscillations appearing as apparent background variation in the final spectrum, but such artifacts may be removed with the response calibrations discussed in Chapter 10.

Dielectric filters may also be designed as *edge filters* having a high optical density at the laser wavelength, then a relatively wide passband at longer wavelengths. These are really bandpass filters designed to cut-on rapidly at wavelengths longer than the laser. As an extreme example, it is possible to use

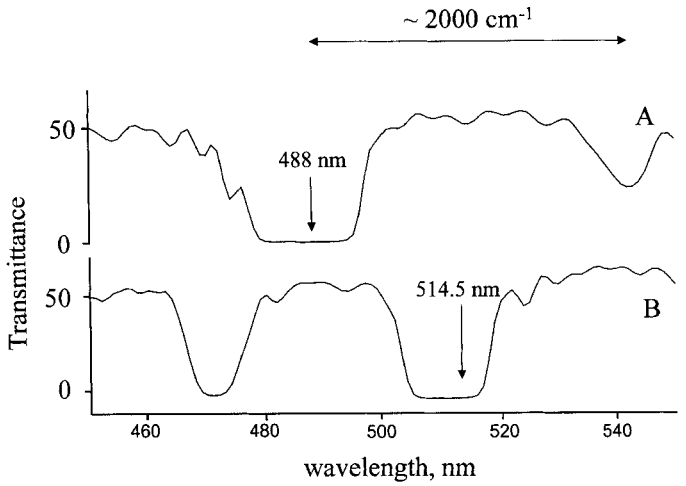

Figure 8.15. Transmission of dielectric notch filter fabricated for rejection of 488 nm (upper curve) or 514.5 nm (lower) light.

a narrow bandpass filter to reject all wavelengths except a particular Raman feature. The detector would then "see" only light scattered over some narrow frequency range, say 900 to 1100 cm^{-1}. This approach is used in a commercial Raman microscopy instrument but will be discussed in more detail in Chapter 11.

8.2.5.2 Holographic Notch Filters

The holographic technology discussed in sections on laser bandpass filters (7.6.2) and holographic gratings (8.2.1.4) was first applied to Raman spectroscopy to build laser rejection filters (9–12). Holographic notch filters are similar in qualitative behavior to dielectric notch filters but generally have superior performance in optical density, high off-laser transmission, and low Raman shift performance. Holographic notch filters may be purchased with several levels of optical density and rejection bandwidth. For example, the transmission curves for holographic filters with different cut-on slopes are shown in Figure 8.16. The sharper cut-on permits lower Raman shifts to be observed but also makes the filter more sensitive to the incidence angle of the light. Figure 8.17 shows a plot of optical density at the laser line as a function of filter angle relative to the optical axes. The maximum OD is relatively forgiving of incident angle over the range of about $\pm 10°$, then falls off rapidly. However, the cut-on wavelength does depend on angle as shown in Figure 8.18. As the angle is increased, the laser is blocked less effectively,

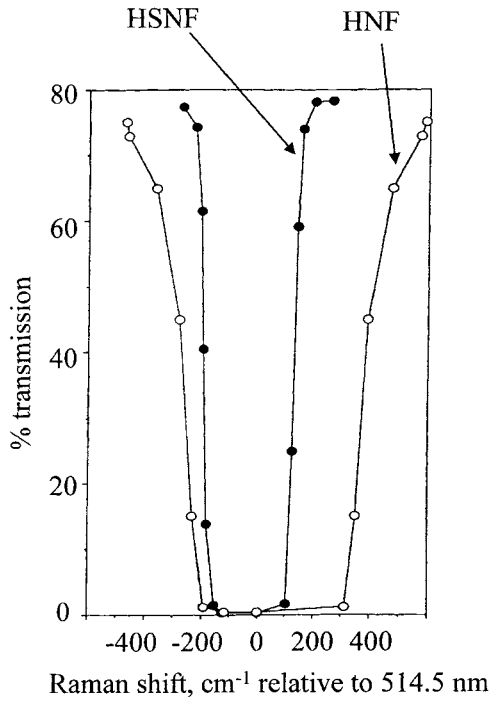

Figure 8.16. Transmission curves for holographic notch filter (HNF) and holographic super notch filter (HSNF) for a 514.5 nm laser. (Adapted from Reference 11, with permission.)

but the lowest observable Raman shift also decreases. Although there is a trade-off of maximum laser rejection and minimum observable Raman shift, it is often possible to observe quite low Raman shifts with holographic filters. Figure 8.19 is the low-frequency region of naphthalene recorded with an angle-tuned holographic filter, demonstrating a Raman shift of 46 cm^{-1}. In terms of wavelength, 46 cm^{-1} is only 1.2 nm above the 514.5 nm exciting line.

As was the case for dielectric filters, the performance parameters of interest for holographic rejection filters are maximum OD at the laser wavelength, minimum observable Raman shift, transmission at unrejected wavelengths, and the smoothness of the transmission curve above the cut-on wavelength. Although holographic filters are wavelength tunable over a limited range, it is nearly always necessary to purchase a different filter when the laser line is changed. Continuous laser tunability requires the use of a double or triple spectrometer, with accompanying complexity and reduction of transmission. Due to their attractive properties, holographic notch filters currently dominate Raman applications involving a single spectrograph.

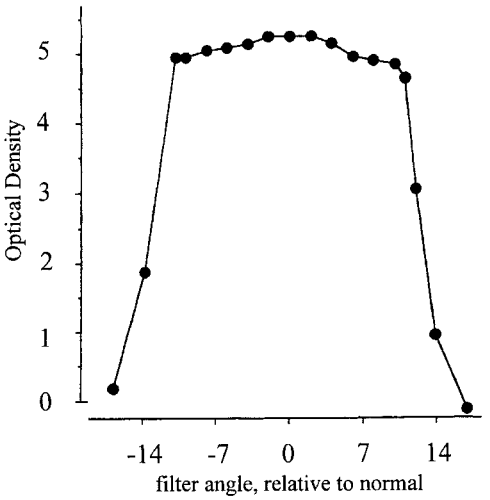

Figure 8.17. Optical density at 514.5 nm of HNF filter designed for a 514.5 nm laser, as a function of the angle of the filter. (Adapted from Reference 11, with permission.)

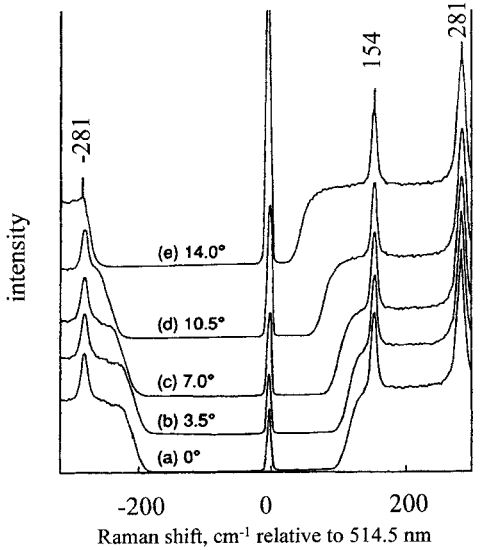

Figure 8.18. Effect of HNF angle on Raman spectrum of calcite. Increasing the angle shifts the rejection band to lower Raman shift but also decreases the optical density at the laser wavelength. (Adapted from Reference 11, with permission.)

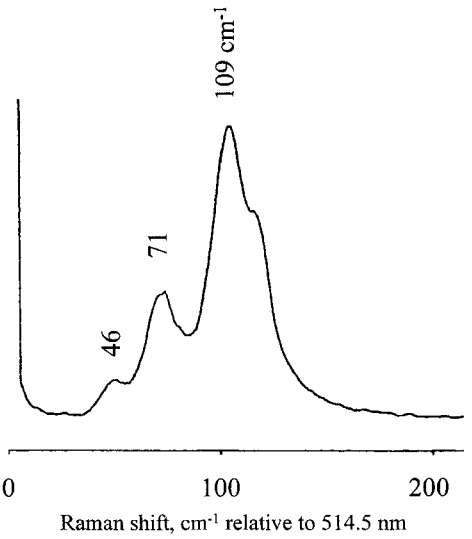

Figure 8.19. Low Raman shift bands of naphthalene, obtained by angle tuning a HSNF filter. (Adapted from Reference 11, with permission.)

8.2.5.3 Absorption Filters

The classical "color filters" in their "long-pass" configuration can be used to block the laser and transmit Raman scattering, but their cut-on curves are generally too gradual, and much of the Raman spectrum below ca. 1000 cm^{-1} is lost. However, if an absorption feature can be made sharp enough to avoid this problem, significant advantages result. An absorption filter is not angle sensitive, so it may be positioned in the uncollimated region of the optical system. The absorber thickness may be increased to achieve very high optical density at the laser wavelength if necessary. Since light absorption is usually an inherent property of the filter material, one cannot choose from a wide range of rejection wavelengths as is the case for dielectric and holographic filters.

Organic liquids and solutions have been reported as laser absorption filters for ultraviolet (UV) Raman in the 280 to 360 nm region (13,14). Figure 8.20 shows absorption spectra for several organic solutions, which permit long-pass operation between 290 and 350 nm. Figure 8.21 is a spectrum of CCl_4 obtained with a 299 nm laser, with and without an absorption filter (14). In this case, a Raman shift of 218 cm^{-1} was observable, and transmission above 800 cm^{-1} exceeded 30 per cent. Since the Raman spectral range is quite narrow in terms of nanometers in the UV, a 200 cm^{-1} shift corresponds to only a 1.8 nm displacement from 299 nm.

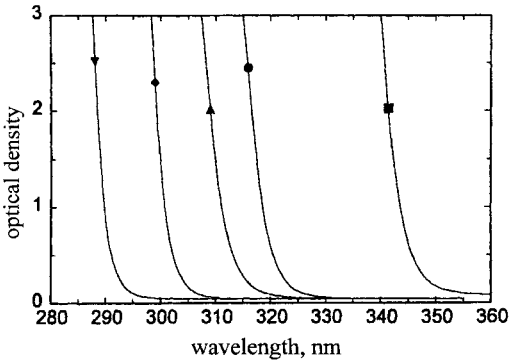

Figure 8.20. Optical density curves for various mixtures of organic liquids. From left to right: 1,2-dichlorobenzene/heptane; 1,2,4-trichlorobenzene/heptane; potassium hydrogen phthalate in water; hydroquinone/ethanol, and 2-naphthol/hexanol. (Adapted from Reference 14 with permission.)

Gas-phase absorbers such as iodine and mercury have very narrow absorption features that may be used to block scattered laser light if their absorptions coincide with the laser wavelength (15–17). For example, mercury vapor in a buffer gas at 760 torr, and room temperature has an absorption at 253.7 nm with a bandwidth of about 1 cm^{-1} (16). A 1 to 5 cm path length gas cell preceding the spectrograph provides strong attenuation at 253.7 nm, with an optical density above 5. Similarly, iodine vapor absorbs 514.5 nm (15) and Rb vapor absorbs 794.8 nm (17). Gaseous absorption filters have been demonstrated as effective laser rejection filters, and in one case it was possible to obtain a Raman spectrum using a very weak Hg pen lamp as a source (16). For the I_2 filter, features within a few reciprocal centimeters of the exciting line were observable, with minimal laser interference. A problem with gaseous absorption filters is they can be "too narrow." The laser source has weak emission off-resonance due to pressure broadening of plasma emission that passes through the laser's bandpass filter. These weak "wings" may lie outside the narrow absorption band of the rejection filter. In effect, the maximum attenuation of laser light by the rejection filter is determined by these linewidth effects rather than the peak absorbance (16).

In summary, vapor-phase absorption filters can be very effective when they coincide with an available laser wavelength but are very restricted in tunability. They can be useful for special cases, such as a need to observe scattering at very low Raman shift.

A third type of absorption filter useful for laser rejection is based on a semiconductor with a band gap slightly lower in energy than the laser photons (18). Scattered laser photons are strongly absorbed by the semiconductor, while

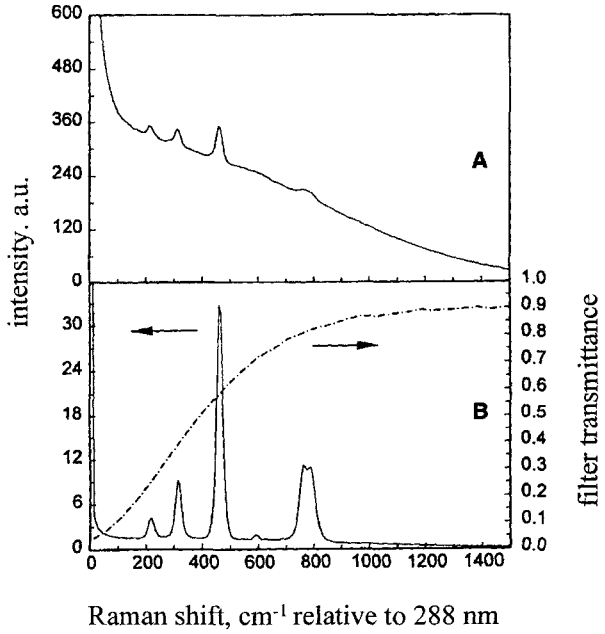

Figure 8.21. Performance of organic liquid filter for the Raman scattering of 288 nm light by CCl_4. (A) No filter. (B) With 10 per cent (v/v) 1,2,3-trichlorobenzene/heptane filter between sample and entrance slit. (Adapted from Reference 14 with permission.)

those at slightly longer wavelengths are transmitted. For example, cadmium telluride has a band gap of 1.4 eV, or 868 nm in terms of wavelength. CdTe transmits (>50 per cent) photons with wavelengths longer than 868 nm, while it strongly absorbs shorter wavelengths. Detailed absorption measurements are not readily available, but a 2 mm-thick crystal of CdTe has an OD above 4 for $\lambda < 840$ nm. Very high optical densities are achievable, since the CdTe thickness may be increased. Figure 8.22 shows CCl_4 and naphthalene spectra obtained with 841.3 nm excitation and a CdTe rejection filter. Note that Raman shifts as low as 74 cm^{-1} were observable (19). Cadmium sulfide has been used to attenuate 514.5 nm light (20) although its band gap is smaller than optimum, and Raman shifts below about 500 cm^{-1} are attenuated.

Semiconductor absorption filters are solid state, convenient, and have high optical densities but do require a match of material and laser wavelength. They can be quite useful with tunable lasers, as the laser wavelength may be adjusted to just above the band gap (19). The limited choice of suitable semiconductor materials currently restricts their use to a few laser wavelengths.

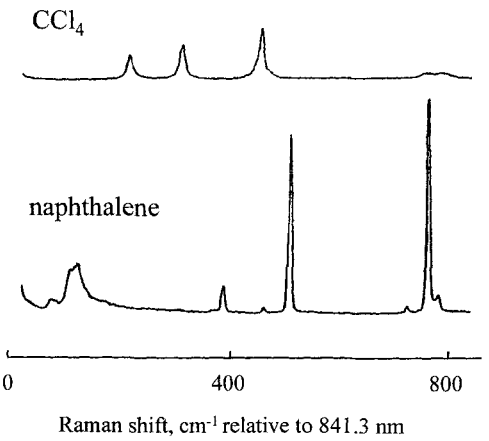

Figure 8.22. Spectra of CCl_4 and naphthalene obtained with a CdTe semiconductor filter and a Ti-sapphire laser tuned to 841.3 nm. (Adapted from Reference 19 with permission.)

8.3. DETECTOR CONSIDERATIONS

With the generally very small signals from Raman scattering, a sensitive and low-noise detector is of obvious importance. Not only is it important to have a high quantum efficiency (photoelectrons generated per Raman photon), but the dark signal must be minimized so the Raman features are not buried in dark noise. The requirement for low dark signal (and accompanying noise) leads to some constraints on detectors that are fundamental in origin. As the laser and Raman-shifted wavelengths extend deeper into the red (in order to reduce fluorescence), the energy of the photons decreases. A detector that is sensitive to those low-energy photons is also prone to thermally generated dark signal. The small energy required for "detection" means that random thermal fluctuations in the detector are sufficient to generate a "photoelectron." Generally speaking, the longer the wavelength to be detected, the colder the operating temperature of the detector, and the higher its dark signal.

Another fundamental detector issue that has been mentioned in several contexts previously is the number of simultaneous acquisition channels. We noted in Chapter 4 that the multichannel advantage can greatly increase signal/noise ratio (SNR) for a given acquisition time or greatly reduce acquisition time to achieve a given SNR (Section 4.3.1). However, as the number of channels increases, the size of each detector element must decrease to avoid a detector of unreasonable size. Even if a large multichannel detector could be made, the flat field of most dispersive spectrographs would limit the useful area.

It should also be noted at this point that a multichannel detector can have multiple detector elements along two axes, one parallel to the direction of wavelength dispersion, and one perpendicular. The latter is parallel to the entrance slit in most dispersive instruments. For example, a CCD may have 1024 pixels along the wavelength axis and 256 along the vertical axis, for a total of 262,144 independent elements. This second dimension of the detector may be used in a variety of applications involving Raman imaging, multiple detection tracks, or echelle spectrometers.

The list below defines most of the detector properties important to Raman applications, particularly for dispersive spectrometers. Specifications of particular devices will be discussed in subsequent sections. More specific definitions are provided for CCD detectors in Section 8.5.2.

1. *Quantum Efficiency, Q.* Probability that a photon striking the detector generates an electronically measurable signal, usually a photoelectron. Units are photoelectrons/photon, often stated as a percentage.
2. *Response Curve or Quantum Efficiency Curve.* Variation of Q with wavelength, or, alternatively, with Raman shift.
3. *Photosensitive Area.* Active area of photodetector, usually in centimeters squared. In cases where the detector area limits light collection, this area will determine the A_D defined in Section 3.2.
4. *Number of Channels, N_C.* For CCD systems, N_C is usually the number of pixels (short for "picture elements") along the wavelength axis. N_C is not necessarily equal to the number of resolution elements (N_R) discussed in Chapters 3 and 4.
5. *Dark Signal.* The average generation rate of electrons when the detector is not exposed to light, equal to ϕ_d as defined in Section 4.2. Usually in electrons/second but can also refer to total electrons collected over a given integration time.
6. *Dark Noise.* Not the same as dark signal but is defined rigorously as the standard deviation of the signal obtained with the laser off.
7. *Readout Noise.* As defined in Section 4.2.5, readout noise is the standard deviation of sequential measurements of a constant number of electrons. Readout noise is generally determined by successive readouts of a dark detector with very short integration time.

8.4. SINGLE-CHANNEL DETECTORS

8.4.1. Photomultiplier Tubes (PMTs)

Given the weakness of Raman scattering, a significant advance in technology occurred with the introduction of photon counting detection in the 1960s.

Photon counting PMTs dominated Raman spectroscopy detection until about 1985, but their use decreased sharply after the introduction of CCDs. A brief review of PMTs is provided here, partly as background for their modern single-channel analog, the avalanche photodiode.

Photon counting PMTs are constructed to have high enough sensitivity to detect single photons but also low enough dark noise to avoid overwhelming the signal of interest. The photon strikes a photocathode, which is a metal surface with a low work function for photoelectron generation. Assuming the energy of the photon exceeds this work function, a photoelectron is ejected from the metal surface with a probability equal to Q. The ejected electron is then accelerated and amplified as in a conventional PMT, until a pulse of several thousand electrons strikes the anode (Fig. 8.23). This pulse is then detected by a pulse height discriminator, set to recognize pulses with a height expected for an amplified photoelectron. This discriminator allows rejection of spurious electrons or other electronic noise (22).

The rate of detected pulses equals the rate of photons striking the photocathode times Q. In other words, Q is the fraction of photons that ejects photoelectrons and results in an output pulse. The dark signal results from thermal ejection of electrons from the photocathode. Since Raman spectrometers often operate in the red and near infrared wavelength regions, the work function of the photocathode surface must be quite low. This small work function makes it difficult to prevent dark electron generation. Photon counting

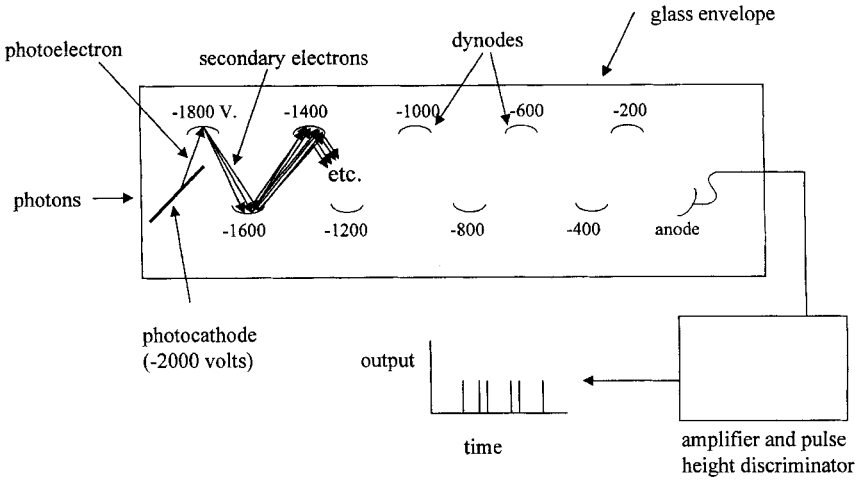

Figure 8.23. Schematic of photon counting photomultiplier tube with detection electronics. A high-voltage power supply holds the photocathode potential at about −2000 V, and the decreasing dynode voltages are provided by a resistor ladder.

PMTs are usually cooled to approximately −20°C, and the high quality of the photocathode adds significantly to the cost. Low dark signal PMTs are often selected from a given batch for use in Raman spectrometers. The PMTs used in the scanning Raman spectrometers of the mid-1980s had dark signals of less than 10 e^-/sec, and a tube with a level of 1 e^-/sec was truly exceptional. A practical problem with such sensitive PMTs is their susceptibility to damage by high light levels. Exposure to scattered laser light or room lights with the PMT active can permanently damage a detector costing several thousand dollars.

An often unappreciated advantage of a PMT is its large photosensitive area, about 2 × 8 mm. With a proper optical design, this large area can translate into a high A_D at the sample or an overall high $A_D\Omega$ (14). Although the smaller area of a CCD pixel is more than compensated by the multichannel advantage, this area difference does decrease the expected advantage based solely on an $N_R^{1/2}$ prediction [as in Eq. (4.18)].

Table 8.5 lists some characteristics of the most popular photon counting PMT used for Raman, the RCA 31034 (now manufactured by Burle Industries). As noted above, PMTs have been largely superseded by semiconductor devices, and low-noise, red-sensitive PMTs are becoming difficult to locate.

8.4.2. Avalanche Photodiodes

Avalanche photodiodes (APDs) are recently developed detectors that show promise for Raman spectroscopy in both single and multichannel formats. An APD is a highly modified photosensitive diode that has internal gain like a PMT. Light striking a photodiode generates an electron/hole pair in a small silicon substrate. If there are enough photoelectrons, the resulting current may be amplified and read as a signal proportional to the incoming photon flux. However, since an incident photon generates at most one photoelectron, photon counting as practiced in many Raman applications requires

Table 8.5. Single-Channel Detector Specifications for Dispersive Raman Spectrometry

	Photon Counting PMT[a]	Avalanche Photodiode
Maximum Q	25%	90%
Response Range	185–930 nm	<300–1050 nm
Photosensitive area	3 × 15 mm	5–20 mm diameter
Dark signal	<10/sec	<25/sec
Maximum count rate	$>10^5$/sec	$>10^6$/sec

[a]RCA 31034a (now Burle C31034a).

detection of single electrons by the associated circuitry. Measurement of such small currents entails substantial noise, and the noise floor for conventional photodiodes prevents photon counting.

A PMT addresses this problem by amplifying a single photoelectron by a large factor (10^4 to 10^6) by the dynode chain (Fig. 8.23). These large groups of electrons are easily counted after detection by a pulse height discriminator. Similarly, an APD amplifies the photoelectron before detection. Additional layers of semiconductor are applied under the photosensitive layer and biased at a high voltage (1000 to 3000 V). Once the photoelectron is generated, it is accelerated by the high voltage and generates secondary electrons by impact ionization. The resulting "avalanche" of electrons yields a gain of a factor of 50 to 350, meaning that each photoelectron generates 50 to 350 secondary electrons.

APDs are physically much smaller than PMTs and are more rugged due to their solid-state construction. Their quantum efficiency is determined by the photosensitive silicon layer and is often above 80 per cent from 400 to 950 nm. Modern APDs have sufficiently large photosensitive area (5 to 20 mm diameter) to be attractive to Raman applications. The current shortcoming of APDs is their relatively high dark signal from thermally generated (then amplified) electrons. This dark signal and associated noise is much lower than conventional photodiodes, but still larger than photon counting PMTs. Some specifications for APDs are compared to those for PMTs in Table 8.6. Cooling and device selection permit APDs to approach photon counting performance, and future developments may further decrease dark signal. Currently available APDs provide a compact and less expensive alternative to the PMT, with wider spectral range and quantum efficiency (23). They are likely to find useful applications in single-channel spectrometers where size and cost are important. Two-dimensional arrays of APDs have been reported for nuclear radiation detection and may be adapted to visible light applications (24).

8.5. MULTICHANNEL DETECTORS AND CCDS

Early multichannel detectors for Raman were based on diode array or vidicon technology derived in part from the television industry. Vidicons are sometimes considered "first-generation" array detectors and provided the first multichannel advantage and accompanying increase in signal and SNR. These detectors were fairly quickly superceded by "second-generation" systems based on the intensified photodiode array (IPDA), also known as an intensified linear diode array. Unintensified diode arrays are in wide use in rapid scanning spectrophotometers and are rugged and inexpensive. A popular format is a 1024-pixel array of 3 mm $\times$ 24 μm elements, in a 3 $\times$ 25 mm stripe. Such

Table 8.6. Some Representative CCDs Used in Raman Spectroscopy

	Format	Pixel Size (μm)	Maximum Quantum efficiency	Dark Current (e^-/pixel/sec)
EEV 15-11	256 × 1024	27 × 27	0.45 (FI)[a]	< 0.002 (LN)[b]
			0.92 (BI)[a]	< 0.02 (TE)[b]
ISA "MRC"	2000 × 800	15 × 15	0.45 (FI)	< 0.001(LN_2)
			0.88 (BI)	< 0.01 (TE)
ISA/SITE	512 × 512	24 × 24	0.45 (FI)	< 0.001 (LN_2)
			0.88 (BI)	
			0.75 (BI-UV)	< 0.2 (TE)

[a]FI = front illuminated; BI = back illuminated; BI-UV = back illuminated, UV enhanced.
[b]LN_2 = liquid nitrogen cooling; TE = thermoelectric cooling.

arrays are fast and reasonably sensitive but are unsuitable for Raman due to high readout noise (1000 to 3000 e^-). Addition of an intensifier amplifies Raman photons by a factor of approximately 3000, such that the Raman signal exceeds the readout noise. IPDAs were popular for Raman spectroscopy before CCDs were developed and have the advantage of providing 1024 (or more) simultaneous channels that can be gated in time by the intensifier (4,25). However, IPDA dark signal is high compared to CCDs, and the intensifier is subject to easy (and expensive) damage by overexposure to laser or room light. Furthermore, existing intensifiers have relatively low quantum efficiency compared to CCDs, which rarely extend into the NIR region. The attractive performance of CCDs established them as "third-generation" multichannel detectors, and CCDs have replaced nearly all other detector configurations in dispersive Raman spectrometers used for chemical analysis.

8.5.1. CCD Basics

Charge-coupled devices are based on storage and manipulation of electrons and holes in a photosensitive semiconductor, usually silicon. Their construction and characteristics are described in other sources in detail (26–29), but their properties relevant to Raman are reviewed here. The basic event of importance to photodetection is generation of an electron/hole pair in silicon by a photon of sufficient energy. The incident photon energy must exceed the band gap of silicon at 1100 nm, and photons of longer wavelength (lower energy) merely pass through the silicon. Photons in the 200 to 1100 nm range generate photoelectrons in the silicon with a probability that varies with wavelength and ultimately determines the quantum efficiency curve. There are other factors that contribute to this curve, but an example is shown in Figure 8.24. Recall

that Q is the probability of generating a photoelectron from a photon, sometimes expressed as a percentage. Also shown in Figure 8.24 are the Raman shift ranges for several common laser wavelengths.

A circuit pattern is deposited on the silicon surface during CCD construction, which consists of an array of metal pads held at positive potential. Each pad forms a potential well that attracts photoelectrons and holds them in the region of positive potential, shown in Figure 8.25. These potential wells can store approximately 10^4 to 10^6 photons before their "full well capacity" is exceeded. So the potential well acts as an integrative detector that patiently collects and holds photoelectrons generated by incoming photons. Since the potential wells form an array across two dimensions of the silicon, each column of potential wells corresponds to a different wavelength. A two-dimensional CCD positioned at the focal plane of a dispersive spectrometer is depicted in Figure 8.26, based on the configuration of Figure 8.3. The squares in Figure 8.26 represent the photosensitive areas, which are partially covered by the circuit mask. In the example shown, the slit image for a particular wavelength (or Raman shift) covers a little more than one column of elements (*pixels*). The pixels in this column detect the same wavelength (or Raman shift), but the detected wavelength increases as one moves along the X axis. It is often the case that the vertical pixels are added together during readout, resulting in a larger signal. The end result is a detector with a large number (256 to 2000) of tall, narrow pixels, each of which corresponds to a different wavelength or Raman shift value. These combinations of pixels are often referred to as *superpixels*.

If the CCD is permitted to integrate the incident photons for a while, it will accumulate photoelectrons in its array of potential wells that corresponds

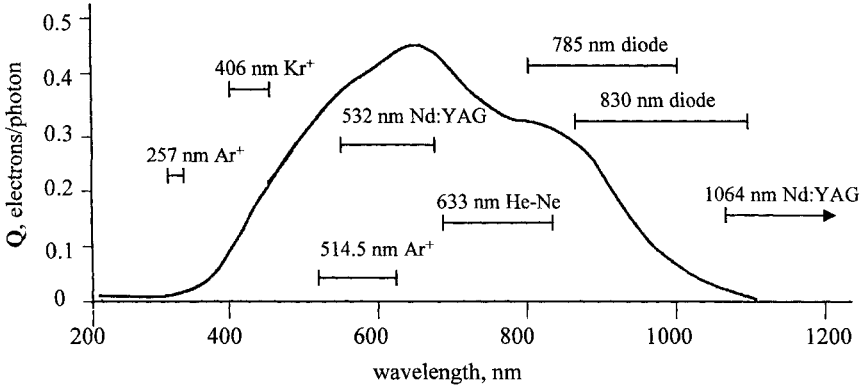

Figure 8.24. Typical of Q vs. λ curve for a front-illuminated silicon CCD, with Raman shift ranges (0 to 3000 cm^{-1}) for several common lasers.

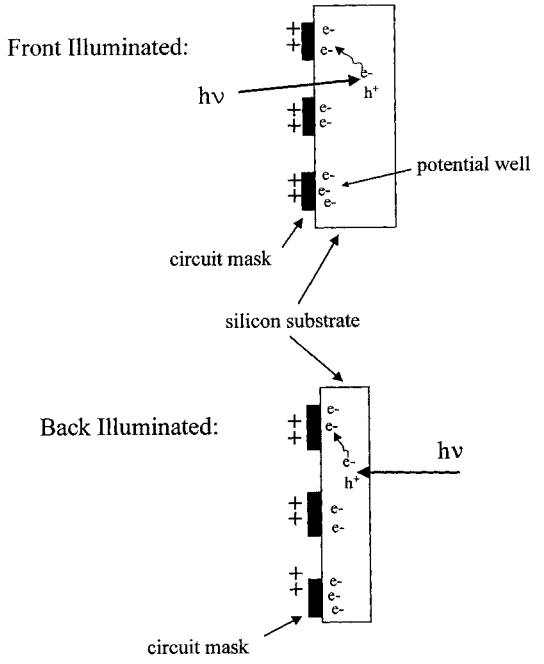

Figure 8.25. Schematic of front-illuminated and back-illuminated CCD construction. h^+ and e^- indicate holes and electrons, respectively.

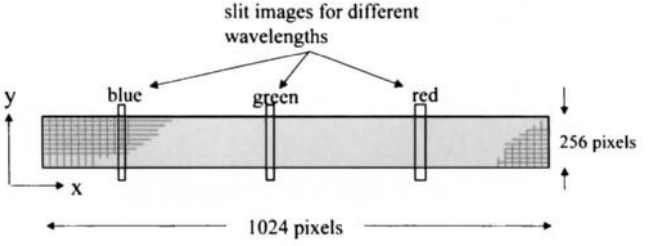

Figure 8.26. An example of the orientation of a CCD at the focal plane of a spectrograph, showing the images of the entrance slit for incident light of three wavelengths.

to particular Raman shifts. After this integration period, the CCD is "read out" electronically and the electrons accumulated in each potential well are converted to a digital value for storage in a computer. This process involves variation of the potentials on the metal pads so the potential wells are sequentially "shifted" to the edge of the photoactive area. Each bundle of stored

electrons is amplified and digitized by an analog-to-digital converter, and the result is a digital value related to the number of stored electrons. The *gain* of a CCD is the number of stored electrons required to yield one digital unit, often stated as electrons per count (e^-/count). Since each pixel location is rigidly related to a wavelength, the spectrum may be reconstructed as a plot of the number of stored electrons vs. the position on the CCD. By various means discussed in Chapter 10, the CCD position may be calibrated in terms of Raman shift, and the resulting spectrum is a plot of electrons vs. Raman shift. Since the basic measurement involves counting photoelectrons, the intensity axis, and most of the signal expressions [e.g., Eq. (3.6)] have units of "electrons."

8.5.2. CCD Definitions

Several terms of importance to Raman applications will be defined in this section. The list is not intended to be comprehensive.

8.5.2.1 CCD Format

A basic specification of CCDs is the number and size of pixels in the two-dimensional photoactive area. A common format is 256 × 1024 square pixels that are 25 μm on each side, for an overall area of 6.4 × 25.6 mm. Several formats are listed in Table 8.6.

8.5.2.2 Gain

As noted earlier, the stored electrons in each potential well are converted to a digital value by an analog-to-digital (A/D) converter, with the gain, γ, usually stated as e^-/count or electrons per analog to digital unit (e^-/ADU):

$$S(\text{e}^-) = \gamma \left(\frac{\text{e}^-}{\text{count}} \right) S'(\text{counts}) \tag{8.12}$$

(analog-to-digital units); where S' designates the observed CCD signal in terms of ADU. There is little point in having a gain of less than 1 e^-/count, and the gain is usually in the range of 1 to 16 e^-/count. Note that gain refers to photoelectrons, not photons, so

$$S(\text{photons}) = \frac{\gamma S'(\text{counts})}{Q} \tag{8.13}$$

where Q must be known to assess the number of photons required to generate a "count." For example, a gain of 4 e^-/count and a Q of 0.40 e^-/photon yields

an overall response of 10 photons/count, or 10 photons/ADU. The gain may be determined by observing a broadband source (e.g., a tungsten bulb) to determine the signal and its standard deviation. The gain in e^-/count equals the average signal (in counts) divided by the square of the observed standard deviation (also in counts), with both measured in a flat region of the broadband spectrum. This simple relation is valid when shot noise is the dominant noise source.

8.5.2.3 Dark Current

At any temperature above 0°C, there will be spontaneous generation of electron/hole pairs that is unrelated to incident light intensity. In addition, defects in the silicon may be sources of electrons and contribute "dark" electrons. Both of these processes are exponentially dependent on temperature, and CCDs must be actively cooled to reduce dark current to acceptable levels. The *dark current* is usually expressed as e^- $pixel^{-1}$ s^{-1} (electrons per pixel per second) and depends both on the specific device and the temperature. A few examples are listed in Table 8.6. As an approximate rule of thumb, the dark current doubles for each 5°C increase in temperature.

It should be noted that dark current is one of the factors that significantly affects CCD cost. Inexpensive CCDs used in video cameras and such have high dark current due to relatively numerous defects and uncooled operation. The dark current provides a "noise floor" that limits the use of such CCDs for the very low light level applications encountered in Raman spectroscopy. "Scientific grade" CCDs are much lower in defect concentration and are often physically larger than video CCDs. Making large pieces of defect free single-crystal silicon is expensive, and this requirement is the main reason why CCD devices for Raman spectroscopy cost several thousand dollars for the chip alone, while a consumer video camera CCD costs less than $100.

8.5.2.4 Bias

When a packet of electrons is "read out", the amplifiers usually introduce an offset which appears as a constant value independent of the number of electrons. This *bias* is constant for a given pixel, but may vary across the CCD. A bias *vs* pixel curve is usually obtained by reading out the CCD following a very short (near zero) dark integration, then stored. This bias is usually subtracted from each spectrum immediately after it is acquired. It is often quite large, but nearly noiseless, so it can be subtracted but not ignored.

8.5.2.5 Readout Noise

As discussed in Section 4.2.5, the act of reading out the packet of electrons (*digitizing* is probably a better term) incurs some noise, sometimes called

quantization noise. For successive readouts of exactly the same number of photons, there will be some variation in the resulting digital value. This readout noise is generally independent of the number of electrons being counted and is usually a few electrons for scientific grade CCDs. It is only a significant factor when the number of electrons being counted is very small and approaches the magnitude of the readout noise itself. For nearly all Raman applications, the signal is at least several hundred electrons, and readout noise is negligible. The readout noise (in electrons) is often determined as the standard deviation of the difference between two short exposure dark integrations, divided by $2^{1/2}$.

8.5.2.6 Full Well Capacity

As noted earlier, there is a limit to the number of electrons that can be stored in a given potential well, generally 10^4 to 10^6 electrons. After this limit, additional photoelectrons will spill over into adjacent potential wells, a process known as *blooming*. The full well capacity is generally equal to the maximum signal that can be digitized and defines the upper signal limit for a given pixel. Full well capacity can be a significant limitation when pixels are added together before readout (*binning*, defined below).

8.5.2.7 Dynamic Range

The effective range of intensities observable with a given CCD pixel is effectively defined by the ratio of the full well capacity to the readout noise. For example, if a full well capacity of 250,000 e^- is digitized with an 18-bit A/D converter, the gain is approximately 1 e^-/ADU, since $2^{18} = 262{,}144$. If the readout noise is 4 e^-, then the minimum useful signal is roughly 4 to 8 e^-. The best-case dynamic range is the ratio of the maximum to minimum signals, or 250,000/4 = 63,000. This range can also be stated as a power of 2, in this case "16 bits." For comparison, an inexpensive video CCD might have a dynamic range of 8 bits (256) due to its larger dark and readout noise.

8.5.2.8 Binning

Since the Raman-scattered photons of a particular frequency are often spread over some or all of a CCD column, it is often desirable to add the signals from each pixel in the column. *Binning* refers to the addition of electrons in two or more pixels during or after readout. In *hardware binning*, the electrons are collected in one potential well before the combined electrons are digitized. This might be advisable with weak signals in order to increase the total signal to a value much larger than the readout noise. In *software binning* each pixel is read out individually, then the resulting digital values are added numerically. If the number of electrons in each pixel greatly exceeds readout noise, hardware

and software binning yield the same signal and SNR. However, hardware binning can easily exceed the full well capacity of the readout register if a large number of pixels are summed. In both spectroscopic and imaging applications, it is often possible to bin pixels along either (or both) the X and Y axes of the CCD.

8.5.2.9 Front-Illuminated CCDs

The most common configuration of CCDs used in Raman spectroscopy is that shown in the upper drawing in Figure 8.25. The *front* of the CCD refers to the side of the silicon wafer containing the circuit mask, and a CCD collecting photons incident on this side is *front illuminated.* The circuit mask covers approximately half of the silicon area, and the circuits themselves are not photoactive, so the silicon is exposed to about half of the incident photons and the maximum possible Q is about 50 per cent. A typical Q vs. λ curve for a front-illuminated CCD is shown in Figure 8.27, with a maximum Q of 43 per cent at 770 nm. Front-illuminated CCDs are the most common because they are the most rugged and least expensive. Since a low defect, scientific-grade CCD is difficult to make at all, any further processing steps add to their expense.

8.5.2.10 Back-Illuminated CCDs

A front-illuminated CCD may be *back thinned* by ion etching on the side of the silicon wafer opposite the circuit mask. If the silicon is thin enough after

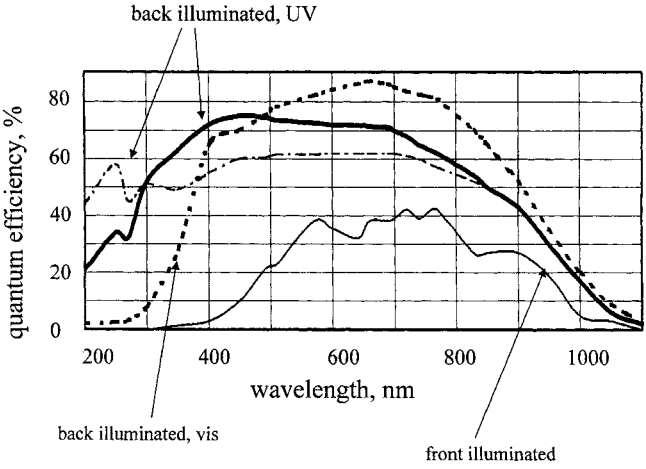

Figure 8.27. Quantum efficiency curves for several CCD types. (Adapted from Horiba/ISA product literature.)

etching ($\sim$ 15 μm), electrons generated by back illumination may migrate to the potential wells on the circuit side and be stored as before. As shown in Figure 8.25, photons enter the CCD from the "back," and there is no obstruction by the circuit mask. The maximum quantum efficiency may be quite high as a result, in the range of 80 to 95 per cent. Furthermore, the processing required to fabricate the circuit results in layers that absorb UV photons, thus constraining the front-illuminated CCD to detecting wavelengths longer than about 400 nm. Back-illuminated CCDs do not have this restriction, and quite high Q is maintained well into the 200 to 400 nm range. Figure 8.27 compares Q vs. λ curves for front- and back-illuminated CCDs. Back-illuminated CCDs often have an antireflection (AR) coating on their photosensitive surface to further improve Q by reducing reflection. The term *back-illuminated AR coated* refers to the most sensitive CCD designs.

Unfortunately, back thinning adds significant expense to already costly devices, and the thin CCD that results is quite fragile. Back-thinned CCDs often cost twice as much as their front-illuminated precursors. In addition, the thin layer of silicon can cause interference effects that appear as gain oscillations, shown in Figure 8.28. These gain oscillations are known as *etaloning* and generally occur in back-thinned CCDs at longer wavelengths (e.g., >700 nm). Some CCD manufacturers have managed to reduce the effect, but the user should verify the absence of etaloning for a given CCD at the time of purchase.

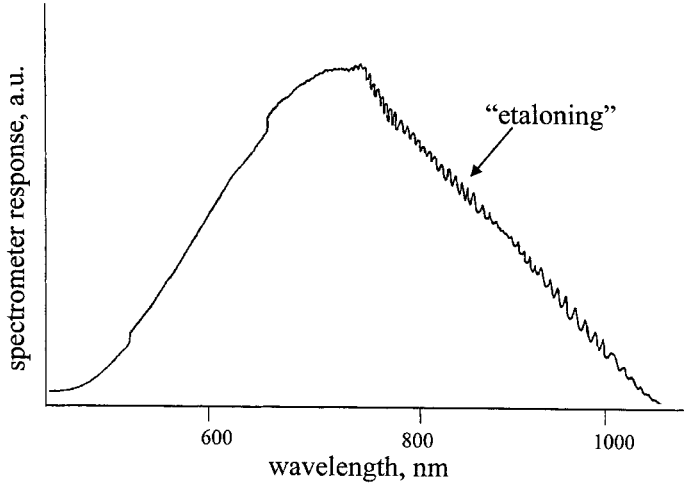

Figure 8.28. Response curve for a back-illuminated CCD on an $f/4$ spectrograph. Response oscillations above 700 nm are caused by "etaloning."

8.5.2.11 Deep Depletion CCDs

Deep depletion refers to controlled doping of the silicon to enhance long wavelength response, usually applied to front-illuminated CCDs. A Q vs. λ curve for a deep depletion CCD is compared to a conventional front-illuminated response in Figure 8.29. Although deep depletion CCDs cost approximately the same as the conventional front-illuminated CCDs, they have higher dark current and generally must be cooled to lower temperatures.

8.5.2.12 Multipinned Phase Operation

Multipinned phase (MPP) is an electronic technique that significantly reduces the dark current, with some cost in the full well capacity. MPP devices exhibit dark currents that are 1 to 2 orders of magnitude lower than similar non-MPP CCDs at the same temperature. Conversely, an MPP CCD may be operated at higher temperature and exhibit as low a dark current as a much cooler non-MPP device. This feature is attractive when the user wants to avoid liquid nitrogen cooling. MPP CCDs cooled by an air-cooled thermoelectric cooler can easily exhibit dark currents in the region of 1 e^-/pixel/sec.

8.5.2.13 Cosmetic Quality

Cosmetic defects refer to imperfections in the silicon layer or circuit mask of the CCD that cause variations in response at certain positions on the CCD

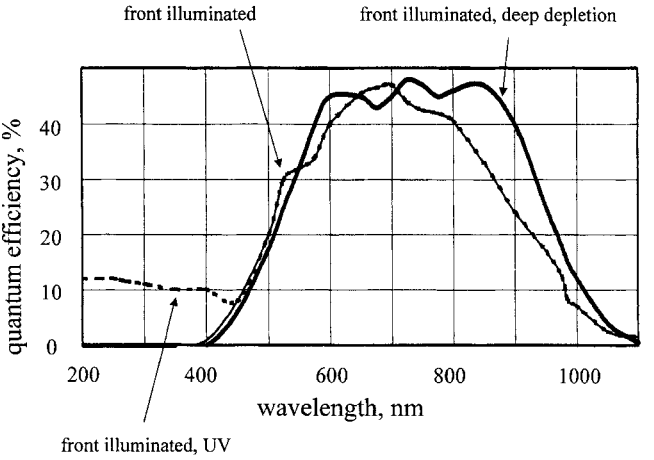

Figure 8.29. Quantum efficiency curves for conventional, deep depletion, and UV-enhanced front-illuminated CCDs. (Adapted from Horiba/ISA product literature.)

photoactive area. *Dead pixels* are completely nonresponsive, while *hot pixels* are close to saturation even without incoming light. A *dead column* is an entire column of pixels that is unresponsive or exhibits much lower gain than adjacent columns. *Charge traps* prevent electrons from reaching the readout registers. Depending on number and size, a few cosmetic effects are often tolerable, and for the more exotic or larger CCD designs they might be unavoidable. Scientific CCDs are often graded according to the number and type of defects, and a user may specify cosmetic quality at the time of purchase. CCD manufacturing techniques have improved rapidly, and many CCDs are available free from defects, but generally at a premium in cost.

8.5.2.14 Cosmics

Silicon detectors, including CCDs, are quite sensitive to high-energy radiation from local or extraterrestrial sources. So-called *cosmics* can in fact be cosmic rays but may also be background high-energy radiation from the lab or the CCD housing. Such events are generally infrequent but have sufficient energy to generate many electrons in the Si substrate that are stored and analyzed as if they were photoelectrons from Raman scattering. The result is a large signal in one or a few pixels, which appears as a spike in the spectrum. A typical rate for such events is roughly $1/\text{min}^{-1}$ cm^{-2} of silicon, but this value may increase wildly if radioisotopes or their residues are nearby. As noted in Section 8.5.3.4, cosmics or *noise spikes* can be rigorously removed from Raman spectra without loss of spectral information provided their density is not too high.

8.5.3. CCD Signal Processing

After a Raman spectrum is collected as a distribution of photoelectrons across the CCD face, then digitized to obtain a digital array of points, several mathematical manipulations are generally applied to correct for bias, dark signal, and Q variations on the CCD. Such processes may be included in the detector software or the acquisition program, but the user should be aware of their effects on observed spectra.

8.5.3.1 CCD Output Signal

The signal following CCD readout will be in digital units (often called *counts*), proportional to the number of photoelectrons according to Eq. (8.12). This signal consists of contributions from Raman scattering, dark signal and CCD bias, as in

$$\gamma S'(i) = S(i) + S_{\text{dark}}(i) + S_{\text{bias}}(i) \tag{8.14}$$

where $S'(i)$ is the digitized signal of the ith CCD element, γ is the gain in e^-/ADU, $S(i)$ is the number of photoelectrons resulting from incident light described in Chapter 3, S_{dark} is the number of dark electrons in each pixel, and S_{bias} (i) is the bias for each element; S_{dark} and S are dependent on integration time, so Eq. (8.14) can be restated as:

$$\gamma S'(i) = \dot{S}(i)t + \dot{S}_{dark}(i)t + S_{bias}(i) \tag{8.15}$$

with $\dot{S}$ and $\dot{S}_{dark}$ having units of electrons per second (e^-/sec). As noted in Section 8.5.2.8, pixels are often *binned* before readout, so the ith element may contain the electrons from several pixels. A common case is binning of the pixels along the slit axis, resulting in a *superpixel* with dimensions equal to 1 real pixel wide by 256 (or more) high. For a 1024 wide × 256 high CCD binned in this fashion, there would be 1024 elements, and 1024 digital values in the $S'(i)$ array.

8.5.3.2 Removing CCD Bias and Dark Signal

The term S_{bias} (i) is not time dependent since it results from the process of amplifying and digitizing the electrons in the CCD potential wells. It may vary across the CCD, however, so it must be recorded and subtracted from the observed signal. Usually S_{bias} is recorded for a CCD integration time of 0 sec and stored for mathematical subtraction. The S_{bias} (i) term should be recorded again if the binning parameters or CCD gain are altered, but need not be updated following changes in integration time. Acquisition of S_{bias} is often automatically included in the CCD software.

The S_{dark} term increases linearly with time and can contribute to the observed signal unless the CCD is very cold and $\dot{S}_{dark}$ approaches zero. A common procedure is acquisition of a signal with the CCD shutter closed, for the same integration time as that used to observe Raman scattering. Strictly speaking, the dark spectrum should be obtained identically to the Raman spectrum, but with the laser off. This procedure will correct for contributions from ambient light, but such sources should be absent in a well-designed experiment. The dark spectrum, consisting of $\dot{S}_{dark}$ (i) t may be stored for later subtraction from $S'(i)$. It is common practice to obtain S_{dark} and S_{bias} simultaneously, by obtaining a dark spectrum with the same integration time as the Raman spectrum, then subtracting both from the observed Raman signal.

Although these corrections are easily implemented, they carry some consequences with respect to noise and SNR. Each CCD acquisition has readout noise, so two successive readouts will not be identical. Figure 8.30A and 8.30B are successive uncorrected CCD readouts with short integration time so the dark signal is negligible. Curve B is offset for clarity by −100 ADU. The bias

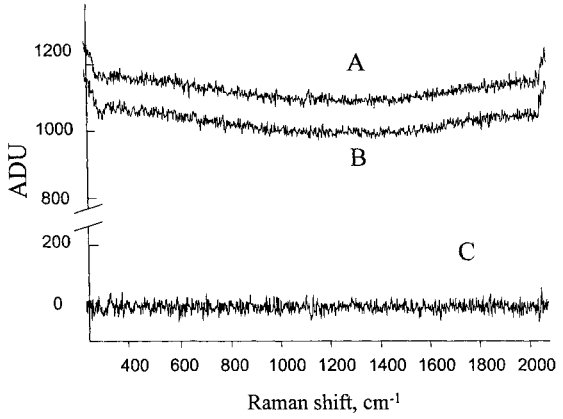

Figure 8.30. A and B are successive readouts of 10 msec dark exposures of a front-illuminated CCD. B is displaced downward by 100 units for clarity. C is the difference between A and B.

accounts for about 1200 ADU for both curves, but readout noise causes differences between the two curves. These differences are obvious when the two bias spectra are subtracted to yield curve C. The standard deviation of curve C is equal to $\sqrt{2}$ times the readout noise, σ_r. In most cases, $S(i)$ is much larger than σ_r, so readout noise may be neglected. For very weak signals, however, the readout noise may contribute significantly, and degrade the SNR. In this case, the integration time should be increased so $S(i)$ greatly exceeds σ_r. Alternatively, more CCD pixels may be binned to boost $S(i)$ relative to σ_r.

Figure 8.31 illustrates dark signal for two integration times. Curve A is a bias spectrum obtained with negligible (10 msec) integration time, while curve B is a dark integration (laser off) of 60 sec. The approximately 100 ADU increase over the bias spectrum is from dark electrons generated randomly during the 60 sec integration. Curve C is a 180 sec dark spectrum, with the expected three fold increase above the bias, but two additional features are observable. First, the noise is larger, as it should be for shot noise. In fact, the dark *noise* (as opposed to dark *signal*) is $\sqrt{3}$ larger for 180 sec than for 60 sec. Second, the sharp spikes are cosmics that happened to arrive during the 3 min integration period. Such spikes are by nature unpredictable but can be removed with the procedure described in Section 8.5.3.4.

Figure 8.32 illustrates the exponential increase in dark signal with CCD temperature. Each curve is a raw spectrum obtained from a 60 sec dark integration, but the CCD temperature was varied from −90 to −58°C. The barely visible bottom curve (−90°C) is the same as curve B of Figure 8.31. The dark signal increases about a factor of 10 for each 14°C increase in temperature for this particular device. Notice that the number of cosmics does not

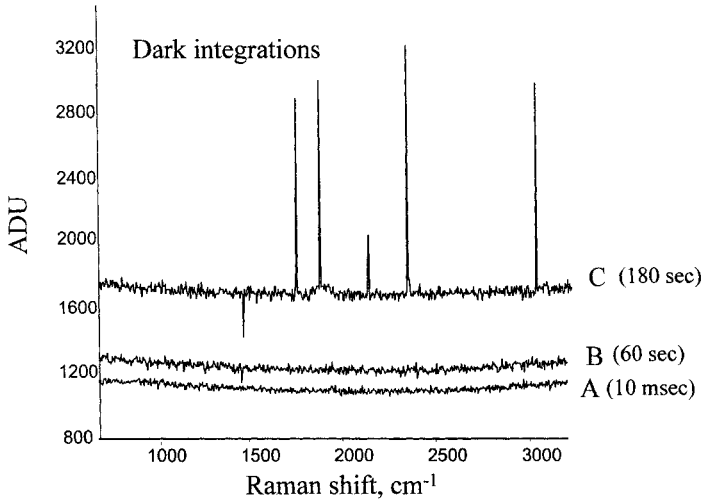

Figure 8.31. Dark spectra from a CCD for 10 msec (A), 60 sec (B), and 180 sec (C) integrations, without bias correction. A is the bias spectrum, while B and C show additional signal due to thermally generated electrons. As explained in the text, the spikes on curve C result from cosmics.

vary with temperature (nor should it), but both dark level and dark noise are strongly temperature dependent. Although Figure 8.32 indicates that dark signal is always lower at lower temperature, it is not necessarily desirable to run an experiment at the lowest possible temperature. A fairly minor problem with low temperature is a decrease in the charge-transfer efficiency of the CCD. As electrons are shifted along the series of potential wells, a few are lost, and this loss is larger at lower temperatures. A more serious consequence of low temperature is illustrated in Figure 8.33, which shows the temperature dependence of the quantum efficiency, Q. The Q for a front-illuminated silicon CCD was divided by the Q at 25°C, then plotted versus wavelength. Notice that the Q for longer wavelengths decreases at lower temperatures by as much as 60 per cent at 1000 nm. At long wavelengths (e.g., a Raman experiment with a 785 nm laser), the user faces a trade-off of dark signal and Q, and the temperature should be chosen to optimize this trade-off.

The statement that the dark noise equals $S_{\text{dark}}^{1/2}$ is simple enough, but it does have some practical consequences. When the dark spectrum is subtracted from the Raman spectrum obtained with the same integration time, the noise on the spectrum will increase according to:

$$\sigma(S - S_{\text{dark}}) = \sqrt{S + S_{\text{dark}}} \tag{8.16}$$

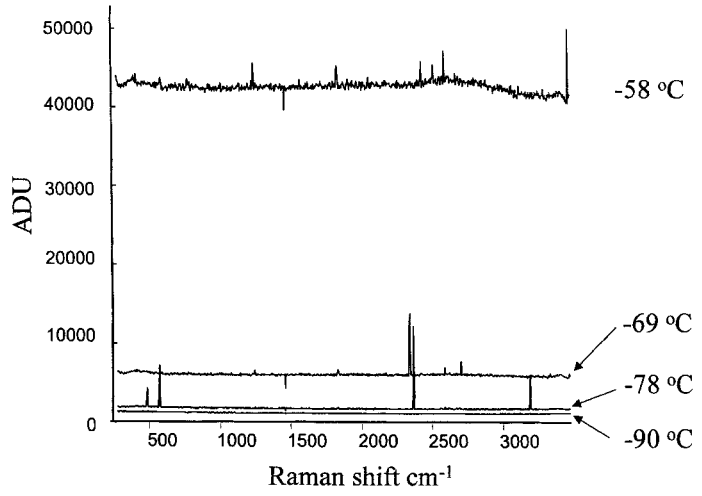

Figure 8.32. Temperature dependence of dark spectrum for an EEV 15-11 deep depletion CCD. Integration time was 60 sec in all cases. Positive spikes are due to cosmics; negative spike at ~1450 cm^{-1} is due to a column in this CCD with weak response.

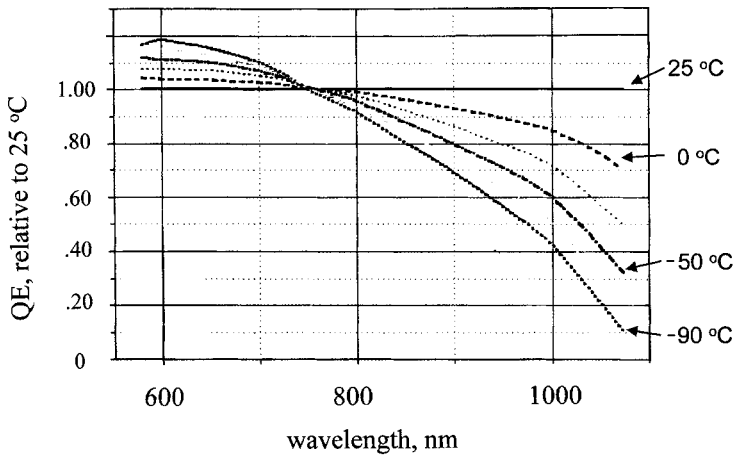

Figure 8.33. Temperature dependence of quantum efficiency for front-illuminated silicon CCD. Spectra of a broadband source with the CCD at the indicated temperatures were divided by a spectrum of the same source taken at 25°C. The observed Q at ~750 nm was nearly independent of temperature. (Adapted from Andor Technologies product literature.)

where $\sigma(S - S_{dark})$ is the standard deviation of the dark-corrected spectrum. Equation (8.16) results from the fact that variances add for addition and subtraction, and S and S_{dark} equal the variances of the total signal and dark signal respectively, since both are shot noise limited. Readout noise is neglected in Eq. (8.16). If the S_{dark} and S are comparable in magnitude, dark subtraction will increase $\sigma(S - S_{dark})$ and noise by a factor of $\sqrt{2}$. If $S_{dark} \ll S$, as might be the case for low CCD temperature or short integration times, dark subtraction is not necessary.

An additional consequence of Eq. (8.16) relates to signal averaging, in which several CCD acquisitions are summed to improve SNR. One is effectively increasing the integration time by combining the electrons from repeated acquisitions. If dark signal is subtracted from a signal-averaged spectrum, the dark spectrum must also be averaged. It would degrade the SNR if $S_{dark}^{1/2} \gg S^{1/2}$ in Eq. (8-16), so one must reduce the noise in S_{dark} as much as possible. Ideally one would signal average S_{dark} for a very long time so that it does not contribute significantly to the overall noise. In practice, however, it is generally sufficient to use the same total acquisition time for the Raman spectrum and the dark spectrum.

The nuances of bias, dark signal, and binning can be complex at times, and detailed discussions are available (21, 26–29). A simple procedure that avoids most pitfalls is subtraction of a blank from the observed Raman spectrum obtained under the same conditions of binning, temperature, and total integration time. The blank includes the dark spectrum and bias, as well as scattering from solvent, cell, optics, and the like.

8.5.3.3 Gain and Q Corrections

The $\dot{S}(i)$ term in Eq. (8.15) is the rate of electron generation for the ith element of the CCD. It contains the quantum efficiency Q, via Eq. (3.6), and is not necessarily constant across the entire CCD. Quantum efficiency Q varies with wavelength as illustrated in Figures 8.27 and 8.29 but also varies from pixel to pixel. Even if the CCD were absolutely evenly illuminated with monochromatic light, there would be variations in the number of electrons collected in each pixel. These variations sometimes repeat in groups of pixels (so-called *fixed pattern noise*) or may be caused by random defects in the Si substrate. These effects appear as variations in the slope of a plot of the number of electrons vs. the number of photons for different pixels. Fortunately, both fixed pattern and random Q variations are reproducible and may be corrected by recording the spectrum of a known source. The response function calibration described in Chapter 10 using either a tungsten bulb or a luminescent standard is straightforward and corrects for most Q variations encountered in CCDs,

with the obvious exception of "dead" or "hot" pixels, which do not produce a useful signal to correct.

In summary, the CCD output, $S'(i)$, expressed by Eq. (8.15) is recorded as an array of points, each equaling an analog-to-digital conversion value proportional to the number of photoelectrons in a CCD pixel or superpixel. Also, S_{bias} and S_{dark} may be determined independently and subtracted from the $\gamma \dot{S}(i)$ to obtain the dark and bias-corrected signal, $\dot{S}(i)t$. In order to avoid degrading the SNR during these corrections, S_{dark} and S_{bias} should have noise levels well below that of $S(i)$. In practice, this condition is met when S_{dark} and S_{bias} are much smaller than $S(i)$, or they have been signal averaged to sufficiently reduce their noise levels.

8.5.3.4 "Spike" or "Cosmic" Removal

As noted earlier, the spikes apparent in Figure 8.32 are caused by high-energy radiation and occur randomly. They can be a particular nuisance when observing weak signals using long integration times. Even a CCD in an environment with a low density of such high-energy events will produce one or so each minute somewhere on the detector face, so a spectrum acquired in >10 min will nearly always be contaminated with cosmics. Several methods have been reported for automatic removal or rejection of these problematic cosmics.

Signal averaging of a series of spectra will decrease the size of a spike, since two spikes are very unlikely to occur on the same pixel. However, spikes are generally quite large (e.g., Fig. 8.31) and averaging can dilute but not remove them. So simple averaging is generally an inadequate approach. Smoothing procedures have the advantage of working on a single CCD spectrum, without requiring signal averaging. Typically a raw spectrum is mathematically smoothed with a Savitsky-Golay or a similar moving-average algorithm. An example is shown in Figure 8.34B. These routines can improve the appearance of noisy spectra but have difficulty with cosmics because they are usually large and sharp. As the extent of Savitsky-Golay smoothing is increased, the spike is diminished but cannot be removed completely without significantly distorting the spectrum.

More sophisticated spike removal may be achieved with *missing point* filters in which a spike is identified by some statistical criterion, then a moving average is carried out on the surrounding points, not including the outlier (30,31). In effect, these procedures are similar to a conventional Savitsky-Golay approach, but they remove the problematic point before applying the moving average. The lower spectrum of Figure 8.34 illustrates effective spike removal using a missing point filter, with minimal distortion of the spectrum.

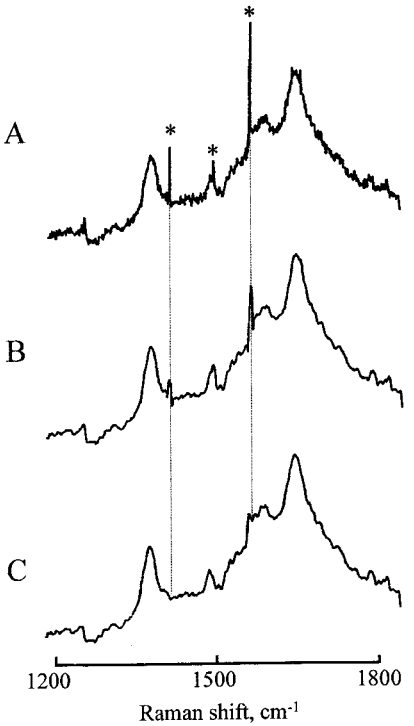

Figure 8.34. Cosmic removal from a single spectrum of bacteriorhodopsin by smoothing routines. A is original spectrum, with asterisks indicating cosmics. B is after a conventional quadratic, 9 point Savitsky Golay smooth. C is after a similar smooth, but including the "missing point" routine. Adapted from Reference 30 with permission.

A different but effective approach for removing cosmics is based on comparing several repetitive spectra of the same sample. Provided readout noise is not significant, there is no SNR penalty for obtaining multiple spectra before averaging. If these multiple spectra are added directly, the result is a simple average or sum, and cosmics will only be diluted, as noted earlier. However, the multiple spectra may be compared *before* adding, and cosmics may be detected. There are several mathematical methods for this process, a few of which are available in commercial instruments.

Consider a total integration time of 60 sec, but acquired as six 10 sec integrations. A simple way to combine the six and remove spikes is to compare the first two and retain the *lower* value of intensity at each wavelength in a new spectrum labeled "result." If a spike occurs in one spectrum, it will be much larger than the same point in the companion spectrum, and only the smaller value is retained in the "result" spectrum. Then the second and

third spectra are compared, and the smaller value at each wavelength is added into the "result." After the sequence is repeated for all six spectra, the result will be the sum of five data points at each Raman shift value, and cosmics will be removed. Although this method is statistically nonrigorous, it has the advantage of permitting spike removal during signal acquisition. If a large number of spectra are to be averaged, the de-spiked result may be displayed dynamically, as it develops. A statistical procedure has been presented for more rigorous rejection of such outliers, based on the distance of the outlier from the mean, relative to the noise level (32). This procedure is conceptually very similar to the statistical Q test for outlier rejection and is quite effective since cosmics are usually large compared to the real noise level.

A simple but less rigorous procedure is rejection of outliers based on a threshold, usually expressed in ADU. After repetitive spectra are collected, the intensities at a particular Raman shift are compared. An example is shown in Figure 8.35. The spikes apparent in the raw spectrum are removed in the average, and the SNR improves during averaging. Only a few points are rejected, since only a few cosmics occurred during the 10 runs to be averaged. For those few wavenumber values when cosmics occurred, one fewer intensity was averaged to arrive at the final spectrum.

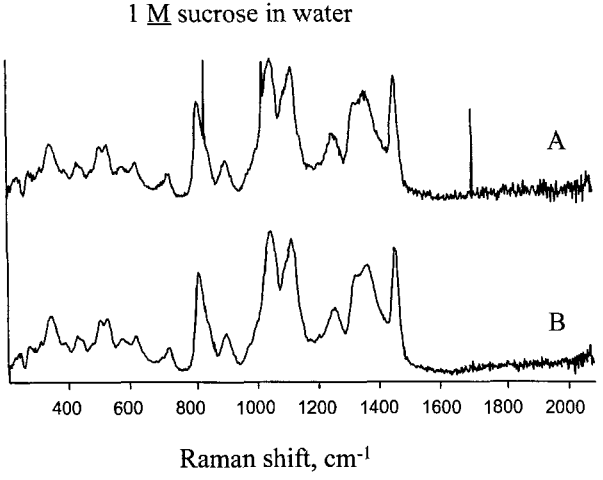

Figure 8.35. Spectra of sucrose in water, with water and cuvette spectrum subtracted. Spectrum A is a single 10 sec integration, containing cosmics at ~800 and ~1700 cm^{-1}. Spectrum B is an average of ten 10 sec spectra, with the spikes filtered by comparing successive spectra. See text for details.

These methods differ in the criteria for rejecting outlier data points, but they share the process of obtaining multiple spectra, detecting and removing outliers, then averaging. If readout noise is negligible, there is no SNR penalty for acquiring multiple spectra, compared to one spectrum for the combined integration time. For the great majority of Raman spectra, the signal from the analyte and background is much larger than the readout noise, so multiple spectral acquisitions do not degrade SNR. For very weak signals and very low background, multiple readouts can degrade SNR due to multiple contributions from readout noise. However, this situation is rare in analytical Raman, and spike removal based on multiple spectral acquisition is effective. Figure 8.36 shows the gain in SNR resulting from both longer integration time and signal averaging. The top spectrum is a single 1 sec integration of sucrose obtained with low laser power, with the CCD bias subtracted. Increasing the integration time to 10 sec increases the SNR by $\sqrt{10}$, but also increases the likelihood of interference from cosmics. The average of 10 acquisitions of 1.0 sec each yield the same SNR (provided readout noise is negligible), but any cosmics are removed.

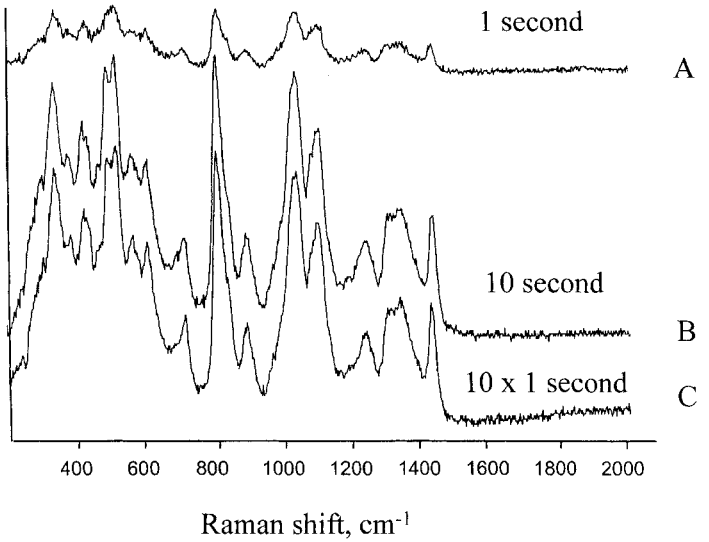

Figure 8.36. Raman spectra of 1 M sucrose in water plotted on the same intensity scale, illustrating signal averaging. Spectrum A was obtained in 1 sec, and a water spectrum was subtracted. Spectrum B is a 10 sec integration, showing a signal increase of a factor of 10 and an SNR increase of a factor of 3. Spectrum C is the average of ten 1 sec CCD exposures and has approximately the same SNR as spectrum B.

8.6. RECORDING METHODS FOR DISPERSIVE SPECTROMETERS

8.6.1. Single-Channel Spectrometers

When a PMT or an avalanche photodiode is coupled with a single or double monochromator, the system is either operated at fixed wavelength, or the spectrum is acquired sequentially with wavelength scanning. Fixed wavelength operation may be adequate for monitoring a single Raman feature as a function of time, or for transient experiments in which a Raman scatterer is generated by some external stimulus, then monitored vs. time. Fixed wavelength operation obviously sacrifices information about the evolution of the Raman spectrum with time, but can provide excellent time resolution. Advanced techniques in time-resolved Raman have extended the time scale to the picosecond regime, but such methods are generally not applied to problems in chemical analysis.

The generally weak Raman signal leads to a fundamental problem with time resolution at fixed wavelength, which can also extend to multichannel operation. If a Raman signal is quite weak, say 1000 photons/sec at the detector, then a photon is arriving every millisecond, on average. If one desires 500 points in a plot of intensity vs. time for 1 sec, the observation window is only 2 msec. So a photon counting detection system will have extreme statistical noise if the photon arrival rate is small compared to the width of the acquisition window. In most cases, a large number of transients are signal averaged to acquire a useful plot of intensity vs. time.

Many time-resolved Raman configurations have been reported, but an example is shown in Figures 8.37 and 8.38. The Raman scatterer of interest was generated electrochemically, then it reacted with a solution species to form a spectroscopically distinguishable product (4,33). Figure 8.37 shows the evolution of the spectra, acquired with a multichannel system as described later. The peak at 1572 cm^{-1} is due to dopamine orthoquinone (DOQ), which reacts with Br^- in the solution to form a new species with a Raman band at 1539 cm^{-1}. The transition from one species to another with time is apparent in Figure 8.37. Fixed wavelength transients were obtained by monitoring the output of a photon counting PMT vs. time after a potential pulse that generated DOQ. A multichannel scaler stored "counts" from the PMT in 50 sequential time windows with widths of 20 msec. Each window stored the Raman signal for a particular wavelength, arriving during time increments of 20 msec after the reaction was initiated. The two species could be monitored independently using two different experiments, one at 1572 and one at 1539 cm^{-1}. The resulting transients (Fig. 8.38) permitted determination of the reaction kinetics and mechanism (25).

Wavelength scanning with single-channel detectors was the most common mode for Raman spectroscopy before multichannel detectors arrived in the

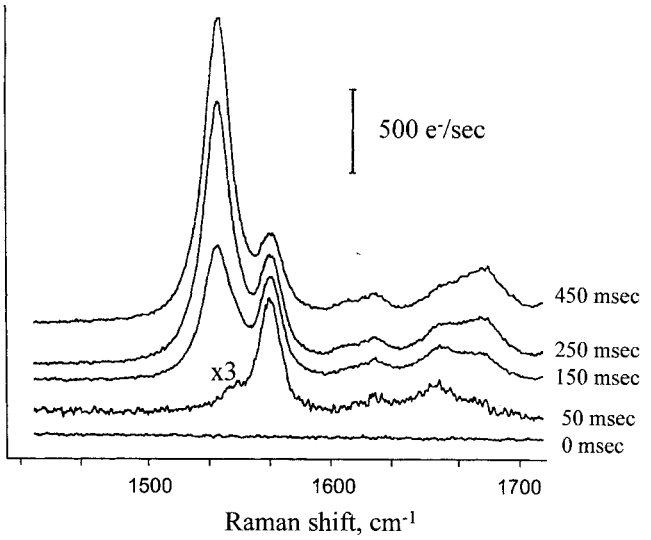

Figure 8.37. *In situ* Raman spectra of dopamine oxidation in 1 M HBr at a carbon electrode surface. An IPDA detector was gated for 50 msec time increments ending at the times indicated after initiation of DA oxidation. The band at 1572 cm^{-1} is from the electrogenerated orthoquinone, that at 1539 cm^{-1} is from brominated quinone. (Adapted from Reference 33 with permission.)

1980s. Assuming both the laser intensity and the sample are invariant with time, the Raman spectrum may be collected as a series of integrations conducted at a series of wavelengths. Generally speaking, the monochromator is stepped in wavelength increments of a few reciprocal centimeters, and photons are collected for a particular time at each wavelength. For example, the monochromator might stay at one wavelength for 5 sec, during which the counts from the detector are collected and stored; then the monochromator is stepped to the next wavelength. Figure 8.11 is an example of a spectrum collected in this manner. The integration time is the *single-channel acquisition time* discussed in Section 3.4 and will determine the SNR as described in Chapter 4. Usually the wavelength increment between integrations is approximately equal to the monochromator bandpass, in order to optimize the trade-off between spectral resolution and total acquisition time. If the bandpass is small compared to the wavelength increment, there will be significant gaps between points. On the other hand, an increment much smaller than the bandpass will add to the total acquisition time without an improvement in spectral resolution.

As discussed in Section 3.4 and Chapter 4, the total acquisition time (t_M) for a single-channel spectrometer is the integration time, t_S, times the number of resolution elements. Operation at higher resolution will require more data

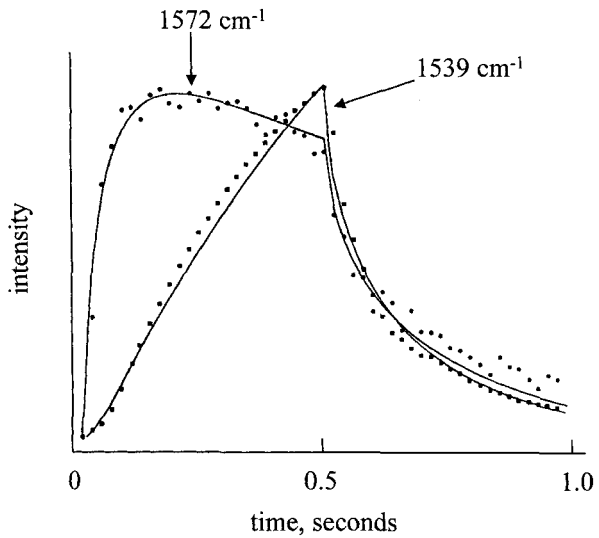

Figure 8.38. Transient Raman intensity recorded with a PMT during the electrochemical oxidation of dopamine in 1 M HBr. Each point represents a 20 msec integration of photons arriving at either 1572 or 1539 cm^{-1}. Solid curves are simulated for a mechanism involving bromination of electrogenerated orthoquinone (1572 cm^{-1}) to yield a monobromo orthoquinone (1539 cm^{-1}). Applied potential was returned to a reducing value at $t = 0.55$. (Adapted from Reference 33 with permission.)

points, increasing N_R and t_M. The rapid and nearly complete transition from single-channel to multichannel spectrometers has been driven primarily by the gain in speed and SNR. An additional factor is the sensitivity of scanning single-channel spectrometers to laser power fluctuation. Any laser noise or drift occurring on the time scale of the integration time or wavelength scan will appear as variations in the peak heights and baseline of the scanned spectrum.

8.6.2. Dispersive Multichannel Acquisition

Once the grating density and position have been selected using the criteria described in Section 8.2.1, the CCD is ready to acquire a spectrum. Some experimentation with integration time is usually required to adjust for the strength of Raman scattering from a particular sample. The integration time must be long enough for the Raman signal to exceed readout and dark noise, and to achieve adequate SNR. For samples with strong background or Raman scattering, the integration time must be short enough to avoid reaching the full well capacity of any CCD pixels. For such strong signals, one can average several shorter integrations or bin fewer vertical pixels. As a rule of thumb,

the maximum signal of a given spectrum should be in the range of 10 to 90 per cent of the full well capacity. The full well capacity often equals the full-scale range of the A/D converter in the CCD electronics, so a signal in the range of 10 to 90 per cent of full scale will generally be large enough to exceed readout and dark noise but small enough to avoid saturation. The extremes of integration time are illustrated in Figure 8.39. The intensity scales are quite different for the three spectra in order to compare them visually. For a short integration time, the SNR is low due to significant shot noise and readout noise. For the 15 sec integration, the full well capacity was exceeded, and the larger peaks are truncated.

Processing of the raw spectrum following CCD acquisition was discussed in Section 8.5.3 but is summarized graphically in Figure 8.40 for a solution of sucrose. The raw spectrum is $\gamma S'(i)$, as given by Equation 8.14, and is shown in figure 8.40A. Subtraction of the bias and dark contributions described in Section 8.5.3 yields Figure 8.40B, governed by:

$$\gamma S' = \gamma P_D \beta D K A \Omega T Q t_M \tag{8.17}$$

The bias and dark contributions in this case are fairly small (about 1000 e^-), hence the small offset between spectra A and B. To correct for CCD gain and quantum efficiency, as well as other instrumental variables, the

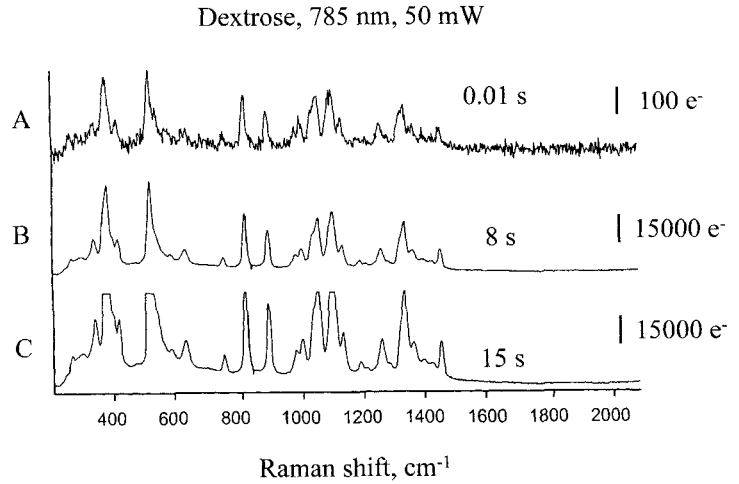

Figure 8.39. Raman spectra of solid dextrose obtained at 785 nm (50 mW) and a dispersive/CCD spectrometer, with a range of integration times. Note the large change of intensity scale between spectra A and B. The short integration time (0.01 sec) yields poor SNR, while the long integration time (15 sec) yields truncated peaks.

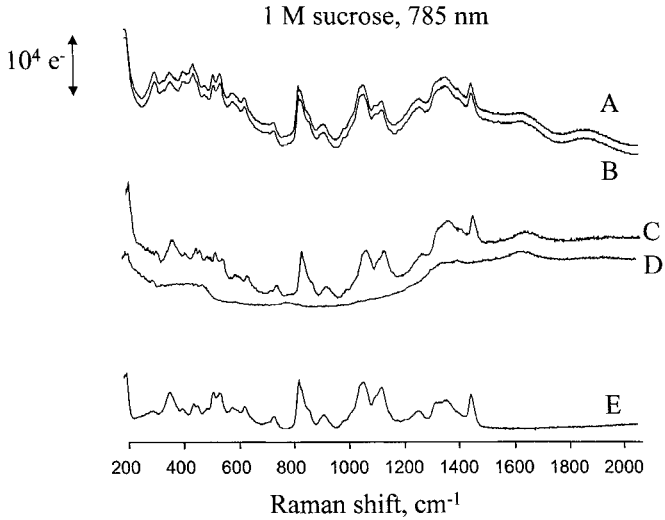

Figure 8.40. Spectra of sucrose solution illustrating several processing steps: A is the raw spectrum of 1 M sucrose in water in a quartz cuvette; B is after the ~1000 e^- bias and dark signal was subtracted; C is after the instrument response correction (described in detail in chapter 10); D is the water/cuvette background after the same processing steps; E is spectrum C minus spectrum D, and is the final spectrum after bias, dark, response, and background corrections.

product $KA\Omega TQ/\gamma$ may be determined with a standard source as outlined in Section 10.3. This instrument response correction yields spectrum C of Figure 8.40 in which the effects of Q variation as well as spectrometer transmission have been removed. Notice that some features (such as the broad band at ~1900 cm^{-1}) are due to the instrument rather than the sample, and such artifacts are removed by the response correction. The final step of Figure 8.40 illustrates background subtraction in which the contribution from the cell and water are subtracted, based on a separate spectrum acquired from a blank solution (spectrum 8.40D). It is important that both sample and background be acquired under identical conditions of laser power, sampling geometry, and the like, and that both be subjected to the same response correction. The operations that lead to the bias, dark, response, and background-corrected spectrum of Figure 8.40 are often automated in the instrument's software and may be performed routinely.

8.6.3. Segmented Acquisition

As described in Section 8.2.1.1, there is a trade-off between resolution and spectral coverage for a dispersive CCD spectrometer. For a given grating

position and CCD acquisition, the finite number of CCD pixels means that one can either obtain a wide spectral range with relatively low resolution or a limited spectral range at high resolution, but not both at once. Several methods for mitigating this trade-off are discussed in this and the following two sections, all of which are implemented in commercial spectrometers. The methods are based on segmented acquisition, multitrack acquisition, and scanning/multichannel operation.

Segmented acquisition involves acquisition of several spectra with limited coverage, then combination to form a complete spectrum. For example, the grating is positioned to observe the 100 to 900 cm^{-1} Raman shift range on the CCD, and a spectrum is acquired as described in Section 8.6.2. Then the spectrum is stored and the grating repositioned to acquire the 900 to 1700 cm^{-1} range. The process is repeated until the desired total spectral range is acquired; then the segments are combined to arrive at a complete spectrum. Any number of segments may be combined in this fashion, but the practical range is 2 to about 10. Segmented acquisition has the advantage of improving resolution in that each pixel collects a smaller Raman shift range than if the entire spectrum were collected in one CCD acquisition. The price of this advantage is time, as the total acquisition time increases by a factor equal to the number of segments, plus the time required to reposition the grating. An example of a segmented spectrum is shown in Figure 8.41A, with the vertical arrows indicating the locations of segment boundaries.

The discontinuities between segments apparent in Figure 8.41A are caused by variations in transmission and focusing across the CCD detector. The upper Raman shift limit for one segment is nearly the same as the lower limit for the adjacent segment, but they are acquired from different ends of the CCD, with slightly different optical geometry and focus. Such discontinuities are most apparent when there is a significant broad baseline or when a segment boundary occurs on a Raman peak. Segments may be "combined" mathematically by some smoothing routine, but such a procedure is nonrigorous and can distort spectroscopic information. Some instruments combine the segments by overlapping a portion of each segment with adjacent spectra, then averaging the overlapped regions. An example is shown in Figure 8.41B for which the overlap was about 50 pixels out of a total of 2000. This procedure improves the accuracy of the multisegment spectrum, but there still are baseline shifts and peak height variations caused by variations in spectral response across the segments.

A rigorous means for removing discontinuities between segments is the use of luminescent standards described in Section 10.3. The standard has a known emission spectrum, which is recorded with the same set of segments as the Raman spectrum of interest (34). The standard emission experiences the same response variations as the Raman scattering, so its spectrum includes the same

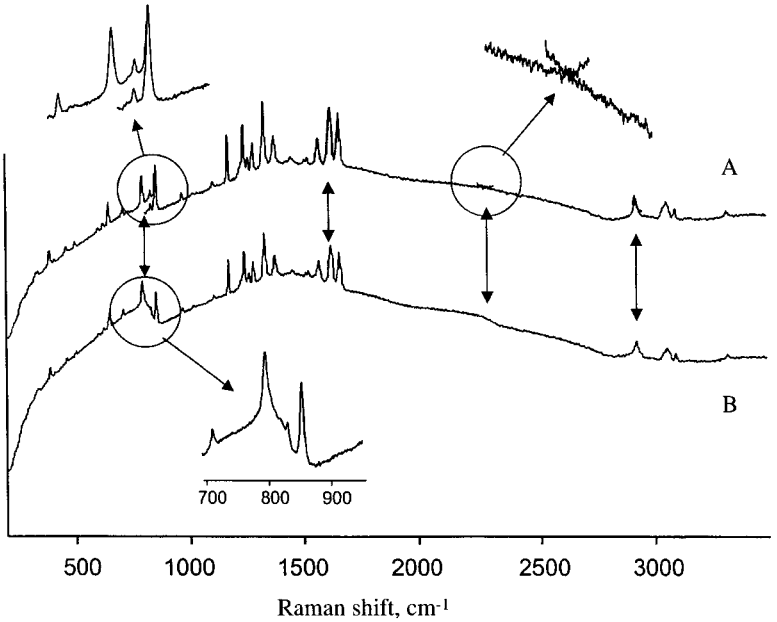

Figure 8.41. Spectra of an aged, impure acetaminophenol tablet, obtained by combining five CCD acquisitions into a single, wide-band spectrum. Vertical arrows indicate Raman shifts where spectral segments were spliced. In spectrum A, the segments were merely superimposed, and the slight overlaps between segments are apparent in the magnified insets. In spectrum B, the overlap regions were averaged and replotted. Some distortion of the spliced region near 825 cm^{-1} remains after averaging.

optical aberrations. Figure 8.42 compares the raw spectrum of Figure. 8.41A with a spliced spectrum resulting from an average of overlapping regions (spectrum 8.41B) and with a spliced spectrum corrected with a luminescent standard. In principle, the luminescent standard should provide accurate correction regardless of the acquisition procedure, since the response function of the instrument is applied to both sample and standard spectra. As is apparent from the insets of Figure 8.42, the luminescent standard provides smooth and accurate combination of segments and also corrects for the overall instrument response function (see Section 10.3.3 for details).

8.6.4. Multitrack Acquisition

The discussion of dispersive CCD spectrometers presented thus far has considered the CCD to be one dimensional, with N_C pixels along the wavelength axis. The vertical (slit) axis of the CCD is usually binned into one (or a few)

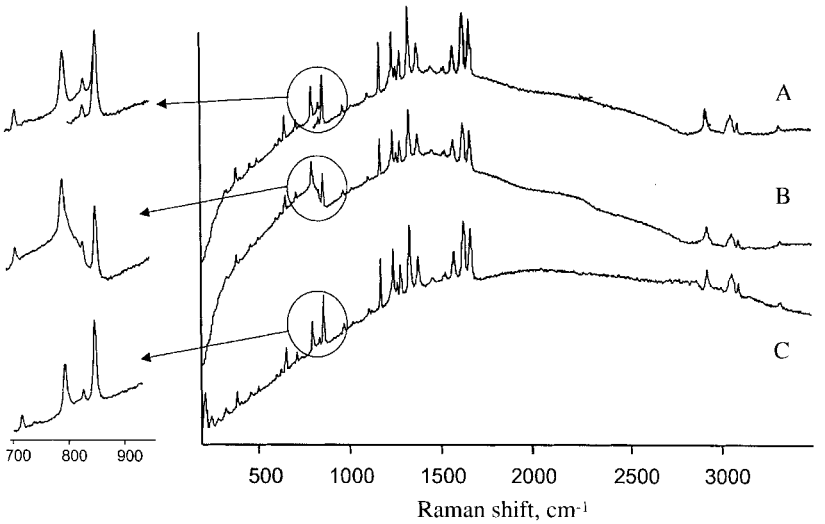

Figure 8.42. Elimination of splicing artifacts with an intensity standard. Spectra A and B are from Figure 8.41, but *C* was obtained by applying an instrument response function correction (with Coumarin 540a as described in Section 10.3.3). The magnified insets for the region near 825 cm^{-1} show the lack of distortion compared to an uncorrected or averaged splice.

"superpixels" to yield a $1 \times N_C$ detector. Multitrack acquisition exploits the two-dimensional nature of CCDs by using the ability to monitor the vertical pixels individually or in groups. This results in two or more *tracks* across the face of the CCD, which may be digitized independently. Multiple tracks may be used to acquire spectra from more than one source or to simultaneously monitor several spectral segments.

8.6.4.1 Multiple Input Sources

As discussed in Section 8.2, an imaging spectrograph maintains the slit image during dispersion and focusing, so a single point on the entrance slit corresponds to a single point on the CCD. If two or more optical fibers carry the Raman light to the entrance slit, the ends of these fibers will be imaged on the CCD. Each fiber's light is also dispersed along the wavelength axis, so each fiber image becomes a spectrum that may be projected onto a CCD track. The image on the CCD is presented schematically in Figure 8.43. In this case, four spectra may be collected simultaneously, and the binning parameters are set to digitize and store the four spectra independently. As described in Chapter 12, fiber optics may be used to carry Raman light over long distances (>100 m), so a multitrack spectrometer could simultaneously acquire spectra from widely separated samples.

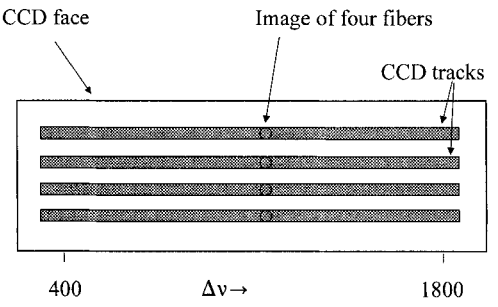

Figure 8.43. Depiction of multitrack image on a CCD. Four optical fibers at the entrance slit are imaged on four different vertical positions, and their light is dispersed horizontally.

8.6.4.2 Simultaneous Multiple-Segment Acquisition

Instead of monitoring multiple samples, multitrack operation may also be used to monitor a single sample over different Raman shift ranges. The simplest example involves two tracks that cover different halves of the Raman shift range. By using two gratings with different angles, or a highly modified single grating, it is possible to disperse the 0 to 1800 cm^{-1} Raman shift range onto the upper half of the CCD, and the 1800 to 3600 cm^{-1} range onto the lower half. This arrangement avoids the sequential acquisition of segments and associated mechanical operations. Since the spectrograph and CCD have no moving parts, the system is rugged and stable.

A sophisticated variation of this approach employs holographic optics to create a grating with two focal planes and dispersion ranges. Since the dispersion process is encoded in the grating holographically, the entire grating area is used for both tracks, and the Ω of the system is maintained. In principle, one retains the signal magnitude and resolution of the single-track holographic spectrometer with the significant bonus of twice the spectral coverage (1).

Dispersive Raman spectrometers based on echelle spectrographs are examples of the multitrack approach applied more extensively (35). An echelle spectrograph separates the spectrum into many more than two segments, in the range of 8 to 20; then these segments are monitored individually by a CCD track. For example, if a 3600 cm^{-1} spectrum is divided into 10 segments on a 256 × 1024 CCD, then each 360 cm^{-1} spectrum is monitored by a 20 (approximately) × 1024 pixel detector. The spectrum may be collected with high resolution, since each pixel covers only ~0.3 cm^{-1} of Raman shift range. In effect, the CCD is converted to a 10,240-pixel detector, with a height of 20 pixels. The advantage is the ability to achieve wide spectral coverage and high resolution simultaneously. Provided the sample image is fairly short (20 pixels × 25 μm/pixel = 500 μm in the example), the echelle signal will be

as large as that from a single-track instrument which covers only 360 cm^{-1}. Like the holographic system, the echelle has no moving parts and is relatively rugged.

Echelle spectrographs have been used extensively in astronomy and atomic spectroscopy (36), and a few applications in Raman have been reported (35). All echelles have a grating that operates in a high order to achieve low reciprocal linear dispersion [according to Eq. (8.3)] and therefore disperses a relatively small Raman shift range over a typical CCD. However, this leads to overlapping orders in which the spectral segments are superimposed on each other at the detector. A cross disperser (a second grating or a prism) is added to spread the orders out vertically on the CCD. The result is 8 to 20 stripes on the CCD, each representing a different Raman shift segment (and a different diffraction order). The grating line densities for the echelle and cross disperser are chosen to match the laser and Raman shift range of interest.

Throughput for different orders and within one order (or segment) can vary significantly, so a response function calibration is important. In addition, a wavelength calibration is essential, often using an atomic line source as described in Chapter 10. An echelle spectrometer has been described for Raman spectroscopy with a 514.5 nm laser (35). Full spectral widths of 5000 cm^{-1} were collected with 2 cm^{-1} resolution on a 516 × 516 pixel detector. If a single track were used, the best resolution possible would be $2500/516 = 5$ cm^{-1}. Spectra from this instrument are shown in Figure 8.44 and demonstrate the wide coverage and high resolution.

Many Raman experiments involve fairly tightly focused lasers, so the image of the sample on the slit is often quite small. The restriction of an echelle to relatively small slit height does not impose a significant constraint for such systems. Fiber-optic coupling is an example where the "sample" at the slit is a 50 to 200 μm fiber, and the fiber image may be separated effectively into 8 to 20 tracks. However, if the sample image is higher, the tracks will overlap or the slit height must be restricted. For example, the cylindrical lens geometry of Figure 6.17 can produce a 50 × 3000 μm laser stripe on the sample, which is too large to collect with an echelle system. Stated more generally, a multitrack system has a smaller $A\Omega$ product than a single-track spectrometer since the photosensitive area for a given wavelength is smaller.

8.6.5. Scanning Multichannel Acquisition

As the heading implies, acquisition methods discussed in this section involve hybrids of multichannel and scanning techniques. Physically, they amount to a CCD on a scanning monochromator without an exit slit. As such, they are quite

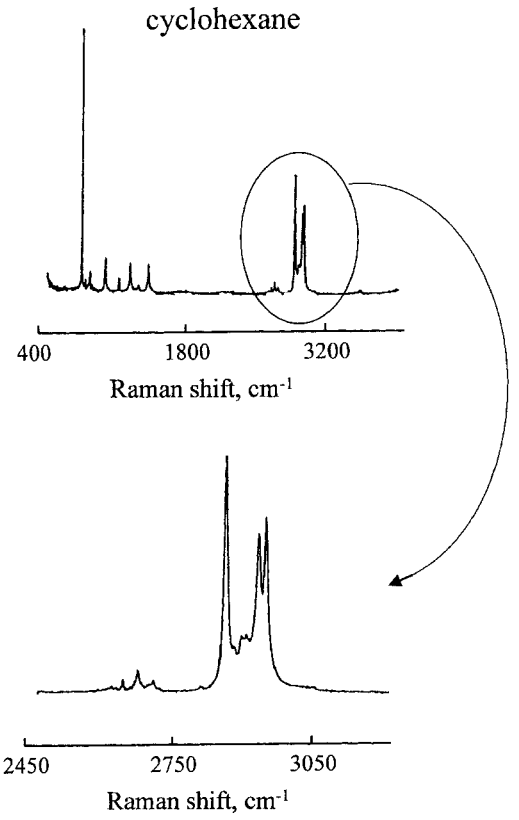

Figure 8.44. Spectrum of cyclohexane obtained with an echelle spectrograph and one CCD exposure. Magnified spectrum demonstrates high spectral resolution. (Adapted from Reference 35 with permission.)

similar to the spectrograph/CCD combinations used for static multichannel acquisition (Section 8.6.2). The difference arises in how grating motion is combined with CCD acquisition and readout. In standard multichannel acquisition with a dispersive/CCD system, the grating is moved only to vary the spectral range and remains static during spectral acquisition. The resolution and spectral range are determined by the dispersion, CCD size, number of pixels, and so forth, as discussed earlier in this chapter. In scanning/multichannel acquisition, the grating is repositioned over a predetermined spectral range *during* acquisition, either in steps or continuously. By synchronizing grating motion and CCD readout, a wide spectral range may be covered without sacrificing resolution. In addition, certain benefits result involving fixed pattern noise, lineshape, and response uniformity.

The first scanning/multichannel acquisition technique (SMT) is essentially an extension of segmented acquisition (Section 8.6.3), but with a very important difference (37). Like segmented acquisition, the grating is stationary during CCD acquisition and readout and is incremented between a series of acquisitions. However, the increment is quite small, possibly less than 1 pixel, and the spectral segments are severely overlapped. As the series of CCD exposures is collected, a given Raman band moves across the CCD, and a particular Raman shift value is observed many times by many different pixels. After the entire spectral range is scanned, the stored CCD exposures are reconstructed into a spectrum by the computer, which had kept track of the wavelength and pixel locations. It is true that the total acquisition time lengthens due to multiple CCD exposures, but this factor is largely mitigated by the overlapping segments. Ignoring the overhead associated with CCD readout, the total acquisition time for SMT is comparable to the same spectral range observed with segmented acquisition. The real cost in terms of SNR is the extra readout noise from the greater number of CCD readouts, which might be serious for weak spectra.

The benefits of this SMT technique can be significant for certain applications. First, a wide spectral range may be covered without the "splicing" illustrated in Figures 8.41 and 8.42. If a grating yielding a narrow spectral range (for a single CCD exposure) is combined with a large number of acquisitions, a wide total spectral range may be observed with high resolution. Like multisegment acquisition, SMT avoids the resolution/spectral coverage trade-off, but with the cost of increased total acquisition time. Second, the spectrum is essentially "swept" over the entire CCD, so variations in either throughput or pixel sensitivity are averaged out. A particular Raman shift is observed at many positions, and the resulting intensity is spatially averaged over the entire CCD. Third, small grating increments may be used to increase the data density and improve the accuracy of the lineshape of narrow Raman bands. For example, a typical static dispersive/CCD system may operate with a dispersion of 2 cm^{-1}/pixel, and a fairly narrow Raman band (say, 10 cm^{-1}) may have only 5 pixels that define its shape. With SMT, a 1 cm^{-1} increment between acquisitions will provide effectively 10 pixels to define the same band. Early work on the SMT approach demonstrated excellent resolution and lineshapes for rotational fine structure bands with linewidths of $\sim$0.5 cm^{-1} (37).

The practice of synchronizing grating motion with CCD readout is carried a significant step further in the "continuous extended scanning" approach (38), which has been implemented in a commercial instrument (39). The grating is scanned continuously during CCD readout such that a given wavelength is scanned across the CCD, synchronously with the shifting of the pixels collecting light from that wavelength. For longer integration times, the scan

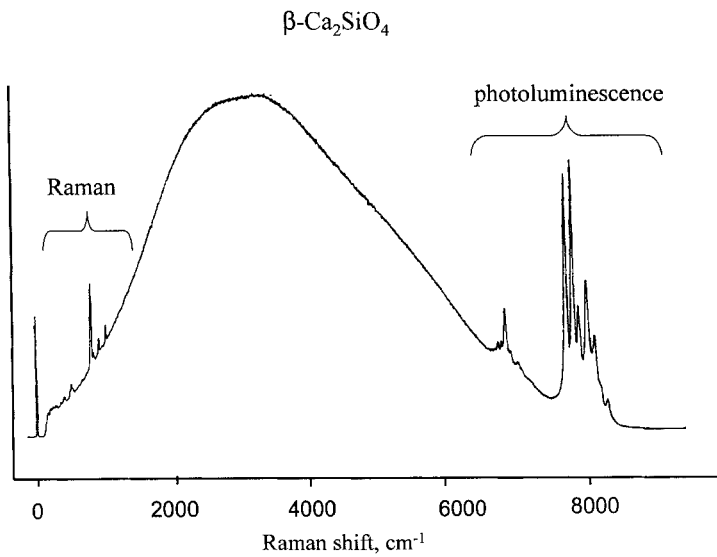

Figure 8.45. Spectrum of calcium silicate obtained with the scanning multichannel technique. A very wide shift range was covered during continuous grating scanning and CCD readout. The features at 6000 to 9000 cm^{-1} are due to photoluminescence, not Raman scattering. (Adapted from Reference 38.)

occurs more slowly, but CCD readout and grating motion are still synchronized. A given wavelength is effectively monitored by all of the CCD pixels along the spectral axis, thus averaging out sensitivity variations. A wide spectral range may be covered without splices, but with an increase in time comparable to that of segmented multichannel acquisition. Furthermore, light of a given Raman shift is read out only once, so readout noise does not accumulate as it does for the multiple readouts of SMT. Figure 8.45 shows a very wide band spectrum of calcium silicate obtained with the continuous extended scanning technique, which shows both Raman (0 to 3000 cm^{-1}) and photoluminescence (~8000 cm^{-1}) features. Note the absence of discontinuities from splicing, which would occur in an uncorrected segmented spectrum such as that of Figure 8.41A.

8.7. EXAMPLES OF DISPERSIVE RAMAN APPLICATIONS

In this and several subsequent chapters, a short list of applications is presented, along with a few experimental details and comments. The available array of applications from the literature is very large, and the lists presented are not intended to be comprehensive. Their purpose is merely to provide examples

Table 8.7. Examples of Dispersive Raman Application

Laser Wavelength (nm)	Application	Reference
217–450	Trace aromatic hydrocarbons	40
255	Aromatic hydrocarbons in coal liquids	41
257.3	Amino acids, myoglobin	42
418.5	Bacteriochlorophyll	43
457.9–514.5	Resonance Raman of Fe^{III} and Ru^{III} complexes	44
457.9–647.1	Metal/ammine complexes in metal refining	45
488 nm	Amorphous carbon films	46
514.5	Database of minerals and inorganic crystals	47
514.5	Glucose in serum and plasma (anti-Stokes)	48
514.5	Li intercalation in graphite, *in situ*	49
514.5	Postconsumer plastics identification	50
514.5	Vapor-deposited diamond film characterization	51
514.5, 632.8	β-Carotene, related polyenes	52
532, 355	*In situ* Vapor deposited diamond	53
632.8	Temperature measurement of polyethylene, methyl cyclohexane	54
647	Aviation turbine fuel composition	55
780	Naphthalene, phenyl triethoxysilane	56
785	Noninvasive identification of pharmaceuticals	57
785	Human tissue biopsy samples	58, 59
830	Human tissue, elastin, coronary artery	60
Various	Dispersive Raman spectroscopy applications in microscopy and imaging	Table 11.3
Various	Applications of dispersive Raman coupled with fiber-optic sampling	Table 12.4
Various	Dispersive Raman applications for surface analysis	Table 13.6

and illustrate some analytical situations where the techniques described in the relevant chapter are useful. Table 8.7 lists some applications of dispersive Raman spectroscopy, without the fiber-optic or microscope attachments described later. The list is not prioritized but is organized in terms of laser wavelength.

REFERENCES

1. J. D. Ingle and S. R. Crouch, *Spectrochemical Analysis*, Prentice-Hall, Englewood Cliffs, NJ, 1988, p. 67ff.
2. J. D. Ingle and S. R. Crouch, *Spectrochemical Analysis*, Prentice-Hall, Englewood Cliffs, NJ, 1988, p. 69.

3. J. D. Ingle and S. R. Crouch, *Spectrochemical Analysis*, Prentice-Hall, Englewood Cliffs, NJ, 1988, p. 54.
4. R. T. Packard and R. L. McCreery, *Anal. Chem.*, **59**, 2631 (1987).
5. R. L. McCreery, in J. J. Laserna, ed., *Instrumentation for Dispersive Raman Spectroscopy*, Wiley, New York, 1996, pp. 41–72.
6. B. Yang, M. D. Morris, and H. Owen, *Appl. Spectrosc.*, **45**, 1533 (1991).
7. J. Williamson, R. Bowling, and R. L. McCreery, *Appl. Spectrosc.*, **43**, 372 (1989).
8. Y. Wang and R. L. McCreery, *Anal. Chem.*, **61**, 2647 (1989).
9. M. Carraba, K. Spencer, C. Rich, and D. Rauh, *Appl. Spectrosc.*, **44**, 1558 (1990).
10. M. J. Pelletier and R. C. Reeder, *Appl. Spectrosc.*, **45**, 765 (1991).
11. C. Schoen, S. K. Sharma, C. Helsley, and H. Owen, *Appl. Spectrosc.*, **47**, 305 (1993).
12. J. Tedesco, H. Owen, D. M Pallister, and M. Morris, *Anal. Chem.*, **65**, 441A (1993).
13. P.-T. Chou, S. L. Studer, and M. Martinez, *Appl. Spectrosc.*, **45**, 513 (1991).
14. J. Klemeyer, J. Fister, J. Zimmerman, and J. Harris, *Appl. Spectrosc.*, **50**, 1597 (1996).
15. K. F. Wall and R. K. Chang, *Optics Lett.*, **11**, 493 (1986).
16. M. Pelletier, *Appl. Spectrosc.*, **46**, 395 (1992).
17. R. Indralingam, J. B. Simeonsson, G. A. Petrucci, B. W. Smith, and J. D. Winefordner, *Anal. Chem.*, **64**, 964 (1992).
18. A. Schulte, T. J. Lenk, V. M. Hallmark, and J. Rabolt, *Appl. Spectrosc.*, **41**, 721 (1987).
19. A. Schulte, *Appl. Spectrosc.*, **46**, 891 (1992).
20. M. Kagan and R. L. McCreery, *Anal. Chem.*, **66**, 4159 (1994).
21. P. M. Epperson and M. B. Denton, *Anal. Chem.*, **61**, 1513 (1989).
22. J. D. Ingle and S. R. Crouch, *Spectrochemical Analysis*, Prentice-Hall, Englewood Cliffs, NJ, 1988, pp 141–144, pp. 514–404.
23. B. Koren and M. Szawlowski, *Laser Focus World*, **November**, 71 (1998).
24. S. Vasile, P. Gothoskar, R. Farrell, and D. Sdrulla, *IEEE Trans. Nucl. Sci.*, **45**, 720 (1998).
25. R. T. Packard and R. L. McCreery, *J. Phys. Chem.*, **92**, 6345 (1988).
26. J. V. Sweedler, K. L. Ratzlaff, and M. B. Denton, *Charge Transfer Devices in Spectroscopy*, VCH, New York, 1994, Chapters 2 and 3.
27. P. M. Epperson, J. V. Sweedler, R. B. Bilhorn, R. G. Sims, and M. B. Denton, *Anal. Chem.*, **60**, 327A (1988).
28. J. V. Sweedler, R. B. Bilhorn, P. M. Epperson, G. R. Sims, and M. B. Denton, *Anal. Chem.*, **60**, 282A (1988).
29. W. P. Acker, B. Yip, D. H. Leach, and P. K. Chang, *J. Appl. Phys.*, **64**, 2263 (1988).
30. G. R. Philips and J. M. Harris, *Anal. Chem.*, **62**, 2351 (1990).

31. W. Hill and D. Rogalla, *Anal. Chem.*, **64**, 2573 (1992).
32. H. Takeuchi, S. Hashimoto, and I. Harada, *Appl. Spectrosc.*, **47**, 129 (1993).
33. R. L. McCreery and R. T. Packard, *Anal. Chem.*, **61**, 775A (1989).
34. K. G. Ray and R. L. McCreery, *Appl. Spectrosc.*, **51**, 108 (1997).
35. M. J. Pelletier, *Appl. Spectrosc.*, **44**, 1699 (1990).
36. J. D. Ingle and S. R. Crouch, *Spectrochemical Analysis*, Prentice-Hall, Englewood Cliffs, NJ, 1988, pp 76 ff.
37. V. Deckert and W. Kiefer, *Appl. Spectrosc.*, **46**, 322 (1992).
38. C. Dyer and B. J. E. Smith, *J. Raman Spectrosc.*, **26**, 777 (1995).
39. Renishaw plc, Wotton-under-Edge, Gloucestershire, UK.
40. S. A. Asher, *Anal. Chem.*, **56**, 720 (1984).
41. S. A. Asher and C. R. Johnson, *Science*, **225**, 311 (1984).
42. C. R. Johnson, M. Ludwig, S. O'Donnell, and S. A. Asher, *J. Am. Chem. Soc.*, **106**, 5008 (1984).
43. Y. Misono, L. Limantara, Y. Koyama, and K. Itoh, *J. Phys. Chem.*, **100**, 2422 (1995).
44. C. Jones, C. Johnson, S. A. Asher, and R. E. Shepherd, *J. Am. Chem. Soc.*, **107**, 3772 (1985).
45. K. J. Schmidt, K. H. Michaelian, and G. R. Loppnow, *Appl. Spectrosc.*, **53**, 139 (1999).
46. B. Marcus, L. Fayette, M. Mermoux, L. Abello, and G. Lucazeau, *J. Appl. Phys.*, **76**, 3463 (1994).
47. A. Wang, J. Han, L. Gua, J. Yu, and P. Zeng, *Appl. Spectrosc.*, **48**, 959 (1994).
48. X. Dou, Y. Yamaguchi, H. Yamamoto, H. Uenoyama, and Y. Ozaki, *Appl. Spectrosc.*, **50**, 1301 (1996).
49. W. Huang and R. Frech, *J. Electrochem. Soc.*, **145**, 765 (1998).
50. V. Allen, J. H. Kalivas, and R. G. Rodriguez, *Appl. Spectrosc.*, **53**, 672 (1999).
51. L. Fayette, M. Mermoux, B. Marcus, F. Brunet, P. Germi, M. Pernet, L. Abello, G. Lucazeau, and J. Garden, *Diamond Relat. Mater.*, **4**, 1243 (1995).
52. S. F. Parker, S. M. Tavender, N. M. Dixon, H. Herman, K. P. J. Williams, and W. F. Maddams, *Appl. Spectrosc.*, **53**, 86 (1999).
53. M. Mermoux, L. Fayette, B. Marcus, N. Rosman, L. Abello, and G. Lucazeau, *Phys. Status Solidi A*, **154**, 55 (1996).
54. F. LaPlant, G. Laurence, and D. Ben-Amotz, *Appl. Spectrosc.*, **50**, 1034 (1996).
55. W. M. Chung, Q. Wang, U. Sezerman, and R. H. Clarke, *Appl. Spectrosc.*, **45**, 1527 (1991).
56. J.-C. Panitz, F. Zimmerman, F. Fischer, W. Häfner, and A. Wokaun, *Appl. Spectrosc.*, **48**, 454 (1994).
57. R. L. McCreery, A. J. Horn, J. Spencer, and E. Jefferson, *J. Pharm. Sci.*, **87**, 1, (1998).

58. C. J. Frank, R. L. McCreery, and D. C. B. Redd, *Anal. Chem.*, **67**, 777 (1995).
59. C. J. Frank, D. C. B. Redd, T. S. Gansler, and R. L. McCreery, *Anal. Chem.*, **66**, 319 (1994).
60. J. F. Brennan III, Y. Wang, R. R. Dasari, and M. S. Feld, *Appl. Spectrosc.*, **51**, 201 (1997).

Raman Spectroscopy for Chemical Analysis. Richard L. McCreery

ISBN: 0-471-25287-5

CHAPTER

9

NONDISPERSIVE RAMAN SPECTROMETERS

The relative merits of dispersive and nondispersive Raman spectrometers were introduced in Sections 5.1 and 5.3, and dispersive systems were addressed in some detail in Chapter 8. Nondispersive systems in the form of Fourier transform (FT)–Raman had a major impact on the increased interest in Raman as an analytical technique starting in 1986 (1–4). FT-Raman combined the low-fluorescence interference that commonly occurs with 1064 nm excitation with the highly developed instrumentation of FT infrared (FTIR) spectroscopy to yield a major increase in the utility of Raman spectroscopy. The broader applicability of Raman to industrial samples available with FT-Raman was partly responsible for the Raman renaissance, which is the main topic of this book. More recently, nondispersive wavelength analyzers have been combined with charge-coupled devices (CCDs) to provide new methods for Raman imaging (5), discussed in Chapter 11. In the current chapter, nondispersive spectrometers are discussed as a group, with particular strengths and weaknesses of each approach addressed in individual sections. The three main subsections are based on three distinct types of wavelength analyzers: filters, interferometers, and multichannel FT spectrometers.

9.1. TUNABLE BANDPASS FILTERS

Most implementations of filter-based nondispersive spectrometers occur in Raman microscopy and imaging, where their large clear aperture is particularly valuable. These applications are discussed further in Chapter 11, but the nature and performance of tunable filters as wavelength analyzers are outlined here.

9.1.1. Interference Filters

A narrow bandpass filter chosen to match a Raman band can serve as a very simple Raman spectrometer, provided only a limited range of Raman shifts is of interest. For example, a 900 nm bandpass interference filter transmits a band centered at 1627 cm^{-1} relative to a 785 nm laser. The center of the passband may be angle tuned over a limited range, and it is possible to construct a spectrum from several measurements of intensity vs. angle (6). However, the

bandpass of an interference filter is wide compared to most Raman features, so a spectral analysis based on such filters has inherently low resolution. For example, if Eq. (8.1) is applied at 900 nm, Eq. (9.1) results:

$$d\bar{\nu}(\text{cm}^{-1}) = 12.3 d\lambda(\text{nm}) \tag{9.1}$$

where $d\lambda$ is the filter bandpass in nanometers. A filter with $d\lambda = 2$ nm is exceedingly narrow for an interference filter and would have low transmission. Even this extreme case would have a bandpass of 24.6 cm^{-1} at 900 nm, and a low-resolution spectrum would result (such as that shown in the bottom spectrum of Fig. 5.18). So the tuning range is limited, and the resolution is poor for interference-filter-based wavelength analyzers, making them suitable only for special applications.

One such application is a dedicated quantitative analyzer that monitors only a few Raman shifts (using different filters) of anesthesia gases (7). In this case, the identity of the analyte is known and unvarying, so a spectrum is unnecessary. The Raman analyzer is built into a commercial anesthesia gas delivery system, and filters are selected to monitor particular gaseous components. Another application exploits the large aperture of interference filters for wavelength analysis in Raman microscopy (6). Several filters may be interchanged mechanically and each one may be angle tuned. The instrument is described in more detail in Section 11.4.2. An alternative to tuning the filter is to tune the laser frequency while keeping the filter passband fixed (8). As the excitation frequency is turned toward the blue, for example, the Raman shift transmitted by the filter increases.

9.1.2. Acousto-optic Tunable Filter (AOTF)

The AOTF is based on a completely different principle from interference filters and permits wavelength tuning over the entire Raman shift range (9,10). A schematic of an AOTF Raman spectrometer is shown in Figure 9.1, and the entire system has no moving parts. The AOTF element is a crystal of TeO_2, which is excited acoustically with an ultrasonic generator. The ultrasound establishes a standing-wave pattern of local refractive index in the crystal, whose wavelength is determined by the ultrasonic frequency. This standing-wave pattern acts as a diffraction grating, which is governed by the usual Bragg equation for the incident light. As shown in Figure 9.1, light entering the AOTF is diffracted in mainly $+1$, 0, and -1 orders, and the system may be optimized to concentrate ~80 per cent of the light into the $+1$ order. The light from the $+1$ order is then directed onto a single-channel detector such as a photomultiplier tube (PMT) or avalanche photodiode (APD) and monitored by a computer. The spectrum may be scanned merely by incrementally changing the ultrasonic frequency and recording intensity vs. frequency. Scanning the entire 0 to 3500 cm^{-1} shift range requires less than 1 sec for sufficiently

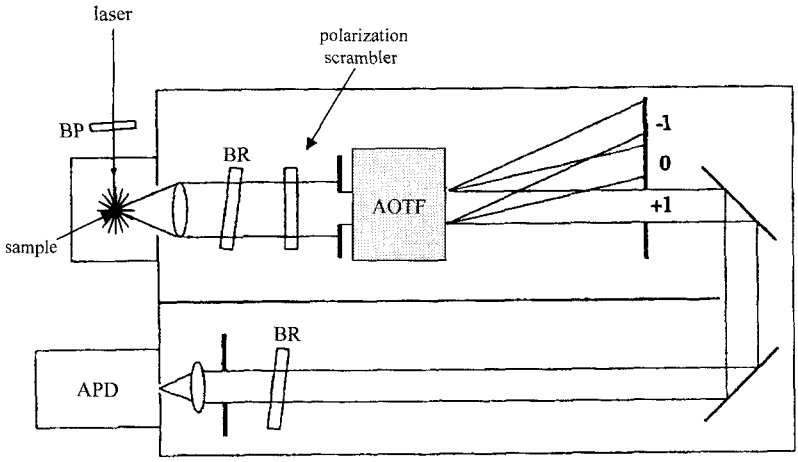

Figure 9.1. Schematic of Raman spectrometer based on an acousto-optic tunable filter (AOTF). BP, bandpass filter; BR, band reject filters; APD, avalanche photodiode. (Adapted from Reference 9, with permission.)

strong scatterers. In addition, the frequency may be switched rapidly among several Raman bands to provide near-simultaneous monitoring of several spectral features.

In addition to electronic tuning, the AOTF has the advantages of small size and high throughput. There is no slit, so the $A\Omega$ product is higher than that of a typical dispersive system. The spectrometer must be large enough to allow spatial separation of the +1 and 0 orders, but at least one working system has a footprint of 7 × 12 in. (9). The disadvantage of current AOTF systems is modest spectral resolution of 25 to 50 cm^{-1}, with a theoretical limit of $\sim$10 cm^{-1}. In addition, the AOTF is inherently a scanning system; hence it loses the multichannel and multiplex advantages of dispersive/CCD or FT-Raman spectrometers. An example of an AOTF Raman spectrum is shown in Figure 9.2. Overall, the AOTF achieves solid-state operation, compact size, and rapid scanning by sacrificing resolution and the multichannel advantage. Its major advantage over interference filters is its electronic tuning.

9.1.3. Liquid Crystal Filters

A third type of tunable filter that has been applied to Raman spectroscopy is a conceptual extension of the interference filter. A conventional dielectric interference filter transmits light most efficiently when Eq. (9.2) is satisfied (11):

$$2d(n^2 - \sin^2\theta)^{1/2} = m\lambda \tag{9.2}$$

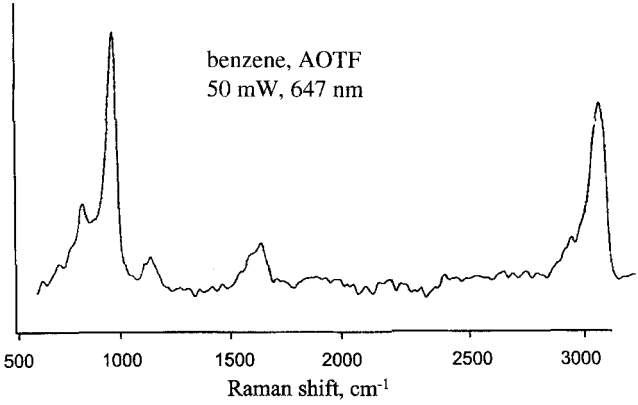

Figure 9.2. Spectrum of benzene obtained with AOTF spectrometer of Figure 9.1 (Adapted from Reference 9, with permission.)

where m is the order (1, 2, 3 . . .), λ the wavelength, n the refractive index of the medium between two partially reflective mirrors, d the distance between the mirrors, and θ the angle of incidence. The transmitted wavelength may be varied by angle tuning (θ), changing the spacing (d), or changing the refractive index (n). Liquid crystals have provided a means to vary the refractive index electronically, with a low-voltage, computer-controlled potential. Combination of two liquid crystal filters results in an electronically tunable bandpass filter with a bandpass of 11 to 14 cm^{-1}, a transmission of 60 to 70 per cent, and a tuning range sufficient to observe at least a 3000 cm^{-1} Raman shift range (12). While the spectral resolution of this liquid crystal filter is modest, its application to Raman microscopy has been demonstrated (12).

A different approach to liquid crystal filters led to the development of a nondispersive Raman spectrometer used commercially in a Raman microscope (13). Tunable liquid crystals are used to rotate light of particular wavelengths between crossed polarizers (5). The rotation is controlled by the applied voltage, and several stages are generally cascaded to provide a narrower bandpass. Current technology provides liquid crystal tunable filters (LCTFs) with a bandpass in the 7 to 9 cm^{-1} range, >6000 cm^{-1} spectral range relative to 532 nm, and relatively low transmission of 16 to 20 per cent (5). As with the other tunable filters described earlier, the LCTF is not intended for conventional Raman spectroscopy of a pure material or solution, since it does not enjoy a multichannel advantage and has modest resolution and transmission. However, the LCTF has excellent characteristics for Raman imaging, and some examples are presented in Section 11.4.2.

9.2. FOURIER TRANSFORM RAMAN SPECTROSCOPY

By far the most common type of nondispersive Raman spectroscopy is FT-Raman, and the importance of the approach has been noted several times in previous chapters. As discussed in Chapters 3 and 4, a major advantage of FT-Raman is the simultaneous monitoring of many wavelengths and the beneficial effects on signal and signal/noise ratio (SNR). FT-Raman is a multiplex technique in which many wavelengths are modulated by an interferometer to generate a complex "interferogram" that is monitored by a single detector. As noted earlier in Figure 5.2, the interferogram may be converted to a spectrum by a Fourier transform, hence the name *FT-Raman* (1–4, 14–18). The process of multiplexing is analogous to encoding and decoding in which a particular wavelength is encoded as a relatively low-frequency sine wave by the interferometer, then decoded by the computer. The interferometer has the effect of downshifting the light frequency ($\sim 10^{14}$ Hz) to a low frequency (several kilohertz), which may be monitored electronically. Each wavelength has a different modulation frequency, so the spectral information is retained in the interferogram. The benefit of multiplexing is the detection of all wavelengths simultaneously, so the total optical signal reaching the detector may be increased above detector noise. Some additional advantages and shortcomings of FT-Raman are discussed later in the chapter.

9.2.1. FT-Raman Principles

A schematic drawing of an FT-Raman spectrometer is shown in Figure 9.3. The wavelength analyzer is a Michelson interferometer adapted from an FT-IR spectrometer. FTIR was developed to a high level of refinement before FT-Raman was introduced in 1986, and many components were transferred from FTIR to FT-Raman with minor modification. Many vendors offer FT-Raman attachments to otherwise conventional FTIR spectrometers, so that both techniques share the same interferometer. Dedicated FT-Raman spectrometers are also available but still share many components with FTIR systems.

Interferometer operation is discussed in many texts (4,11) and will be described here only briefly. Modulation of a particular wavelength is accomplished by linear motion of the moving mirror in Figure 9.3 at a constant velocity. The two light paths shown in the figure (path a and b) differ in path length by $2x$, where x is the mirror travel from the point where a and b are of identical lengths. The beamsplitter is 50 per cent reflective; so the two light paths have equal intensity when they recombine after reflection from the moving (path a) or fixed (path b) mirrors. For the light directed toward the detector, there is a path length difference given by:

$$a - b = 2x \tag{9.3}$$

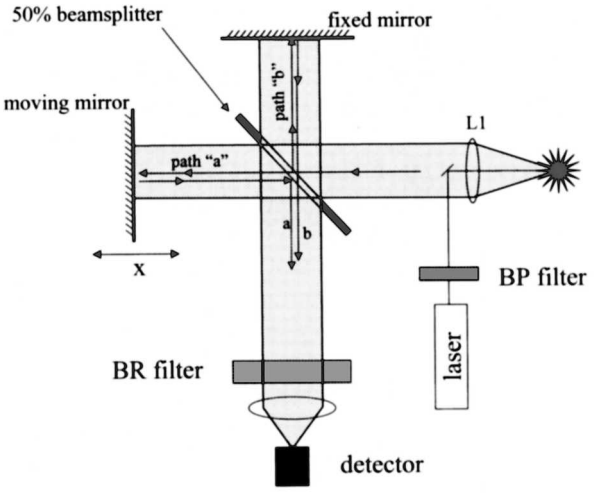

Figure 9.3. Schematic of FT-Raman spectrometer based on a Michelson interferometer: x is the moving mirror displacement, a and b describe two different paths of light split by the beamsplitter.

With motion of the moving mirror, the two beams undergo constructive and destructive interference, so that the detector signal will be maximum when $2x = m\lambda$ (m is an integer) and a minimum when $2x = (m + 1/2)\lambda$. For a single input wavelength, the detector output is a sine wave of the form:

$$\text{signal}(x) = A \cos \frac{(4\pi x)}{\lambda} = A \cos(4\pi x \bar{\nu}) \tag{9.4}$$

Assuming the mirror velocity is constant, equal to Γ (centimeters per second), then $x = \Gamma t$, and

$$\text{Signal}(t) = A \cos(4\pi \Gamma \bar{\nu} t) \tag{9.5}$$

where $\bar{\nu}$ is the wavenumber of the incident light (19). For example, a Raman feature with $\Delta\bar{\nu} = 1500$ cm^{-1} has an absolute $\bar{\nu}$ of 7898 cm^{-1} when observed with a 1064 nm laser. For a mirror velocity of 0.1 cm/sec, the detector signal for this feature would have a frequency of $2\Gamma\bar{\nu}$ or 1580 Hz. So the very high optical frequency of the Raman scattering (2×10^{14} Hz) has been converted to 1580 Hz, which is easily monitored electronically. The detector output is monitored with an analog-to-digital (A/D) converter and computer, then stored for subsequent analysis.

When many wavelengths are present in the input spectrum, the interferogram is a sum of many sine waves of different frequency and phases. An example is shown in Figure 9.4A, for the Raman scattering from cyclohexane.

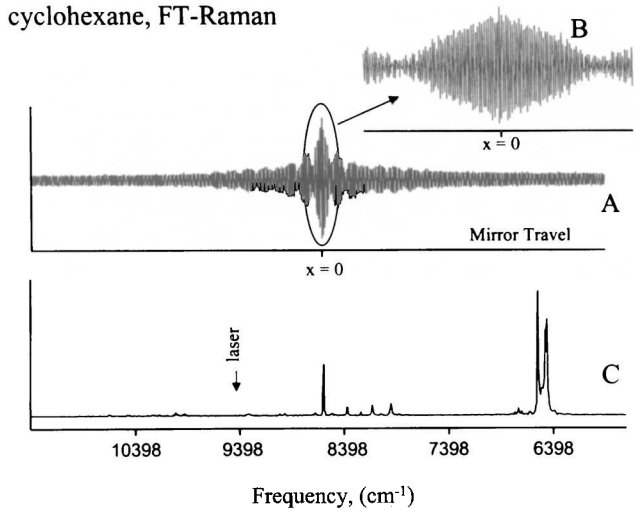

Figure 9.4. Interferogram (spectrum A) and its expansion (b) obtained from cyclohexane excited at 1064 nm. The Raman spectrum resulting from Blackman-Harris apodization (4-term), 2 × zero filling and Fourier transformation is shown as spectrum C, plotted against the absolute wavenumber rather than Raman shift.

The *center-burst* at $x = 0$ corresponds to zero path length difference, where all wavelengths constructively interfere. Magnification of the center burst region (Fig. 9.4B) shows the complex oscillations characteristic of the raw interferogram. Even a simple spectrum generates a fairly complex interferogram that is uninterpretable without Fourier transformation. There are several data processing steps between the interferogram and the spectrum, including apodization, zero-filling, phase correction, and Fourier transformation, but these are generally automated within the spectrometer software. The Raman spectrum resulting from Figure 9.4A is shown in 9.4C, obtained with a Bruker IFS/66 spectrometer, 245 mW of 1064 light at sample.

Of fundamental importance to FT-Raman performance is the relationship between mirror travel and resolution. The precision with which a sine wave frequency may be determined increases as the number of wave periods increases, for reasons ultimately related to the uncertainty principle. The longer the mirror travel, the more periods are observed, and the greater the precision. Increased precision takes the form of higher resolution and smaller instrumental linewidth. Mathematically, the resolution of an interferometer, $\delta\bar{\nu}$, is related to the maximum mirror travel, $\Delta x_{\max}$, according to Eq. (9.6) (20):

$$\delta\bar{\nu} = 1/(\Delta x_{\max}) \tag{9.6}$$

For example, 0.1 cm^{-1} resolution is attainable with 10 cm of mirror travel. Spectral coverage in FT-Raman is determined by the optical materials used for the beamsplitter and other components and by the rate of digitization of the interferogram. The Nyquist criterion dictates that a sine wave must be sampled at least twice per cycle to accurately define its frequency. If a sampling rate lower than the Nyquist criterion is used, the frequency in question will appear at an incorrect position on the frequency axis after Fourier transformation. This error is known as *aliasing* and is easily avoided by using sufficiently fast analog-to-digital converters or slow mirror velocities.

Since sampling rate and mirror travel are controlled independently in FT-Raman, there is no trade-off between resolution and spectral coverage, as there is with dispersive/CCD spectrometers (Section 8.2.1.1). Assuming sufficient sampling rate, any Δx_{max} yields complete spectral coverage, and the resolution may be improved independently by increasing mirror travel up to the limits of the instrument. Long mirror travel does generate a large number of data points, but this issue is minor with modern computers. The ability to freely vary resolution while maintaining full spectral coverage is a major attraction of FT-Raman spectrometers compared to dispersive/CCD systems.

9.2.2. FT-Raman Advantages and Pitfalls

The nearly total conversion from dispersive infrared spectrometers to FTIR instruments occurred because of some inherent advantages of the FT approach, some of which also apply to Raman spectroscopy. Already noted is the multiplex (Felgett) advantage in which many wavelengths are detected simultaneously. For the common case of detector noise limited operation, the multiplex advantage leads to an SNR improvement governed by Eq. (4.37). The SNR expressions derived in Chapter 4 relate to the SNR observed for particular resolution elements and are governed by the signal collected in each such element. A higher resolution spectrum results in fewer photons collected per resolution element, hence lower SNR. Partly for this reason, FT-Raman acquisition is usually stated in terms of the number of interferometer scans added together before the Fourier transformation. A *scan* is defined as one excursion to the maximum mirror displacement, Δx_{max}. At higher resolution, each scan requires more time, since Δx_{max} is larger according to Eq. (9.6). Figure 9.5 shows the improvement in SNR with the number of scans when operating at fixed resolution (and therefore fixed mirror travel). In this case, the SNR is proportional to the square root of the number of scans (and to the square root of the total measurement time), since the resolution is constant. Figure 9.6 shows the decrease in SNR for fixed measurement time as the resolution is improved, since each resolution element is collecting fewer photons. The dependence of SNR on resolution is a sometimes complex

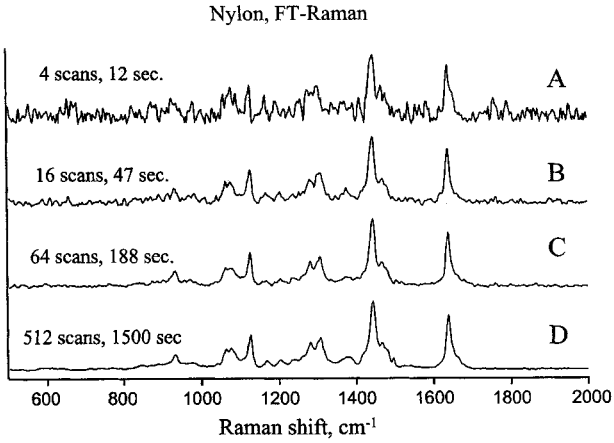

Figure 9.5. FT-Raman spectra of solid nylon obtained with 1064 nm excitation (245 mW) and a Bruker IFS/66 FT-Raman spectrometer with a germanium detector. Resolution was 4 cm^{-1} in all cases, and the number of scans and associated total measurement time are shown. Blackman-Harris apodization, 2 × zero filling.

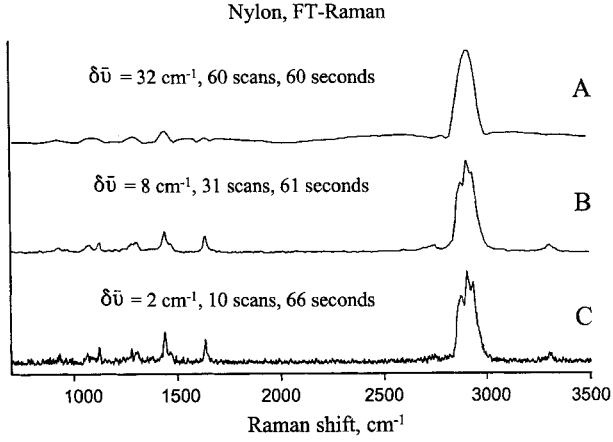

Figure 9.6. Effect of resolution on SNR for FT-Raman spectra of nylon, when total measurement time is kept constant.

function of spectrometer throughput and the Raman band shape but has been considered in some detail for FTIR spectrometers (21). All else being equal, the SNR for a constant observation time is proportional to $\delta\bar{\nu}$ or in some cases $(\delta\bar{\nu})^{3/2}$. For the case of Figure 9.6, an increase in resolution from 8 to 2 cm^{-1} has decreased the SNR by approximately a factor of 4.

As discussed in Section 4.6, the multiplex advantage does not apply as the detector noise decreases toward the shot noise limit and can be a disadvantage when detector noise becomes negligible, and Eq. (4.38) applies. Since current detectors that function above wavelengths of 1 μm are noisy, it is correct to say that a multiplex advantage occurs in this region via Eq. (4.37). However, if a new detector were invented that had zero noise in the 1000 to 1700 nm range relevant to 1064 nm excitation, FT-Raman would lose the multiplex advantage, and the SNR would be no better than the analogous scanning experiment, subject to the conditions outlined in Section 4.6.

A second advantage of FT-Raman over dispersive techniques is the throughput (or Jacquinox) advantage. Spectral resolution does not depend on a narrow slit (as with dispersive/CCD systems), and an interferometer has a larger $A\Omega$ product as a result. In practical terms, the larger aperture means the focus need not be as tight nor as accurate as that for a dispersive system. A larger aperture is related to the "blur diameter," which governs depth of focus (Section 6.3.2), so the focus for an FT-Raman spectrometer can be more forgiving than many dispersive systems. The relatively large depth of focus illustrated in Figure 6.13 for FT-Raman results from the larger aperture.

A third advantage is the excellent frequency precision of interferometers compared to dispersive systems. The observed frequency does not depend on precise positioning of a grating and detector, rather it is determined from the observation of many sine wave periods in the interferogram. Most interferometers incorporate a reference beam, such as a He–Ne laser, to monitor the moving mirror position. The analog-to-digital converter readings may be synchronized with interference fringes of this reference beam, so the interferogram acquisition time is very precise. A practical consequence of frequency precision is spectral subtraction, in which small frequency offsets between two spectra can cause residues in the resulting subtracted spectrum (Fig. 5.5). Figure 9.7 illustrates subtraction of two FT-Raman spectra in which strong scattering from one component was subtracted from the spectrum of a mixture with minimal effect on the spectrum of the other component. The absence of a residue from the bis-phenyliminoterephthalaldehyde (BPT) spectrum after subtraction indicates excellent frequency precision.

The disadvantages of FT-Raman compared to dispersive systems lie mainly in the area of SNR and detection limits. The various expressions for SNR for FT-Raman were discussed in Section 4.6, but some additional comments are useful here. Division of the signal for a particular wavelength, $\dot{S}_i t_M$, by the noise given by Eq. (4.34) yields

$$\mathrm{SNR_{FT}} = \frac{\dot{S}_i t_M^{1/2}}{\left[\sum_{N_R} \dot{S}_i + \dot{B}_i + \phi_d\right]^{1/2}} \tag{9.7}$$

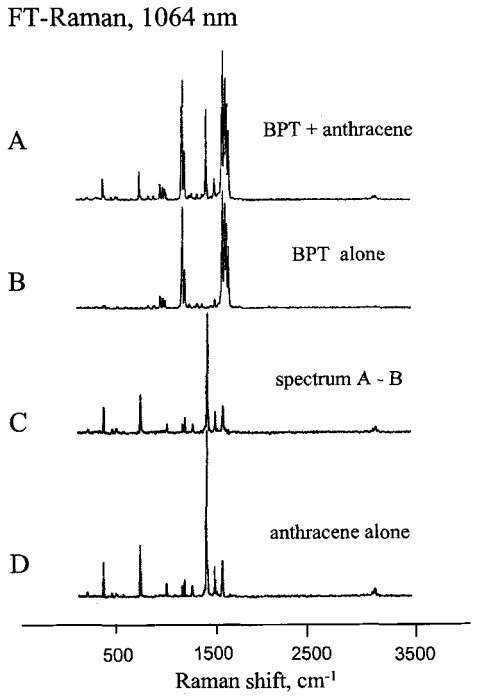

Figure 9.7. Example of spectral subtraction of FT-Raman spectra after subtraction of a spectrum of pure BPT (bis-phenyliminoterephthalaldehyde, spectrum B) from that of a mixture of BPT and anthracene (A). The resulting spectrum (C) is nearly identical to that of pure anthracene (D). (Adapted from Reference 2, with permission.)

where $\dot{S}_i$ is the time derivative of Eq. (3.6), $\dot{B}_i$ refers to background scattering, and ϕ_d is the dark signal in e^-/sec. As noted in Section 5.2, a major advantage of FT-Raman is operation at longer laser wavelengths where $\dot{B}_i$ is often significantly reduced due to lower sample fluorescence. For some samples, $\dot{B}_i$ may be so large that the SNR approaches zero unless a long wavelength laser is used. However, longer wavelength lasers also yield less signal [according to the ν^4 factor, Eq. (2.14)], and ϕ_d increases sharply when the scattering to be detected exceeds the CCD cut-off at 1100 nm. Stated generally, the SNR is maximized when $\dot{B}_i$ and ϕ_d in Eq. (9.7) are minimized and $\dot{S}_i$ is maximized. For fluorescent samples, shorter wavelengths will increase $\dot{S}_i$ but may prohibitively increase $\dot{B}_i$. And $\dot{B}_i$ may decrease sufficiently for longer wavelengths, but ϕ_d may become significant and the SNR degrades. In the case of FT-Raman with a 1064 nm laser, sample fluorescence ($\dot{B}_i$) is usually much lower than that for visible lasers, but current detectors yield a significant ϕ_d.

Even with this reduced SNR, there are many samples where fluorescence is too large to permit useful SNR with CCD/dispersive systems. Figure 9.8 shows the case of a polymer composite for which a useful spectrum was acquired with 1064 nm excitation and FT-Raman, while a dispersive/CCD system operating at 514.5 or 785 nm yielded mainly (or entirely) broadband fluorescence.

The sensitivity problem arises when the sample of interest does not fluoresce significantly and does not require the 1064 nm wavelength of FT-Raman to reduce $\dot{B}_i$ to an acceptable level. In this case, Eq. (9.7) predicts an SNR lower than a dispersive/CCD system [Eq. (4.20)] because of the contribution from detector noise (which is negligible in most CCD systems). If background is *not* a major contribution to the noise, an FT-Raman spectrometer yields significantly lower SNR than a CCD system operated at shorter wavelength (e.g., see Fig. 5.4). Unfortunately, this problem is not easily solved due to the inherent properties of a multiplex spectrometer. If the detector noise is reduced to zero, then the multiplex advantage is lost and the SNR reverts to its single channel value [Eq. (4.39)]. The pragmatic conclusion drawn from this discussion centers on the important consequences of background scattering on the observed SNR. If the background is low enough to use a multichannel dispersive/CCD spectrometer, the SNR will be higher than that for a multiplex FT-Raman spectrometer. However, if the laser wavelength must be increased to 1064 nm to reduce the background, the only option currently available is FT-Raman. As noted in Chapter 5, current multichannel technology places

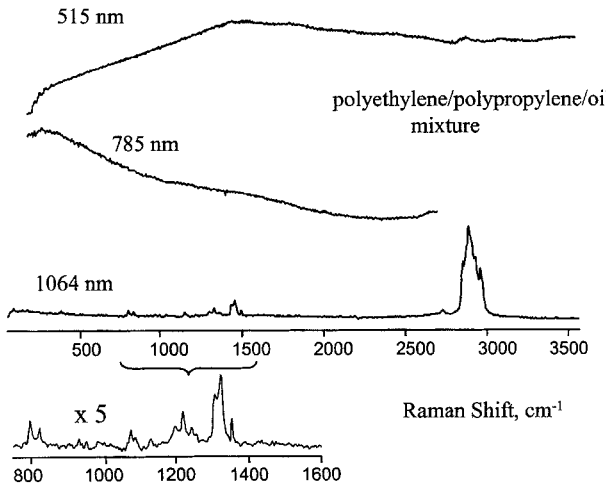

Figure 9.8. Raman spectra of an polyethylene/polypropylene/oil mixture obtained with three laser wavelengths. The lower spectrum is an expansion of the FT-Raman (1064 nm) spectrum showing detail that was obscured by fluorescence at the other wavelengths.

special significance on the silicon CCD cut-off at 1100 nm. If the Raman scattering occurs at wavelengths shorter than this cut-off, a dispersive/CCD system will generally yield higher SNR than an FT-Raman system with similar experimental parameters. Stated more simply, a dispersive/CCD spectrometer will yield a spectrum with higher SNR than FT-Raman unless sample fluorescence is significantly stronger than Raman scattering at the laser wavelength used for the dispersive/CCD experiment.

An additional aspect of FT-Raman may be viewed as an advantage or a pitfall, depending upon the situation. For the common case of the detector noise limit [Eq. (4.37)], the SNR_{FT} depends linearly on the laser power density, P_D. For most dispersive/CCD systems, which operate under a shot noise limit, the SNR is proportional to $P_D^{1/2}$ [e.g., Eq. (4.20)]. So an increase in P_D has a larger effect on SNR in FT-Raman because the signal is being boosted above a noisy detector. As a consequence, laser powers used in FT-Raman can be quite high and sample heating can be a problem. Figure 9.9 shows a spectrum that exhibits black-body radiation at longer wavelengths (and larger Raman shift) due to sample heating. Since the focus in FT-Raman is not as tight as in dispersive spectrometers, the sample can often tolerate higher laser power. Furthermore, 1064 nm light is not strongly absorbed by many samples, so the FT-Raman beam generally causes less thermal and photochemical damage than a visible beam of similar power. The requirement for relatively high laser power makes FT-Raman generally less suitable for the

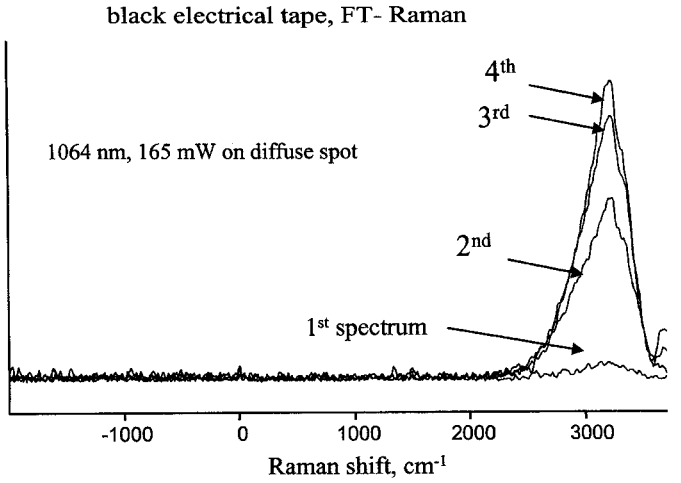

Figure 9.9. FT-Raman spectra of black electrical tape, 16 cm^{-1} resolution. Four spectra were acquired successively, each composed of eight scans. Sample heating causes black-body radiation above 2500 cm^{-1}. Rolloff above 3000 cm^{-1} is due to detector response.

Raman microscopy techniques, discussed in Chapter 11, in which the laser is usually tightly focused.

9.2.3. FT-Raman Instrumentation

In part because many FT-Raman instruments were adaptations of existing FTIR spectrometer, there is a fairly wide variety of instrument configurations in current use. However, they all share the components shown in the block diagram of Figure 9.10. While all of the components shown are represented in the generic spectrometer of Figure 1.7, there are some important differences between the FT and dispersive spectrometers, beyond the obvious case of the wavelength analyzer itself.

9.2.3.1 Excitation Laser

All currently available commercial FT-Raman spectrometers use Nd:YAG lasers operating at 1064 nm, and most of those are diode pumped (Section 7.4.1). Such lasers are compact (approximately 3 × 3 × 12 in.), air-cooled, and operate on standard 110 VAC power. Commercial spectrometers generally have a laser power range of up to 1 W, with 300 to 500 mW being typical during spectrum acquisition. The laser output is filtered by a 1064 nm bandpass filter (Section 7.6.1) to remove spontaneous emission, then directed to the sample. As shown in Figure 9.10, some spectrometers have provision for either 180° geometry (using M1) or 90° geometry (using M2). Since an

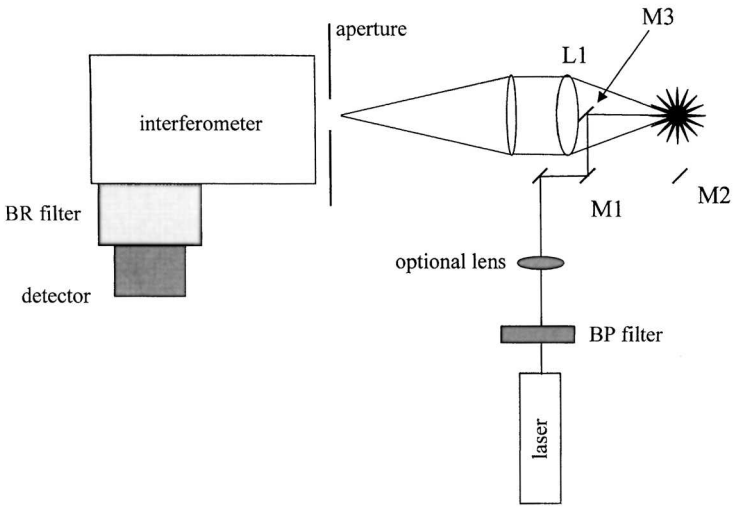

Figure 9.10. Black diagram of an FT-Raman spectrometer with 180° collection (M1 in place) or 90° collection (M1 absent). Optional lens permits tight or weak laser focus at sample.

interferometer has a larger aperture than the slit of a dispersive/CCD system, it is not always necessary to focus the laser to a small spot. For this reason, the beam steering mirror (or prism) M3 is placed to the right of the collection lens (L1) in Figure 9.10. An optional focusing lens that may be easily removed and replaced is often placed in the laser beam path as shown. An unfocused or weakly focused laser is advantageous in FT-Raman because it lowers the power density at the sample and relaxes the tolerances on alignment of laser, collection optics, and sample.

9.2.3.2 Collection Optics

Although direct coupling of the collected light with the parallel path of the interferometer is possible (as shown in Fig. 9.3), the light usually passes through an aperture as shown in Figure 9.10. This aperture, often called a *Jacquinox stop* permits control of the degree of collimation in the interferometer and excludes severely off axis light. The collection optics preceding this aperture can have quite low $f/\#$ and large collection angles to exploit the relatively large $A\Omega$ product of the interferometer. For example, L1 might have a short focal length and low $f/\#$, resulting in magnification of the laser spot at the aperture. Since the aperture is large compared to a slit, this magnification does not overfill the spectrometer. Both the weak laser focus and the high Ω of L1 exploit the relatively large $A\Omega$ product of the interferometer. As the resolution of the interferometer improves, the collimation requirement becomes more stringent, and the aperture diameter (and consequently the $A\Omega$ product) is decreased.

The configuration of the collection optics is certainly not restricted to that shown in Figure 9.10. Reflective optics such as an off-axis paraboloid, similar to Figure 6.6, or spherical and elliptical optics similar to those of Figure 9.3 are also available. Collection through a microscope is possible with FT-Raman, using techniques similar to those described in Chapter 11. However, Raman microscopes usually focus the laser very tightly, since the spatial resolution is usually directly related to spot size. For FT-Raman instruments, the generally high laser powers lead to sample damage when small spots are involved. Furthermore, the tight focus of a microscope usually underfills an FT-Raman spectrometer, thus "wasting" their high $A\Omega$ product. Fiber-optic sampling has also been demonstrated for FT-Raman (16,22), similar to that described in Chapter 12, but is not in common use at this writing.

9.2.3.3 Interferometers

Excellent interferometers were developed for FTIR and adapted for FT-Raman with minimal change. Since many FT-Raman spectrometers are configured as accessories to FTIR spectrometers, the interferometers are identical. An

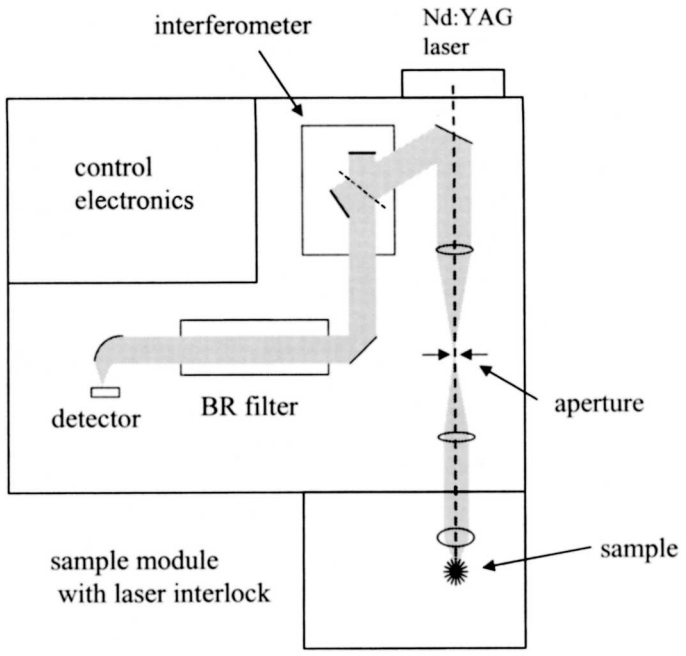

Figure 9.11. Optical schematic of Bruker FT-Raman spectrometer based on an IFS 66 FTIR system.

example is shown in Figure 9.11 in which the FT-Raman accessory consists of a laser, sample chamber, filter, and detector that are added to a stand-alone FTIR spectrometer. The optics of FTIR interferometers are optimized for use in the 400 to 4000 cm^{-1} range, while FT-Raman involves the range from 9398 cm^{-1} (1064 nm) to 5898 cm^{-1} (1695 nm). Usually a different beamsplitter is required for the FT-Raman range than for the mid-IR and, of course, a different detector (discussed below).

9.2.3.4 Laser Rejection Filter

As was the case for dispersive spectrometers, a laser rejection filter serves the essential function of reducing the strong elastically scattered laser light relative to the weak Raman scattering. The problem is more severe in FT-Raman, however, because the laser light is distributed over the entire interferogram and contributes to the noise at every observed frequency. It was noted in Chapter 4 and Eq. (4.36) that the noise in an FT-Raman spectrum is proportional to the square root of the *average* intensity of light across the entire spectrum. So if significant laser intensity enters the interferometer, the SNR of

the entire spectrum is degraded. This problem of *distributed noise* requires FT-Raman spectrometers to have excellent laser rejection filters, either between the sample and the interferometer or immediately preceding the detector.

The laser rejection filters used in FT-Raman are variations on the dielectric and holographic notch filters described in Section 8.2.5. Since the laser rejection required is higher than that for a dispersive system, filter designs are often multistage and proprietary. High optical density for the laser is in conflict with the objective of observing low Raman shift values, and the designer faces a trade-off between distributed noise and low Raman shift performance. For a strong scatterer such as sulfur (Fig. 9.12), an FT-Raman instrument is capable of observing the band at 85 cm^{-1}. While this performance is impressive, it is not likely to match that of the triple spectrograph for low Raman shift observations (e.g., Fig. 8.14).

Filters often have variable transmission across the relevant spectral range, which can appear in the spectrum as a varying background. Figure 9.13A shows a spectrum of impure dinitrobenzene, which has a broad fluorescent background. The transmission of the rejection filter (dielectric in this case) oscillates 6 to 7 times over the 400 to 3300 cm^{-1} Raman shift range, thus generating artifacts in the baseline. This problem is easily corrected by calibrating the instrument response function as described in Chapter 10. Such a procedure was used to correct the spectrum of Figure 9.13A to yield 9.13B (4,14). Corrections of this type are important for both FT-Raman and dispersive spectrometers, but they are not in common use at this time.

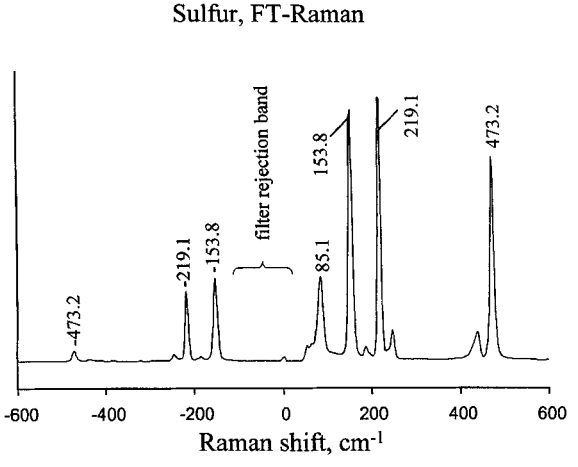

Figure 9.12. FT-Raman spectrum of solid sulfur, obtained with a Bruker 66 FTIR and Raman attachment. Filter rejection band blocks Raman shifts from +55 to −130 cm^{-1}. Small feature at zero shift is the residual elastic scatter transmitted by the rejection filter.

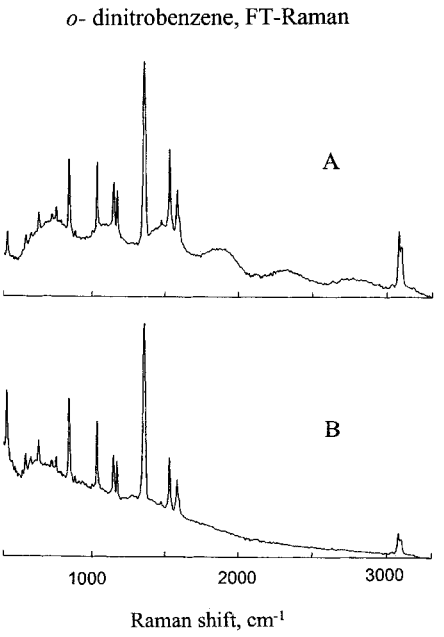

Figure 9.13. FT-Raman spectra of a mildly fluorescent, impure sample of ortho dinitrobenzene before (A) and after (B) correction for instrumental response. Modulation at A is caused by the laser rejection filter. (Adapted from Reference 4, p. 104.)

9.2.3.5 FT-Raman Detectors

Currently available detectors for the 1100 to 1700 nm wavelength range appropriate to FT-Raman are low band gap semiconductors, particularly germanium (Ge) and indium gallium arsenide (InGaAs). When the band gap becomes small enough to detect the low-energy photons involved, dark signal increases due to the ease of thermal electron/hole generation. Even when Ge and InGaAs are cooled, the dark signal significantly exceeds that of silicon. In addition to photometric linearity, the important specifications for FT-Raman detectors are the dark signal and the quantum efficiency (QE), curve. QE curves for Ge and InGaAs are shown in Figure 9.14. These curves are quite dependent on temperature and also vary somewhat with doping and other aspects of fabrication. It is common practice to select one or a few units out of a batch of apparently identical detectors, on the basis of low dark noise or an attractive QE curve. As a consequence, relative intensities and SNR can vary after a detector is replaced.

As was the case with CCDs, the QE curve of an FT-Raman detector can significantly affect the appearance of an uncorrected spectrum. Figure 9.15

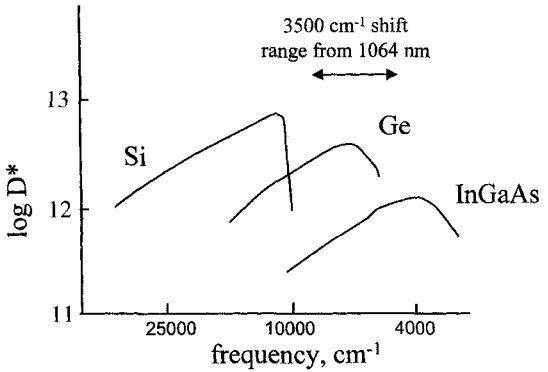

Figure 9.14. Response curves of semiconductor detectors, with Raman shift range shown relative to 1064 nm. D^* is proportional to quantum efficiency and is defined in the FTIR literature (21). Note the logarithmic D^* axis and the nonlinear frequency axis.

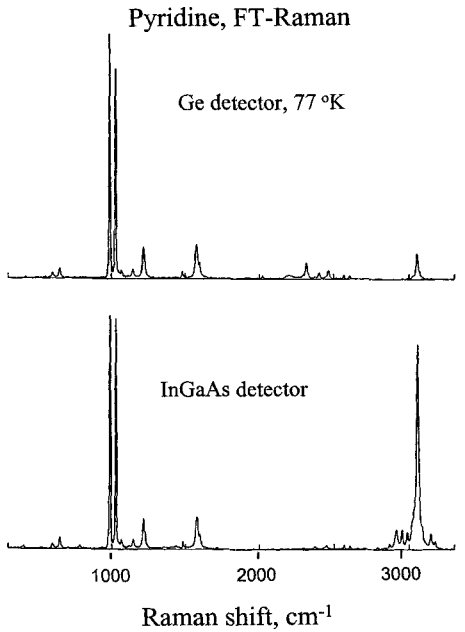

Figure 9.15. Uncorrected FT-Raman spectra of pyridine obtained with different detectors, showing distortion of relative intensities caused by quantum efficiency variation across the spectrum. (Adapted from Reference 4, p. 92.)

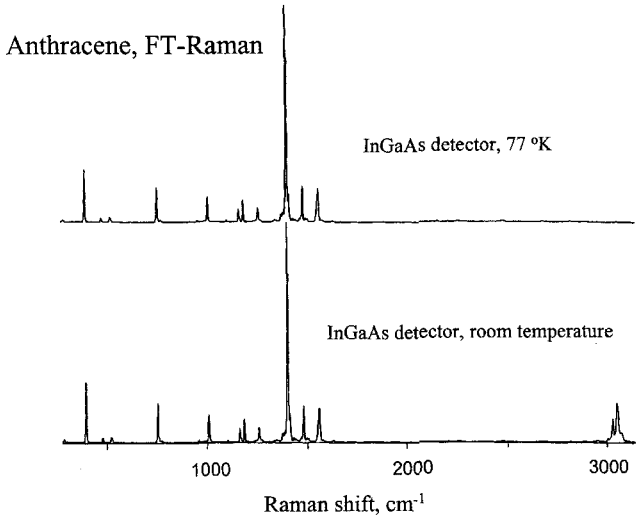

Figure 9.16. Uncorrected FT-Raman spectra of anthracene, showing variation in detector response with detector temperature. (Adapted from Reference 4, p. 99.)

shows spectra of pyridine acquired with Ge and InGaAs detectors under otherwise similar conditions. Note the large difference in C—H stretch intensity, since this Ge detector has diminished sensitivity at ~1600 nm (~3000 cm^{-1}). Figure 9.16 shows that a given detector can be affected by temperature, in this case causing disappearance of the C—H region for a cooled InGaAs detector. Fortunately, these effects are generally correctable using a response function correction (Section 10.3), provided there is adequate signal to analyze.

9.3. MULTICHANNEL FOURIER TRANSFORM RAMAN SPECTROSCOPY

A general comparison of dispersive and FT-Raman spectrometers reveals some complementary properties inherent in the two methods of wavelength analysis. A dispersive/CCD system has a multichannel advantage arising from parallel detection of many wavelengths but requires a small slit to match small detector elements, thus limiting the $A\Omega$ product. FT-Raman has a large $A\Omega$ and excellent precision, but a noisy detector and the multiplex disadvantage lead to lower SNR. There is obvious merit in techniques that might unify the two methods and maintain the positive points of both. A step toward this goal is the multichannel Fourier transform (MCFT) spectrometer, which uses a CCD to detect an interferogram, then FT techniques to analyze the results (22,23).

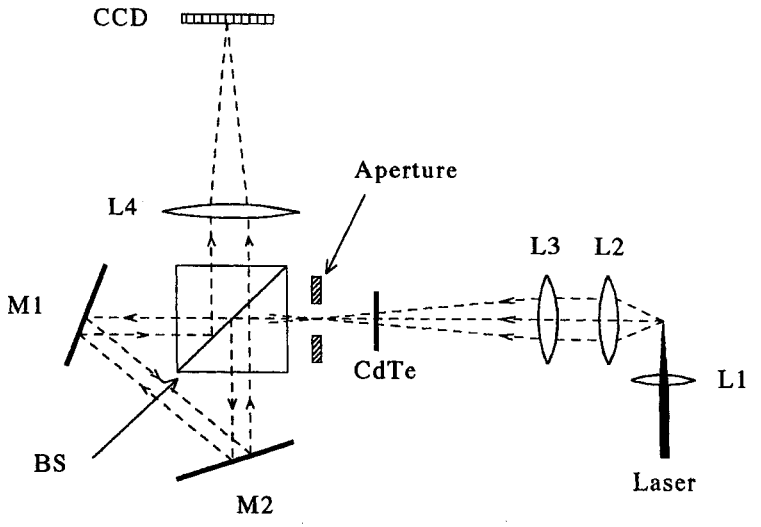

Figure 9.17. Common path (Sagnac) interferometer used for multichannel FT-Raman: '*a*' and '*b*' indicate two paths followed by light leaving the beamsplitter (BS). CdTe acts as a long pass filter. (Adapted from Reference 22 with permission.)

The apparatus for MCFT Raman is shown in Figure 9.17. A *Sagnac* or *common path* interferometer generates an interferogram by splitting the incident beam and recombining the two halves after introducing a path length difference. Without the need for a moving mirror, an interferogram is generated at the focal plane of L4 and is detected by a CCD. The entire apparatus is static, and data acquisition is controlled electronically by the CCD. Instead of monitoring a single detector during mirror movement, the MCFT approach reads the static interferogram with many CCD pixels. An interferogram resulting from Raman scattering from naphthalene is shown in Figure 9.18, and its Fourier transform is shown in Figure 9.19.

Although the MCFT system and conventional FT-Raman generate and monitor the interferogram in different ways, they share certain properties. First, the MCFT has no slit, and the aperture is comparable to that of a Michelson interferometer, so the large $A\Omega$ product is retained. Experimentally, minimal signal loss (<10 per cent) was observed when the laser spot size was increased from 0.1 to 1.0 mm (23). Second, the spectral coverage is large for both MCFT and FT-Raman and is independent of mirror travel (for the Michelson system) or the number of pixels (for MCFT). Third, observed frequency is determined from the entire interferogram, so frequency precision and stability are excellent for both MCFT and conventional FT-Raman.

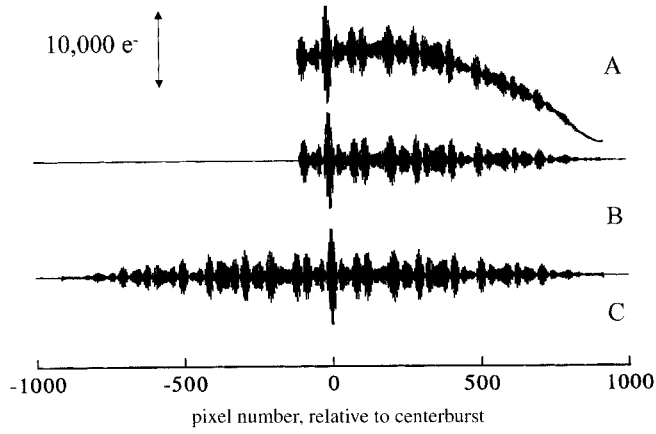

Figure 9.18. Raw interferogram (A) obtained with 1024-pixel CCD using MCFT. Sample is naphthalene illuminated by 135 mW of 830 nm light, 5-sec integration; B is the same data after removal of low-frequency components and zero filling to 2000 points; C is after reflection of the right half of the interferogram through the centerburst. (Adapted from Reference 22 with permission.)

The two main differences between MCFT and conventional FT-Raman are both derived from the characteristics of the CCD, and both are fundamental. First, the resolution depends on the number of CCD elements along the interferogram axis. Since one cannot arbitrarily vary the size of the CCD or the pixel spacing, there is less flexibility than with a Michelson system, where mirror travel and sampling rate are variable. For the configuration shown in Figure 9.17, Eq. (9.8) applies (23):

$$\delta\bar{\nu} = \frac{2\bar{\nu}_{\mathrm{MAX}}}{N_C} \tag{9.8}$$

where $\delta\bar{\nu}$ is the resolution (in reciprocal centimeters), $\bar{\nu}_{\mathrm{MAX}}$ is the maximum observed frequency (in reciprocal centimeters), and N_C is the number of CCD pixels along the axis of the interferogram. For a 785 nm laser ($\bar{\nu}_{\mathrm{MAX}} = 12740\ \mathrm{cm}^{-1}$) and a 1024-element CCD, $\delta\bar{\nu}$ is 25 cm^{-1}. This modest resolution may be improved by increasing N_C by mathematical techniques during the FT to about 14 cm^{-1}. The best resolution achieved thus far with MCFT is 8 cm^{-1} (Fig. 9.20), achieved with an optical heterodyne approach (24). Resolutions in the 8 to 14 cm^{-1} range can certainly be useful for many applications, but MCFT resolution is unlikely to exceed or even approach that of the best FT-Raman and dispersive techniques.

The second fundamental issue of MCFT bears on the now familiar question of SNR. Since the CCD operates at or near the shot noise limit, the SNR is

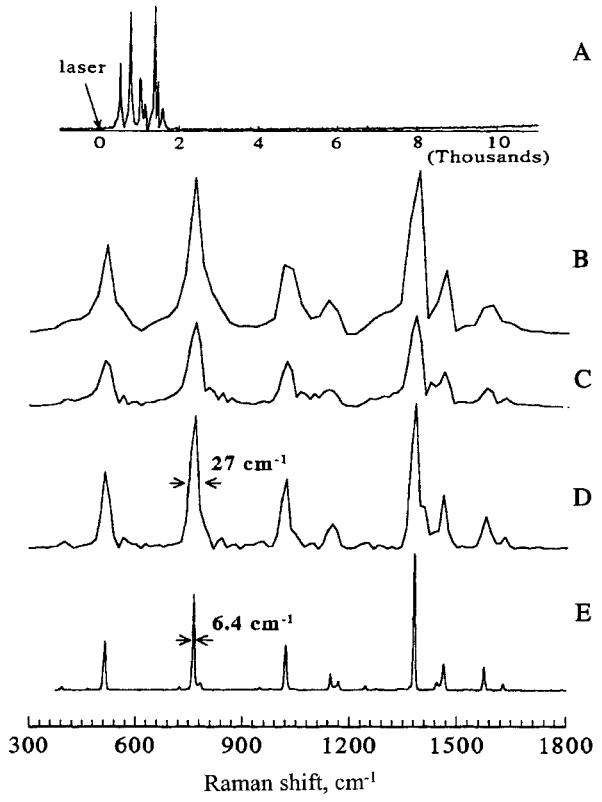

Figure 9.19. (A) Fourier transform of interferogram of Figure 9.18A, showing entire Raman shift range; (B) expansion of A over 300- to 1800 cm^{-1} range. (C) FT of Figure 9.18B. (D) FT of Figure 9.18C showing resolution improvement from data reflection. (E) Spectrum of naphthalene obtained with dispersive/CCD spectrometer, 5 sec, 135 mW. (Adapted from Reference 22 with permission.)

not controlled by detector noise. However, the noise is still distributed over the entire interferogram, so the SNR is dictated by Eq. (4.38). The SNR of the MCFT is similar to that of a conventional FT-Raman system if both instruments use a shot-noise-limited detector. So the SNR depends on the density of spectral features, as discussed in Section 4.6. In general, the SNR for MCFT will be lower than the analogous dispersive experiment due to the contribution of distributed noise. This shortfall is compensated somewhat by the higher $A\Omega$ product of MCFT, but the resulting SNR is still lower than a dispersive experiment for typical conditions.

Since MCFT offers lower (and fixed) resolution compared to conventional FT-Raman, and it is currently limited to the silicon detection range, it is

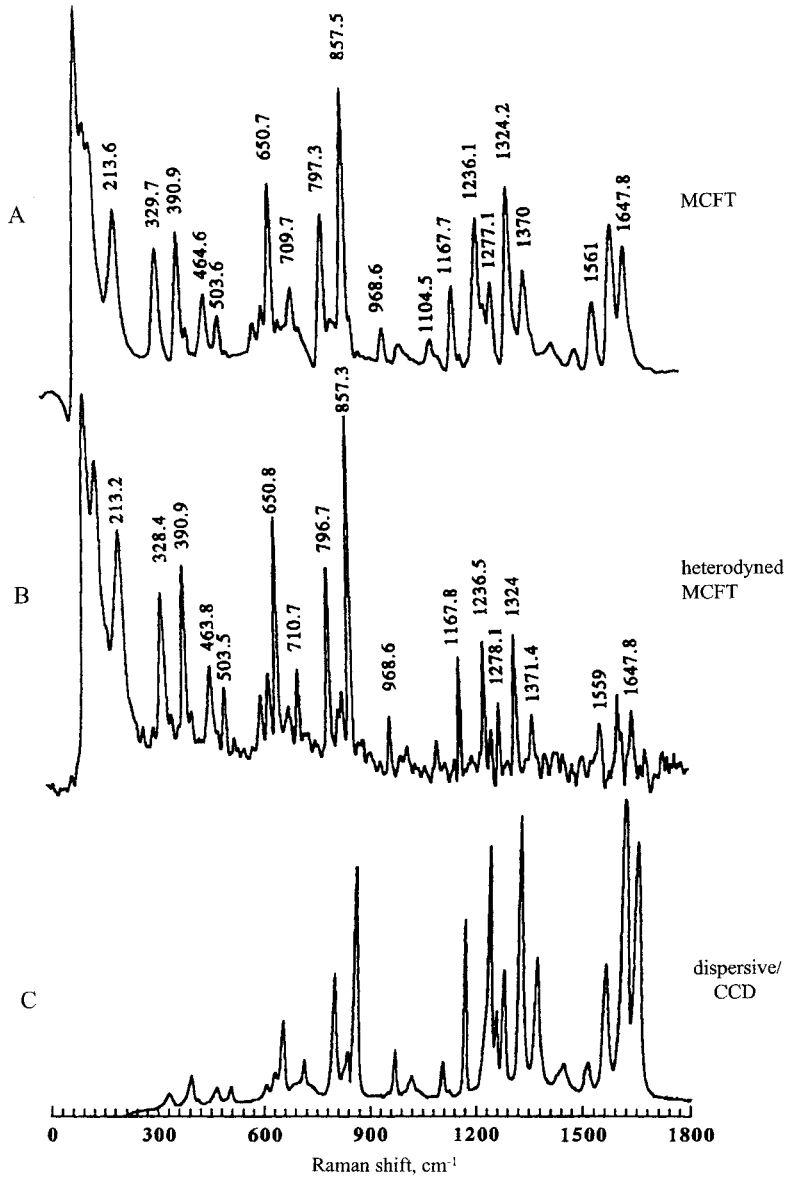

Figure 9.20. Resolution improvement in MCFT using an optical heterodyne resulting from a beat frequency caused by a transmission diffraction grating imaged at the CCD. Spectra are not response corrected, resulting in variation of relative intensities. Sample was a commercial Tylenol tablet. (Adapted from Reference 23 with permission.)

unlikely to compete favorably with existing dispersive or FT-Raman techniques in the laboratory. However, the rugged design, lack of moving parts, excellent stability, and large entrance aperture may be useful for certain dedicated applications where resolution is not a high priority (24).

9.4. EXTENSIONS OF FT-RAMAN FOR LONGER WAVELENGTH OPERATION

After consideration of the properties of dispersive/CCD Raman spectroscopy and FT-Raman, questions about alternative approaches to conventional FT-Raman often arise. First, can fluorescence be further reduced by using still longer laser wavelengths? Second, wouldn't the best solution be a shot-noise-limited multichannel system operating above 1000 nm? Both of these questions have been addressed experimentally, but given current technology the associated hardware developments are not yet ready for widespread use.

A conventional Nd:YAG laser may be modified to operate at 1339 nm by changing its mirrors, and a germanium detector is suitable for detecting the resulting Raman scattering up to a Raman shift of 1800 cm^{-1} (25). By using a longer laser wavelength, the likelihood of sample fluorescence is reduced and a wider range of samples should be accessible. The cross section is lower by a factor of 2 (for ν^3) or 2.5 (for ν^4) for a 1339 nm laser compared to 1064 nm. In the case of a germanium detector, the cross-section loss is compensated by increased detector efficiency, at least up to 1800 cm^{-1}. The benefit of 1339 nm operation is shown in Figure 9.21 for a sample of copper phthalocyanine. Raman scattering is barely visible above the fluorescence for 1064 nm excitation, while the Raman scattering is dominant for the longer laser wavelength.

The generality of this benefit to a wide range of samples is difficult to assess in any quantitative manner. There are samples that fluoresce deep into the infrared, such as near-infrared (NIR) laser dyes and will defeat any existing Raman spectrometer. On the other hand, if the mix of anticipated samples includes large molecules or fluorescent impurities, a longer laser wavelength is more likely to yield useful Raman spectra. At least with current technology, shorter wavelengths and multichannel spectrometers favor high sensitivity but risk fluorescence, while long laser wavelengths reduce both fluorescence and sensitivity.

So why not use a multichannel detector above 1000 nm? The ν^4 factor would still yield lower cross sections, but the multichannel detector would boost SNR without the distributed noise problem of FT-Raman. An array detector with negligible dark (and readout) noise that is sensitive in the 1000 to 1700 nm range would seem ideal, yielding the sensitivity of multichannel detection and the low fluorescence of 1064 nm excitation. Such detectors

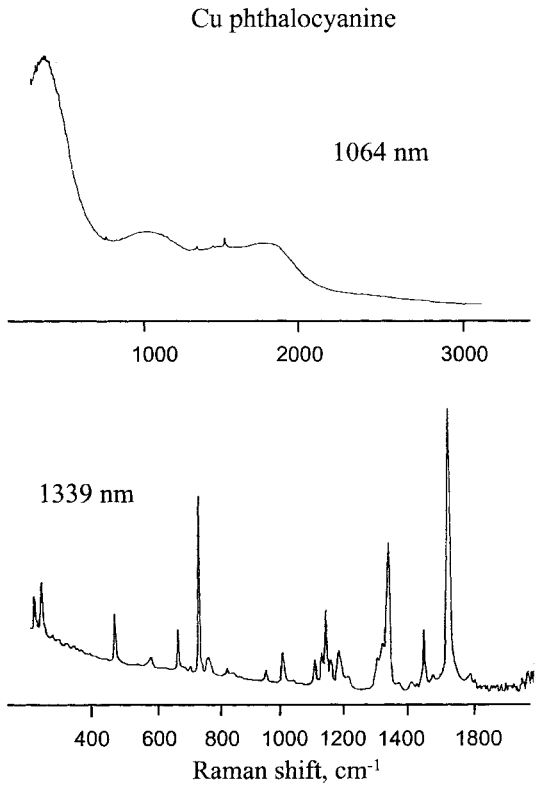

Figure 9.21. FT-Raman spectra of copper phthalocyanine obtained with 1064 and 1339 nm excitation. (Adapted from Reference 24 with permission.)

would indeed be attractive, but they do not yet exist. There are red-sensitized CCDs based on platinum silicide that have adequate red response but low quantum efficiency. Ge and InGaAs arrays are available but have high dark noise compared to silicon CCDs (26). Perhaps because NIR detectors are not of interest to the consumer video industry, their development has lagged that of high-quality visible CCDs. The goal of a low-noise, multichannel detector for the region above 1000 nm is certainly attractive for Raman spectroscopy but has so far remained elusive.

9.5. FT-RAMAN EXAMPLES

Table 9.1 lists some applications of FT-Raman to a variety of samples. The list is illustrative rather than comprehensive, but it does indicate the wide range of problems amenable to FT-Raman.

Table 9.1. Examples of FT-Raman Applications

Application	Comments	Reference
Lipids, solvents	Fiber-optic sampling	16
Pure solids, liquids	Fiber-optic sampling	22
Polyethylene, PET		27
Cimetidine polymorphs		28
Fluorescent samples	Pulsed, step-scan	29
Adsorbed monolayers	Surface-enhanced FT-Raman	30–32
Biological macromolecules		33
Food analysis	Carotenoid, fatty acids	34
Sugars, proteins	2-D correlation with NIR absorption	35
Oxygenates in gasoline	Compared to NIR	36
Petroleum additives	Compared to mid-IR and NIR	37
Low-density polyethylene	Multivariate data analysis	38
Oxygenates in gasoline	Compared to FT-IR, NIR	39
Basal cell carcinoma	Diagnostic	40
High-temperature polymerization	>250°C	41

REFERENCES

1. D. B. Chase, J. F. Rabolt, *Fouries Transform Raman Spectroscopy: From Concept to Experiment*, Academic Press, New York, 1994.
2. D. B. Chase, *Anal. Chem.* **59,** 881A (1987).
3. P. Hendra, C. Jones, and G. Warnes, *FT-Raman: Instrumentation and Chemical Application,* Ellis Harwood, New York, 1991.
4. P. Hendra, in J. J. Laserna, ed., *Modern Techniques in Raman Spectroscopy,* Wiley, London, 1996.
5. M. Schaeberle, H. Morrison, J. Turner III, and P. J. Treado, *Anal. Chem.*, **71,** 175A (1999).
6. D. N. Batchelder, C. Cheng, and G. D. Pitt, *Adv. Mater.*, **3,** 565 (1991).
7. Datex/Ohmeda, Inc., Madison, Wisconsin.
8. G. J. Puppels, M. Grond, and J. Greve, *Appl. Spectrosc.*, **47,** 1256 (1993).
9. E. N. Lewis, P. J. Treado, and I. W. Levin, *Appl. Spectrosc.*, **47,** 539 (1993).
10. M. Schaeberle, V. F. Kalasinsky, J. L. Luke, E. N. Lewis, I. W. Levin, and P. J. Treado, *Anal. Chem.*, **68,** 1828 (1996).
11. J. P. Ingle and S. R. Crouch, *Spectrochemical Analysis,* Prentice-Hall, Englewood Cliffs, NJ, 1988, p 61.
12. K. Christensen, N. Bradley, M. D. Morris, and R. V. Morrison, *Appl. Spectrosc.*, **49,** 1120 (1995).
13. ChemIcon Inc., 7301 Penn Avenue, Pittsburgh, PA 15208.

14. C. J. Petty, G. M. Warnes, P. J. Hendra, and M. Judkins, *Spect. Acta,* **47A,** 1179 (1991).
15. D. B. Chase and B. A. Parkinson, *Appl. Spectrosc.,* **42,** 1186 (1988).
16. N. Lewis, V. F. Kalasinsky, and I. W. Levin, *Anal. Chem.,* **60,** 2658 (1988).
17. B. Schrader, A. Hoffman, A. Simon, and J. Sawatzki, *Vibrational Spec.,* **1,** 239 (1991).
18. B. Schrader, A. Hoffman, and S. Keller, *Spect. Acta,* **47A** 1135 (1991).
19. J. P. Insle and S. R. Crouch, *Spectrochemical Analysis;* Prentice-Hall, Englewood Cliffs, NJ, 1988, p. 81.
20. J. P. Insle and S. R. Crouch, *Spectrochemical Analysis;* Prentice-Hall, Englewood Cliffs, NJ, 1988, p. 83.
21. P. Jaakola, J. D. Tate, M. Paakunainen, J. Kauppinen, and P. Sirenian, *Appl. Spectrosc.,* **51,** 1159 (1997).
22. D. D. Archibald, L. T. Lin, and D. E. Honigs, *Appl. Spectrosc.,* **42,** 1558 (1988).
23. J. Zhao and R. L. McCreery, *Appl. Spectrosc.,* **50,** 1209 (1996).
24. J. Zhao and R. L. McCreery, *Appl. Spectrosc.,* **51,** 1687 (1997).
25. K. J. Asselin and B. Chase, *Appl. Spectrosc.,* **48,** 699 (1994).
26. B. Chase and Y. Talmi, *Appl. Spectrosc.,* **45,** 929 (1991).
27. B. A. Barrera and A. J. Sommer, *Appl. Spectrosc.,* **52,** 183 (1998).
28. G. Jalsovsky, O. Egyed, S. Holly, and B. Hegedus, *Appl. Spectrosc.,* **49,** 1142 (1995).
29. A. Sakamoto, Y. Furukawa, M. Tasumi, and K. Masutani, *Appl. Spectrosc.,* **47,** 1457 (1993).
30. S. M. Angel, L. F. Katz, D. D. Archibald, L. T. Lin, and D. E. Honigs, *Appl. Spectrosc.,* **42,** 1327 (1988).
31. S. M. Angel, L. F. Katz, D. D. Archibald, and D. E. Honigs, *Appl. Spectrosc.,* **43,** 367 (1989).
32. S. M. Angel and D. D. Archibald, *Appl. Spectrosc.,* **43,** 1097 (1989).
33. E. N. Lewis, V. F. Kalasinsky, and I. W. Levin, *Appl. Spectrosc.,* **48,** 1188 (1988).
34. Y. Ozaki, R. Cho, K. Ikegaya, S. Muraishi, and K. Kawauchi, *Appl. Spectrosc.,* **46,** 1503 (1992).
35. W. F. McClure, H. Maeda, J. Dong, Y. Liu, and Y. Ozaki, *Appl. Spectrosc.,* **50,** 467 (1996).
36. S. J. Choquette, S. N. Chesler, D. L. Duewer, S. Wang, and T. C. O'Haver, *Appl. Spectrosc.,* **68,** 3525 (1996).
37. J. B. Cooper, K. L. Wise, W. T. Welch, M. B. Sumner, B. K. Wilt, and R. R. Bledsoe, *Appl. Spectrosc.,* **51**, 1613 (1997).
38. K. Sano, M. Shimoyama, M. Ohgane, H. Higashiyama, M. Watari, M. Tomo, T. Ninomiya, and Y. Ozaki, *Appl. Spectrosc.,* **53**, 551 (1999).

39. J. B. Cooper, K. L. Wise, W. T. Welch, R. R. Bledsoe, and M. B. Sumner, *Appl. Spectrosc.*, **50**, 917 (1996).
40. M. Gniadecka, H. C. Wulf, and N. N. Mortensen, *J. Raman Spec.*, **28**, 125 (1997).
41. J. F. Aust, J. B. Cooper, K. L. Wise, and B. J. Jensen, *Appl. Spectrosc.*, **53,** 682 (1999).

Raman Spectroscopy for Chemical Analysis. Richard L. McCreery

ISBN: 0-471-25287-5

CHAPTER

10

CALIBRATION AND VALIDATION

10.1. OVERVIEW

Calibration is used here to describe whatever process is used to relate observed spectral frequencies and intensities to their true values, and *validation* is a procedure to verify the calibration and determine the magnitude of experimental error. Raman spectroscopy is a demanding technique in terms of reproducibility and accuracy and involves a variety of instrumental configurations. Calibration is often the source of irreproducibility and inconsistency in reported Raman spectra. This chapter is divided into four general sections: frequency calibration (10.2), response function calibration (10.3), absolute response calibration (10.4), and a summary of procedures (10.5). For each section, standards and procedures for instrument validation are considered.

10.2. FREQUENCY AND RAMAN SHIFT CALIBRATION

Even a cursory examination of Raman shift values reported in the literature reveals significant variations, often greater than ± 5 cm^{-1}. Even small changes in true Raman shift can be scientifically informative, so it is quite unfortunate if such effects are obscured by instrumental or random error. Reported Raman shift values are currently more prone to error than Fourier transform infrared (FTIR) frequencies for two reasons. First, Raman shift involves the difference of two frequencies (laser and Raman scattering), each of which may be subject to measurement error, while FTIR is usually a measurement of one frequency. Second, the higher absolute frequencies involved in Raman must be determined to a higher degree of relative accuracy. For example, measurement of a 1000 cm^{-1} vibration with FTIR to an accuracy of ± 1 cm^{-1} requires relative frequency error of 0.1 per cent. The same observation with Raman spectroscopy and a 514.5 nm laser requires a frequency measurement accurate to 1 cm^{-1} in 18,435 cm^{-1} (19, 435–1000), or 0.005 per cent. Such accuracy is readily achievable with modern Raman instruments but does require extra care.

10.2.1. Frequency Calibration with Absolute Frequency Standards

The most common approach to frequency calibration is based on known frequency standards, usually atomic emission from gases. Neon, argon, and mercury lamps are readily available, and a large number of accurate frequencies ($\geq$6 significant figures) are available (1–4). The atomic source is placed at (or in the vicinity of) the normal sample position, and the resulting spectrum is recorded using the same optical conditions to be used for the sample. Using a table of known frequencies (or wavelengths), an appropriate mathematical function is then fit to the observed frequencies, thus relating observed to actual frequency. In order to calibrate Raman shift, the laser frequency must be known accurately or determined with the spectrometer. Apparent Raman shifts for several neon lines are shown in Figure 10.1, relative to the Ar^+ laser at 514.532 nm.

The simplest case of an absolute calibration employs the laser line itself to calibrate a dispersive spectrometer. With the system positioned so the laser line is on the spectrum, the spectrometer is fine tuned so the laser

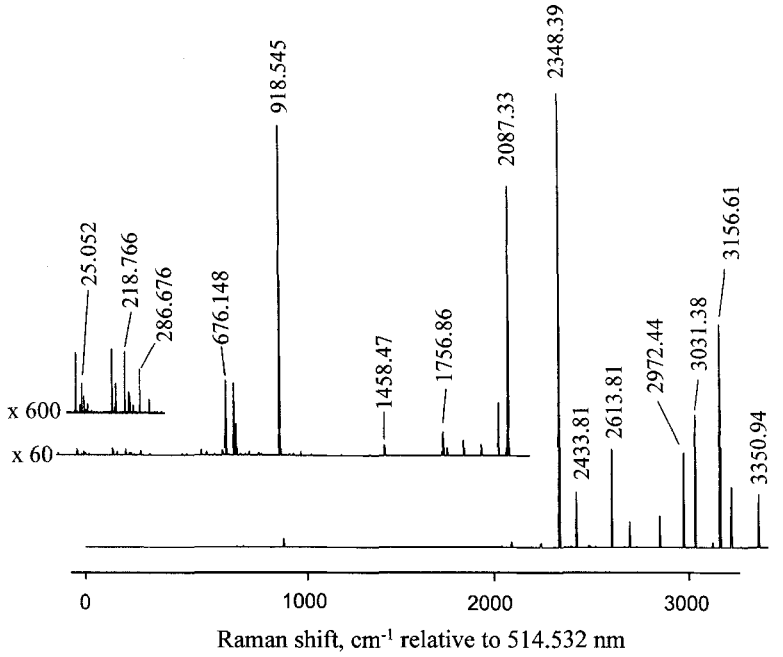

Figure 10.1. Spectra of neon bulb emission, expressed as Raman shift (in air) relative to 514.532 nm. Obtained with Spex 1402 double monochromator, RCA 31034 PMT. Indicated values were calculated from Reference 2.

corresponds to zero Raman shift. Once the position of zero Raman shift is known, observed Raman shifts may be calculated from the dispersion relationships from Chapter 8. The accuracy of the calibration for the entire Raman shift range depends on the accuracy of the optomechanical system, particularly positioning accuracy of the grating. For high-quality dispersive spectrometers, this one-point frequency calibration can be quite accurate, in the range of ± 1 cm^{-1}. However, random variations in the mechanical drive, expansion with temperature, and optical aberrations can easily generate errors of several wavenumbers, and a one-point calibration is risky for many dispersive systems.

For FT-Raman spectrometers, an equivalent one-point calibration is more reliable because interferometers are less prone to mechanical errors. Nearly all interferometer designs include a well-defined reference wavelength (often a He–Ne laser at 632.8 nm), which is used to control data acquisition. In addition, observed FT frequencies are calculated from a large number of individual measurements, so minor mechanical jitter and random timing errors are averaged out. Provided the laser and reference frequencies are known accurately, an observed FT-Raman frequency is quite accurate, and the one-point calibration is usually adequate.

Returning to the dispersive case, it is far more reliable to use many calibration lines than to use only one. Ideally, a large number of accurately known frequencies would be dispersed across the spectrum, then observed under the same conditions as the sample. Assuming the optical and data acquisition conditions are precisely reproduced for the standard and the sample, the sample frequencies may be accurately calculated from the standard spectrum. As noted earlier, Raman shifts may then be determined from the equally accurately known laser frequency.

Extensive tables of atomic emission wavelengths for Ne, Ar, Ar^+, and the like are available for both vacuum and atmospheric conditions. Since the wavelength analyzer is nearly always operating in air, the appropriate frequency values obtained in air should be used. The difference between vacuum and air frequencies is about 5 cm^{-1} at 20,000 cm^{-1} (500 nm) and can represent a substantial error. Note that the *analyzer* atmosphere is what counts, not the *sample* atmosphere, as far as frequency calibration is concerned. Table 10.1 lists frequencies for neon emission in the region of 514.5 to 624 nm, stated in terms of Raman shift relative to the Ar^+ laser line at 514.532 nm. Since Raman shift is a nonlinear function of position on the charge-coupled device (CCD) or focal plane for a dispersive spectrometer, the calibration function must itself be nonlinear. Second- and third-order polynomials are generally used to fit the observed detector output to the known Raman shifts of the standard. The use of polynomials higher than third order leads to "overfitting" and poorer shift

Table 10.1. Frequency Shifts (in Air) of Neon Emission Lines Relative to 514.532 nm

Raman shift (cm^{-1})[a]	Approximate Relative Intensity (2348.4 cm^{-1} = 100)
25.0520	0.10
162.161	0.12
218.766	0.12
243.369	0.03
286.676	0.16
496.049	0.02
560.764	0.08
584.136	0.048
676.148	1.0
720.053	0.32
740.766	0.024
778.463	0.048
918.545	2.4
1031.31	0.06
1458.47	0.2
1744.06	0.06
1756.86	0.40
1859.88	0.32
1950.25	0.2
2038.68	0.48
2087.33	3.2
2206.98	0.48
2253.47	1.6
2348.39	100.
2407.56	0.8
2433.81	40
2493.06	1.6
2504.43	0.6
2525.06	0.32
2540.12	0.32
2613.81	48
2661.18	0.2
2672.00	0.8
2700.23	12
2734.81	0.48
2745.25	0.2
2851.38	20
2972.44	48

(*continued next page*)

Table 10.1. *(continued)*

Raman shift (cm^{-1})[a]	Approximate Relative Intensity (2348.4 cm^{-1} = 100)
3031.38	60
3117.80	4
3156.61	60
3210.84	40
3259.52	0.8
3350.94	40

[a]Calculated from Ne and Ar^+ wavelengths in air, from Reference 2.

accuracy (5). Since the frequency is related to $1/\lambda$, the calibration function is monotonic and smooth, so high-order polynomials are unnecessary.

Atomic emission sources have the advantage of numerous calibration lines covering a wide spectral range, but they do have a problem that affects ultimate Raman shift accuracy. All spectrometers, including dispersive and interferometric, exhibit small apparent frequency shifts that depend on sample position. If the light being analyzed enters the spectrometer from different directions, a given frequency will be imaged at slightly different points on the detector. For an FT-Raman system, variations in input angle result in differences in optical path length, and therefore small apparent frequency shifts. It is difficult to position the atomic emission source at exactly the same point as the laser focus, so these small positioning errors arise. The errors can rage from near zero to a few reciprocal centimeters but are impossible to eliminate unless the standard and the sample illuminate the spectrometer with exactly the same geometry.

When the laser itself is based on atomic emission (e.g., Ar^+, Kr^+, He–Ne), a convenient alternative to an atomic emission lamp is available. The "background" atomic emission from the laser (often called *plasma lines*) are normally filtered out with a bandpass filter before reaching the sample. If the filter is temporarily removed, these lines will be focused at the sample position. A white material (e.g., Teflon, paper, even glass) will scatter this light into the spectrometer and provide the same calibration lines as an atomic emission lamp (3,6). Table 10.2 lists many of the plasma lines for an Ar^+ laser in terms of Raman shift relative to 514.532 nm. Not only does the laser provide a "built-in" calibration source (accessible simply by removing the bandpass filter and perhaps detuning the laser to reduce 514.5 nm output), but the calibration light "automatically" reproduces the sample geometry. Several tables of Raman shifts of plasma lines from common lasers have been published (3,6).

Table 10.2. Argon Emission Lines[a]

Raman Shift cm^{-1}, Relative to 514.532	Relative Intensity (514.532 nm = 100)
−319.76	140
0	100
116.07	4.1
266.36	2
520.44	15
908.12	1.8
1101.00	1.9
1442.33	3.0
1599.44	4.8
1738.23	2.9
2111.10	6.9
2521.63	3.8
3051.22	9.1
3233.69	140
3417.52	59
3808.22	16

[a]Calculated from data in Reference 6.

Whatever the atomic line source, it is up to the user or instrument designer to decide how many calibration lines to use. The availability of lines depends somewhat on the spectral region, but there are usually enough available for Ne, Ar, and Hg sources. The number required depends on the desired accuracy, but generally at least 10 lines spread across the spectral range of interest are required. It is difficult to generalize for the many types of instruments and applications, but some guidance on designing a calibration procedure is provided in Section 10.2.3. A calibration based on an atomic line source is built into some commercially available spectrometers (e.g., Kaiser, Chromex). Automatic frequency calibration is important for correcting for drift caused by temperature changes or vibrations, particularly in a process monitoring application where environmental control is lacking.

Figures 10.2 and 10.3 demonstrate the value of frequent calibration for the case of an unstable laser. An unstabilized single-mode diode laser exhibited mode hops over several hours, causing a laser frequency shift of 13 cm^{-1}. If the Raman shift axis was not recalibrated after a mode hop, the apparent Raman shift also changes by 13 cm^{-1}. Spectra before and after a mode hop are shown in Figures 10.2A and 10.2B, along with their difference. The mode hop caused a severe subtraction artifact due to the imprecise Raman shifts. Figure 10.3 shows spectra before and after the mode hop, but with the laser and

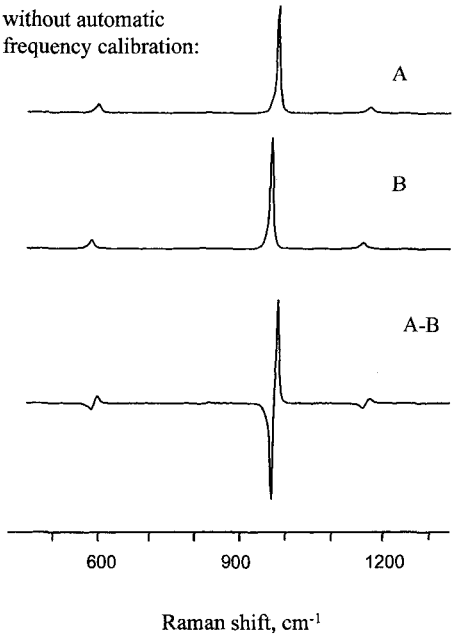

Figure 10.2. Spectra of benzene obtained one hour apart from a spectrometer with an unstable diode laser. Raman shift axis was not recalibrated between A and B, causing a 13 cm^{-1} shift due to a laser mode hop. Both spectra and their difference use the same intensity scale.

Raman wavelengths recalibrated frequently (and automatically). Although the laser frequency shifted by 13 cm^{-1}, the shift was compensated by recalibration, and the observed Raman shift was unchanged to <0.3 cm^{-1}. Automatic recalibration can also correct for thermal or mechanical drift of the grating and several other effects that cause Raman shift imprecision.

The procedures used to calibrate the Raman shift axis with neon lines can be fairly complex, due to subtleties introduced by the use of CCDs (5, 7–10). The image of the entrance slit usually covers more than one CCD pixel along the wavelength axis, and the Raman bandshape might be distributed over several pixels as well. So the observed Raman peak is a convolution of the slit function, the pixel width, and the line shape. These issues can become important when <1 cm^{-1} accuracy is required or when comparing spectra from different insturements (7,9).

10.2.2. Frequency Calibration with Raman Shift Standards

Determination of Raman shift with absolute wavelength standards always requires subtraction of two frequencies, those for the laser and the Raman

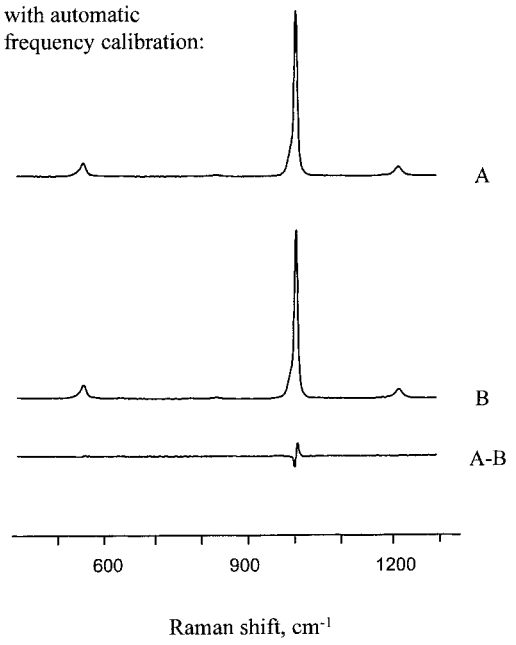

Figure 10.3. Same as Figure 10.3, but the instrument automatically recalibrated the shift axis against argon emission lines, compensating for the mode hop. Results obtained on a Chromex "Sentinel" spectrometer. Both spectra and their difference use the same intensity scale.

scattering. In many cases (e.g., Ar^+, He–Ne), the laser frequency is known very accurately and the subtraction of the scattering frequency does not incur additional error. However, the growing popularity of diode lasers raises the possibility that the laser frequency is not known accurately and may even vary with time, temperature, and so forth. For cases where the laser frequency is not fixed inherently by an atomic line (or similar), both the laser and Raman frequencies must be determined to the desired accuracy before the Raman shift is calculated.

Raman shift standards provide a different means of calibration that does not depend on accurate knowledge of the laser frequency provided it is constant. Given a set of accurately known Raman frequencies for convenient standard samples, one may calibrate the Raman shift axis without knowing the laser frequency. Of course, the laser must be stable during the time between calibration and use, at least as stable as the desired accuracy. An additional advantage of Raman shift standards is their duplication of the sampling geometry. Since the standard is "just another sample," it can precisely reproduce the optical geometry used for actual samples.

A working group of the ASTM (American Society for Testing and Materials) selected and analyzed several readily obtainable materials as Raman shift standards. Materials from different sources and/or batches were examined by at least six independent laboratories, using both dispersive and FT-Raman spectrometers. These labs used whatever calibration procedure they had in place, and the operators did not have access to predetermined accurate Raman shift values. The committee collected and tabulated the results and the eight sets of Raman shifts were published as an ASTM standard (11). A typical data set is shown in Table 10.3 for the case of naphthalene. The average Raman shift for those peaks exhibiting standard deviations of <1 cm^{-1} for eight different standard materials are listed in Table 10.4. A few frequencies at the extremes of the Raman shift range are based on fewer than six determinations or have standard deviations larger than 1 cm^{-1}, as indicated in the table. Spectra of six of the eight ASTM standards are shown in Figures 10.4, 10.5, and 10.6. The other two are 4-acetamidophenol (Fig. 5.7) and sulfur (Fig. 8.14). These eight standards were chosen for a variety of reasons, including wide spectral coverage (benzonitrile, acetonitrile/toluene), low Raman shift values (sulfur), low toxicity (4-acetamidophenol, polystyrene), strong Raman scattering [sulfur, bis-(2-methylstyryl) benzene], and compatibility with ultraviolet (UV), visible, and near-infrared (NIR) excitation (cyclohexane). Indene has been proposed as a shift standard based on a different procedure (3), and several of its peak frequencies are included in Table 10.4.

The Raman shifts listed in Table 10.4 are quite useful for verifying frequency accuracy, but there are some caveats associated with their use. They were determined with 1064- and 514.5 nm lasers, and changes in observed frequencies are possible at other wavelengths due to resonance effects. The procedures used for peak frequency determination are not part of the standard and can affect observed frequency. For example, a peak frequency taken from the maximum scattering intensity may differ slightly from the center-of-gravity frequency determined from the entire Raman band. Finally, the laboratories reporting results that contributed to Table 10.4 did not use a standard calibration procedure, thus contributing to the observed standard deviation of 0.3 to 1 cm^{-1}. More accurate shift standards than these are necessary for measurements requiring shift accuracy less than a few tenths of a wavenumber.

With a set of standard Raman shifts in hand, an instrument's Raman shift axis may be calibrated from a spectrum of one or more standards from Table 10.4. The same mathematical procedure used for atomic emission standards is employed, usually involving a quadratic or cubic fit of the observed to the actual frequencies from Table 10.4. As noted earlier, Raman shift standards provide a more direct calibration than an atomic emission lamp, with no need to accurately determine the laser frequency. The disadvantage of calibration

Table 10.3. Raw Data for Naphthalene Raman Shifts from Seven Independent Labs (All Raman Shifts in cm^{-1})

Scanning/PMT[a]	FT-Raman[b] A	FT-Raman B	FT-Raman C	FT-Raman D	FT-Raman E	FT-Raman F	Mean[c]	Literature[d]
74.3								
513.6	513.5	513.7	513.5	514.3	513.6	514.1	513.8 ± 0.3	512.2
763.5	763.8	763.8	763.6	764.4	763.8		763.8 ± 0.3	762.2
1021.3	1022.2	1021.5	1021.3	1022.3	1021.0	1021.4	1021.6 ± 0.5	1023.0
1147.3	1147.3	1146.9	1146.8	1147.7	1146.9	1147.5	1147.2 ± 0.3	1144.2
1382.3	1381.9	1382.2	1382.0	1382.6	1381.7	1382.4	1382.2 ± 0.3	1379.2
1464.3	1464.6	1464.5	1464.3	1465.0	1464.2	1464.8	1464.5 ± 0.3	1461.3
1576.3	1576.7	1576.6	1576.3	1577.1	1576.4	1576.8	1576.6 ± 0.3	1576.8
3056.0	3056.7	3056.6	3056.3	3057	3055.9	3056.1	3056.4 ± 0.4	3055.0

[a]514 nm excitation.
[b]All FT-Raman at 1064 cm^{-1}.
[c]Average of values from References 12 to 15.
[d]Mean of experimental values, with standard deviation.

Table 10.4. Raman Shifts of Standard Samples (ASTM E1840-96)[a]

Sample	Average (cm^{-1})± Standard Deviation	Number of Points	Relative Instensity[b]
4-Acetamidophenol	213.3 ± 1.77	5	17
(active ingredient of	329.2 ± 0.52	6	11
Tylenol)	390.9 ± 0.76	6	25
	465.1 ± 0.30	6	11
	504.0 ± 0.60	6	11
	651.6 ± 0.50	6	33
	710.8 ± 0.68	6	17
	797.2 ± 0.48	6	45
	834.5 ± 0.46	6	14
	857.9 ± 0.50	6	82
	968.7 ± 0.60	6	12
	1105.5 ± 0.27	6	7
	1168.5 ± 0.65	6	70
	1236.8 ± 0.46	6	75
	1278.5 ± 0.45	6	42
	1323.9 ± 0.46	6	100
	1371.5 ± 0.11	6	38
	1515.1 ± 0.70	6	9
	1561.5 ± 0.52	6	37
	1648.4 ± 0.50	6	73
	2931.1 ± 0.63	6	29
	3064.6 ± 0.31	6	26
	3102.4 ± 0.95	6	20
	3326.6 ± 2.18	3	7
Acetonitrile/Toluene	378.5 ± 0.92	7	4 (A)[c]
(50/50 v/v)	521.7 ± 0.34	7	10 (T)
	786.5 ± 0.40	7	39 (T)
	919.0 ± 0.40	7	11 (A)
	1003.6 ± 0.37	7	100 (T)
	1030.6 ± 0.36	7	23 (T)
	1211.4 ± 0.32	7	16 (T)
	1605.1 ± 0.47	7	6 (T)
	2253.7 ± 0.42	7	44 (A)
	2292.6 ± 0.89	7	5 (A)
	2940.8 ± 0.25	7	64 (A)
	3057.1 ± 0.63	7	30 (T)
Benzonitrile	460.9 ± 0.73	6	15
	548.5 ± 0.82	6	7

(continued next page)

Table 10.4. (*continued*)

Sample	Average (cm^{-1})± Standard Deviation	Number of Points	Relative Instensity[b]
	751.3 ± 0.74	6	10
	767.1 ± 0.59	6	10
	1000.7 ± 0.98	6	100
	1026.6 ± 0.81	6	13
	1177.9 ± 0.82	6	20
	1192.6 ± 0.56	6	25
	1598.9 ± 0.70	6	36
	2229.4 ± 0.39	6	67
	3072.3 ± 0.41	6	26
1,4 Bis(2-methylstyryl)	456.0 ± .56	6	3
benzene	642.4 ± .12	6	3
	841.6 ± .28	6	4
	950.1 ± .13	6	4
	978.0 ± .16	6	6
	1104.1 ± .31	6	5
	1177.7 ± .56	6	49
	1290.7 ± .28	6	9
	1316.9 ± .94	6	10
	1334.5 ± .16	6	12
	1555.2 ± .19	6	18
	1593.1 ± .44	6	100
	1627.9 ± .23	6	56
Cyclohexane	384.1 ± 0.78	6	2
	426.3 ± 0.41	6	3
	801.3 ± 0.96	6	95
	1028.3 ± 0.45	6	15
	1157.6 ± 0.94	6	6
	1266.4 ± 0.58	6	14
	1444.4 ± 0.30	6	12
	2664.4 ± 0.42	6	8
	2852.9 ± 0.32	6	100
	2923.8 ± 0.36	6	58
	2938.3 ± 0.51	6	67
Indene[d]	730.4 ± 0.5		97
	1018.3 ± 0.5		100
	1205.6 ± 0.5		67
	1552.7 ± 0.5		50
	1610.2 ± 0.5		47

(*continued next page*)

Table 10.4. (*continued*)

Sample	Average (cm^{-1})± Standard Deviation	Number of Points	Relative Instensity[b]
	2892.2 ± 1.0		28
	3054.7 ± 1.0		28
Naphthalene	513.8 ± 0.31	7	29
	763.8 ± 0.31	6	30
	1021.6 ± 0.49	7	11
	1147.2 ± 0.34	7	6
	1382.2 ± 0.31	7	100
	1464.5 ± 0.29	7	12
	1576.6 ± 0.29	7	16
	3056.4 ± 0.41	7	32
Polystyrene	620.9 ± 0.69	6	16
	795.8 ± 0.78	6	10
	1001.4 ± 0.54	6	100
	1031.8 ± 0.43	6	27
	1155.3 ± 0.56	6	13
	1450.5 ± 0.56	6	8
	1583.1 ± 0.86	6	12
	1602.3 ± 0.73	6	28
	2852.4 ± 0.89	5	9
	2904.5 ± 1.22	5	13
	3054.3 ± 1.36	6	32
Sulfur	85.1 ± 2.6	3	17
	153.8 ± 0.50	6	38
	219.1 ± 0.57	7	100
	473.2 ± 0.49	7	36

[a]From Reference 11.
[b]For 514.5 nm laser, RCA 31032 PMT, uncorrected for spectral response.
[c](A) denotes acetonitrile band; (T) denotes toluene band.
[d]From Reference 3, p. 64.

with shift standards is the lower density of available frequencies compared to atomic emission lamps. There are many more frequencies available for an atomic emission source, and they cover the entire spectrum with reasonable density. For example, only a few shift standards are available between 1800 and 2700 cm^{-1}, and fewer shift standards are available overall, compared to atomic emission lines. So the fit used for calibration is usually based on fewer, less well distributed points. That said, the shift standard is "just another sample" and is easy to implement. The shift standard reproduces the sample observation geometry more accurately than an atomic emission

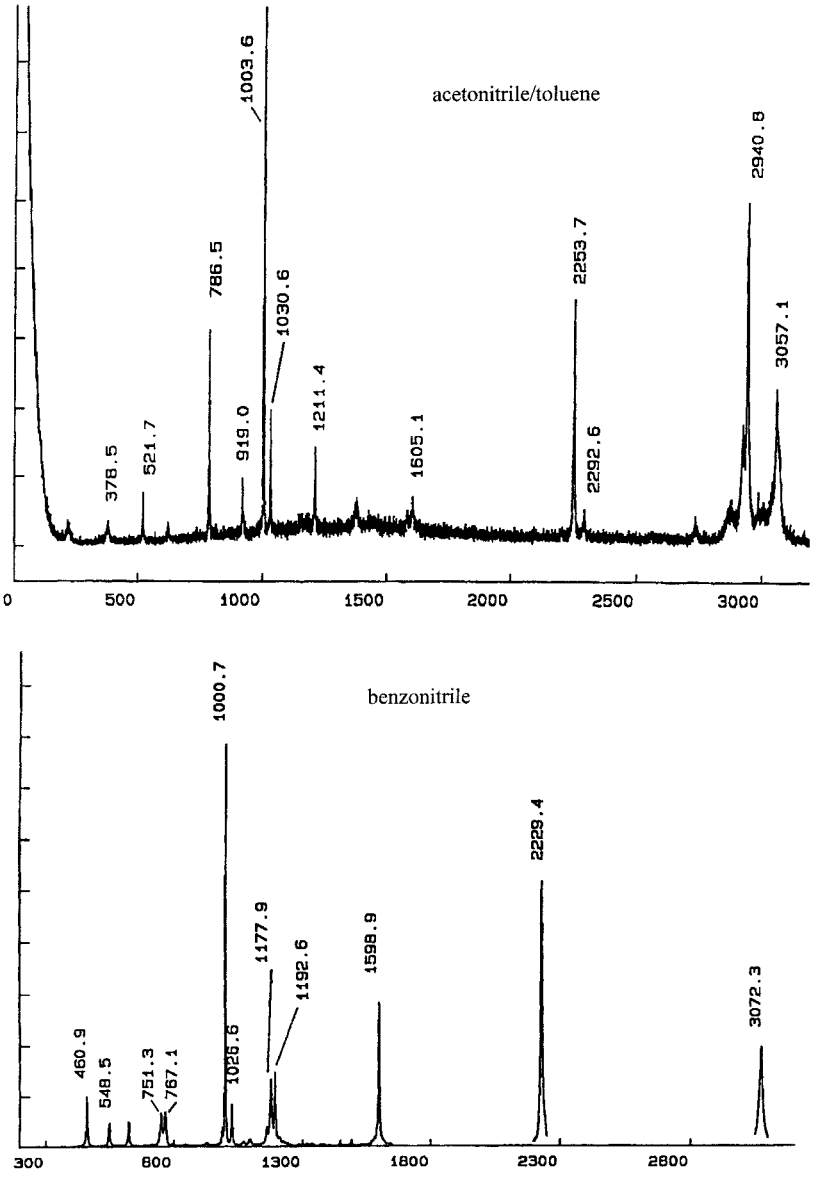

Figure 10.4. Uncorrected spectra of a 50/50 acetonitrile/toluene mixture and neat benzonitrile obtained with a Spex 1403, RCA 31034A PMT, and 514.532 nm laser. Raman shift values are from ASTM E1840 standard (11).

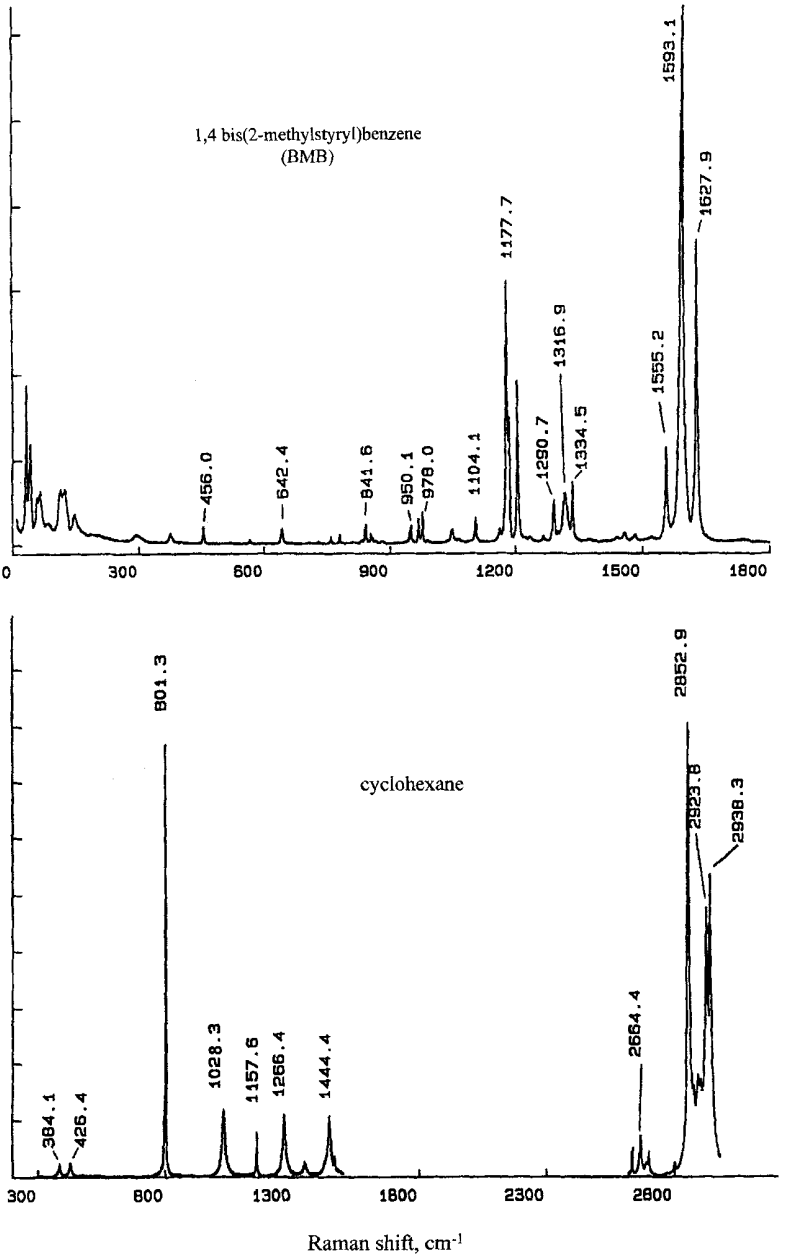

Figure 10.5. Spectra of 2,4-bis(2-methylstyryl)benzene and cyclohexane. Same conditions as Figure 10.4, with ASTM standard frequencies accompanying each peak.

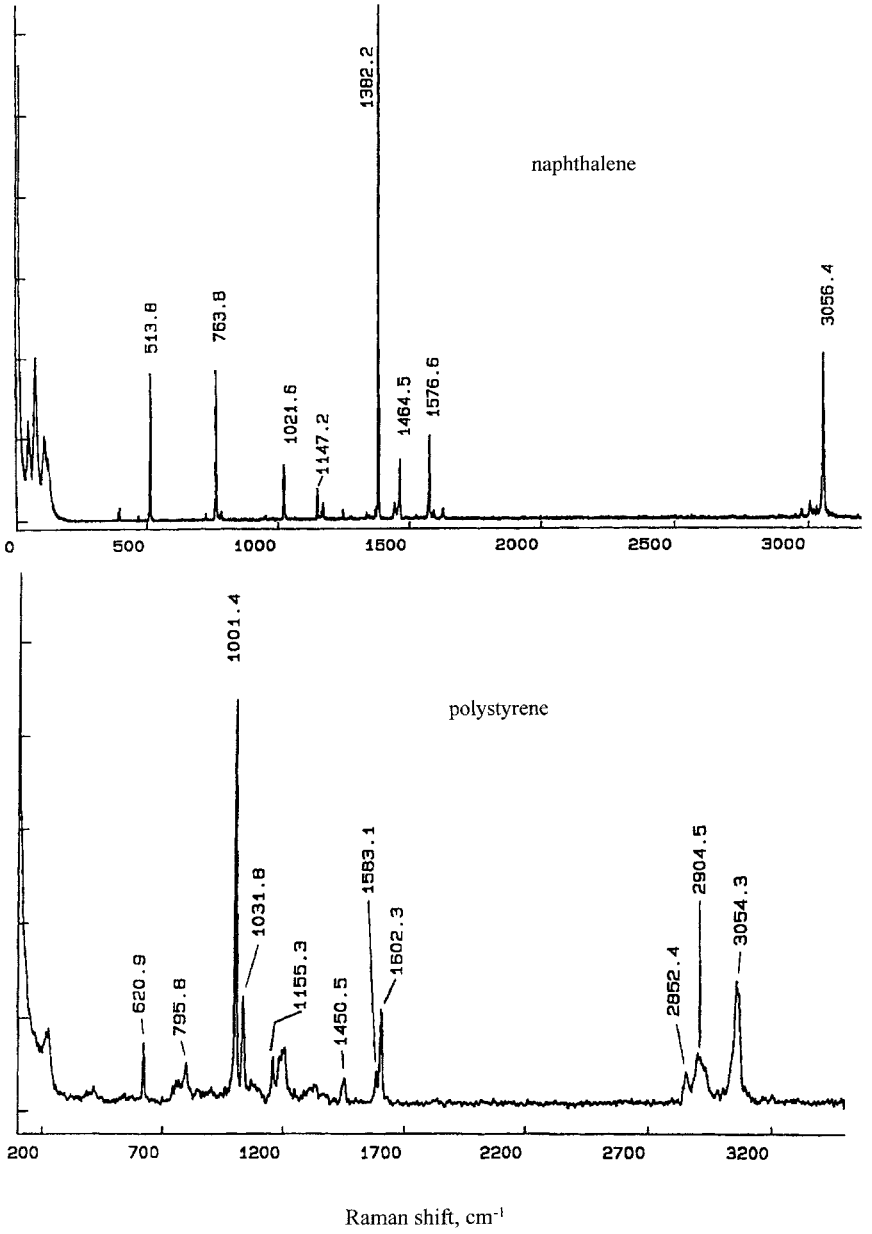

Figure 10.6. Spectra of naphthalene and polystyrene solids; conditions as in Figure 10.4.

source, thus reducing small frequency shifts resulting from sample position. Once the computer software is written, a shift calibration may be incorporated nearly automatically, with the user required only to run a calibration standard periodically.

10.2.3. Validation of Raman Shift Calibration

Validation and *qualification* are terms often used to describe procedures for verifying instrument performance. *Qualification* will be used here to describe a procedure for testing the initial performance of an instrument as it is received from a vendor or configured from components for the first time. The qualification procedure establishes the best performance achievable for a fully functional instrument in terms of frequency, accuracy, resolution, and the like. *Validation* is a simpler procedure repeated periodically to verify that instrument performance has not degraded over time. For example, the peak frequency of a particular Raman band of a standard might be determined at the beginning of each working day to check if some error (e.g., a mechanical offset) has arisen since the previous use. Under these definitions, qualification establishes the level of instrumental accuracy achievable when functioning properly, and validation provides a periodic check that accuracy has not degraded over time. When a particular instrument or analytical procedure is to be used to meet quality control or regulatory requirements, it is important that qualification and validation protocols be established clearly. When regulatory or patent issues are involved, the procedures are likely to be included in the user's permanent record.

For the case of Raman shift accuracy, the simplest criterion for tracking instrument performance is the standard deviation of several observed Raman shifts for standard samples. The standard should be examined under the same experimental conditions as subsequent experimental samples, and cover at least as large a Raman shift range. For example, 4-acetamidophenol has peaks covering the Raman shift range of most common samples (see Fig. 5.7), and ASTM shift values are available with standard deviations $<1.0\ \text{cm}^{-1}$ (Table 10.4). If the user needs to qualify an instrument for very low or very high Raman shift, or for greater precision, different standards must be used.

Once the criteria for validation are selected, qualification is usually carried out with a new instrument known to be operating properly. The specific procedure depends on the application, but it might include measures of short-term and long-term accuracy. As an example, consider determination of the Raman spectra of powders inside amber vials, such as the case shown in Figure 5.16. The qualification procedure could include several steps:

1. Raman shift calibration by a particular procedure.
2. Observation of an ASTM standard to verify compliance to $\pm 1\ \text{cm}^{-1}$.

3. Observation of a material similar to the samples of interest, as a secondary standard. In this example, calcium ascorbate was selected as a stable, reliable material similar to the samples of interest. One of the ASTM standards could also be used for qualification if convenient.
4. Determination of standard deviation for 10 successive spectra of the secondary standard, without adjustment of sample position. This result indicates short-term repeatability of spectrum acquisition.
5. Determination of standard deviation of 10 successive spectra, with recalibration between runs.
6. Determination of standard deviation of spectra obtained over a longer period of time, chosen to be relevant to the application. For example, if the instrument is recalibrated once a day, it is important to determine any drift in Raman shift occurring on a time scale of minutes and hours.

The example is illustrated by the results of Table 10.5. The Raman shift range from 400 to 2000 cm^{-1} was calibrated with the 4-acetamidophenol shift standard, and the calibrated spectrum was recorded and stored on disk. Then calcium ascorbate was observed, with and without recalibration between spectra. Finally, spectra of calcium ascorbate were obtained approximately daily (each after recalibration) over a period of 2 months. The 769- and 1582 cm^{-1} peaks were chosen for analysis, and their peak frequencies were determined by a center-of-gravity criterion included in the data analysis software (GRAMS 32). It is important that these qualification spectra duplicate the instrumental conditions to be used for real samples, at least as far as optical geometry, sampling mode, and calibration procedure. The objective is to provide an accurate indication of instrument performance in the intended application.

Table 10.5. Qualification Results for Frequency Accuracy of Dispersive/CCD Spectrometer

Sample: Solid Calcium Ascorbate	767-band (cm^{-1})	1582-band (cm^{-1})
15 repeated spectra, sample removed and replaced, without calibration between runs	767.0 ± 0.18	1582.6 ± 0.20
6 spectra over 10 days, recalibrated between spectra[a]	767.2 ± 0.11	1582.6 ± 0.32
23 spectra over 60 days, recalibrated before each spectrum[a]	767.27 ± 0.14	1582.67 ± 0.22

[a]Calibrated with 10 peaks of 4-acetamidophenol.

The first line of Table 10.5 indicates short-term repeatability. The second line indicates the reproducibility of the calibration procedure, based on six recalibrations over a 10-day period. Long-term drift is indicated by the third line, over a period of time selected by the user, with recalibration. These results may be used to verify specifications claimed by the manufacturer and to provide a baseline for future measurements. Table 10.5 provides an assessment of the Raman shift accuracy of a particular instrument, obtained using samples and procedures that should be similar to the intended application.

Once the qualification results such as those in Table 10.5 are in hand, validation of instrumental accuracy should be conducted periodically. In the current example, a spectrum of the calcium ascorbate standard might be obtained each day, and stored in an archive. These spectra provide an immediate check on the position of the 767 and 1582 cm^{-1} bands and may be accessed at a future date. If a particular sample spectrum comes into question, the calcium ascorbate spectrum for that day may be examined for any discrepancies. As noted earlier, a particular validation procedure will depend on the application, but a possible daily routine might include:

1. Start up instrument and allow stabilization.
2. Calibrate Raman shift by established procedure.
3. Obtain and record validation spectrum of an ASTM or secondary standard, verifying peak frequencies against qualification values.
4. Obtain sample spectra.
5. Obtain and record validation spectrum at end of day, to detect possible drift.

10.3. INSTRUMENT RESPONSE FUNCTION CALIBRATION

The instrument response function, $R(\Delta\bar{\nu})$, was introduced in Section 5.4.2 in the context of the reproducibility of relative peak intensities. As noted in Chapter 1, Raman spectroscopy is a single-beam technique in which the observed spectrum is the product of the true spectrum and the response function. Since the response function depends on several instrumental variables, such as detector quantum efficiency curve, laser wavelength, grating efficiency, and the like, the magnitude and shape of $R(\Delta\bar{\nu})$ can vary greatly for different instruments. In addition, $R(\Delta\bar{\nu})$ can vary for the same instrument over time or when a particular component (such as the detector) is replaced. As a consequence, Raman spectra for the same sample and the same laser wavelength obtained on different spectrometers can vary significantly. As example is shown in Figure 10.7 for cyclohexane observed with 514.5- and 785 nm excitation. Note the large difference in relative intensities of the 801- and

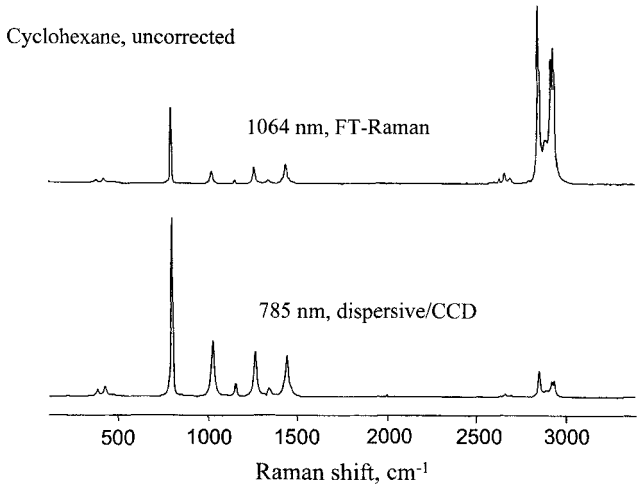

Figure 10.7. Spectra of cyclohexane obtained on FT-Raman and dispersive/CCD spectrometers, without correcting for instrument response function.

2853 cm^{-1} bands, due mainly to the weaker CCD response in the deep red for the 785 nm spectrum.

10.3.1. General Procedure

The majority of Raman spectra reported in the literature are uncorrected for instrument response, so one could argue that the most common response correction is none at all. Uncorrected spectra are still valuable for qualitative applications involving comparison of peak frequencies and for quantitative comparisons where the response function is unknown but constant. For example, a quantitative analysis of two components based on the relative heights (or areas) of two Raman bands can be calibrated with known solutions and applied to unknowns without determination of the response function. However, there are many situations in which response function calibration is important, including variations in relative intensity with different instruments, variations caused by instrumental drift or repair, and subtraction of library spectra (see Fig. 5.6). If a quantitative analysis is based on a calibration curve without response correction, a new curve must be collected if a change in response

* As discussed later in Section 10.3.4.3, a small part of this relative intensity difference is due to cross-section changes between 514.5 and 785 nm, but this effect is usually much smaller than the response distortion from the instrument.

functions occurs. On a fundamental level, uncorrected spectra are not accurate representations of Raman scattering as a function of frequency and are therefore one step removed from reality.

In principle, the response function could be calculated from the response functions of each relevant component, including collection optics, wavelength analyzer, detector, and the like, but this procedure is both tedious and difficult. The response or efficiency curves for each component are often known to a low degree of accuracy and are generally hard to measure. A more practical approach involves a standard with known emission of intensity vs. wavelength. Given such a standard, the correction procedure is straightforward, as illustrated in Figure 10.8. Using the same conditions as those for the real sample, the observed spectrum of the standard (S_L) is recorded. This spectrum is the product of the response function and the standard output [$\Phi_S(\Delta\bar{\nu})$], as in Eq. (10.1):

$$S_L(\Delta\bar{\nu}) = R(\Delta\bar{\nu})\Phi_L(\Delta\bar{\nu}) \tag{10.1}$$

where $R(\Delta\bar{\nu})$ includes all of the contributions from individual components (grating, detector, etc.). Since $\Phi_S(\Delta\bar{\nu})$ of the standard is known, $R(\Delta\bar{\nu})$ may be calculated from the observed spectrum. The standard source is replaced by the sample, and the uncorrected sample spectrum [$S_S(\Delta\bar{\nu})$] is recorded. The corrected sample spectrum, $\Phi_S(\Delta\bar{\nu})$, may then be calculated from the known response function via Eq. (10.2):

$$\Phi_S(\Delta\bar{\nu}) = \frac{S_s(\Delta\bar{\nu})}{R(\Delta\bar{\nu})} \tag{10.2}$$

This step is illustrated in Figure 10.8, at the point labeled R^{-1}. Equations (10.1) and (10.2) may be combined to yield Eq. (10.3), which illustrates that the response function need not be explicitly determined in order to correct a sample spectrum:

$$\Phi_S(\Delta\bar{\nu}) = \frac{S_S(\Delta\bar{\nu})\Phi_L(\Delta\bar{\nu})}{S_L(\Delta\bar{\nu})} \tag{10.3}$$

In practice, the corrected sample spectrum may be determined from the ratio of sample and standard spectra and the known standard emission curve.

Specific procedures for implementing Eqs. (10.1), (10.2), and (10.3) differ according to the nature of the standard source. The most common source is a black-body radiator, often approximated by a tungsten bulb. A less common alternative with some attractive advantages is a standard material which luminesces in response to laser excitation. These approaches will be addressed separately.

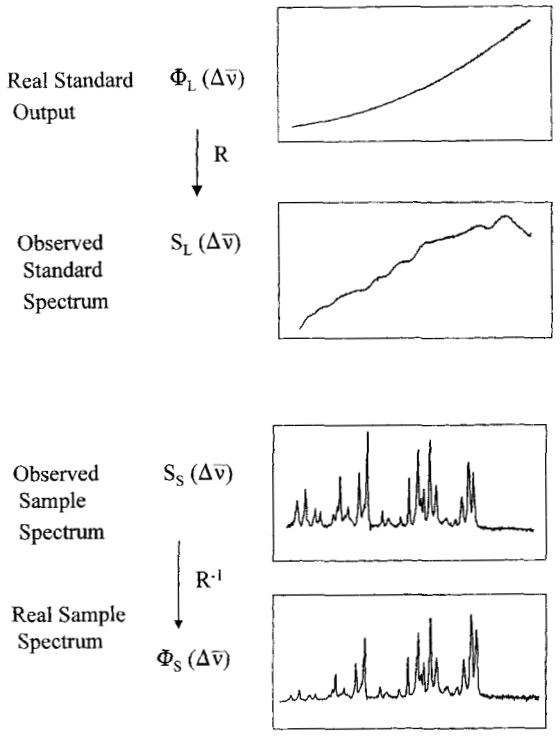

Figure 10.8. Schematic of procedure for correction of spectra for instrumental response variation. R represents the response function; ϕ_L and ϕ_S are the actual output of the sample and standard (intensity vs. Raman shift) and S_S and S_L the observed spectra.

10.3.2. Response Calibration with a Black-Body Source

Since the thermal emission curve from a black-body radiator may be calculated from first principles, it can serve as a primary standard for an intensity vs. wavelength curve. Petty et al. (16) described a procedure for intensity calibration of an FT-Raman spectrometer using such a source. Provided the source acts as a black body to the required accuracy, its temperature is known, and the laser wavelength is known accurately, the black-body provides a known $\Phi_L(\Delta\bar{\nu})$ curve to use in Eq. (10.3). Since most modern spectrometers measure photons/second rather than watts, the proper units for $\Phi_L(\Delta\bar{\nu})$ are photons per second per wavenumber.*

* The solid angle and area are sometimes included in the emission curve, yielding photons per second per wavenumber per square centimeter per steradian.

Black-body sources have the attraction of being primary standards but are rather cumbersome. A quite hot furnace is required to produce sufficient intensity, particularly at visible wavelengths. In addition, the source is usually too large to be positioned near the sample region (assuming the spectrometer could tolerate the heat!), so coupling optics are required. These optics should attempt to position the source image at the normal laser and collection focus and may not introduce their own response function. At least for routine use, a black-body radiator is unlikely to be practical.

A tungsten bulb approximates a black body, and calibrated tungsten sources are available with traceability to National Institute of Science and Technology (NIST) standards. Once a given bulb is calibrated, its output will remain constant to a few percent for perhaps 10 to 100 h of operation. Control of lamp current is critical, as the emission curve is strongly temperature (and current) dependent. Generally, the user purchases a regulated power supply, bulb mount, and calibrated bulb from a vendor who conducts the calibration. As with the black-body radiator, it is impractical or inconvenient to place the bulb at the Raman sample position, so optics are required to project a bulb image to the sample location. The calibration will be most accurate when the source duplicates the sample position and fills the spectrometer collection angle and aperture in a fashion similar to Raman scattering from a real sample. A convenient example of coupling optics involves using a fiber optic to couple the source to the spectrometer, with the end of the fiber optic positioned at the laser focus (17).

The vendor of the calibrated source provides a table of output vs. wavelength for a particular bulb current. It is usually convenient to determine a polynomial that reproduces this output curve, to permit calculation of bulb output at any wavelength within the calibration range. Figure 10.9A shows an emission curve for a 100 W tungsten source operated at 6.50 A. The calibrated intensities provided by the vendor are usually in terms of watts per cubic centimeter, meaning watts per square centimeter (at a distance of 50 cm from the source) per centimeter of wavelength. Conversion of these values to more useful units of photons per square centimeter per nanometer per second is accomplished by dividing by $h\nu$ and 10^7 nm/cm. The resulting curve for a typical source is spectrum B of Figure 10.9. According to the discussion of Section 8.2.1 and Eq. (8.1), curve B of Figure 10.9 may be further converted to units of photons per square centimeter per second per wavenumber by multiplying by λ^2 to yield curve C of Figure 10.9.* The magnitude of the two curves is obviously different, but more importantly their shape is different. The

* Combination of these conversion factors yields a composite factor of 50.35 λ^3 for conversion of watts per cubic centimeter for the tungsten source to photons per square centimeter per second per wavenumber, with λ stated in nanometers.

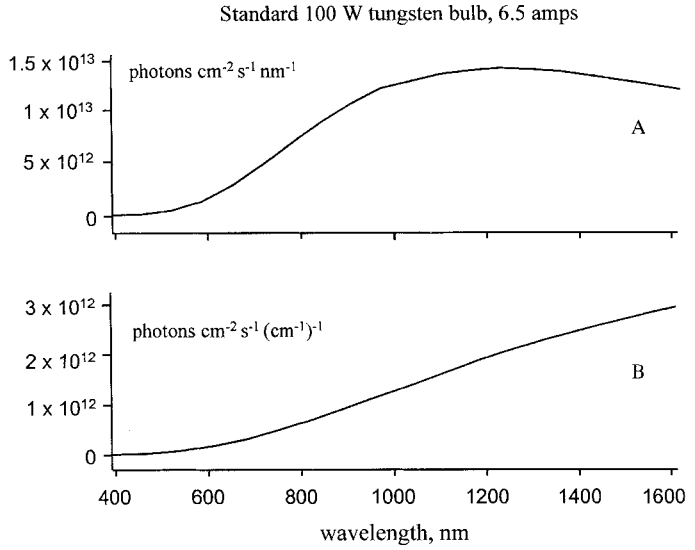

Figure 10.9. Emission output of a calibrated tungsten bulb plotted using different intensity units.

wavenumber range per nanometer of wavelength differs across the spectral range of Figure 10.9, which causes the change in shape.

To implement an instrument response correction using a standard tungsten source, the curve of Figure 10.9B is usually fit to a polynomial, so Φ_L may be calculated at any wavelength within the calibration range. Knowing the laser wavelength and Raman shift range of the sample spectrum to be corrected, the function $\Phi_L(\Delta\bar{\nu})$ may be calculated (17). Then a spectrum of both the tungsten source and the sample are obtained, and Eq. (10.3) is used to calculate the corrected sample spectrum, $\Phi_S(\Delta\bar{\nu})$. In practice, the data analysis is easily automated, usually as part of the spectrometer software. So the user need only acquire a spectrum of the tungsten source for a given spectrometer configuration, then store the results. A series of sample spectra may be corrected from a single tungsten spectrum provided conditions remain constant for sample and standard. Response correction of an entire day's spectra may require only one tungsten spectrum, possibly acquired during instrument start-up and validation. Raman spectra of CH_2Cl_2 before and after response correction with a standard tungsten source are shown in Figure 10.10. Notice that the raw spectra differ greatly in relative peak intensities, mainly because of variation in detector Q for the two wavelength ranges involved. After correction, however, the relative intensities vary only slightly, by an amount predicted from the ν^3 dependence.

Response correction based on a tungsten bulb is currently the most common procedure (when correction is undertaken at all) but is not without some

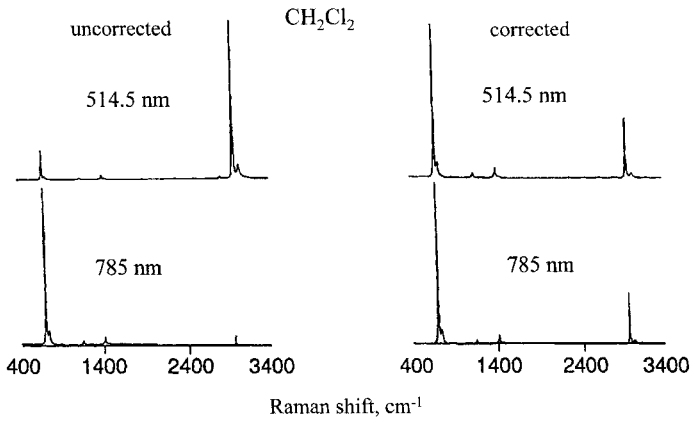

Figure 10.10. Spectra of methylene chloride with 514.5- and 785 nm lasers before and after response correction with a standard tungsten source coupled to the spectrometer with fiber optics. (Adapted from Reference 17 with permission.)

disadvantages. First, it is difficult to precisely reproduce the Raman sampling geometry with the tungsten source, so the standard will "fill" the spectrometer differently from a real sample. The response function varies somewhat with sample position, so the standard will not yield an accurate response function without perfect positioning. Second, a tungsten source requires some manual manipulation for positioning and control and may be inconvenient on a routine basis. Third, a tungsten emission source (or its image) is usually significantly larger than a focused laser spot, again causing a mismatch of sample and standard optical geometry. Finally, the tungsten source output has no relation to the laser intensity, so the magnitude of the source spectrum has no significance with regard to the Raman sample cross section (more on this in Section 10.4). These difficulties with tungsten calibration standards stimulated development of an alternative based on luminescent sample materials.

10.3.3. Response Calibration with Luminescence Standards

Luminescent standards have been established for use in calibrating fluorescence spectrometers and have been suggested for Raman spectroscopy in the past (18). The standard is a luminescent material, usually a solid or liquid, that emits a broad reproducible luminescence spectrum when excited by a laser. Once the standard is calibrated for a particular laser wavelength, its emission spectrum is known, and it can provide the "real standard output", $\Phi_L(\Delta\bar{\nu})$ depicted in Figure 10.8. In practice, a spectrum of the standard is acquired with the same conditions as an unknown; then the unknown spectrum is corrected for instrument response function using the known standard

output via Eq. (10.3). Examples of two luminescence standards are shown in Figure 10.11. Coumarin 540a is a laser dye suitable for 514.5 nm excitation and Kopp 2412 glass is a common filter glass material useful at 785 nm (15,16). Such standards are most useful when provided with a polynomial representing their emission spectra expressed as intensity vs. Raman shift (in reciprocal centimeters) relative to a specified laser wavelength. Polynomials for coumarin 540a and Kopp 2412 glass are listed in Table 10.6. The spectra reconstructed from these polynomial coefficients are shown in Figure 10.11 as "corrected" output. Both raw and corrected curves are normalized to the maximum output within the indicated Raman shift range.

An ideal luminescent standard for Raman intensity calibration would have several characteristics (17), some of which are difficult to achieve:

1. A broad, featureless output over the relevant wavelength range.
2. Exactly reproduce the Raman sampling geometry.
3. Simple and easy to implement.

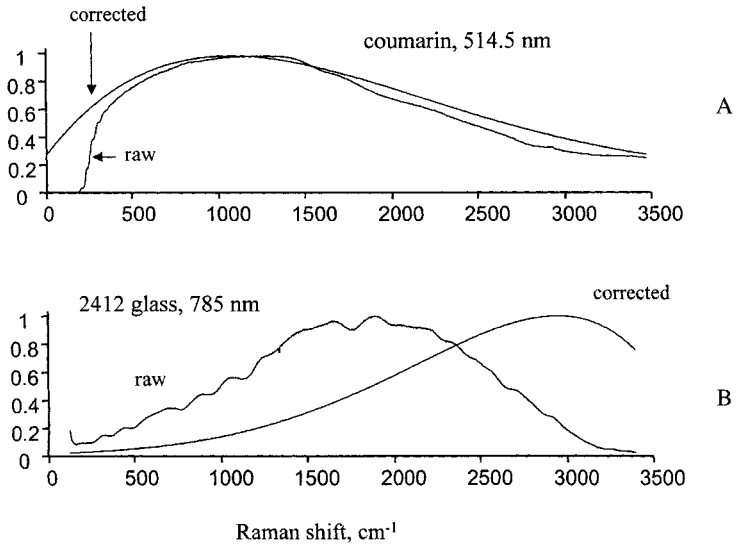

Figure 10.11. Observed and corrected emission curves for two luminescent standards. "Raw" curves were recorded for coumarin 540a solution excited by 514.5 nm light, and for Kopp 2412 glass excited by 785 nm light. Raman shift is stated relative to the appropriate laser wavelength. "Corrected" output was calculated by comparison to a standard tungsten source. All curves are normalized to their maximum output. See Reference 20 for details. Spectrum A was determined on a Dilor X-Y spectrometer, B was acquired with a Chromex 2000.

Table 10.6. Polynomial Coefficients for Intensity Standards, Normalized to Maximum Intensity

Raman Shift[a]	Coumarin 540a (514.5 nm)	Kopp 2412 #1 (785 nm)[b]
$(\Delta\bar{\nu})^0$	0.2701196431	0.015647
$(\Delta\bar{\nu})^1$	1.5743416716e-3	6.284845e-5
$(\Delta\bar{\nu})^2$	−1.0957287534e-6	−1.515732e-8
$(\Delta\bar{\nu})^3$	2.5681273909e-10	8.564479e-11
$(\Delta\bar{\nu})^4$	−2.0594831955e-14	−9.472784e-15
$(\Delta\bar{\nu})^5$		1.594599e-18
$(\Delta\bar{\nu})^6$		−1.375663e-21

[a]In wavenumbers relative to indicated laser. Standard emission curve (with maximum equal to 1.0 arbitrary units) is reconstructed from the coefficients and the Raman shifts (relative to 514.5 or 785 nm) raised to the indicated powers. From Reference 20.

[b]Coefficients vary for individual samples of 2412 glass.

4. Require no additional equipment other than what is required to take the Raman spectrum.
5. Reproducible luminescence output, no sample heterogeneity.
6. The source should exhibit long-term stability, both with and without laser illumination.

The reproducibility and stability requirements can be particularly problematic. Since luminescence requires light absorption and electronic excitation of the material, photochemical degradation is possible. This is a particular problem with the high laser power densities encountered in Raman microscopy or even conventional sampling. For example, luminescence from the Kopp 2412 standard decreases upon prolonged laser exposure, even after a few minutes at higher power (19, 20). At this writing, there are no NIST traceable luminescence standards available for common Raman wavelengths, although a few (e.g., quinine) are available for UV excitation. Currently, there is an ongoing effort at NIST to establish and eventually sell luminescent standards for common laser wavelengths, and glasses containing rare earth oxides appear to be promising candidates.

Compared to the tungsten lamp, luminescence standards are quite simple to use. The polynomial and associated mathematical manipulations are usually implemented automatically in the spectrometer software (21). The user need only acquire a spectrum of the standard under the same conditions as the sample of interest, usually once per session. After the spectrum $[S_L(\Delta\bar{\nu})]$

is acquired, response correction may be automatic until conditions (such as grating position) are changed. As noted earlier, a luminescence standard is generally calibrated for only one laser wavelength, while a tungsten bulb may be used for many laser wavelengths. With both tungsten and luminescent standards, the accuracy of the response correction will depend on the accuracy of the standard's emission spectrum.

An additional advantage of a luminescent standard over a tungsten source is the ability to closely mimic the optical conditions existing when the sample was observed. If the sample is in a container or at the end of an optical fiber, the luminescent standard may also be observed under the same conditions, and any attenuations or aberrations will apply to both sample and standard. Figure 10.12 illustrates the case of a powdered sample inside an amber vial. The vial attenuates the laser and the scattered light, and will cause distortion of relative intensities if not corrected. However, if the standard is also inside a similar vial when its spectrum is obtained, then the response correction will include the effects of the vial. Figure 10.13 shows corrected spectra of acetaminophenol as an open powder and inside an amber vial. Despite the fact that the vial attenuates the overall signal by about 60 per cent, the corrected relative and absolute peak heights are the same to better than 5 per cent. A similar correction would be difficult or impossible with a tungsten source, since the source would have to be positioned inside a vial, and even then would not exactly duplicate the optical geometry used for the sample.

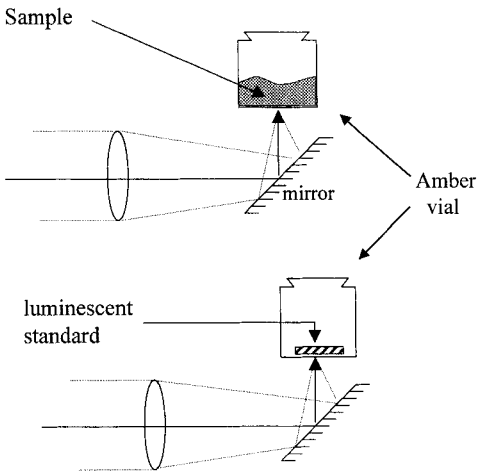

Figure 10.12. Correction for vial absorption using luminescent standard. Upper drawing shows 180° sampling of a powder inside an amber vial. Lower drawing is the same arrangement, but with a luminescent standard substituted for the sample, to correct the response function for vial absorption.

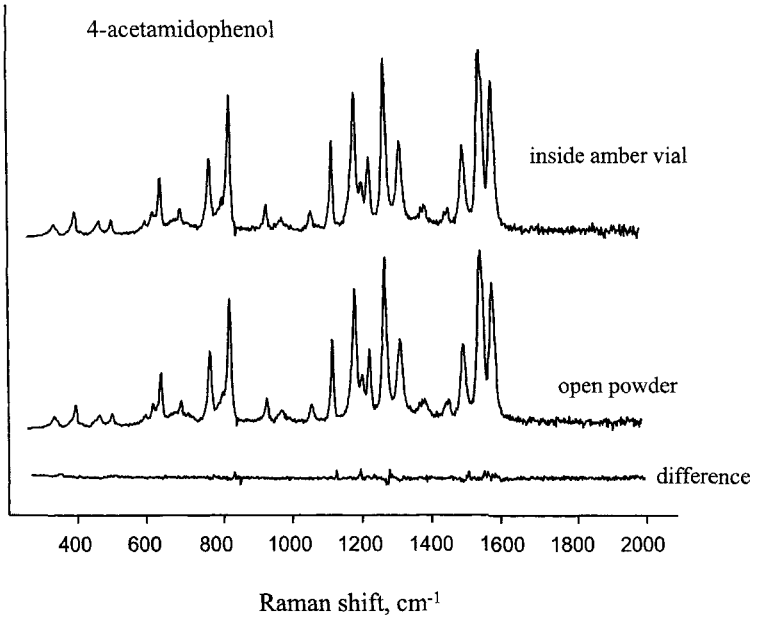

Figure 10.13. Spectra of 4-acetamidophenol as an open powder and inside an amber vial. Both spectra are corrected for response function with Kopp 2412 glass. For the vial spectrum, the standard was inside the vial when the response function was determined. Bottom spectrum is the difference of the corrected spectra. Optical geometry was that of Figure 10.12; laser wavelength was 785 nm.

The corrected cyclohexane spectrum of Figure 5.17 is shown in more detail in Figure 10.14. The peak areas relative to the 801 cm^{-1} band are indicated, based on the average of corrected spectra from two different spectrometers (Chromex 2000 and Dilor X-Y). The results for cyclohexane are listed in Table 10.7, along with some reported values from the literature (20). Corrected spectra of several additional solvents are shown in Figure 10.15, with peak area ratios obtained with 785 nm excitation. Notice that the integration ranges for each peak are indicated, and that the C—H stretch region of most compounds are combined into one "peak" area. Since response function corrections are fairly difficult, and many variables are involved, literature values often disagree significantly. Nevertheless, it is clear that the agreement between relative peak areas for corrected spectra is far better than that for uncorrected spectra, as illustrated by Figures 10.7 and 10.10. The importance of response function correction lies in the ability to compare results from different labs and different instruments. Whether the correction employs a tungsten source or a luminescent standard, the result is a spectrum that is closer

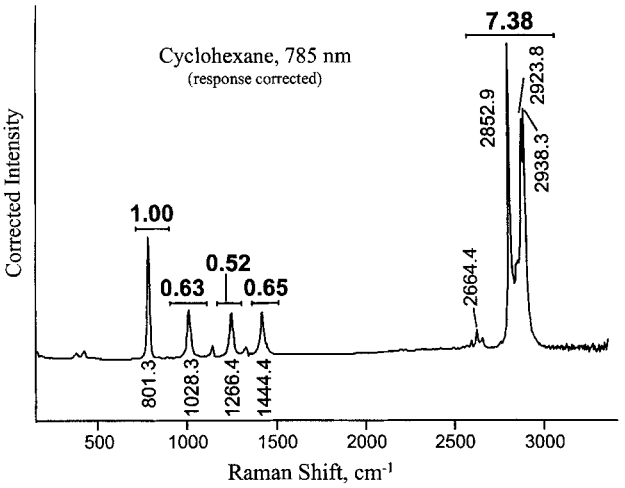

Figure 10.14. Cyclohexane spectrum following correction with Kopp 2412 glass standard. Horizontal numbers are the peak areas (integrated over the shift range indicated by the horizontal bars), relative to the 801 cm^{-1} peak area. Vertical numbers are the ASTM frequencies for cyclohexane listed in Table 10.4 and Reference 11. Intensity data is average of two spectrometers calibrated independently, as described in Reference 20. (See footnote *e* of Table 10.7.)

to reality, less affected by instrumental distortion. As Raman spectroscopy is used more widely, both frequency calibration and response function correction will become more important. Fortunately, both may be implemented simply (even automatically) provided the instrument is stable.

10.3.4. Validation of Instrument Response

Qualification and validation of Raman intensities may be approached according to several criteria, three of which will be considered here. First, the magnitude of the Raman signal for a given standard or sample should be observed with a well-tuned instrument upon installation, and checked for short- and long-term reproducibility. This test provides an indication of the absolute signal magnitude expected for a particular set of conditions and permits detection of instrumental changes. Second, the reproducibility of relative peak heights (or areas) of two or more peaks may be examined to evaluate the stability of the instrument response function. Third, a corrected spectrum of a standard (such as cyclohexane) may be obtained and compared to accepted values. The combination of these three qualification tests provides quantitative measures of the reproducibility of the absolute and relative intensities, as well as the compliance of a corrected spectrum with a known standard spectrum.

Table 10.7. Relative Peak Areas for Cyclohexane, 785 nm

Cyclohexane	Literature[a]	Chromex 2000	Dilor X-Y	Mean[b]
801 (700–900)[c]	1.00	1.00	1.00	
1028 (925–1125)	0.58	0.62 ± 0.03 ($N = 7$)[d]	0.64 ± 0.01 ($N = 4$)[d]	0.63 ± 0.03 ($N = 11$)[d]
1267 (1180–1315)	0.49	0.51 ± 0.02 ($N = 7$)	0.53 ± 0.02 ($N = 4$)	0.52 ± 0.02 ($N = 11$)
1444 (1380–1525)	0.64	0.63 ± 0.03 ($N = 7$)	0.67 ± 0.04 ($N = 4$)	0.65 ± 0.04 ($N = 11$)
All CH (2587–3068)	6.50	7.17 ± 0.77 ($N = 7$)	7.74 ± 0.68 ($N = 4$)	7.38 ± 0.76 ($N = 11$)[e]

[a]Calculated from Reference 22, using $\bar{\nu}_0(\bar{\nu}_0 - \bar{\nu}_j)^3$ dependence.

[b]Mean of Chromex and Dilor values. From Reference 20. Also illustrated in Figure 10.14.

[c]Raman shift range for peak integration.

[d] Mean $\pm$ standard deviation. N is number of measurements.

[e]As this book goes to press, NIST is testing new luminescent standards and verifying relative cyclohexane intensities. NIST results have not been finalized, but currently show a deviation of approximately +25% from these values.

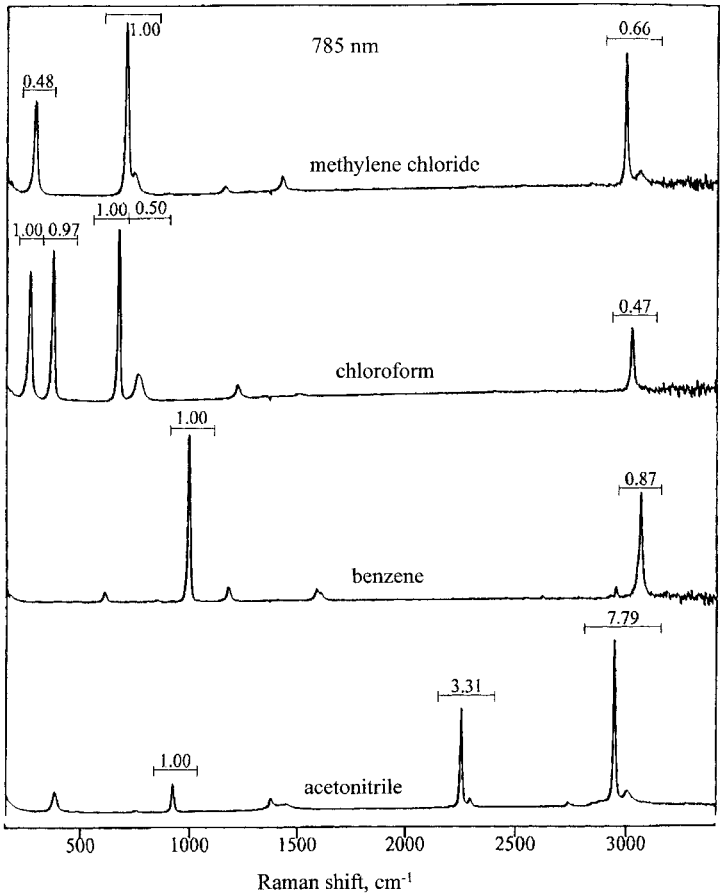

Figure 10.15. Response-corrected spectra of four common solvents obtained on a Chromex 2000 spectrometer and corrected with Kopp 2412 glass. Numbers are peak areas (integrated over the shift range shown) after normalizing to the band area indicated by "1.00." (Adapted from Reference 20 with permission.)

10.3.4.1 Validation of Signal Magnitude

Since so many instrumental variables determine the magnitude of the Raman signal (as discussed in Chapter 3), it is difficult to predict the magnitude of a Raman signal for a given instrument and sample. However, it is important to determine the signal magnitude for a new instrument and to determine its reproducibility. As the spectrometer is used in different applications, its alignment, optics, or active components (e.g., laser and detector) may change. If

the initial signal for a given sample is known, that sample may be observed again to detect a possible decline in performance. Short- and long-term reproducibility are of obvious importance for any quantitative applications.

As with Raman shift qualification, the procedure for response qualification will depend on the application, but some possible criteria are as follows:

1. Standard deviation of repetitive runs of a given sample to test short-term reproducibility.
2. Standard deviation of many runs of a given sample obtained over extended periods, perhaps days or months.
3. Linearity of signal with integration time to check photometric linearity of the detector.
4. Linearity of signal with laser power.

To illustrate the first two criteria, consider the example of calcium ascorbate. The results of several tests of quantitative reproducibility are listed in Table 10.8. In this case, the signal magnitude for the calcium ascorbate sample is reproducible to about 5 per cent over both long and short term. The absolute signal in electrons for a particular set of conditions provides a benchmark for future checks of instrument performance and alignment. When absolute signal is recorded for future use, it is essential to record all relevant variables, such as slit width, laser power, grating choice, and CCD gain. Additional examples of short-term reproducibility for various samples observed with the 180° geometry were listed in Table 6.4. For clear, homogeneous samples,

Table 10.8. Calcium Ascorbate Powder, 785 nm, Chromex 2000 Spectrometer[a]

rsd[b] for 767 cm^{-1} peak height, 15 successive runs	4.3%
rsd for 1582 cm^{-1} peak height over 3 weeks ($N = 9$)	4.9%
rsd for 1582 cm^{-1} peak height, 15 successive runs	4.8%
absolute magnitude of 1582 cm^{-1} peak over 3-week period, for 50 mW laser, 30 sec exposure, 50 μm slit, 600-line/mm grating, in electrons	35,800 ± 1700[c]

[a]Sample inside USP amber vial, illuminated through bottom of vial in 180° geometry.
[b]Relative standard deviation.
[c]Standard deviation of nine measurements.

quantitative reproducibility was <1 per cent, while homogeneous translucent solids increased variation to ~5 per cent.

Once the absolute signal strength for a given sample and conditions are known for a newly installed or newly tuned instrument , daily validation might consist simply of a check of signal strength for the original qualification sample. The signal magnitude for the same conditions as the qualification spectrum indicates the general health of the spectrometer and can also warn the operator of any errors in setting spectrometer parameters.

10.3.4.2 Validation of Relative Response

Even if the instrument response function is not calibrated with the methods described in Section 10.3, the user should be aware of any changes caused by misalignment or instrument repair. Some important analyses are based on the ratio of two or more peak intensities, such as the relative concentrations of two components in a mixture, or identification of a compound by comparison to a reference spectrum. In such cases, the user must be aware of changes in instrument response that may alter the relative intensities of peaks in different locations on a spectrum. A first-order approach to this issue is quantitative comparison of two peaks of a standard sample, recorded during instrument qualification and periodically for instrument validation. The two peaks might be from a standard relevant to the analysis at hand, such as a known mixture of two components. Periodic checks of one or more peak height ratios will detect changes in response function, at least at the Raman shift regions involved. However, this simple approach is useful only for a particular instrument and does not permit comparison to other instruments or even to the same instrument after adjustment or repair.

Recalibration of the instrument response function reduces or eliminates most of the instrumental factors that lead to relative intensity variations over time. For example, a luminescent standard could be used at the beginning of each session as described in Section 10.3.3. Use of the same standard and correction procedure during qualification could establish the true value of one or more peak ratios for future reference. Table 10.9 shows results for this approach applied to the example of calcium ascorbate. The ratio of the 767- and 1587 cm^{-1} peak intensities was monitored after calibration of the response function with a luminescent standard. The standard deviations listed in Table 10.9 for the 767/1582 peak height ratio provide indications of the reproducibility of the response correction and sample spectra.

10.3.4.3 Standards for Response Function

Regardless of the method used to calibrate response function, it is useful to have standard corrected spectra of readily available materials to verify that the

Table 10.9. Calcium Ascorbate, 785 nm, Chromex 2000, Calibrated with Luminescent Kopp 2412 Glass

	Peak Height of 767 cm^{-1}	1582	767/1582 Ratio[a]
15 successive spectra, one response calibration	0.00548[a] ± 0.0002	0.01185[b] ± 0.00053	0.462 ± 0.030
9 spectra over 29 days, response recalibrated before each run	0.00523 ± 0.0007	0.0124 ± 0.0022	0.432 ± 0.0096
23 spectra over 40 days, recalibrated before each spectrum	0.00543 ± 0.0004	0.0116 ± 0.0009	0.466 ± 0.011

[a]Based on peak height, not area.

[b]Peak height expressed relative to maximum Kopp 2412 emission intensity.

response calibration was accurate. The cross sections listed in Tables 2.2 and 2.3 can be used to calculate spectra for any laser wavelength (in principle) where resonance is not involved, but this process is not trivial, and the range of valid wavelengths may be limited. Ideally, corrected spectra for common samples and a variety of laser wavelengths could be determined, along with tabulations of relative peak area ratios. A comparison of the observed spectra for a given spectrometer to those of the standard would provide assessment of response accuracy.

Unfortunately, a set of standard, corrected spectra does not exist at this writing. Figure 10.14 represents a tentative standard for cyclohexane at 785 nm, which is currently being verified by different labs, including NIST. The horizontal bars above each peak in Figure 10.14 represent the range of Raman shifts used during integration of a given peak, and the accompanying number is the peak area relative to that of the 801 cm^{-1} band. If one assumes that all of the Raman bands of cyclohexane are not resonance enhanced, relative peak areas for other laser wavelengths may be predicted. Since cyclohexane absorbs light deep in the UV, its cross section is likely to follow the $\nu_0(\nu_0 - \nu_j)^3$ dependence indicated by Eq. (2.14) for at least the visible and NIR wavelength regions. At a particular laser wavelength, the peak area ratio of any cyclohexane feature to the 801-band area is given by:

$$\frac{A_j}{A_{801}} = \frac{\sigma_j}{\sigma_{801}} = \frac{\sigma_j^\circ}{\sigma_{801}^\circ} \frac{(\bar{\nu}_0 - \bar{\nu}_j)^3}{(\bar{\nu}_0 - 801)^3} \tag{10.4}$$

where A_j and A_{801} represent peak areas and σ_j° is the laser independant cross section defined in Chapter 2. Equation (10.4) follows from Eqs. (2.13) and (2.14), since all measurement variables are the same for two bands in the same molecule.

To adjust the peak area ratios determined for one laser wavelength to those expected for another wavelength, Eq. (10.4) is written for two ν_0 values and rearranged to yield

$$\frac{A'_j}{A'_{801}} = \frac{A_j}{A_{801}} \frac{(\bar{\nu}'_0 - \bar{\nu}_j)^3(\bar{\nu}_0 - 801)^3}{(\bar{\nu}'_0 - 801)^3(\bar{\nu}_0 - \bar{\nu}_j)^3} \tag{10.5}$$

where (A'_j/A'_{801}) is the peak area ratio at a different laser frequency, $\bar{\nu}'_0$. The peak areas of cyclohexane features relative to the 801 peak area may be calculated from Eq. (10.5) for any wavelength where resonance effects are absent. The experimental peak area ratios noted in Figure 10.14 were adjusted by this procedure to yield Table 10.10. The peak ratios shown in Figure 10.14 and Table 10.10 apply to spectrometers that detect photons, such as dispersive spectrometers with CCDs or photon counting detectors. However, most

Table 10.10. Calculated Peak Area Ratios for Cyclohexane, Relative to 801 cm^{-1} Band, for Different Laser Wavelengths

Shift	Integration Range (cm^{-1})	488 nm	514.5 nm	532 nm	632.8 nm	647 nm	785[a] nm	1064 nm (photons)	1064[b] (watts)
2900	2567–3068	9.400	9.211	9.087	8.387	8.290	7.38	5.692	4.30
1444	1380–1525	0.694	0.690	0.688	0.672	0.670	0.65	0.607	0.600
1267	1180–1125	0.545	0.543	0.542	0.533	0.531	0.52	0.495	0.492
1028	925–1125	0.644	0.643	0.638	0.637	0.636	0.63	0.615	0.613
801	700–900	1	1	1	1	1	1	1	1

[a]This column is experimental average from Reference 20, other columns calculated via Eq. (10.5). (See also footnote *e* of Table 10.7.)

[b]Calculated ratios for a detector sensitive to watts rather than photons, as is the case for most FT-Raman spectrometers.

FT-Raman spectrometers are based on detectors that detect power (watts) rather than photons. As noted in Section 2.2, the varying energy per photon across a Raman spectrum yields different relative intensities when measuring power rather than photons. For the common case of a 1064 nm laser in an FT-Raman spectrometer with a power-sensitive detector, the predicted peak ratios for cyclohexane are included in the final column of Table 10.10.

10.4. ABSOLUTE RESPONSE CALIBRATION

In principle, one could calculate an absolute Raman cross section from the response of an instrument calibrated with a standard radiometric source. This approach is difficult but has been used to provide the cross sections in Table 2.2. If the relative response function is calibrated accurately, however, it is much simpler to determine cross sections by comparison to standards. Provided the sample positioning and optics permit quantitative Raman signal reproducibility, cross sections of liquids may be determined by comparing the response-corrected peak area to a band with known absolute cross section, such as the benzene 992 cm^{-1} band. For response-corrected spectra, the ratio of the peak areas under identical experimental conditions equals the ratio of the absolute cross sections.

In the practice of Raman spectroscopy for chemical analysis, absolute cross sections are rarely determined, in part because the task is difficult. In addition, translucent samples, solids, refractive index effects, and local field effects can cause significant errors that are tedious or impossible to correct. Furthermore, many applications depend on peak *heights*, rather than *areas*, which are affected by spectral resolution as well as cross section. Although absolute cross sections are not often useful to the analytical chemist (partly due to their rarity), it is valuable to have semiquantitative information about relative scattering intensity. Even if the cross section of a particular material is not known accurately, a knowledge of where it falls in the wide range of cross sections listed in Tables 2.2 and 2.3 will permit the analyst to assess the difficulty of obtaining useful Raman signals.

A less rigorous but more pragmatic approach to the problem of assessing the comparative Raman cross sections of various samples is the use of a "standard scatterer" to define a quantitative scale. For example, if the benzene 992 cm^{-1} band in neat benzene were considered to have a scattering coefficient of 1.0 arbitrary unit, other samples could be evaluated and tabulated relative to benzene. One is effectively measuring βD for the sample, normalized to βD for benzene. By measuring both sample and benzene on the same spectrometer and adjusting for any differences in laser power and integration time, this normalized βD provides a comparison of the scattering strength of

a given sample to benzene for a particular laser wavelength. Of course, the approach does not consider differences in transparency, path length, refractive index, and so forth but will nevertheless be useful in practical applications. The approach has been described for FT-Raman, using a standard with a broad Raman feature in order to reduce the effects of instrumental resolution (23).

10.5. SUMMARY OF CALIBRATION AND VALIDATION PROCEDURES

There is no single standard procedure for Raman spectrometer calibration, since instrument configurations and applications vary so widely. Nevertheless, it is useful to summarize typical procedures, some of which resulted in the spectral results presented in this chapter.

10.5.1. Qualification of a New Instrument

Once a new instrument is installed by the vendor or set up for the first time, several benchmark measurements should be conducted and saved for future reference:

1. After frequency calibration by a recommended (or established) procedure, obtain and store a spectrum of an ASTM standard, such as cyclohexane or 4-acetamidophenol.
2. Repeat acquisition of the standard over a period of several minutes to test short-term frequency reproducibility.
3. Repeat acquisition of the standard over several days, using whatever frequency calibration technique and interval are to be used in real applications.
4. For a particular set of conditions, acquire and store the spectrum of a sample similar to those involved in the application, either an ASTM standard or a stable material of reliable purity. The peak height or area of a particular Raman feature will serve as an indication of quantitative reproducibility and sensitivity. *Be sure* to record all relevant instrumental parameters, such as laser power, slit width, grating position, laser focusing parameters, integration time, CCD gain, and the like. The intent is to be able to reproduce these conditions at a future date, to check for response degradation.
5. Repeat step 4 several times, with sample removal and replacement between runs, to determine the quantitative reproducibility for repetitive sampling.

6. If desired, or required for a particular application, repeat step 4 for a range of integration times, from near the detection limit to near detector saturation. The detector response should be linear with integration time. For an FT-Raman system, a similar test may be performed by varying the laser power to check photometric linearity.
7. If response correction will be used in the application, carry out the correction with a tungsten source or luminescent standard. Acquire a corrected spectrum of cyclohexane for future reference and to compare to Figure 10.14 or Table 10.10.

10.5.2. Daily Calibration and Qualification

The procedure below was developed for a dispersive CCD spectrometer used daily to acquire response-corrected Raman spectra. The calibration procedure was conducted at the beginning of each session or after the grating was repositioned to cover a different Raman shift range. The calibration steps were automated for the most part, so the time required from the user was approximately 5 min before each session. This procedure may be adapted to a particular spectrometer and application, guided by the objective of resulting in a known level of accuracy of Raman shift and relative intensity, and providing a daily record of instrument performance.

1. Calibrate Raman shift axis with neon source or Raman shift standard. Record spectrum of 4-acetamidophenol (or alternative ASTM standard from Table (10.4) to provide a record of Raman shift calibration.
2. Obtain an uncorrected spectrum of cyclohexane and verify that peak intensity compares well to qualification spectrum obtained on new instrument. Store this spectrum as a permanent record. Be sure to note relevant experimental parameters.
3. Execute procedure for response function calibration with tungsten source or luminescent standard. Acquire corrected spectrum of cyclohexane (or an alternative standard) and compare relative peak areas to established values. Store corrected spectrum.

Once this procedure is complete, the user has a permanent record of Raman shift accuracy, absolute instrument response, and instrument response function for a given experimental session. Over time, these periodic records provide an indication of instrumental drift and performance changes. In addition, they may be checked at a future date if a particular sample appears to deviate from expected behavior. If the instrument was at fault, the daily qualification spectra may provide insight into the origin of the deviation.

REFERENCES

1. *MIT Wavelength Tables*, MIT Press, Cambridge, MA, 1982.
2. H. M. Crosswhite, *J. Res. NBS-A*, **79**, 17 (1975) .
3. D. P. Strommen and K. Nakamoto, *Laboratory Raman Spectroscopy*, Wiley, New York, 1984, pp. 66 ff.
4. K. Burns, K. B. Adams, and J. Longwell, *J. Opt. Soc. Am.*, **40**, 339 (1950).
5. S. T. Wollman and P. W. Bohn, *Appl. Spectrosc.*, **47**, 125 (1993).
6. N. C. Craig and I. W. Levin, *Appl. Spectrosc.*, **33**, 475 (1979).
7. C. K. Mann and T. J. Vickers, *Appl. Spectrosc.*, **53**, 856 (1999).
8. C. Shen, T. J. Vickers, and C. K. Mann, *Appl. Spectrosc.*, **46**, 772 (1992).
9. C.-H. Tseng, J. F. Ford, C. K. Mann, and T. J. Vickers, *Appl. Spectrosc.*, **47**, 1808 (1993).
10. T. J. Vickers, C. A. Rosen, and C. K. Mann, *Appl. Spectrosc.*, **50**, 1074 (1996).
11. ASTM, Standard Guide for Raman Shift Standards for Spectrometer Calibration, ASTM Designation E 1840-96 (1998).
12. D. B. Scully and D. H. Whiffen, *Spectrochim. Acta*, **16**, 1409 (1960).
13. E. Lippincott and E. O'Reilley, *J. Chem. Phys.*, **23**, 238 (1954).
14. F. R. Dollish, W. G. Fateley, and F. F. Bentley, *Characteristic Raman Frequencies of Organic Compounds*, Wiley, New York, 1974.
15. B. Schrader, *Raman/IR Atlas of Organic Compounds*, 2nd ed., VCH, New York, 1989.
16. C. J. Petty, G. M. Warnes, P. J. Hendra, and M. Judkins, *Spect. Acta.*, **47A**, 1179 (1991).
17. M. Fryling, C. J. Frank, and R. L. McCreery, *Appl. Spectrosc.*, **47**, 1965 (1993).
18. H. Hamaguchi, *Appl. Spec. Rev.*, **24**, 137 (1988).
19. K. G. Ray and R. L. McCreery, *Appl. Spectrosc.*, **51**, 108 (1997).
20. K. J. Frost and R. L. McCreery, *Appl. Spectrosc.*, **52**, 1614 (1998).
21. Software and Polynomials for GRAMS implementation are available at: http://chemistry.ohio-state.edu/~rmccreer/Raman.html.
22. J. R. Nestor and E. R. Lippincott, *J. Raman Spectrosc.*, **1**, 305 (1973).
23. C. T. Petty, P. J. Hendra, and T. Hawhari, *Spectrochim. Acta*, **47A**, 1189 (1991).

Raman Spectroscopy for Chemical Analysis. Richard L. McCreery

ISBN: 0-471-25287-5

CHAPTER

11

RAMAN MICROSCOPY AND IMAGING

11.1. OVERVIEW OF RAMAN MICROSCOPY

It was recognized quite early that the 180° sampling geometry provides a means to combine a Raman spectrometer with an optical microscope, thus permitting Raman analysis of very small regions of a sample (1). Raman microscopy has been used widely for analysis of very small samples or small heterogeneities in larger samples. For example, a small visible impurity in a pharmaceutical tablet might be identified after visual observation with a microscope, then a Raman spectrum may be acquired through the same microscope. Since Raman spectroscopy often involves visible light, and optical microscopes are very well developed, there is a natural match between the two techniques.

The simplest form of Raman microscopy is acquisition of a spectrum from a single point on the sample. Although the spot size is usually much smaller for microscopic sampling than for the conventional 180° arrangement discussed in Section 6.3, the two experiments are conceptually identical. The user has the option of obtaining spectra from several points on the sample, but only at one location at a time. The experiment is often called *microspectroscopy*, and collection of spectra from several points is often dubbed *point-to-point mapping*. The advent of two-dimensional detectors permits a variety of more efficient methods for Raman microscopy in which the instrument monitors more than one point on the sample. These methods are categorized broadly as *Raman imaging*, and the result is a sample image based on spectroscopic information (2). For example, the image may be derived from light having a particular Raman shift, so that the spatial distribution of a particular component may be observed. Alternatively, it is possible with some instruments to choose any point on the stored spectroscopic image and then display its Raman spectrum. A third possibility is *profiling*, where the variation of intensity of a particular Raman feature is observed along a straight line on the sample.

Considered in a general context, these methods amount to different ways to acquire or display results from a data set of intensity as a function of four independent variables: x, y, z (depth), and Raman shift. A complete spectroscopic description of the sample is a hypercube of Raman intensity as a function of Raman shift and three spatial axes. Some authors refer to experiments

combining spectral and spatial information as *hyperspectral imaging* because the end result is a hypercube of intensity, Raman shift, and two or three spatial dimensions. The mode of data acquisition and presentation as well as the spatial and spectral resolution vary greatly for different microscopy techniques, and many of these issues are discussed below.

Several examples of imaging methods are shown in Figure 11.1 for the case of two spatial variables, x and y. The point-to-point profile is a sequence of single-point acquisitions, and the complete spectrum of each point is stored for subsequent analysis. In *line imaging* the laser is focused to a line, then the scattering is projected through an imaging spectrograph onto a charge-coupled device (CCD) to generate a two-dimensional data set of intensity vs. Raman shift and position along the line (x in the case shown). As with the point-to-point profiling, line imaging provides spectra at many points along a line, but it does so with simultaneous rather than sequential data acquisition. *Global imaging* or *direct imaging* refers to a group of techniques that illuminate a relatively large sample area, then collect spatially resolved spectra over the entire illuminated area. For example, a filter that transmits only a particular Raman shift might precede the CCD. The end result is a two-dimensional image of Raman scattering intensity over a narrow band of Raman shifts. If

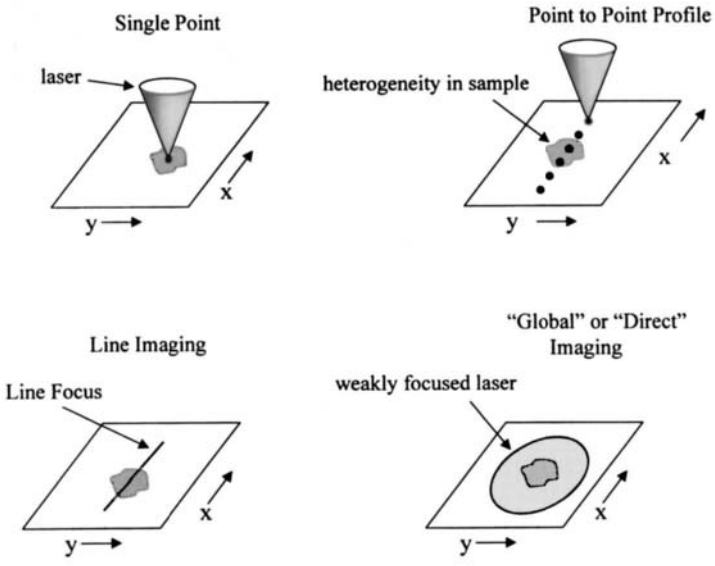

Figure 11.1. Several imaging modes for Raman microscopy. Gray circle in global imaging case represents a defocused laser spot covering a large area compared to a point or line focus.

the observed shift corresponds to a specific sample component, then global imaging results in a chemically selective two-dimensional image.

In this chapter, some general principles and instrumentation for Raman microscopy are considered initially, in the context of a discussion of single-point microspectroscopy. After that, several varieties of imaging modes and data presentation are addressed.

11.2. SINGLE-POINT RAMAN MICROSPECTROSCOPY

11.2.1. Objective Lenses and Spatial Resolution

The first step in combining a microscope and a Raman spectrometer is orienting the laser beam along the microscope optical axis to result in a 180° geometry. A method for combining the laser and spectrometer optical axes using a beamsplitter was introduced in Figure 6.3, and a similar configuration is common in Raman microscopes. Most Raman microscopes use a beamsplitter to inject the laser into the collection axis, and "infinity-corrected" objective lenses are used to permit a collimated beam path within the microscope. There are several variations on the design of Figure 6.3, but all of them direct the laser beam through the objective lens and collect scattered light through the same objective lens in 180° backscattered geometry. The spatial resolution in single-point sampling is determined by the optical characteristics of the objective lens and associated optics, and the divergence of the laser.

The spatial resolution is determined by either the laser spot size or the collection optics, both of which are ultimately limited by diffraction. The laser beam diameter at the focal spot (twice the "beam waist," w_0) was discussed in Chapter 6, and is given by Eq. (6.2):

$$2w_0 = f\theta_d \tag{6.2}$$

An alternative expression relates w_0 to the *pupil* (or aperture) of the objective lens, w_e:

$$2w_0 = 1.27\lambda f/w_e \tag{11.1}$$

where f is the objective lens focal length (3). If the laser beam diameter does not fill the lens pupil, then w_e should be the laser beam diameter at the lens. Table 11.1 lists a few calculated laser spot diameters for various objectives, under the assumption that the laser beam fills the objective pupil. Some experimental values are listed in Table 11.1 for comparison.

For single-point microscopy, the laser spot size often defines the spatial resolution, and the spectrometer is designed to collect light from an area

Table 11.1. Calculated Beam Parameters for Various Microscope Objective

Microscope Objective	Working Distance (mm)[a]	Spot Diameter ($2\ w_0$, μm, for 514.5 nm laser)		Observed Depth of Focus (δa)[b]	Power Density[c] (W cm^{-2})
50 mm camera lens[d]	40	50[e]		10,000 μm	250
10×[f]	8	33[i]	40[j]	220 μm	597
50×[g]	0.4	6.5[i]	6[j]	10 μm	15,000
100×[h]	0.25	3.3[i]	3.1[j]	4 μm	59,700

[a]Distance between lens surface and object.
[b]Experimental full width of half maximum (FWHM) of plot of signal vs. focal position of silicon 521 cm^{-1} band in μm.
[c]For 5 mW at sample.
[d]Canon $f/1.4$, 50 mm camera lens.
[e]Calculated with Eq. (6.2), using ray optic limit.
[f]$NA = 0.25$, $f/\# = 1.94$, Olympus Mplan.
[g]$NA = 0.75$, $f/\# = 0.44$, Olympus Mplan.
[h]$NA = 1.00$, $f/\# = 0.25$, Olympus Mplan.
[i]Calculated from Eq. (11.1), assuming $w_e = 6$ mm.
[j]Observed with video micrograph of calibrated grid.

equal to or larger than this spot size. The *underfilled* case governed by Eq. (3.8) usually applies, and the signal is independent of the spot size provided it is smaller than A_D. It is also possible that the spatial resolution is controlled by the collection optics, and $A_D < A_L$. Figure 11.2 illustrates both situations, which are microscopic analogs of the "macro" cases from Figure 3.2. Most commonly, both laser and collection beams are collimated above the objective lens, and the spectrometer aperture is larger than the laser spot size.

Microscope objectives have short focal lengths and small $f/\#$, so the depth of focus is very short (see Section 6.3.2). By convention, the $f/\#$ of the objective is restated as a numerical aperture (NA), defined as the sine of the half-angle of the collection cone. For transparent samples, the depth of focus, δa, is usually determined by the diffraction limit of the focused laser beam, given by Eq. (6.3) or by the depth of focus of the collection optics, whichever is smaller. Absorption or scattering by the sample can reduce the effective path length below δa, as discussed in Chapter 6. Since the power of the microscope objective determines its focal length and beam waist, Eq. (6.3) predicts that higher power (and smaller w_O) objectives yield smaller depth of focus. The beam parameters listed in Table 11.1 vary greatly for different optical components and experimental conditions, but a few trends are of general value. First, the laser spot diameter is a strong function of the choice of objective lens focal length, with diameters of a few microns predicted only for

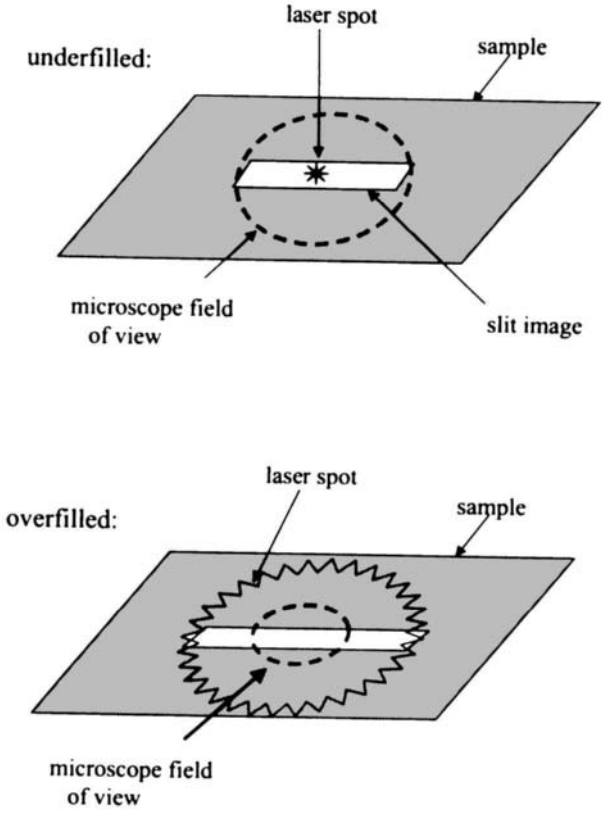

Figure 11.2. Microscopic analogs of underfilled and overfilled cases described in Chapter 3 and Figure 3.2.

the 100 × objective.* Second, the depth of focus is also a strong function of focal length, for the reasons discussed in Section 6.3.2. Third, the spot size and depth of focus increase with the laser wavelength, since diffraction effects increase with wavelength as well. Fourth, the power density increases rapidly with the "power" of the objective, as noted earlier in general terms in Table 6.1. Finally, it should be noted that the observed depths of focus reported in Table 11.1 are experimental values for a particular wavelength and microscope design. The effective sampling depth is determined by a combination of laser focal depth and collection optics and will vary significantly

* The objective lens "power" is based on a standard image distance, usually 150 mm. So "100 ×" corresponds to an effective objective focal length of 1.5 mm.

for different spectrometers. The achievable spatial resolution (both lateral and depth) also depends on the spectrometer and confocal techniques, discussed later. The properties of microscope objectives for observing solids may be illustrated with some simple experimental observations. The short depth of focus for microscope objectives is demonstrated graphically in Figure 11.3, which shows the Raman signal for the silicon 521 cm^{-1} band as a function of focal position. For comparison, the $f/4$ macro system from Figure 6.13 is included, and the intensities are normalized to their values at optimal focus. Over the range of focal positions shown, the signal from the macro system decreases only about 3 per cent, while the microscope objectives are much more sensitive to focus. This variation of signal with focus is more dramatic as the power becomes higher, as apparent in Figure 11.3 and from the values of δa listed in Table 11.1. With the focus adjusted for optimum signal, spectra of silicon and polystyrene were obtained and plotted in Figure 11.4. The signal for silicon depends dramatically on the microscope objective, while that for polystyrene varies only slightly.

The obvious difference in the dependence of the signal on focus between the opaque (silicon) and transparent (polystyrene) samples is described more quantitatively in Table 11.2. The signals were divided by laser power and integration time to permit direct comparison of sensitivity. The NA of each objective was converted to $f/\#$ by:

$$f/\# = \frac{0.5}{\tan[\sin^{-1}(\mathrm{NA})]} \tag{11.2}$$

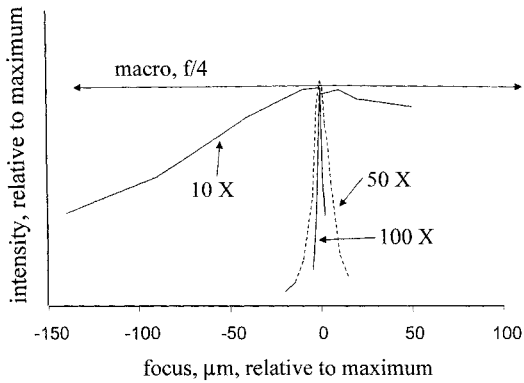

Figure 11.3. Silicon 521 cm^{-1} band intensity for a macro sampling (50 mm camera lens) and three microscope objectives, as functions of focus. The signals were determined for a range of sample positions along the z axis, then normalized to their maximum value for each lens. Zero on the focus scale corresponds to maximum signal.

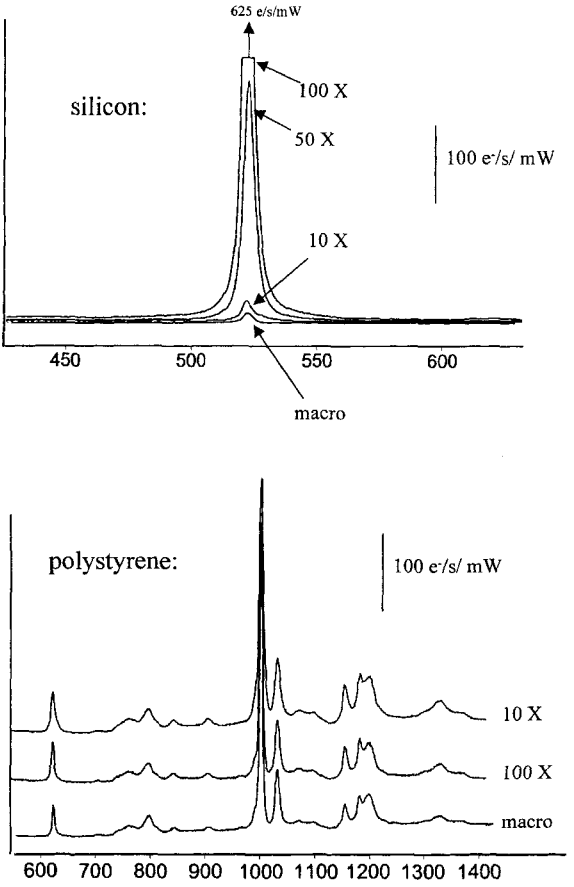

Figure 11.4. Spectra of silicon and polystyrene at optimum focus, for various objective lenses, all on the same spectrometer. Macro is a 50 mm camera lens, and all intensities were divided by integration time and power at the sample.

Insertion of the $K\Omega_D$ value from Table 6.2 for an optically dense sample such as silicon into Eq. (3.8) yields

$$S = \frac{P_0 \beta D T Q t_s \pi}{4(f/\#)^2(\alpha_L + \alpha_D)} \tag{11.3}$$

With all else equal, Eq. (11.3) predicts that the signal is proportional to $(f/\#)^{-2}$ for an optically dense or thin sample, such as silicon. This prediction is supported by the data in Table 11.2, with the signal increasing rapidly for the higher NA (lower $f/\#$) objectives. For thin or optically dense samples,

the sample opacity or depth limits the effective path length, and the more powerful objective improves signal due to higher Ω_D.

The observations are quite different for a thick, transparent sample such as polystyrene. As the $f/\#$ decreases, so does the depth of focus and the effective path length. The shorter path length partially offsets the higher Ω_D of higher power objectives. Table 6.3 predicts a $(f/\#)^{-1}$ dependence of signal on the $f/\#$ of the objective lens for the underfilled case and a clear sample. The variation of signal with $f/\#$ in Table 11.2 is scattered and shows no clear trend. This simple experiment has enough uncontrolled variables that Table 6.3 may not apply directly, but it is certainly clear that the signal from a microscope is strongly dependent on sample transparency and thickness. A practical consequence of this fact is the observation that microscopes exhibit good sensitivity for the usually thin or opaque samples common to microscopy but have much lower sensitivity for the thick samples commonly examined with conventional Raman spectrometers. As apparent from the last line of Table 11.2, a spectrometer optimized for macro performance is significantly more sensitive than the microscope. Although such comparisons depend on a variety of instrumental variables, the fact remains that microscopic sampling has an inherently short path length.

11.2.2. Microscope/Spectrometer Interface

Insertion of the laser into the optical axis of a microscope is relatively straightforward for single-point microspectroscopy and does not differ fundamentally

Table 11.2. Signal Comparison for Various Microscope Objectives on Dilor *X-Y* Raman Microscope

Objective	NA	$f/\#$[a]	Polystyrene Peak Area, 1004 cm^{-1} (e^-/sec/mW)[b]	Silicon Peak Area, 521 cm^{-1} (e^-/sec/mW)[b]
macro[c]		6[c]	3040	159
10×	0.25	1.94	5410	203
50×, LWD[d]	0.5	0.87	3160	1190
50×	0.75	0.44	5500	2920
100×	0.9	0.24	3425	6450
Macro[e]		4	21,500	951

[a]Calculated using Eq. (11.2).

[b]Peak area was divided by integration time and power at sample.

[c]Macro optics ($f/1.4$ camera lens) on same 600 mm, $f/6$ spectrometer used with microscope objectives.

[d]LWD = long working distance.

[e]$f/4$ collection on 250 mm, $f/4$ spectrometer optimized for macro operation.

from the approach used for macro 180° sampling (Fig. 6.4 and 6.5). The aperture of a microscope objective is generally much smaller than a typical macro lens, so the small mirror depicted in Figure 6.4B or the "mirror with hole" in Figure 6.5D will block most of the collected light. The two methods in common use employ a broadband beamsplitter or wavelength-selective reflectors such as dichroic mirrors or holographic optical elements.

A broadband beamsplitter is a 50 per cent reflective mirror on a thin substrate, usually silica or BK-7 glass. The geometry shown in Figure 6.3 employs a broadband beamsplitter to reflect the laser into the objective lens. Fifty per cent of the backscattered Raman is transmitted through the beamsplitter for analysis by the spectrometer. The beamsplitter mount has adjustments to precisely align the laser beam to match the image of the spectrometer aperture at the sample (as in Fig. 11.2). A broadband beamsplitter provides a fairly simple means to combine the excitation and collection axes, but it also causes significant signal loss. Only half of the laser light reaches the sample (at most) and half of the collected light is reflected back to the laser. So at best, the signal is attenuated by 75 per cent compared to what is available. In addition, the beamsplitter is positioned directly in the collection axis, so it can create significant background signal. Inelastic scatter of the laser by the beamsplitter can enter the spectrometer and appear as both broadband luminescence or silica Raman.

The losses of the broadband beamsplitter can be significantly reduced by using a "smart" beamsplitter based on a dichroic mirror or holographic optical element (4). The reflectivity of these devices is strongly dependent on wavelength, as shown in Figure 11.5. The beamsplitter is fabricated to have a high reflectivity for the laser and a high transmission for the Raman-shifted light. For example, if the beamsplitter reflects 90 per cent of the laser light and 20 per cent of the Raman light, the signal loss will be $[1 - (0.9)(0.8)] = 28$ per cent instead of the 75 per cent of the broadband beamsplitter. Of course, this benefit comes with the requirement that the beamsplitter be matched to the laser wavelength. So the beamsplitter would need to be changed and realigned when the laser wavelength is changed, and a tunable laser would be impractical. In addition, the transition from high reflectivity at the laser wavelength (zero on the x axis of Fig. 11.5) is not infinitely sharp, so a significant fraction of the light with low Raman shift is reflected back to the laser, rather than transmitted into the spectrometer. The result is serious attenuation of the low Raman shift region of the spectrum. In the case shown in Figure 11.5, the holographic beamsplitter transmits 50 per cent of its maximum at about 200 cm^{-1}, while the dichroic mirror is not at 50 per cent until 800 cm^{-1}. The dichroic arrangement can be improved to transmit scattered light at $\sim$500 cm^{-1} by sacrificing the anti-Stokes region of the spectrum, and tuning the rising transmission on the Stokes side closer to the laser frequency.

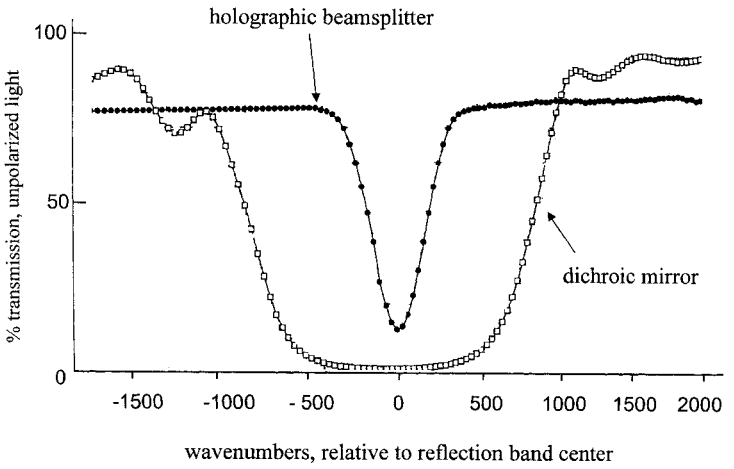

Figure 11.5. Transmission curves for dichroic mirror (squares) and holographic beamsplitter (dots). (Adapted from Kaiser product literature and described in Reference 4.)

An alternative to the smart beamsplitter exploits the high reflectivity of a holographic notch filter (Section 8.2.5.2) at the laser wavelength. When positioned as shown in Figure 11.6, a notch filter serves to insert the laser beam into the collection axis. Since the filter is at a near-normal angle to the collection axis, it transmits a high fraction of the Raman-shifted light into the spectrometer. In addition, the filter rejects elastically scattered light from the sample. So the notch filter is acting as both an efficient "beamsplitter" to combine the excitation and collection axes and as a notch filter to reduce stray light in the spectrograph. As with a dichroic mirror, the notch filter must be matched to the laser wavelength, taking into account the angle of the filter relative to the collection and laser axes.

An example of single-point Raman microspectroscopy is shown in Figure 11.7, in this case with a broadband beamsplitter. The sample is a pharmaceutical tablet pressed from a mixture of powdered acetamidophenol (active) and microcrystalline cellulose (excipient). The particle size is in the range of 10 to 50 μm, and the distribution of active and excipient is random. A conventional spectrometer with a spot size of ~100 μm yields a spectrum containing Raman features from both components, since it is spatially averaging over the <50 μm heterogeneities. The video micrograph shown in Figure 11.7 (often called a "bright-field" image) shows few features, as the two components are visually indistinguishable in this case. A typical macro spectrum, which sampled a 50 × 50 μm region of the tablet surface,

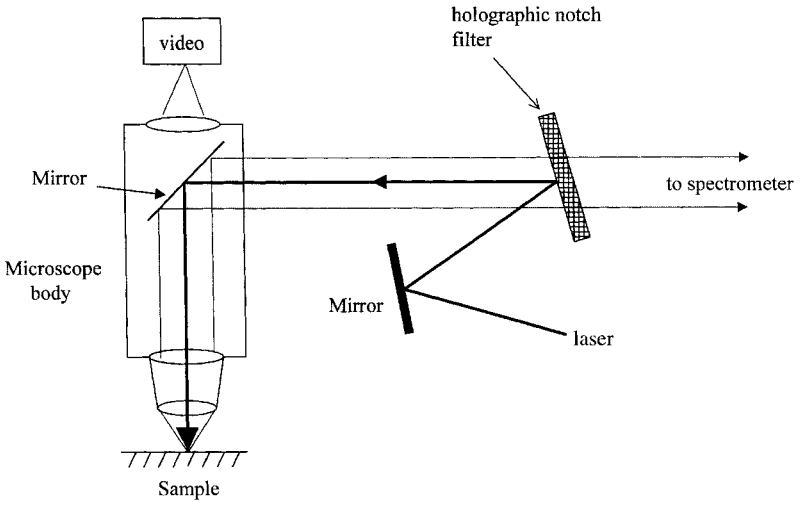

Figure 11.6. Schematic of holographic notch filter used to inject laser beam into the collection axis of a microscope (similar to an arrangement in a Renishew Raman microscope system).

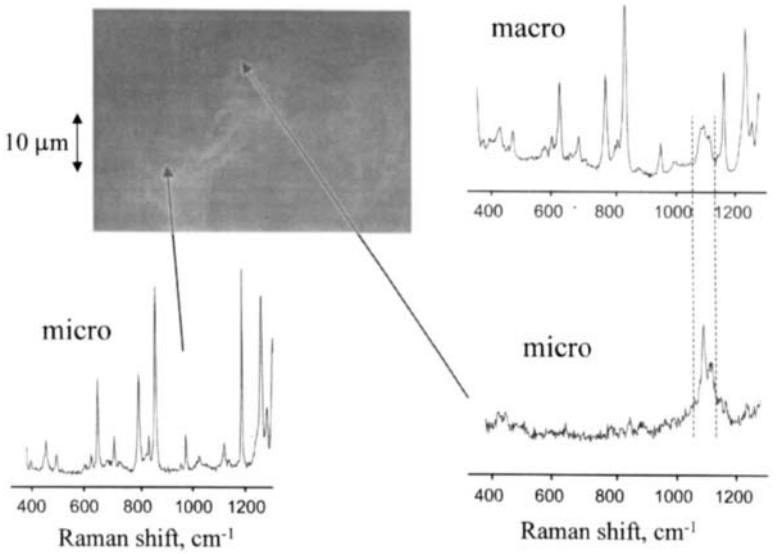

Figure 11.7. Single-point Raman microspectroscopy of a pressed tablet containing acetamidophenol and microcrystalline cellulose. The macro was obtained with an ~100 μm-diameter sampling area, and the micro spectra were obtained at the locations indicated.

shows features from both components of the mixture. Microprobe spectra of two locations on the tablet show distinct spectra for each component, since the spot size in this case is <10 μm. Notice that the "excipient" peak in the region of 1100 cm^{-1} is absent from the "active" spectrum, indicating nearly complete spatial segregation of the two compounds. Some additional examples of single-point Raman microspectroscopy are listed in Table 11.3. A specialized but impressive application is Raman microspectroscopy of single microdroplets with picoliter volumes that were laser trapped in an immiscible liquid (5). The microprobe provided a three-dimensional distribution of the Raman scatterer within the microdroplet with a spatial resolution in terms of solution volume of a few femtoliters.

A rudimentary type of Raman imaging is the line profile, consisting of a series of single-point spectra acquired along a line selected by the user. The total acquisition time equals the number of sample positions observed times the single-point acquisition time, plus any overhead associated with sample motion. Several commercial instruments automate the process with a computer-controlled microscope stage that positions the sample under the laser spot according to a video image. A line profile is shown in Figure 11.8, constructed of 31 spectra along a 90 μm line on an integrated circuit. All

Table 11.3. Examples of Raman Microscopy Applications

Configuration	Sample	Reference
Single-point sampling	Poly(ethylene terephthalate)	6
Single-point sampling of microdroplet	Toluene in water	5
Single point, confocal	Multilayer polymer film	7
Single point, confocal	Poly(ethylene terephthalate)	8
Single point	Borate minerals (caforsite)	9
Global and line imaging	Polystyrene/polyacrylate composite	10
Global imaging	Gallium arsenide semiconductor dots	11
Single point	Human dentin and resin composite	12
Line imaging		13
Line imaging	Polyvinyl chloride	14
Hadamard imaging	Benzoic acid	15
Mechanical line scan	TiO_2, zirconia	16
Single point	Carbon fibers	17
x-y image reconstruction from line scan	Glassy carbon and graphite surfaces	18
Hadamard imaging	Graphite surfaces	19
Global imaging	Human lymphocytes	20
Line imaging	CuSCN on platinum electrodes	21
Single point	Microorganisms	26

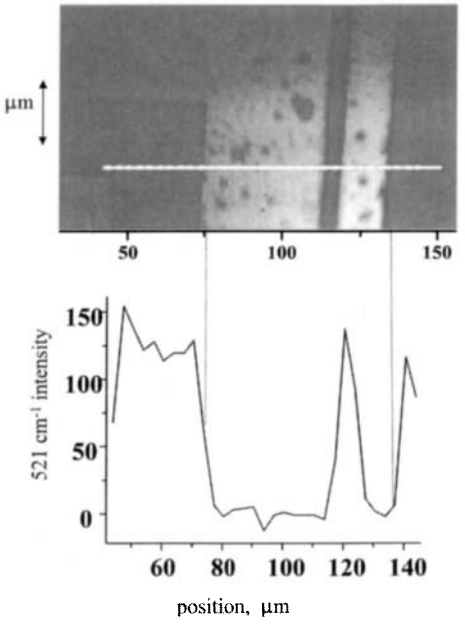

Figure 11.8. Line profile consisting of 31 single-point spectra, each acquired between stage motions. The spectra were obtained with 3-sec acquisitions along the line shown in the video image. The lower plot is the 521 cm^{-1} peak intensity as a function of position on the line.

31 spectra were stored, so the data may be analyzed *post facto* and plotted in various formats. Shown is a plot of 521 cm^{-1} intensity as a function of position along the line to illustrate the spatial distribution of silicon. In this example, the silicon intensity decreases drastically when the microprobe is positioned over an aluminum circuit feature.

11.2.3. Confocal Raman Microspectroscopy

A *confocal* microscope has an additional aperture, sometimes called a *confocal hole*, that has the effect of decreasing the depth of focus (22). For some applications, sampling depth and depth resolution are important to the analytical problems involved. For example, a laminated polymer material may consist of two or more thin films, and the analyst may need to obtain spectra of each layer. If the layers are thinner than the depth of focus, then the spectrum will represent an average of the layers. In order to restrict the measurement to a particular polymer layer, the depth resolution must be improved.

The principle of a confocal microscope is illustrated by Figure 11.9, by comparison to a conventional, infinity-corrected microscope. Light scattered from two sample depths, z_1 and z_2, is indicated by the solid and dashed lines.

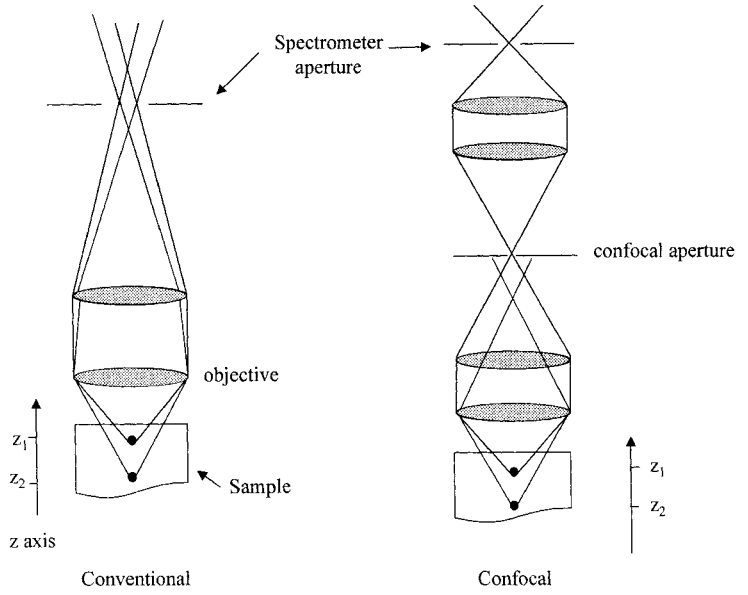

Figure 11.9. Schematic of confocal microscope optics, showing addition of a "confocal aperture" that restricts sampling depth; z_1 and z_2 represent two depths in a transparent sample.

For the spectrometer aperture shown (usually the slit), light from both z_1 and z_2 may enter the spectrometer. If both points are within the focal cylinder of the laser beam, the spectrum will reflect the average sample composition between z_1 and z_2. The confocal aperture limits sampling depth by blocking the light from z_2 before it enters the spectrometer. If the sample were homogeneous, the confocal aperture will also decrease signal, since it decreases the effective path length. But for a sample whose composition varies with depth, the confocal aperture restricts the sampling depth to a region smaller than that for conventional optics. The depth resolution depends on the confocal aperture diameter, among other factors, and some instruments have provision for varying the aperture diameter. The confocal aperture need not be located exactly as shown in Figure 11.9, and a variety of configurations for confocal microscopy have been explored. The aperture may be located farther away from the objective lens, as will be described later for a confocal imaging system. In fact, the "conventional" spectrometer is to some extent confocal, as the entrance slit and the pixel height can act as apertures to decrease the sampling depth.

Figures 11.10 and 11.11 demonstrate the confocal effect for Raman microspectroscopy of polymer films (7). In Figure 11.10, the Raman intensity of a

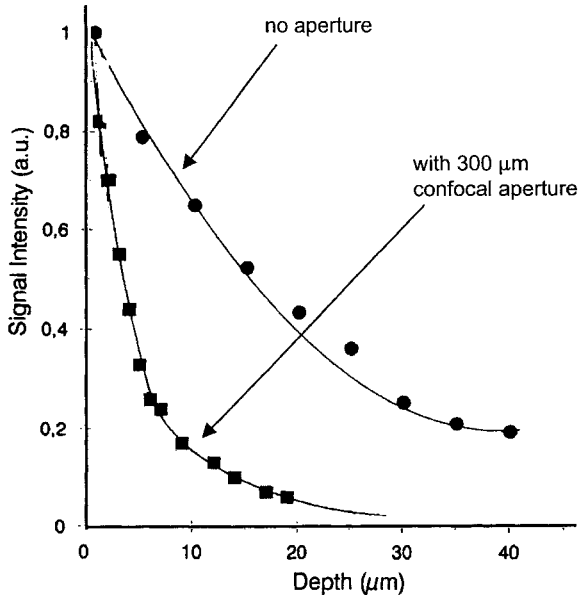

Figure 11.10. Effect of a confocal aperture on the signal for a 10 μm-thick polyethylene film as a function of focus. An infinitesimal depth of field would yield a step function at zero depth. (Adapted from Reference 7.)

polyethylene band is plotted as a function of focal distance from the surface of a 10 μm-thick polyethylene film. If the depth of focus were infinitesimal, the intensity vs. distance plot should be a step function. For a real Raman microscope and 50 × objective, the signal decreases over a >40 μm range (upper plot in Fig. 11.10). When a 300 μm confocal aperture was in place, the depth of focus was significantly decreased, as shown in the lower curve of Figure 11.10. The utility of this improvement in depth resolution is shown in Figure 11.11, for a sample consisting of a three-layer film of polyethylene (26 μm thick), polyamide (30 μm), and polyethylene (26 μm). Without the confocal aperture, the spectra are quite similar for different focal positions, since the depth of focus covers all three layers, and the spectrum represents the average composition of all three layers. With the aperture present, distinct features for the polyamide layer are apparent when the focus is in the middle of the three polymer layers.

The degree to which the sampling depth is restricted by a confocal aperture is a fairly complex function of objective power and NA, as well as the position and size of the confocal aperture. Some experimental observations of sampling depth for two microscope configurations are listed in Table 11.4. The

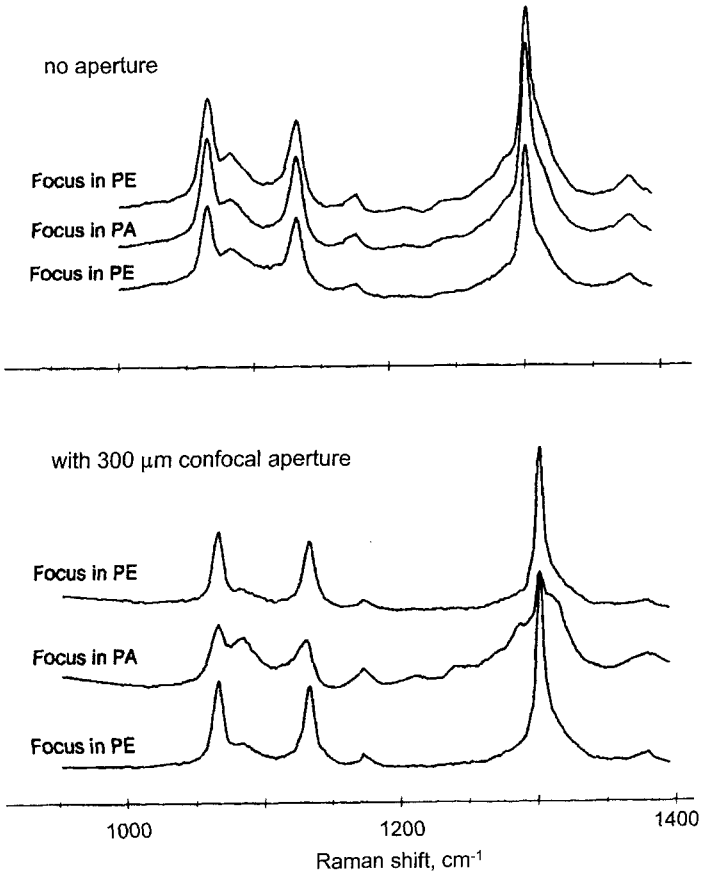

Figure 11.11. Raman spectra of a polyethylene (26 μm thick)/ polyamide (30 μm)/polyethlylene (26 μm) laminate with and without a confocal aperture. The improved depth resolution with the aperture permits discrimination of polyethylene and polyamide spectral features. (Adapted from Reference 7.)

Table 11.4. Depth Resolution (μm)

	Confocal Diameter (μm)			
Objective	500	300	100	Reference
50 × LWD	>16			7
50 ×	>8	<6		7
100 ×	≈2	<2		7
100 ×			1.8	10

values listed vary widely for different spectrometers but the trends are valid in general. The depth resolution improves (i.e., shorter sampling depth) for higher objective power, higher numerical aperture, and smaller confocal aperture.

11.3. LINE IMAGING

The technique of obtaining a series of single-point spectra to produce a line profile was discussed earlier and represents a simple extension of point-to-point sampling. At first glance, line imaging appears quite similar, with an end result of a data set consisting of intensity vs. Raman shift and position along a line. However, true line imaging is substantially more sophisticated than a point-to-point line profile and is a precursor to several of the global imaging techniques to be discussed later. Furthermore, it illustrates some useful principles that apply to virtually all Raman imaging methods, and it provides a useful intermediate step before considering more complex approaches.

11.3.1. Line Imaging Based on a Line-Focused Laser

Consider a flat sample illuminated by a line focus similar to that discussed in Section 6.3. As demonstrated in Figure 6.20, the scattering from this line may be collected and imaged onto the entrance slit of a dispersive/CCD spectrometer. If the user's objective is a single Raman spectrum with no spatial resolution, the slit image on the CCD would normally be binned vertically to collect light over the entire line focus. The resulting spectrum represents a spatial average of the sample over the line illuminated by the laser and monitored by CCD. Now, suppose the CCD is *not* binned along the slit axis, and the spectrograph has imaging ability as described in Section 8.2.1. As shown in Figure 11.12, each pixel of the CCD along the slit axis collects scattered light from a particular position on the line focus. The vertical axis of the CCD is a map of the position along the line (labeled "X" in Fig. 11.12), and the horizontal axis of the CCD remains proportional to wavelength. If the imaging capability of the spectrograph and collection optics are perfect, then the CCD is collecting as many Raman spectra as there are vertical pixels, and each spectrum originates at a discrete position on the line focus. For example, a 256 (vertical) $\times$ 1024 (horizontal) CCD could simultaneously collect 256 spatial positions and 1024 Raman shift values during a single CCD integration. The image stored from the CCD after integration is a 256 $\times$ 1024 data set of intensity vs. 1024 Raman shifts and 256 positions along the line focus. This experiment is an example of "hyperspectral" acquisition, since it adds a spatial dimension to the spectroscopic results, with simultaneous acquisition of spatial and spectral data (14,16,23).

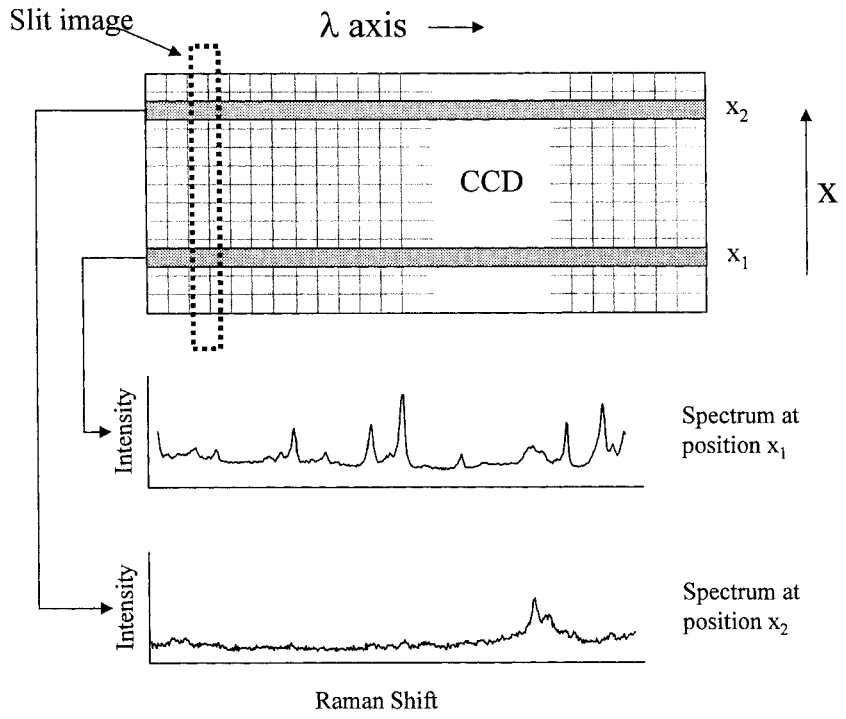

Figure 11.12. Schematic of line imaging onto a CCD. A line focus at the sample projected onto the slit of an imaging spectrograph generates a two-dimensional image of intensity vs. x and $\Delta\bar{\nu}$.

A line image obtained with the arrangement of Figure 11.12 is shown in Figure 11.13 for a uniform sample of diamond (14). Approximately 200 Raman spectra were collected simultaneously along a 600 μm line and plotted to show only the prominent 1332 cm^{-1} band of diamond. The variation of intensity with spatial position is due to laser power variation along the line, a common consequence of the use of a cylindrical lens to form the line focus. The center 100 μm section of the line, shown as a magnified inset, indicates an intensity variation of about ±5 per cent over the line center. An application to a reaction between polyvinyl chloride (PVC) and triethylamine diamine is shown in Figure 11.14. A PVC sheet was cut and the edge was polished before examining the edge with line imaging. The spatial axis shown in Figure 11.14 represents depth into the PVC sheet, with the extremes representing the PVC/air interface. An initial line image shows uniform Raman intensity with depth, as expected for an untreated sample. After exposure of the PVC sheet to triethylene diamine for 21 days followed by cutting and polishing, a new feature at 1521 cm^{-1}

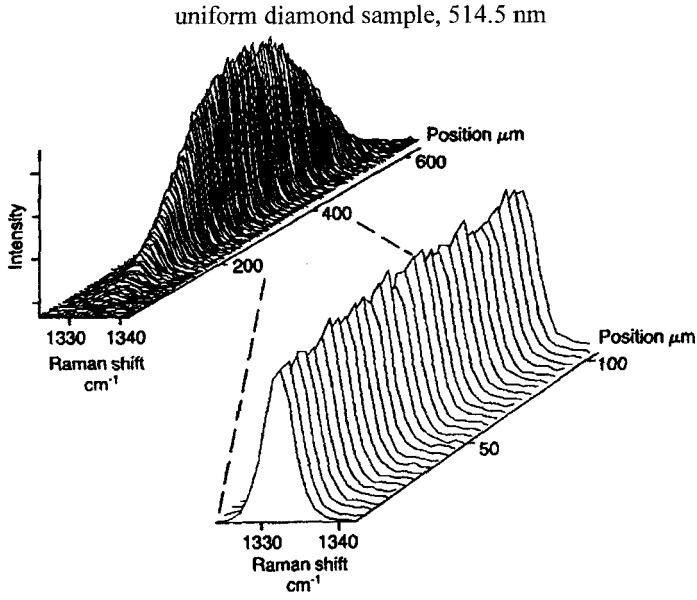

Figure 11.13. 200 Raman spectra of the 1332 cm^{-1} feature of diamond obtained with a 600 μm-long line focus. The expansion of the middle 100 μm of the line demonstrates relatively constant laser intensity. (Adapted from Reference 14.)

is observed due to C=C bonds resulting from dehydrochlorination. This band shows a strong depth dependence, while the weaker 1436 cm^{-1} band from the plasticizer remains constant with depth. So the Raman line image provides information not only about the chemical changes occurring with triethylene diamine exposure, but also the extent of those changes with sample depth. Similar information could be obtained with a confocal single-point experiment, but it would require many (~100) spectral acquisitions to generate the same data set as that obtained with a single line image.

An important feature of the line imaging configuration is the achievement of multichannel acquisition of many Raman shifts along one CCD axis, combined with multichannel acquisition of spatial positions with the other CCD axis. With some qualifications, the multichannel advantages of speed and improved signal/noise ratio (SNR) apply to both the spatial and Raman shift axes. At first glance, the simultaneous acquisition of N spectra along a line requires $1/N$ as much time as acquisition of the same N spectra by point-to-point sampling. For example, acquisition of Raman spectra from 256 points on a line with a point-to-point spectrometer would require 256 times longer than acquisition of the same data set with the line imager depicted in Figure 11.12.

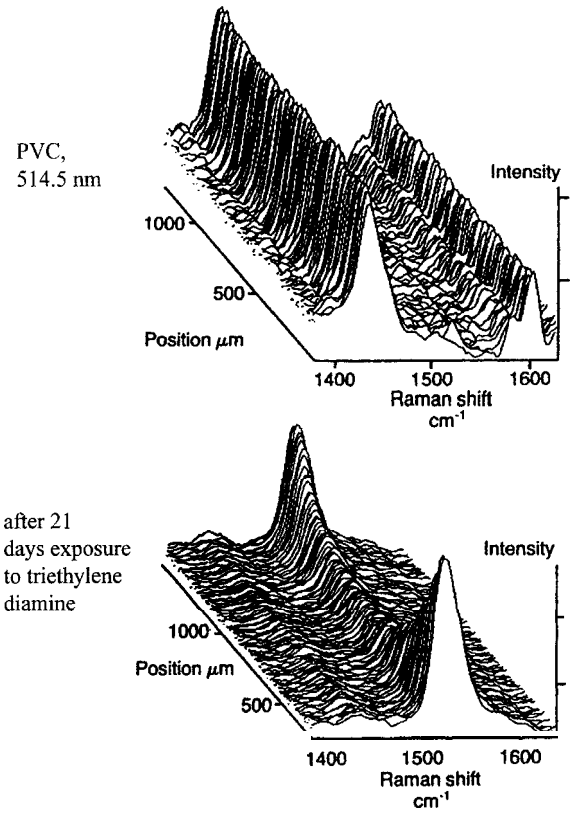

Figure 11.14. Raman line images of polyvinyl chloride, before and after exposure to triethylene diamine. Line focus was applied to the edge of the sample after cutting and polishing, so the "position" axis represents depth, between the original PVC/air interfaces at 0 and 1500 μm. (Adapted from Reference 14.)

Note that a total data set of over 262,000 Raman intensities as functions of position and Raman shift are obtained in a single CCD exposure with line imaging, for the case of a 256 × 1024 CCD at maximum resolution.

These multichannel advantages indeed apply under certain conditions, but the situation is rarely so simple. If the power density (P_D) is the same for a point-to-point profile compared to a line image, the point-to-point approach will require N times as long to acquire spectra from N positions along the line. However, the total laser power must be increased to achieve the same P_D for the line focus, by a factor of approximately N. If the same total power (rather than power density) is used for both experiments, the two techniques have comparable total acquisition times for the same SNR. Line imaging would

still have certain advantages over point-to-point scanning, such as lower power density and relative immunity to laser power fluctuations and/or mechanical drift that might change the signal intensity during a series of single-point spectra. On the other hand, it is not trivial to generate a constant laser intensity along a line focus (as apparent in Fig. 11.13), so special optics such as a Powell lens (discussed in Section 11.4.3.1) or calibration of intensity variation is required to construct an accurate plot of intensity vs. position for the line focus.

The spatial resolution along the line focus is ultimately limited by the number of CCD pixels available along the appropriate axis. The spatial resolution of the collection optics and the imaging spectrograph may degrade the achievable spatial resolution at the sample below the number of CCD pixels, but the CCD determines the upper bound. For example, a 256 × 1024 CCD might be used to obtain 1024 Raman shift values from a maximum of 256 points along a line focus, when arranged as shown in Figure 11.12. However, each pixel corresponds to a very small A_D, so a long acquisition time would be required. More commonly, the CCD is binned along the spatial dimension to yield fewer, larger spatial elements along the line focus. For example, binning of four pixels would yield 64 spatial elements along the line focus, each of which captures four times as much light as a single pixel. So there is a trade-off between sensitivity (or time) and spatial resolution. Better spatial resolution along a given line focus requires less binning, smaller superpixels, lower sensitivity, and ultimately more time to achieve the required SNR.

11.3.2. Line Imaging with Mechanical Scanning

Line imaging based on a line focus of the laser involves relatively simple apparatus, with the software and CCD doing most of the "work" of generating a data set of intensity vs. position and Raman shift. Provided the laser power density along the line is constant, or its variations are correctable, significant qualitative and quantitative chemical information about the sample along the line of focus is obtainable. However, the line focus is not amenable to confocal operation since a confocal aperture would truncate the line. In order to vary the length of the line focus, the focusing optics must be modified, and the collected light will fill a larger (or smaller) fraction of the CCD. In order to maintain confocal operation as well as permit a line of user-selected length to completely fill the CCD, a mechanical method for generating a line focus has been developed and is available commercially.

The apparatus shown in Figure 11.15 generates a line focus mechanically rather than optically. A beamsplitter injects the laser beam into the collection axis as before, but then the laser is directed to a motor-driven mirror,

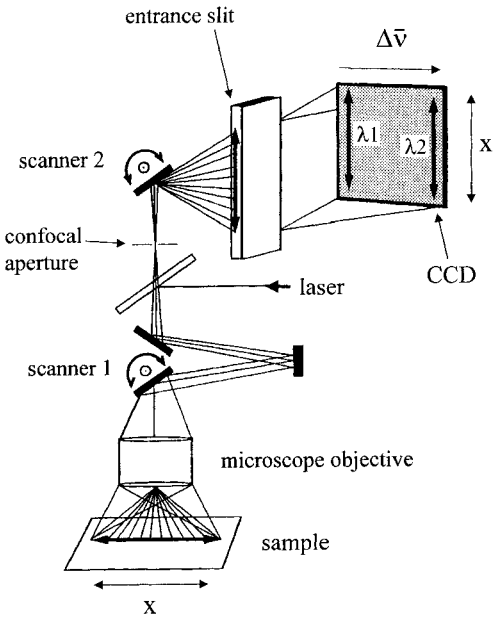

Figure 11.15. Apparatus for generating a line focus with mechanically scanned mirrors. Scanner 1 and scanner 2 are computer-controlled oscillating mirrors. The grating and mirrors of the imaging spectrograph are located between the entrance slit and CCD but are not shown. (Adapted from Reference 10.)

labeled scanner 1. As the mirror angle is changed electrically, the laser scans a line at the sample, along the x axis in Figure 11.15. As the mirror is oscillated, the laser focal point rapidly sweeps out a line at the sample, although at any instant in time the focus remains a point. The amplitude of the mirror oscillation is controlled electronically, so the user may select a line of arbitrary length, within the limits of the field of view provided by the microscope objective. The backscattered light reflects off the same mirror, so it focuses at the confocal aperture regardless of the mirror position. The confocal aperture controls the depth resolution in the manner shown in Figure 11.9, but it is doing so over the entire line swept out by the oscillating mirror. Once past the confocal aperture, the collected light is scanned along the long axis of the entrance slit by scanner 2. The two scanners are synchronized in phase (position along the sample line and entrance slit) but may have different amplitudes. So scanner 2 may be used to magnify sample lines of different length so they fill the entire x dimension of the CCD. The wavelength analysis is carried out by an imaging spectrograph, so each x position on the CCD corresponds to a particular x position on the sample line. The computer that controls the

scanners keeps track of the relationship between the CCD and laser spot positions with respect to the line, and the experiment is usually set up by the user during video observation of the sample. A line image obtained with mechanical scanning is shown in Figure 11.16 for the same sample observed with point-to-point sampling (Fig. 11.8).

This mechanical approach to line imaging has the same qualitative outcome as the line focus described in Figure 11.12, but there are some significant differences in practicality and performance. The mechanical scanner is much more complex to implement than the line focus, but it does permit confocal operation if desired. The scanning approach is more flexible, since the line length may be varied electronically and can fill the full height of the CCD. The power density is much higher for the scanning approach, since the laser is still focused to a point rather than spread over the line. However, the scanners

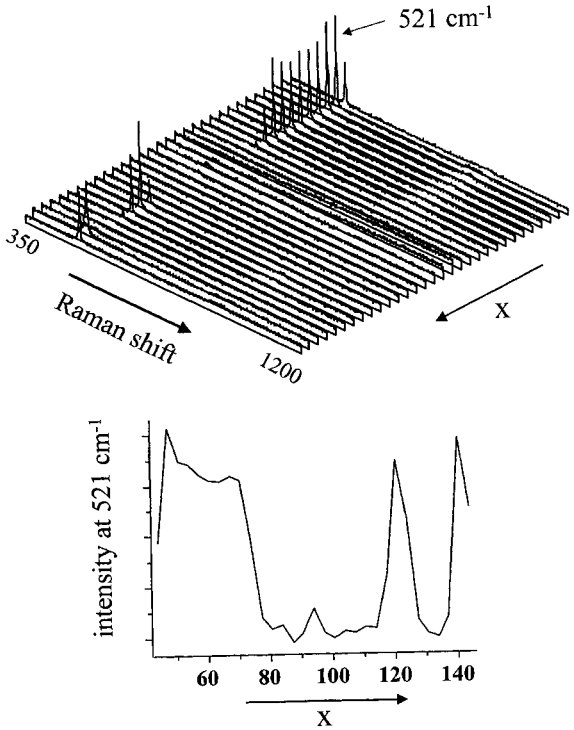

Figure 11.16. Line image data from the line shown in Figure 11.8. Laser beam was oscillated along the line, and a two-dimensional image of intensity vs. position and $\Delta\bar{\nu}$ was collected at the CCD. Upper plot shows individual spectra; lower plot is the intensity of the 521 cm^{-1} band vs. position: at 90-sec total acquisition time, 5 mW at sample, 50 × objective.

can operate fairly quickly (e.g., several sweeps per second) so possible sample damage is reduced by a low duty cycle at each point. Finally, the instantaneous power density along the line of focus is constant and equal to the single-point power density. So the spectra obtained along the line may be directly quantitatively compared.

11.4. TWO-DIMENSIONAL RAMAN IMAGING

The addition of a second spatial dimension to the line imaging experiment yields the technique most commonly referred to simply as "Raman imaging" (1,2). Although several approaches to the problem are available commercially, they share a common objective of providing Raman intensities as a function of $\Delta\bar{\nu}$, x, y, and sometimes depth (z). To illustrate an example of two-dimensional Raman imaging, Figure 11.17 shows both a Raman image

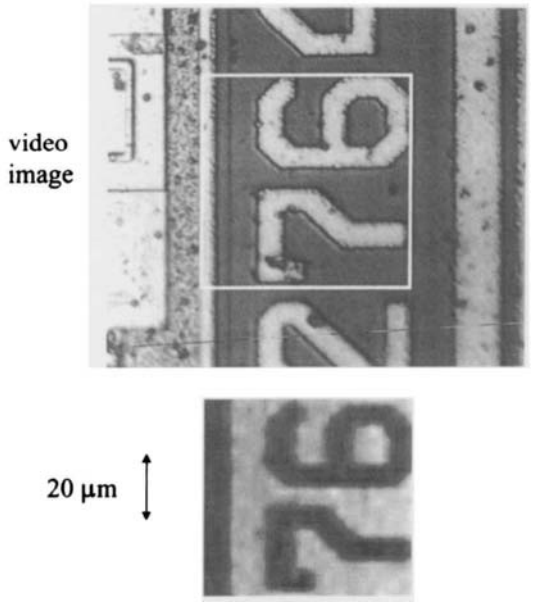

Figure 11.17. Video and Raman image of an integrated circuit, obtained with line scanning and stage translation on a Dilor "XY" spectrometer. Area in white box was observed with a 28 × 28 spatial grid, and the Raman image was reconstructed from 28 CCD exposures. White regions in the Raman image correspond to higher Raman intensity in the 501 to 536 cm^{-1} Raman shift range.

and a video image of an integrated circuit. The video image shows microscopic lettering used to label the device and is quite clear in the bright-field image. The lower image was formed from light scattered in the range of 501 to 536 cm^{-1} relative to the 514.5 nm laser, which includes the silicon 521 cm^{-1} Raman band. It is obvious that the dark regions in the video image correspond to exposed silicon. Instrumental techniques for generating Raman images similar to that of Figure 11.17 differ substantially in their characteristics, and there is no current consensus on the "best" approach. Before considering specific methods, some general observations are worthwhile.

A generalized imaging experiment has one, two, or even three independent spatial variables (x, y, and depth) plus one independent spectral variable (Raman shift). The hypercube of intensity as a function of these variables comprises the global spatially resolved Raman information for a given sample or sample region. The instrument has a CCD with pixels covering two spatial dimensions that are interrogated to provide intensity at each CCD position after some measurement time. The general imaging problem becomes one of how to acquire Raman intensities as a function of x, y, z, and $\Delta\bar{\nu}$ with a two-dimensional detector and some manageable measurement time. Stated colloquially, the CCD has a finite amount of "real estate" (in area and in the number of pixels); how should it be used to obtain the spatially and spectrally resolved image? In single-point acquisition, the multichannel nature of one axis of the CCD is used to obtain multiple Raman shifts simultaneously, and the other axis is used to increase A_D, if it is used at all. In line imaging, one CCD axis is $\Delta\bar{\nu}$, the other x, and a multichannel advantage applies to two of the four (x, y, z, $\Delta\bar{\nu}$) independent variables in the hypercube. The remaining two variables must be examined sequentially, for example, by changing focal position to probe deeper along the z axis. As will be discussed below for the case of two-dimensional rather than line images, one can invest the two CCD axes toward obtaining x and y spatial information, then scan wavelength, or use the CCD for x and $\Delta\bar{\nu}$, then scan y. The labels used to identify imaging approaches are not completely consistent in the literature, but "global imaging" or "direct imaging" are generally used to describe the approach where a relatively large sample area is illuminated, and the CCD monitors the x and y spatial coordinates for a single Raman shift region at a time. Methods in which the CCD monitors one spatial and one spectral coordinate simultaneously are generally referred to as "hyperspectral imaging" or "image reconstruction" (20,23). Global imaging will be discussed first, followed by several types of image reconstruction.

11.4.1. Global Raman Imaging

A general schematic of a global imaging apparatus is shown in Figure 11.18. The laser is defocused to cover most of the microscope's field of view. The

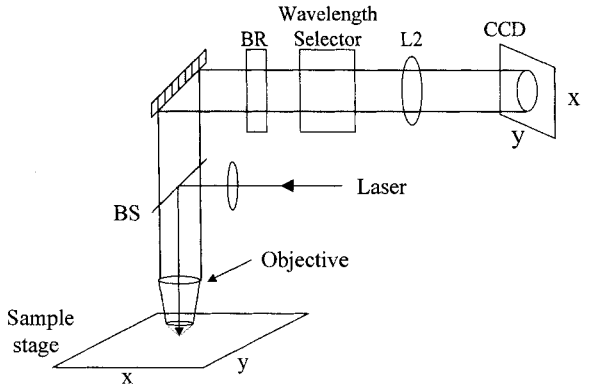

Figure 11.18. Schematic of global imaging Raman microscope in which one CCD exposure yields an x-y map of a particular Raman shift range. The laser is generally defocused to produce a relatively large spot at the sample.

laser spot diameter at the sample can vary widely in different applications, but is often in the range of 50 to 500 μm. Light scattered by the illuminated area is collected by the objective and passed through a laser rejection filter and wavelength selector, then imaged onto a CCD. If the BR filter and wavelength selector were absent, the CCD would produce an image of the sample from backscattered laser light (mostly), plus a small amount of Raman shifted light. The BR filter rejects most of the elastically scattered laser light, and the wavelength selector is tuned to transmit a particular range of Raman shift. With both the BR filter and wavelength selector in place, the CCD produces an image derived solely (in principle) from Raman-shifted photons. In the general terms of Section 11.4, the apparatus of Figure 11.18 uses the multichannel advantage for x and y and yields a two-dimensional Raman image at fixed $\Delta\bar{\nu}$ and z. In order to obtain Raman spectra as well as two-dimensional images, the wavelength selector must be stepped through a series of Raman shifts, and a CCD image obtained at each shift value. Similarly, a depth profile would require stepping the focus between successive CCD acquisitions.

Several characteristics of global imaging result from the decision to use the multichannel advantage of the CCD for spatial information rather than Raman shift. Acquisition of a two-dimensional image at one Raman shift is often very rapid, since a large number of sample spots are observed simultaneously. On the other hand, acquisition of complete spectra requires many CCD exposures, particularly for high spectral resolution. Since global imaging uses a weakly focused laser, the power density is much lower than a single-point experiment, greatly reducing the risk of sample damage. However, lower power density means less signal from each spatial resolution element, so the acquisition

time is longer than that for a single point. Finally, large area illumination is not amenable to confocal operation, but still retains the relatively short depth of focus inherent in microscopes. Several detailed assessments of the trade-offs involved in global imaging designs are available in the literature (10,20), and the choice of a particular mode is often sample dependent. Overall, global imaging has a major advantage in the speed of an acquisition of two-dimensional images at selected values of Raman shift, but some compromises of spectral performance are required to achieve this speed advantage.

11.4.2. Wavelength Analysis for Global Imaging

The wavelength selector is obviously critical to converting a conventional microscope with CCD recording into a Raman imager that records images of a particular Raman shift value. The important properties of a wavelength selector for Raman imaging include transmission, bandpass, and stray light level, defined in the same manner as in Chapter 8. Wavelength analyzers in commercially available spectrometers include nondispersive devices based on angle-tuned interference filters or tunable liquid crystals and dispersive systems that use gratings or acoustically generated diffraction grating (acousto-optic tunable filter, AOTF). The nondispersive global imager based on interference filters is the simplest system conceptually and uses a bandpass filter selected to transmit light of a particular range of Raman shift values. This approach was introduced in Section 9.1.1 as a means of nondispersive wavelength analysis and has been adapted for imaging. For example, an interference filter with a bandpass of 2 nm centered at 540 nm transmits Raman-shifted light from a 514.5 nm laser in the range of 883 to 952 cm^{-1}. Such a filter would generate a Raman image from shifted light over a bandpass of $\sim$60 cm^{-1}, and the center Raman shift could be tuned by changing the angle of the filter relative to the optical axis. With refinements in filter design plus the use of several rapidly interchangeable filters, images over the entire Raman shift range are obtainable, with $\sim$20 cm^{-1} resolution. An example of a Raman image obtained with this approach is shown in Figure 11.19.

A recent approach to wavelength selection for Raman imaging is based on the liquid crystal tunable filter (2). A stack of liquid crystals and polarizers is configured to permit electronic tuning of the transmitted wavelength, as described earlier in Section 9.1.3. The tuning range is significantly wider than that of an angle-tuned interference filter, and a single liquid crystal tunable filter (LCTF) can cover the entire Raman shift range. Like an interference filter, the aperture of an LCTF is large enough to be positioned in the collimated region of the collection axis, as in Figure 11.18. The bandpass of the LCTF is $\sim$10 to 20 cm^{-1}, but its transmission is currently fairly low, <20 per cent. One advantage of the LCTF is wide tunability under computer control, so that

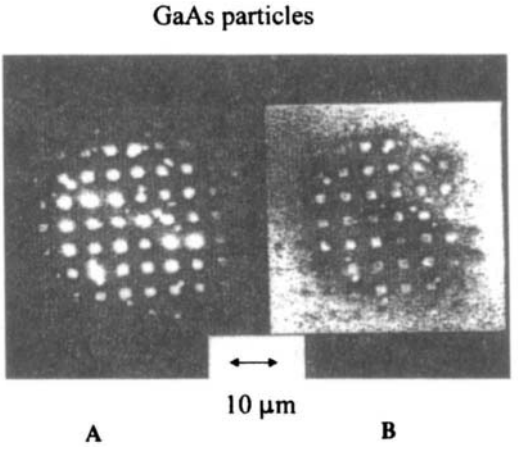

Figure 11.19. Global images of an array of GaAs semiconductor dots (diameter = 1.4 μm), using a Renishaw microscope with wavelength selection by interference filters. Image A is light from the 269 cm^{-1} GaAs phonon, after subtraction of the 200 cm^{-1} background. Image B is after correction for response variation across the image. (Adapted from Reference 11.)

a series of images over a range of Raman shifts may be acquired automatically. So it is straightforward to generate a data set of intensity vs. x, y, and $\Delta\bar{\nu}$, with the acquisition time depending on signal strength, spectral range, and resolution. A second advantage is the small size of the LCTF and associated optics, so that the entire spectrometer and CCD may be mounted on the top of a standard microscope body. An example of a Raman image from an LCTF instrument is shown in Figure 11.20. The ability to distinguish two polystyrene spheres spaced 200 nm apart indicates excellent spatial resolution, near the diffraction limit.

A wavelength filter for global imaging may also be constructed from a diffraction grating, but the process is complicated by the conflict between a narrow slit required for spectral resolution and a relatively large field of view desired for imaging. If the spectral resolution is decreased to ~20 cm^{-1} using a wide (~400 μm slit), the entire image may be passed through the spectrograph, and the grating may select the desired wavelength range. A schematic of a commercial instrument based on this approach is shown in Figure 11.21. The wavelength range is selected by rotating the grating, and the slit width is large enough to collect the entire field of view. An additional feature of the instrument is a multimode fiber-optic loop between the laser and the beamsplitter, which is vibrated mechanically. The varying mode structure in the fiber averages out intensity variations across the laser beam and results in a constant laser intensity across the illuminated sample area.

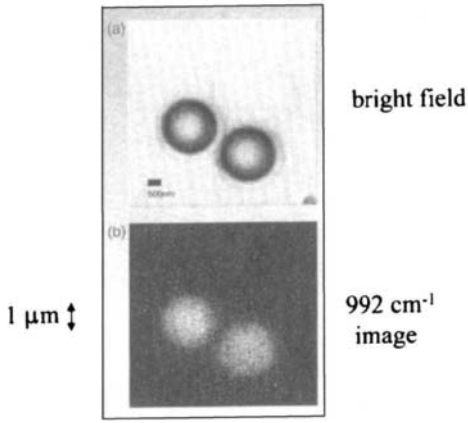

Figure 11.20. Bright-field and Raman image of polystyrene beads; 992 cm^{-1} light was selected with a liquid crystal tunable filter. (Adapted from Reference 2.)

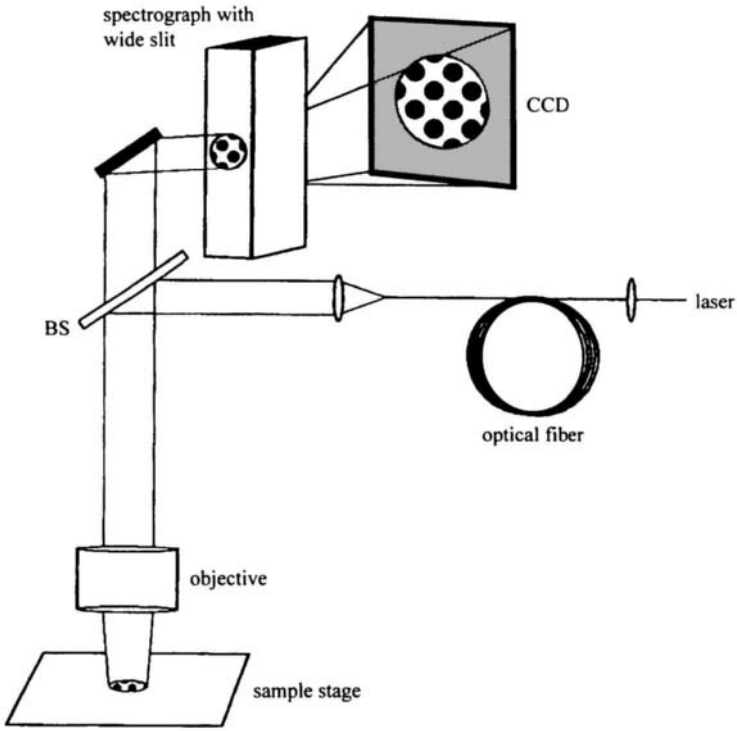

Figure 11.21. Global imaging with a grating spectrograph. Wide entrance slit transmits entire image into spectrograph, which selects desired Raman shift range. (Adapted from Reference 10.)

11.4.3. Raman Image Reconstruction

Several methods for constructing a two-dimensional Raman image from point or line spectra have already been described, and several examples are presented here. A wide variety of reconstruction methods have been reported and the examples below are certainly not comprehensive. In particular, those techniques available in commercial instruments are emphasized. Furthermore, the case of image reconstruction from an x-by-y array of single-point spectra is conceptually trivial and is not presented here.

11.4.3.1 Reconstruction from a Line Focus

The line focus illustrated in Figures 11.12 to 11.14 has been used to obtain two-dimensional Raman images from a series of line images. The spectra shown in Figure 11.13, for example, represent Raman intensity along a line with a width of 1 to 50 μm and were obtained with a single CCD exposure. By adding a motorized translation stage, the sample may be moved along an axis perpendicular to the slit axis. A series of line images is obtained to fill in the y axis data of the Raman intensity hypercube. The number of points along the y axis equals the number of CCD acquisitions and is governed by the desired spatial resolution. The end result is a hypercube of intensity vs. x, y, and $\Delta\bar{\nu}$, which may be manipulated by the software and to yield presentations in various formats.

The trade-off between spatial resolution and acquisition time arises again with two-dimensional image reconstruction, and with even greater impact. As noted in Section 11.3.1, spatial resolution for a line image is determined by how the pixels are binned along the line image, and the greater the number of spatial resolution elements, the longer the acquisition time for a given signal or SNR. For example, dividing a line into 100 spatial elements would reduce the signal per element by a factor of 10 compared to division into 10 elements. So the 100-element line requires 10 times the acquisition time to achieve the same signal in each spatial element. Similarly, 100 spatial elements along the y axis require 100 CCD exposures and 100 movements of the translation stage. Although many factors affect the acquisition time, the trade-off between time and spatial resolution is significantly greater for the two-dimensional area.

A refinement of the two-dimensional line imaging experiment addresses the nonuniform laser intensity apparent in Figure 11.13. A Powell lens is designed to have variable divergence across the region illuminated by the laser, such that a Gaussian intensity profile is converted to a "flat-topped" profile (23). The laser intensity along the line is constant to ±10 per cent or less, as shown in Figure 11.22A. A Raman image of two 6.7 μm diameter polystyrene spheres obtained with the Powell lens is shown in Figure 11.22B.

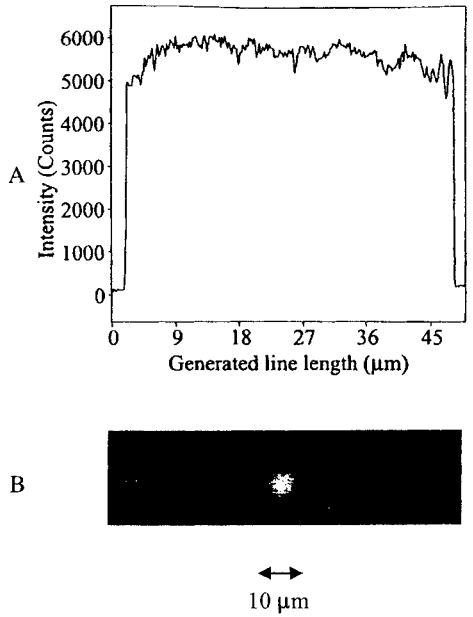

Figure 11.22. Illustration of the use of a Powell lens to flatten the intensity profile of a Gaussian laser beam. A is the observed laser intensity along a line focus at the sample, and B is a Raman image of two 6.7 μm diameter polystyrene spheres reconstructed from a collection of line images. (Adapted from Reference 23.)

In this case, a particularly sensitive spectrometer and an intensified CCD were used, so the images were obtained quite rapidly (8 sec to 2 min).

The mechanical line scanning technique described in Section 11.3.2 has also been extended to two-dimensional Raman imaging by the addition of a computer-controlled translation stage. The result is shown in Figure 11.23 for the same pressed pharmaceutical tablet used to illustrate microspectroscopy in Figure 11.7. In this case, the laser spot was mechanically scanned along a 60 μm line, and the corresponding image on the CCD was binned into 28 spatial elements. The line was monitored for a total of 180 sec, to produce 28 spectra, each containing 500 intensities as functions of Raman shift. The translation stage was incremented 28 times, and the 180 sec acquisition was repeated after each step. The result was a hypercube of intensity vs. x, y, and $\Delta\bar{\nu}$, with 28 × 28 spatial elements and 500 Raman shifts. So the total data set contained 392,000 intensity values, which could be accessed and manipulated after the experiment was over. Figure 11.23A shows the intensity of the 839 to 875 cm^{-1} region, which includes the 858 cm^{-1} band of the active ingredient, 4-acetamidophenol. The false color scale represents the most intense Raman

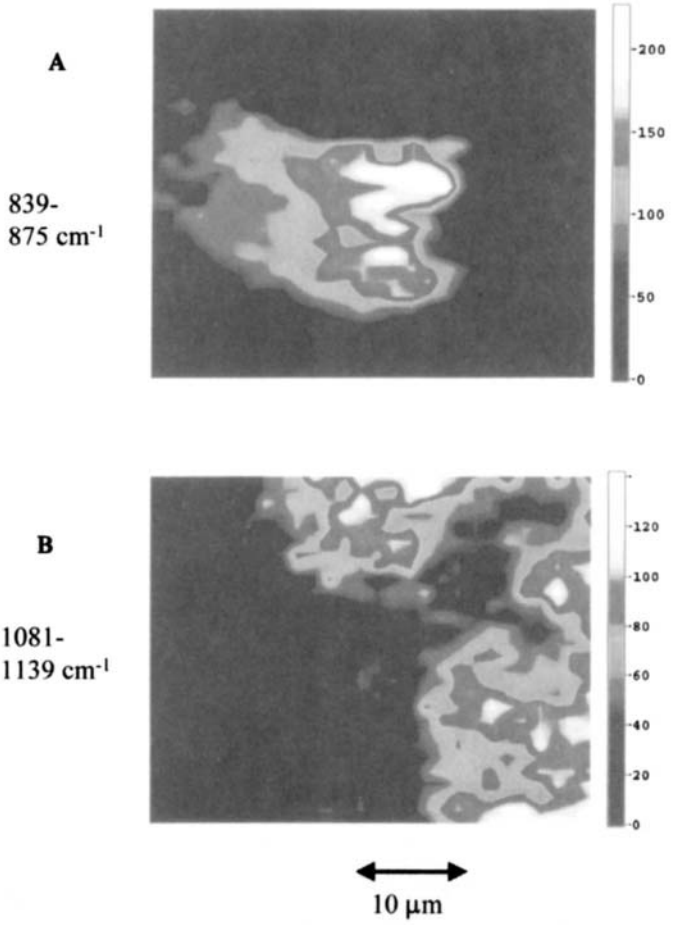

Figure 11.23. Raman images of a pharmaceutical tablet reconstructed from 28 line images obtained with mechanical line scanning in a Dilor "XY" spectrometer. Both images are of the same area on the tablet, but image A is derived from an acetamidophenol band, while image B is from an excipient band. False color intensity scale is shown to the right of both images. Individual spectra are shown in Figure 11.7. (See color plates.)

scattering as white and yellow and the weakest as black. It is clear from Figure 11.23A that the active ingredient is localized in a ~30 μm particle. The 1081 to 1139 cm^{-1} shift region contains a band due primarily to the excipient (Avicel), whose spatial distribution complements that of acetamidophenol. Two alternative representations of the data of Figure 11.23A are shown in Figure 11.24. The 839 to 875 cm^{-1} image in Figure 11.23A is

actually a spatially smoothed version of the raw 28 × 28 matrix shown in Figure 11.24A. The smoothing process is mathematically objective but cannot generate any new information. Figure 11.24B is a histogram of intensity vs. x and y, with intensity indicated by both height and color.

Both optical and mechanical line scans generate large data sets when used to construct a two-dimensional Raman image, but computer power and storage is inexpensive in the post-PC world. An advantage of such large data sets is the retention of complete spectra for each spatial element, with often high spectral

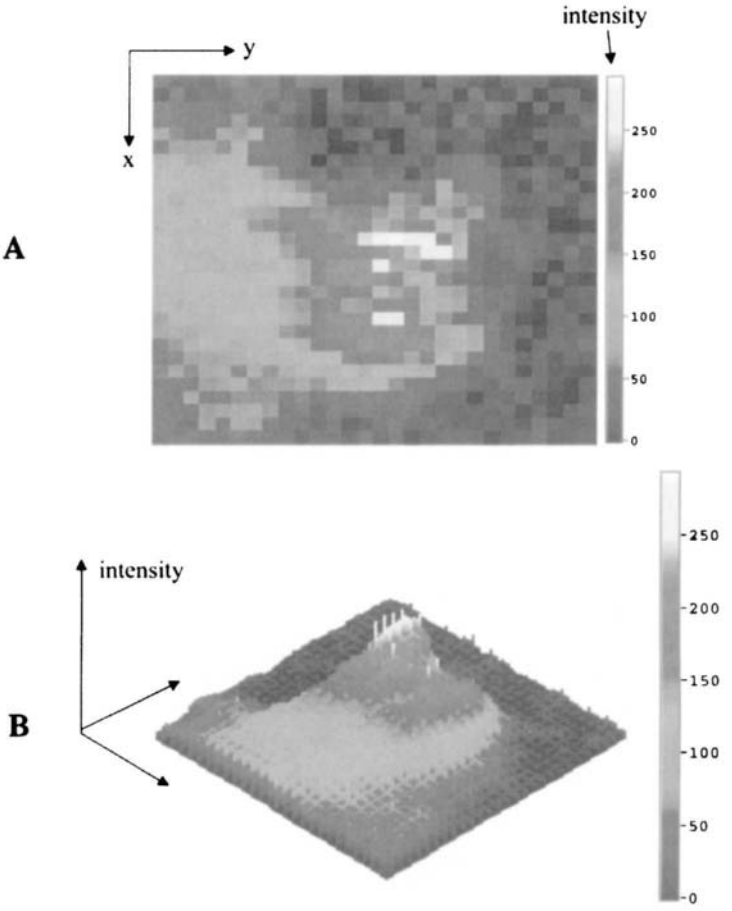

Figure 11.24. Alternative representations of the data in Figure 11.23A. Image A is the raw 28 × 28 spatial grid, with white representing the most intense 858 cm^{-1} band. Image B is an axonometric plot showing intensity as both a height above the x-y plane and as a false color scale, shown on the right. (See color plates.)

resolution. Data analysis techniques based on chemometrics and factor analysis may be applied to such data sets to provide greater chemical selectivity. A simple example is baseline subtraction in which a broad or sloping baseline is subtracted from each spectrum in each spatial element, leaving only Raman scattering. Fitting and subtracting baselines is more difficult with the limited spectral data from global imaging. Factor analysis is a general term that refers to the process of decomposing a series of spectra into components that describe variations among the spectra. In principle, every spectrum in an image may be described as a linear combination of a relatively small number of "factors," and each factor is often associated with a chemical component in the sample. The hyperspectral Raman data set is amenable to factor analysis, so that the spatial distribution of chemical components may be determined. Instead of observing the distribution of a particular Raman band (as in Fig. 11.23), the distribution of an entire *spectrum* is determined. The Raman image is more specific for a particular component when based on factor analysis, resulting in greater ability to localize particular chemical species.

The image of Figure 11.22B is based on the polystyrene "factor" and is obviously limited spatially to the polystyrene sphere itself. Factor analysis has the added benefit of automatic background correction, since the background is often due to a different sample component than the factor of interest. The ability of factor analysis to discriminate among similar chemical components is illustrated in Figures 11.25 and 11.26. A section of human biopsy tissue was mounted in paraffin for conventional analysis by a pathologist. The tissue slice contained paraffin plus several structurally similar biological lipids, all of which were distributed nonuniformly in the tissue section. The bright-field micrograph of Figure 11.25 shows both fibrous tissue and a region suspected of being a prostate tumor. Figure 11.25 also shows three single-point spectra obtained at different regions on the sample, as indicated. Since paraffin and the two naturally occurring lipids have long aliphatic chains, their spectra in the spectral region shown are similar but not identical. The software was instructed to determine the contribution of each of these three spectra to the spectrum observed at each spatial coordinate in the entire image. Figure 11.26 shows an overlay of the Raman analysis on the video image. Each color corresponds to the contribution from each of the three components, based on the entire spectrum. Although the spectra are similar to the eye, their spatial distributions based on factor analysis are clearly distinct. Assignment of each of the 28×28 spatial points to a particular lipid component by eye would have been at least tedious and probably inaccurate as well.

11.4.3.2 Hadamard Image Reconstruction

Hadamard transform spectroscopy existed long before Raman imaging, as a form of multiplex spectroscopy. A Hadamard mask is an array of clear and

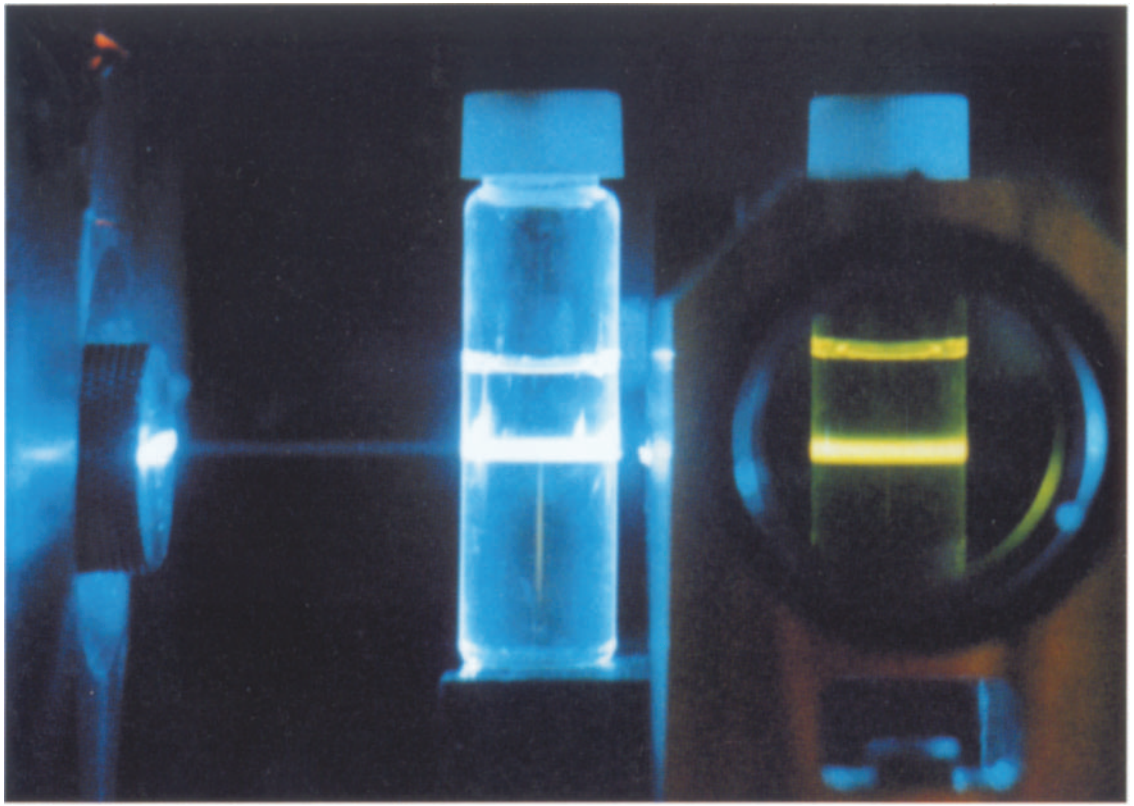

Raman scattering visible to the unaided eye, from a 488 nm laser beam passing through liquid cyclohexane. Left vial exhibits mostly Rayleigh scattering which obscures much weaker Raman scattering. Right vial is viewed through a 488 nm band rejection filter, which permits observation of longer wavelength Raman scattering.

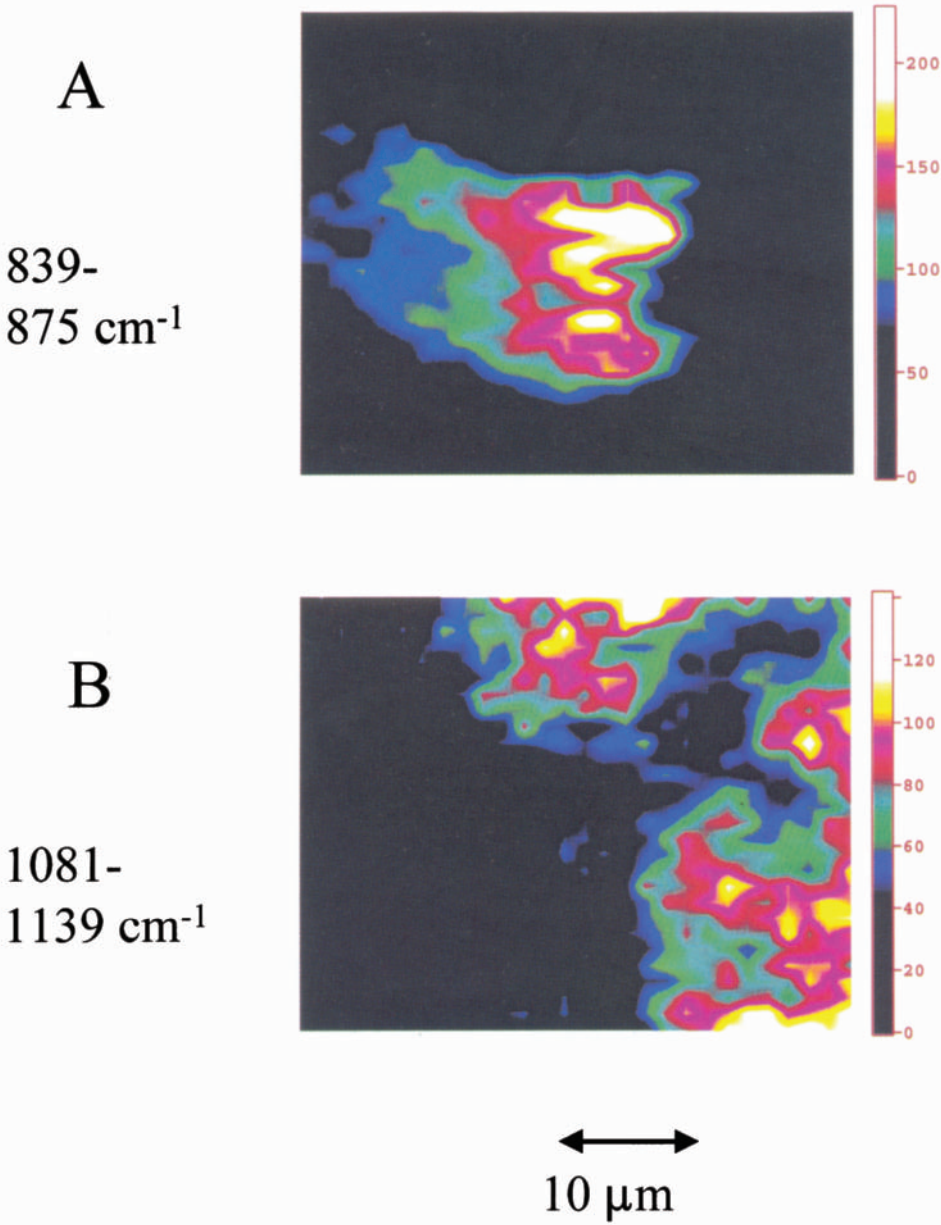

Figure 11.23. (See page 324.) Raman images of a pharmaceutical tablet reconstructed from 28 line images obtained with mechanical line scanning in a Dilor "XY" spectrometer. Both images are of the same area on the tablet, but image A is derived from an acetamidophenol band, while image B is from an excipient band. False color intensity scale is shown to the right of both images. Individual spectra are shown in Figure 11.7.

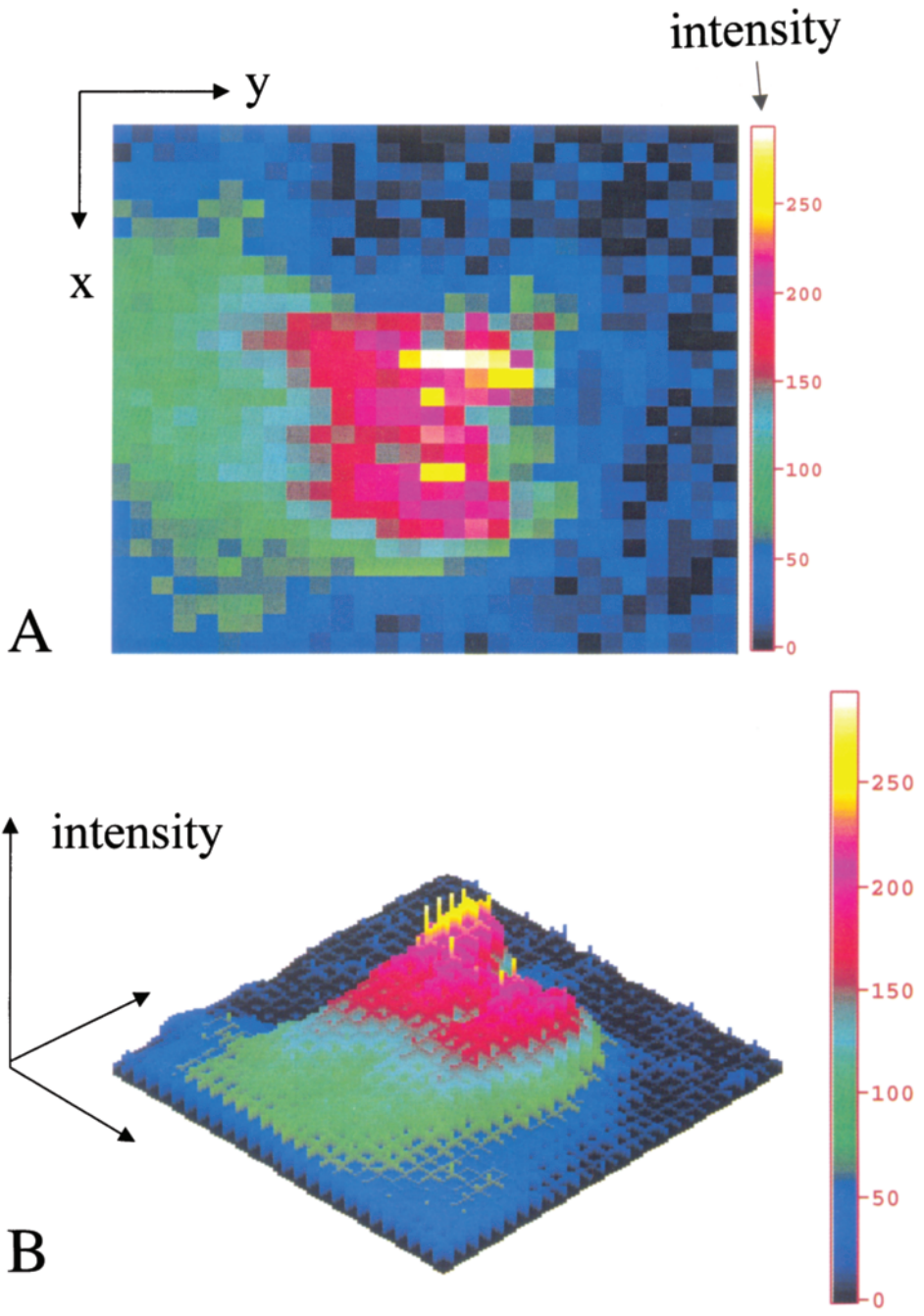

Figure 11.24. (See page 325.) Alternative representations of the data in Figure 11.23A. Image A is the raw 28 x 28 spatial grid, with white representing the most intense 858 cm-1 band. Image B is an axonometric plot showing intensity as both a height above the *x*-*y* plane and as a false color scale, shown on the right.

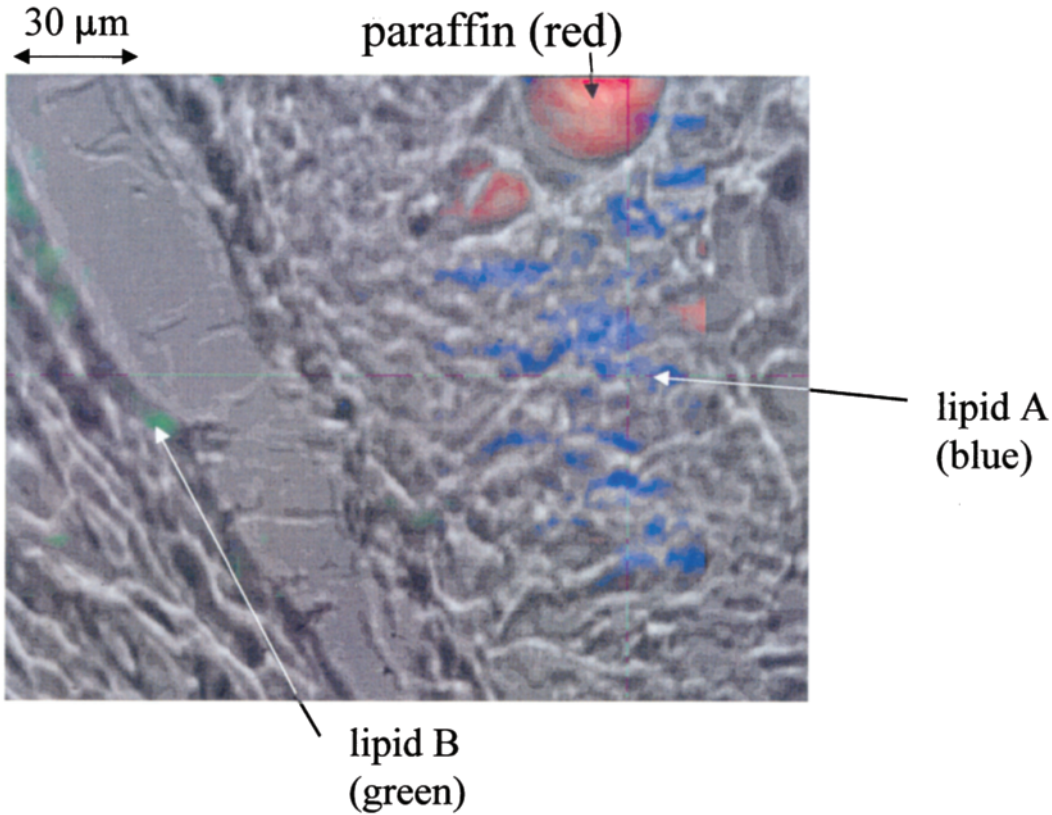

Figure 11.26. (See page 327.) Distribution of components indicated in Figure 11.25 overlaid on the video image. Each color represents the contribution of a particular component to the Raman spectrum observed at each position of a 28 x 28 grid. Obtained with a Dilor "XY" imaging spectrometer.

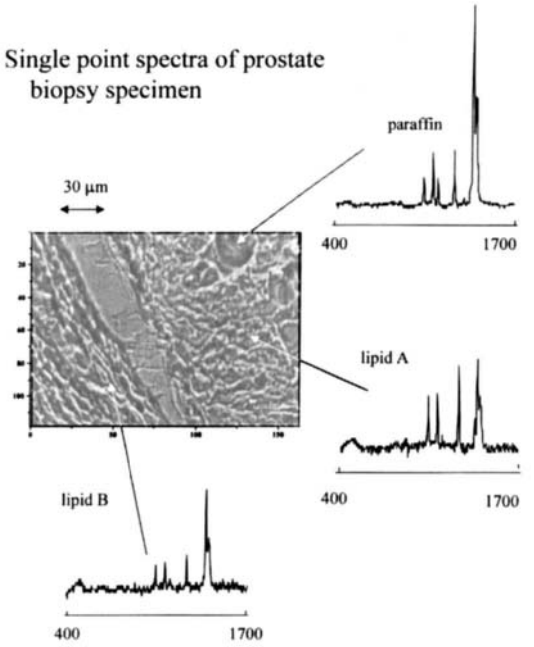

Figure 11.25. Raman microspectroscopy of a human tissue slice from a prostate cancer biopsy specimen mounted in paraffin. Scale on video image is in microns.

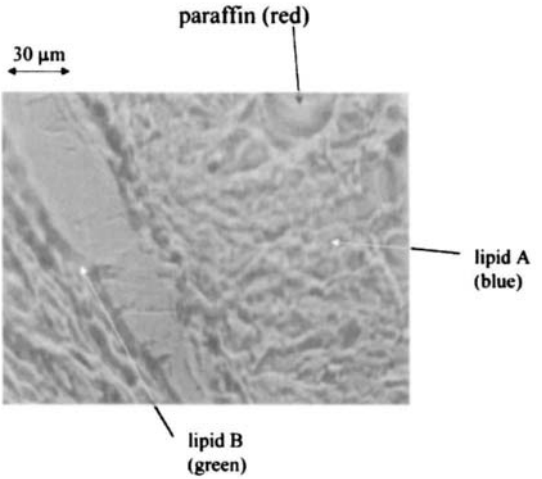

Figure 11.26. Distribution of components indicated in Figure 11.25 overlaid on the video image. Each color represents the contribution of a particular component to the Raman spectrum observed at each position of a 28 × 28 grid. Obtained with a Dilor "XY" imaging spectrometer. (See color plates.)

opaque lines resembling a modern bar code placed at the focal plane of a dispersive spectrometer, preceding a single detector. A sequence of mask translations between detector readings permits mathematical reconstruction of the spectrum. The SNR characteristics are similar to those of a Fourier transform (FT) spectrometer, with a multiplex advantage resulting when detector noise is important. Hadamard transform spectroscopy has not been used extensively for Raman, mainly because of the superior noise characteristics of CCDs. However, a sophisticated combination of the Hadamard transform with CCD detection has been implemented for Raman imaging (19,24,25). Instead of using the Hadamard technique to multiplex *wavelength*, it is used to multiplex *space*, thereby providing spatially resolved Raman spectra.

Consider the apparatus of Figure 11.27, which shows an adaptation of Hadamard transform techniques to Raman imaging. The laser is defocused at the sample so it illuminates a relatively large spot, as is the case for global imaging. The Hadamard mask is a two-dimensional pattern of opaque and clear regions, which is placed at the image plane of the microscope. Light passing through the mask represents a pattern of spatial regions on the sample, which

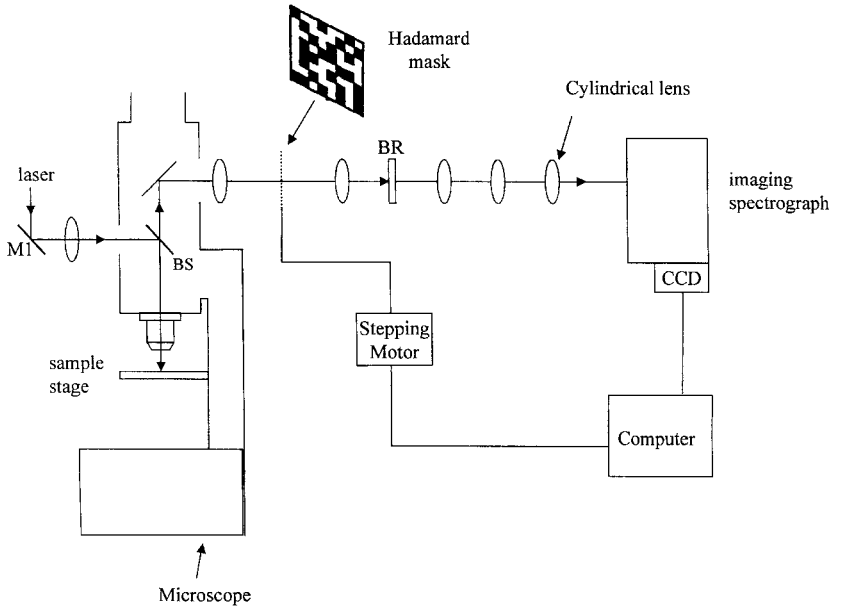

Figure 11.27. Schematic of a Hadamard transform imaging Raman spectrometer. The mask is moved between CCD exposures by the stepping motor, and the cylindrical lens creates a line focus along the entrance slit to an imaging spectrograph. (Adapted from Reference 24.)

is then focused to a line at the entrance slit of a spectrograph. This line is then dispersed according to Raman shift and imaged onto the CCD. During data acquisition, the Hadamard mask is translated along an axis perpendicular to the entrance slit, and a CCD image is acquired for each position of the mask. Each exposure represents a different set of spatial elements on the sample, all analyzed spectrally for Raman shift. Once the set of CCD exposures is complete, the Raman hypercube of intensity vs. x, y, and $\Delta\bar{\nu}$ is reconstructed mathematically. The spatial and spectral resolution depend on the CCD binning and the Hadamard mask, and the now-familiar trade-off between acquisition time and resolution still exists.

Although Hadamard image reconstruction is mathematically complex, it is implemented in software and is essentially automatic. Since a relatively large sample area is illuminated, the high power densities of point-to-point methods are avoided. This can be a major advantage for photo- or thermolabile samples. While Hadamard imaging operates with the low power density of global imaging techniques, it also can acquire a large number of spectral elements simultaneously. The combination of low power density with potentially high spectral resolution is a significant advantage of the Hadamard technique.

11.5.4. Relative Speed of Global and Reconstruction

The trade-offs among spatial resolution, acquisition time, and spectral resolution were pointed out several times in this chapter. In addition, image acquisition techniques vary significantly in power density, which affects both acquisition time and the likelihood of sample damage. With so many techniques and acquisition variables, there is a very large number of possible combinations, and it is difficult to generalize about "typical" or "desirable" parameters. As is so often the case, the optimum choice of imaging technique and acquisition parameters depends on the sample and the information desired. Nevertheless, it is useful to compare three of the common imaging techniques in order to illustrate some common trends.

Table 11.5 lists relative acquisition times for point-to-point reconstruction, line focus reconstruction, and global imaging for several different conditions. A hypothetical case of up to 50×50 spatial and 150 spectral resolution elements is considered, all at a single point along the z (depth) axis. The first three columns list the number of $\Delta\bar{\nu}$, x, and y resolution elements acquired in a given experiment. For example, line 1 represents acquisition of a spectrum with 150 Raman shifts at a single spatial point on the sample, while line 5 represents a 50×50 element Raman image at a single Raman shift value. The last three columns list the relative acquisition times to achieve a particular signal from a sample with a certain βD product. The actual acquisition

Table 11.5. Acquisition Times for a Given Signal Level (150 spectral resolution elements, 50 × 50 spatial elements, 1 depth)[a]

	Spectral Elements	x Elements	y Elements	Global imager 50 × 50 μm Area	Line Focus Reconstruction 50 μm Line	Point-to-point Reconstruction, from 1 μm Spot
			Constant Power Density			
1.	150	1	1	150	1[a]	1
2.	150	50	1	150	1	50
3.	150	50	50	150	50	2500
4.	1	50	1	1	1	50
5.	1	50	50	1	50	2500
			Constant Total Power			
6.	150	1	1	375,000	50	1
7.	150	50	1	375,000	50	50
8.	150	50	50	375,000	2,500	2,500
9.	1	50	1	2,500	50	50
10.	1	50	50	2,500	2,500	2,500

[a]All acquisition times listed are relative; actual times will vary greatly with cross section, concentration, power, etc.

time depends on many spectrometer and sample variables, but if these are held constant, the table entries reflect the relative acquisition times.

Lines 1 to 5 of Table 11.5 represent experiments where the laser power density is kept constant, even when the laser is focused onto a line or a two-dimensional area. In this case, the line focus would require 50 times the total laser power as a single-point observation, and a 50 × 50 μm area 2500 times. With constant power density, the global imager is much faster than a line or point focus when an image with only one Raman shift is acquired (line 5) but much slower if a complete spectrum is acquired at a single sample position (line 1). In the latter case, much of the data from the global imager is being "wasted," since all but one of the 2500 simultaneously monitored spatial points are ignored. For the case of constant power density, the acquisition times for a Raman image with n pixels and m Raman shift values are related simply by:

$$T_g = \frac{m}{n} T_p = \frac{m}{n^{1/2}} T_l \tag{11.4}$$

where T_g, T_p, and T_l are the acquisition times for the same image acquired in global, point–point, and line imaging modes (2).

The opposite extreme from constant power density is constant laser power, in which the available photon flux is merely distributed over different areas. The much lower power density of global compared to point imaging significantly increases the global acquisition time. For the case of a single spectral element and a 50 × 50 spatial grid (line 10), the power density changes and spatial multichannel advantage compensate exactly, leading to the same acquisition time for each imaging mode. In any real global imaging experiment, the total power would be substantially increased over that for a point or line focus, to reduce the acquisition time from that listed in Table 11.5. A typical point focus power might be 3 mW on a 3 μm-diameter spot (42 kW/cm^2) while a global imager might use 500 mW on a 60 μm spot (17 kW/cm^2). In most practical situations, the effect of spatial and spectral resolution on acquisition time is somewhere between the "constant power' and "constant power density" cases shown in Table 11.5.

As a final generalization on global imaging vs. image reconstruction, it is sometimes stated that global techniques stress the spatial information while reconstruction techniques stress the spectral information. For rapid, often high spatial resolution images of a few Raman shifts (such as line 5 in Table 11.5), the global approach is faster and often superior. But when detailed spectroscopic analysis or baseline subtraction is required, the necessary information is present in the line or point focus data sets. Point focus techniques, including the mechanically scanned line image, maintain the ability to allow confocal operation and can be important when depth resolution is critical to the application.

REFERENCES

1. G. Turrell and J. Corset, *Raman Microscopy: Developments and Applications*, Academic Press, San Diego, 1996.
2. M. Shaeberle, H. R. Morris, J. F. Turner, and P. J. Treado, *Anal.Chem.*, **71**, 175A (1999).
3. G. Turnell and J. Corset, *Raman Microscopy: Developments and Applications*, Academic Press, San Diego, 1997, p. 57.
4. D. M. Pallister, K.-L. Liu, A. Govil, M. D. Morris, H. Owen, and T. R. Harrison, *Appl. Spectrosc.*, **46**, 1469 (1992).
5. K. Ajito, *Thin Solid Films*, **331**, 181 (1998).
6. N. Everall, K. Davis, H. Owen, M. J. Pelletier, and J. Slater, *Appl. Spectrosc.*, **50**, 388 (1996).
7. R. Tabaksblat, R. J. Meier, and B. J. Kip, *Appl. Spectrosc.*, **46**, 60 (1992).
8. N. J. Everall, *Appl. Spectrosc.*, **52**, 1498 (1998).
9. J. T. Kloprogge and R. L. Frost, *Appl. Spectrosc.*, **53**, 356 (1999).

10. L. Markwort, B. Kip, E. Da Silva, and B. Roussel, *Appl. Spectrosc.*, **49**, 1411 (1995).
11. P. D. Wang, C. Cheng, C. M. Sotomayor Torres, and D. N. Batchelder, *J. Appl. Phys.*, **74**, 5907 (1993).
12. Y. Leung and M. D. Morris, *J. Biomed. Optics*, **2**, 120 (1997).
13. C. A. Drumm and M. D. Morris, *Appl. Spectrosc.*, **49**, 1331 (1995).
14. M. Bowden, P. Donaldson, and D. J. Gardiner, *Anal. Chem.*, **63**, 2915 (1991).
15. A. Govil, D. M. Pallister, L.-H. Chen, and M. D. Morris, *Appl. Spectrosc.*, **45**, 1604 (1991).
16. M. Bowden, D. J. Gardiner, and G. Rice, *J. Raman Spectrosc.*, **21**, 37 (1990).
17. A. Cuesta, P. Dhamelincourt, J. Laureyns, A. Martínez-Alonso, and J. M. D. Tascón, *Appl. Spectrosc.*, **52**, 356 (1998).
18. K. G. Ray and R. L. McCreery, *Anal. Chem.*, **69**, 4680 (1997).
19. P. J. Treado, A. Govil, M. D. Morris, K. Sternitzke, and R. L. McCreery, *Appl. Spectrosc.*, **44**, 1270 (1990).
20. C. J. Puppels, M. Grond, and J. Greeve, *Appl. Spectrosc.*, **47**, 1256 (1993).
21. S. M. Haight and D. T. Schwartz, *J. Electrochem. Soc.*, **142**, L156 (1995).
22. G. Turrell and J. Corset, *Raman Microscopy: Development and Applications*, Academic Press, San Diego, 1996, p. 39ff.
23. K. Christensen and M. Morris, *Appl. Spectrosc.*, **52**, 1145 (1998).
24. K.-L. Lee, K. Liu, L.-H. Chen, R.-S. Sheng, and M. D. Morris, *Appl. Spectrosc.*, **45**, 1717 (1991).
25. P. J. Treado and M. D. Morris, *Appl. Spectrosc.*, **43**, 190 (1989).
26. K. Maquelin, L. Choo-Smith, T. Vreeswijk, H. Endtz, B. Smith, R. Bennett, H. Bruining, and G. J. Puppels, *Analy. Chem.*, **72**, 12 (2000).

Raman Spectroscopy for Chemical Analysis. Richard L. McCreery

ISBN: 0-471-25287-5

CHAPTER

12

FIBER-OPTIC RAMAN SAMPLING

12.1. OVERVIEW OF FIBER-OPTIC SAMPLING

Figure 6.2 and associated text (Section 6.1) introduced the utility of fiber optics for coupling the Raman spectrometer to the sample. The laser and the wavelength analyzer do not differ fundamentally for fiber-optic compared to conventional sampling, although they may be optimized for fiber-optic use. The laser light is carried to the sample by an "excitation" optical fiber, and the scattered light is returned to the spectrometer by one or more "collection" fibers. At the sample, the fibers might be terminated as a simple bundle of parallel fibers, or a more sophisticated probe head containing focusing optics and filters. The various fiber-optic sampling configurations will be discussed in subsequent sections.

Several advantages of fiber-optic Raman sampling were recognized early, before charge-coupled devices (CCDs), Fourier transform (FT)–Raman and diode lasers, and provided some of the driving force for the development of Raman spectroscopy for chemical analysis (1). First, transmission of visible and near-infrared (NIR) light is quite efficient in modern optical fibers, so the spectrometer may be located a significant distance from the sample. It is not unusual to use fiber optical cables of 10 to 100 m lengths without severe signal attenuation. Second, the sample may be located in hazardous or difficult to access environments and still be efficiently coupled to the spectrometer. Some examples include radioactive storage tanks and human arteries. In the latter case, the fiber probe was only 1 to 3 mm in diameter, permitting Raman sampling of whole blood or arterial walls in living patients (2). Third, the alignment of laser, fibers, and spectrometer may be designed so that sampling requires little or no additional alignment. For example, an 18-around-1 parallel probe (described below) may be simply immersed in a liquid sample to obtain a spectrum. In this case, Raman spectroscopy is no more difficult for the operator than acquiring the sample's temperature with a thermometer. Fourth, fiber optics can be used to increase sensitivity by increasing the sampled volume, usually by increasing the effective path length. In some cases, the laser power density may also be reduced significantly, while maintaining signal. Fifth, fiber optics permit a single spectrometer to monitor several sampling points,

either sequentially or in parallel using the multitrack method illustrated in Figure 8.43.

These features have considerable value in many analytical applications, and have driven both instrumental design and industrial applications. Fiber-optic sampling often is a key feature in the development of "process Raman" in which Raman spectroscopy is used to monitor chemical production, often in-line. Current fiber technology limits transmission of the mid-infrared (IR) wavelengths used in FTIR to lengths of a few meters, while the visible and NIR light used most often for Raman spectroscopy can travel hundreds of meters. When vibrational spectroscopy is appropriate for process monitoring, Raman affords significant advantages over FTIR when the sample cannot be brought to the spectrometer. After describing some basic fiber properties and probe designs, we will illustrate several applications of fiber-optic sampling.

12.2. FIBER-OPTIC BASICS

The principles of light conduction in fiber optics are discussed thoroughly elsewhere (3), but a few issues relevant to Raman spectroscopy will be summarized here. Figure 12.1 shows a generic optical fiber, consisting of a core with a diameter of 5 to 600 μm and a cladding chosen to have a refractive index less than that of the core. Light entering the fiber at an angle less than the critical angle for the core–cladding interface is totally internally reflected and is conducted down the fiber. Since internal reflection is essentially 100 per cent efficient, the only loss mechanism of light within the fiber is absorption and scattering by the core material. The major interest in fiber optics for communication has resulted in very low loss fibers capable of efficiently conducting light for many kilometers at certain wavelengths.

The range of acceptance angles for an optical fiber is generally stated as the numerical aperture (NA). For the case of the square-cut fiber shown in

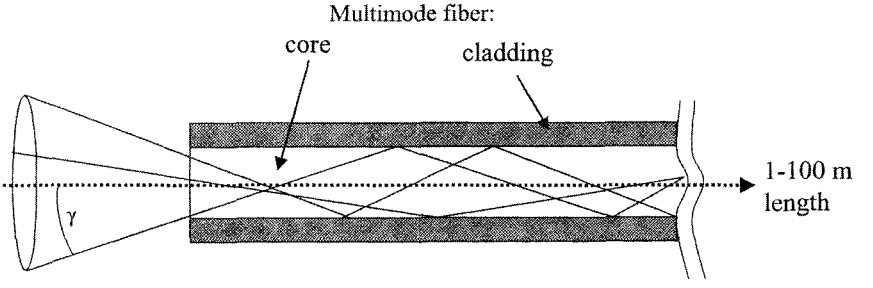

Figure 12.1. Schematic of light propagation in a typical multimode fiber. γ is the acceptance angle and is related to the numerical aperture.

Figure 12.1, the numerical aperture is given by:

$$\text{NA} = n_M \sin \gamma_M \tag{12.1}$$

where n_M is the refractive index of the medium in which a half-angle γ_M is observed. Only light entering the fiber at angles of γ_M or less relative to the fiber axis will be conducted down the fiber. Similarly, γ_M is the maximum half-angle of light exiting the fiber into a medium with a refractive index n_M. Optical fibers commonly used in Raman applications have numerical apertures of approximately 0.1 to 0.5, corresponding to half-angles of acceptance of 6° to 30° in air.

Multimode fibers have core diameters in the range of 50 to 600 μm and derive their name from the fact that light may take one of many possible paths down the fiber. The paths differ in the distance between internal reflections and in their entrance and exit angles. Multimode fibers do not retain the polarization of the light except over very short fiber lengths. The diameters of multimode fibers are large enough to permit straightforward coupling of laser and collected scattering into the fiber. Furthermore, multimode fibers in the 50 to 250 core diameter range are flexible and quite rugged. When the core exceeds about 300 μm in diameter, the minimum bend radius of the fiber increases, and the fiber becomes less flexible without damage. *Single-mode* fibers have small core diameters, <20 μm, and support only a single conduction mode. They retain polarization of the light, but they are much more difficult to align and use. Although single-mode fibers are of primary importance to communication applications, their use in Raman spectroscopy is limited to a few special cases.

Transmission by optical fibers is generally a strong function of wavelength, with the most efficient communication fibers operating in the region of 1100 to 1300 nm. Fiber transmission follows Beer's law, but the absorptivity is usually expressed in decibels per kilometer or decibels per meter. Equation (12.2) relates the intensity incident on the fiber, I_0 (ignoring coupling losses), the transmitted intensity, I_t, the fiber length, L (meters), and the attenuation, α_F, in decibels per meter:

$$\frac{I_t}{I_0} = 10^{-0.1\alpha_F L} \tag{12.2}$$

Curves of α_F vs. wavelength for a few optical fibers are shown in Figure 12.2 (4). Losses in the ultraviolet (UV) are quite high, and fiber lengths of only a few meters are practical (and quite expensive). Above about 2.5 μm, silica absorbs strongly so the core material must be changed to fairly exotic materials such as metal halides and chalcogenides. At present, these materials are also quite expensive and are useful for lengths of a few meters at most.

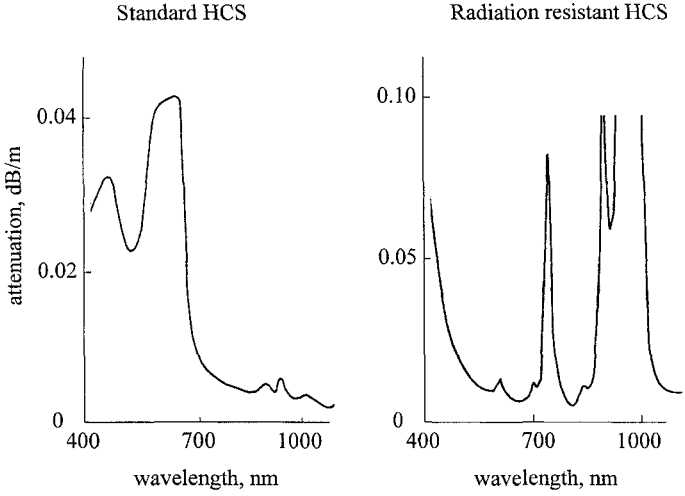

Figure 12.2. Attenuation curves for hard clad silica (HCS) fibers, plotted as dB/m vs. wavelength. Peaks correspond to losses caused by fiber absorption. Curves vary greatly for different fiber types and compositions. [Adapted from Ensign Bickford product literature (4)].

Table 12.1. Measured Transmission of 200 μm Core Diameter Optical Fiber[a] at Ar^+ Wavelengths

		Transmittance over	
λ (nm)	α_F (dB/m)[b]	3 m	100 m
514.5	0.018	0.988	0.66
496.0	0.014	0.990	0.72
488.0	0.014	0.990	0.72
476.5	0.020	0.986	0.63
457.9	0.021	0.985	0.62

[a]Ensign-Bickford HC 212-T fiber, NA = 0.4.
[b]Data from Reference 5.

Fortunately, low-loss fibers are available over most of the visible and NIR wavelengths in common use for Raman spectroscopy. As an example, some measured attenuation values for a commercial, 200 μm fiber at argon ion laser wavelengths are listed in Table 12.1 (5). Over a 3 meter fiber length appropriate to laboratory use, light loss is trivial, while 100 meter lengths are possible with moderate light loss. Since commercial Raman probes are

available for a variety of common laser wavelengths in the 450 to 1064 nm range, the probe manufacturers generally offer suitable fibers for a particular application or installation. In many cases, the fiber-optic sampling head and fibers are designed to be integrated to a particular manufacturer's spectrometer, so the fiber assembly is sold as an integrated unit, including cables.

12.3. FIBER–SPECTROMETER INTERFACE

The fiber-optic spectrometer configuration introduced in Figure 6.2 is shown in slightly more detail in Figure 12.3. The bandpass (BP) and band reject (BR) filters may be located as shown or integrated into the probe head. Probe head designs will be discussed in later sections, but they range from a simple bundle of square-cut fibers to quite sophisticated heads containing filters and focusing optics. Of interest in the current section are the "launching" optics, which direct the laser light into the excitation fiber, and the collection optics, which direct the scattered light from the collection fiber into the spectrometer.

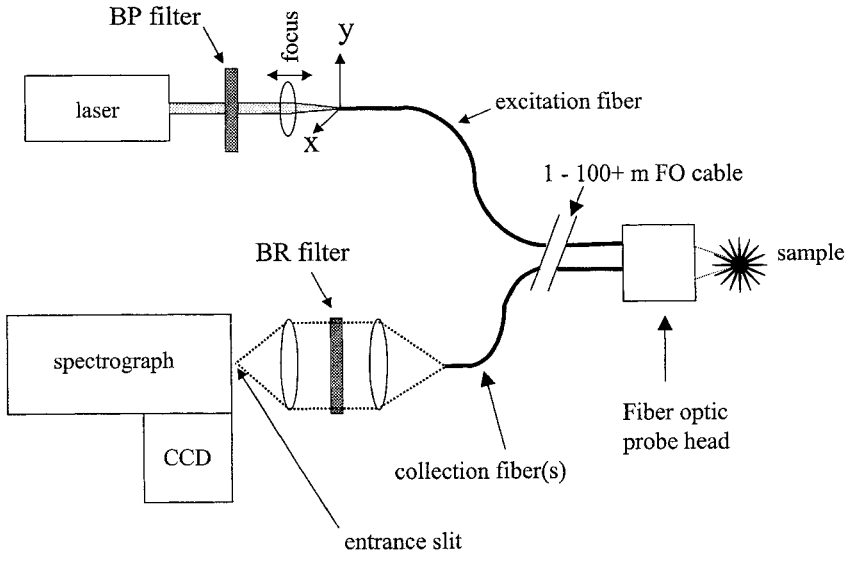

Figure 12.3. General schematic of fiber-optic Raman sampling, showing the laser–fiber interface and the fiber–spectrometer interface. The bandpass (BP) and band reject (BR) filters are sometimes integrated into the probe head. The fiber-optic (FO) length can vary over a wide range, from less than 1 m to greater than 100 m, depending on the application.

12.3.1. Laser–Excitation Fiber Interface

Ion, He–Ne, and Nd:YAG lasers (Sections 7.3 to 7.5) have well-collimated beams of a few millimeter diameters, while diode lasers often have diverging beams emanating from an area of a few tens or hundreds of square micrometers. The objective of the laser–excitation fiber interface is to couple a maximum fraction of total laser light into the fiber, at angles within the numerical aperture of the fiber. For "unfiltered" probes (Section 12.4), a laser bandpass filter is necessary for the reasons described in Section 7.6. The laser–fiber interface is governed by $A\Omega$ considerations in a manner similar to the spectrometer described in Chapter 6, so that the *étendue* through the laser optics and fiber remains constant, equal to the smallest value of the component parts. For the laser, A is related to the beam cross section and Ω to the divergence. For the fiber, A is determined by the fiber cross section and Ω by the numerical aperture. For the generic fiber shown in Figure 12.1, maximum coupling of laser light into the fiber occurs when the laser is focused on an area smaller than the fiber cross section, and the input light cone remains within the numerical aperture of the fiber. This condition is relatively easy to meet for multimode fibers but becomes significantly more difficult for single-mode fibers.

Assuming the $A\Omega$ requirement is met, an additional consideration is the optimum divergence of the light exiting the excitation fiber at the probe head or sample (1). Within the limit imposed by the numerical aperture, the range of exit angles approximately equals the range of entrance angles for the incident laser light, so the coupling optics can significantly affect the divergence of light exiting the fiber. This divergence can affect both the sampling depth and the probe efficiency at the sampling end of the fiber-optic assembly, so it is a fairly important design issue. Figure 12.4 illustrates two examples, both involving a collimated laser beam (e.g., Ar^+, 514.5 nm) and a 100 μm fiber with NA = 0.3. The laser spot size at he fiber end is given by Eq. (6.2), and equals 50 μm for the 100 mm lens and 12.5 μm for the 25 mm lens. Both lenses must meet the $A\Omega$ requirement that the spot size be smaller than the fiber end and the incident angle be smaller than γ_M. Both lenses should produce comparable coupling efficiency of laser light into the fiber. However, the 100 mm lens produces a divergence half-angle at the probe end of 0.6°, while the 25 mm lens yields 2.3°. This angle may be important to how the laser light penetrates the sample or to how it fills the probe head optics.

The mechanics of the laser–excitation fiber interface include a lens mount and a fiber mount with the three translation adjustments shown in Figure 12.3, plus yaw and pitch. In some cases, these five fiber adjustments are independent, and the procedure for alignment is often painstaking. However, a

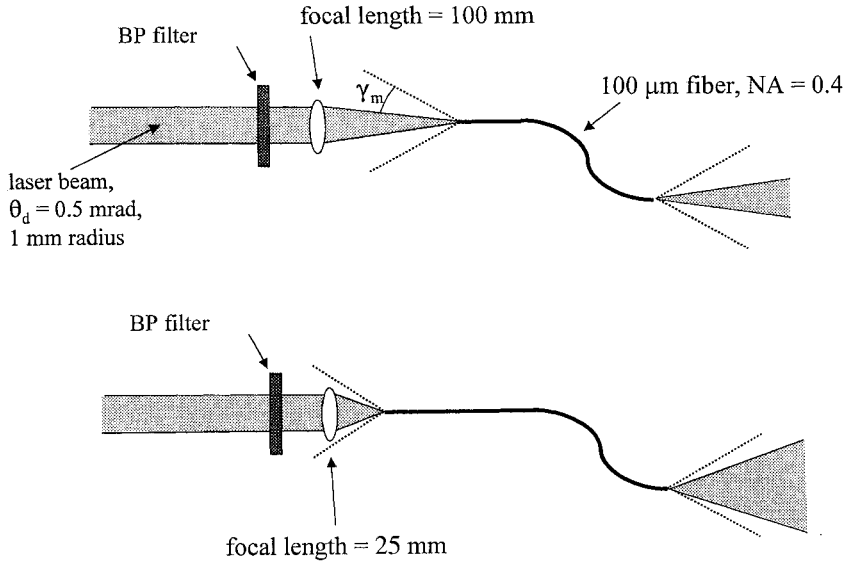

Figure 12.4. Effect of the focusing lens at the laser–fiber interface on the size of the light exit cone at the sample or probe head. (Angles not drawn to scale.)

variety of simpler devices are available that are completely adequate for Raman applications. For example, the lens may be integrated with a fiber-optic connector (e.g., SMA type) so the X, Y, and Z adjustments are prealigned (6). Efficient coupling is achieved with only the yaw and pitch adjustments. Laser manufacturers often sell fiber-optic couplers that attach directly to the laser and require minimal adjustment, if any. Provided the $A\Omega$ requirement is met and the fiber position is aligned with sufficient accuracy, it is usually possible to couple >80 per cent of the laser light into the fiber, not counting losses that occur in the BP filter, if present.

12.3.2. Fiber–Spectrometer Interface

Depending on the probe head configuration, the collection fibers returning scattered light to the spectrometer range from a single fiber of 50 to 200 μm diameter to a bundle of as many as 36 fibers with diameters of 50 to 500 μm. Furthermore, the spectrometer input aperture may be a slit of perhaps 25 to 200 μm width in a dispersive spectrometer or a circular aperture of a few millimeter diameter for an FT-Raman system. All spectrometers have an Ω determined by their $f/\#$ as well. The goal of the optics that couple the collection fiber(s) to the spectrometer is to maximize efficiency by matching the

fiber output to the size and shape of the input aperture and filling the spectrometer Ω as much as possible. Stated differently, the *étendue* ($A\Omega$) of the spectrometer should be met or exceeded by that of the collection fibers (5). Since the spectrometer *étendue* usually limits that of the overall system, it should not be degraded by the optical-fiber system.

In principle, the collection fiber can be placed directly at the spectrometer input aperture, as shown in Figure 12.5A. In this case, the light cone leaving the fiber should fill the collimating optic of the spectrometer, effectively matching the $f/\#$ of the fiber and spectrometer. While this direct coupling method works, it is more common to insert optics between the fiber and spectrometer aperture, to permit the use of a filter or slit, or to adjust the fiber numerical aperture to that of the spectrometer. Figure 12.5B shows coupling optics that change an $f/2$ fiber output to $f/4$ to enter the spectrograph and allow insertion of a filter and slit. For the example of Figure 12.5B, the fiber diameter would be magnified by a factor of 2 when imaged onto the slit. The lens may also be chosen to image the fiber without magnification (or even with demagnification), but the $A\Omega$ product will remain constant.

An additional feature of fiber-optic collection is the ability to change the shape of the sample area from which scattering is collected before the light

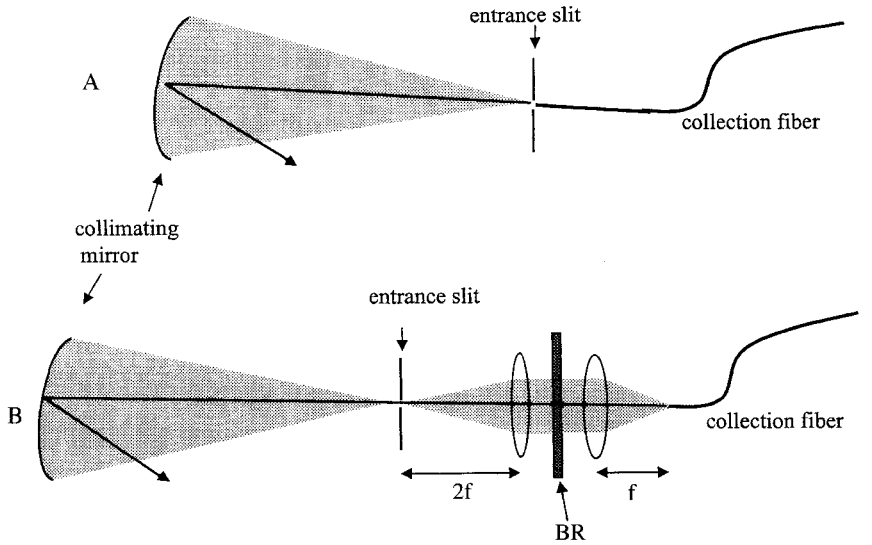

Figure 12.5. Two methods for directing light exiting the collection fiber into the spectrometer slit or aperture. Case A is simple and direct but does not allow adjustment of the numerical aperture of the fiber to match the $f/\#$ of the spectrometer. Case B is more common both because of greater flexibility and because it provides a parallel path region in which to place a BR filter.

enters the spectrometer. For example, a circular bundle of 18 fibers that collect the scattered light may be reconfigured as a line to match the entrance slit of a dispersive spectrometer (1,5). This operation does not violate the constancy of $A\Omega$ but does permit reshaping the observed area into one more amenable to the spectrometer. A few arrangements of input fibers are shown in Figure 12.6. Either these configurations are input to the spectrograph directly (as in Fig. 12.5A) or imaged onto the entrance slit of a dispersive spectrograph or the aperture of an interferometer.

It is useful at this point to note the relationship between fiber diameter and slit width for the case of a dispersive spectrometer. As described by Eq. (8.7), the resolution of a dispersive spectrometer is determined by the slit width. In addition, the area (and *étendue*) of collection depends on how much of the cross section of the fiber is analyzed by the spectrometer. As shown in the upper diagrams of Figure 12.6, the slit may block part of the fiber when the slit width is smaller than the fiber diameter. As the slit width is increased beyond the fiber diameter, the slit no longer functions, and the resolution is determined by the fiber diameter. If a particular application uses small diameter fiber (e.g., <50 μm), the slit may be deleted from the system altogether. If high resolution requires a slit narrower than the fiber diameter, some scattered light intensity must be sacrificed. For FT-Raman systems, the resolution depends on the aperture size very weakly, so a relatively large fiber bundle area may be monitored. In fact, a drawback of fiber-optic sampling with FT-Raman systems is that the large available *étendue* of the spectrometer is usually underfilled by the fibers and effectively wasted.

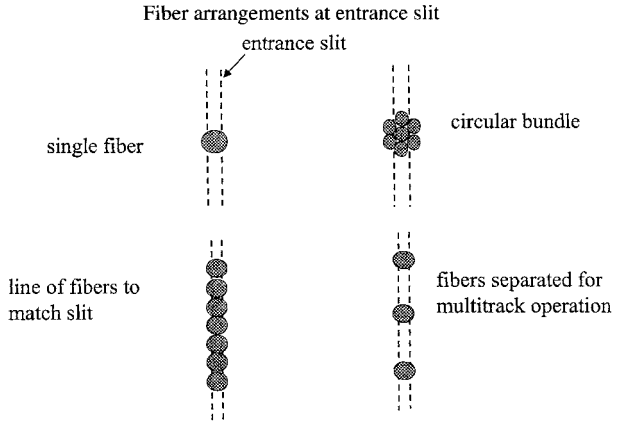

Figure 12.6. Four configurations of the collection fibers at the entrance slit (or slit image).

12.4. FIBER-OPTIC PROBES

The interface of the excitation fiber, collection fibers, and sample occurs at a "probe" or "sampling head" located at some distance from the spectrometer, ranging from a few meters to hundreds of meters. The probe must duplicate many of the functions of the sampling optics described in Chapter 6, such as laser focusing, collection of scattered light, and associated alignment. The probe is usually compact and rugged and is often intended for applications in uncontrolled or harsh environments such as chemical production facilities. A wide variety of probe designs have been reported and evaluated, but they may be classified into two general types. *Unfiltered* probes were developed first and have the advantage of small size, low cost, and simplicity. However, inelastic scattering within the excitation and collection fibers generates a background signal that is difficult to avoid in many practical situations. *Filtered* probes have optical filters built into the probe head to remove the fiber background. The sampling head may also include focusing optics that reproduce the 180° geometry (Fig. 6.4) at the sample. Filtered probes are larger and more complex than the unfiltered variety but are useful in a wider range of applications.

12.4.1. Unfiltered Fiber-Optic Raman Probes

Some early examples of fiber-optic collection of Raman light scattered by a conventional open laser beam exist (7,8) but will not be discussed here. In addition, fiber optics have been used for absorption and fluorescence experiments (9,10), resulting in the term *optrode*. The first example of Raman spectroscopy in which both the excitation light and collected scattering are carried by optical fibers appeared in 1983 (11), shortly before an independent patent submission by Dow Chemical (12). These early designs were subsequently modified and enhanced by many laboratories and became known as the *"parallel"* or "*n*-around-1" probe geometries. Several basic configurations are shown in Figure 12.7. The probe may be immersed in a liquid sample or placed near a solid sample. The central fiber carries laser light to the sample, with the excitation light exiting the central fiber as a cone whose size depends on the numerical aperture or laser to fiber coupling optics. The surrounding collection fibers collect backscattered light and return it to the spectrometer. If all of the fibers have the same diameter, the 6-around-1, 18-around-1, and 36-around-1 packing arrangements provide maximum packing density for a given total diameter. Figure 12.7 also shows a photograph of an 18-around-1 probe illuminated by a desk lamp at the spectrometer end of the fiber bundle (5). The 200 μm core diameter fibers used in this case have a quite thin cladding (15 μm) to permit close packing into a bundle with a total diameter of ~1 mm. The 19 fibers were encased in epoxy in a melting point capillary tube.

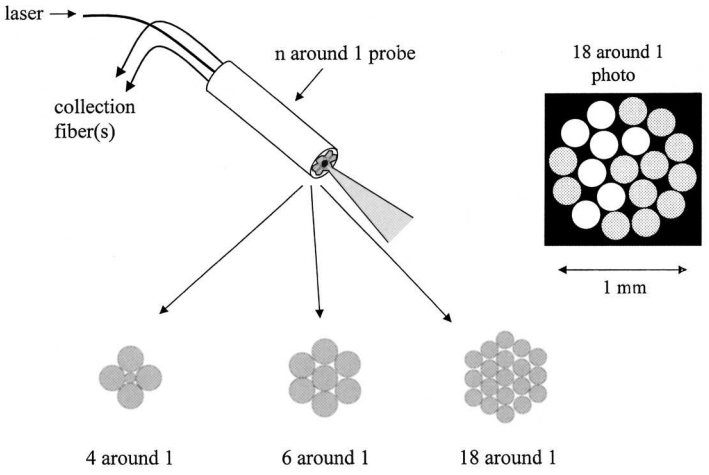

Figure 12.7. Schematic of the n-around-1 unfiltered fiber-optic probe. The excitation and collection fibers need not be the same diameter, but usually are. The inset shows a photo of an 18-around-1 probe illuminated with white light conducted from the spectrometer end of the fiber cable. (Adapted from Reference 5).

Figure 12.8 shows a spectrum of four samples obtained with an 18-around-1 probe and a dispersive/CCD spectrometer (13). The spectra are nearly identical in both appearance and signal magnitude to those obtained with conventional 90° or 180° geometry, even though the fiber spectrum required minimal sample alignment. The fiber probe is actually collecting more scattered light than the conventional sampling optics, but the overall signal is limited by the *étendue* of the spectrometer. Hence the greater collection efficiency of the fiber probe is overfilling the spectrometer, and the two signal strengths are identical. The suitability of the unfiltered probe for harsh environments is demonstrated in Figure 12.9. An 18-around-1 probe immersed in acetonitrile was lowered into liquid nitrogen, thus freezing the acetonitrile around the probe. An excellent spectrum was obtained, without the need for a specialized cryogenic cell, windows, or the like.

Several theoretical analyses of the characteristics of n-around-1 probes have been reported, and they illustrate some important points about probe characteristics (5,14,15). The relevant variables are illustrated in Figure 12.10. The scattered light entering the collection fiber originates in the overlap region of the excitation beam and the collection cone determined by the NA of the collection fiber(s). For a sample molecule located at a point within this overlap region, the incident laser intensity is determined by the distance from the excitation fiber, and the scattered light entering the collection fiber is determined by the inverse square of the distance to the collection fiber face. Integration

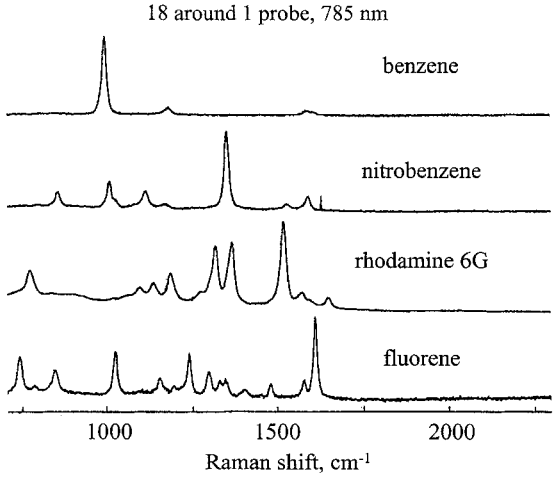

Figure 12.8. Spectra of two liquids and two solids obtained in rapid succession with an 18-around-1 probe and a Chromex spectrometer operating at 785 nm. Acquisition time for each spectrum was 1 sec or less, and the probe was either immersed in the liquids or directed at the powdered solids from distance of about 5 mm. (Adapted from Reference 13 with permission.)

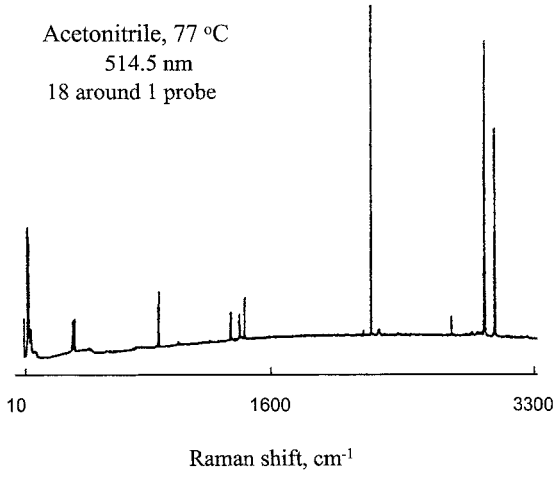

Figure 12.9. Spectrum of acetonitrile obtained with an immersed 18-around-1 probe after lowering both sample and probe into liquid nitrogen. Spex 1403 scanning/PMT spectrometer, 514.5 nm laser, about 10 min total acquisition time. (Adapted from Reference 5 with permission.)

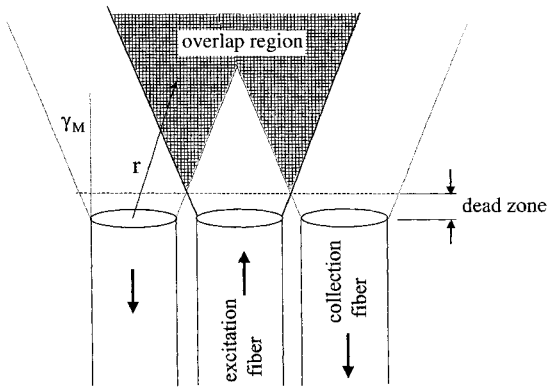

Figure 12.10. Parameters governing light collection from an n-around-1 probe, which are also used in most theoretical calculations of probe efficiency; r represents a point within the overlap of the excitation light and the numerical aperture of the collection fiber(s). The signal may be predicted by integrating Eq. (2.19) over the entire overlap region, taking into account the laser power density and the distance from the collection fibers.

of Eq. (2.19) for each point r within the overlap region yields the theoretical signal magnitude as a function of probe parameters such as fiber radii, NA, and fiber spacing.

Several results of the theoretical analysis deserve special note. First, there is a "dead zone" near the fiber face from which no Raman light is collected. The sample must be deep enough and transparent enough to permit overlap of the excitation and collection cones. Second, collection is most efficient when the excitation and collection fibers are close together, so thin fiber cladding results in closer packing and larger signal. Third, the signal is larger for a large collection fiber area, resulting from either large collection diameters or many collection fibers. This advantage diminishes as collection fibers are added because additional fibers are necessarily farther from the excitation fiber. Also, the collection fiber area is ultimately limited by the spectrometer aperture, as the signal will not increase once the fiber $A\Omega$ exceeds the spectrometer $A\Omega$. Fourth, the n-around-1 geometry probes fairly deeply into the sample because the overlap region increases in size with distance from the probe tip, and a larger number of sample molecules is observed. Figure 12.11 shows the relative signal as a function of sample depth for an excitation NA of 0.075. Each curve corresponds to a different collection NA, which is determined by the collection fiber or the spectrometer (whichever is less). Notice that the signal is still increasing at a sample depth of 1 cm. Experimentally observed points for a particular case (collection NA = 0.15) are also shown in Figure 12.11. Not surprisingly, the lower collection NA (narrower cone) collects deeper into the sample but yields a smaller total signal.

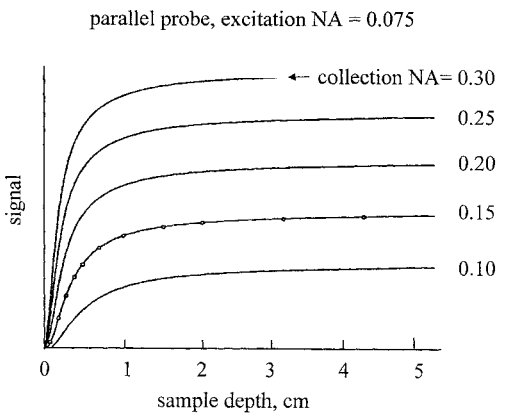

Figure 12.11. Calculated Raman signal for an n-around-1 probe as a function of numerical aperture and sample depth. Penetration into the sample for unfocused probes is quite deep, often exceeding 1 cm. (Adapted from Reference 5 with permission.)

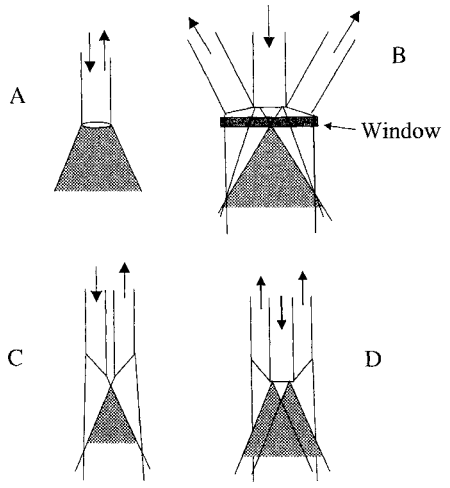

Figure 12.12. Variations on the n-around-1 probe, which increase the overlap of the excitation light and the collection region. A is a single fiber arrangement, B is based on the Dow patent (12), and C and D use beveled fibers (16).

The already fairly efficient collection efficiency of parallel n-around-1 probe has been further improved by modifications to the probe tip, four of which are shown in Figure 12.12. The *single-fiber* configuration has the advantage of complete overlap of excitation and collection regions and has been used successfully for fluorescence experiments. However, the background scattering

from the fiber is severe due to the long path length in the fiber, and only very short lengths of fiber are tolerable (<10 cm). The *angled* arrangement (Fig. 12.12B) is the basis of the early Dow patent (12). It increases the overlap of the excitation and collection regions, and also reduces reflections when a window is placed on the end of the probe. As discussed below, reflection or scattering of laser light by a window back into the collection fibers can be a serious issue with unfiltered probes, and the angled probe mitigates the problem somewhat. The remaining arrangements shown in Figure 12.12 involve beveling one or more fibers so the fiber face is not perpendicular to the fiber axis. For the case of Figure 12.12C, refraction of the laser light directs it toward the center of the probe, and the collection fiber preferentially samples light from the region near the probe center (16). Hence the overlap of excitation and collection is increased over the same probe with square-cut fibers. A window is often added to the probe to reduce contamination of the fibers. The design of Figure 12.12C is effective for only a pair of fibers and is not amenable to employing a bundle of collection fibers to improve collection. The design in Figure 12.12D uses a square-cut excitation fiber and beveled collection fibers to create an efficient 6-around-1 probe (16).

12.4.2. Problem of Fiber Background

As noted above, an issue with fiber-optic Raman sampling is the background generated by inelastic scattering within the fiber. The silica used to make most optical fibers of interest here is not a particularly strong Raman scatterer, but the path length relevant to Eq. (3.6) can be very large. Much of the scatter from the fiber occurs within the NA of the fiber, so it is efficiently returned to the spectrometer, resulting in the long effective path length. Furthermore, the silica spectrum is broad and occurs over most of the useful Raman shift range with varying intensity. A typical spectrum of a silica fiber is shown in Figure 12.13 (17). While the strongest features occur below $\sim$1100 cm^{-1}, weak scattering is present over the entire 0 to 3500 cm^{-1} range. Obviously, the extent of interference from fiber scattering increases with fiber length, but it is also a strong function of the properties of the sample. For clear samples, the silica background generated in the excitation fiber is not efficiently scattered back into the collection fibers, and fiber background is often quite low (e.g., Fig. 12.8). However, if the same probe is used to examine a white powder, much more of the fiber scattering returns to the spectrometer and the background is significant or prohibitive. Figure 12.14B shows a spectrum of an acetaminophen tablet obtained with a relatively short (1 m) unfiltered probe (18). The additional scattering from silica is obvious and overwhelms the acetaminophen signal with longer fiber lengths.

It is useful to point out that the fiber background does not result from scattering solely in the excitation fiber, which then enters the collection fibers

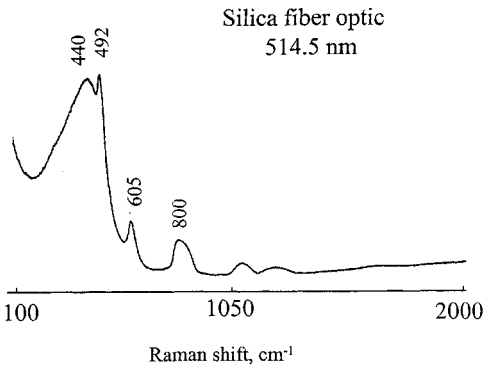

Figure 12.13. Raman spectrum of a typical silica optical fiber, showing common Raman features from silica; 514.5 nm excitation. (Adapted from Reference 17 with permission.)

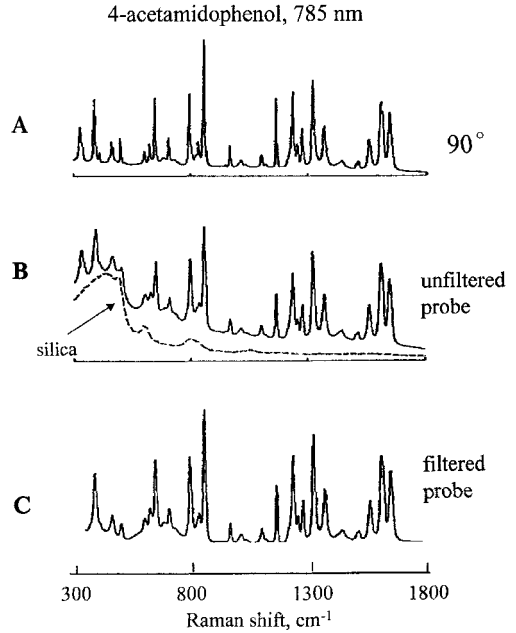

Figure 12.14. Raman spectra of 4-acetamidophenol obtained with a Chromex spectrometer at 785 nm. Spectrum A is from conventional, nonfiber 180° geometry; spectrum B was obtained with an 18-around-1 unfiltered probe and a short (<1 m) fiber-optic cable; and spectrum C with a DLT filtered probe and a 17 m cable. Dashed line in spectrum B is the spectrum of silica. (Adapted from Reference 18 with permission.)

after scattering from the sample. An additional source is unshifted laser light, which is elastically scattered into the collection fibers by the sample, then is Raman shifted within the collection fiber. In fact, we can show that these two contributions are equal for the case of equal excitation and collection fiber lengths. Suppose s_e is the fraction of light that is Raman scattered by the excitation fiber (per meter) and conducted down the fiber to the sample (length l_e), and e_s is the fraction of light that is elastically scattered by the sample and collected. The inelastic silica background (including Raman) from the excitation fiber, which is detected by the spectrometer (B_e), is

$$B_e = P_0 s_e l_e e_s \tag{12.3}$$

where P_0 is the laser intensity incident on the excitation fiber, and losses within the fibers are ignored. Unshifted laser light leaving the excitation fiber will also be scattered into the collection fiber, with an intensity of $P_0 e_s$. This light will then generate silica Raman scattering equal to B_c:

$$B_c = P_0 e_s s_c l_c \tag{12.4}$$

with s_c and l_c being the scattering efficiency and length of the collection fiber:

$$B_T = B_c + B_e = P_0 e_s (s_e l_e + s_c l_c) \tag{12.5}$$

If the excitation and collection fibers have the same length and scattering properties, their contributions to fiber background are equal, and the total fiber background is $2P_0 e_s s_e l_e$. For a clear sample, e_s is determined only by Rayleigh scattering and is often small enough to make B_T negligible. For solid samples, however, e_s may increase by several orders of magnitude, and silica background may become prohibitive. Even for small values of e_s, long fibers will increase $s_e l_e$ enough to cause serious fiber background. In practical terms, the maximum acceptable fiber length for a given experiment is determined by e_s and the size of the desired Raman signal relative to the fiber background. For clear samples (low e_s) with strong Raman scattering, relatively long fiber lengths (and therefore large $s_e l_e$ and $s_c l_c$) may be tolerable. But for samples with weak Raman scattering and high e_s (such as white powders), short fiber lengths are required to reduce fiber background below the desired Raman signal when an unfiltered probe is used. For many real samples, an unfiltered probe generates unacceptable background even for very short lengths.

To summarize the characteristics of unfiltered probes, their advantages stem from simplicity and efficiency, while their limitations are due to inelastic scattering background from the fibers themselves. When this background is tolerable, unfiltered probes are useful in applications requiring small probe size (<1 mm total diameter) or high efficiency. The signal for unfiltered probes can be significantly larger than that from filtered designs because less light

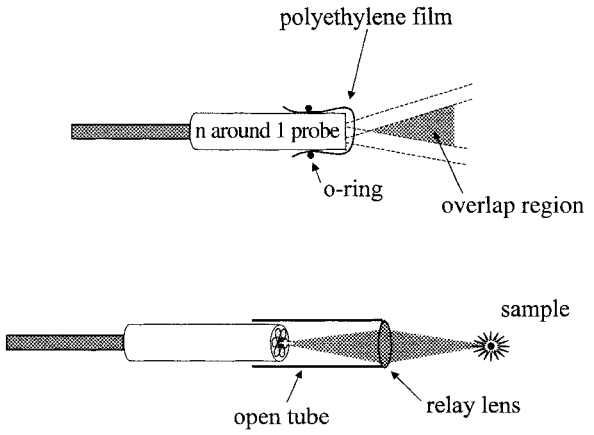

Figure 12.15. Two accessories for the n-around-1 probe that broaden applicability. A clear, thin, protective membrane may be placed over the probe end (19) such that it does not enter the overlap region and is not detected (upper drawing). The lower drawing shows a simple relay lens that refocuses the probe end in the sample, possibly after passing through a sampling window.

is lost in optical components and the sampled volume can be large. Unfiltered probes often result in low power density at the sample, which might be important for photolabile samples. The dead zone for n around 1 and related probes can be a problem for thin or absorbing samples but can also be used to advantage for insertion of a thin plastic film to protect the probe when immersed in a sample (Fig. 12.15) (19). Since the film is not within the sampling region, its Raman scattering does not contribute to the observed spectrum. Conversely, the n-around-1 probes are constrained to sample within about 1 cm of their tips, and are not directly compatible with thick windows or a working distance greater than ~1 cm. A solution to this constraint is a relay lens (Fig. 12.15B), which images the fiber probe face at a distance determined by the thin lens equation applied to the relay lens. This lens can be mounted in a simple attachment that may be quickly placed over the probe when desired.

While unfiltered probes can perform very well for clear samples and relatively short fiber lengths, the silica background is prohibitive for many applications. Process monitoring is one of the primary applications driving Raman spectrometer development in which the probe head is located in a chemical plant (e.g., at the side of a pipe or reactor) and the spectrometer is in a more controlled environment. such applications generally require fiber lengths greater than 10 m, and unfiltered probes are unacceptable. Filtered fiber-optic Raman probes were developed to overcome the limitations imposed by silica background scattering.

12.4.3. Filtered Fiber-Optic Raman Probes

The variety of combinations of filters, fiber optics, and sampling optics will be divided here into two types, involving either in-line filters or integrated probe heads. In-line filter designs are conceptually similar to the unfiltered probes of Section 12.4.1 but add bandpass and band reject filters to the fibers, near or at the sample location. Probe heads are often similar to the 180° sampling geometries described in Chapter 6, and the fibers are used to convey light from the laser to the probe head and the head to the spectrometer. When a probe head is used, the fibers serve the function of separating the sample and spectrometer by a possibly long distance, but they are not directly involved in directing laser light into the sample or collecting Raman scattering.

12.4.3.1 In-Line Filtered Probes

An effective in-line filtered probe design is shown in Figure 12.16 for two sampling configurations. Miniature lenses, filters, and housings are available for fiber-optic applications, which permit insertion of filters with little increase in physical size. Graded index (GRIN) lenses collimate or focus the light to permit filtering by bandpass or band reject filters, usually miniature dielectric interference filters. A bandpass filter is used on the sample end of the

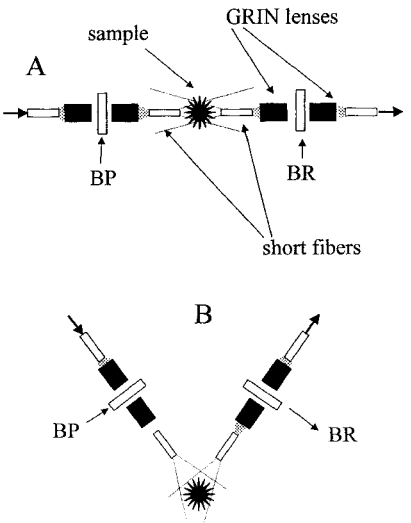

Figure 12.16. Two sampling geometries that use in-line filters near the sample region and graded index (GRIN) lenses. For details, see the text as well as Reference 20.

excitation fiber to remove inelastically scattered laser light, and a band reject filter precedes the collection fiber to avoid inelastic scattering during transit back to the spectrometer. Both linear (Fig. 12.16A) and "V" configurations (Fig. 12.16B) have been evaluated (20). In-line filtering yielded excellent reduction of fiber background, such that weak scatterers were observable with a fiber length of 100 m. Since the filters and GRIN lenses may be quite small (<5 mm in diameter), they do not greatly increase the size of the overall probe.

An alternative in-line arrangement uses the fibers themselves as filters. Fibers containing rare-earth oxides can be fabricated to absorb light of particular wavelength ranges. For example, a short (several centimeters) length of such fiber may be used to attenuate laser light before transmission between the sample and spectrometer, thus reducing fiber background in the "collection" fiber. This design avoids coupling losses in the GRIN lenses and filters and maintains the small diameter of the fiber bundle (21). At present, the design is limited in versatility, since the availability of absorbing fibers is limited. Since filtering is based on absorption, the low Raman shift range is generally inaccessible.

A major improvement of the in-line filtering approach occurred with a patent by Carrabba and Rauh in 1992 (22). The excitation and collection fibers were filtered with BP and BR filters as before, but the filtered laser light axis was combined with the collection axis with a dichroic mirror, as shown in Figure 12.17. The dichroic transmits laser light but reflects Raman-shifted light, thus directing it into the collection fiber. This approach has several significant advantages over the in-line filtered or unfiltered designs. First, the overlap of the excitation and collection regions in the sample is not dependent on fiber positioning, and the coaxial geometry leads to more reproducible sampling and scattering intensity. Second, the focal length of the objective lens may be varied, to permit sampling through a window to vary the effective path length. Third, the entire assembly is small and rugged, with an outside diameter of ~15 mm. These advantages occur while the fiber filtering is maintained, so long fiber lengths may be employed. The Carrabba and Rauh design was the forerunner of the probe head designs in most common use currently, and it incorporates most of their features. The probe head configurations discussed next are physically larger and generally more versatile.

12.4.3.2 Fiber-Optic Probe Heads

The most popular probe heads in current use are conceptually similar to the Carrabba and Rauh design, with the excitation and collection axes combined to form a coaxial 180° sampling geometry. The integration of fiber connections, lenses, and filters into a small probe in the Carrabba and Rauh design

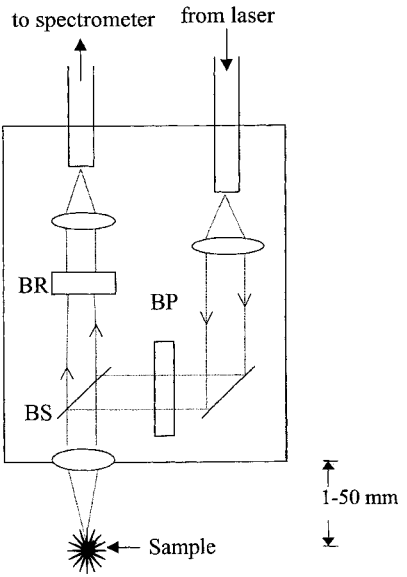

Figure 12.17. Integrated probe containing filters and focusing optics developed by Carrabba and Rauh (22). The external diameter is small (<2 cm) and the probe is very rugged compared to laboratory optics.

limits the range of compatible optics and filters and makes probe modification and internal alignment difficult. Subsequent designs were directed toward a larger probe head, often containing holographic optics, which permitted an interchangeable objective lens. The result is a probe head that is roughly the size of a flashlight and that may be connected to the laser and spectrometer with fiber-optic cables. Once the head itself is aligned internally, it may be easily connected to the spectrometer and laser without further alignment. The fiber-optic cables are usually terminated with standardized connectors (e.g., SMA), so connection of probe head to spectrometer becomes as easy as interconnecting electronic components with BNC cables. When configured this way, the optical fibers are serving to spatially separate the spectrometer and laser from the focusing and collection optics, and the probe head is duplicating the function of conventional focusing optics, at possibly great distance from the spectrometer.

Perhaps the simplest (but not the first) example of this approach is a direct descendant of the 180° geometry used in microscopes (Fig. 6.3). A partially reflective mirror or dichroic mirror combines the excitation and collection axes, as shown in Figure 12.18 for a probe built by DLT, Inc. This mirror is commonly referred to as a "beamsplitter," even though its function is

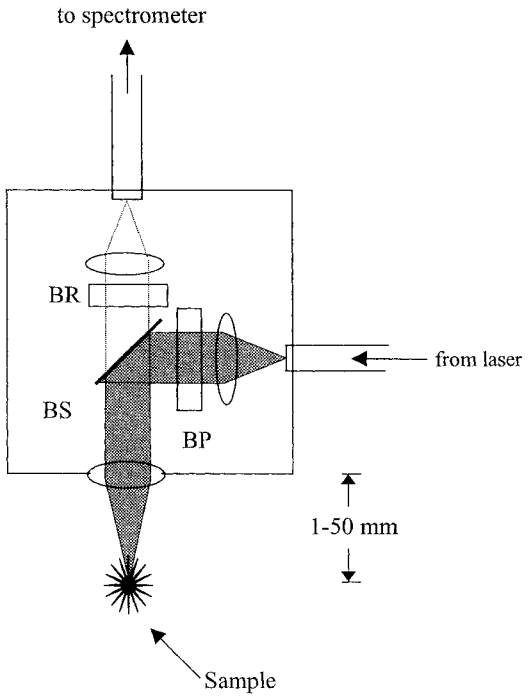

Figure 12.18. Probe head based on a cube about 5 cm on a side and incorporating filters, beamsplitter, and focusing optics. The probe is designed to accept standard fiber-optic cables terminated with SMA connectors. Designed by DLT, Inc. (23) and used to acquire Figure 12.14C.

beam "combination" in this case. A discrete lens and bandpass filter direct the filtered laser light onto the beamsplitter, then another lens focuses the scattered light into the collection fiber. The combination of excitation and collection axis into a collimated beam at the objective lens is a significant advantage of the design of Figure 12.18, which is shared by the nonfiber 180° geometry of Figure 6.4A and the probe heads discussed below. The objective lens may be interchanged easily to vary the working distance and depth of focus, as described in Section 6.3.2. This feature is very useful when the probe is used for different applications, where the probe to sample distance may need to vary. For example, a transparent window, which is thin compared to the working distance, may be used to protect the probe and contain the sample, with generally small contribution to the Raman signal.

With the proper choice of filters, the probe head of Figure 12.18 can greatly reduce interference from silica. Figure 12.14B showed such interference for the case of an unfiltered probe and short (1 m) fiber-optic cable

length. Figure 12.14C is a spectrum of the same sample obtained with the DLT probe head of Figure 12.18, and 17 m cable length. The contribution of silica is negligible, even with the long fiber-optic length. The beamsplitter in Figure 12.18 is often a weak point in the design, due both to low efficiency and to contributions to the background. A simple 50 per cent reflective mirror will sacrifice 50 per cent of the laser light and 50 per cent of the Raman light, thus decreasing the possible signal by 75 per cent. This loss contributes to the significantly weaker signal apparent in Figure 12.14C compared to 12.14B. A dichroic mirror reduces this loss somewhat but must be changed for different laser wavelengths. Both types of mirrors generate inelastically scattered light, and their optical materials must be selected carefully to have low background. Overall, the simple design of Figure 12.18 provides reasonable performance at relatively low cost and has many of the attractions of more expensive probe heads based on holographic optics.

A more efficient design from Chromex, Inc. shown in Figure 12.19 uses a periscope arrangement to inject the laser beam into the collection beam axis. The turning mirror in the collection path is small, and represents a fairly small fraction of the collection lens area (~10 per cent). This injection loss is much smaller than that of a 50/50 beamsplitter, leading to higher overall probe efficiency. In addition, the fiber bundle used for collection may be reconfigured at the spectrometer to match the entrance slit, thus increasing the $A\Omega$ product. As with the design of Figure 12.18, the filters are less expensive than holographic optical elements and the probe design is quite versatile in terms of working distance and laser wavelength.

A spectrum of 4-acetamidophenol obtained with the Chromex probe head of Figure 12.19 is shown in Figure 12.20. The signal magnitude is comparable

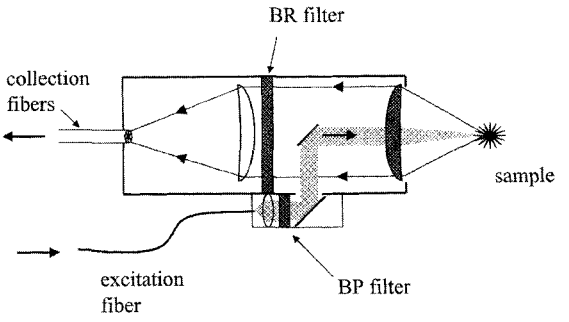

Figure 12.19. Schematic of the Chromex distally filtered fiber-optic probe, which uses a periscope arrangement to inject the laser beam into the collection axis (24). The collection fibers are arranged as a circular bundle in the probe, and a line at the spectrometer, matched to the entrance slit.

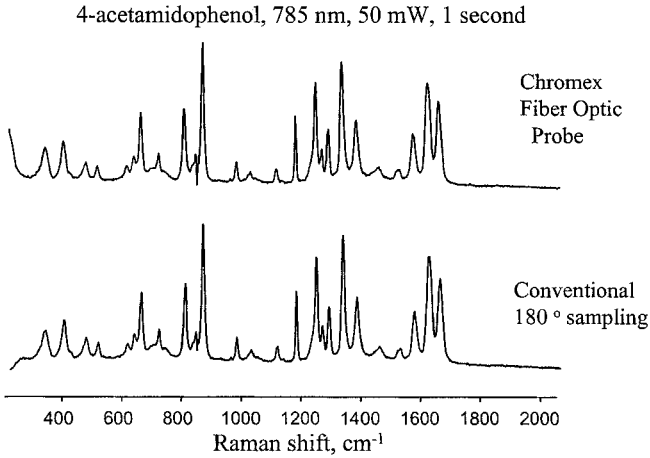

Figure 12.20. Spectra of acetamidophenol obtained with the fiber-optic probe of Figure 12.19 (upper spectrum) and with conventional 180° sampling (similar to that of Fig. 6.5D). In both cases, 50 mW of 785 nm laser power impinged on the sample, and other acquisition conditions were identical.

to that obtained with conventional 180° sampling, for the same integration time and laser power at the sample. A detailed study investigating quantitative analysis of intact pharmaceutical capsules using this probe has appeared (24), and the Raman results were of comparable accuracy to those from diffuse reflectance infrared spectroscopy. A significant advantage of the Raman approach was the lack of sample preparation and rapid, nondestructive data acquisition. Spectra of the active drug (bucindolol) at three different concentrations in an excipient are shown in Figure 12.21.

The high optical density of holographic rejection filters for laser light described in Section 8.2.5.2 is accompanied by a high reflection efficiency for the same laser light. So a holographic rejection filter may also be used as a very efficient mirror that selectively reflects a narrow band of wavelengths and transmits all others. This property of holographic filters is exploited in the Dilor "Superhead" design shown in Figure 12.22 (25). The excitation and collection fibers enter the probe head parallel but not coaxial, and the laser light is filtered to remove silica background. A holographic filter serves to combine the laser and collection axes, as well as reject much of the elastic scatter returning from the sample. An additional notch filter precedes focusing onto the collection fiber. As with the DLT and Chromex designs, the working distance may be varied easily by changing the objective lens.

A further refinement in head design improves the laser filtering by adding an additional holographic element. The Kaiser Mark II head shown in

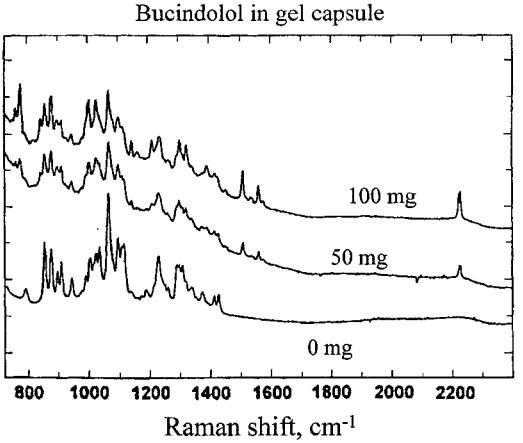

Figure 12.21. Raman spectra of bucindolol capsules with the Chromex probe and Raman 2000 spectrometer. The active drug had three different concentrations (0, 50, and 100 mg) in an excipient similar to lactose. The bands at ~2200 and 1400 to 1500 cm^{-1} are due to bucindolol, as are other less obvious bands overlapping the excipient features. The spectra were obtained on intact capsules, with the beam transmitted through the thin (and weakly scattering) gel capsule material. The 50 and 100 mg spectra are offset for clarity. (Adapted from Reference 24 with permission.)

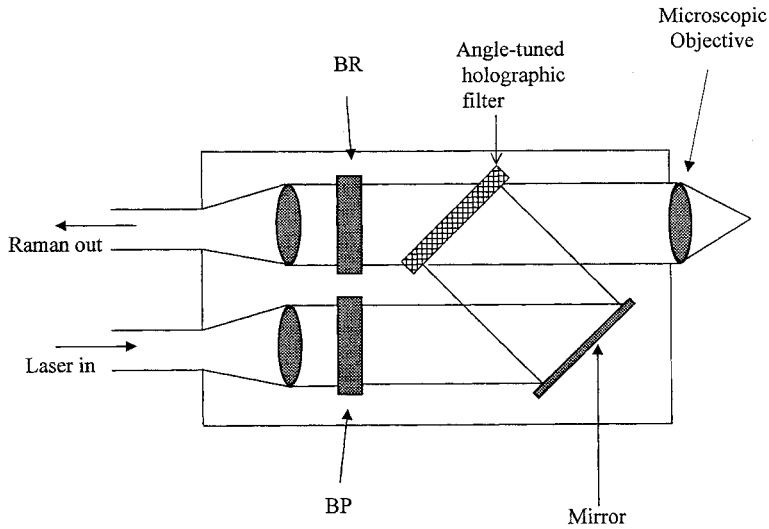

Figure 12.22. Schematic of Dilor "Superhead" fiber-optic probe head. The objective lens may be replaced to permit different working distances and focal spot diameters.

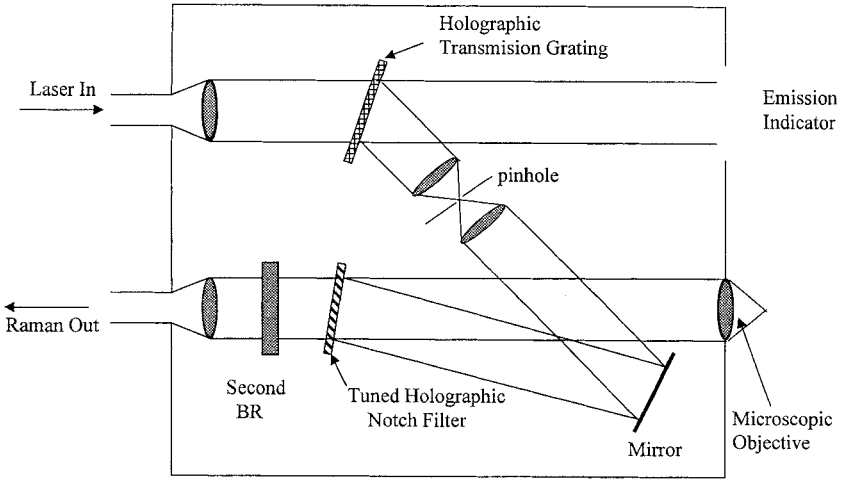

Figure 12.23. Schematic of Kaiser Mark II fiber-optic probe head. A holographic diffraction grating and pinhole act to remove silica scattering from the laser light and improve beam quality by spatial filtering. (Adapted from Reference 1 with permission.)

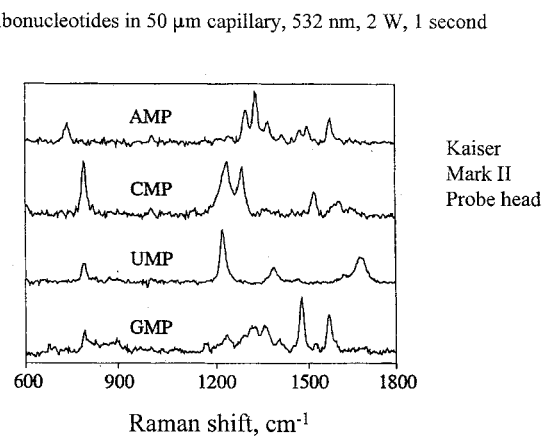

Figure 12.24. Spectra of dilute solutions of ribonucleosides obtained with the Kaiser Mark II probe and Kaiser spectrograph. Solutions were in a 50 μm capillary in which they had been concentrated by isotachophoresis. (Adapted from Reference 27.)

Figure 12.23 combines the holographic bandpass filter described in Chapter 7 (and Fig. 7.11) with an already efficient probe head (26). The holographic BP filter transmits a greater fraction of the laser light than a dielectric BP filter, and the spatial filtering yields a high-quality beam (in terms of collimation and profile) for the objective lens. The Kaiser design is available with a variety of

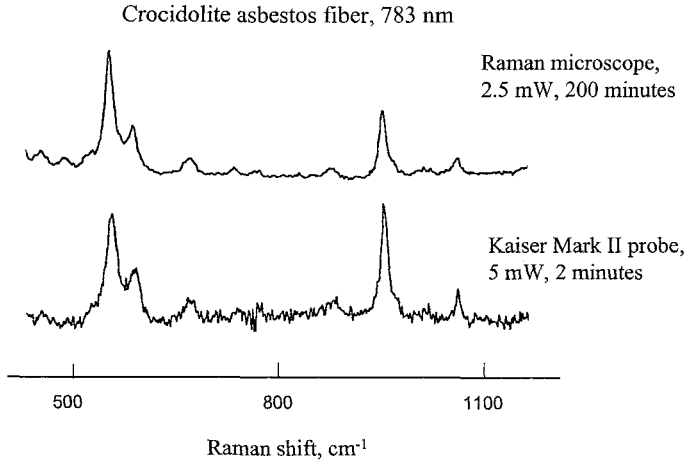

Figure 12.25. Spectra of an asbestos fiber illustrating the focus of a Kaiser Mark II probe. A 2 min acquisition at low power (5 mW) with the fiber-optic probe yielded a useful spectrum that compares well (except for SNR) to a dedicated Raman microscope requiring much longer acquisition time and higher power. (Adapted from Reference 1 with permission.)

focusing lenses and other sampling attachments to interface to a potentially wide range of samples. Figure 12.24 shows spectra of four ribonucleotides in aqueous solution obtained with a Mark II probe (27). The sample was contained in a 50 μm capillary during isotachophoresis, so extremely small quantities of sample were involved (much less than one nanomole). The tight focus of the Mark II was used to advantage to obtain Figure 12.25, a spectrum of a single asbestos fiber. The spectrum is comparable to that from a dedicated Raman microscope. The high noise for the probe is attributable to the much shorter integration time.

12.5. COMPARISONS OF FIBER-OPTIC SAMPLING PROBES

It is clear from previous discussions that fiber-optic probe designs differ substantially in sensitivity, background interference, acceptable fiber length, size, and fragility, not to mention cost. As always, the choice of probe depends on the requirements of the application, so there is no "best" design. Nevertheless, it is useful to address some general comparisons of probe performance.

12.5.1. Probe Figure of Merit

In principle, the signal and signal/noise ratio (SNR) figures of merit discussed in Sections 3.4 and 4.4 can be applied to fiber-optic sampling. Equation (3.11)

defined a figure of merit for a Raman spectrometer that normalized the observed signal for laser power, sample concentration and cross section, and measurement time. One may draw the same distinction between a F'_S [based on total laser power, Eq. (3.11)] and F_S [based on power density, Eq. (3.10)]. As with conventional sampling, probe heads vary significantly in the power density to which the sample is subjected, with possibly large effects on signal and sample radiation damage. A pragmatic approach is to determine a figure of merit empirically by substituting observed parameters for a particular sample into Eq. (12.6), using the variables defined in Section 3.4:

$$F'_S = \frac{S_{\text{obs}}(e^-)}{P_0 \beta_A D_A t_M} \tag{12.6}$$

The observed F'_S depends on several variables, particularly the fiber numerical aperture, sample depth, interfiber distances, filter losses, and so fourth Similarly, an SNR figure of merit may be determined empirically, which would incorporate SNR degradation due to fiber background. Equation (12.7) for F'_{SNR} is identical to Eq. (4.25), and both are based on experimetnally determined variables:

$$F'_{\text{SNR}} = \frac{\text{SNR}_{\text{obs}}}{(P_0 \beta_A D_A t_M)^{1/2}} \tag{12.7}$$

It is theoretically possible to predict F'_S and F'_{SNR} for different probes, but it is difficult to achieve generality because the results depend on sample properties such as transparency and inelastic scattering efficiency. Nevertheless, for a given type of sample, such as a clear, deep liquid, F_S or F'_S can provide a direct prediction of relative signal strength.

12.5.2. Comparisons of Fiber-Optic Probes

Cooney and co-workers (14,15) performed a detailed theoretical and experimental analysis of probe variations similar to the designs of Figures 12.7, 12.12, and 12.17. These designs do not involve a separate probe head (such as those of Figs. 12.20 and 12.21), but some do involve distal filtering. A figure of merit was calculated for each design, including the n-around-1 probe with flat or beveled tips, and covering a range of fiber diameters and numerical apertures. Their predictions of the dependence of the figure of merit on fiber diameter and interfiber spacing were consistent with those discussed in Section 12.4.1. Several examples are shown in Table 12.2, based on calculations similar to those shown in Figures 12.10 to 12.12. Notice that F'_S increases for the beveled tip over the flat tip due to the increased overlap shown in Figure 12.12. Increased numerical aperture and closer fiber spacing

Table 12.2. Calculated F_S' for Several Probe Designs[a]

Type	Design	Excitation Radius μm	Collection radius μm	Interfiber spacing (center to center) μm	F_S' (relative to type 1)
1	1 around 1[a,b], flat tip	100 (NA = 0.22)	100 (NA = 0.22)	200	1.00
2	1 around 1[a,b], flat tip	100 (NA = 0.33)	100 (NA = 0.33)	200	1.53
3	1 around 1[a,b], flat tip	100 (NA = 0.33)	100 (NA = 0.33)	500	0.63
4	18 around 1	100 (NA = 0.22)	100	—	13.0
5	36 around 1	100 (NA = 0.22)	100	—	18.6
6	1 around 1[a,b], beveled	100	100	200	1.5
7	1 around 1[a,b], beveled	100	100	500	0.83

[a]Data from reference 14, with F_S' assumed to scale with the normalized Raman power of Figure 1 of reference 14.
[b]One excitation fiber, one collection fiber, adjacent and parallel.

also increase F_S'. Not surprisingly, the largest F_S' occurs with multiple collection fibers, such as the 18-around-1 design.

Some valuable experimental results for various probes are shown in Figures 12.26 and 12.27. Seven spectra of an acetaminophen tablet observed by different probes are plotted on the same intensity scale. The observed intensities track the predictions, with larger fibers and beveling resulting in stronger signals. Filtering reduces the signal but has the major benefit of reducing background. In Figure 12.27, the spectra are replotted after normalizing to the intensities of the sample band at $\sim$1300 cm^{-1}. Strong silica features are apparent at $\sim$400 to 600 cm^{-1} for the unfiltered probes. For example, the Carrabba and Rauh design (probe) has about 40 per cent the signal of an unfiltered 6-around-1 design (probe), but the silica background is reduced by a much larger factor, to negligible levels in this case. The trade-off between sensitivity and background rejection is fairly general for fiber-optic probes of the types in general use.

12.5.3. Comparisons of Fiber-Optic Probe Heads

The utility and sensitivity of fiber-optic probe heads are more difficult to compare than those of the fiber-optic probes of Section 12.5.2 because there are a greater number of configurations and variables to consider. Since a

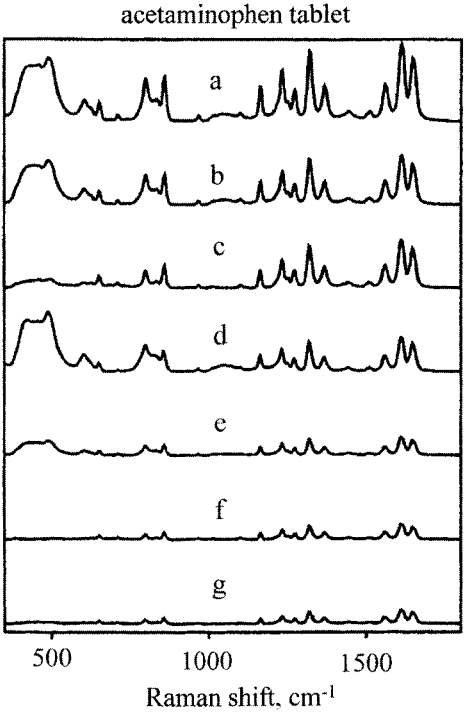

Figure 12.26. Spectra of an acetaminophen tablet obtained with different fiber-optic probes, with the same acquisition conditions and plotted on the same intensity scale. Relative intensities indicate probe efficiency. Probe configurations are: (a) 6 around 1, beveled, 400 μm diameter fibers, unfiltered; (b) 6 around 1 flat tipped, 400 μm, unfiltered; (c) 6 around 1 beveled, 400 μm, filtered; (d) 6 around 1, flat tipped, 200 μm, unfiltered; (e) two-fiber beveled, 400 μm, unfiltered; (f) Carrabba and Rauh design (Fig. 12.17); (g) two-fiber, beveled, 400 μm, filtered. (Adapted from Reference 15, with permission.)

probe head is essentially a 180° sampling system located remotely from the spectrometer, most of the issues discussed in Section 6.3 apply. Probe heads can differ in working distance, laser spot size (and therefore power density), depth of focus, size and number of collection fibers, and the like. A given probe is often modified for samples with varying properties. For example, a longer focal length objective lens may be more sensitive for thick, transparent samples, while a shorter focal length may provide better response for thin, opaque samples. So a comparison of probe heads would need to include several different sample types and optical variables and would probably lose generality. A figure of merit for signal or SNR [as in Eqs. (12.6) and (12.7)] could certainly be defined for probe heads, but any comparisons of such parameters

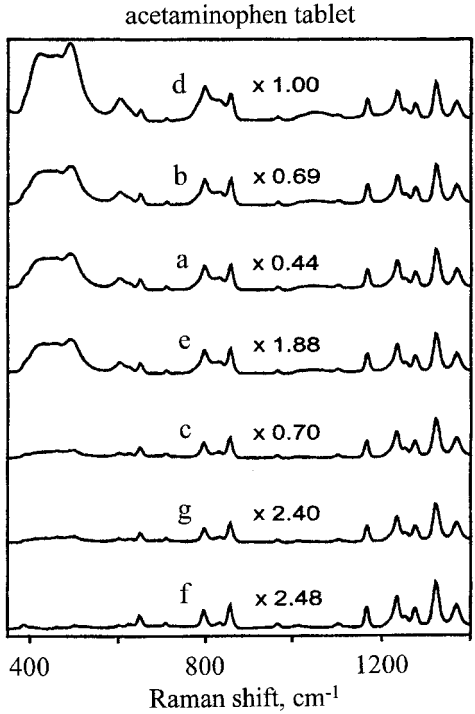

Figure 12.27. Spectra of Figure 12.26 replotted after normalization to the intensity of the 1324 cm^{-1} band. Note the variation of the contribution of the silica features in the 400 to 700 cm^{-1} region for different probe types. The probes are labeled as in Figure 12.26 and ranked according to the degree of silica interference. (Adapted from Reference 15 with permission.)

for competitive head designs would have to precisely specify sample types and acquisition conditions.

That said, there are some useful criteria to consider when evaluating fiber-optic probe heads, including:

1. Physical size
2. Environmental stability (temperature, humidity, etc.)
3. Working distance between probe head and sample and the ability to vary with interchangeable lenses
4. Available laser wavelengths and the ability to change wavelengths (if desired)
5. Provision for polarization analysis (if desired)
6. Laser spot size and its effects on power density and depth of focus

7. Compatibility with spectrometer and laser and ease of alignment
8. Sensitivity to alignment between probe and sample
9. Sensitivity for a given sample type

The sensitivity criterion (item 9) is best evaluated with samples of interest to the user, as sample properties can greatly affect the signal. It is good practice to compare probes in terms of signal per unit of laser power and acquisition time (e.g., in electrons per milliwatt per second, or e^{-} mW^{-1} sec^{-1}) for a given sample. It is usually possible to send particular samples to instrument manufacturers for examination with their probe heads and spectrometers. It is important to know the laser power and acquisition time used by the manufacturer when making such comparisons.

12.6. WAVEGUIDE SAMPLING FOR ANALYTICAL RAMAN SPECTROSCOPY

The term *waveguide* applies to the fiber optic itself but is also used to describe sampling arrangements that modify the interactions between the excitation light, the sample, and the collected light in one of several ways (1,9). In the context of analytical Raman spectroscopy, waveguides have been used to increase sensitivity, localize the measurement spatially, and deal with hostile or difficult sample environments. Several examples will be described in this section, and their potential analytical value will be noted. Throughout the section the term *waveguide* will be used somewhat loosely and is not restricted to phenomena that localize or direct light by total internal reflection. Although there are notable examples of exploiting total internal reflection to localize a measurement to a flat surface (9), the majority of analytical Raman applications use waveguides to increase effective path length for bulk liquid samples in order to increase sensitivity. The discussion below is limited to such cases.

A very early application of a waveguide for Raman spectroscopy occurred in 1972 by Walrafen, who used a tubular fiber optic to contain the sample (28,29). The laser was directed into one end of the tubular fiber optic and the light collected from the other end, then directed into a dispersive/photomultiplier tube (PMT) spectrometer. The sample was chosen to have a refractive index higher than the silica tube, so the laser light and much of the scattered light was totally internally reflected within the tube. The consequence was a very long path length, in the region of several meters, and very high sensitivity. For clear liquids with refractive index greater than silica ($\sim$1.5), strong Raman signals were achieved with a weak He–Ne laser and a spectrometer with much lower sensitivity than a modern dispersive/CCD system.

The requirement that the sample have a refractive index higher than the sample tube material is essential to completely constrain the light inside the sample. This is a stiff constraint, and it rules out the use of aqueous samples ($n \sim 1.33$) in silica ($n = 1.55$) unless the requirement for total internal reflection is relaxed (see below). Some modern variations of Walrafen's approach broaden the technique to aqueous samples by reducing the refractive index of the sample tube below that of water. Specially formulated fluoronated copolymers with $n = 1.29 - 1.31$ can be extruded as capillaries to contain the sample (30,31). Total internal reflection is maintained for most aqueous solutions, since they have a refractive index greater than the tube material.

An example of a polyfluorocarbon based waveguide sampler is shown in Figure 12.28. In this case, a 180° fiber-optic probe head directs laser light into the sample tube and collects the backscattered Raman light. The tube may be part of a small flow system that may be filled by a syringe or pump. Waveguide

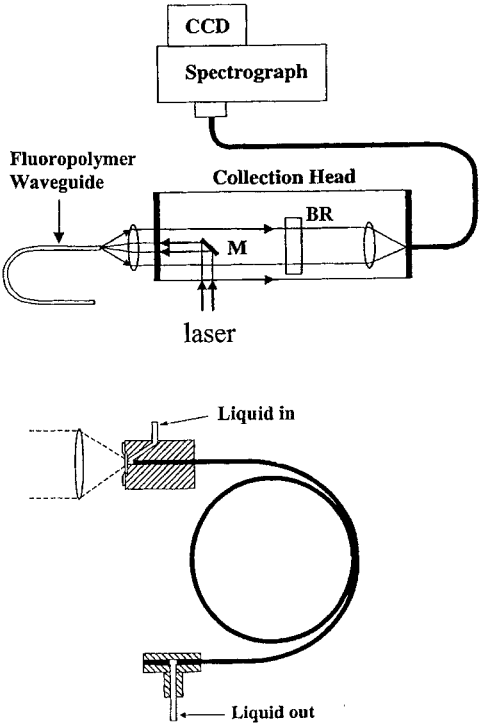

Figure 12.28. Schematic of fluorocarbon waveguide for enhancing sensitivity of liquid and aqueous samples. May be used as a flow cell as shown in lower drawing. (Adapted from Reference 30 with permission.)

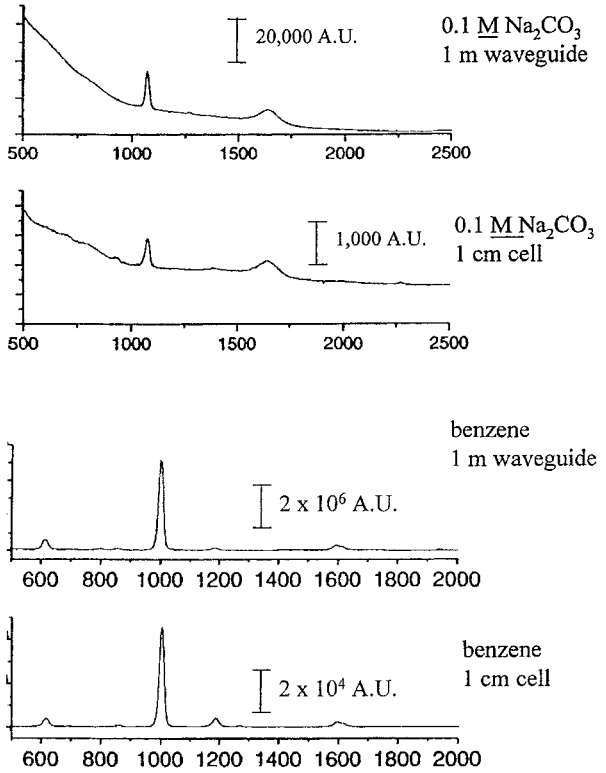

Figure 12.29. Spectra of 0.1 M Na_2CO_3 and neat benzene in the waveguide of Figure 12.28, with comparison spectra in a 1 cm cuvette; 40 mW laser power in all cases, 1 sec integration for benzene, 10 sec for Na_2CO_3. (Adapted from Reference 30 with permission.)

Table 12.3. Observed Raman Sensitivity Enhancements[a] for Various Waveguide Sampling Techniques

Configuration	Laser Wavelength	Sample	Enhancement	Reference
Tubular silica fiber	632.8	CCl_4	100–1000	29
Fluorocarbon waveguide	785	C_6H_6	120	30
Fluorocarbon waveguide	785	0.1 M Na_2CO_3	20	30
Melting point capillary	488	Acetonitrile	8	5
Silica tube	488	0.1 M KNO_3	33	32
Silica tube	488	CCl_4	45	32

[a]Magnitude of Raman signal with waveguide compared to that without, for same spectrometer, laser power, acquisition time, etc.

arrangements based on low index materials have shown impressive sensitivity gains for both aqueous and nonaqueous samples. Figure 12.29 shows spectra of 0.1 M aqueous sodium carbonate and neat benzene obtained with the configuration shown in Figure 12.28. For benzene ($n = 1.50$), the Raman signal was 120 times that for conventional sampling without the tube. Representative sensitivity enhancements for several waveguide sampling arrangements are listed in Table 12.3. A problem arises with the long effective path lengths of these waveguides when aqueous samples are observed with NIR lasers. The overtones of IR transitions in water create NIR absorption bands in the 780 to 1064 nm region, thus reducing transparency of both the laser and scattered light. The effective path length becomes limited not by the waveguide but by sample absorption. For the configuration of Figure 12.28, the sensitivity gain for aqueous samples and 785 light is 20, much lower than that observed for benzene.

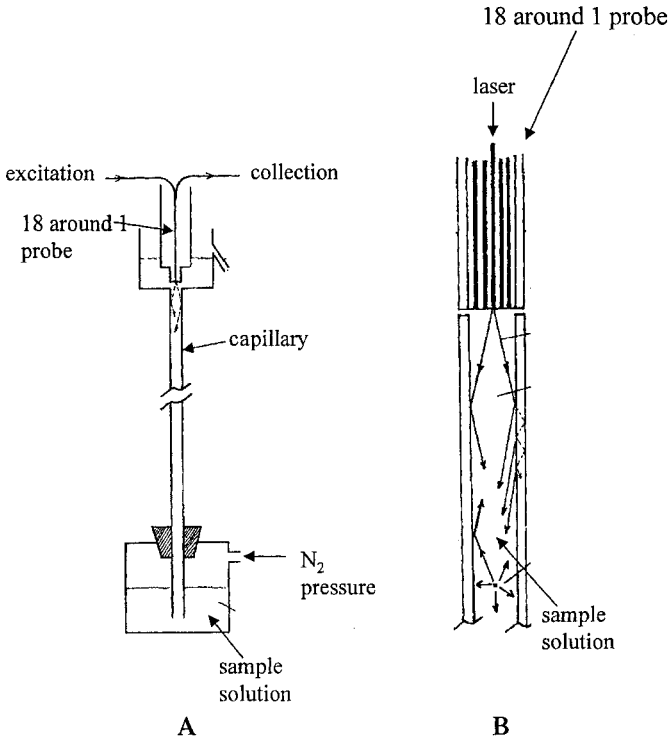

Figure 12.30. Sensitivity enhancement using partial reflection inside a glass capillary with ~1 mm inside diameter. Sample depth was controlled by N_2 pressure. (Adapted from Reference 32 with permission.)

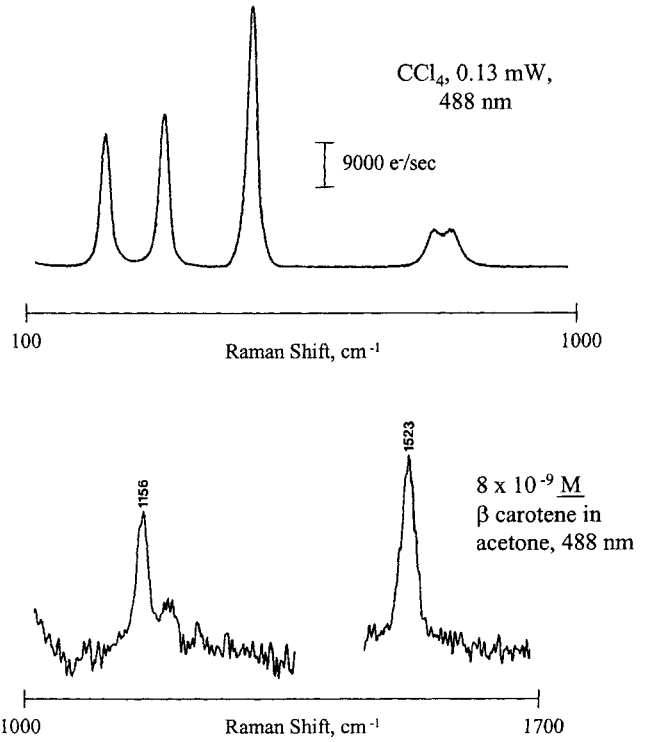

Figure 12.31. Spectra from apparatus of Figure 12.30, obtained with a scanning/PMT spectrometer. Gap in β-carotene spectrum occurred when shutter was closed to avoid large solvent band. (Adapted from reference 32 with permission.)

If the requirement that the sample refractive index be higher than the waveguide material can be relaxed, the approach may be broadened to more samples while retaining some of the sensitivity gain. A quite simple arrangement was reported in 1984 (5) and an improved variation in 1987 (32), based on an 18-around-1 fiber-optic probe directed into a capillary containing a liquid sample. As shown in Figure 12.30, the laser light is partially reflected at the sample–capillary interface, then totally internally reflected at the capillary–air interface. Since the incident angle of light on the sample–capillary interface is quite large (i.e., grazing incidence), the reflectivity is quite high and a large fraction of light is propagated through the sample rather than the capillary. A standard melting point capillary attached to the end of an

unfiltered 18-around-1 probe yielded an increase of a factor of 9 compared to the signal without the capillary (5), even though the RI of the sample (1.33) was lower than the capillary (1.5). This approach was extended to much longer tubes using a sample tube drawn from silica with a capillary puller intended for making gas chromatography columns. The arrangement of Figure 12.30B combines an 18-around-1 fiber probe with a 1 m sample tube. Spectra obtained with this apparatus are shown in Figure 12.31. Even with a low-sensitivity dispersive/PMT spectrometer, good-quality spectra were observed at low laser power (0.13 mW) for CCl_4 and a very low concentration (8×10^{-9} M) for resonance enhanced β-carotene. The signal increased with sample depth up to about 45 cm, indicating a large effective path length. The enhancement ranged from 33 for 0.1 M KNO_3 in water (488 nm) to 45 for CCl_4 (32).

12.7. EXAMPLES OF FIBER-OPTIC SAMPLING

The chapter thus far has addressed fiber-optic sampling techniques and hardware, illustrated with a few applications. As noted earlier, there has been a wide range of fiber-optic Raman applications presented in the literature, and new reports continue to appear at an accelerating rate. Table 12.4 lists some examples of applications to illustrate the wide variety and breadth of fiber-optic samples. The list is by no means comprehensive, but it should provide the reader with a starting point to explore applications in particular areas.

Table 12.4. Examples of Fiber-Optic Raman Applications

Probe Type	Analytical Target	Reference
Unfiltered bundle	Coronary artery composition	33, 34
Fiber-coupled microscope	Polyethylene terephthalate fibers	35
Filtered probe head, robotic	Lunar and Martian soil	36
18 around 1 unfiltered	NIR Raman of liquids, solids	37
Filtered probe head	Capillary isotachophoresis of ribonucleotides	27
Filtered probe head	Bucindolol in gel capsules	24
Single fiber with waveguide	epoxy curing	38
Filtered probe head	high-temperature monitoring of minerals	39
Diamond coated, dual fiber	Diamond deposition	40
n around 1 unfiltered	FT-Raman sampling	41
6 around 1	Phosphonates adsorbed on alumina	42
6 around 1	Balsa wood, FT-Raman	43

REFERENCES

1. I. R. Lewis and P. R. Griffiths, *Appl. Spectrosc.*, **50**, 12A (1996).
2. J. P. Salenius, J. F. Brennan, A. Miller, Y. Wang, T. Aretz , B. Sacks, R. R. Dasari, and M. S. Feld, *J. Vasc. Surg.*, **27**(4), 710 (1998).
3. P. Halley, *Fiber Optic Systems*, Wiley, New York, 1987.
4. Ensign Bickford Optics Co, Avon, CT.
5. S. D. Schwab and R. L. McCreery, *Anal. Chem.*, **56**, 2199 (1984).
6. For example, Thor Labs, OZ Optics, etc.
7. G. R. Trott and T. E. Furtak, *Rev. Sci. Inst.*, **51**, 3215 (1980).
8. A. C. Eckbreth, *Appl. Optics*, **18**, 3215 (1980).
9. R. E. Dessy, *Anal. Chem.*, **61**, 1079A (1989).
10. Z. Y. Zhu and M. C. Yappert, *Appl. Spectrosc.*, **46**, 912 (1992).
11. R. L. McCreery, P. H. Hendra, and M. Fleischmann, *Anal. Chem.*, **55**, 146 (1983).
12. R. D. McClachan, G. L. Jewett, and J. C. Evans, U.S. Pat. 4,573,761, submitted September 14, 1983, granted March 4, 1986.
13. C. D. Newman, G. G. Bret, and R. L. McCreery, *Appl. Spectrosc.*, **46**, 262 (1992).
14. T. F. Cooney, H. T. Skinner, and S. M. Angel, *Appl. Spectrosc.*, **50**, 836 (1996).
15. T. F. Cooney, H. T. Skinner, and S. M. Angel, *Appl. Spectrosc.*, **50**, 849 (1996).
16. P. E. O'Rourke, and R. R. Livingston, U.S. Pat. 5,402,508 (1995).
17. S. D. Schwab, Ph.D. Dissertation, The Ohio State University, 1994.
18. C. J. Frank, Ph.D. Dissertation, The Ohio State University, 1986.
19. B. Yang, and M. D. Morris, *Appl. Spectrosc.*, **45**, 512 (91).
20. M. L. Myrick, and S. M. Angel, *Appl. Spectrosc.*, **44**, 565 (1990).
21. Visionex, Inc., Atlanta, GA.
22. M. N. Carrabba and R. D. Rauh, U.S. Pat. 5,112,127, 1992.
23. DLT, Inc., Laramie, WY.
24. T. M. Niemczyk, M. Delgado-Lopez, F. S. Allen, J. T. Clay, and D. L. Arneberg, *Appl. Spectrosc.*, **52**, 513 (1998).
25. Dilor, Inc., Lille, France and Metucheon, NJ.
26. Kaiser Optical Systems, Ann Arbor, MI, H. Owen, J. M. Tedesco, and J. B. Slater, U.S. Pat. 5,337,004 (1994).
27. P. A. Walker and M. D. Morris, *J. Chromatog. A*, **805**, 269 (1998).
28. G. E. Walrafen and J. Stone, *Appl. Spectrosc.*, **22**, 585 (1972).
29. G. E. Walrafen, *Appl. Spectrosc.*, **29**, 179 (1975).
30. L. Song, S. Liu, V. Zhelyaskov, and M. A. El-Sayed, *Appl. Spectrosc.*, **52**, 1364 (1998).
31. R. Attkorn, I. Koev, R. P. Van Duyne, M. Litorja, *Appl. Optics* **36**, 8992 (1997).

32. S. D. Schwab and R. L. McCreery, *Appl. Spectrosc.*, **41**, 126 (1987).
33. J. F. Brennan, T. J. Romer, R. S. Lees, A. M. Tercyak, J. R. Kramer, and M. S. Feld, *Circulation*, **96**, 99 (1997).
34. J. P. Salenius, J. F. Brennan, A. Miller, Y. Wang, T. Aretz, B. Sacks, R. R. Dasari, and M. S. Feld, *J. Vasc. Surg.*, **27**, 710 (1998).
35. N. Everall, K. Davis, H. Owen, M. J. Pelletier, and J. Slater, *Appl. Spectrosc.*, **50**, 388 (1996).
36. A. Wang, L. A. Jasken, and E. Cortez, *Appl. Spectrosc.*, **52**, 477 (1998).
37. C. D. Allred and R. L. McCreery, *Appl. Spectrosc.*, **44**, 1229 (1990).
38. J. F. Aust, K. S. Booksh, and M. L. Myrick, *Appl. Spectrosc.*, **50**, 382 (1996).
39. S. K. Sharma, C. L. Shoen, and T. F. Cooney, *Appl. Spectrosc.*, **47**, 377 (1993).
40. H. Xiao, S. Dai, J. P. Young, C. S. Feigerle, and A. G. Edwards, *Appl. Spectrosc.*, **52**, 626 (1998).
41. C. G. Zimba and J. F. Rabolt, *Appl. Spectrosc.*, **45**, 162 (1991).
42. K. J. Ewing, D. M. Dagenais, F. Buchholtz, and I. D. Aggarwal, *Appl. Spectrosc.*, **50**, 614 (1996).
43. I. R. Lewis and P. R. Griffiths, *Spectrochem. Acta*, **50**, 1943 (1994).

Raman Spectroscopy for Chemical Analysis. Richard L. McCreery

ISBN: 0-471-25287-5

CHAPTER

13

RAMAN SPECTROSCOPY OF SURFACES

13.1. OVERVIEW

By definition, surface Raman spectroscopy deals with samples that are very thin, generally ranging from a single molecular layer (or less) to a few microns in thickness. The term *monolayer* is used here to refer to a single layer of molecules on a surface, and *submonolayer* to denote a surface that is partially covered by a molecular layer. A *multilayer* is more than one monolayer thick and in the extreme limit approaches a bulk solid or liquid. Figure 13.1 shows schematic drawings of surface films of varying thickness. Surface Raman spectroscopy has received significant attention, in part because of the importance of surfaces to many areas of science, but also because of the observation that certain surfaces yield much larger Raman intensities than expected. "Surface enhancement" can yield increases in intensity of greater than a factor of 10^6 for certain molecules relative to their solution intensity, and many investigators have attempted to exploit the resulting gain in sensitivity for chemical analysis.

Since Raman intensity is proportional to path length [Eq. (2.19)], the very thin "samples" encountered in surface Raman are expected to yield very weak Raman intensities. A typical molecular monolayer is ~10 Å thick, corresponding to a path length of 10^{-3} μm or 10^{-7} cm. A typical path length for a clear sample and 180° sampling (Fig. 6.13) is at least 100 μm, so the

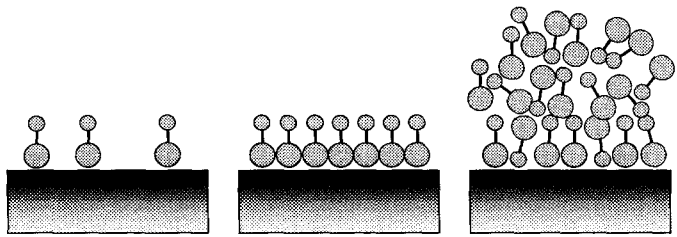

Figure 13.1. Schematic drawings of molecular films on surfaces. A *monolayer* is a close-packed single layer of molecules, while a *multilayer* may extend to thick films or even bulk material.

surface monolayer is expected to produce a Raman intensity roughly 10^5 weaker than a typical bulk sample, if no enhancements were present. Obviously, the problem of observing Raman spectra of monolayers on surfaces presents a formidable challenge with regard to sensitivity. A second issue is the potential background from the substrate itself. Even opaque solids can have sampling depths of several hundred angstroms, much greater than the monolayer itself. If the substrate or the sample environment (solution or gas) has a significant Raman cross section, it can interfere with the surface signal and degrade the signal to background ratio.

As will be discussed in Section 13.2, these sensitivity and background issues make surface Raman spectroscopy without enhancement difficult, but still possible and useful. Long before unenhanced surface Raman spectra were acquired, however, spectra of surface monolayers were acquired with surface enhanced Raman spectroscopy (SERS) (1–5). For reasons that were initially mysterious, Raman spectra of molecules adsorbed on certain metals, mainly silver, gold, and copper, were observed to be much stronger than expected. For roughened silver surfaces, small adsorbed molecules such as pyridine and CN^- ion exhibited Raman features approximately 10^6 times more intense than those for an equal number of molecules in solution. This huge effect boosted the surface signal above that of the substrate and solvent and permitted Raman spectra of surfaces to be acquired with relatively insensitive spectrometers. Because of its fundamental and practical importance, SERS generated thousands of studies on its origin and applications over a 25-year period, and the phenomenon is largely understood. Several aspects of SERS that bear on analytical applications will be discussed in Section 13.5, but some introductory notes are given here.

The enhancement observed with SERS is attributable to two effects, often called *field enhancement* and *chemical enhancement. Field enhancement* is the larger of the two effects and occurs when metal particles or roughness on a metal surface are exposed to laser light of an appropriate wavelength. If the metal has suitable optical properties, the electric field of the incident light is increased at the particle surface, particularly near regions of surface curvature that occur on small particles (1,2,6,7). The local increase in electric field is highest at the surface, right where the adsorbed molecules are present. An enhanced local field corresponds to an enhanced intensity, effectively increasing the power density (P_D) in Eq. (2.19). The end result is an increase in observed Raman scattering of approximately 10^4 under optimum conditions, but the effect is strongly dependent on several variables, as discussed later. *Chemical enhancement* results from interaction between the adsorbate molecule and the metal, usually involving electronic effects such as charge transfer. These effects may result in resonance Raman enhancement if adsorption of the molecule to the surface shifts its optical absorption maximum closer

to the incident laser. Whatever the origin of chemical enhancement, the result is an increase in cross section [β in Eq. (2.19)] for the adsorbed molecule compared to the gas or solution phase. Chemical enhancement factors also vary greatly but are often in the region of 10 to 100. As a very rough rule of thumb, the 10^6 enhancement commonly quoted for SERS is partitioned into factors of 10^4 from field enhancement and 10^2 from chemical enhancement.

In the context of chemical analysis, surface Raman applications may be divided into two general groups: those with surface enhancement and those without. Non-SERS examples are more limited due to sensitivity constraints but are of interest when the substrate does not support field enhancement. Areas of particular interest include electrochemistry and heterogeneous catalysis. Analytical SERS applications exploit field enhancement for a large gain in sensitivity but require some special properties of the substrate. In many cases, an SERS analysis involves a prefabricated substrate introduced into a solution or gas sample, followed by absorption and Raman spectroscopy. Some examples of this approach are discussed in Section 13.6. To close this brief introduction, a few warnings about nomenclature are useful. First, *enhancement* is a matter of degree and may refer to factors ranging from greater than 10^6 down to just above 1.0 (no enhancement at all). While *surface-enhanced* usually denotes large effects, one could argue that a small factor (1.1 to 10, say) is still "enhanced." Second, *surface* or *surface species* may refer to a monolayer or less or to a relatively "thick" film such as a polymer coating. Clearly, a monolayer or less is affected by the presence of the substrate, and special techniques are required to observe its Raman spectrum due to short path length. Once the layer becomes large compared to molecular dimensions, one could argue that it is a bulk rather than surface material, and it may be completely unaffected by the substrate. The path length approaches that in a bulk material as the surface film increases in thickness. So the terms *surface* and *surface species* depend on the thickness of the layer of interest, and its relation to the sampling depth, the range of enhancement effects (if any), and the influence of the substrate–adsorbate interaction on molecular properties of the sample layer.

13.2. SURFACE SENSITIVITY

The equations developed in Chapters 2 and 3 relating Raman signal to sample and instrumental variables were derived by integration of the Raman scattering from an incremental sample thickness. For example, Eq. (2.19) states that the Raman signal P_R is proportional to the sample number density (D, molecules per cubic centimeter) and the incremental thickness (dz, centimeters). This integration depends on sampling geometry, depth of field, and so forth, as

discussed in Chapter 6. For surface Raman spectroscopy, the sample thickness is almost always much less than the spectrometer depth of field, and the equations for Raman intensity may be rewritten in more convenient form. Equation (2.19) becomes

$$P_R \text{ (photons cm}^{-2} \text{ sr}^{-1} \text{ sec}^{-1}) = P_D \beta_S D_S \tag{13.1}$$

where P_D = laser power density at surface (photons cm^{-2} sec^{-1})
β_S = cross section of surface species (cm^2 molecule^{-1} sr^{-1})
D_S = surface number density (molecules cm^{-2})

D_s combines D and dz from Eq. (2.19) and is independent of layer thickness. In effect, D_s is the volume number density (D) times the layer thickness (dz), under the assumption that the entire layer thickness is within the laser and spectrometer depths of focus. Since *surface* refers to a depth of a few angstroms to much less than 1 μm, the assumption is easily satisfied. Note also that P_R in Eq. (13.1) equals the specific intensity, as defined by Eq. (2.20), with the same units.

When considering the collection and detection of Raman scattering from a surface, the cases of an *underfilled* and *overfilled* spectrometer discussed in Chapter 3 and Figure 3.2 still apply. The most common geometry is external

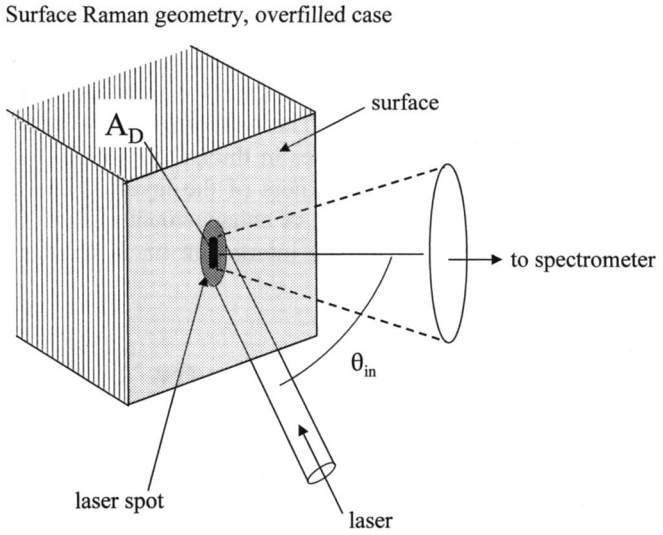

Figure 13.2. External reflection geometry for surface Raman in which the laser spot "overfills" the area collected by the spectrometer (A_D). θ_{in} is the laser incidence angle relative to the surface normal.

reflection from a flat surface, shown schematically in Figure 13.2. For the overfilled case shown, the laser spot on the sample surface is larger than the area detected by the spectrometer, A_D. In this case, P_D at the sample is reduced by a factor $(\cos\theta_{in})^{-1}$, where θ_{in} is the incident angle of the laser relative to the surface normal. Equation (3.6) becomes (13.2) for surface Raman with an overfilled spectrometer:

$$S(e^-) = P_D \beta_S D_S A_D \Omega_D T Q t_s \tag{13.2}$$

where β_s and D_s are defined as in Eq. (13.1), and the other terms in (13.2) have the same meaning as in Eq. (3.6). Notice that for 180° backscattering geometry, Eq. (13.2) applies directly, while for other incident angles P_D must be multiplied by the factor $(\cos\theta_{in})^{-1}$, and the signal decreases.

For the underfilled case, with the laser spot being smaller than the area detected by the spectrometer, the surface signal expression becomes a modified form of Eq. (3.8):

$$S(e^-) = P_0 \beta_s D_s \Omega T Q t_s \tag{13.3}$$

Recall that P_0 is laser power (photons per second) not power density. Note that the Raman signal no longer depends on laser spot size or spectrometer A_D [since $A_L = A_D$ in Eq. (3.7)], nor does it vary with incidence angle (8).

It is instructive to consider predicted intensities based on Eqs. (13.1) and (13.2) for several realistic examples. Table 13.1 lists calculated specific intensities in the absence of enhancement mechanisms, and the expected Raman signal for an efficient dispersive/charge-coupted device (CCD) spectrometer (9). Recall from Chapter 2 and Table 2.2 that benzene is a moderate Raman scatterer that is nonresonant at 514.5 nm, so it provides an estimate for a "typical" surface monolayer. The surface signal is weaker than that from a bulk solution by a large factor ($\sim 10^7$), due to the very short path length inherent to a monolayer. The predicted signal is obviously dependent on the product $\beta_s D_s$, so a resonant adsorbate such as β-carotene is relatively easily observed due to its large cross section (11). For monolayers D_s is in the range of 6×10^{13} to 6×10^{14} molecules cm^{-2} (10^{-10} to 10^{-9} mol/cm^2), while multilayers can yield much higher surface densities. Using the units of molecules cm^{-2} for D_s, a multilayer has a D_s equal to the monolayer coverage times the number of molecules along the axis normal to the surface. For a 1000 Å thick benzene multilayer (about 300 molecular layers), the predicted signal is 300 times larger than a monolayer.

Although the signals predicted in Table 13.1 are indeed small, they are observable experimentally with modern equipment and a low background. The multichannel advantage and low detector noise of CCDs are critical in this regard, as they permit sufficiently long integration times to accumulate

Table 13.1. Predicted Raman Intensities for Surface Species

	L_s^a, (photons cm^{-2} sec^{-1} sr^{-1})	S^b (e^- sec^{-1})
Neat liquid benzene,[c] 992 cm^{-1} ($\beta = 2.9 \times 10^{-29}$ cm^2 $molecule^{-1}$ sr^{-1})	1.0×10^{13}	3×10^7
Benzene monolayer (1×10^{-10} mol/cm^2)[d]	9×10^5	2.7
β-Carotene monolayer ($\beta = 1.1 \times 10^{-23}$)	3.4×10^{11}	1.0×10^6
Bis-(methyl styryl) benzene (BMB, $\beta = 2 \times 10^{-27}$)	6×10^7	190
Anthraquinone-2,6,disulfonate[e]	1.6×10^7	46
Benzene multilayer (1000 Å thick)	3×10^7	900

[a] 100 mW, 514.5 nm (2.6×10^{17} photon sec^{-1}), 50 μm × 1 mm laser focus, 180° backscattering, from Eq. (13.1). Adapted in part from Reference 9.
[b] From Eq. (3.6), with $A_D = 5 \times 10^{-4}$ cm^2, $Q = 0.4$, $T = 0.32$, $\Omega = 0.049$ sr ($f/4$).
[c] For liquid benzene, path length assumed to be 0.1 cm.
[d] Monolayers assumed to have $D = 1.0 \times 10^{-10}$ mol/cm^2.
[e] From Reference 10.

sufficient signal and signal/noise ratio (SNR). Surface Raman spectra may involve integration times up to an hour or more, but scientific-grade CCDs have low enough dark and readout noise that detector noise contributes negligibly to the total noise even with such long integration times. In this case, the SNR is given by a modified form of Eq. (4.20), which applies to the case where the dominant noise sources are signal and background shot noise:

$$\text{SNR} = \frac{\beta_s D_s}{(\beta_s D_s + \beta_B D_B)^{1/2}} (P_D A_D \Omega T Q t)^{1/2} \tag{13.4}$$

Equation (13.4) applies to the overfilled case, and $\beta_B D_B$ refers to an effective cross section–number density product for the background. Table 13.2 shows the effect of relative signal and background strengths for a range of cross sections. It is clear that even if the detector contributes no background or noise, a large substrate or solution background can reduce the SNR to unacceptable levels. The SNR tracks $t^{1/2}$, so the longer integration times allowed by low detector dark signal are important. Furthermore, when the background is larger than the analyte signal, the SNR is nearly linear with $\beta_s D_s$, as expected from Eq. (13.4) when $\beta_s D_s \ll \beta_B D_B$. Since the multichannel advantage of CCD detectors effectively increases the measurement time over a scanning instrument by a large factor (e.g., 1024), multichannel detection is essential for acquiring Raman spectra of unenhanced monolayers.

Table 13.2. Predicted SNR for Various Sample and Background Combinations[a]

Sample[b]	$\beta_s D_s (sr^{-1})$	Background[c] (e^- sec^{-1})	Observation Time (sec.)	Predicted SNR[d]
Benzene monolayer	1.7×10^{-15}	0	100	14.5
Benzene monolayer	1.7×10^{-15}	10	100	6.6
Benzene monolayer	1.7×10^{-15}	1000	100	0.7
Benzene monolayer	1.7×10^{-15}	1000	3600	4.2
BMB monolayer	1.2×10^{-13}	1000	100	48
Benzene multilayer, 1000 Å thick	5×10^{-13}	1000	100	165

[a]Assumes negligible noise contribution from detector.
[b]Conditions same as those for Table 13.1.
[c]1 e^- sec^{-1} corresponds to a $\beta_B D_B$ of 6.3×10^{-16} sr^{-1}.
[d]From Eq. (13.4).

Reconsideration of Eq. (13.4) in the context of typical surface Raman experiments reveals that two major factors dictate the success of the measurement: the magnitude of $\beta_s D_s$ and the background from the sample. The cross section–number density product of the surface species of interest ($\beta_s D_s$) determines the signal magnitude, while the background strongly affects the SNR. Clearly, all sources of background noise not derived from the sample such as room lights, detector dark signal, and the like must be reduced to negligible levels. Even then, Eq. (13.4) and Table 13.2 show that background from the substrate or solution degrades the SNR. That said, this degradation of SNR may be compensated by increasing the product $P_D A_D \Omega T Q t$. As the $\beta_s D_s$ product decreases or the background increases, the collection and detection performance of the spectrometer must be improved to maintain an acceptable SNR. As noted in Chapters 3 and 4, large increases in the $A_D \Omega T Q$ product combined with multichannel detectors have provided the necessary improvement in sensitivity.

13.3. SAMPLING CONSIDERATIONS

Surface Raman sampling has many of the same considerations as the conventional Raman arrangements discussed in Chapter 6, particularly the case of a thin or optically dense sample. In some cases, surface spectra may be acquired in air using external reflection geometry, as shown in Figure 13.3A. It is often necessary to minimize the laser power density to reduce possible sample damage. One approach is the cylindrical focus of Figure 6.19, which couples well to the slit on a CCD/dispersive spectrometer. If the focal line image does

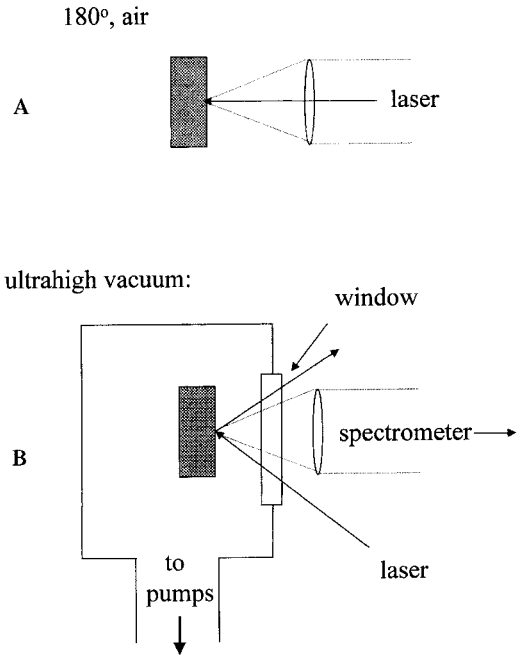

Figure 13.3. Two sampling geometries for surface Raman spectroscopy. (A) is 180° backscattering, and (B) uses a non-normally incident laser and normal collection through a window in a UHV chamber.

not overfill the CCD, the signal strength is the same for a line focus compared to a point focus, with much lower power density (e.g., Fig. 6.20).

The susceptibility of solid surfaces to contamination often results in a requirement for an ultrahigh vacuum (UHV) chamber for preparation and observation of particular samples. For many materials, including metals such as platinum and nickel, adsorption of hydrocarbons and chemisorption of oxygen are quite fast at atmospheric pressure, and the surface must be isolated in UHV to prevent rapid degradation. In addition, a sample in UHV may be subjected to surface analytical techniques such as X-ray photoelectron and Auger spectroscopy to verify or corroborate Raman results. As a result, much of the early and well-characterized surface Raman experiments were carried out in UHV chambers operating below 10^{-9} torr (12).

Raman spectroscopy interfaces for UHV chambers are not fundamentally difficult to design, since Raman sampling is generally tolerant of the window required in the UHV chamber. As shown in Figure 6.7, the window need not be near the focal point of the incident laser, so window background may be avoided. Some ingenious designs for the UHV–Raman interface have evolved

for special purposes, such as the study of SERS as a function of laser and scattering angles (12,13). Since UHV equipment is generally quite specialized, there is no "standard" design. UHV sampling has been very important for revealing fundamental properties of surface Raman scattering and enhancement, but the associated constraints on the sample and the complexity of UHV equipment make it unlikely that UHV–Raman will have widespread utility in analytical applications.

Surface-enhanced Raman was discovered during Raman observation of electrochemical processes at a silver electrode, so surface Raman in electrolyte solutions has been studied very extensively (1,2,5,7). Two configurations for Raman spectroscopy of electrode surfaces in solution are shown in Figure 13.4. These designs permit control of electrode potential during Raman monitoring as well as electrochemical preparation of the electrode surface. Electrochemical roughening of silver electrodes by an oxidation/reduction cycle in chloride solution is a common method for generating an active SERS substrate, so variations on the design of Figure 13.4A have been used in hundreds of publications. Fiber-optic coupling of Raman scattering from a planar electrode in solution is shown in Figure 13.4B in which the scattered light is carried to the

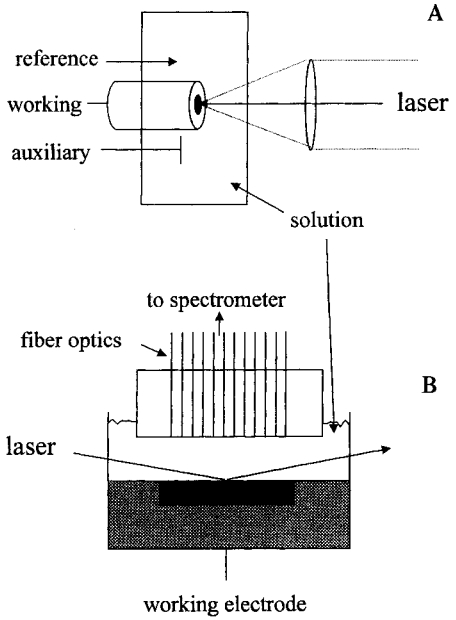

Figure 13.4. Electrochemical cells for Raman spectroscopy based on (A) 180° geometry and (B) fiber-optic collection of scattered light.

spectrometer by 27 optical fibers. This arrangement permitted efficient light collection and a relatively simple interface to the spectrometer (14).

13.4. SURFACE RAMAN SPECTROSCOPY WITHOUT FIELD ENHANCEMENT

Raman spectra of monolayers were first obtained on roughened silver surfaces that exhibit strong field enhancement, since the scanning/photomultiplier tube spectrometers of the time needed the gain in sensitivity of a factor of $\sim 10^4$ to provide useful spectra (3,4). Multichannel spectrometers permitted spectrum acquisition without field enhancement about 8 years later (12), for the reasons discussed in Section 13.2. Surface Raman without field enhancement is conceptually simpler, so it will be discussed first. Section 13.5 describes the requirements and additional benefits when field enhancement occurs.

The simplest case of surface Raman would exhibit no field enhancement, and the cross section of the adsorbed molecule would equal that of the same molecule in solution. This simple condition was assumed for the predictions of signal strength listed in Table 13.1 and serves as a useful indicator of the required experimental sensitivity. However, the assumption of equal surface and solution cross sections is valid only if the interaction between substrate and adsorbate is weak and the adsorbate electronic or vibrational characteristics are unaltered by adsorption. Since adsorption onto a surface inherently involves some adsorbate–substrate attraction, the adsorbate must be perturbed in some way. The resulting change in cross section (which may be positive or negative) is the chemical enhancement described earlier, and may be as large as a factor of 10^3. The conditions leading to changes in cross section upon adsorption are of obvious importance to the magnitude of a surface Raman signal, and ultimately to the success of a surface Raman experiment.

Adsorbate–substrate interactions may be loosely classified as *physisorption* or *chemisorption*, depending on the strength of the adsorbate–substrate bond. *Physisorption* refers to relatively weak and nonspecific attraction of the adsorbate to the substrate, such as dipole–dipole, electrostatic, or hydrophobic interactions. In *chemisorption*, there is usually a bond formed between the adsorbate and the surface, analogous to those formed in free molecules. For example, a pyridine molecule adsorbed on silver interacts through the lone pair of the nitrogen atom, forming a coordinate Ag—N bond. Chemisorption is more specific than physisorption in that it requires a site on the molecule (often a lone pair) and may also occur at specific sites on the surface. Both physi- and chemisorption perturb the molecular orbitals and electron distributions of both the adsorbate and the substrate and are expected to modify the optical properties of the adsorbed molecule compared to its free state. The issue at the moment is how those changes in electronic structure that

accompany adsorption affect the Raman cross section and/or the vibrational spectrum.

The molecular orbitals of the adsorbate and the electronic band structure of the substrate may be complex and often poorly understood. So predicting interactions between the two is nontrivial and inexact. Stated generally, the adsorbate–substrate complex has a different electron distribution from the isolated components, resulting in a different cross section. While the details are usually complex and often undefined, at least one theory of the effects of adsorption on Raman cross section has yielded useful explanations and predictions. The theory attributes chemical enhancement of cross sections to charge transfer between adsorbate and substrate orbitals (or vice versa) and is generally known as *charge-transfer theory* (1,15,16).

Consider Figure 13.5, which depicts the energy levels of an adsorbate and a metallic substrate. The metal has a band structure resulting from combinations of atomic orbitals of metal atoms. The Fermi level is the boundary between the filled and unfilled orbitals within the conduction band, and the Fermi level moves up or down as the electrical potential on the metal is altered. When the adsorbate is widely separated from the metal, it has discrete energy levels that are involved in normal and resonance Raman as shown in Figure 1.1. Also shown in Figure 13.5A is the energy corresponding to an incident laser photon ($h\nu_0$) involved in a normal Raman experiment. A higher energy photon, $h\nu_0'$, is shown to match a molecular absorption, leading to resonance enhancement in the free molecule.

Upon adsorption, the orbitals of the metal and adsorbate interact to some degree, as required to form a metal–adsorbate bond. Overlap of metal and adsorbate orbitals permits electrons to be transferred from the molecule to the

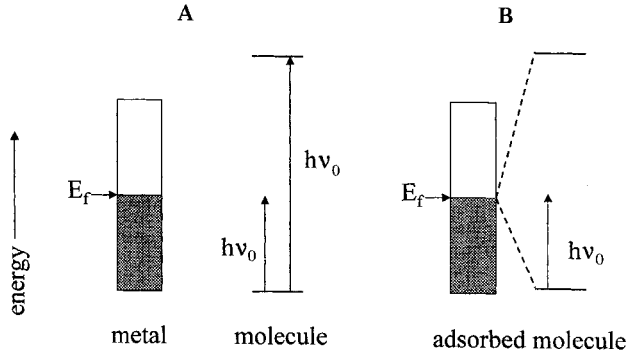

Figure 13.5. Energy level diagrams of a widely separated metal and organic molecule (A) and after adsorption of the molecule to the surface (B). E_f is the Fermi level of the metal; $h\nu_0$ is the incident laser energy.

metal (and vice versa), hence the name *charge transfer*. For the case shown in Figure 13.5B, $h\nu_0$ may excite an electron from the ground state of the adsorbate into the Fermi level of the metal. Since the adsorbate–metal complex absorbs the photon by this charge-transfer process, the cross section may be enhanced by resonance. In effect, adsorption of the molecule has created a new species that is subject to resonance enhancement for photons of the original energy $h\nu_0$. The adsorbate–surface interaction has shifted the process from normal to resonance Raman, with an accompanying increase in cross section. An analogous process may occur for metal-to-adsorbate charge transfer as well as for the adsorbate-to-metal charge transfer depicted in Figure 13.5B.

Several characteristics of chemical enhancement, via charge transfer or otherwise, distinguish it from the field enhancement discussed in Section 13.5. First, chemical enhancement depends on interactions of adsorbate and substrate orbitals, not directly on the optical properties of the substrate. Chemical enhancement is therefore possible on a wider range of substrates, beyond the silver, gold, and copper surfaces that commonly exhibit field enhancement. Second, chemical or charge-transfer enhancement requires a specific adsorbate–surface interaction, usually involving a specific chemical site on the surface. An example is an *adatom* site on a metal, where the relatively bare atom is more susceptible to complexation with the adsorbate. Third, chemical enhancement is very short range and is usually limited to the first layer of adsorbed molecules. As noted later, field enhancement can extend into the solution for distances of several hundred angstroms. Fourth, charge-transfer enhancement is expected to depend on the potential of the electrode, since potential varies the Fermi level depicted in Figure 13.5. The case of a silver electrode in piperidine solution is shown in Figure 13.6. The intensity of the 1008 cm^{-1} Raman band of pyridine adsorbed on silver varies by a factor of about 3 within a 0.8 V potential range, as E_f is tuned by the applied potential. In effect, the potential is shifting the pyridine-to-metal charge-transfer transition in and out of resonance with the incident laser light, resulting in variation in resonance Raman enhancement.

An early example of surface Raman without field enhancement is shown in Figure 13.7. This measurement predated the development of CCD detectors and represents a major achievement in terms of sensitivity (12). The adsorption of nitrobenzene on a well-defined nickel surface was carried out in UHV; then Raman scattering was observed with a single spectrograph and an intensified Vidicon detector. Unenhanced spectra were obtained from 7.5×10^{13} molecules cm^{-2} of nitrobenzene (1.1×10^{-10} mol cm^{-2}), corresponding to a submonolayer. Examples of surface Raman spectroscopy with resonance enhancement include monolayers of phthalocyanines on gold (17) and ordered graphite (18), and multilayers of metalloporphyrins (19).

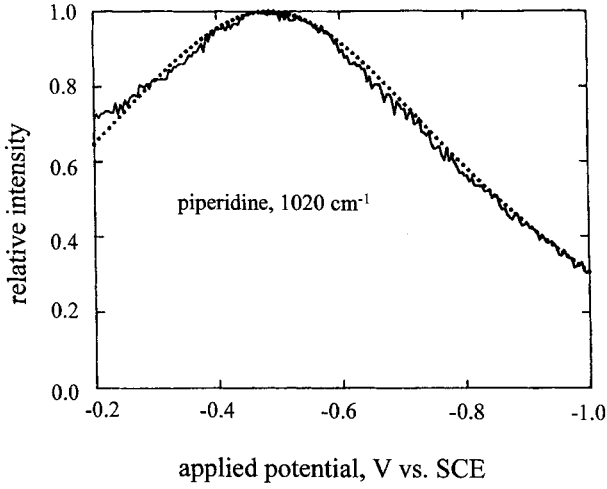

Figure 13.6. Intensity of the 1020 cm^{-1} band of piperidine adsorbed on roughened silver as a function of applied potential. Intensity is relative to the maximum at −0.45 V vs. SCE. Line is experimental, dots are a fit to the predictions of the charge-transfer theory for chemical enhancement. (Adapted from Reference 1, with permission.)

The nature of chemical enhancement of surface species was examined for adsorbates on smooth metal surfaces that have negligible field enhancement. Surface Raman spectra of pyromellitic dianhydride (PMDA) on Cu(111) obtained at different laser wavelengths showed significantly different enhancements (15). The results support the charge-transfer theory described earlier in which the molecular orbitals of PMDA interact with the metal orbitals to yield resonance enhancement. A similar study of pyridine on smooth silver concluded that a chemical enhancement of a factor of 15 to 65 resulted from pyridine adsorption and a charge-transfer interaction (20). The enhancement of pyridine scattering on electrochemically roughened copper and silver surfaces as a function of both potential and laser wavelength concluded that the charge-transfer effects for the two metals depend on their band structure (16). A detailed examination of surface Raman spectra of benzene, pyrazine, and *s*-triazine on silver revealed that the selection for adsorbed molecules differs from those in bulk solution due to several factors, including symmetry reduction, image dipoles, and quadrupole polarizability contributions (21).

The application of confocal Raman microscopy to surface Raman has led to some promising results for transition-metal surfaces that yield weak or negligible field enhancement. High-performance CCD detection provided high SNR, and the confocal sampling reduced the background from the solution or gas over the surface (22, 23). Metals such as platinum, rhodium, and ruthenium

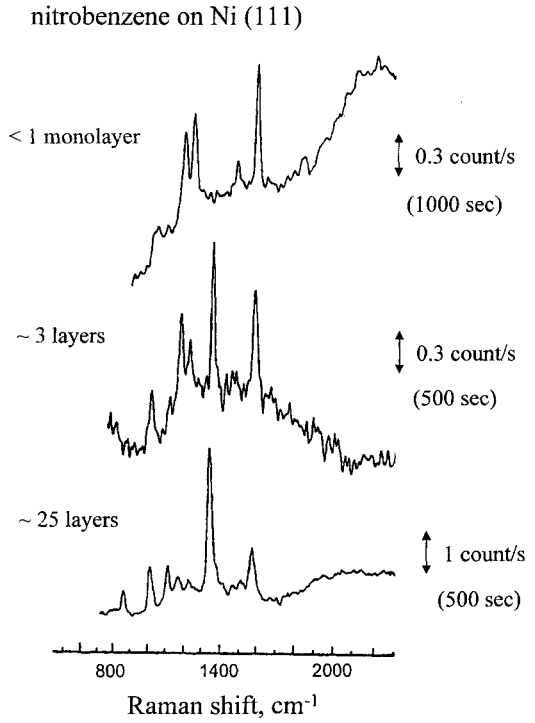

Figure 13.7. Surface Raman spectra from nitrobenzene on flat Ni (111) in UHV, following controlled deposition from the gas phase. Field enhancement is negligible in this case. (Adapted from Reference 12 with permission, including reversal of x axis.)

were electrochemically roughened, but the expected field enhancement was quite low (see below). Although this development is quite recent, the prospect of obtaining Raman spectra from monolayer adsorbates on metals other than silver, gold, and copper is quite promising and may lead to important insights into catalysis and surface chemistry.

Additional examples of surface Raman spectroscopy without field enhancement involve carbon as a substrate. Although sp^2 carbon materials such as glassy carbon, activated carbon, and graphite are well known to adsorb a wide range of organic and inorganic molecules, carbon does not support field enhancement for any currently accessible laser wavelength. So surface Raman on carbon is guaranteed to lack field enhancement but may still exhibit charge-transfer or resonance effects. A useful illustration is the case of rhodamine 6G (R6G) adsorbed on graphite. When examined with a 514.5 nm laser, R6G is strongly fluorescent (Fig. 1.5) and Raman scattering is unobservable. Figure 13.8 illustrates the dramatic change that occurs when photoexcited R6G

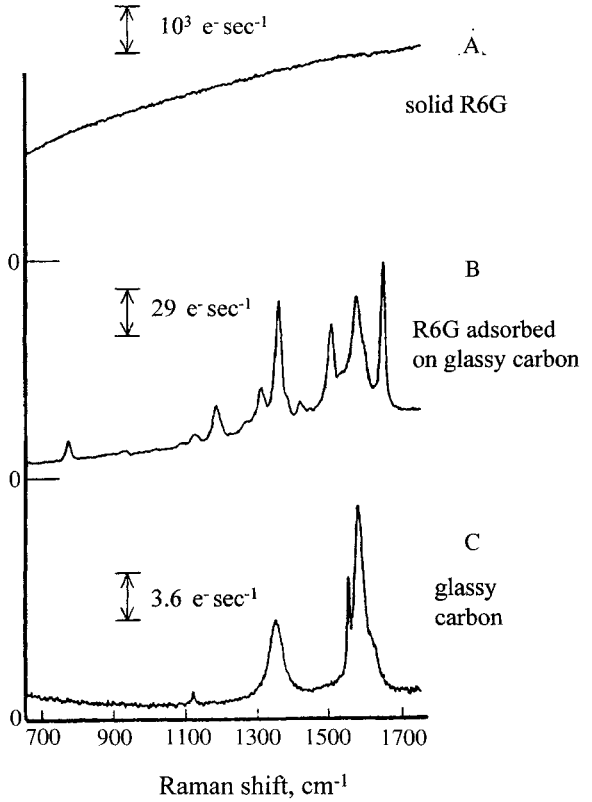

Figure 13.8. Raman spectra of R6G adsorbed from a methanol solution onto glassy carbon (B). The fluorescence normally encountered with 514.5 nm excitation is quenched upon adsorption to the conducting surface. Spectra of (A) solid R6G and (C) clean glassy carbon are shown for comparison. (Adapted from References 10 and 25 with permission.)

transfers its energy to the conducting carbon and does not emit fluorescent light (11,24). What remains is a well-defined Raman spectrum of R6G adsorbed on carbon (Fig. 13.8B). The R6G layer was shown to be a monolayer by demonstrating its adherence to a Langmuir isotherm. R6G is an example of a molecule that exhibits quite strong resonance enhancement in solution or on a surface, but the Raman scattering is overwhelmed by fluorescence for the solution case. Figure 13.8C represents a surface Raman spectrum with resonance enhancement of the adsorbate. The surface interaction may enhance (or decrease) the resonance effect, but we cannot say without knowing the solution cross section.

The spectra of Figure 13.8 are more intense than those of Figure 13.7 partly because of improvements in instrumentation, but more because of the

high cross section afforded by resonance enhancement. As the cross section decreases, observation of surface spectra on carbon becomes more difficult due to reduced SNR. Surface spectra for adsorbates with a range of cross sections are shown in Figures 13.9 to 13.11. 1,4-Bis (2 methylstyryl) benzene (BMB) and 2-(4-biphenylyl)-5-(4-tertbutylphenyl)-1,3,4 oxadiazol (BPBD)

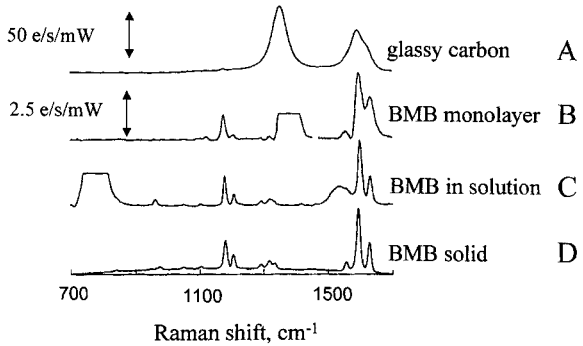

Figure 13.9. Spectra of BMB adsorbed on glassy carbon (B) in solution (C) and as a solid (D). The glassy carbon spectrum (A) was subtracted from the raw spectrum of adsorbed BMB to produce spectrum B. BMB has a cross section about 65 times that of benzene. (Adapted from References 10 and 11 with permission.)

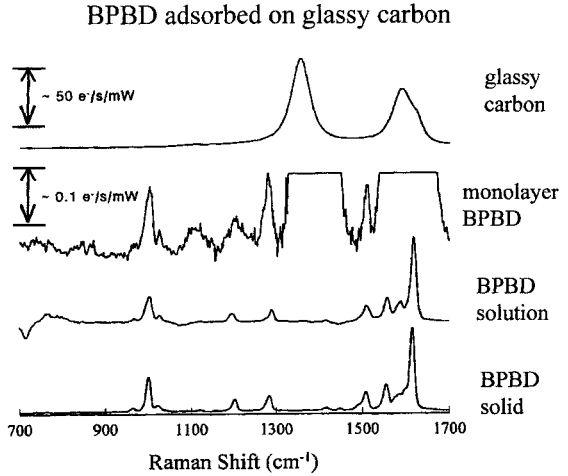

Figure 13.10. Spectra similar to those of Figure 13.9, except for the laser dye BPBD adsorbed on glassy carbon. BPBD has a cross section about 13 times that of benzene. The large bands in the monolayer spectrum are partly due to incomplete subtraction of the glassy carbon spectrum. (Adapted from References 10 and 11 with permission.)

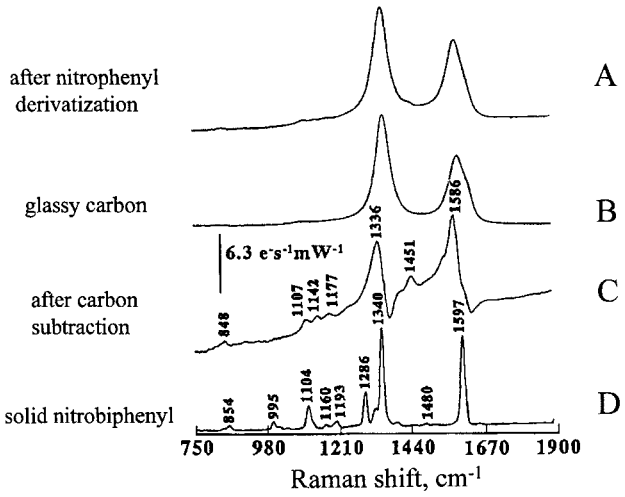

Figure 13.11. Raman spectra of glassy carbon (B) before and (A) after covalent modification with a monolayer of nitrophenyl groups. Subtraction of carbon spectrum reveals small nitrophenyl bands (spectra C). Nitrophenyl is a model compound for nitrophenyl bonded to sp^2 carbon. (Adapted from Reference 26 with permission.)

are preresonant at 514.5 nm and have cross sections in solution that are 65 and 13 times that of benzene. Nitrophenyl (Fig. 13.11) is analogous to chemisorbed nitrobenzene, although the bonding differs from that on nickel (12). Nitrobenzene has a cross section about four times that of benzene, so spectrum 13.11 represents a case with weak or negligible enhancement. Table 13.3 lists several surface species that have been observed without field enhancement, along with a comparison of solution and surface cross sections where available. For nonresonant adsorbates, the observed surface cross section was higher than that in solution, while a resonant surface scatterer (β-carotene) exhibited decreased cross section (10,11). These cross-section changes are consistent with the conclusion that the adsorption interaction can lead to changes in cross section due to changes in the electronic structure of the adsorbate. As noted earlier, *chemical enhancement* can be explained as a shift of the molecule's optical properties that promote resonance enhancement.

From the perspective of chemical analysis, the ability to observe spectra from surface monolayers without requiring field enhancement demonstrates the high sensitivity of modern Raman instrumentation. In addition, it indicates that multilayer films such as polymer coatings, lubricants, or metal oxides are readily observable on a variety of substrates, provided the multilayer is reasonably transparent. However, the sensitivity constraints in the absence of field enhancement are generally severe when dealing with monolayers,

Table 13.3. Examples of Surface Monolayers Observed without Field Enhancement

Adsorbate/surface	β_{rel}[a]	LOD, Monolayers	β_s^b/β_{sol}	Reference
	Resonance Enhanced			
Magnesium phthalocyanine/Au	$\sim 10^4$			17
Cobalt phthalocyanine/graphite	10^4	<0.1		18
β-Carotene, 1522	4×10^5	<0.1	0.12	11
Rhodamine 6G (1184 cm^{-1})/GC	>1000	0.003		11
Dinitrophenylhydrazine (1140 cm^{-1}/GC	>1000	~0.01		25
Bis-methyl styryl benzene (1178 cm^{-1})/GC	66	0.02	3.6	11
	Unenhanced			
Nitrobenzene/Ni	~4			12
BPBD[c](1000 cm^{-1})/GC	13	0.11	3.2	11
Anthraquinone disulfonate (1179 cm^{-1})/GC	4.5		~4	10
Nitrophenyl (1107 cm^{-1})/GC		0.1		26
Nitroazobenzene/GC	19 (solution) 1600(chemisorbed)		84	27
Phenyl (1184 cm^{-1})/GC	1.0			28
Pyridine (1008 cm^{-1})/Ag	0.5		15–65	20

[a]Cross section relative to neat benzene, 992 cm^{-1}.
[b]Ratio of observed surface cross section to that observed in solution.
[c]BPBD = 2-(4-biphenyl)-5-(4-tert-butylphenyl)1,3,4oxadiazol.

and Raman may be applicable only to special analytical applications at the monolayer level. Much greater interest in surface Raman for chemical analysis results from the combination of chemical enhancement with electromagnetic field enhancement. The additional factor of up to 10^5 from field enhancement is the subject of the next section.

13.5. ELECTROMAGNETIC FIELD ENHANCEMENT

Surface-enhanced Raman scattering was first observed by Fleischmann, et al. (3) for pyridine adsorbed on a silver surface that had been roughened by repeated electrochemical oxidation and reduction in chloride solution. The

strong scattering was initially attributed to a high microscopic surface area produced by repeated cycling between AgCl and Ag metal and the known ability of pyridine to adsorb on silver through the nitrogen atom. Jeanmaire and Van Duyne later established that the signal was much too strong to be attributed solely to surface area, and a new enhancement phenomenon was proposed (4,5). The unexplained enhancement was too large to attribute to the chemical enhancement discussed in Section 13.4, although the distinction between chemical and field enhancement came much later (1,2).

13.5.1. Field Enhancement Characteristics

A great deal of research by many investigators led to the formulation of a theory of electromagnetic field (EM) enhancement, which occurs when small metal particles are illuminated by light of suitable wavelength. The following characteristics are a distillation of approximately 15 years of research into the origin of enhanced Raman results of EM field enhancement that are relevant to analytical applications.

1. Field enhancement is strongest on metals with high reflectivity at the laser and Raman-shifted wavelengths, particulary Ag, Au, and Cu.
2. Field enhancement can increase scattering intensity by a factor of $\sim 10^5$ or more, in addition to any chemical enhancement.
3. The molecule of interest need not be in direct contact with the surface to exhibit enhanced scattering. Field enhancement is longer range than chemical enhancement, extending several tens of nanometers away from the metal surface.
4. Field enhancement magnitude depends on the optical properties of the metal and their variation with wavelength. For example, Ag surfaces exhibit strong field enhancement with midvisible lasers (514.5 nm, 532 nm), while Au and Cu show field enhancement in the red (>600 nm).
5. Field enhancement depends strongly on the presence of small metal particles or at least regions with high curvature of the metal surface. Enhancement magnitude is significant when the particles are much smaller than the laser wavelength, in the region of several hundred angstroms. The optimum particle size depends on the metal and laser wavelength, as well as particle shape (see below).
6. The shape of metal particles affects field enhancement magnitude in a manner that depends on both the identity of the metal and the wavelengths of both the laser and the Raman-shifted light. For example, spherical and elliptical particles have different radii of curvature for

the same average diameter, and curvature affects field enhancement. A micrograph of a silver electrode surface roughened by electrochemical oxidation and reduction is shown in Figure 13.12B. Microscopy of such surfaces reveals a range of particle sizes and shapes that produce a range of field enhancements. The observed enhancement is a weighted average of the enhancements from each particle size and shape, combined with any chemical enhancement.

Figure 13.13 shows normal and SERS spectra of a monolayer of pyridine on roughened silver demonstrating the large magnitude of surface enhancement. The predicted peak intensity of the 1008 cm^{-1} band in the absence of enhancement is about 0.1 e^{-} sec^{-1}, and the observed intensity is about 4×10^4, indicating a total enhancement of a factor of 4×10^5 (5). The peak frequencies are shifted slightly due to the interaction of pyridine with the surface. The SERS spectrum has different selection rules and polarization behavior compared to the solution, since the pyridine–Ag complex has different orientation and electronic structure. In addition, the relative intensities vary with applied potential, as discussed in Section 13.4. The main enhancement results from field enhancement caused by perturbation of the incident electric field by the metal surface. Significant progress has been made to explain the origin of the characteristics of field enhancement using electromagnetic theory.

13.5.2. Field Enhancement Theory

A detailed theoretical treatment based on both electrostatic and electrodynamic effects of an optical electric field on a metal particle is beyond the scope of this chapter, but such approaches have been discussed extensively (1,5–7). Several of the main theoretical points are of value to analytical applications and will be summarized here.

Consider Figure 13.14, which depicts the electric field of the incident light interacting with a spherical particle of diameter a and molecule positioned at a distance r from the particle center. If the wavelength is much larger than the particle (e.g., $\lambda > 10a$), the incident field will polarize electrons to one side of the particle, and this polarization will track the incident field. Provided the metal has high conductivity at the optical frequency, its electrons will oscillate along with the field, to create a *dipolar surface plasmon* (DSP). This localized electron polarization in the particle produces a local electric field that is synchronized with the optical field, but may be much larger. The enhanced field depends on the optical conductivity of the metal (which depends on wavelength) and the size and shape of the particle. In particular, the DSP field is maximized when

$$\epsilon_i(\lambda_L) = -2\epsilon_0(\lambda_L) \tag{13.5}$$

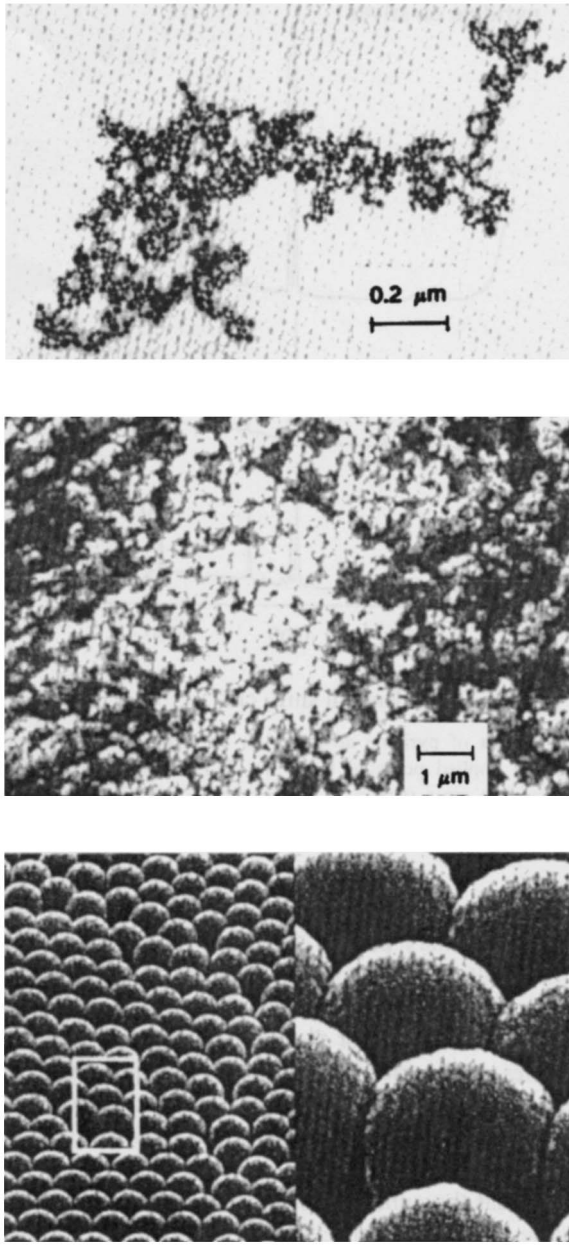

Figure 13.12. Micrographs of (A) gold colloids and (B) electrochemically roughened silver and (C) silver-coated polystyrene spheres. White box is expanded in right half of micrograph C. Diameter of spheres range from 38 to 482 nm (37). (Adapted from Reference 2 with permission.)

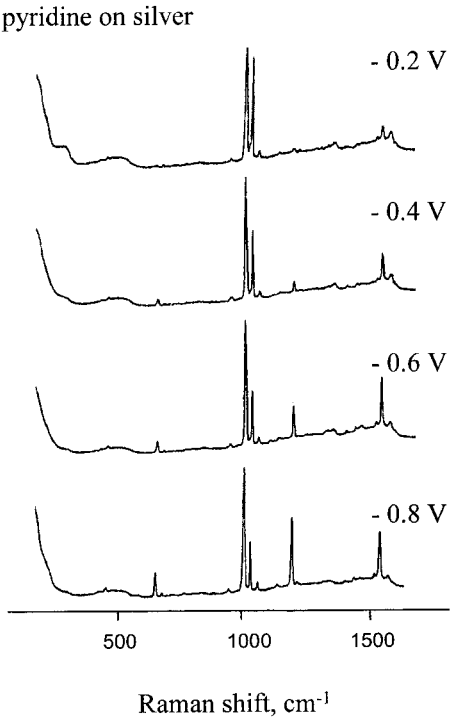

Figure 13.13. SERS spectra of pyridine adsorbed on an electrochemically roughened silver surface as a function of applied potential (volts vs. SCE). Spectra are $>10^5$ more intense than expected from pyridine cross section in the gas phase. (Adapted from Reference 5 with permission, including reversal of x axis.)

where $\epsilon_i(\lambda_L)$ is the imaginary part of the metal dielectric constant and ϵ_0 is the real part of the dielectric constant of the surrounding medium (1). Since ϵ_i depends on both the identity of the metal and the laser wavelength, the condition of Eq. (13.5) accounts for the dependence of field enhancement on the optical properties of the metal. For a silver sphere in water, the DSP is maximized for $\lambda = 382$ nm, while for gold, it is maximized at ~550 nm. In practice, particle shape effects shift the maximum field enhancement to longer wavelengths (6), as discussed later.

We noted above that the enhanced electric field resulting from the DSP is not restricted to the immediate particle surface but should extend away from the particle. For the case of field enhancement at a spherical particle, theory predicts that the field enhancement should track $(a/r)^3$. Figure 13.15 shows the predicted field enhancement relative to the surface ($r = a$) for various

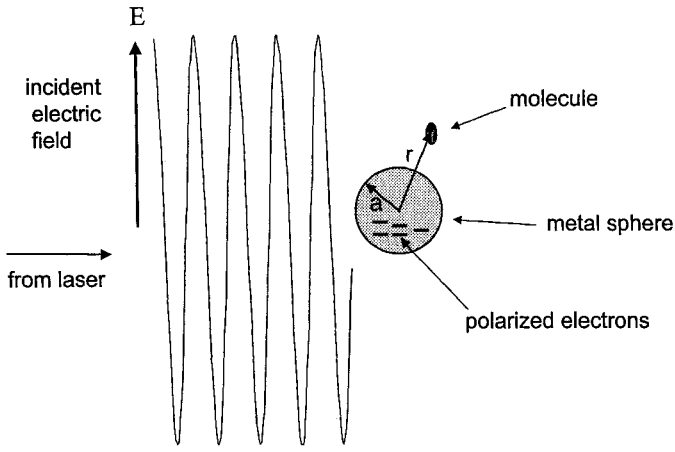

Figure 13.14. Schematic of laser light incident on a metal particle whose diameter is much smaller than the laser wavelength. Electrons are polarized by the incident field and oscillate at the laser frequency: a is the particle diameter, and r is the distance of the molecule from the particle center.

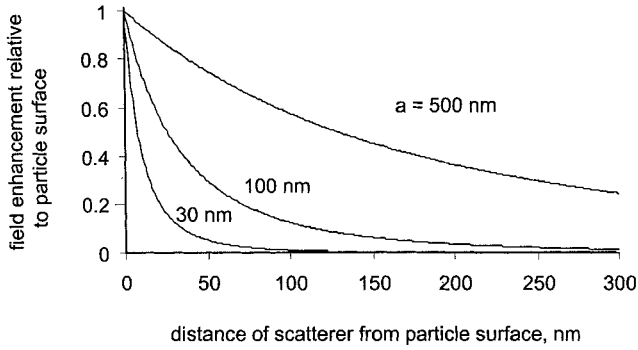

Figure 13.15. Dependence of EM field enhancement on distance form the particle surface for spherical particles of three different radii. The enhancement is normalized to that at the particle surface, which itself depends on particle radius. Based on $(a/r)^3$ dependence (1).

diameters of spherical particles. Note that enhancement can extend several tens of nanometers away from the surface, a fact exploited in certain analytical applications described in Section 13.6. Recall that the field enhancement depends strongly on particle size, so the enhancements for different particle sizes in Figure 13.15 cannot be compared directly. In addition, the distance

dependence varies with particle shape and the identity of the metal. The extension of field enhancement away from the particle surface has been verified experimentally, but the theory has not been tested quantitatively (29).

In addition to the surface plasmon resonance, other phenomena contribute to the field enhancement. The oscillating dipole of the molecular vibration induces an image field in the metal, sometimes called the antenna effect (1). These effects have also been treated theoretically, leading to a combined theory that predicts overall field enhancement. Detailed discussions of these considerations have been presented and should be consulted by the interested reader (6,7).

As noted above several times, the field enhancement depends on particle shape, as well as size, metal, and wavelength. A roughened metal surface such as that shown schematically in Figure 13.12 consists of spheres, ellipsoids, and irregular particles of a range of sizes. For most real surfaces beyond the idealized case of a sphere, the theory must be extended to other shapes. The effects on field enhancement are significant, since particle shape (particularly the degree of curvature) has major effects on both the plasma resonance and the antenna effect. Zeman and Schatz considered elliptical particles of various metals and predicted the field enhancement as a function of wavelength (6). The ellipsoid eccentricity was described by the ratio of the semimajor axis (b) to the semiminor axis (a), shown in Figure 13.14B. Values of b/a from 1:1 to 5:1 were considered, as were values of b from 10 to 1000 nm. The treatment presented by Zeman and Schatz represents a comprehensive prediction of field enhancement magnitude for spherical and elliptical particles of 10 metals of various sizes and illuminated with wavelengths from the ultraviolet (UV) to the near-infrared (NIR). A few of their results are presented here to illustrate some useful predictions.

Figure 13.16 shows the predicted electric field enhancement (R) for silver particles of various sizes and b/a ratios. The observed signal enhancement equals $R(\nu_0)R(\nu_0 - \nu_j)$, determined from the R values at the laser and Raman-shifted frequencies. Notice that the maximum enhancement is larger and occurs at longer wavelengths for more elliptical particles. Note that a 30 nm radius spherical particle of silver yields maximum enhancement at about 370 nm (circular points shown on Fig. 13.16). For a 3:1 ellipsoid, the maximum enhancement is about 5 times that of the sphere and occurs for a 70 × 210 nm ellipsoid and a wavelength of about 480 nm. These effects are presented in different form in Figure 13.17, which shows the electric field $[R(\nu_0)]$ and signal enhancement $[R(\nu_0)R(\nu_0 - \nu_j)]$ vs. wavelength for $b = 60$ nm and $\Delta\bar{\nu} = 1500\ \text{cm}^{-1}$. As before, greater ellipticity yields larger enhancement at longer wavelengths. For the common case of 514.5 nm (2.4 eV) light on silver, signal enhancement is in the region of 10,000 to 30,000, for $b = 60$ nm, depending on ellipticity.

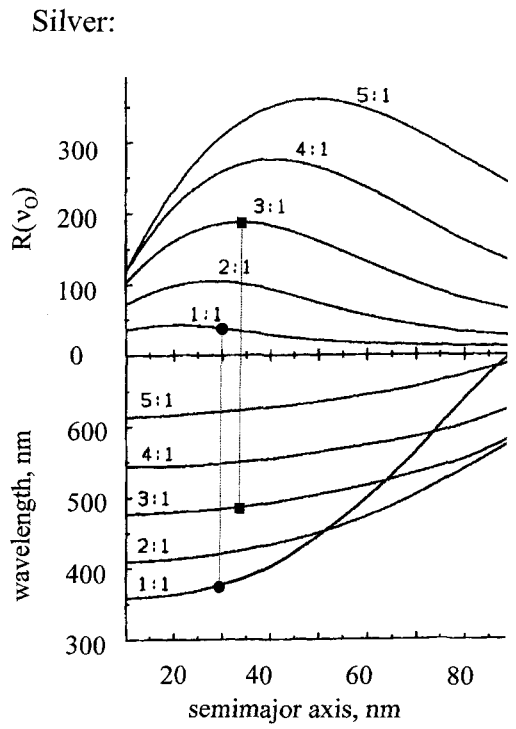

Figure 13.16. Optimum field enhancement $R(\nu_0)$ for silver (optimized with respect to wavelength), and the optimum wavelength for various ellipticities and particle sizes. Labels (e.g., 3:1) indicate the ratio of the semimajor to the semiminor axis, b/a. The large dots indicate the enhancement and optimum wavelength for a 30 nm-diameter sphere, while the squares indicate those for a 3:1 ellipsoid with a 35 nm semimajor axis. (Adapted from Reference 6 with permission.)

A similar plot for gold is shown in Figure 13.18. The enhancement is more strongly dependent on ellipticity and occurs at longer wavelength. For example, the 3:1 ellipsoid has maximum enhancement at about 600 nm (2.1 eV) for $b = 60$ nm. These effects are even more pronounced for copper, shown in Figure 13.19. Enhancements for 10 metals are shown in Figure 13.20 as functions of wavelength. The size and shape of the particle has been optimized for each metal. At least at present, monodisperse collections of metal particles of most of the metals in Figure 13.20 have not been prepared, so the theory is not completely tested (see also page 404). However, it successfully predicts field enhancement magnitude for several combinations of metal and particle shape and provides useful guidance when considering new SERS substrates.

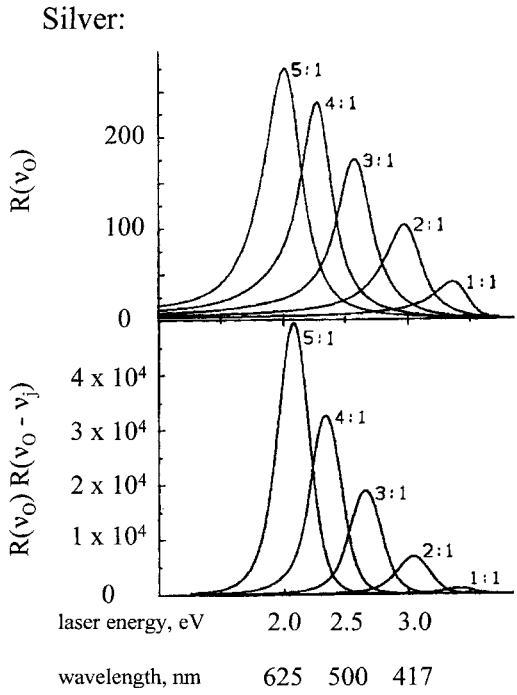

Figure 13.17. Field enhancement $R(\nu_0)$ and signal enhancement, $R(\nu_0)R(\nu_0 - \nu_j)$ for silver as a function of laser energy and wavelength. Signal enhancement is plotted for $\nu_j = 1500$ cm^{-1}. (Adapted from Reference 6 with permission.)

13.5.3. SERS Materials for Analytical Applications

The observation and understanding of SERS are clearly very important developments in the study of surface chemistry and surface physics. The combination of molecular information and extraordinary sensitivity provides a valuable probe of surface structure and behavior. Out of the broad study of SERS by both chemists and physicists have emerged several approaches to using SERS for chemical analysis. A common analytical situation involves preparation of a SERS active substrate by one of several methods, then exposure of the substrate to a liquid or gaseous sample. Subsequent Raman spectroscopy of the adsorbed layer provides the analytical signal, enhanced by whatever chemical or field enhancement is provided by the adsorbate–substrate interaction. The current and next section are not intended to address SERS substrates comprehensively, but several of analytical interest are described.

When considering substrates for analytical applications of SERS, several properties are important (30). First, the magnitude of the enhancement and any

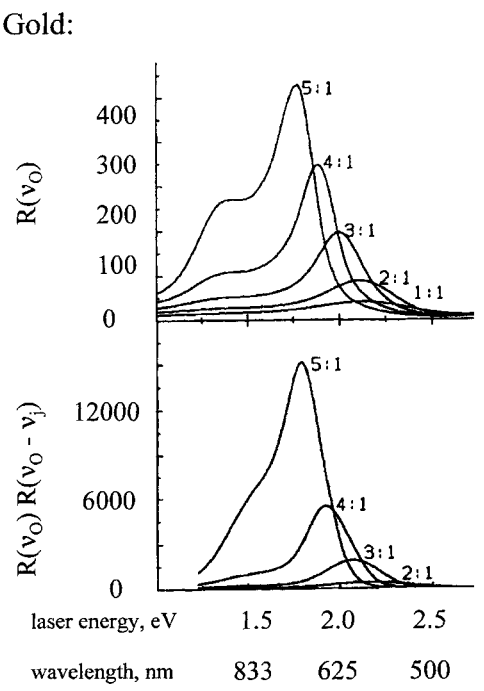

Figure 13.18. Same as Figure 13.17 but for gold particles. (Adapted from Reference 6 with permission.)

associated background determine the limit of detection for a given analyte. Second, various substrates differ significantly in their ease of preparation, and some are more amenable to large-volume commercial production. Third, the enhancement should be reproducible to whatever level is required by a given application. Fourth, substrates vary in their stability after preparation, and an ideal substrate has an indefinite "shelf-life," with no loss of enhancement with storage time. Fifth, substrates may be modified to provide selectivity, by which certain analytes exhibit much larger enhancement than others. Sixth, substrates are usually optimized for particular laser wavelengths, so the choice of substrate may depend on the available Raman instrumentation.

Since chemical and field enhancement are sensitive to a number of variables, including substrate material, particle size and shape, laser wavelength, and the nature of the adsorbate–substrate interaction (including those requiring active adsorption sites), there is wide latitude in how a given substrate may be designed and optimized. Conversely, the observed enhancement can vary by orders of magnitude if the important substrate variables are not adequately controlled. Examples of SERS substrates that have been proposed for chemical analysis

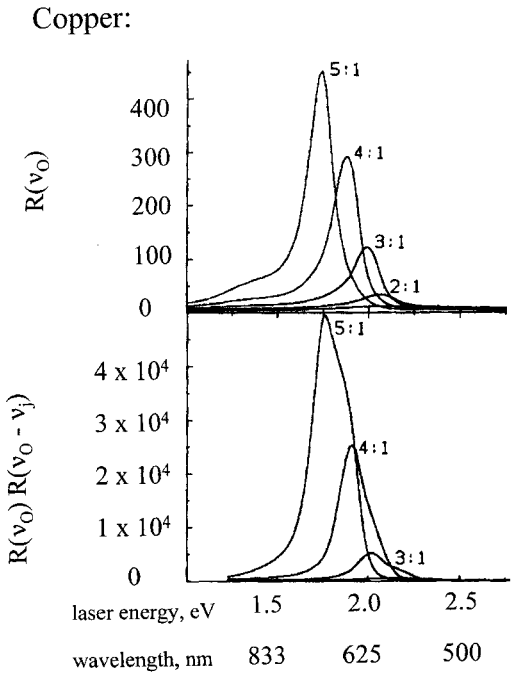

Figure 13.19. Same as Figure 13.17 but for copper particles. (Adapted from Reference 6 with permission.)

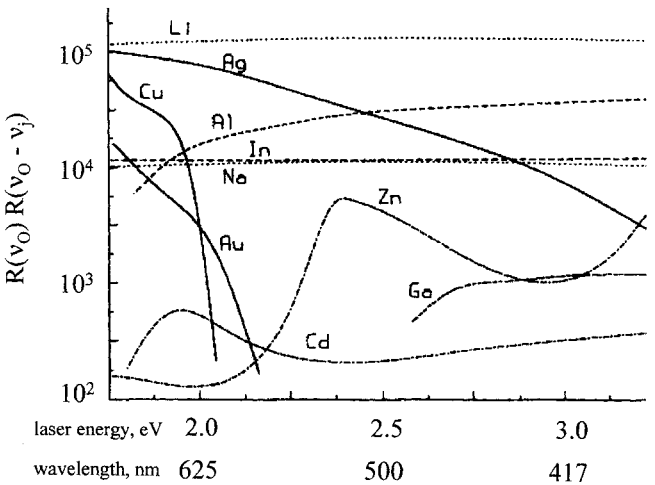

Figure 13.20. Magnitude of signal enhancement from EM field effects for 10 metals as a function of laser wavelength, with $\Delta\nu_j = 1500\ \text{cm}^{-1}$. For each metal, the particle size and shape were optimized for maximum enhancement. (Adapted from Reference 6 with permission.)

are presented below, with attention to preparation, enhancement magnitude, reproducibility, and stability. To date, nearly all analytical SERS materials are made from silver or gold, with the great majority derived from silver.

13.5.3.1 Electrochemically Roughened Silver

As the first, but not the simplest, procedure for fabricating an active SERS substrate, electrochemical roughening is probably the most studied. A polished silver electrode is placed in a cell similar to that shown in Figure 13.4A, containing a chloride solution such as 1 M KCl. Application of a potential of +0.2 V (typically) vs. a saturated calomel electrode (SCE) causes oxidation of Ag to AgCl, which forms a film on the Ag surface. After a certain time or oxidation charge has passed, the potential is switched to about −0.3 V vs. SCE, where the AgCl is reduced back to Ag metal. This process yields a collection of silver particles such as that shown in Figure 13.12B, with a range of particle diameters of approximately 10 to 100 nm (2,6,30). A wide variety of oxidation and reduction procedures has been presented, which come under the general name *oxidation–reduction cycle* or ORC. The results of one such procedure are shown in Figure 13.21 in which the Raman intensity for adsorbed *trans*-1,2-bis(4-pyridyl)ethene (BPE) is plotted as a function of the oxidation charge of the ORC. The maximum signal occurred after about 100 mC/cm^2 of oxidation charge was passed, preceding reduction back to Ag metal. This charge corresponds to the oxidation and reduction of approximately 1000 layers of silver atoms.

The analyte of interest may be present in the ORC solution itself, or the roughened electrode may be removed from the ORC solution and rinsed. The analyte solution is generally applied to the surface and dried, or the Raman spectrum is obtained from the roughened electrode in an analyte solution. A calibration curve of SERS intensity vs. BPE amount is shown in Figure 13.22 for an electrochemically roughened Ag electrode. The BPE was applied to the surface as a dilute solution in a 3 μl drop, then allowed to dry before acquiring a Raman spectrum. The amount of BPE required for a useful signal was impressively low, corresponding to a limit of detection (LOD) of 1×10^{-6} M BPE in 3 μl of solution applied to the SERS substrate. In terms of the amount of BPE actually in the laser spot, this corresponds to 25 fmol (25×10^{-15} mol). However, the reproducibility was poor, with a standard deviation across eight different electrodes of 40 per cent (30). The magnitude of the enhancement decreased rapidly (~5 min) after roughening but exhibited some enhancement for at least 3 days. An advantage of the electrochemical process is relatively easy renewability, as the ORC may be repeated many times between samples.

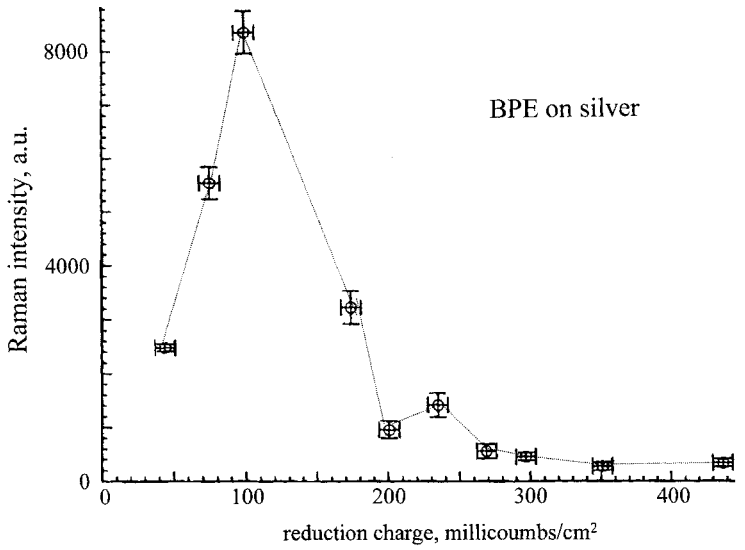

Figure 13.21. Strength of SERS signal from 1,2-bis(4-pyridyl)ethene (BPE) adsorbed on electrochemical roughened silver as a function of the charge required for reduction of AgCl to Ag. (Adapted from Reference 30 with permission.)

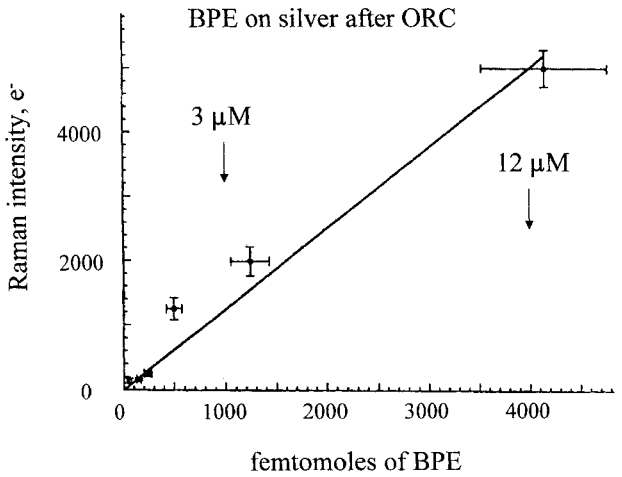

Figure 13.22. Calibration curve for BPE on electrochemically roughened silver. The x axis is the femtomoles of BPE contained within the area illuminated by the laser. Arrows indicate concentrations of BPE solutions applied to the roughened silver. (Adapted from Reference 30 with permission.)

As noted earlier, a wide variety of electrochemical roughening procedures have been devised. Some examples of analytical interest include an electrochemical preparation of roughened silver for Fourier transform (FT)–Raman at 1064 nm (31) and electrochemical etching of silver microelectrodes with 1- to 2 μm tip diameters (32). Fractal characterization of electrochemically roughened silver revealed that SERS activity begins increasing when the fractal dimension of the surface morphology exceeds about 1.7 (33). A quantitative comparison of electrochemical roughening to other fabrication techniques (1) concluded that electrochemical roughening showed poor reproducibility and stability but moderate sensitivity and LOD, at least for the quantitative analysis of BPE. Table 13.4 summarizes some of the results of this comparison.

Although less common than silver, electrochemically roughened gold is also useful as a SERS active surface. In some cases, the gold may be coated with a thin layer of a transition metal, often by electrochemical deposition (34,35,36). Since field enhancement can extend well beyond a thin layer of a few nanometer thickness, the roughened gold substrate enhanced the Raman scattering from adsorbates on the transition-metal film. The result was enhanced spectra of adsorbates on metals used widely in heterogeneous catalysis (e.g., Pt, Rh), without a requirement for significant field enhancement by the transition metal itself (36).

13.5.3.2 Metal Vapor Deposition

Vapor deposition of an SERS active metal onto various substrates is more versatile than electrochemical roughening and sometimes permits control over

Table 13.4. SERS Results for *trans*-1,2bis(4-pyridyl)ethene (BPE) on Various Substrates[a]

	Sensitivity[b] (counts/fmol)[c]	Lowest Detected Amount[d] (fmol)[c]
Annealed Ag islands	152	0.6
Unannealed Ag islands	150	1.3
Electrochemically roughened Ag	1.25	23
HNO_3 etched Ag foil	0.485	170
Tollens reagent	0.38	480
Photoreduction of $AgNO_3$ on TiO_2	—[e]	50

[a]From Reference 30.
[b]Slope of plot of intensity vs. BPE amount.
[c]Femtomoles present on surface, within the 1 μm-diameter laser beam; 100 fmol corresponds to deposition of 3 μl of a 5×10^{-6} M solution of BPE.
[d]SNR >3.
[e]Nonlinear calibration curve.

particle size and morphology. When a very thin (~50 nm) film is vapor deposited on glass, the Ag segregates into particles, usually referred to as *islands*. These islands have a range of sizes and shapes, but many fall into the size range required for field enhancement. Figure 13.23 shows a spectrum of 6 fmol of BPE (within the laser spot) on a vapor-deposited Ag film with an average silver thickness of ~50 nm. The material onto which the metal is deposited is certainly not limited to flat glass, and many other materials have been explored, including frosted glass (30), polystyrene spheres (37), fumed silica (38), alumina (39), transition metals (39), and the ends of fiber optics (40). Figure 13.12C shows the example of silver-coated polystyrene microspheres.

A sophisticated enhancement of metal vapor deposition involves silver deposition over an ordered array of polystyrene spheres with submicron diameters (41–43). The Ag atoms deposit both on the spheres and on the flat substrate below the spheres. After deposition, the spheres may be removed to leave an ordered array of microscopic Ag pyramids with regular size and shape. The pyramids have dimensions of a few hundred nanometers, in the range required for EM field enhancement. These arrays of Ag microparticles have provided a direct test of EM field enhancement theory (44), and have been modified with platinum and organic thin films (45).

After vapor deposition and cooling in a vacuum chamber, the SERS substrate is usually removed, exposed to the sample solution or gas, and then the Raman spectrum is acquired. Exposure to air and/or water vapor

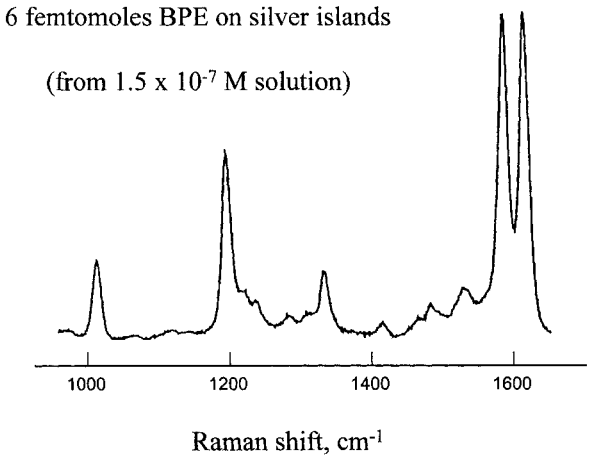

Figure 13.23. SERS spectrum of BPE on vapor-deposited silver islands, from 6 fmol of BPE contained within the laser spot; 514.5 nm, 43 mW on a 1 μm spot, 5 sec integration on a dispersive/CCD spectrometer. (Adapted from Reference 30 with permission.)

may change the metal surface, either by surface rearrangement, oxidation, or contamination. For the BPE example listed in Table 13.4, high sensitivity and low detection limits were achieved for Ag island films. Reproducibility of the Raman signal following exposure of Ag island films to 1.2×10^{-6} M BPE was 14 per cent for annealed films and 27 per cent for unannealed films (30). The stability of the films depended on storage conditions, with good stability over extended periods when stored in a vacuum. Exposure to air or water decreased SERS intensity and increased the background from contamination.

A promising modification of the silver island approach involves protection of the island film with a very thin layer of silica (46). The silica layer is thin enough so that molecules on its surface are still subject to field enhancement, although the chemical enhancement between silver and adsorbate is lost. The silver islands are protected from adsorption of atmospheric impurities and the field enhancement is quite stable with time. Silica-protected Ag island films do not exhibit the large enhancements encountered with bare Ag islands or electrochemical roughening, but the decreased enhancement may be more than compensated by improved reproducibility for many analytical applications.

In order to enhance or modify the chemical selectivity of an SERS substrate, it is possible to chemically derivatize the metal surface. For example, covalent bonding of a hydrocarbon to a silver island film should selectively adsorb nonpolar analytes from an aqueous solution. The general approach is shown schematically in Figure 13.24 for the case of metal ions detected by a surface-bound complexing agent (47). Field enhancement is provided by the substrate, while adsorption selectivity results from the chemistry of the derivatized

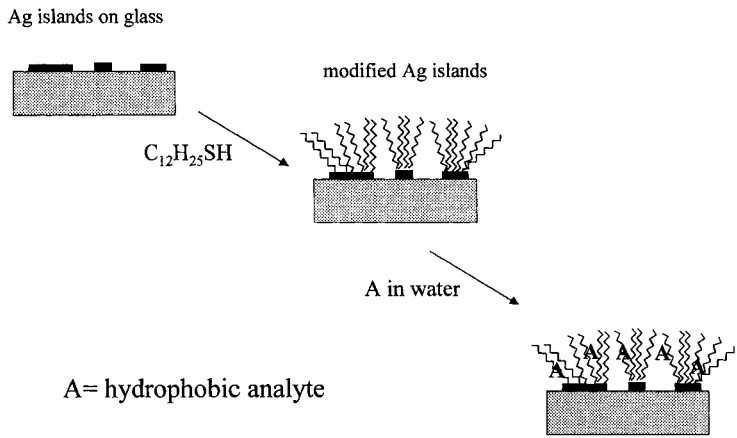

Figure 13.24. Procedure for forming a self-assembled monolayer on a silver island film, followed by adsorption of a hydrophobic analyte (A) preceding SERS analysis. See References 53, 57 and 58.

surface. Many procedures similar to that depicted in Figure 13.24 are based on *self-assembled monolayers* (SAMs) made when thiols adsorb irreversibly to gold, silver, or copper. Quite sophisticated SERS methods exploiting both field enhancement and chemical selectivity have been devised using SAMs on vapor-deposited silver islands (47–49), electrochemically roughened metals (50,51), and silver roughened with nitric acid (52,53). A further extension of SERS to silica surfaces involved alkylsilane layers bonded to mechanically roughened silver, as a model for a chromatographic stationary phase (54).

13.5.3.3 Metal Colloids

Colloidal suspensions of metal particles may be formed in aqueous solution by chemical reduction of metal salts (30,55,56). The distribution of particle diameter depends on conditions but may be controlled to a range suitable for EM field enhancement. An example of an aggregate of colloidal silver is shown in Figure 13.12A. Colloidal suspensions of silver and gold are available commercially but most commonly are prepared shortly before use. A common diagnostic of colloidal properties is a UV–Vis absorption spectrum, which depends on the particle size and density. Visible light absorption by small metal particles results from interactions of the optical electric field with particles having diameters smaller than the wavelength and is related to the same phenomena that underlie EM field enhancement. When used for chemical analysis, the metal colloid may be added to an analyte solution or immobilized before exposure to the analyte. Metal colloids have been studied extensively with visible (2,57,58) and NIR excitation (59,60).

Depending on conditions, many procedures for preparing colloids lead to particles that are too small to exhibit large field enhancement, so an aggregating agent is sometimes added to produce structures similar to that shown in Figure 13.12A. Much of the variability in Raman intensities observed with colloids is due to variations in the agglomeration time and procedure. Jones and co-workers compared several agglomeration procedures to determine the reproducibility of the SERS enhancement of resonant Raman dyes based on azobenzotriazole (61). The agglomerating agent was either added to the colloid–dye solution or the colloid was preagglomerated before adding the dye. The Raman intensities were monitored as a function of agglomeration time, and the standard deviation was determined for repeated spectra and colloid preparations. Typical spectra are shown in Figure 13.25 for three concentrations of an azo dye adsorbed on an agglomerated silver colloid. The combination of surface and resonance enhancement yields high SNR spectra in the concentration range of 10^{-4} to 10^{-9} M. A calibration curve of intensity vs. dye concentration was linear (Fig. 13.26) over about 3 orders of magnitude but leveled off sharply when the dye formed a monolayer on the colloid

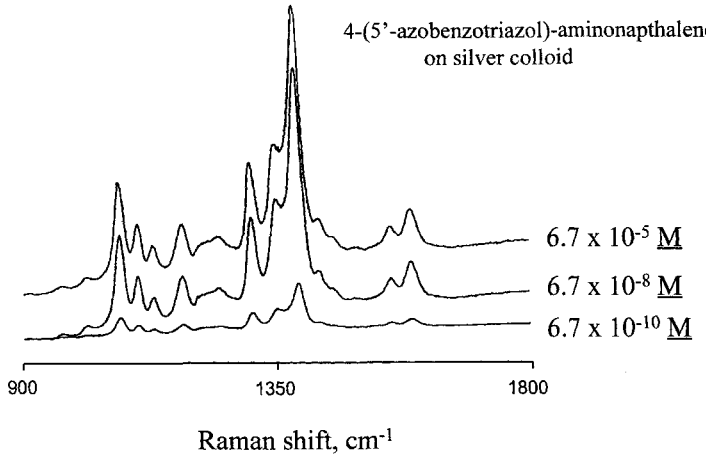

Figure 13.25. Surface-enhanced resonance Raman spectra (SERS) of an azo dye adsorbed on silver colloids from solutions of the indicated concentrations; 514.5 nm, 25 mW, 10 sec integrations on CCD/dispersive Raman microscope (Renishaw). (Adapted from Reference 61.)

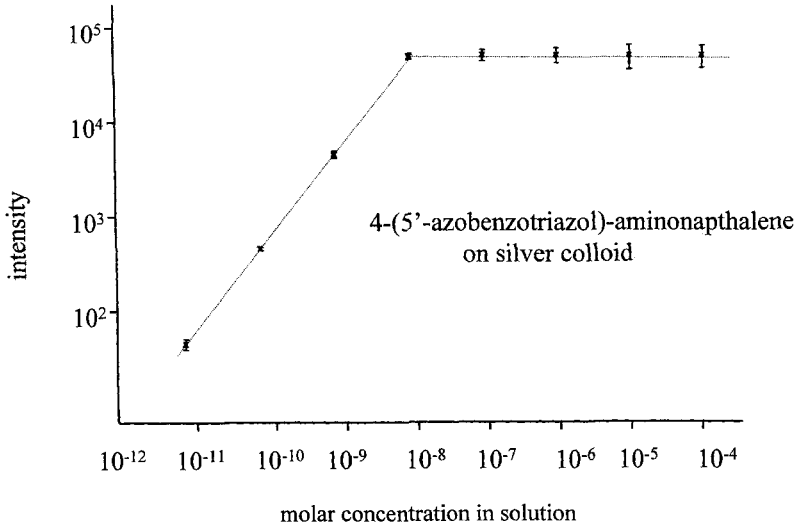

Figure 13.26. Calibration curve based on spectra similar to those in Figure 13.25. (Adapted from Reference 61 with permission.)

surface. The most sensitive Raman spectroscopy ever reported uses SERS on silver colloids to detect single molecules of adsorbed dyes (60,62,63).

Reproducibility of the Raman intensity for the 1424 cm^{-1} band of a particular dye at 10^{-8} M is summarized in Table 13.5. Relative standard deviations of five spectra of a given colloid solution as well as the relative standard deviation (rsd) for five different colloid solutions are listed. Significantly higher (rsd) was observed for different colloid solutions, implying that the particle agglomeration and analyte adsorption are quite sensitive to uncontrolled changes in conditions. The authors (61) concluded that preaggregation with poly-(L-lysine) yields quite reproducible intensities (rsd <5 per cent).

13.5.3.4 Etched Metal Surfaces

Mechanical polishing (50,51) and etching in nitric acid (30,47,48,52,53) have been used to prepare roughened surfaces that exhibit EM field enhancement. The enhancement factors are significantly smaller than those observed for electrochemical roughening, but nitric acid etching is simple and reproducible. A quantitative comparison of etching of silver with other methods is shown in Table 13.4. The sensitivity and limit of detection were about a factor of 100 worse than the best silver island films, but the reproducibility was better. Eight silver foil samples etched with nitric acid showed a relative standard deviation of 17 per cent for a given sample concentration. Etched foils were stable for a few days but showed slow degradation over longer periods due to surface contamination (30). Etched silver modified with self-assembled monolayers exhibited the chemical selectivity noted in Section 13.5.3.3 (53,54). The modification layer appears to protect the active surface and extend the shelf life.

Table 13.5. Relative Standard Deviation (rsd) of the 1424 cm^{-1} Band of 10^{-8} M 4-(5′azobenzotriazol)aminonapthalene on Silver Colloid[a]

Aggregation Agent	rsd, 5 Spectra of one Colloid Solution (%)	rsd, 5 Spectra each of 5 Solutions (%)
None	1–4	7–8
HNO_3	12–25	31–41
NaCl	14–18	28–35
Poly(L-lysine)	1–4	17–18
Preaggregation with poly(L-lysine)	1–3	3–5

[a]From Reference 61.

13.5.3.5 Photoreduced Metal Particles

Since photoreduction of silver salts to metallic silver is the basis of most photographic emulsions, the phenomenon has been studied extensively. Several preparations of SERS substrates have been developed, based on photoreduction of $AgNO_3$ under various conditions. In some cases, a $AgNO_3$ solution was photoreduced prior to exposure to the analyte (64) or in the presence of analyte (65). In the latter case, the "photocolloid" was found to produce about 4 times the Raman scattering intensity as a colloid produced by chemical reduction. Silver particles may also be produced by photoreduction on TiO_2 with UV light in the presence of sodium formate. A quantitative study of silver on TiO_2 (30,66) showed a nonlinear response to BPE concentration, with a detection limit of about 2 μM in 3 μL of solution (Table 13.4). Photoproduced films were quite reproducible (rsd ~8 per cent), despite the nonlinear response, which was attributed to analyte adsorption by TiO_2.

13.6. EXAMPLES OF ANALYTICAL APPLICATIONS

The large signal enhancements often encountered with SERS have stimulated many investigations of analytical applications, examples of which are listed in Table 13.6. Many of these involve biological or environmental analysis, where low concentrations of analytes preclude the use of unenhanced or even resonance-enhanced Raman spectroscopy witout the added benefit of surface enhancement. Despite the great promise of a technique that increases Raman intensity by 10^6 or more, SERS has not yet resulted in widely used or routine analysis of real samples. SERS has been a very important and valuable probe of surface structure and has stimulated new discoveries about the behavior of metal–gas and metal–liquid interfaces, but its incursion into practical chemical analysis has been limited. It is worth considering why SERS has encountered formidable barriers to widespread analytical utility (2).

First, there are many variables that determine SERS enhancement, not all of which are controlled. Even if particle size and shape can be reproduced, surface chemistry is difficult to control and is generally unstable. Chance exposure to contaminants or reconstruction of the metal surface can significantly vary the observed enhancement over time. Second, chemical enhancement depends on the adsorbate–surface interaction and varies both with surface chemistry and with adsorbate structure. Analytes differ greatly in the strength of this interaction, and surface contamination can prevent it altogether. SERS is not a general phenomenon as far as the wide range of species encountered in chemical analysis. Third, relative intensities and even peak frequencies can be quite different for an adsorbed molecule compared to the spectrum observed in bulk.

Table 13.6. Examples of Analytical Applications of SERS

Analyte	SERS Substrate	Reference
Peptides	Silver colloid	2
p-Nitrobenzoic acid	Silver islands	29
Co phthalocyanine	Silver islands	29
Bis (4-pyridyl)ethene	Various	30
Adenine	ORC[a]	31
Nicotonic acid	ORC	31
Glycine	ORC	31
Anthracene	ORC	31
Pyridine	Ag microelectrode	32
Glycine	ORC, microelectrode	33
Benzoic acid	Ag on fumed silica	38
Phthalic acid	Ag on fumed silica	38
Anthracene	Ag on fumed silica	38
pH (with indicator)	Ag on fiber optic	40
Cyanine dye	Ag colloid	59
Adenine	Colloidal Ag and Au	61
Azobenzotriazole	Colloidal Ag	62
Pyrene, and related compounds	Colloidal Ag	67
Organophosphorous toxins	Colloidal Ag	68
Chlorinated hydrocarbons	ORC	69
SCN^-	Sputtered Ag	39
Cu^{2+}, Pb^{2+}, Ca^{2+}	Modified Ag islands	47
Alkali metal ions	Modified Ag islands	49
Chlorinated ethylenes	Nitric acid etched Ag	52
Benzoic acid	Fumed silica	70
p-Nitrophenol, pyrene	Chemically reduced Ag	71
Benzoic acid	Ag coated Al_2O_3	72
Terephthalic acid	Ag coated Al_2O_3	72
Viologens	ORC	73
DNA sequences	Ag coated Al_2O_3	74
Isophthalic acid	Ag on TiO_2	75
Osmium complexes	ORC	76
Ruthenium complexes	ORC	76

[a]ORC = oxidation reduction cycle.

So spectrum interpretation or library searching may be frustrated unless SERS reference spectra are available. Fourth, a practical substrate for routine analysis should be available commercially and have a long shelf life. At this writing, all SERS substrates are prepared by individual labs, usually immediately before use. The world needs a stable, reproducible, and probably disposable SERS substrate in commercial quantities, but so far none of the various substrates

have reached this goal. At the time of this writing, SERS remains a spectacular phenomenon with limited applications in routine chemical analysis.

REFERENCES

1. R. L. Birke and J. R. Lombardi, in R. J. Gale, ed., *Spectroelectrochemistry Theory and Practice*, Plenum, New York, 1988, pp. 263–328.
2. R. L. Garrell, *Anal. Chem.*, **61**, 401A (1989).
3. M. Fleischmann, P. J. Hendra, and A. J. McQuillan, *Chem. Phys. Lett.*, **26**, 163 (1974).
4. D. L. Jeanmaire and R. P. Van Duyne, *J. Electroanal. Chem.*, **84**, 1 (1977).
5. R. P. Van Duyne, in L. B. Moore, ed., *Chemical and Biochemical Applications of Lasers*, Vol. IV, Academic Press, New York, 1979, Chapter 4.
6. E. J. Zeman and G. C. Schatz, *J. Phys. Chem.*, **91**, 634 (1987).
7. M. Moscovitz, *Rev. Mod. Phys.*, **57**, 784 (1985).
8. M. Fryling, C. J. Frank, and R. L. McCreery, *Appl. Spectrosc.*, **47**, 1965 (1993).
9. R. L. McCreery, in J. J. Laserna, ed., *Instrumentation for Dispersive Raman Spectroscopy*, Wiley, New York, 1996, pp. 41–72.
10. M. R. Kagan, Ph.D. Dissertation, The Ohio State University, 1996.
11. M. R. Kagan and R. L. McCreery, *Langmuir*, **11**, 4041 (1995).
12. A. Campion, J. K. Brown, and V. M. Grizzle, *Surf Sci. Lett.*, **115**, L153 (1982).
13. D. R. Mullins and A. Campion, *J. Phys. Chem.*, **88**, 8 (1984).
14. S. D. Schwab, R. L. McCreery, and F. T. Gamble, *Anal. Chem.*, **58**, 2486 (1986).
15. A. Campion, J. E. Ivanecky III, C. M. Child, and M. Foster, *J. Am. Chem. Soc.*, **117**, 11807 (1995).
16. J. C. Ingram and J. E. Pemberton, *Langmuir*, **8**, 2034 (1992).
17. J. L. Kahl, L. R. Faulkner, K. Dwarakanath, and H. Tachikawa, *J. Am. Chem. Soc.*, **108**, 5434 (1986).
18. J. Zhao and R. L. McCreery, *Langmuir*, **11**, 4036 (1995).
19. D. Melamed, B. Darlington, D. J. R. Brook, H.-L. Pan, A. Campion, and M. A. Fox, *J. Phys. Chem.*, **98**, 8971 (1994).
20. X. Jiang and A. Campion, *Chem. Phys. Lett.*, **140**, 95 (1987).
21. V. M. Hallmark and A. Campion, *J. Chem. Phys.*, **84**, 2933 (1986).
22. W. B. Cai, B. Ren, X. Q. Li, C. X. She, F. M. Liu, and X. W. Cai, *Surf. Sci.*, **406**, 9 (1998).
23. Z. Q. Tian, B. Ren, and B. W. Mac, *J. Phys. Chem. B*, **101**, 1338 (1997).
24. M. R. Kagan and R. L. McCreery, *Anal. Chem.*, **66**, 4159 (1994).
25. M. A. Fryling, J. Zhao, and R. L. McCreery, *Anal. Chem.*, **67**, 967 (1995).
26. Y.-C. Liu and R. L. McCreery, *J. Am. Chem. Soc.*, **117**, 11254 (1995).
27. Y.-C. Liu and R. L. McCreery, *Anal. Chem.*, **69**, 2091 (1997).

28. T.-C. Kuo, Ph.D. Dissertation, The Ohio State University, 1999.
29. H. Bercegol and F. J. Boerio, *Langmuir*, **10**, 3684 (1994).
30. K. L. Norrod, L. M. Sudnik, D. Rousell, and K. L. Rowlen, *Appl. Spectrosc.*, **51**, 994 (1997).
31. E. Roth, G. A. Hope, D. P. Schweinsberg, W. Kiefer, and P. M. Fredericks, *Appl. Spectrosc.*, **47**, 1797 (1993).
32. E. A. Todd and M. D. Morris, *App. Spect.*, **47**, 855 (1993).
33. Y. Yamaguchi, M. K. Weldon, and M. D. Morris, *Appl. Spectrosc.*, **53**, 127 (1999).
34. S. Zou, C. T. Williams, E. K.-Y. Chen, and M. J. Weaver, *J. Am. Chem. Soc.*, **120**, 3811 (1998).
35. S. Zou and M. J. Weaver, *Anal. Chem.*, **70**, 2387 (1998).
36. M. Weaver, S. Zou, and H. Chan, *Analytical Chem.*, **72**, 39 (2000)
37. R. L. Moody, T. Vo-Dinh, and W. H. Fletcher, *Appl. Spectrosc.*, **41**, 966 (1987).
38. A. M. Alak and T. Vo-Dinh, *Anal. Chem.*, **61**, 656 (1989).
39. J. P. Davies, S. J. Pachuta, R. G. Cooks, and M. J. Weaver, *Anal. Chem.*, **58**, 1290 (1986).
40. K. I. Mullen, D. Wang, L. G. Crane, and K. T. Carron, *Anal. Chem.*, **64**, 930 (1992).
41. T. Jensen, G. Schatz, and R. Van Duyne, *J. Phys. Chem.*, **103**, 2394 (1999).
42. J. Hulteen, D. Treichel, M. Smith, M. Duval, T. Jensen, R. Van Duyne, *J. Phys. Chem. B*, 3854 (1999).
43. J. Hulteen, R. Van Duyne, *J. Vac. Sci. Technol A.*, **13**, 1553 (1995).
44. T. Jensen, M. Duval, K. Lance Kelly, A. Lazarides, G. Schatz, R. Van Duyne, *J. Phys. Chem. B*, **103**, 9846 (1999).
45. P. Freunscht, R. Van Duyne, S. Schneider, *Chem. Physics Letters*, **281**, 372 (1997).
46. W. B. Lacy, J. M. Williams, L. A. Wenzler, T. P. Beebe, Jr., and J. M. Harris, *Anal. Chem.*, **68**, 1003 (1996).
47. L. G. Crane, D.-X. Wang, L. M. Sears, B. Heyns, and K. Carron, *Anal. Chem.*, **34**, 360 (1995).
48. T. T. Ehlre, N. Malmburg, K. Carron, B. P. Sullivan, and L. J. Noe, *J. Phys. Chem. B.*, **101**, 3174 (1997).
49. J. B. Heyns, L. M. Sears, R. C. Corcoran, and K. T. Carron, *Anal. Chem.*, **66**, 1572 (1994).
50. M. A. Bryant and J. E. Pemberton, *J. Am. Chem. Soc.*, **113**, 3629 (1991).
51. M. A. Bryant and J. E. Pemberton, *J. Am. Chem. Soc.*, **113**, 8284 (1991).
52. K. Mullen and K. Carron, *Anal. Chem.*, **66**, 478 (1994).
53. K. T. Carron and B. J. Kennedy, *Anal. Chem.*, **67**, 3353 (1995).
54. W. R. Thompson and J. E. Pemberton, *Anal. Chem.*, **66**, 3362 (1994).
55. M. J. Angebranndt and J. D. Winefordner, *Talanta*, **39**, 569 (1992).
56. W. S. Sutherland, J. J. Laserna, M. J. Angebranndt, and J. D. Winefordner, *Anal. Chem.*, **62**, 689 (1990).

57. R. G. Freeman, K. C. Grabar, A. P. Guthrie, K. J. Allison, R. M. Bright, J. A. Davis, M. B. Hommer, M. A. Jackson, P. C. Smith, D. Walter, and M. J. Natan, *Science*, 267, 1629 (1995).
58. L. A. Lyon, M. D. Musick, and M. J. Natan, *Anal. Chem.*, **70**, 5177 (1998).
59. K. Kneipp, H. Kneipp, G. Deinum, I. Itzkan, R. R. Dasari, and M. S. Feld, *Appl. Spectrosc.*, **52**, 175 (1998).
60. K. Kneipp, R. R. Dasari, and Y. Wang, *Appl. Spectrosc.*, **48**, 951 (1994).
61. J. C. Jones, C. McLaughlin, D. Littlejohn, D. A. Sandler, D. Graham, and W. Ewen Smith, *Anal. Chem.*, **71**, 596 (1999).
62. S. Nie and S. R. Emory, *Science*, **275**, 1102 (1997).
63. S. R. Emory, W. E. Maskins, and S. M. Nie, *J. Am. Chem. Soc.*, **120**, 8009 (1998).
64. X. Gao, C. Wan, T. He, J. Li, H. Xin, and F. Liu, *Chem. Phys. Lett.*, **112**, 465 (1996).
65. A. M. Ahern and R. G. Garrell, *Anal. Chem.*, **59**, 2816 (1987).
66. L. M. Sudnik, K. L. Noirod, and K. L. Rowlen, *Appl. Spectrosc.*, **50**, 422 (1996).
67. T. Vo-Dinh, A. Alek, and R. L. Moody, *Spectrochim. Acta B*, **43B**, 966 (1988).
68. A. M. Alak and T. Vo-Dinh, *Anal. Chem.*, **59**, 2149 (1987).
69. M. M. Carraba, R. B. Edmonds, and R. D. Rauh, *Anal. Chem.*, **59**, 2559 (1987).
70. A. M. Alak and T. Vo-Dinh, *Anal. Chem*, **61**, 656 (1989).
71. Y.-S. Li and Y. Wang, *Appl. Spectrosc.*, **46**, 142 (1992).
72. J. M. Bello, D. L. Stokes, and T. Vo-Dinh, *Appl. Spectrosc.*, **43**, 1325 (1989).
73. X. Tang, T. Schneider, and D. A. Buttry, *Langmuir*, **10**, 2235 (1994).
74. T. Vo-Dinh, K. Houck, and D. L. Stokes, *Anal. Chem.*, **66**, 3379 (1994).
75. J. M. Bello, D. L. Stokes, and T. Vo-Dinh, *Anal. Chem.*, **61**, 1779 (1989).
76. S. Farquharson, K. L. Guyer, P. A. Lay, R. H. Magnuson, and M. J. Weaver, *J. Am. Chem. Soc.*, **106**, 5123 (1984).

Raman Spectroscopy for Chemical Analysis. Richard L. McCreery

ISBN: 0-471-25287-5

INDEX